

UNCLASSIFIED

AD NUMBER
AD904747
NEW LIMITATION CHANGE
TO Approved for public release, distribution unlimited
FROM Distribution authorized to U.S. Gov't. agencies only; Test and Evaluation; OCT 1972. Other requests shall be referred to Air Force Flight Dynamics Lab., Wright-Patterson AFB, OH 45433.
AUTHORITY
AFWAL ltr 7 Mar 1976

THIS PAGE IS UNCLASSIFIED

THIS REPORT HAS BEEN DELIMITED
AND CLEARED FOR PUBLIC RELEASE
UNDER DOD DIRECTIVE 5200.20 AND
NO RESTRICTIONS ARE IMPOSED UPON
ITS USE AND DISCLOSURE.

DISTRIBUTION STATEMENT A

APPROVED FOR PUBLIC RELEASE;
DISTRIBUTION UNLIMITED,

AD904747

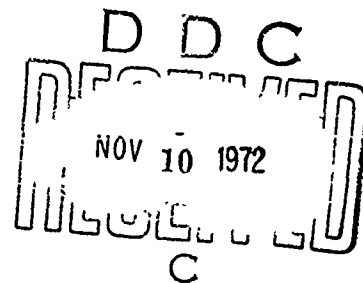
AFFDL-TR-72-101 - Vol I

EXPERIMENTAL AND ANALYTICAL DETERMINATION OF INTEGRATED AIRFRAME NOZZLE PERFORMANCE

E. R. GLASGOW, D. M. SANTMAN, AND L. D. MILLER, et al.
LOCKHEED-CALIFORNIA COMPANY

TECHNICAL REPORT AFFDL-TR-72-101 - VOL I

OCTOBER 1972



Distribution limited to U. S. Government agencies only; test and evaluation;
statement applied (October 1972). Other requests for this document must
be referred to AF Flight Dynamics Laboratory, (FXM), Wright-Patterson AFB,
Ohio 45433

AIR FORCE FLIGHT DYNAMICS LABORATORY
AIR FORCE SYSTEMS COMMAND
WRIGHT-PATTERSON AIR FORCE BASE, OHIO

NOTICE

When Government drawings, specifications, or other data are used for any purpose other than in connection with a definitely related Government procurement operation, the United States Government thereby incurs no responsibility nor any obligation whatsoever; and the fact that the Government may have formulated, furnished, or in any way supplied the said drawings, specification, or other data, is not to be regarded by implication or otherwise as in any manner licensing the holder or any other person or corporation, or conveying any rights or permission to manufacture, use, or sell any patented invention that may in any way be related thereto.

Copies of this report should not be returned unless return is required by security considerations, contractual obligation, or notice on a specific document.

EXPERIMENTAL AND ANALYTICAL DETERMINATION OF INTEGRATED AIRFRAME NOZZLE PERFORMANCE

E. R. GLASGOW, D. M. SANTMAN, AND L. D. MILLER, et al.
LOCKHEED-CALIFORNIA COMPANY

Distribution limited to U. S. Government agencies only; test and evaluation;
statement applied (October 1972). Other requests for this document must
be referred to AF Flight Dynamics Laboratory, (FXM), Wright-Patterson AFB.
Ohio 45433

FOREWORD

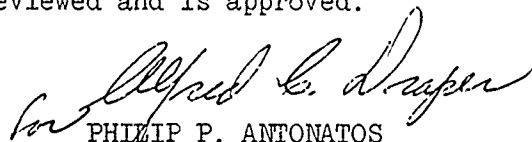
The experimental and analytical effort reported herein was performed by the Lockheed-California Company (Calac), Burbank, California, under Contract No. F33657-70-C-0511 of Project No. 668A. The contract was administered by the Air Force Flight Dynamics Laboratory (AFFDL), Wright-Patterson Air Force Base, Ohio, with P. C. Everling (FXM) and J. A. Laughrey (FXM) as Project Engineers. Subcontract support was provided by Pratt and Whitney Aircraft (P&WA), East Hartford, Connecticut; and all testing was conducted in the 16-foot Propulsion Wind Tunnels (PWT) at the Arnold Engineering Development Center (AEDC), Arnold Station, Tennessee. The project engineers for the various contributing organizations were E. R. Glasgow of Calac; W. M. Presz, Jr., of P&WA; and L. L. Galigher of the Arnold Research Organization, Inc. (ARO), which is the organization contracted to operate the AEDC tunnel.

This is the final report to be submitted under the contract. The report documents the results obtained during each phase of the three-phase program, which was conducted during the period from 1 November 1969 to 31 July 1972. In addition to the three principal authors, the following Calac personnel made significant contributions toward preparation of the report manuscript: R. A. Fox, R. D. Grennan, D. K. Hill, R. F. Smith, and S. J. Smyth.

The authors are indebted to the following Calac personnel for their assistance during the study: E. L. Bragdon, A. L. Busby, and M. H. Scott, Jr. of Propulsion; G. L. Dougherty of Aerodynamics; V. E. Arnold, L. H. Brown, Jr., T. W. Jensen, and B. H. Robinson of the Fluid Dynamics Laboratory; O. B. Cox and J. R. Gorman of Model Fabrication; G. Heathcock, L. H. Michel, D. Tappeiner, and M. L. White of Computer Services; L. L. Rogge and L. E. Campbell of Engineering Administration; and A. W. Campbell of Government Contracts. Special acknowledgements are due to T. P. Higgins, Jr., J. E. May, and T. A. Sedgwick who, in their supervisory positions, have made significant contributions to the program.

This report was submitted by the authors for AFFDL approval on 31 July 1972. A Calac report number, LR 25370, has been assigned to identify the report prior to approval.

This technical report has been reviewed and is approved.



PHILIP P. ANTONATOS
Chief, Flight Mechanics Division
Air Force Flight Dynamics Laboratory

ABSTRACT

An experimental and analytical investigation of the installed thrust and drag of various isolated nozzle and twin-nozzle/aftbody configurations indicated that empirical correlations provide the best means of predicting aft-end performance, especially for the early stages of the aircraft design. Although theoretical methods were evaluated which adequately predicted external pressure distribution trends, the MOC (method of characteristics) was the only method which provided reasonably good drag estimates. Time dependent methods combined with the MOC accurately predicted the nozzle internal pressure distributions, thrust, and discharge coefficients; however, similar results were more rapidly computed using empirically corrected one-dimensional methods which also accounted for the effects of flow separation.

Both subsonic and transonic isolated nozzle drag data were correlated using IMS (integral mean slope) as the geometric parameter. A correlation of twin-nozzle/aftbody drag data at subsonic and transonic speeds was developed by combining Spreiter's transonic similarity parameters with the IMS of the equivalent body of revolution. A correlation of inviscid MOC pressure drag, achieved through use of IMS combined with similarity parameters obtained from linearized supersonic flow theory, provided an accurate and rapid means of estimating drag for arbitrary axisymmetric boattail contours at supersonic speeds. Twin-nozzle/aftbody drag data at supersonic speeds was correlated with the equivalent body drag obtained from the axisymmetric MOC correlation.

Improved thrust and drag performance was obtained by modifying the aft-end design of five selected aircraft configurations. The rationale for these modifications was derived from design guidelines and criteria developed during the program. Improvements in mission radius for a fixed takeoff gross weight aircraft were obtained, in general, by utilizing convergent-divergent nozzles, a horizontal wedge interfairing with the trailing edge terminating at the exit plane of the nozzles, a single vertical stabilizer, and a narrow lateral nozzle spacing.

VOLUME I
TABLE OF CONTENTS

<u>Section</u>	<u>Title</u>	<u>Page</u>
1	INTRODUCTION	1
	1.1 PROGRAM BACKGROUND AND OBJECTIVES	1
	1.2 PROGRAM PLAN AND SCHEDULE	2
	1.3 REPORT ORGANIZATION	4
2	ISOLATED NOZZLE INVESTIGATION	5
	2.1 APPARATUS AND PROCEDURE	5
	2.2 EXPERIMENTAL RESULTS AND DISCUSSION	35
	2.3 PERFORMANCE PREDICTION METHODS	55
3	TWIN-NOZZLE/AFTBODY INVESTIGATION	107
	3.1 APPARATUS AND PROCEDURE	109
	3.2 EXPERIMENTAL RESULTS AND DISCUSSION	150
	3.3 PERFORMANCE PREDICTION METHODS	207
4	TWIN-NOZZLE/AFTBODY DESIGN TECHNIQUES	239
	4.1 DEVELOPMENT OF DESIGN TECHNIQUES	239
	4.2 APPLICATION OF DESIGN TECHNIQUES	253
	4.3 EXPERIMENTAL PROGRAM FOR VERIFICATION OF DESIGN TECHNIQUES	308
5	CONCLUSIONS AND RECOMMENDATIONS	313
	5.1 TEST FACILITY AND APPARATUS	313
	5.2 EXPERIMENTAL RESULTS	314
	5.3 PERFORMANCE PREDICTION METHODS	316
	5.4 IMPROVED AIRCRAFT DESIGNS	317
	REFERENCE LIST	319

LIST OF ILLUSTRATIONS

<u>Figure</u>	<u>Title</u>	<u>Page</u>
1	Program Schedule	3
2	Photograph of Isolated Nozzle Test Rig and Nozzle Model Installed in AEDC 16T Propulsion Wind Tunnel	6
3	Isolated Nozzle Model and Support Strut	9
4	Model Reynolds Number Simulation	12
5	Phase II Airplane Model and Support Strut Tunnel Blockage	13
6	Axisymmetric Nozzle Design Identification	15
7	Basic Axisymmetric Nozzle Designs	18
8	Model Nozzle Designs	23
9	Total Drag Summary Chart - Mach 0.9	36
10	Total Drag Summary Chart - Mach 1.2	37
11	Total Drag Summary Chart - Mach 1.8	38
12	Total Drag Summary Chart - Mach 2.5	39
13	Effect of Nozzle Pressure Ratio On Nozzle Boattail Drag	40
14	Effect of Nozzle Pressure Ratio On Pod Aftbody Drag	41
15	Thrust Minus Total Nozzle Drag Summary Chart - Mach 0.9	42
16	Thrust Minus Total Nozzle Drag Summary Chart - Mach 1.2	43
17	Thrust Minus Total Nozzle Drag Summary Chart - Mach 1.8	44
18	Thrust Minus Total Nozzle Drag Summary Chart - Mach 2.5	45
19	Effect of Nozzle Pressure Ratio on Thrust	46
20	Effect of Angle of Attack on Aftbody/Nozzle Drag for Nozzles at Normal Power - Mach 0.8	48
21	Effect of Angle of Attack on Aftbody/Nozzle Drag for Nozzles at Maximum A/B - Mach 0.6	49
22	Effect of Boundary-Layer Trip on Pod Aftbody Drag	51
23	Effect of Boundary-Layer Trip on Total Pressure Profiles - Mach 0.9	52
24	Effect of Boundary-Layer Trip on Total Pressure Profiles - Mach 1.6	53

LIST OF ILLUSTRATIONS (Continued)

<u>Figure</u>	<u>Title</u>	<u>Page</u>
25	Comparison of Potential Flow - Gothert and Crown Mesh Method Predicted Boattail Pressures with Test Data	58
26	CD_1 Aftbody/Boattail Predicted and Experimental Pressure Profiles - Mach 0.8 - Nozzle Pressure Ratio 4.0	59
27	Comparison of P&WA Spreiter-Alksne and Measured Pressure Distributions at Mach 1.0	62
28	Comparison of Flow Computation Methods - 6% Circular Arc Airfoil	64
29	Comparison of Crown Mesh Method and P&WA Spreiter-Alksne Predicted Boattail Pressures with Test Data	65
30	UP_{A3} Aftbody/Boattail Predicted and Experimental Transonic Pressure Distributions - Mach 0.9 - Nozzle Pressure Ratio 5.0	67
31	CI_1 Aftbody/Boattail Predicted and Experimental Transonic Pressure Distributions - Mach 0.9 - Nozzle Pressure Ratio 5.0	68
32	CI_1 and CI_3 Aftbody/Boattail Analytical and Experimental Transonic Total Drag - Mach 0.9	69
33	CD_3 Aftbody/Boattail Predicted and Experimental Pressure Profile - Mach 1.8	70
34	IMS/Supersonic Similarity Correlation of Conical Boattail MOC Pressure Drag	72
35	Correlation of Circular Arc and Conical Boattail MOC Pressure Drag - Axisymmetric Boattails - Mach 1.2	73
36	Correlation of Circular Arc and Conical Boattail MOC Pressure Drag - Axisymmetric Boattail - Mach 2.0	74
37	IMS/Transonic Similarity Correlation of Circular Arc Boattail Scaled MOC Pressure Drag - Axisymmetric Boattails	76
38	Ponner-Karger Separation Correlation	79
39	CD_3 Nozzle Predicted and Experimental Internal Pressure Profiles	81
40	Comparison of Predicted and Measured Nozzle Thrust Coefficients	83
41	Convergent-Divergent Ejector Nozzle Shroud Designs	84
42	Comparison of Ejector Nozzle Pumping Characteristics Prediction Methods	86

LIST OF ILLUSTRATIONS (Continued)

<u>Figure</u>	<u>Title</u>	<u>Page</u>
43	CDE ₁ Ejector Nozzle Predicted and Experimental Internal Pressure Distributions	87
44	Comparison of Plume Shape Prediction Methods for Supersonic External Flow	90
45	Comparison of Isentropic Shock MOC and Shock-Expansion-ID Plume Shapes for Still Air	93
46	Annular Base Correlation for Cylindrical and 3-Degree Conical Aftbodies	95
47	Annular Base Pressure Correction for Noncylindrical Afterbodies	96
48	Comparison of Subsonic Base Pressure Prediction Methods with CF ₁ Test Data	98
49	Comparison of Base Pressure Prediction Methods	101
50	Isolated Plug Nozzle Base Pressure Correlations	103
51	Plug Nozzle Locked-in Base Pressures	104
52	Photograph of Phase II Aircraft Model Installed in AEDC 16T Propulsion Wind Tunnel	108
53	Diagram of Phase II Aircraft Model External Components	110
54	Diagram of Phase II Aircraft Model Internal Arrangement	112
55	High Horizontal Wedge Interfairing	124
56	Center Horizontal Wedge Interfairing	125
57	Modified High Horizontal Wedge Interfairing with Trailing Edge Along Nozzle Radial Lines	126
58	Vertical Wedge Interfairing	127
59	Schematic of Phase II Model and Support Strut	131
60	Model Cross-Sectional Area Distribution - Effect of Nozzle Spacing and Support Strut	132
61	Model Cross-Sectional Area Distribution - Effect of Wing, Empennage, and Nozzle Power Setting Position	133
62	Pressure Tap and Rake Locations	137
63	Effect of Nozzle Type on Total Drag - Normal Power Nozzles - Mach 0.9	151
64	Effect of Nozzle Type on Total Drag - Maximum A/B Nozzles - Mach 0.9	152

LIST OF ILLUSTRATIONS (Continued)

<u>Figure</u>	<u>Title</u>	<u>Page</u>
65	Effect of Nozzle Type on Total Drag - Maximum A/B Nozzles - Mach 1.2	153
66	Effect of Nozzle Type on Total Drag - Maximum A/B Nozzles - Mach 1.6	154
67	Total Drag - Typical Mission Applications - Normal Power Nozzles	156
68	Total Drag - Typical Mission Applications - Normal Power and Maximum A/B Nozzles	157
69	Nozzle Pressure Ratio Schedule for Typical Mission Applications	158
70	Effect of Nozzle Type on Thrust - Normal Power Nozzles - Mach 0.9	159
71	Effect of Nozzle Type on Discharge Coefficients - Normal Power Nozzles - Mach 0.9	160
72	Effect of Nozzle Type on Thrust - Maximum A/B Nozzles - Mach 0.9, 1.2, and 2.0	162
73	Effect of Nozzle Type on Discharge Coefficients - Maximum A/B Nozzles - Mach 0.9, 1.2, and 2.0	163
74	Effect of Nozzle Type on Thrust - CD and UP Nozzles - Mach 0.9, 1.2, 2.0, and 2.5	164
75	Effect of Nozzle Type on Discharge Coefficient - CD and UP Nozzles - Mach 0.9, 1.2, 2.0, and 2.5	165
76	Effect of Nozzle Type on Thrust-Minus-Total-Drag - Normal Power Nozzles - Mach 0.9	167
77	Effect of Nozzle Lateral Spacing on Thrust-Minus-Total-Drag - Maximum A/B Nozzles - Mach 0.9, 1.2, and 1.6	168
78	Effect of Nozzle Lateral Spacing on Total Drag - Normal Power Nozzles - Mach 0.9	170
79	Effect of Nozzle Lateral Spacing on Total Drag - Maximum A/B Nozzles - Mach 0.9	171
80	Illustrative Area and Pressure Distributions for Phase II Aftbody and Nozzle	172
81	Effect of Nozzle Lateral Spacing on Total Drag - Maximum A/B Nozzles - Mach 1.2	174
82	Effect of Nozzle Lateral Spacing on Total Drag - Maximum A/B Nozzles - Mach 1.6	175
83	Effect of Nozzle Lateral Spacing on Thrust - Normal Power Nozzles - Mach 0.9	177

LIST OF ILLUSTRATIONS (Continued)

<u>Figure</u>	<u>Title</u>	<u>Page</u>
84	Effect of Interfairing Type on Total Drag - Normal Power Nozzles - Mach 0.9	179
85	Effect of Interfairing Type on Total Drag - Maximum A/B Nozzles - Mach 0.9	180
86	Effect of Interfairing Type on Total Drag - Maximum A/B Nozzles - Mach 1.2	181
87	Effect of Interfairing Length on Total Drag - Normal Power Nozzles - Mach 0.9	183
88	Effect of Interfairing Length on Total Drag - Maximum A/B Nozzles - Mach 0.9	184
89	Effect of Interfairing Length on Total Drag - Maximum A/B Nozzles - Mach 1.2	185
90	Effect of Vertical Stabilizer Type and Position on Total Drag	187
91	Effect of Empennage Span Reduction on Total Drag - Normal Power Nozzles	188
92	Effect of Empennage Span Reduction on Total Drag - Maximum A/B Nozzles	189
93	Effect of Rudder Deflection on Total Drag	191
94	Effect of Horizontal Stabilizer Deflection on Total Drag	192
95	Effect of Angle of Attack on Total Drag - Normal Power Nozzles - Mach 0.6	193
96	Effect of Angle of Attack on Total Drag - Normal Power Nozzles - Mach 0.9	195
97	Effect of Angle of Attack on Total Drag - Maximum A/B Nozzles - Mach 1.2	196
98	Effect of Angle of Attack on Thrust-Minus-Total-Drag - Normal Power Nozzles - Mach 0.9	198
99	Effect of Angle of Attack on Thrust-Minus-Total-Drag - CD1 Nozzle - Mach 0.9	199
100	Effect of Reynolds Number on Total Drag - CD1 Nozzles - Mach 0.9	200
101	Effect of Reynolds Number on Total Drag - CI3 Nozzles - Mach 0.9	201
102	Effect of Reynolds Number on Total Drag - UPAC3 Nozzle - Mach 0.9	202

LIST OF ILLUSTRATIONS (Continued)

<u>Figure</u>	<u>Title</u>	<u>Page</u>
103	Effect of Reynolds Number on Integrated-Pressure Drags - CD ₃ Nozzle - Mach 2.0	203
104	Effect of Boundary Layer Trips on Total Drag - UPAC1 Nozzle - Mach 0.9	205
105	Effect of Boundary Layer Trips on Integrated Pressure Drags - CI3 Nozzle	206
106	Sectoring Technique	209
107	Comparison of Predicted and Measured Aft-End Drag - A-1 Twin-Jet Body - Subsonic External Flow	210
108	Comparison of Predicted and Measured Row 1 Pressure Distributions - A-1 Twin-Jet Body - Mach 0.8	212
109	Comparison of Predicted and Measured Row 2 Pressure Distributions - A-1 Twin-Jet Body - Mach 0.8	213
110	Comparison of Predicted and Measured Rows 4 and 5 Pressure Distributions - A-1 Twin-Jet Body - Mach 0.8	214
111	Comparison of Sector Analysis and Measured Row 1 Pressure Distributions - A-1 Twin-Jet Body - Mach 0.8	215
112	Transonic Similarity Correlation of Phase II Data - Subsonic Flow - Jet-Off	217
113	Correlation of Drag Increment From Jet-Off to Design Pressure Ratio Operation	219
114	Correlation of Drag Increment From Design to Operating Pressure Ratio	220
115	Correlation of Plug Thrust and Boattail Drag Increment - UPAC ₁ Nozzle	221
116	Equivalent Body Jet-On Drag Correlation of Phase II Data - Mach 1.6	224
117	Comparison of Predicted and Measured Aft-End Drag - A-1 Twin-Jet Body - Supersonic External Flow	225
118	Comparison of Predicted and Measured Total Boattail Drag - NLB/CD ₃ Configuration With Empennage	226
119	Comparison of Predicted and Measured Aft-End Drag - Configuration 1	228
120	Comparison of Sector Analysis and Measured Row 1 Pressure Distributions - A-1 Twin-Jet Body - Mach 1.3	229
121	Equivalent Body Drag Correlation of Phase II Data - Subsonic Flow - Jet-Off	231

LIST OF ILLUSTRATIONS (Continued)

<u>Figure</u>	<u>Title</u>	<u>Page</u>
122	Transonic Similarity Correlation of Phase II Data - Supersonic Flow - Jet-Off	232
123	Correlation of Jet-On Minus Jet-Off Drag Increment - Supersonic Flow	233
124	Comparison of Predicted and Measured Plug Surface Pressure Distributions - I2B/UP _A C ₃ Configuration - Mach 1.6	235
125	Twin Nozzle Base Pressure Correlation - UP _A C ₃ Nozzle	237
126	Chart for Estimating Twin-Jet Aft-End Drag - Narrow Spacing Ratio, Horizontal Interfairing, and Single Vertical Stabilizer	242
127	Chart for Estimating Twin-Jet Aft-End Drag - Narrow Spacing Ratio, Vertical Interfairing, and Single Vertical Stabilizer	243
128	Chart for Estimating Twin-Jet Aft-End Drag - Intermediate Spacing, Horizontal Interfairing, and Single Vertical Stabilizer	244
129	Chart for Estimating Twin-Jet Aft-End Drag - Wide Spacing Ratio, Horizontal Interfairing, and Single Vertical Stabilizer	245
130	Chart for Estimating Twin-Jet Aft-End Drag - Wide Spacing, Horizontal Interfairing, and Twin Vertical Stabilizers	246
131	Effect of Adjusted Nozzle Pressure Ratio on Total Boattail Pressure Drag	249
132	Comparison Between Predicted and Measured Twin-Jet Aft-End Drags - Narrow Spacing Ratio, Vertical Interfairing, and Single Vertical Stabilizer	251
133	Nozzle Thrust Coefficients - Jet Specific Heat Ratio 1.25	254
134	Nozzle Thrust Coefficients - Jet Specific Heat Ratio 1.30	255
135	Nozzle Thrust Coefficients - Jet Specific Heat Ratio 1.35	256
136	Nozzle Thrust Coefficients - Jet Specific Heat Ratio 1.40	257
137	Thrust Function	258
138	Procedure for Developing Improved Twin-Nozzle/Aftbody Installations	259
139	Calac CL-1250 Air Superiority Fighter	261
140	X-1 Baseline Turbofan Configuration	263
141	X-2 Baseline Turbofan Configuration	264
142	X-3 Baseline Turbofan Configuration	265
143	X-4 and X-5 Baseline Turbofan Configuration	266

LIST OF ILLUSTRATIONS (Continued)

<u>Figure</u>	<u>Title</u>	<u>Page</u>
144	Y-1 Candidate Turbofan Configuration	269
145	Y-2 Candidate Turbofan Configuration	271
146	Y-3 Candidate Turbofan Configuration	273
147	Z-1 Candidate Turbojet Configuration	275
148	Configuration X-1 Aero-Model Zero Lift Variation	279
149	Configuration X-2 Aero-Model Zero Lift Drag Variation	280
150	Configuration X-3 Aero-Model Zero Lift Drag Variation	281
151	Configuration X-4 Aero-Model Zero Lift Drag Variation	282
152	Configuration X-5 Aero-Model Zero Lift Drag Variation	283
153	Configuration Y-1 Aero-Model Zero Lift Drag Variation	284
154	Configuration Y-2 Aero-Model Zero Lift Drag Variation	285
155	Configuration Y-3 Aero-Model Zero Lift Drag Variation	286
156	Configuration Z-1 Aero-Model Zero Lift Drag Variation	287
157	Drag Due to Lift Factor	288
158	Increment External Stores Drag	288
159	Second Cone Angle and Throat to Capture Area Ratio Schedules	290
160	Inlet Local Mach Number	291
161	Inlet Total Pressure Recovery	292
162	Additive Drag Coefficient	294
163	Boattail and Base Pressure Drag - Baseline and Candidate Configurations	296
164	Drag Increment Between Propulsion and Aero Models - Baseline and Candidate Configurations	297
165	Nozzle Thrust Coefficients For Baseline and Candidate Configurations	299
166	Nozzle Discharge Coefficients For Baseline and Candidate Configurations	300
167	Breakdown of Basic Air Superiority Mission Profile	302
168	Breakdown of Tactical Air-to-Air Mission Profile	303
169	Breakdown of Supersonic Point Intercept Mission Profile	304

LIST OF TABLES

<u>Table</u>	<u>Title</u>	<u>Page</u>
1	NOZZLE DESIGN PARAMETERS	17
2	NUMBER AND LOCATION OF MODEL STATIC PRESSURE TUBES	27
3	NOZZLE CONFIGURATIONS TESTED - 16T	33
4.	NOZZLE CONFIGURATIONS TESTED - 16S	34
5	STRUT NON-UNIFORMITY DRAG INCREMENT SUMMARY	54
6	SUMMARY LIST OF PERFORMANCE PREDICTION METHODS	56
7	PHASE II MODEL CONFIGURATION SUMMARY	113
8	WING GEOMETRIC CHARACTERISTICS	115
9	HORIZONTAL STABILIZER GEOMETRIC CHARACTERISTICS	118
10	VERTICAL STABILIZER GEOMETRIC CHARACTERISTICS	120
11	INTERFAIRING CONFIGURATION IDENTIFICATION	123
12	OVERVIEW OF PHASE II CONFIGURATIONS TESTED	145
13	PHASE II CONFIGURATIONS TESTED	146
14	SUMMARY LIST OF ANALYTICAL METHODS INVESTIGATED	208
15	MOC/EQUIVALENT BODY RESULTS	222
16	DESIGN GUIDELINES	241
17	GEOMETRIC PARAMETERS FOR PHASE II AFT-END CONFIGURATION	248
18	APPLICATION OF DESIGN CHARTS	250
19	IDENTIFICATION OF BASELINE CONFIGURATIONS	262
20	IDENTIFICATION OF CANDIDATE CONFIGURATIONS	268
21	AIRCRAFT WEIGHT COMPARISON	298
22	MISSION RADIUS COMPARISON	305
23	SPECIFIC EXCESS POWER COMPARISON	307
24	RECOMMENDED RUN SCHEDULE	312

LIST OF SYMBOLS

A	Area.
A_F	LH plus RH nozzle/aftbody boattail projected frontal area.
A_c	Inlet capture area
A_W	Wing reference area, 2667.6 in. ² .
A_1	LH plus RH nozzle boattail cross-sectional area at nozzle exit stations.
A_2	LH plus RH aftbody boattail cross-sectional area at F.S. 133.182, customer connect station.
A_3	LH plus RH fuselage aftbody boattail cross-sectional area at F.S. 132.978, station farthest aft on fuselage aftbody.
A_6	LH plus RH aftbody boattail cross-sectional area at F.S. 133.188, metric break station.
$C_{D_{A_M}}$	Aft-end (pressure plus friction) drag coefficient based on maximum model cross-sectional area.
$C_{D_{A_S}}$	Nozzle/aftbody boattail pressure drag coefficient based on boattail cross-sectional area at nozzle exit stations.
$C_{D_{BA}}, \hat{C}_{D_{BA}}, C_{D_{BA_W}}$	Aftbody base drag coefficients based on cross-sectional area at metric break station (A_6), projected frontal area ($A_3 - A_2$), and wing reference area (A_W), respectively.
$C_{D_{BN}}, \hat{C}_{D_{BN}}, C_{D_{BN_W}}$	Nozzle base drag coefficients based on cross-sectional area at customer connect station (A_2), projected frontal area ($A_1 - A_S$), and wing reference area (A_W), respectively.
$C_{D_{BTA}}, \hat{C}_{D_{BTA}}, C_{D_{BTA_W}}$	Aftbody boattail (pressure and friction) drag coefficients based on cross-sectional area at metric break station (A_6), projected frontal area ($A_6 - A_3$), and wing reference area (A_W), respectively.
$C_{D_{BTN}}, \hat{C}_{D_{BTN}}, C_{D_{BTN_W}}$	Nozzle boattail (pressure and friction) drag coefficients based on cross-sectional area at customer connect station (A_2), projected frontal area ($A_2 - A_1$), and wing reference area (A_W), respectively.
C_{D_P}, \hat{C}_{D_P}	Aft-end pressure drag coefficient based on maximum area, and projected frontal area, respectively.

LIST OF SYMBOLS (Cont.)

$C_{D_{PT}}$, $\hat{C}_{D_{PT}}$, $C_{D_{PT_W}}$ Total boattail pressure drag coefficients - includes total aftbody and nozzle boattail pressure drag - based on cross-sectional area at metric break station (A_6), projected frontal area (A_6-A_1), and wing reference area (A_W), respectively.

C_{D_T} , \hat{C}_{D_T} , $C_{D_{T_W}}$ Total drag coefficients - includes total aftbody and nozzle drag - based on cross-sectional area at metric break station (A_6), projected frontal area (A_6-A_1), and wing reference area (A_W), respectively.

$C_{D_{TA}}$, $\hat{C}_{D_{TA}}$, $C_{D_{TA_W}}$ Total aftbody drag coefficients - includes aftbody boattail and base drag - based on cross-sectional area at metric break station (A_6), projected frontal area (A_6-A_2), and wing reference area (A_W), respectively.

$C_{D_{TBT}}$, $\hat{C}_{D_{TBT}}$, $C_{D_{TBT_W}}$ Total boattail drag coefficients - includes total aftbody and nozzle boattail drag - based on cross-sectional area at metric break station (A_6), projected frontal area (A_6-A_1), and wing reference area (A_W), respectively.

$C_{D_{TN}}$, $\hat{C}_{D_{TN}}$, $C_{D_{TN_W}}$ Total nozzle drag coefficients - includes nozzle boattail and base drag - based on cross-sectional area at customer connect station (A_2), projected frontal area (A_2-A_1), and wing reference area (A_W), respectively.

$C_{D_{W_{SL}}}$ Aircraft zero lift drag coefficient based on wing reference area and sea level operating conditions.

C_L Lift coefficient

C_P Pressure coefficient

C_{d_N} Nozzle discharge coefficient

C_T Nozzle thrust coefficient based on ideal gross thrust, F_i

$C_{(T-ND)}$ Thrust-minus-nozzle-drag coefficient - includes total nozzle drag - based on ideal gross thrust, F_i

$C_{(T-TD)}$ Thrust-minus-total-drag coefficient based on ideal gross thrust, F_i

D Diameter or drag

F_i Nozzle ideal gross thrust based on isentropic expansion of actual mass flow to freestream pressure

LIST OF SYMBOLS (Cont.)

F_g	Gross thrust at nozzle exit
F_s	Stream total momentum
m	Boundary layer velocity profile power law, exponent, $\left(\frac{v}{v_e} = \frac{\Delta R}{\delta}\right)^m$
\dot{m}	Mass flow
M	Mach number
M_∞	Freestream Mach number
P	Pressure
P_s	Separation pressure
P_{T_N}	Nozzle exhaust flow total pressure
P_{T_N}/P_∞	Nozzle pressure ratio
P_∞	Freestream static pressure
q_∞	Freestream dynamic pressure
Re/ft	Reynolds number per foot
R_{mf}	Momentum ratio
ΔR	Radial distance from model surface, inches
S/D	Spacing ratio, distance between nozzle centerlines divided by maximum exposed nozzle diameter of 8 inches
T	Temperature
V	Velocity
W	Weight flow
X	Distance
α	Angle of attack
δ	Boundary layer thickness or pressure ratio
δ^*	Boundary layer displacement thickness,

$$\delta \int_0^1 \left(1 - \frac{\rho V}{\rho_e V_e}\right) d \left(\frac{\Delta R}{\delta}\right)$$

LIST OF SYMBOLS (Cont.)

θ Boundary layer momentum thickness,

$$\delta \int_0^1 \left(1 - \frac{v}{v_e} \right) \left(\frac{\rho v}{\rho_e v_e} \right) d \left(\frac{\Delta R}{\delta} \right)$$

boattail angle, or cone angle, or temperature ratio

ρ Density

τ Shear stress

Subscripts

AERO	Aero-model
axi	Axisymmetric
b	Base
BLD	Bleed
BT	Boattail
ENG	Engine
2	Engine face
e	Exit
LS	Lip section
L	Local or lip
M	Maximum
MB	Metric Break
m	Minimum
T	Total

Abbreviations

A/B	Afterburning
AEDC	Arnold Engineering Development Center
AFFDL	Air Force Flight Dynamics Laboratory
ARC	Arnold Research Organization
B.L.	Buttock line, lateral distance from aircraft vertical plane of symmetry, inches
Calac	Lockheed-California Company
CEESI	Colorado Engineering Experimental Station, Inc.

LIST OF SYMBOLS (Cont.)

Abbreviations (Cont.)

ECS	Environmental Control System
FRL	Fuselage reference line
F.S.	Fuselage station, longitudinal distance aft of a point 1.041 inches aft of model nose
IMS	Integral mean slope
LH	Left-hand portion of model when viewed looking forward
LR	Lockheed report
MOC	Method of characteristics
P&WA	Pratt & Whitney Aircraft
PWT	Propulsion wind tunnel
P ² B	Precision pressure balance
RH	Right-hand portion of model when viewed looking forward
RMS	Root-mean-square
USAF	United States Air Force
W.L.	Water line, vertical distance from FRL, inches
VKF	Von Karman Facility
16S	AEDC 16 ft supersonic PWT
16T	AEDC 16 ft transonic PWT

LIST OF CONFIGURATION SYMBOLS

Airframe Symbols

B_1	Fuselage (nose, forebody, centerbody, and aftbody shell)
C_1	Canopy
N_1	Inlet fairing
S_1	Airframe, $S_1 = B_1 C_1 N_1 W_1$
W_1	Wing

Fuselage Fairing Symbols

Y_1	Basic
Y_2	Alternate (F-111 type) non-metric
Y_{2M}	Alternate - metric
-	Fuselage fairing removed

Horizontal Stabilizer Symbols

$H_{1F}^{-0.4}$	Full stabilizer deflected -0.4 degrees (negative deflection is with trailing edge up)
H_{1F}^{-2}	Full stabilizer deflected -2.0 degrees
H_{1F}^{-5}	Full stabilizer deflected -5.0 degrees
$H_{1P}^{-0.4}$	Partial stabilizer deflected -0.4 degrees
H_{1P}^{-2}	Partial stabilizer deflected -2 degrees
-	Horizontal stabilizer removed

Vertical Stabilizer Symbols

V_{1F}	Forward-mounted single full stabilizer
$V_{1F} r^4$	V_{1F} with rudder deflected +4.0 degrees (positive deflection is with trailing edge right as viewed looking forward)
$V_{1F} r^{+11}$	V_{1F} with rudder deflected ± 11.0 degrees
V_{1P}	Forward-mounted single partial stabilizer
$V_{1P} r^4$	V_{1P} with rudder deflected + 4.0 degrees
V_{2P}	Aft-mounted single partial stabilizer

V _{3PV}	Twin partial stabilizers aligned vertically
V _{3PR}	Twin partial stabilizers canted 15 degrees outboard
-	Vertical stabilizers removed

Interfairing Symbols

N1B	Narrow horizontal wedge interfairing with trailing edge above the nozzle centerline at the customer connect station
N1C	Narrow horizontal wedge interfairing with trailing edge above the nozzle centerline at the unshrouded plug nozzle cowl exit station
N1D	Narrow horizontal wedge interfairing with trailing edge above the nozzle centerline at the convergent-divergent nozzle exit station
N1D/C	N1D interfairing truncated to "C" length
N1E/D	N1E (non-fabricated narrow horizontal wedge interfairing with trailing edge above the nozzle centerline downstream of the convergent-divergent nozzle exit station) truncated to "D" length
N3D	Narrow vertical wedge interfairing with trailing edge at the convergent-divergent nozzle exit station
N3E	Narrow vertical wedge interfairing with trailing edge downstream of the convergent nozzle exit station
N3E/D	N3E interfairing truncated to "D" length
I1B	Intermediate-width horizontal wedge interfairing with the same profile as N1B
I2B	Intermediate-width horizontal wedge interfairing with trailing edge at the nozzle centerline at the customer connect station
I2D	Intermediate-width horizontal wedge interfairing with the trailing edge at the nozzle centerline at the convergent-divergent nozzle exit station
I4B	Intermediate-width horizontal wedge interfairing with the trailing edge along a nozzle radial line and with the same profile as N1B and I1B along the interfairing centerline
W1B	Wide horizontal wedge interfairing with the same profile as N1B and I1B
W2A	Wide horizontal wedge interfairing with trailing edge at the nozzle centerline and upstream of the customer connect station
W2B	Wide horizontal wedge interfairing with the same profile as I2B
W2C	Wide horizontal wedge interfairing with trailing edge at the nozzle centerline at the unshrouded plug nozzle cowl exit station

W2D Wide horizontal wedge interfairing with the same profile as I2D
W2E Wide horizontal wedge interfairing with trailing edge at the nozzle centerline and downstream of the convergent-divergent nozzle exit station

Nozzle Symbols

CF Convergent flap nozzle
CF₁ Normal power
CF₃ Maximum A/B
CI Convergent iris nozzle
CI₁ Normal Power
CI₃ Maximum A/B
CD Convergent-divergent nozzle
CD₁ Normal power
CD₂ Partial A/B
CD₃ Maximum A/B
CD_{1A} CD₁ which is only partially exposed to the freestream flow
CD_{3A} CD₃ which is only partially exposed to the freestream flow
CDE Convergent-divergent ejector nozzle
CDE₃ CDE at maximum A/B
UP Unshrouded plug nozzle
UP_AC₁ Plug (A) and cowl at normal power position
UP_AC₂ Plug (A) and cowl at partial A/B position
UP_AC₃ Plug (A) and cowl at maximum A/B position

Boundary Layer Trip Symbols

- No trips anywhere
T₁ Trips installed on forebody nose
T₂ Trips installed on forebody nose and inlet fairing
T₃ Trips installed on forebody nose, inlet fairing, and wing
T₄ Trips installed on forebody nose, inlet fairing, wing, and empennage (horizontal and vertical stabilizers)

SECTION 1

INTRODUCTION

1.1 PROGRAM BACKGROUND AND OBJECTIVES

The problems of airframe/nozzle integration have become significantly more complex and important with the advent of the multimission aircraft requiring variable geometry nozzles to operate over a broad range of altitudes and Mach numbers. The mutual interactions that occur between the nozzle exhaust and the external flow field can alter the pressure distributions on the aft-end of the fuselage and can produce both internal and external flow separation. Such interactions can result in significant penalties in both aircraft drag and engine thrust. It has been difficult in the past to minimize these losses because adequate analytical methods and empirical information were not available during the aircraft design phase.

In order to improve this situation, a 32 month AFFDL program was initiated on 1 November 1969 for the development and assembly of predictive techniques, design criteria, and guidelines for producing improved nozzle installations. This experimental and analytical program include both isolated nozzle/aftbody configurations and twin-nozzle/airframe installations. A common basic airframe design was used in all the latter studies. This basic airframe design is a generalized version of an advanced, air superiority fighter having twin buried engines and dual nozzles. It was selected from among those designs developed under the AFFDL-sponsored Supersonic Inlet Design and Airframe-Inlet Integration Program (USAF Contract F33657-69-C-1209).

Unheated air was chosen as the exhaust medium for all nozzle testing in this program based on the following technical and economic considerations. The program emphasis is on determining the differences in aftbody drag and nozzle thrust associated with configuration changes, rather than on establishing absolute levels of performance. Further, compensation for the primary effect of using unheated air, the change in plume shape caused by the change of specific heat ratio, can be effected by a small change of nozzle pressure ratio. The jet pressure ratios were varied over a range sufficient to accomplish this and thereby yield the proper external flow field simulation. The jet/freestream viscous mixing is affected through the transport properties; however, the effects of not exactly simulating this phenomenon are of minor importance unless large regions of separated flow are present. For these reasons, the complexity and expense of using a hot exhaust in the contract program could not be justified, especially since the current AFFDL/ARO test program will provide additional insight on hot jet effects and guidance in correcting cold jet results, if necessary.

1.2 PROGRAM PLAN AND SCHEDULE

The program was divided into three distinct, but related phases as follows: Phase I, Isolated Nozzle Investigation; Phase II, Twin-Nozzle/Aftbody Investigation; and Phase III, Development of Improved Twin-Nozzle/Aftbody Designs. For planning, scheduling, and reporting purposes, each of the three program phases was divided into a series of specific work tasks, as shown on the program schedule in Figure 1. Both the 13.6-month Phase I effort and the 28-month Phase II effort, which ran concurrently for the duration of Phase I, consisted of experimental and analytical studies. All testing for these two phases was conducted in the AEDC 16T (16-foot transonic) and 16S (16-foot supersonic) PWT. The four-month Phase III effort was initiated upon completion of Phase II and was followed by a one-month period for preparation of the final report.

The purpose of the Phase I isolated nozzle investigation was to determine the gross thrust, external drag, and internal and external pressure distributions for large scale convergent (flap and iris), convergent-divergent (with and without secondary flow), and plug (shrouded and unshrouded) type exhaust nozzles installed in a single, isolated pod. Sufficient test data were obtained over a 0.6 to 3.0 Mach number range to satisfy each of the following three test objectives: (1) provide large scale isolated nozzle test data for use by the aircraft industry; (2) acquire isolated nozzle test data to substantiate analytical methods; and (3) evaluate the capabilities of the test rig instrumentation for accurately measuring exhaust nozzle performance, since instrumentation and basic hardware was to be utilized in Phase II. The objective of the analytical study was to develop and/or improve methods for predicting isolated nozzle performance, and to select from among the available methods those which appeared most promising for extension to twin-nozzle/aftbody performance analysis. The validity of the experimental and analytical results were partially substantiated by direct comparison. A detailed documentation of the Phase I results is provided in Reference 1.

The purpose of the Phase II twin-nozzle/aftbody investigation was to determine the gross thrust, external aftbody and nozzle drags, and internal and external pressure distributions for a generalized twin-jet air superiority fighter aircraft model. Sufficient test data were obtained over a 0.6 to 2.5 Mach number range to substantiate analytical methods and to develop design criteria and guidelines for aircraft of this type. The configuration variables investigated were as follows: nozzle type, power setting position, lateral spacing, and axial position; aftbody contour, horizontal stabilizer area and deflection; vertical stabilizer type, longitudinal position, area, and rudder deflection; and interfairing type, length, height, and base area. Analytical methods for predicting twin-nozzle aftbody performance were evaluated and improved using available test data, including the Phase II test results, as a basis for comparison. Phase II data correlations were also developed for predicting those performance parameters which could not be easily and/or accurately computed using available analytical methods. A detailed documentation of the Phase II results is provided in Reference 2.

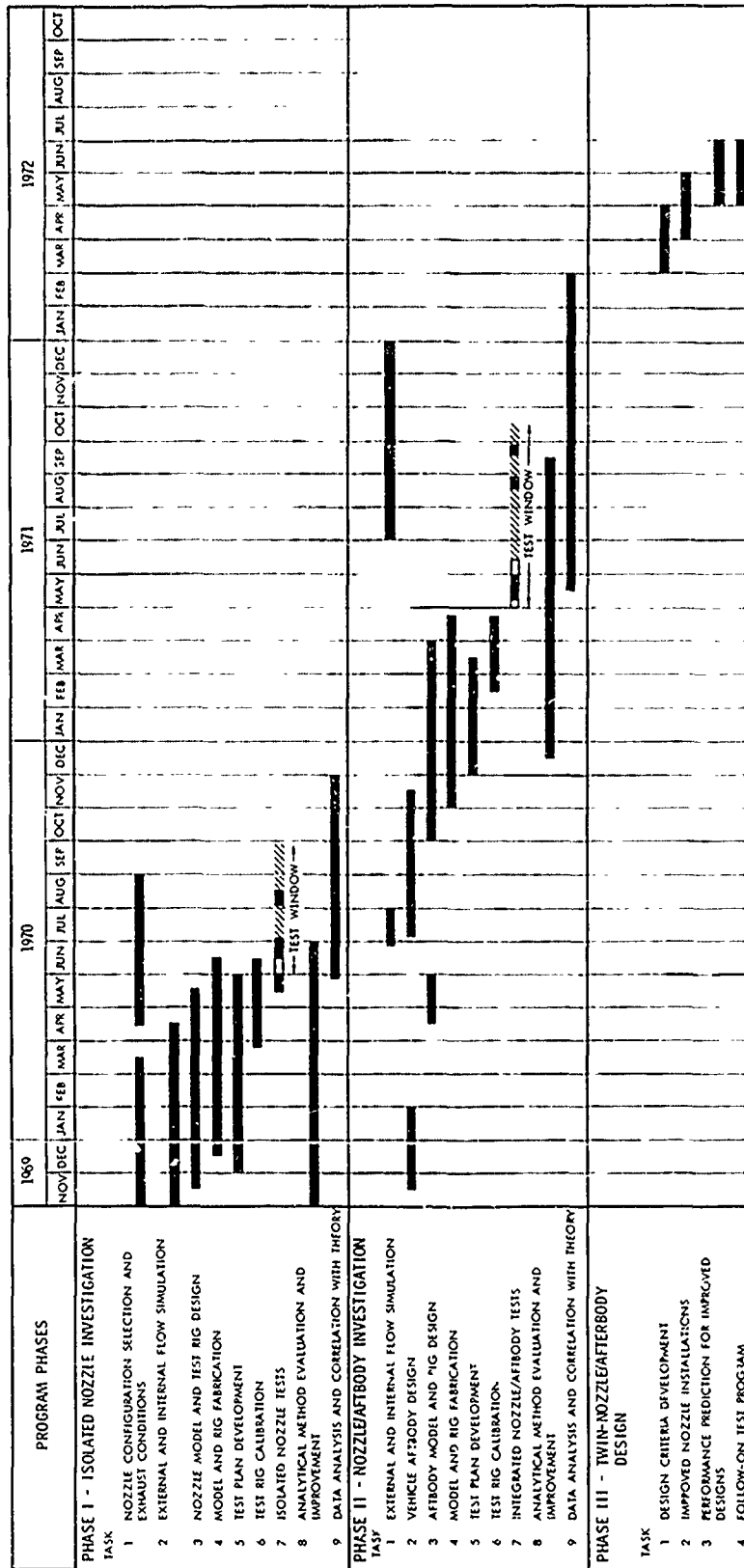


Figure 1. Program Schedule

The purpose of the Phase III investigation was to develop, apply, and verify techniques for improving twin-nozzle/aftbody designs. Predesign guidelines and performance prediction charts were formulated for use in developing or modifying aircraft aft-end arrangements so that a high thrust minus drag can be achieved. Also, post-design methods for predicting the aft-end performance of the final aircraft designs were developed for use in conducting mission analysis studies. Three improved designs were developed during Phase III by applying the design techniques to selected Phase II configurations. New aftbody lines were also developed for one of these designs in which the turbofan engine was replaced by a turbojet engine of equal sea level static thrust. A test program for the improved designs was then recommended from which thrust and aft-end drag would be obtained for verifying the design techniques employed.

1.3 REPORT ORGANIZATION

This report documents the results obtained during all three phases of the AFFDL/Calac Program. The results of the Phase I isolated nozzle and Phase II twin-nozzle/aftbody investigations are summarized in Sections 2 and 3, respectively. Included in these sections are descriptions of the apparatus and procedure, experimental results, and performance prediction methods. The Phase III twin-nozzle/aftbody design techniques are presented in Section 4, and the conclusions and recommendations derived from the program are itemized in Section 5. The operating instructions for the twin-nozzle/aftbody drag and internal nozzle performance computer program are provided in Volume II of this report.

SECTION 2

ISOLATED NOZZLE INVESTIGATION

A strut-supported isolated nozzle test rig was developed for testing large-scale nozzle models (maximum nozzle diameter of 8 inches) over a 0 to 3.0 Mach number range in the AEDC FWT 16-foot wind tunnels. A photograph of the test rig with nozzle model installed in the 16T tunnel is shown in Figure 2. Nozzle performance, including the thrust coefficient and pod aftbody and nozzle boattail drag coefficients, was obtained from force balance data during the test and from pressure/area integrated forces plus calculated skin friction drag subsequent to the test. The apparatus and procedures employed in obtaining and reducing the test data are discussed in this section, in addition to a presentation of experimental results and an evaluation of performance prediction methods.

2.1 APPARATUS AND PROCEDURE

The apparatus utilized during the test, which includes the AEDC 16-foot propulsion wind tunnels, support system, nozzle models, and instrumentation, is described below. Also presented is the data reduction and calibration procedures employed and a description of the test.

2.1.1 Test Facility

The AEDC 16-foot transonic and supersonic propulsion wind tunnels, 16T and 16S, respectively, including their operating characteristics, data acquisition systems, and test support equipment, are summarized in this subsection. A detailed description of the facility capabilities is provided in Reference 3.

2.1.1.1 Operating Characteristics

The 16T and 16S are continuous-flow, closed-circuit wind tunnels with a common main drive system capable of operation within Mach number ranges of 0.2 to 1.6 and 1.5 to 4.75, respectively. The 16T can be operated within a stagnation pressure range from 120 to 4000 psfa and a stagnation temperature range from 80°F to 160°F. The 16S can be operated within a stagnation pressure range from 200 to 2300 psfa and a stagnation temperature range from 100°F to 620°F. These operating limits are dependent upon Mach number. Stagnation temperatures for the isolated nozzle test were approximately 100°F and 140°F in the 16T and 16S, respectively.

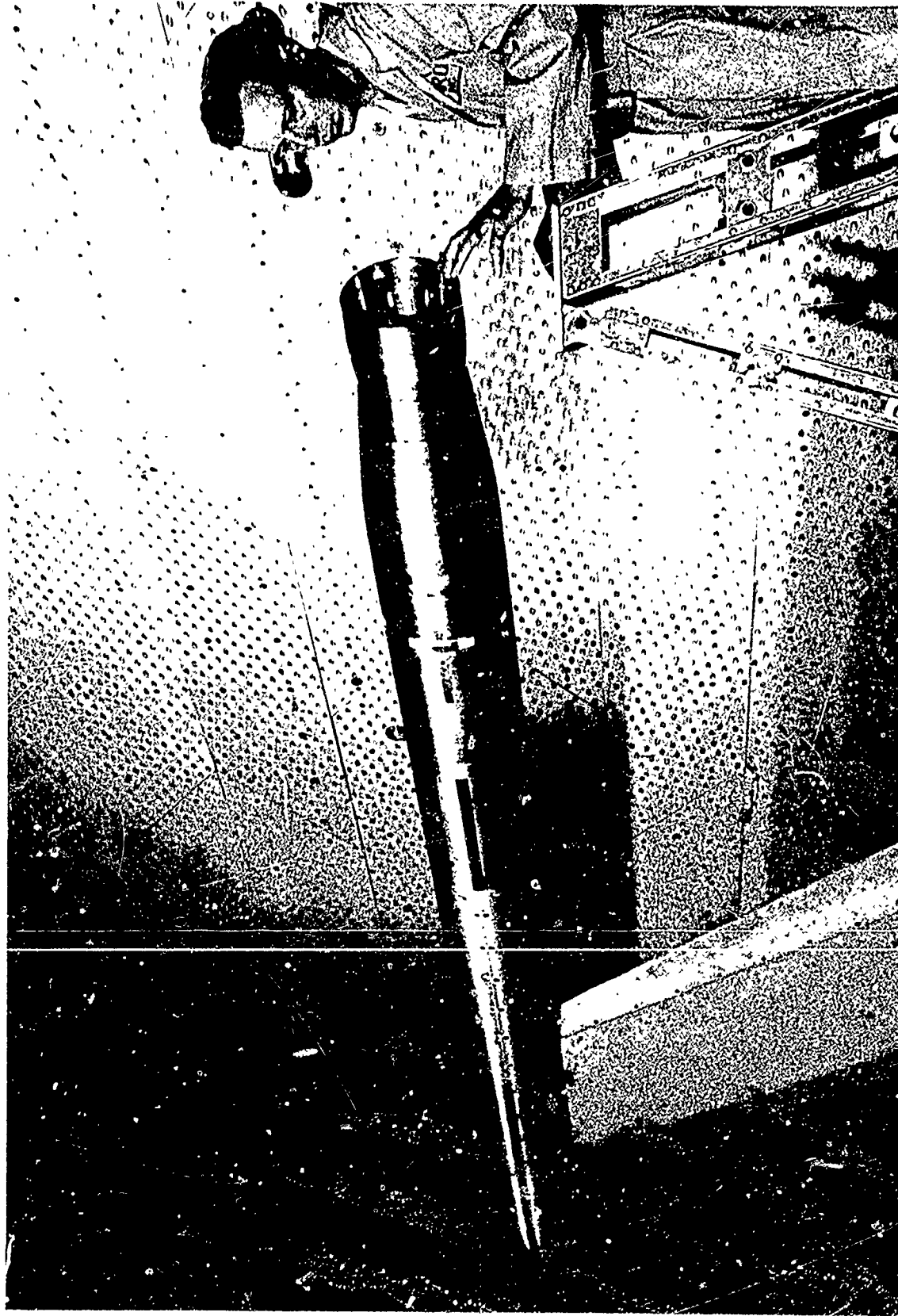


Figure 2. Photograph of Isolated Nozzle Test Rig and Nozzle Model Installed in AEDC 16T Propulsion Wind Tunnel

Due to power limitations, operation of the tunnels is restricted to the period from evening to early morning hours. Reynolds number variations above 2.5 million per foot in 16T and 1 million per foot in 16S are further limited to the middle of this period.

2.1.1.2 Test Support Equipment

Test support equipment was required to provide model angle of attack variations, high pressure air for simulating the nozzle exhaust flow and visual recordings. Support equipment was also required to measure airflow rates, pressures, and temperatures.

Model airflow, at a maximum rate of 60 lb/sec, was supplied either from the PWT or the VKF (Von Karman Facility) air storage systems. These two systems contain 75,000 lb of air at 2300 psia and 134,000 lb of air at 4,000 psia and can be replenished at a rate of 5 lb/sec and 60 lb/sec, respectively. Both systems delivered air to the tunnels at pressures exceeding 1000 psia. An automatic pressure control system was developed to supply air to the flow meters within a pressure range from tunnel static pressure to 500 psia.

Nozzle airflow was metered by orifice meters, venturi meters, and a swirl-meter which were installed in the 16T and 16S tunnel plenums. At least two metering systems were installed in series for each tunnel entry.

For the first tunnel entry, scanivalves, mounted in the test rig nose, were used to measure the majority of the model pressures. For the subsequent tunnel entries, the AEDC precision pressure balance (P²B) system was used to measure the model pressures. Although the pressure instrumentation arrangement using the P²B system was more complicated due to the large range of model pressures, the higher accuracy (0.15 percent of full scale) and stability of the measured pressures outweighed these complications.

All temperatures were measured by iron/constantan (within the model) or copper/constantan (within the airflow meters) thermocouples.

The test rig support strut was attached to the tunnel pitch table which is installed below the floor of the test section. This pitch table has a pitching range of ± 10 degrees. The support strut was constructed such that the ± 10 degree angle range of the pitch table yielded a -4 degree to +16 degree angle-of-attack capability for the test rig.

Schlieren and shadowgraph movies can be recorded in the 16T and 16S, respectively. No schlieren movies were taken, however, since the model was not located within the viewing window. Shadowgraph movies of the aftbody, nozzle, and jet plume were taken in the 16S. Still photographs of each model configuration were also taken.

2.1.1.3 Data Acquisition

The balance force data were digitized by a 20 channel readout system which was operated at a 5 or 10 millivolt signal for a full-scale readout of

10,000 counts. The basic accuracy of the system is the larger of ± 0.1 percent of reading or ± 3 counts with a confidence level of 99.7 percent. The digitized data were transmitted to the central computer in binary-coded form and permanently recorded on magnetic tape. These data were reduced by a Raytheon 520 computer to forces and moments and then transmitted back and printed in the tunnel control room.

Scanivalve transducer pressure signals were digitized and transmitted to the central computer by a Beckman 210 high-speed digital data recording system. The P²B system utilizes a high-speed analog-to-digital converter for signal transmission to the central computer and provides an accuracy of 0.15 percent of full scale at a 99.7 percent confidence level. The digitized pressure data were handled in the same manner as the force data to obtain absolute pressures or pressure coefficients.

The Beckman Model 210 system was used for digitizing each thermocouple analog signal. These signals enter directly into the central computer where they are resolved to one part in 10,000 with an accuracy better than 0.15 percent of full-scale. These data were reduced to temperatures in degrees Rankine and printed out in the control room by the same methods utilized for the force data.

2.1.2 Model and Support System

The various nozzle models were attached to the isolated nozzle test rig, which consisted of a strut supported, cylindrical pod, as shown in Figure 3. The strut swept forward from the tunnel floor upward to the forward end of the pod. The pod has a conical nose which faired into the cylindrical body.

The pod internal arrangement included the air supply ducting and three force balances: thrust, aftbody boattail, and nozzle boattail. The nozzle boattail balance was attached to the flow tube, which was supported by the thrust balance, so that the thrust balance measured nozzle thrust-minus-boattail drag directly.

Four nozzle model arrangements were employed: pressure/force, dummy, force, and pressure. For the convergent flap (CF), convergent-divergent (CD), and convergent-divergent ejector (CDE) nozzles, a two-shell arrangement was used wherein the external shell was attached to the balance, the internal shell was attached to the flow tube, and both shells were pressure instrumented (denoted as pressure/force or "P/F" nozzles). The corresponding nozzles for the Twin-Nozzle/Aftbody Investigation are single shell, non-instrumented designs which attach to the flow tube (denoted as dummy or "D" nozzles). For the convergent iris (CI), unshrouded plug (UP), and shrouded plug (SP) nozzles, the two-shell arrangement was also employed for force measurements (denoted as force or "F" nozzles); however, these shells were too thin for routing pressure tubes. As a result, the corresponding single shell nozzles which attach to the flow tube are pressure instrumented (denoted as pressure or "P" nozzles).

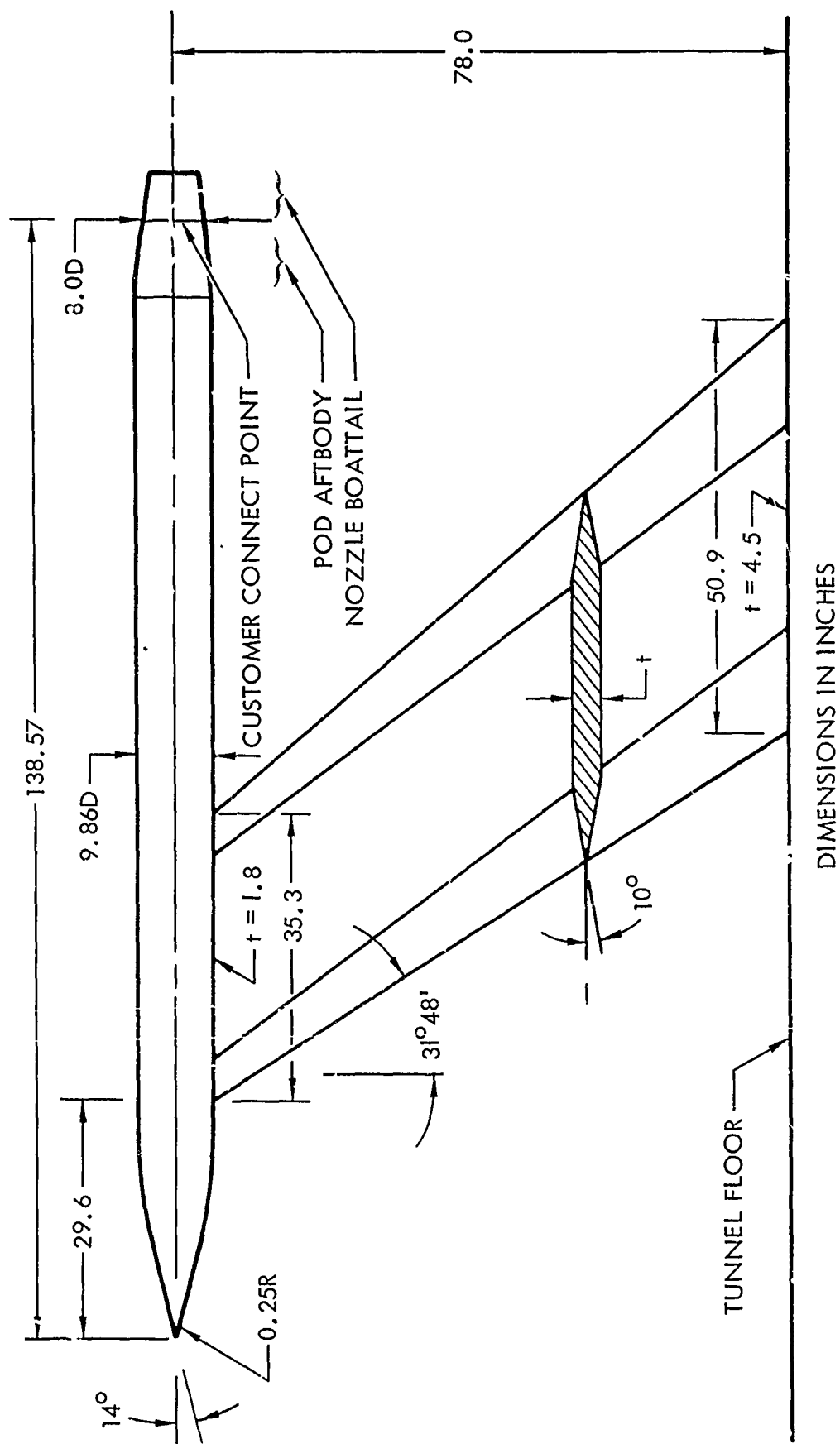


Figure 3. Isolated Nozzle Model and Support Strut

2.1.2.1 Flow Simulation

Prior to development of the test plan and design of the scaled nozzle models, a study was conducted to identify simulation requirements for the external and internal flows. The basic philosophy of the test program was to obtain data which showed the effect of configuration and flow variable changes on the external drag and the interaction effects between the external and internal flows, rather than to establish precise absolute levels of full scale performance. However, the reliability of the data for this purpose can be improved if full scale external flow conditions are closely approached. The inviscid external flow field can be simulated in the wind tunnel if the external geometry is directly scaled, the freestream Mach number and specific heat ratio are duplicated, and the boundary layer and exhaust plume displacement effects are simulated.

External Boundary Layer Simulation - Boundary layer thickness calculations (using the Lockheed MOC/Boundary Layer Program), Reference 4, indicate boundary layer thicknesses equivalent to full scale conditions can be approached in the supersonic wind tunnel even though the model Reynolds numbers are less than the full scale values. Reducing the Reynolds number at otherwise similar conditions (including the same transition point) increases the boundary layer thickness. However, reducing the Reynolds number also moves the boundary layer natural transition point downstream on the model and thus tends to reduce the boundary layer thickness. If transition is forced by means of trips at the proper location upstream of the nozzle, these effects can be made to offset one another and equivalent full scale turbulent boundary layer on the nozzle boattail can be simulated.

Exhaust Plume Shape Simulation - The exhaust plume shape can be properly simulated with a cold jet provided the nozzle pressure ratio is adjusted slightly to compensate for the lower specific heat ratio of the hot jet of the full scale aircraft. A suitable criterion for this adjustment is to match the initial plume boundary angles of the tunnel model and aircraft while maintaining the same nozzle internal geometries. Inviscid jet plume and flow field analyses, using the method of Reference 5, indicate that the full scale boattail pressures will be duplicated on the wind tunnel model by this procedure. The viscous interaction effects between the freestream and the jet are not accurately simulated; however, these effects are significant only when large regions of separated flow exist.

2.1.2.2 Model Scale

Because of nozzles designed for the Phase I Isolated Nozzle Investigation would also be used for the Phase II Twin-Nozzle/Aftbody Investigation, it was necessary to establish the airplane model scale early in the program. A model scale of 8/43, corresponding to a nozzle maximum diameter of 8 inches, was selected based on considerations of full scale Reynolds number simulation, model airflow limitations, model and support strut blockage, and wing span limitations. The rationale used in selecting the model scale is discussed below in terms of these considerations.

The largest possible model is desired in order to approach full-scale Reynolds numbers as closely as possible and thereby simulate full-scale viscous effects. Figure 4 compares the full scale Reynolds number and maximum tunnel freestream Reynolds number (based on airplane and model lengths) for the selected model scale over the range of test Mach numbers. Although only a portion of the full scale flight envelope can be duplicated, in all cases the model Reynolds numbers are high enough to insure a turbulent boundary layer on the external surface of the model.

The maximum airflows available at AEDC are approximately 60 lb/sec for continuous operation and 90 lb/sec for durations less than 1.5 minutes. Airflows above 60 lb/sec were required only for a limited number of test conditions, and no difficulty was encountered in satisfying these requirements without loss of tunnel time.

Tests had been run in the AEDC 16T wind tunnel with wing-body models having up to 1.15 percent blockage without interference effects being evident, and this was selected as a desirable limit of the Phase II model and support strut blockage. The model and strut blockages were calculated as functions of model scale as illustrated in Figure 5. The former was based on the maximum airplane cross-sectional area of the A-1 Tailor-Mate aircraft configuration developed by General Dynamics (Contract No. F33657-69-C-1209), and the latter on a preliminary support strut design. A model scale of 8/43 was selected, with an associated nozzle reference diameter of 8 inches, as equivalent to a combined blockage of 1.15 percent. (The resultant blockage for the Phase I model pod and support strut is approximately 0.65 percent). Subsequent refinement of the Phase II model support strut design resulted in a combined model plus strut blockage of 1.28 percent; however, the additional blockage was not sufficient to warrant changing the model scale.

The usual criterion for holding the interference effects between the wing tips and the tunnel walls to acceptable values is to limit the model wing span to the order of 60 to 70 percent of the tunnel width. The span for the 8/43 scale is 8.2 ft., or 51 percent of the tunnel width.

2.1.2.3 Support Strut Design

The support struts for the two test phases had to satisfy requirements involving structural integrity, airflow, model-strut orientation, and interference. Because these requirements were markedly different for the two test phases, it was decided to provide separate struts. The strut requirements and design are discussed below.

- The strut must withstand steady-state aerodynamic loads and an unsymmetrical tunnel unstart condition with safety factors in accordance with Reference 6.
- The strut must have sufficient internal flow area to pass the maximum airflow required by the nozzle.

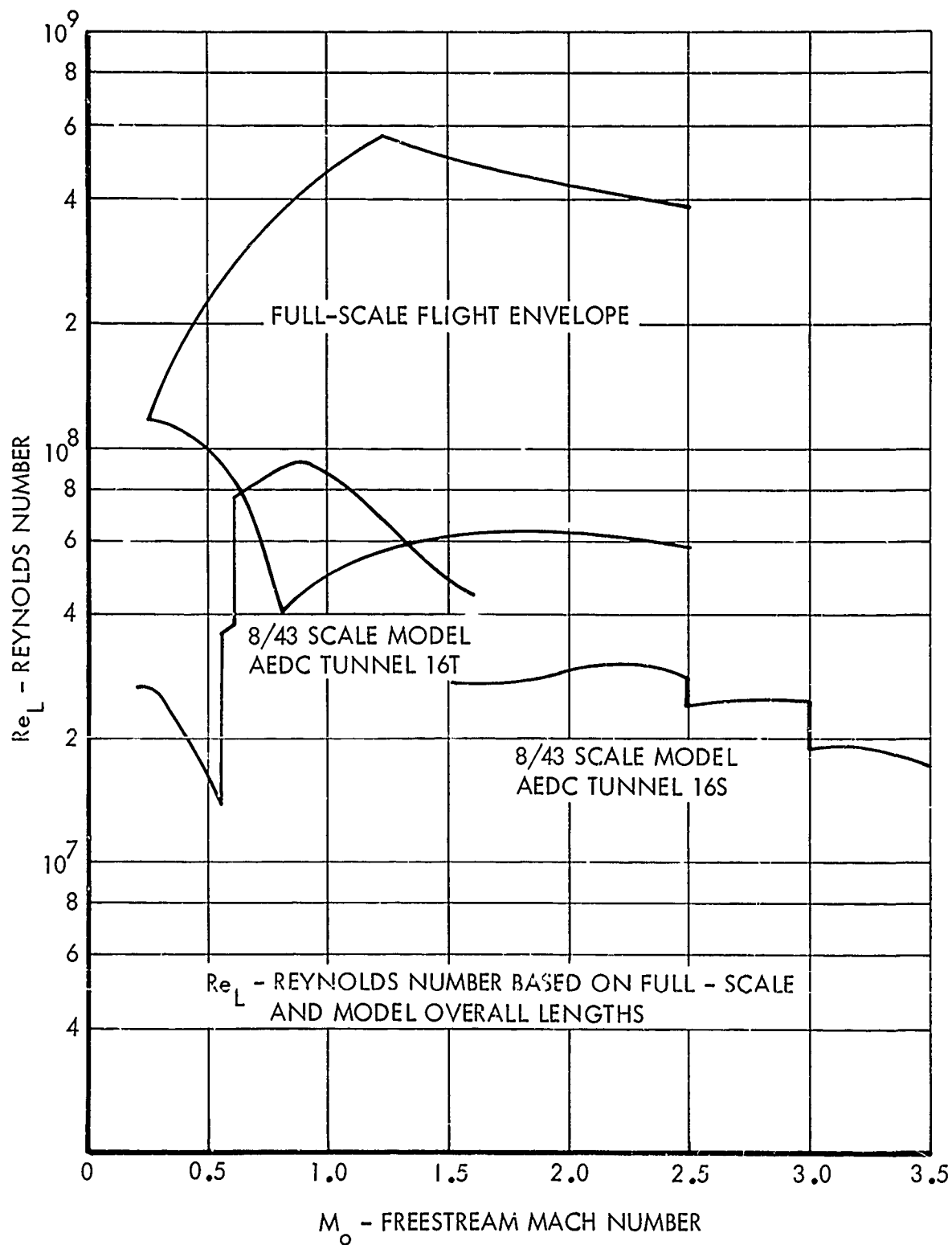


Figure 4. Model Reynolds Number Simulation

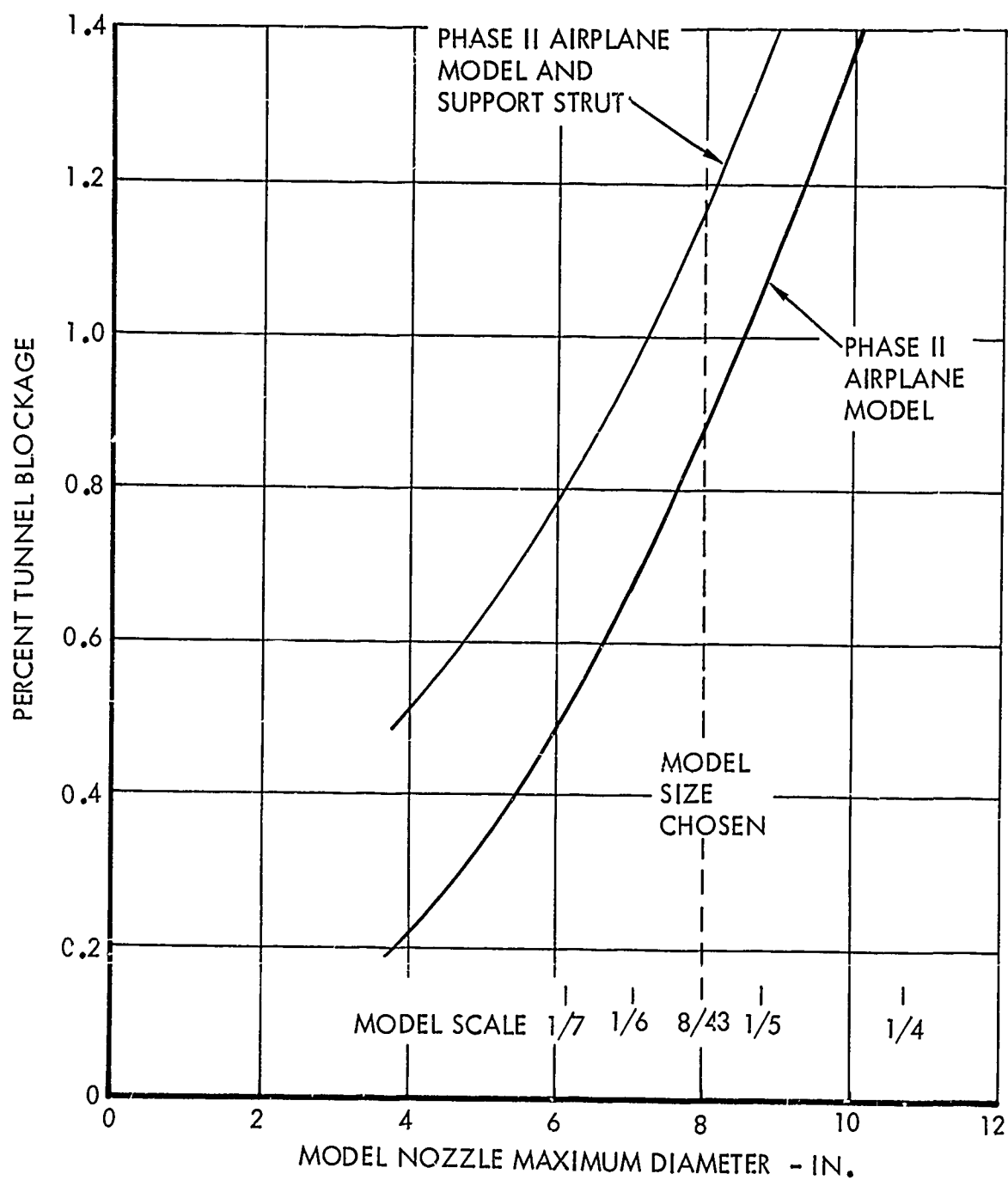


Figure 5. Phase II Airplane Model and Support Strut Tunnel Blockage

- The bow shock reflections from the tunnel walls should pass downstream of the model at Mach 1.6 and above.
- The aft-end of the model must remain in a relatively fixed position in the tunnel with changing angle of attack.
- The attachment of the strut to the model should be as far forward of the nozzles as possible to minimize strut wake effects on the nozzles.
- The interference caused by strut blockage and strut wake must be minimized.

Based on the above requirements, the strut design illustrated in Figure 3 was evolved. The strut thickness was tapered from the model (1.8 inches thick) to the tunnel floor (4.5 inches thick) to minimize the interference near the model while still satisfying the strength requirements. This tapered design had a low thickness to chord ratio varying from 0.051 at the model to 0.089 at the tunnel floor. The wedge-shaped leading and trailing edges had total included angles of 20 degrees and were swept back from the model pod at angles of $31^{\circ}48'$ and $39^{\circ}48'$, respectively. The trailing edge was approximately 8 model pod diameters upstream of the nozzles. The strut blockage was 0.45 percent. The required internal flow area of 18 square inches was provided by 12 tubes within the basic strut structure.

2.1.2.4 Nozzle Design and Philosophy

General Discussion and Ground Rules - The internal and external lines and dimensions for the thirty (30) full-scale nozzle configuration designs illustrated in Figure 6 were developed in sufficient detail to define the corresponding small-scale wind tunnel model geometries. Eighteen of the 30 designs (solid lines in Figure 6) were provided by P&WA. These designs consist of three power setting positions (normal, partial A/B, and maximum A/B) for each of the six nozzle types investigated (CF, CI, CD, CDE, UP, and SP). The remaining twelve (12) configurations (dotted lines in Figure 6) were developed by Calac for the purpose of investigating the effect of nozzle boattail angle and plug angle, shape, and length. Only twenty-nine of the 30 designs were considered for model fabrication since the aerodynamic lines of the unshrouded and shrouded plug nozzles in the normal power position were essentially identical. Geometric similarity was maintained between full-scale and model-scale, except for the plug nozzles where the model shroud base had to be increased in order to insure structural integrity. Twelve sets of nozzle models were designed and fabricated utilizing the "pressure/force" and "dummy" twin-jet arrangement (CF, CD, and CDL), while the remaining 17 sets of configurations employed the "pressure" and "force" arrangement (CI, UP, SP). Thus, a total of 46 nozzle model configurations from which pressure and/or force data could be obtained were available for the Phase I Isolated Nozzle Investigation.

The primary emphasis in formulating the aerodynamic lines of the basic full scale nozzle designs was placed on nozzle performance and weight. Included



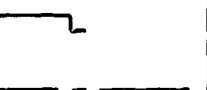




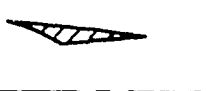
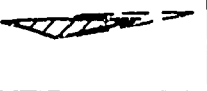



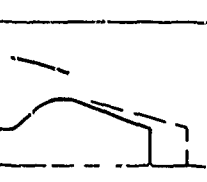
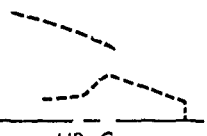
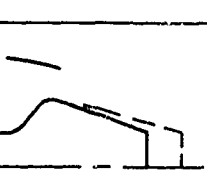
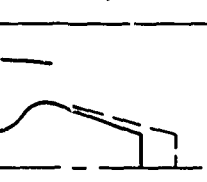
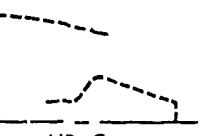
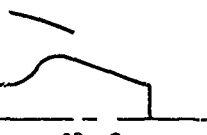
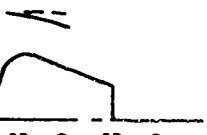
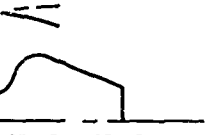
NOZZLE TYPE	NOZZLE POWER SETTING POSITION			NUMBER OF CONFIGURATIONS
	NORMAL	PARTIAL A/B	MAX. A/B	
CONVERGENT FLAP (CF)	 CF ₁	 CF ₂	 CF ₃	3
CONVERGENT IRIS (CI)	 CI _{1S} , CI ₁ , CI _{1E}	 CI ₂	 CI ₃	5
CONVERGENT-DIVERGENT (CD)	 CD ₁ , CD _{1E}	 CD ₂	 CD ₃ , CD _{3E}	5
CONVERGENT-DIVERGENT EJECTOR (CDE)	 CDE _{1S} , CDE ₁	 CDE ₂	 CDE ₃	4
UNSHROUDED PLUG (UP)	 UP _A C ₁ , UP _B C ₁  UP _C C _{1E}	 UP _A C ₂ , UP _B C ₂	 UP _A C ₃ , UP _B C ₃  UP _C C _{3E}	8
SHROUDED PLUG (SP)	 SP _A C ₁	 SP _A C ₂ , SP _A C _{2F}	 SP _A C ₃ , SP _A C _{3F}	5

Figure 6. Axisymmetric Nozzle Design Identification

in the design was an actuation system which provided the required geometric variation. The following ground rules were established to provide a common basis for the design process.

- The design point of the full-scale nozzles must be subsonic cruise (normal power position) at Mach 0.9.
- The full-scale exhaust system must satisfy jet area and operating pressure ratio requirements of the STF 359B 20 mixed flow turbofan engine.
- The external contour of the full-scale nozzle must be designed to mate with a fixed diameter circular opening (8 inch diameter in model scale) and a seven (7) degree surface angle at the aftbody/nozzle juncture (designated as the customer connect point).
- Full-scale nozzles must be designed with an external geometry that is as short as possible, allowing the engine to shift fore and aft, as required, to accommodate the nozzle's internal geometry and actuation system.
- The full-scale afterburner volume must not be less than 68,330 cubic inches, and the constant area section of the afterburner must extend for at least 60 percent of the effective afterburner length (afterburner volume divided by the maximum afterburner cross-sectional area).

The design rationale employed by P&WA and Calac in developing the basic and alternate full-scale nozzle configurations, respectively, is discussed below. A comparison of the major design parameters for all nozzles is provided in Table 1. Two-dimensional and asymmetric nozzle concepts are presented in the P&WA supplement (Reference 7) in addition to a more detailed discussion of the P&WA axisymmetric nozzle design rationale.

Basic Nozzle Designs Developed by P&WA - A schematic of the axisymmetric nozzle designs developed by P&WA is shown with a common customer connect station in Figure 7. The more obvious distinguishing features between nozzle geometries are differences in length forward and aft of the customer connect station, flap thickness, throat position, and area ratio.

The shortest and most compact system is the convergent flap nozzle. The design utilizes a short flap to minimize weight at the expense of high base drag. This weight advantage may be significant, especially for the basic air superiority type mission. The base area, which is a maximum at the normal power position, is still relatively large at the maximum jet area position due to the large structure required to support the nozzle flap assembly. The short flap and stroke required for this nozzle permits the actuation system to be short and located downstream of the customer connect point in a relatively thick envelope.

TABLE 1. NOZZLE DESIGN PARAMETERS

Nozzle Type and Position	Nozzle Configuration Symbol	Internal Expansion Ratio	Total Expansion Ratio	Internal Shroud to Customer Connect Area Ratio	Shroud Length to Customer Connect Diameter Ratio
Convergent Flap					
Normal	CF ₁	1.0	1.0	0.252	0.511
Partial A/B	CF ₂	1.0	1.0	0.386	0.501
Max A/B	CF ₃	1.0	1.0	0.529	0.460
Convergent Iris					
Normal	CI ₁	1.0	1.0	0.252	0.828
Normal - Shortened	CI _{1S}	1.0	1.0	0.252	0.738
Normal - Extended	CI _{1E}	1.0	1.0	0.252	1.028
Partial A/B	CI ₂	1.0	1.0	0.386	0.693
Max A/B	CI ₃	1.0	1.0	0.529	0.551
Convergent-Divergent					
Normal	CD ₁	1.10	1.10	0.278	1.011
Normal - Extended	CD _{1E}	1.10	1.10	0.278	1.125
Partial A/B	CD ₂	1.22	1.22	0.471	1.024
Max A/B	CD ₃	1.60	1.60	0.846	1.028
Max A/B - Extended	CD _{3E}	1.99	1.99	1.054	1.133
CD Ejector					
Normal	CDE ₁	1.51	1.51	0.379	0.695
Normal - Shortened	CDE _{1S}	1.78	1.78	0.448	0.538
Partial A/B	CDE ₂	1.81	1.81	0.697	0.700
Max A/B	CDE ₃	2.14	2.14	1.131	0.695
Unshrouded Plug					
Normal	UP _A C ₁	1.0	2.38	0.601	0.439
Normal - 10° Plug	UP _B C ₁	1.0	2.38	0.601	0.439
Normal - Extended	UP _C C _{1E}	1.0	1.83	0.462	0.631
Shroud, Smaller Plug					
Partial A/B	UP _A C ₂	1.0	1.83	0.733	0.440
Partial A/B-10° Plug	UP _B C ₂	1.0	1.91	0.733	0.440
Max A/B	UP _A C ₃	1.0	1.67	0.870	0.439
Max A/B-10° Plug	UP _B C ₃	1.0	1.67	0.870	0.439
Max A/B-Extended	UP _C C _{3E}	1.0	1.40	0.727	0.641
Shroud, Smaller Plug					
Shrouded Plug					
Normal	SP _A C ₁	1.0	2.38	0.601	0.439
Partial A/B	SP _A C ₂	1.84	2.48	0.971	0.438
Partial A/B-Fantail Shroud	SP _A C _{2F}	2.24	2.91	1.121	0.430
Max A/B	SP _A C ₃	1.25	1.87	0.972	0.438
Max A/B-Fantail Shroud	SP _A C _{3F}	1.53	2.16	1.121	0.430

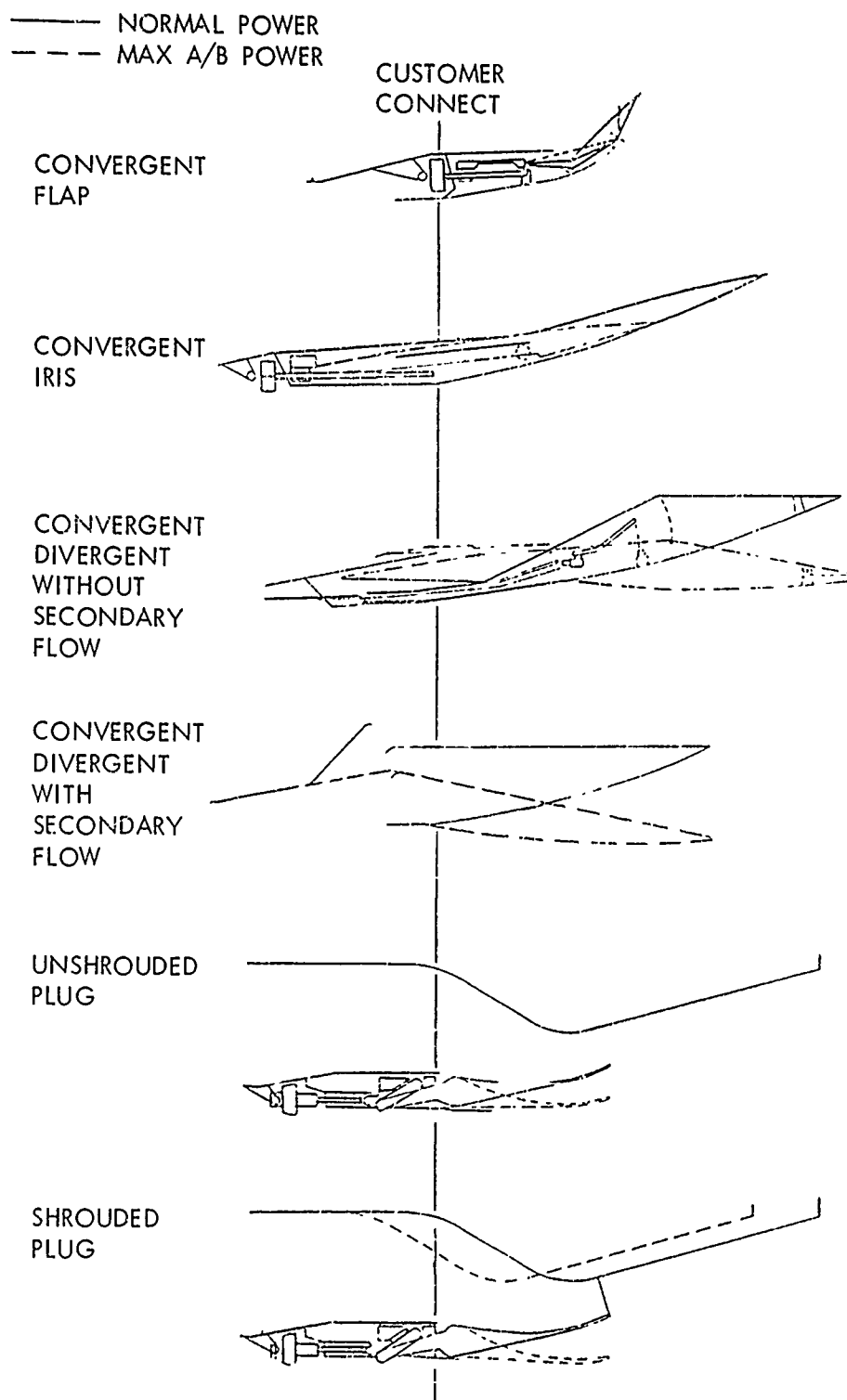


Figure 7. Basic Axisymmetric Nozzle Designs

In contrast, the convergent iris nozzle design utilizes a long iris flap whose external surface follows the circular arc contour originating upstream of the customer connect station. A 12-degree mean boattail angle, which is the angle formed between the horizontal and a line connecting the initial and final points on the boattail surface, was selected as a good compromise in length, weight, and performance. A short conical section at the end of the nozzle was incorporated into the design to reduce weight without significantly affecting the nozzle performance. The long stroke required for obtaining both normal and maximum A/B throat area positions results in a long section upstream of the customer connect point.

The convergent-divergent nozzle without secondary flow is one of the longest exhaust systems. The nozzle's throat position is maintained at about the same axial station during area excursions. The remaining length beyond the throat is used to obtain a low drag external boattail for subsonic cruise and an internal divergent surface for better supersonic performance. At afterburning power settings the external flap forms a slope discontinuity with the fixed nozzle section at the forward external flap hinge point. In addition, the necessity for burying the aft external flap hinge upstream of the trailing edge produces a small base when afterburning. Both the slope discontinuity and base, which result in a performance loss for the afterburning modes, are required for this type of nozzle in order to maintain a clean aerodynamic contour at subsonic cruise. The design area ratio of 1.6 also results in some sacrifice in supersonic performance since the nozzle operates underexpanded for Mach numbers above 1.5; however, a reasonable compromise between performance and weight is achieved.

The convergent-divergent ejector nozzle retains good performance over the complete range of operating conditions at the expense of some increased weight. This is contrasted with the convergent and convergent-divergent nozzle designs where supersonic performance is sacrificed to obtain a lightweight exhaust system with good subsonic performance. The use of secondary flow for the ejector nozzle results in an exit-to-throat area ratio greater than unity for subsonic operation at normal power. The nozzle external boattail, therefore, is relatively short, and as a result, the throat can be placed farther forward than in the other designs. At supersonic speeds, the shorter boattail produces a maximum expansion ratio of 2.2 with less actuated motion required than for the convergent-divergent nozzle. Also, the break in the boattail surface slope (hinge locations) is located farther forward and at a larger diameter than that on the convergent-divergent nozzle, which permits a larger portion of the external surface to be cylindrical, thus reducing the possibility of high supersonic pressure drag.

For this program it was assumed that the secondary flow for the ejector nozzle would be supplied from the inlet bleed flow. Secondary-to-primary corrected mass flow ratios of 10 percent and 5 percent were selected as representative values for fighter aircraft using normal power at subsonic cruise (Mach 0.9) and partial A/B power at intermediate supersonic cruise (Mach 1.6), respectively. It was further assumed that no secondary flow was required for the maximum supersonic cruise condition.

Both plug nozzles required moderately long variable shroud flaps to provide a thin trailing edge and the gradual thickening of the flap in an upstream direction required to support flap loads. Due to the annular throat geometry, the actuation stroke necessary for jet area variation is less than that required for the other nozzle types discussed which have circular throat areas. These short strokes lead to a relatively compact and thin actuation system. The plug with its supersonic expansion surface truncated at 50 percent of cone length, results in a nozzle length downstream of the customer connect point which is equal to the length of the convergent-divergent nozzle. The plug support structure, including the actuation system for the shrouded plug nozzle, extends upstream through the flameholder and into the turbine hub section.

Detailed design drawings and static thrust estimates for all the basic full-scale nozzle configurations are presented in Reference 7.

Alternate Nozzle Designs Developed by Calac - Selected basic nozzle designs supplied by P&WA were modified by Calac for the purpose of investigating the effect of boattail angle and plug angle, shape, and length. The boattail angle for the CI, CD, and CDE nozzles was varied by either shortening or extending the flap length specified for the corresponding basic nozzle designs. Associated with the shorter flap for the CDE nozzle was an increase in the required secondary airflow rate during normal power operation. For the UP nozzles, the external plug angle and corresponding plug length (plug B) were increased over that specified for the basic plug (plug A). Two additional UP nozzle configurations were developed by reducing the basic plug diameter (plug C) and extending the basic cowl length. The alternate SP nozzles were developed by rotating the basic cowl to provide higher expansion ratio. The design rationale employed in the development of these alternate nozzle configurations is discussed below.

No flap length variations to the basic minimum weight convergent flap nozzle design were investigated in the test program. Since the support structure for the flap assembly creates a large base area immediately ahead of the nozzle flap, the external flow, which separates from this base region, generally remains separated on the nozzle flap, resulting in little variation in nozzle drag with flap angle. Thus, an increase in flap length for a given nozzle jet area results in a weight increase, while the nozzle drag remains relatively unchanged.

Two alternate non-afterburning iris nozzle configurations, having mean boattail angles of 10 and 15 degrees compared to 12 degrees for the basic design, were selected for the test program. The basic non-afterburning configuration was selected for further examination since the mean boattail angle has the largest effect on nozzle drag for this area position. The alternate mean boattail angles selected represent the maximum and minimum limits for which a feasible actuation system could be developed by P&WA.

The alternate CD nozzle configuration was designed to maximize the aftbody thrust-minus-drag during maximum A/B operation at Mach 2.5, for a nozzle

pressure ratio of 16.0. The design was developed by trading off aftbody external drag with nozzle flow angularity and underexpansion losses for various flap lengths and expansion ratios. For the selected flap length, an expansion ratio of 2.0 was found to be optimum. This configuration results in an aftbody thrust-minus-drag coefficient which is estimated to be approximately one percent larger than that for the basic design. This performance increase is, of course, obtained at the expense of some increase in nozzle weight since the flap is longer. At the normal power setting, the boattail angle at the nozzle exit is 15 degrees, as compared with 24 degrees for the basic design. Both the maximum A/B and normal power setting of this alternate configuration were modeled and tested.

The alternate CD ejector nozzle design is shorter than the basic design and has a larger shroud exit to primary throat area ratio at the normal power position (1.776 as compared to 1.506). This increased area ratio doubles the secondary mass flow which the nozzle will pump at normal power conditions for a secondary to primary total pressure ratio of 0.25. The length of the alternate shroud was selected such that, at the maximum A/B area ratio of 2.14, an internal shroud angle of 15 degrees was obtained. The 15 degree internal angle was considered to be the maximum allowable to avoid excessive divergence losses. Only the normal power position of this alternate design was modeled and included in the test program. At the maximum A/B position this nozzle does not have secondary flow, and is reasonably close to the alternate CD configuration.

Two variations to the basic unshrouded plug nozzle design were selected. The variations consist of (1) a 10-degree truncated conical plug (Plug B) which is installed with the basic cowl flap design (Cowl A), and (2) a truncated 15-degree conical plug with a reduced diameter (Plug C) which is installed with a lengthened cowl flap design (Cowl B). Both plugs are truncated at 50 percent of the full cone length. Flap positions corresponding to normal, part A/B, and maximum A/B power settings were fabricated for the basic cowl flap design (Cowl A). For the lengthened cowl flap design (Cowl B), flap positions corresponding to normal and maximum A/B power settings were fabricated. Thus, a total of eight unshrouded plug configurations was available for test.

The design variations described above are oriented toward improved nozzle performance at Mach 0.9. For example, as reported in Reference 8, reducing the plug cone angle from 15 degrees to 10 degrees increases the nozzle thrust coefficient by about 1.5 percent at Mach 0.9. (Further, for the same plug cross-sectional area at the throat, the 10 degree plug yields a larger plume diameter immediately downstream of the boattail, and thus may result in more favorable interference effects). Elimination of plug truncation would increase the thrust coefficient about one percent at Mach 0.9; however, it appears that this gain would be just about offset by the weight increase. Also, additional truncation does not appear justifiable since Reference 9 shows about a three percent loss in thrust coefficient for truncation at 30 percent cone length.

Since the basic unshrouded nozzle design is operating highly overexpanded at Mach 0.9, an increased thrust coefficient can be realized by reducing the nozzle expansion ratio. The second design variation is based on this premise and was developed by lengthening the basic flap design (normal power setting) along the mean boattail angle of 14 degrees until an expansion ratio of 1.8 was achieved. This expansion ratio value is approximately midway between the 2.38 expansion ratio for the basic design and the ideal expansion ratio of 1.2 based on the pressure ratio of 4.0 for the Mach 0.9 normal power setting. Although this design variation increases cowl flap weight and boattail projected area, the plug weight is significantly reduced. At the maximum afterburning flap position, this design variation results in an expansion ratio of 1.5, as compared with a value of 1.67 for the basic design.

As with the alternate CD design, the alternate shrouded plug nozzle configuration was designed to maximize the aftbody thrust-minus-drag at Mach 2.5 for a nozzle pressure ratio of 16.0. The design was developed by trading off external boattail drag with flow angularity losses, underexpansion losses, and external plug thrust forces for various cowl flap lengths and exit diameters. The aftbody thrust-minus-drag coefficient is maximized by rotating the basic cowl flap design outward from an exit radius of 20.485 inches to a radius of 22.0 inches. With the plug positioned for maximum A/B operation, the nozzle internal expansion ratios corresponding to the above exit radii are 1.252 and 1.527, respectively.

Nozzle Model Diagrams - Diagrams of all 29 nozzle models (directly scaled from detailed model design drawings) are shown in Figure 8. Only reference model stations and diameters are provided. At the customer connect point (M.S. 138.57), the nozzle external diameter is 8 inches.

2.1.3 Instrumentation and Calibration

A description of the force, pressure, and temperature instrumentation used to measure the flow properties within the flow meters and model is presented in this section. Also, the results from the balance, flow tube, and flow meter calibration tests are summarized.

2.1.3.1 Force Balance Description and Calibration

Three individual force measuring balances were utilized during the test, a thrust balance and two cylindrical drag balances. Duplicates of each balance were fabricated to be used in the event of a primary balance failure.

The six-component thrust balance measures the nozzle internal thrust minus the nozzle external boattail and base drag. The nozzle airflow is routed radially inward into the balance and exits axially. The cylindrical drag balances are used to measure the external pod aftbody and nozzle boattail drags separately. All three balances use metal bellows to seal the gap between the metric and non-metric balance segments.

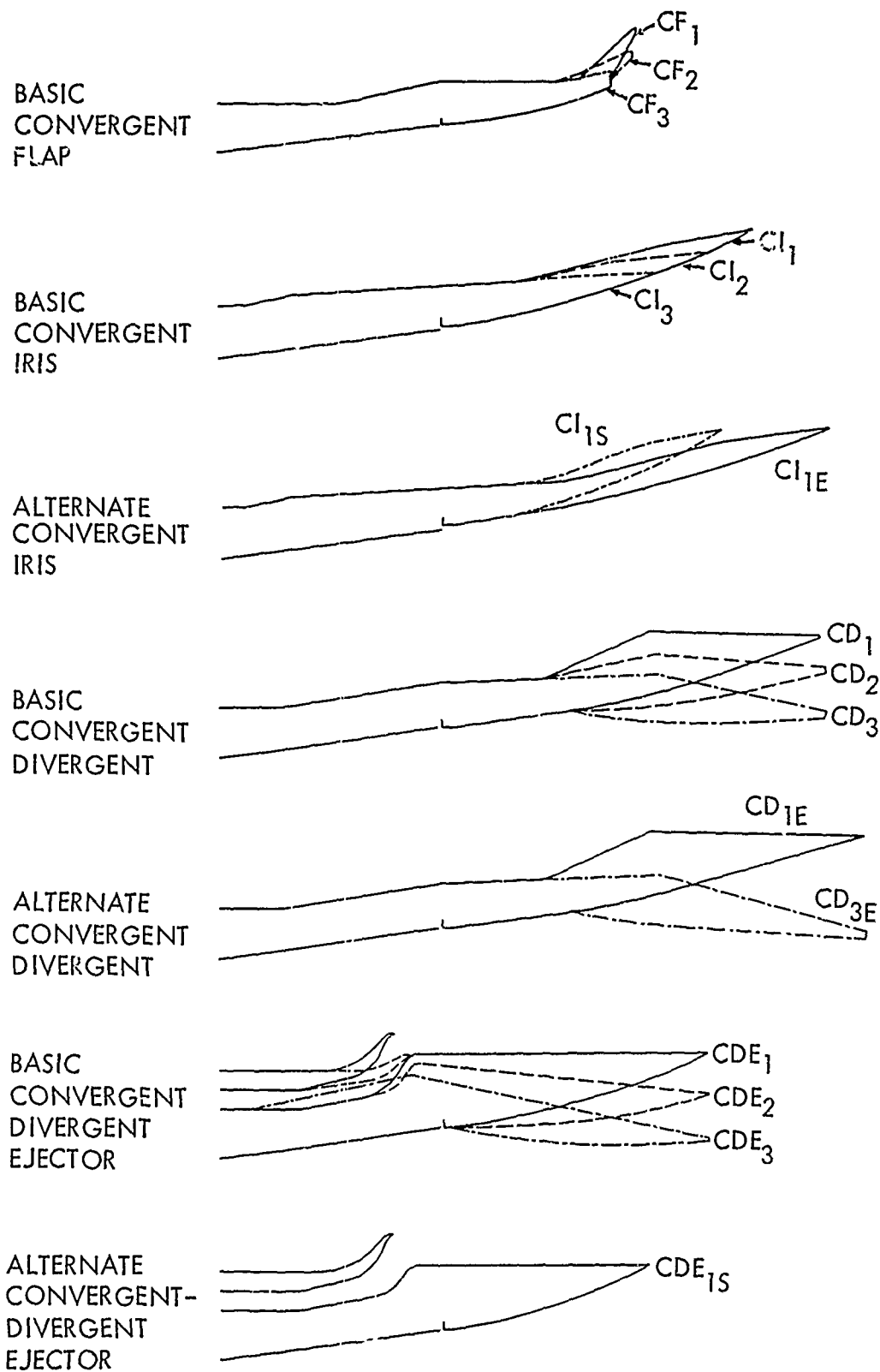
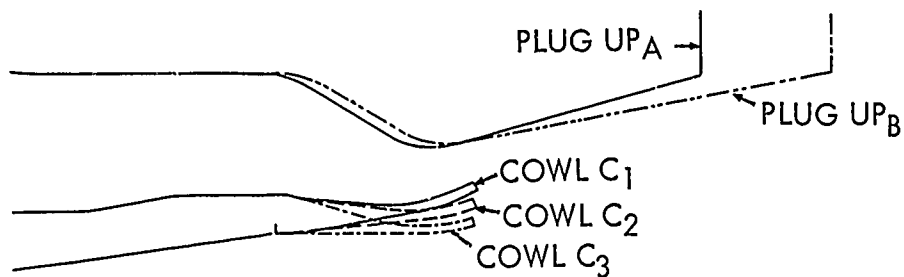
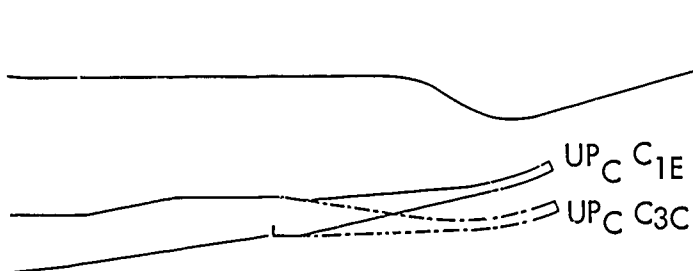


Figure 8. Model Nozzle Designs (Sheet 1 of 2)

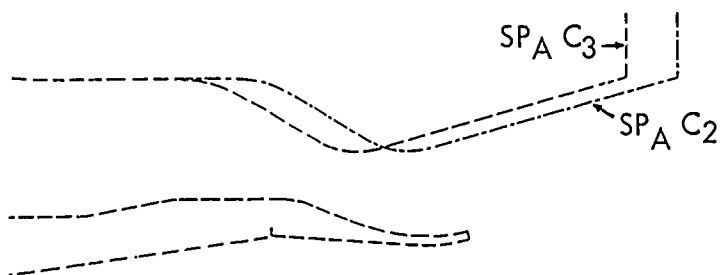
BASIC
UNSHROUDED
PLUG



ALTERNATE
UNSHROUDED
PLUG



BASIC
SHROUDED
PLUG



ALTERNATE
SHROUDED
PLUG

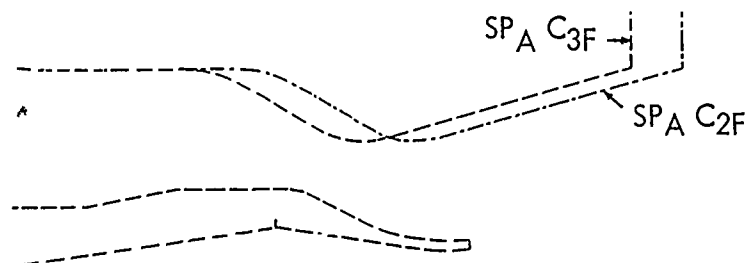


Figure 8. Model Nozzle Designs (Sheet 2 of 2)

The thrust balances used for the 16T and 16S tunnel entries were designed to withstand axial forces of 4000 and 2200 pounds, respectively. The axial force correction required due to internal pressure forces on the 4,000 pound balance was as large as 15 percent of the indicated axial force. To reduce the magnitude of this correction, four nozzles were installed within the 2200 pound balance to cause the incoming air to enter the metric sleeve more nearly perpendicular to its longitudinal axis and thereby substantially reduce the axial component of the entering stream momentum. This reduced the correction to less than 6 percent of the indicated load. The maximum load measured by these balances was approximately 2200 pounds.

Each thrust balance was subjected to a dead weight and flow-through calibration. From a six-component dead weight loading, a 6 by 6 calibration coefficient matrix was established, from which all balance-measured forces and moments were derived. For this application, the axial force was the component of primary interest; consequently, the other five components were loaded principally to establish interaction corrections for the axial force. Results of the calibration showed that no interaction was more than four percent of the primary axial component. Laboratory calibrations of both thrust balances indicated an accuracy in axial force of approximately 0.25 percent of design load.

The flow-through calibration of the thrust balance provides data to correct for the forces acting on the bellows seal and for the momentum of the air-stream entering the nozzle. This correction was developed as a function of the differential pressure across the bellows seal and the airflow rate. The flow-through calibration was done with a "zero thrust" nozzle attached to the thrust balance. The "zero thrust" nozzle consists of a plenum with two nozzles which exhaust the air in opposite directions perpendicular to the balance centerline. Four sets of nozzles with different exit areas were used to obtain airflow data at various internal pressure levels.

The design load for all cylindrical drag balances was 150 pounds. Although the maximum measured axial force estimated for these balances was 40 pounds, the 150 pound design load requirement was dictated by safety factor requirements, tunnel unstart possibilities, and tunnel dynamic conditions.

For the aftbody and boattail balances, a dead weight calibration and an internal pressure versus axial force calibration were performed. The dead weight calibration of electrical readout as a function of applied positive axial force showed that the possible error is within a maximum deviation of 0.10 and 0.30 percent of applied load for the aftbody and boattail balances, respectively. The coefficients in the calibration matrixes for calculation of axial force measured by these balances indicate the interaction terms are less than three percent of the primary component. The internal pressure calibration is required to determine the effective area of the balance bellows. This area is necessary to correct for any differential pressure across the bellows under running conditions.

2.1.3.2 Pressure and Temperature Instrumentation

Rows of static pressure tubes were located along the nose, centerbody, aftbody, and nozzle boattail at positions of 0 (top), 45, 90 (side), 135, 180 (bottom), and 270 degrees. Since these nozzles were also to be tested in the Twin-Nozzle/Aftbody Investigation, a greater concentration of tubes (45 and 135 degree positions) was placed on that portion of the boattail surface which was to be closest to the adjacent twin nozzle. The internal pressure instrumentation consisted of static pressure taps in the flow tube at and near the plane of the total pressure rake and along the nozzle surface. The number and location of the static pressure tubes are indicated in Table 2. Specific longitudinal locations, angle orientations, and orifice identifications of all model internal and external static pressure instrumentation are provided in Reference 10.

Total pressure distributions were obtained near the external model surface immediately upstream of the aftbody at 0, 90, and 180 degrees. Each total pressure rake had 12 probes. Internal total pressure surveys were made in the flow tube and at the convergent-divergent ejector nozzle exit. A 10-tube rake was located in the flow tube at a circumferential station of 180 degrees. The nozzle exit rakes were at 0 and 180 degrees and each rake had 9 tubes. Probe identifications and heights from surface are presented in Reference 10.

Pressures necessary to calculate nozzle performance parameters including pressure forces were measured on scanivalves during the first entry in the 16T tunnel and on P^2B 's for the remaining tests in the 16T and 16S tunnels. A reference pressure system provided two known pressures to each scanivalve for the determination of the transducer calibration constants. The accuracy of the scanivalve measured pressures is estimated to be ± 0.09 psia. This estimate takes into consideration the scanivalve transducer temperature and vibration environment, the low signal to the electrical noise ratio for the lower pressure measurements, and the absence of a pneumatic filter system (plenum) in the pressure leads from the model orifices to the scanivalves.

A known reference pressure was required for each P^2B , since these instruments are differential pressure measuring devices. Three reference pressures were required due to the limited range of the P^2B 's and the wide range of model pressures. The P^2B 's were calibrated prior to each running shift. Since they were contained in a controlled environment cabinet, these calibration constants were used to reduce the data to absolute pressures for all data points obtained during the shift. Based on multiple pressure measurements at the same model station and data repeatability, the accuracy of pressures measured by the P^2B 's is estimated to ± 0.02 psia.

Model airflow total temperatures were measured in the flow tube and at each airflow metering station.

TABLE 2. NUMBER AND LOCATION OF MODEL STATIC PRESSURE TUBES

Model Component	Circumferential Station								Pressure Tube Total
	0	45	90	135	180	225	270	315	
External									
Nose	6		1		2		1		10
Centerbody	2				2				4
Aftbody	8		4		8		3		23
Nozzle Boattail									
*CF	5-6	4	5-6	4	5-6		5-6		28-32
*CI	6-8	3-4	6-8	3-4	6-8		6-8		30-40
CD	9	5	9	5	9		9		46
CDE	9	5	9	5	9		9		46
UP	5	2	5	2	5		5		24
SP	5	2	5	2	5		5		24
Internal									
Flow Tube		3		1		3		1	8
Nozzles									
CF		6				6			12
CI		6-8				6-8			12-16
CD		12				12			24
CDE		12				12			24
UP ~ cowl		5		4		6			15
UP ~ plug	4	8	4	8	4	6	4		38
SP ~ cowl		5		4		6			15
SP ~ plug	4	8	4	8	4	6	4		38

*Maximum and minimum values correspond to normal and max A/B configurations, respectively.

2.1.3.4 Flow Tube Calibration

Prior to the isolated nozzle tests, convergent flap nozzle configurations (CF₁ and CF₃) were assembled with the thrust balance and single flow tube and tested at Calac to determine (1) choke plate effectiveness, (2) adequacy of the nozzle without excessive system pressures, (3) proper function of the nozzle thrust balance and (4) flow tube total and static pressure distributions. A similar test was conducted using the ejector nozzle configurations (CDE₁ and CDE₂) and the primary-secondary flow tube to evaluate (1) operation of the secondary airflow control valve, (2) total and static pressure distributions of the primary and secondary airflows, (3) maximum secondary airflow rate, (4) secondary airflow rate calibration, and (5) effectiveness of the choke plates. These tests indicated satisfactory performance of all components.

2.1.3.5 Flow Meter Description and Calibration

Two orifice plates were installed in series in a 5 inch diameter pipe. In order to measure the full range of flow rates from 0.2 to 60 lb/sec the upstream and downstream orifice diameters were 2.75 and 3.375 inches, respectively. The system was calibrated at Calac using venturi meters which had been calibrated at CEESI (Colorado Engineering Experimental Station, Inc.).

The venturi meters were designed in accordance with procedures outlined in Reference 11 and had diameters of 1.998 and 1.499 inches for the 16T and 16S tests, respectively. Both venturi meters were calibrated at CEESI and had discharge coefficients with accuracies of 0.1 percent. Including the accuracy of the pressure and temperature instrumentation used with the venturi meters, the overall accuracy of the flow measurement is estimated to be ± 0.3 percent.

A Swirlmeter, manufactured by the Fischer and Porter Company, was used in series with the venturi and small orifice plate during the 16S tests. The stated accuracy of this device is ± 0.75 percent of actual flow rate. A check calibration against a venturi meter at AEDC yielded an accuracy of $+0.8$ percent to -0.6 percent of the measured venturi mass flow over a range of flow rates from 2 to 10 lb/sec. During actual testing, the average difference between Swirlmeter and venturi meter indications was 0.2 percent.

2.1.4 Data Reduction

Isolated nozzle test data were reduced using computer programs developed by AEDC for on-site operation and by Calac for off-site operation. The on-site program handled all data reduction calculations which could be performed either during or immediately after the tests. After review and correction of the nozzle pressure data, the off-site program was used to calculate the remaining performance parameters. More specifically, the nozzle thrust, nozzle boattail drag, and aftbody drag were calculated from force balance data using the on-site program and from pressure/area integrated forces plus calculated skin friction drag using the off-site program. A description of the two programs is given below.

2.1.4.1 On-Site Data Reduction Program

On-site data reduction results were printed in tabular form and displayed on a cathode ray tube (CRT) in plotted form during the tests. More comprehensive printed plots of the data were prepared subsequent to the tests. Included in the tabulated (on-line) data were the tunnel properties, model pressures and temperatures, flow meter pressures and temperatures, balance forces and moments, and nozzle performance parameters calculated from force balance data. Both the on-line and off-line plotted data included pressure distributions along the external pod, nozzle boattail, internal nozzle shroud and plug, flow tube total pressure profiles, and various nozzle performance parameters, plotted as a functions of either angle of attack or nozzle pressure ratio.

The more important performance parameters calculated by the on-site data reduction program were nozzle discharge coefficient, nozzle thrust-minus-drag coefficient, nozzle boattail and base drag coefficients, and aftbody boattail and base drag coefficients. The data reduction procedures used to calculate these parameters are summarized below.

Nozzle Discharge Coefficient - The nozzle discharge coefficient is defined as the ratio of actual to ideal primary mass flow rate. The actual primary flow rate is defined as the measured flow for single-flow nozzles and for ejector nozzles as the total measured flow rate (primary plus secondary) less the computed secondary flow rate. The ideal primary mass flow is based on one-dimensional, sonic flow at the nozzle throat. The throat area used in the calculation is the minimum physical area measured within the nozzle.

Nozzle Thrust-Minus-Drag Coefficient - The nozzle thrust-minus-drag coefficient is equal to the thrust minus the nozzle boattail and base drag normalized with the ideal gross thrust based on actual primary and secondary mass flows and isentropic expansion of the flow to ambient pressure. The thrust-minus-drag force is obtained by adjusting the axial force indicated by the thrust-balance for the cavity force and the axial components of the pressure forces and momentum of the incoming flow.

Nozzle Boattail and Base Drag Coefficients - The nozzle boattail drag coefficient is the drag exerted on the boattail surface normalized with the tunnel incompressible dynamic head and nozzle maximum cross-sectional area. The nozzle boattail drag is obtained by adjusting the boattail balance axial force for the cavity forces. The nozzle base drag is calculated from the boattail balance cavity pressure and nozzle base area.

Pod Aftbody and Base Drag Coefficients - The pod aftbody boattail drag coefficient is the drag exerted on the boattail surface normalized with the tunnel incompressible dynamic head and the pod maximum cross-sectional area. The aftbody boattail drag is obtained by adjusting the boattail balance axial force for the cavity forces. The aftbody base drag is calculated from the thrust balance cavity pressure and aftbody base area.

2.1.4.2 Off-Site Data Reduction Program

The off-site data reduction results calculated from surface pressure data and measured boundary layer profiles just upstream of the pod aftbody were obtained primarily for the purpose of validating the performance parameters calculated from force balance data in the on-site data reduction program. The output results from the on-site program were recorded on computer tapes at AEDC and used as input data for the off-site program. Also input to the program were tables of corrected pressure values and nozzle geometric parameters, such as projected areas to be used in pressure/area integrations. The off-site data reduction program calculates pressure/area integrated forces and skin friction drag on the pod aftbody boattail, nozzle boattail, and nozzle internal surfaces. The data reduction procedures used to calculate the more important performance parameters are summarized below. A discussion of the strut induced flow non-uniformity drag increment is also included.

Pod Aftbody and Nozzle Boattail Drag Coefficient - The pod aftbody and nozzle boattail drag coefficients are determined by adding the calculated skin friction drag to the pressure/area integrated forces and normalizing the result with the tunnel incompressible dynamic head and component (aftbody or boattail) maximum cross-sectional area. The skin friction drag coefficient is obtained from the empirical correlations of local skin friction coefficient versus Reynolds number developed by Sivells and Payne (Reference 12) for incompressible turbulent flow over a flat plate with zero pressure gradient. The effect of compressibility is accounted for using the Sommer and Short T' method (Reference 13). The upstream flow properties used to calculate the skin friction drag on the pod aftbody are determined from the boundary layer rake data. The upstream flow properties for the nozzle boattail are the flow properties at the downstream end of the pod aftbody. The initial Reynolds number is obtained from the empirical correlation of Reynolds number versus power law exponent as developed in Reference 14. The power law exponent used in the calculations is the one which yielded a boundary layer displacement thickness most closely agreeing with that calculated from the boundary layer rake data.

Nozzle Thrust Coefficient - The nozzle thrust was obtained by subtracting the pressure and friction forces from the total momentum calculated at the flow tube rake station. The ideal gross thrust and total momentum values were provided by the on-site data reduction program.

The method used for calculating the internal skin friction drag is applicable to convergent and convergent-divergent axisymmetric nozzles. The method was applied to plug nozzles by treating the internal annulus at each station as a circle of equivalent area and extending the shroud horizontally to the exit plane of the plug. Thus the plug nozzle was transformed into an equivalent convergent-divergent nozzle. The secondary flow annulus of the ejector nozzle was treated in a similar manner, and thus was transformed into an equivalent convergent nozzle. Consequently, for CDE nozzles, both the convergent and convergent-divergent options of the internal skin friction routine must be employed.

The procedure for calculating internal skin friction drag (References 15 and 16) involves dividing the duct into a series of cylindrical sections, calculating the pressure loss due to friction for each section, computing the pressure at the beginning of each section by assuming an isentropic compression or expansion, and then determining the friction from the total exit momentum without friction.

Strut Non-Uniformity Drag Increment - The procedure for calculating the decrement in aftbody and nozzle boattail drag resulting from strut-induced flow non-uniformity is as follows. The decrement designated as the strut non-uniformity drag increment, is obtained by calculating the pressure and skin friction drag using all of the external pod aftbody and nozzle pressure tubes and then subtracting the values obtained using only those pressure tubes located at a circumferential station of zero degrees (the strut is located at 180 degrees). It is assumed in this procedure that the pressures measured from tubes located at zero degrees are unaffected by the strut.

2.1.5 Test Description

Two hundred and eighty seven hours of isolated nozzle testing were expended in the AEDC 16T and 16S PWT during the 18 May to 18 August 1970 time period. The test was divided into three tunnel entries - two in 16T (93 and 68 hours) and one in 16S (126 hours). The 16T and 16S portions of the test program are identified by AEDC Project Numbers PTO055-B00 and PTO055-S00 and Test Numbers TF-231 and SF-125, respectively. The following table summarizes the basic testing.

Tunnel	Nozzle Configurations Tested	Mach Number Range	Angle Of Attack Range Degrees	Basic Reynolds Numbers
16T	26	0.6 to 1.6	0 to 12	$2.5 \times 10^6/\text{ft}$
16S	19	1.8 to 3.0	0 to 6	$1.6 \times 10^6/\text{ft}$

Force balance and/or pressure data were obtained for all nozzle configurations at exhaust nozzle total pressure ratios spanning the operation range of a typical advanced technology engine. Reynolds number excursions were made for selected configurations. In addition, boundary layer rake data were obtained on the exterior of the pod aftbody.

2.1.5.1 Test Procedure

For each nozzle configuration, the typical operational procedure was as follows:

1. Obtain static performance at several nozzle total pressure ratios.
2. Establish predetermined tunnel test conditions.

3. Obtain jet-off data.
4. Obtain data at predetermined angles of attack over the required range of nozzle total pressure ratios.
5. Change tunnel test conditions.
6. Repeat steps 3 through 5 for all tunnel test conditions.

Several nozzle configurations were tested each running shift. A typical nozzle configuration change took 30 minutes. During the non-running shift, an installed check calibration of the force balances was performed in addition to a thorough pressure instrumentation leak check.

2.1.5.2 Test Schedule

A run schedule was developed prior to testing for the purpose of indicating the number of configurations, their associated test conditions, and the general sequence in which these configurations should be tested. In addition, an estimate of run time (tunnel start to stop) was made for each set of runs. Since the estimated run time exceeded the scheduled tunnel occupancy hours, the following priority system was established to indicate the relative importance of the information obtained for each configuration.

Priority	Configurations Included
1 (highest)	Force data on basic nozzle configurations
2	Force data on alternate nozzle configurations Boundary layer surveys
3	Reynolds number excursions for basic force and pressure configurations pressure data for basic normal and maximum A/B configurations Effects of boundary layer trip location
4	Exit plane rake data. Reynolds number excursions for basic pressure configurations
5	Pressure data on basic partial A/B configurations Pressure data on alternate nozzle configurations

The idealized run schedule, based on the desirability of the information obtained for each configuration from a data analysis standpoint, was adjusted daily during the test so as to be realistic in terms of tunnel operational requirements. The nozzle configurations tested in the 16T and 16S tunnels are listed in Tables 3 and 4, respectively.

TABLE 3. NOZZLE CONFIGURATIONS TESTED - 16T

Configuration	Model Type	Mach Numbers						
		0.6	0.8	0.9	1.1	1.2	1.4	1.6
CF ₁	P/F	x	x	x				
CF ₃	P/F	x	x	x	x	x	x	x
CI ₁	F	x	x	x				
CI ₁	P	x	x	x				
CI _{1S}	F	x	x	x				
CI _{1E}	F	x	x	x				
CI ₃	F	x		x	x	x	x	x
CI ₃	P	x	x	x	x	x	x	x
CI ₃	B.L. Rake	x	x	x	x	x	x	x
CD ₁	P/F	x	x	x				
CD _{1E}	P/F	x	x	x				
CD ₃	P/F			x	x	x	x	x
CDE ₁	P/F	x	x					
CDE ₁	Exit Rake			x				
UP _A C ₁	F	x	x	x				
UP _A C ₁	P	x	x	x				
UP _B C ₁	F	x	x	x				
UP _C C _{1E}	F	x	x	x				
UP _A C ₃	F	x		x	x	x	x	x
UI _A C ₃	P	x		x	x	x	x	x
UP _B C ₃	F	x		x	x	x	x	\
UP _C C _{3E}	F	x		x	x	x	\	\
SP _A C ₃	F		x	x	x	x	\	\
SP _A C ₃	P				x	\	\	\

TABLE 4. NOZZLE CONFIGURATIONS TESTED - 16s

Configuration	Model Type	Mach Numbers					
		1.8	2.0	2.2	2.5	2.75	3.0
CF ₃	P/F	x	x	x			
CI ₃	P	x	x				
CD ₂	P/F	x	x	x	x		
CD ₃	P/F	x	x	x	x		
CD _{3E}	P/F	x	x	x	x		
CDE ₂	P/F	x	x	x	x		
CDE ₂	Exit Rake	x	x				
CDE ₃	P/F	x	x	x	x		x
UP _A C ₂	F	x	x	x	x		
UP _A C ₂	P	x	x	x	x		
UP _B C ₂	F	x	x	x	x		
UP _A C ₃	F	x	x	x	x		
UP _A C ₃	P	x	x	x	x		
UP _B C ₃	F	x	x	x	x		
UP _B C ₃	P	x	x	x	x		
UP _C C _{3E}	P	x	x	x	x		
SP _A C ₂	F	x	x	x	x		
SP _A C ₂	P	x	x	x	x		
SP _A C ₃	F	x	x	x	x		
SP _A C ₃	P	x	x	x	x	x	

2.2 EXPERIMENTAL RESULTS AND DISCUSSION

The Phase I test data were analyzed to determine of the effects of nozzle type and power setting, angle of attack, Reynolds number and boundary layer trip location, and support strut wake on thrust, drag, and boundary layer total pressure profiles.

2.2.1 Nozzle Type and Power Setting Effects

The effect of nozzle geometry on the total (aftbody-plus-nozzle) drag coefficient and the thrust-minus-total-nozzle-drag coefficient is presented in this section for tunnel Mach numbers of 0.9, 1.2, 1.8, and 2.5. These performance parameters were obtained from force balance data and therefore include both pressure and friction drag components.

2.2.1.1 Total Drag

The effect of nozzle geometry on the total (aftbody-plus-nozzle) drag coefficient is shown in Figures 9 through 12 for Mach numbers of 0.9, 1.2, 1.8, and 2.5, respectively. The total drag at maximum A/B was less than that at normal power for all nozzle configurations due to the generally lower frontal areas of the maximum A/B configurations compared to those of the normal power configurations. The total drag decreased with decreasing mean boattail angle, β , as shown by comparison of the data for CI_{1S} (15 degrees), CI_{1E} (12 degrees), and CI_{1E} (10 degrees) nozzle configurations where the greatest change occurred between the 10 degree and 12 degree boattail angles. The alternate unshrouded plug nozzle has less drag than the corresponding basic configurations for all Mach numbers except Mach 2.5. In general, the plug nozzles had greater subsonic drag, approximately the same transonic drag, and less supersonic drag than the other four nozzle types.

The effects of nozzle pressure ratio on nozzle boattail drag and on aftbody boattail drag are presented in Figures 13 and 14, respectively. The nozzle boattail drag coefficient decreases with increasing pressure ratio, with the largest effect occurring at the lower pressure ratios (generally corresponding to the subsonic freestream Mach numbers). This effect shows up in the aftbody drag coefficient only for maximum A/B at the lowest pressure ratios.

2.2.1.2 Thrust-Minus-Drag Performance

The effect of nozzle geometry on the thrust-minus-total-nozzle-drag coefficient is shown in Figures 15 through 18 for Mach numbers of 0.9, 1.2, 1.8, and 2.5. At Mach 0.9 and a nozzle pressure ratio 4.0, the CD_1 nozzle has not only the lowest drag but the highest thrust. Hence, the CD_1 thrust-minus-nozzle drag is significantly higher than the convergent and plug nozzles. At the supersonic Mach numbers, the convergent-divergent and plug nozzles perform equally well, and both are superior to the convergent nozzles, which have highly underexpanded exhaust streams. The effect of nozzle pressure ratio on thrust coefficient is presented in Figure 19 for normal, part A/B, and

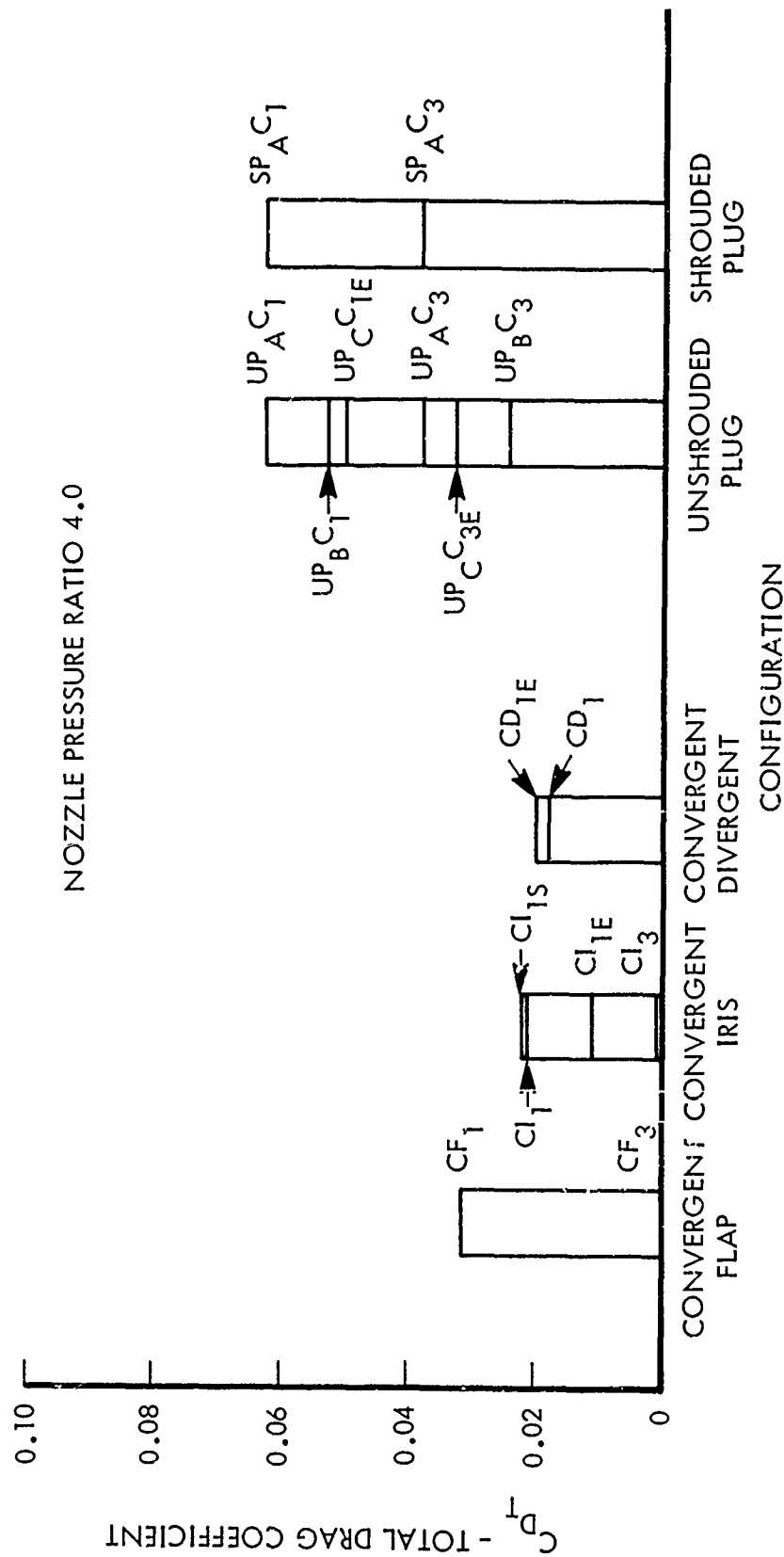


Figure 9. Total Drag Summary Chart - Mach 0.9

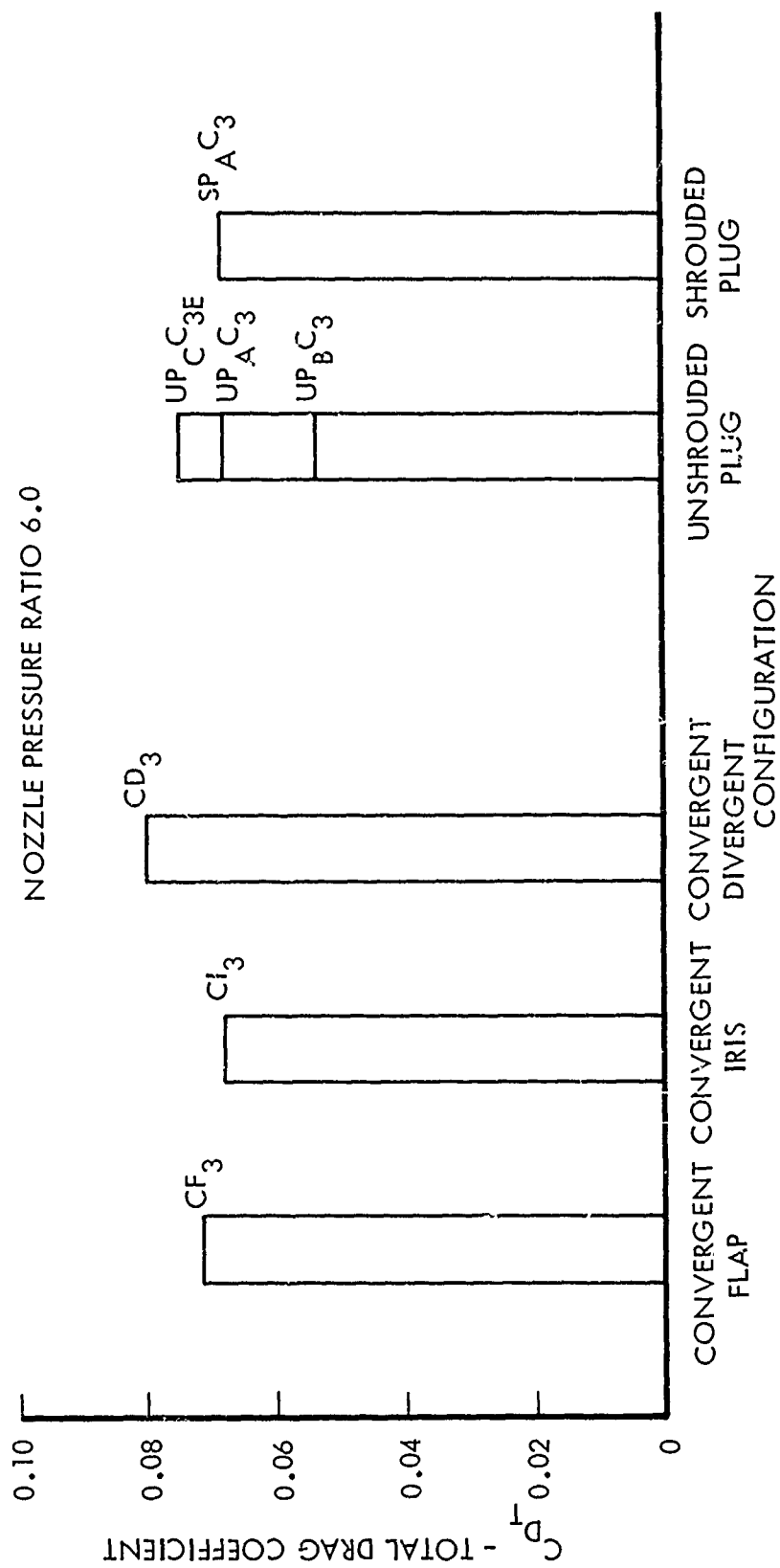


Figure 10. Total Drag Summary Chart - Mach 1.2

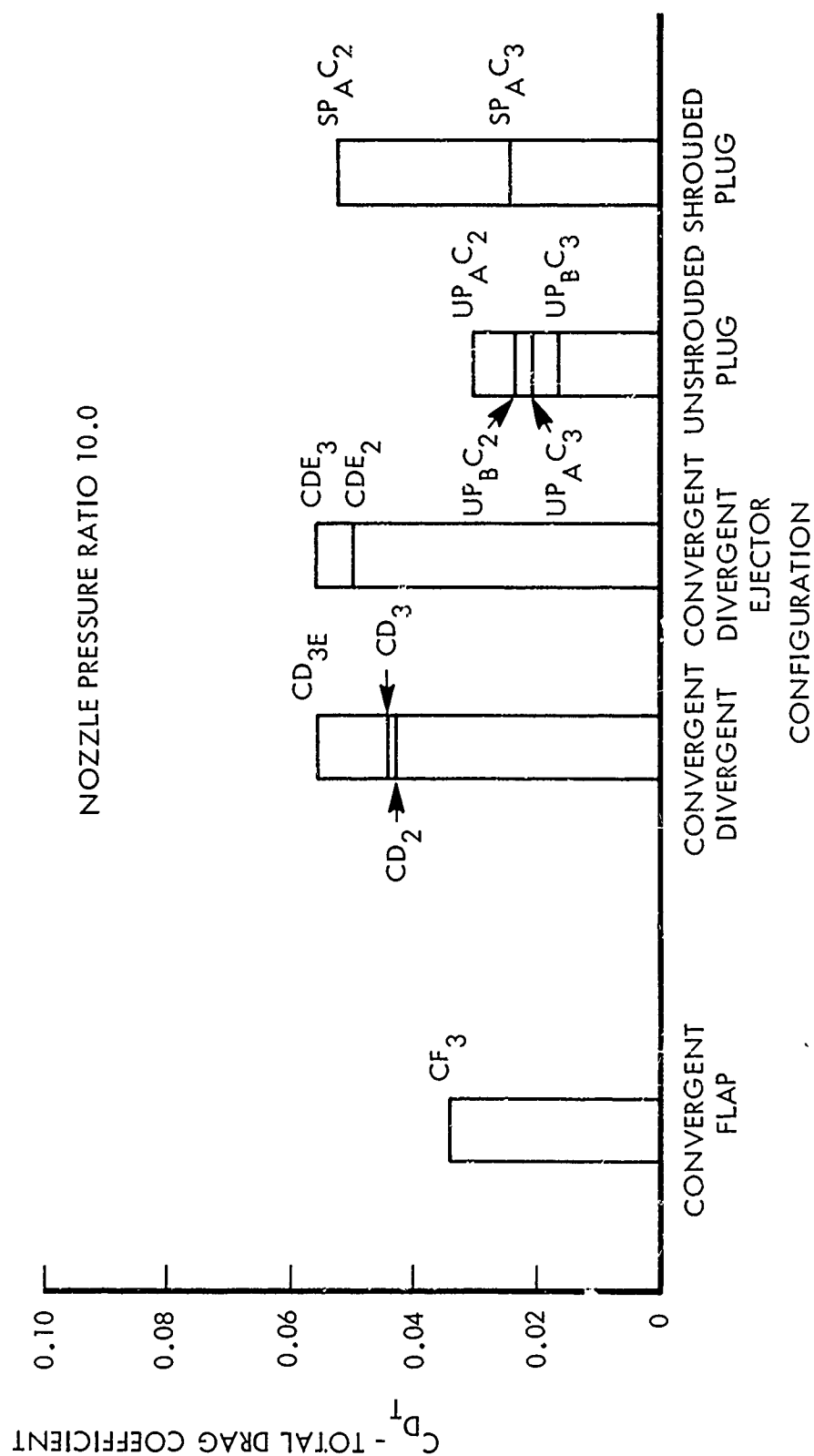


Figure 11. Total Drag Summary Chart - Mach 1.8

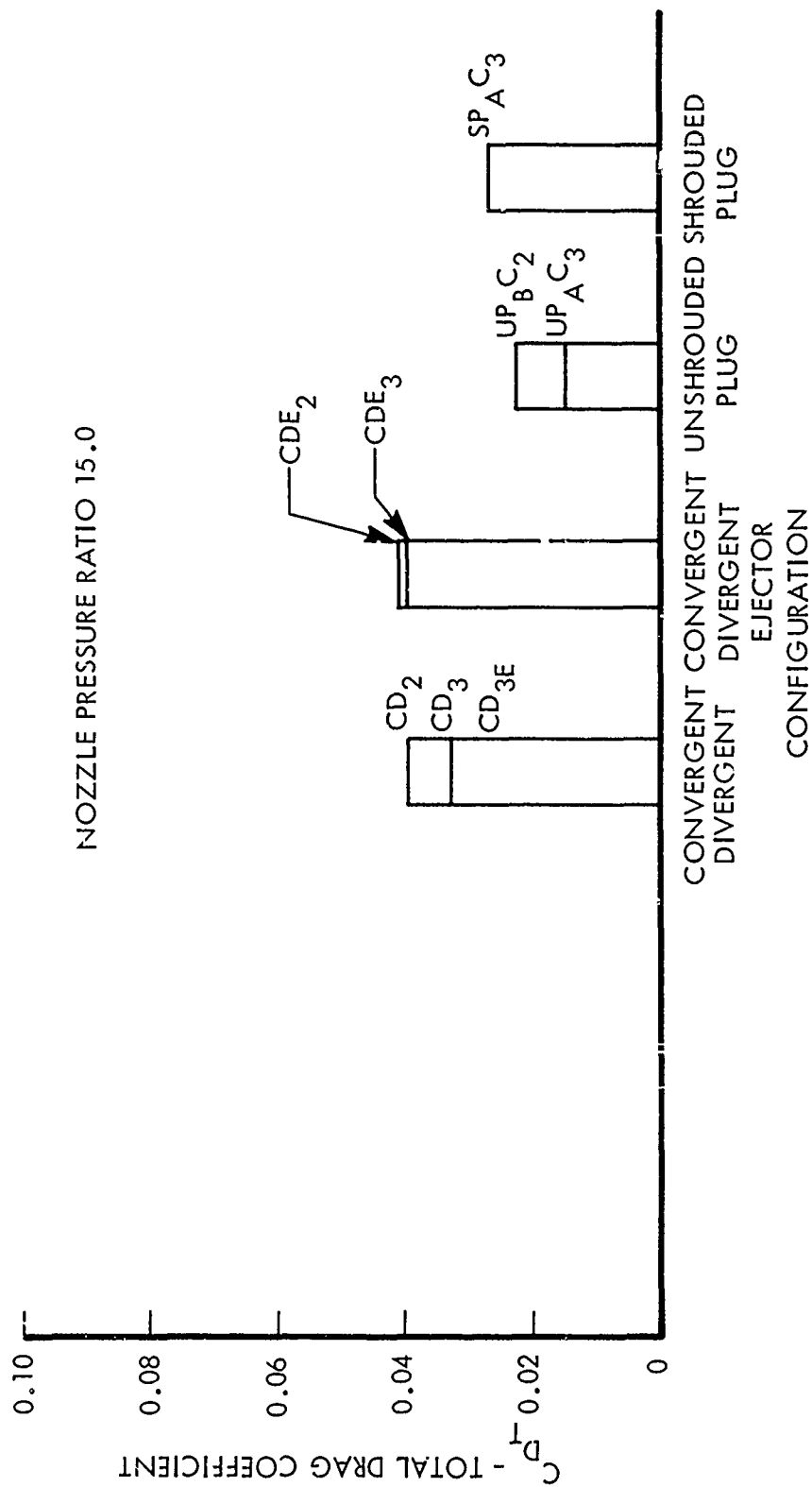


Figure 12. Total Drag Summary Chart - Mach 2.5

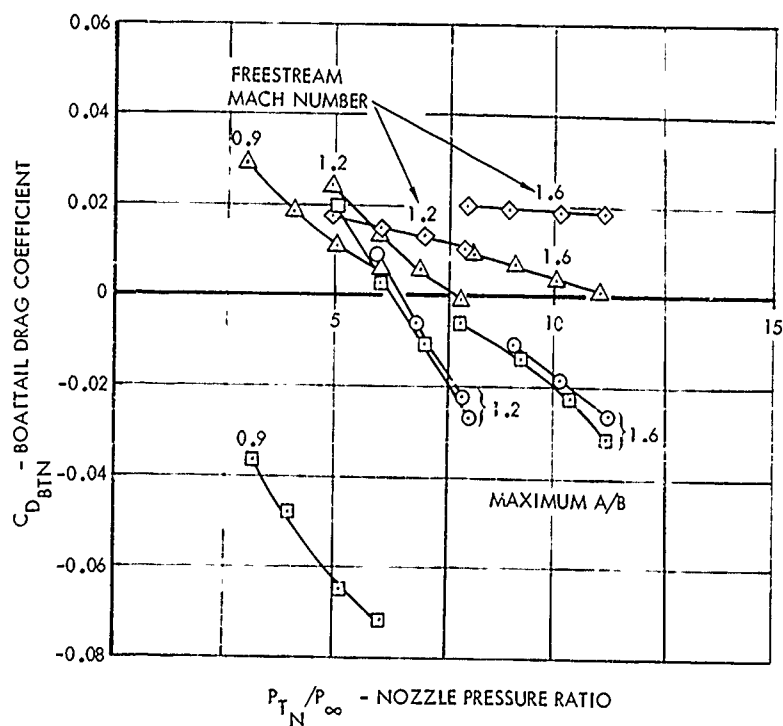
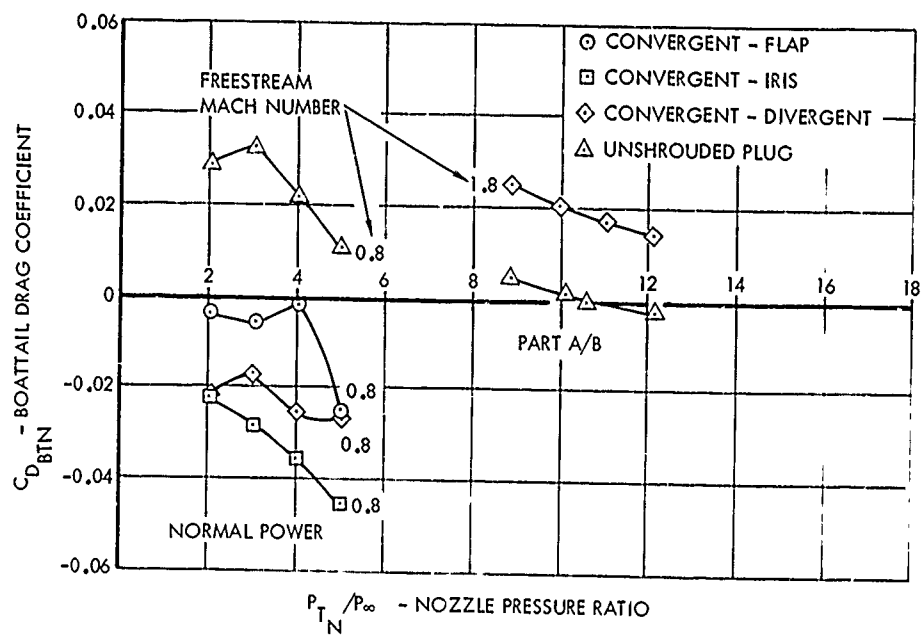


Figure 13. Effect of Nozzle Pressure Ratio On Nozzle Boattail Drag

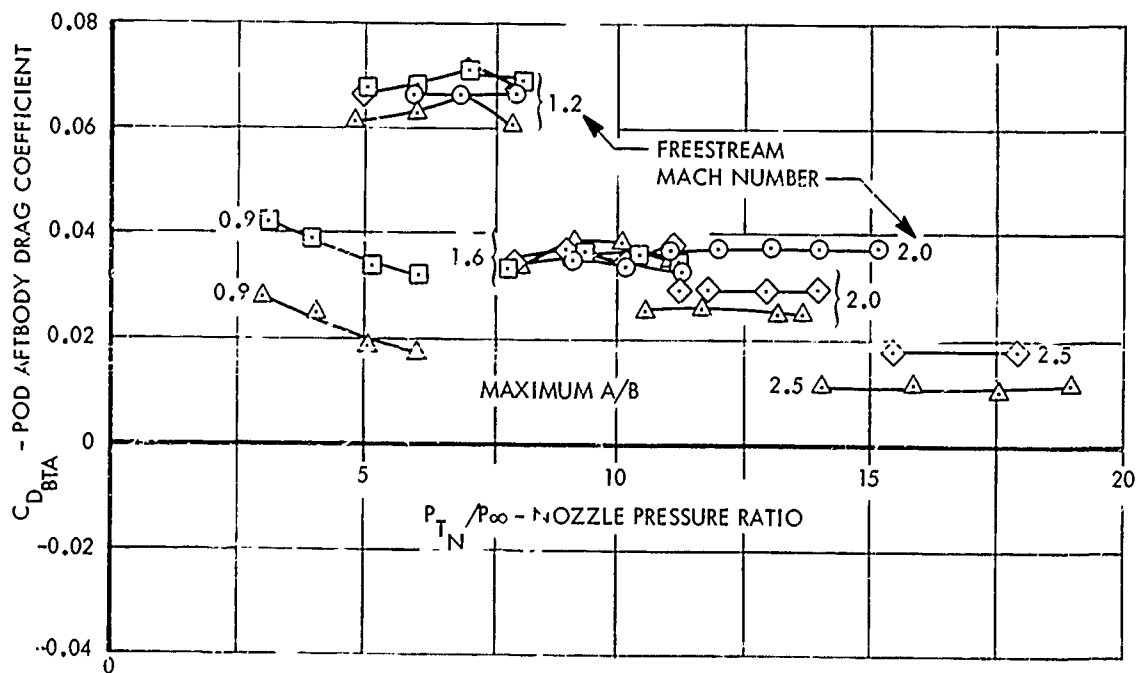
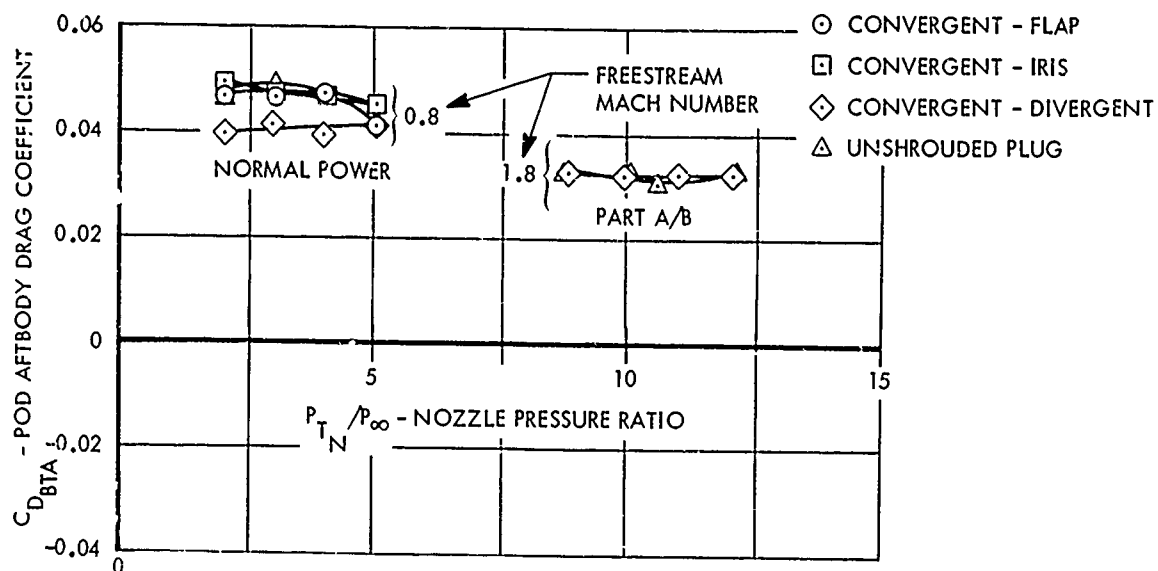


Figure 14. Effect of Nozzle Pressure Ratio On Pod Aftbody Drag

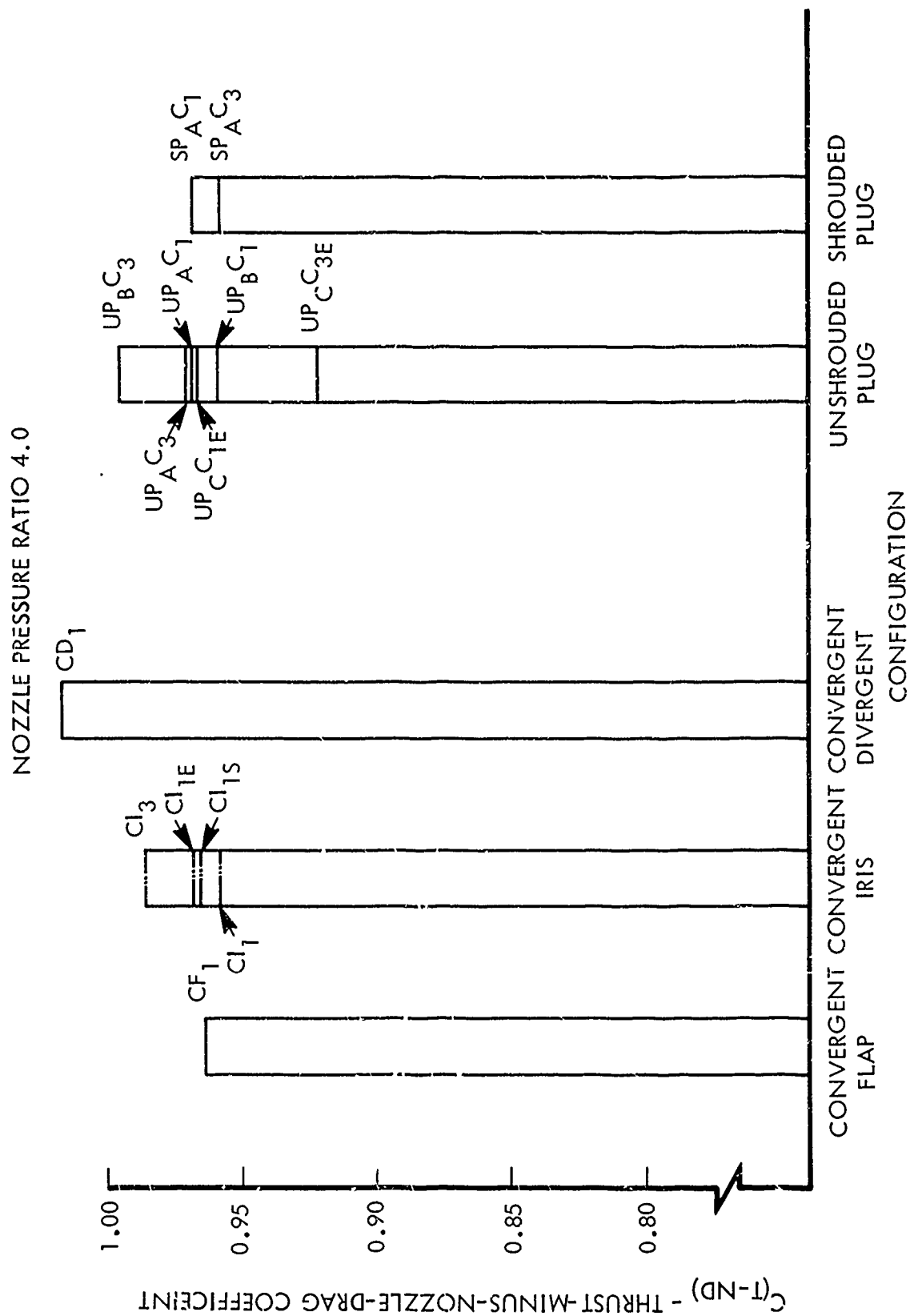


Figure 15. Thrust Minus Total Nozzle Drag Summary
Chart - Mach 0.9

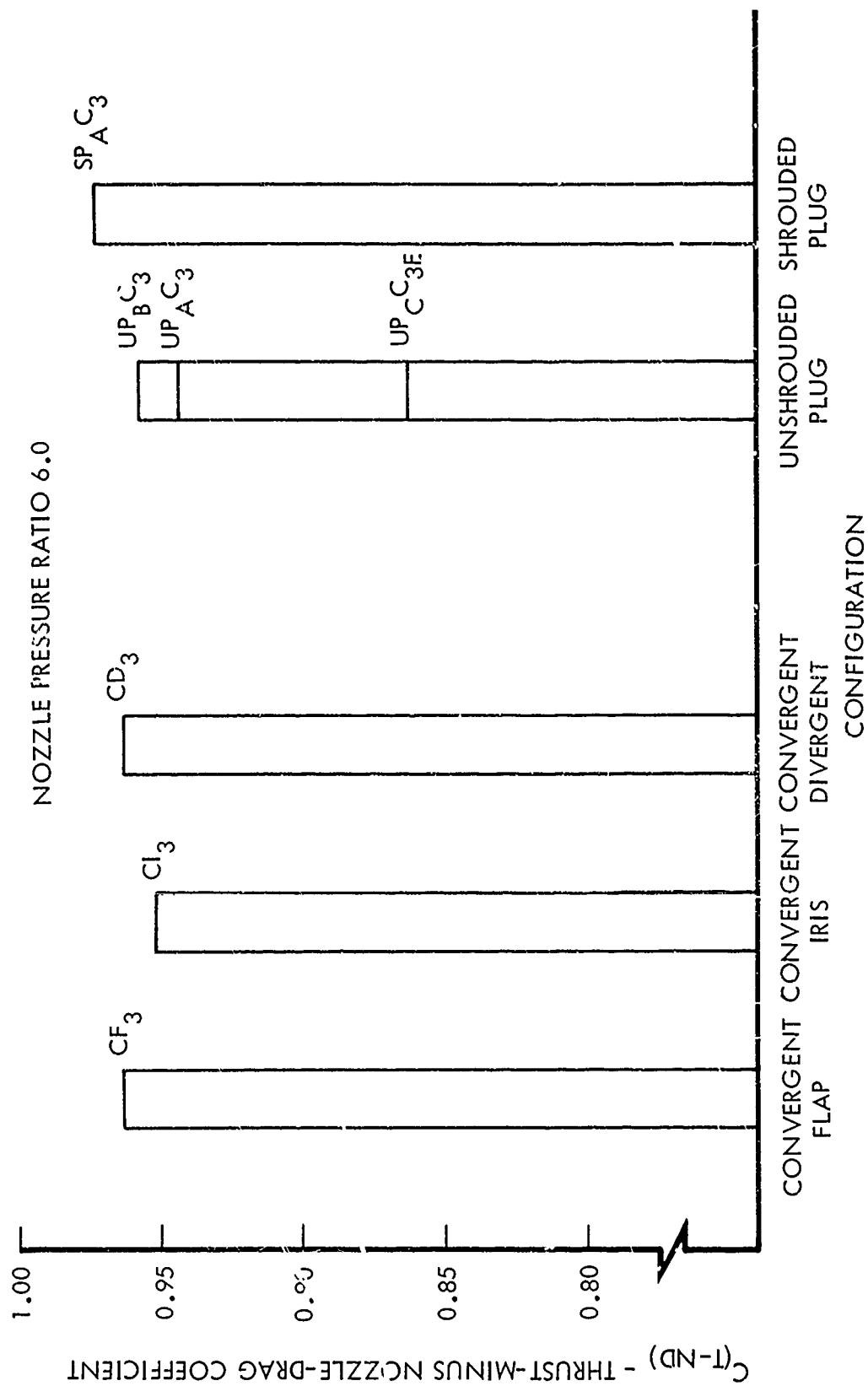


Figure 16. Thrust Minus Total Drag Summary
Chart - Mach 1.2

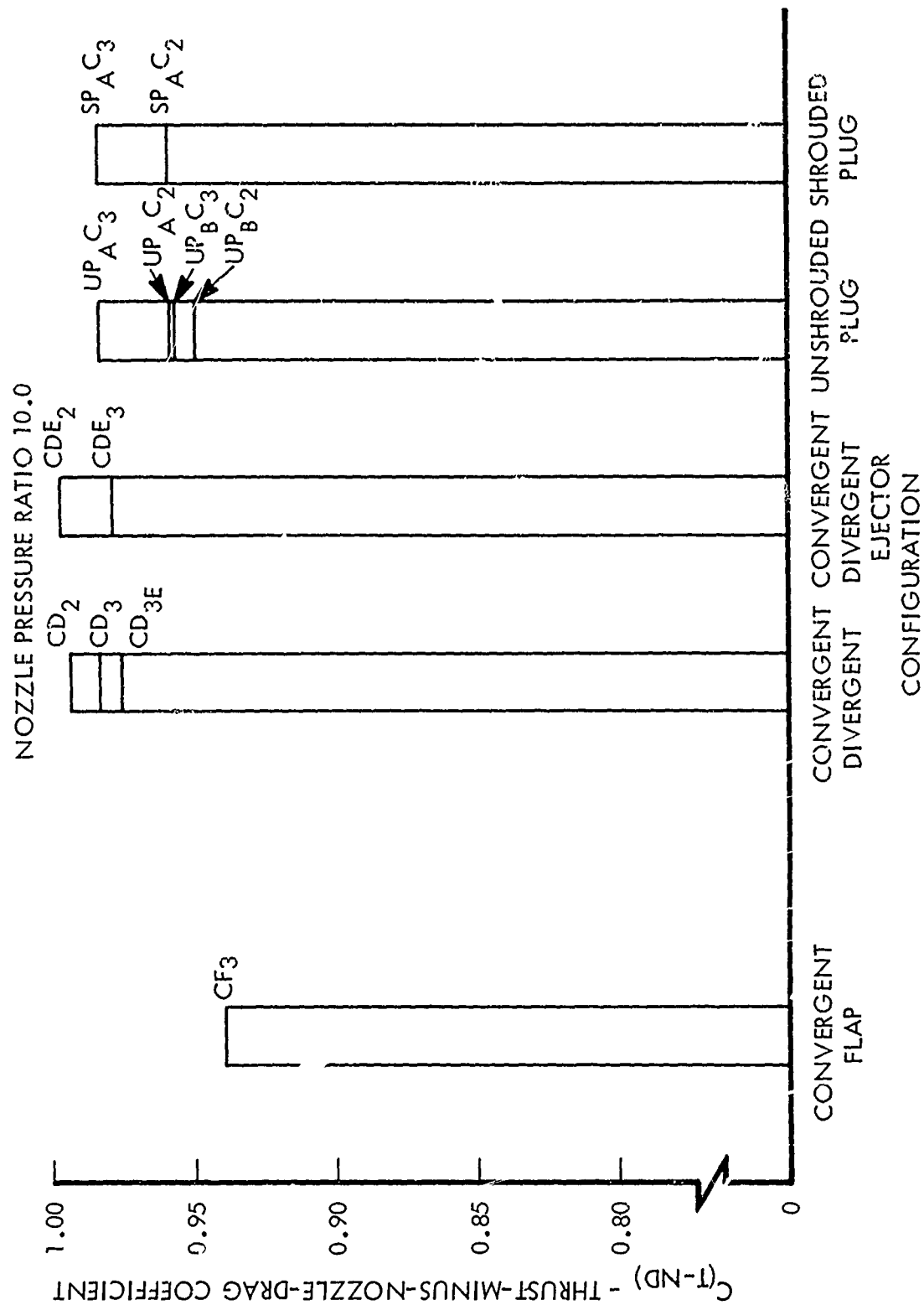


Figure 17. Thrust Minus Total Nozzle Drag
Summary Chart - Mach 1.8

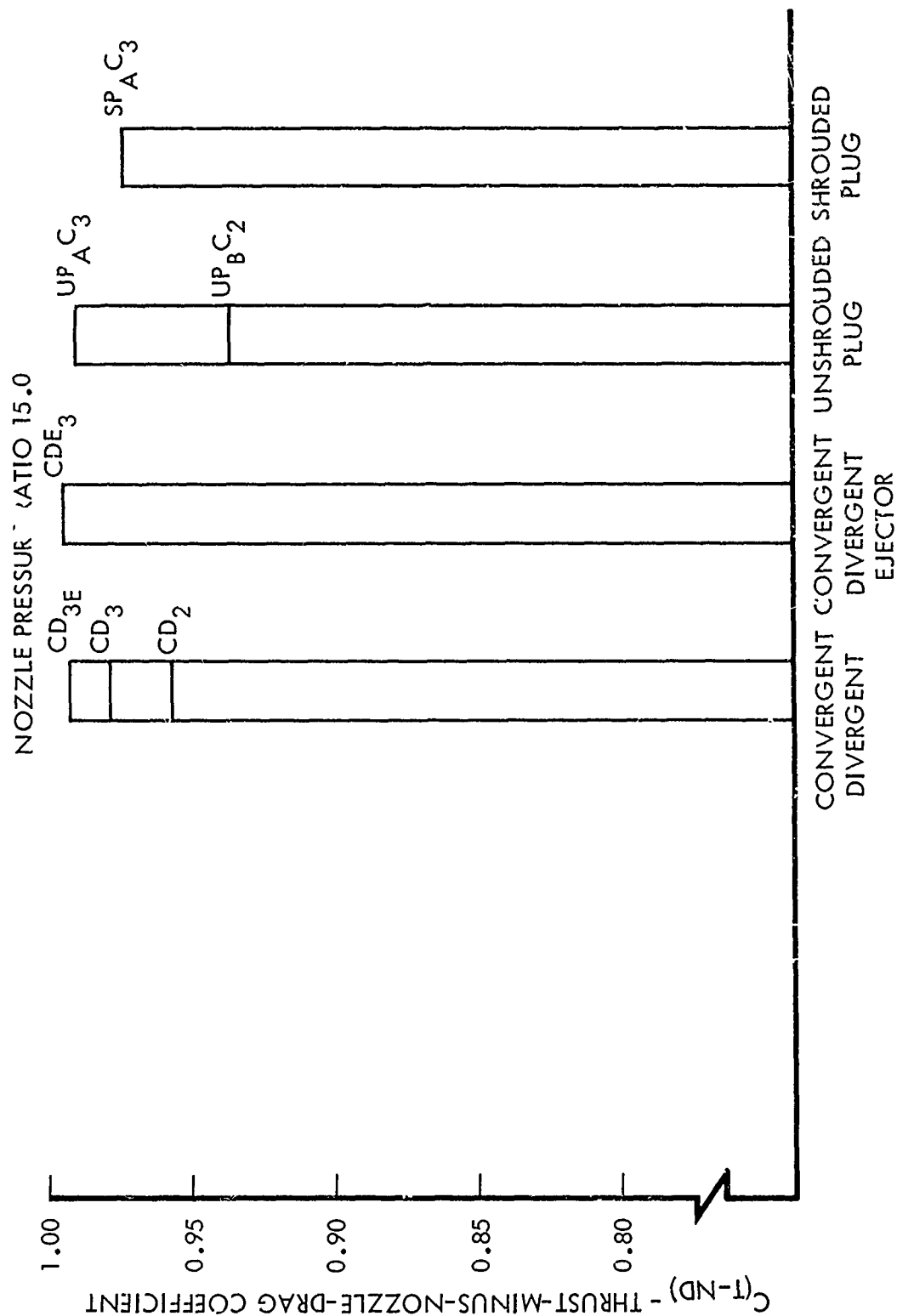


Figure 18. Thrust Minus Total Nozzle Drag
Summary Chart - Mach 2.5

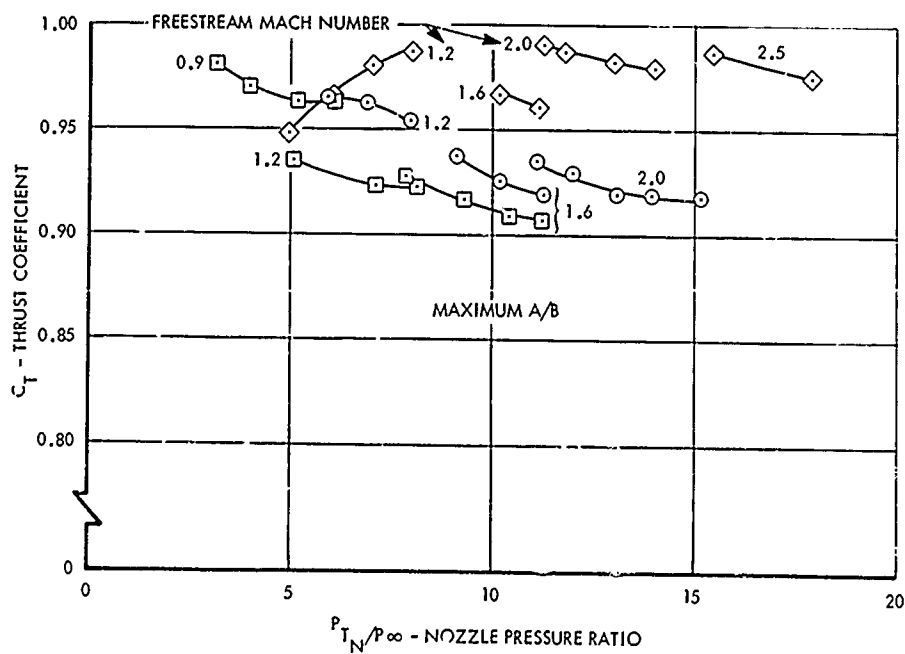
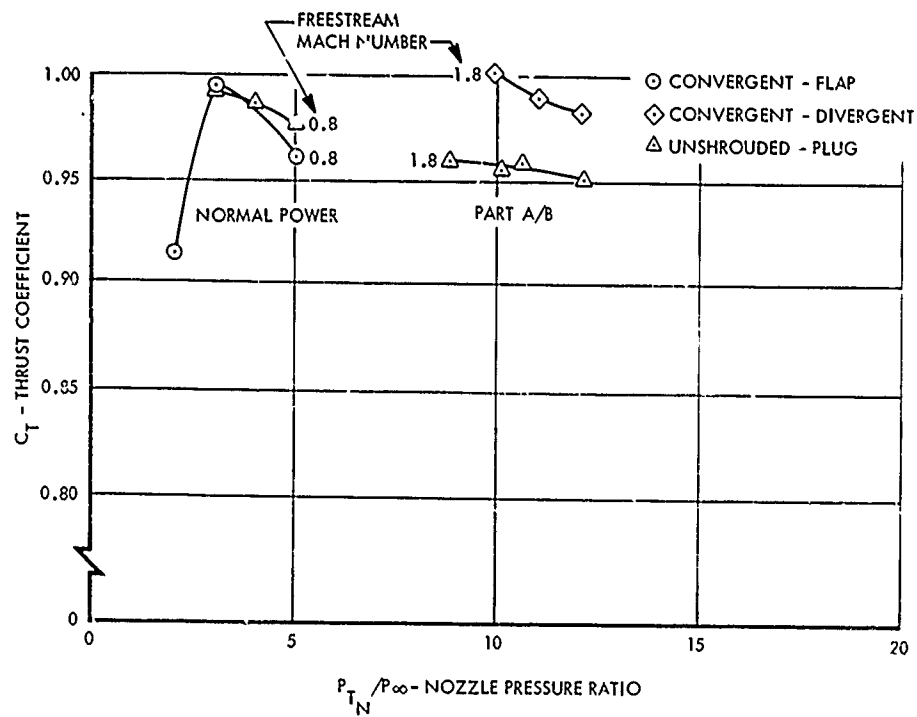


Figure 19. Effect of Nozzle Pressure Ratio on Thrust

Max A/B configurations. The CD nozzle has the highest thrust at the higher pressure ratios (supersonic range, there are too few data points to establish a preference at the lower pressure ratios.

2.2.2 Angle-of-Attack Effects

The effect of angle of attack on the static pressure distribution along the top of the pod aftbody and nozzle boattail has been determined for four nozzle types for both the normal power and maximum A/B configurations. For the convergent-flap nozzle, convergent-iris nozzle, convergent-divergent nozzle, and unshrouded plug nozzle for subsonic flow the pressure decreases on the windward side of the aftbody and boattail as angle of attack is increased. This is consistent with Shrewsbury's test data (Reference 1). For the unshrouded plug at Mach 2.0 and 2.5 an increase in angle of attack appears to retard separation near the end of the boattail, as evidenced by a reduction in pressure near the nozzle exit.

For the same nozzle configurations and test conditions, the angle of attack had little effect on thrust.

Nozzle boattail and aftbody boattail drag coefficients both increase slightly with increasing angle of attack at the subsonic Mach numbers, as shown in Figures 20 and 21. No significant drag variation with angle of attack occurs at supersonic Mach numbers.

The effects on boundary layer total pressure of changing angle of attack from -3 to 12 degrees have been determined from total pressure rake measurements at model station 115.52. At the 0-degree (windward side) and 90-degree rakes, as the angle of attack increases the total pressure in the boundary layer increases, the boundary-layer thickness and displacement thickness decrease, and the form factor increases. The 180-degree rake data show the same trend in the total pressure ratios but not in the boundary layer thickness. The boundary layer thickness at the 180-degree station generally increases and then decreases with increasing angle of attack.

2.2.3 Reynolds Number and Boundary Layer Trip Studies

The effect of Reynolds number on aftbody boattail and nozzle drag coefficients and on boundary layer total pressure profiles at the 0-degree rake is virtually undetectable.

Moving the boundary-layer trips aft from a model station of 12 inches to a model station of 67.2 inches had little effect on the boundary layer thickness, the external static pressure distributions, or the aftbody boattail drag for the range of Mach numbers and Reynolds numbers tested. Moving the boundary-layer trips aft, however, decreased the total pressure ratios in the boundary layer, and this effect became larger with increasing Mach number. It had been intended during the tests to simulate full-scale boundary-layer thickness at the pod aftbody by reducing the tunnel Reynolds number to a value substantially less than the full-scale value and locating the boundary-layer trips at a model station of 67.2 inches. However, it was

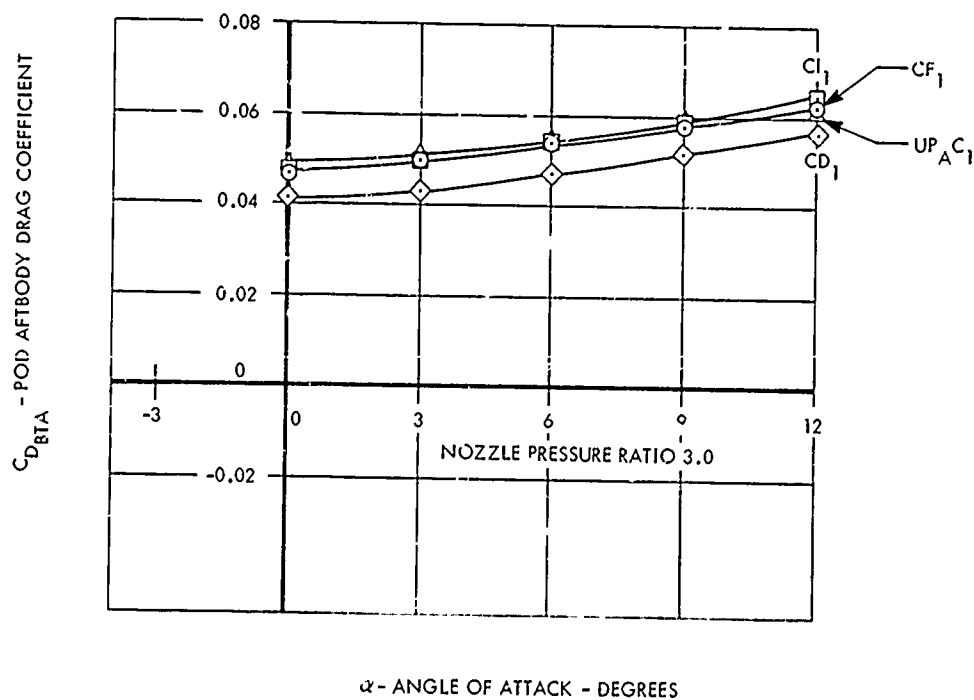
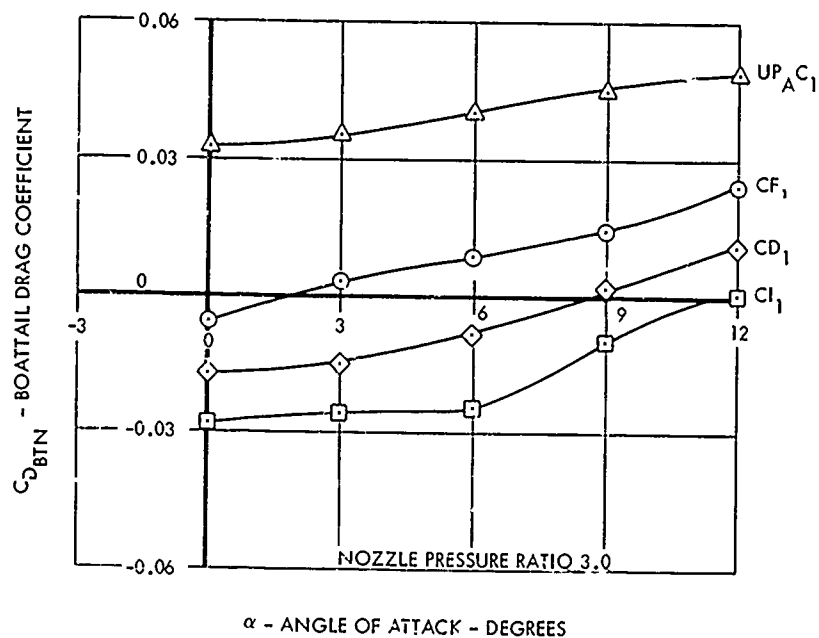


Figure 20. Effect of Angle of Attack on Aftbody/Nozzle Drag for Nozzles at Normal Power - Mach 0.8

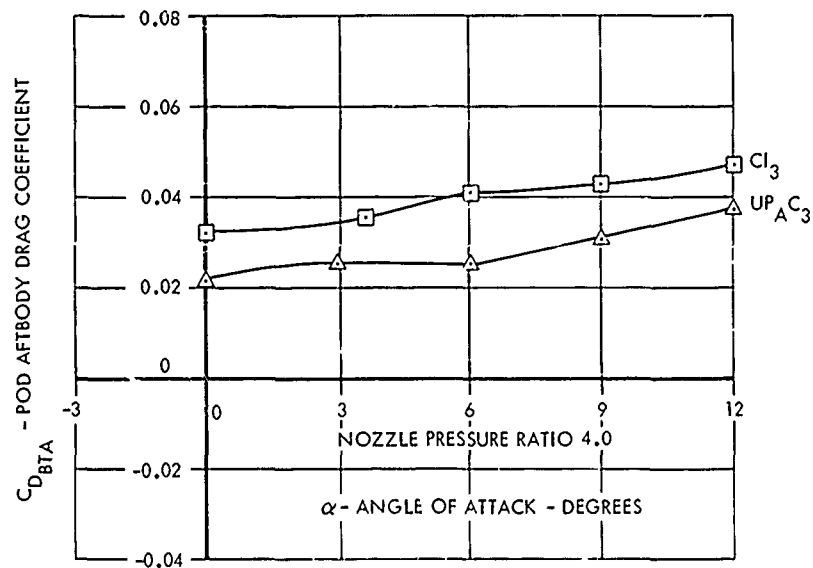
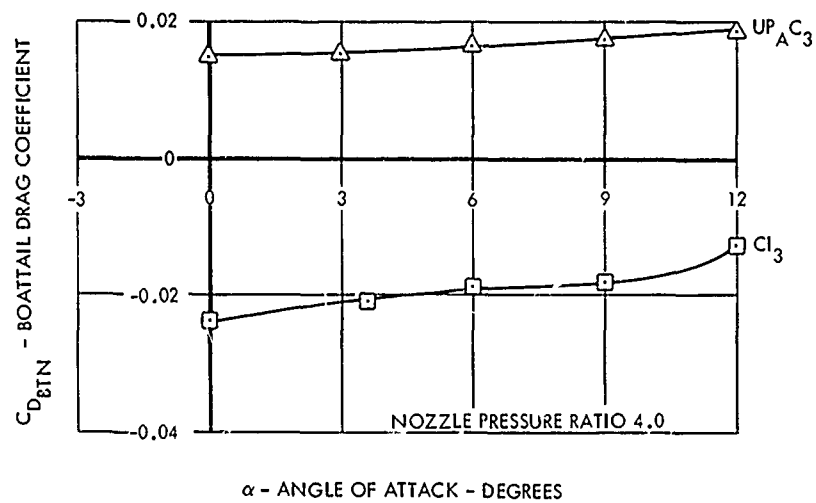


Figure 21. Effect of Angle of Attack on Aftbody/Nozzle Drag for Nozzles at Maximum A/B - Mach 0.6

found that the reduced Reynolds numbers resulted in model forces and pressures which were too low to measure accurately. Therefore, tests were not conducted at Reynolds numbers low enough to simulate the full scale boundary layer. A few tests were made with the boundary-layer trips aft, and the total pressure profiles, external static pressure distributions, and aftbody boat-tail drag with the trips aft were compared with the trips forward, as discussed below.

The effect of the boundary-layer trip location on the aftbody boattail drag coefficient is a slight reduction in drag when the trip is moved from model station 12 inches to station 67.2 inches, as shown in Figure 22. The forward trip data show slightly higher boundary layer total pressure ratios than the aft trip data, and this difference increases with Mach number. For the aft trip location, the effect of reducing Reynolds number is small on both total pressure ratios and boundary-layer thickness. These effects are illustrated with the Mach 0.9 data of Figure 23 and the Mach 1.6 data of Figure 24.

2.2.4 Strut-Wake Effects

2.2.4.1 External Static Pressure Distributions and Drag

The strut wake was found to have a negligible effect upon the external static pressure distributions and drag over the aftbody and nozzle boattails. The circumferential pressure distributions at the beginning (MS 127.77) and end (MS 138.02) of the aftbody and at the ends of the basic convergent-divergent (MS 145.42) and unshrouded plug (MS 141.98) nozzle at zero angle of attack indicate that the pressure distribution is independent of angular position.

Longitudinal pressure distributions at the 0-, 90-, and 180-degree (strut side) positions on the CD_{3E} nozzle were examined for a freestream Mach number of 2.0 to determine if the strut wake effects on external pressure distributions were different between a positive and negative 3-degree angle-of-attack orientation. No significant difference was found.

The strut non-uniformity effect or drag increment was obtained from the pressure instrumented nozzles by subtracting calculated pressure and skin friction drag using only the pressure tubes located at the zero-degree position (the strut is located at 180 degrees) from the drag computed using all pod aftbody and nozzle pressure tubes. It is assumed in this procedure that the pressures measured from tubes located at zero degrees are unaffected by the strut. The nozzle boattail pressure, friction, and total (pressure-plus-friction) drag increments are tabulated in Table 5 for the configurations and conditions investigated. In general, the magnitudes of the drag increments are extremely small and well within the limits attributed to data scatter. Consequently, it is concluded that the strut has no significant effect on nozzle drag.

2.2.4.2 External Boundary-Layer Profiles

The total pressure profiles from the 0-degree, 90-degree, and 180-degree (strut side) pod boundary-layer rakes at model station 115.52 inches show the

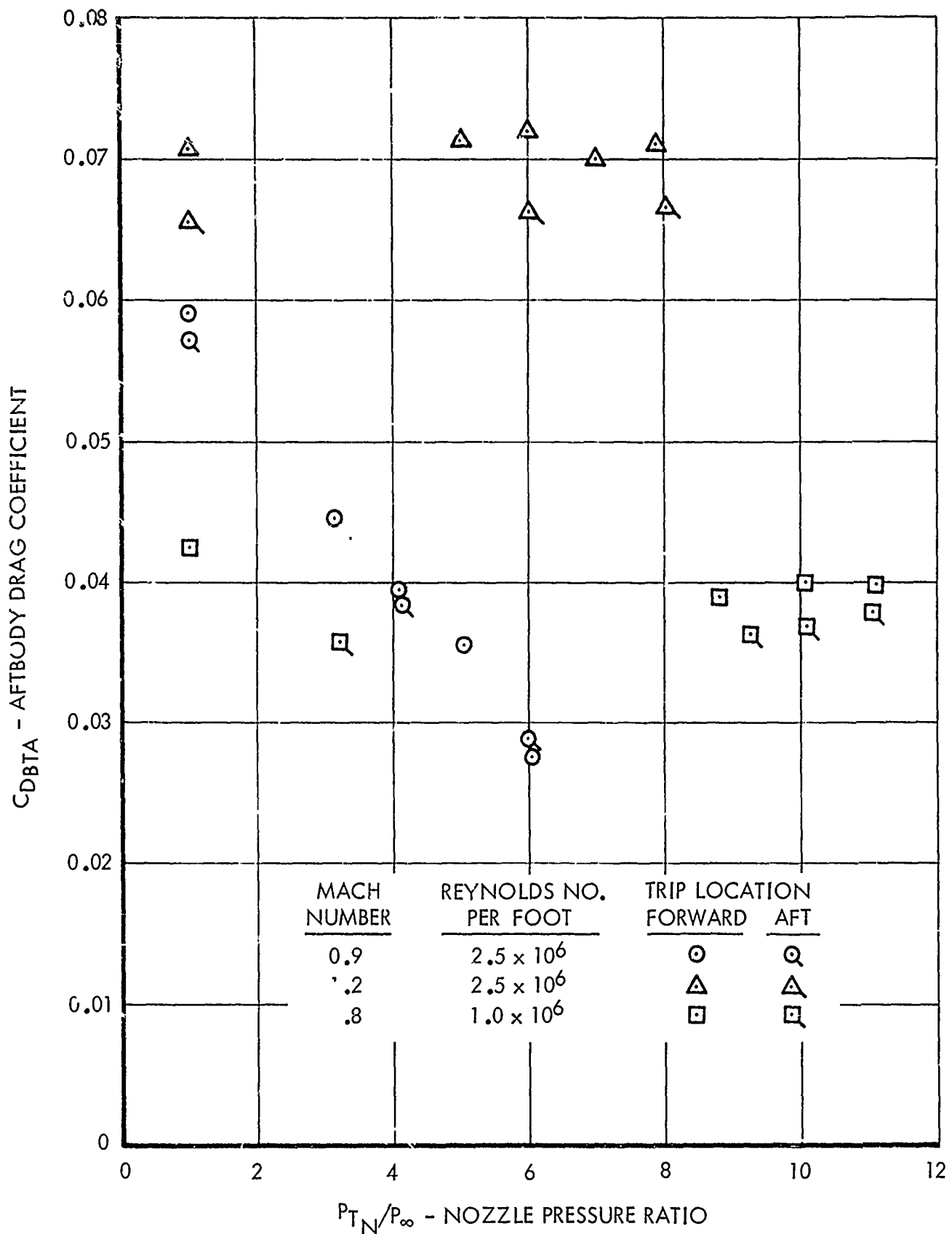


Figure 22. Effect of Boundary-Layer Trip on Pod Aftbody Drag

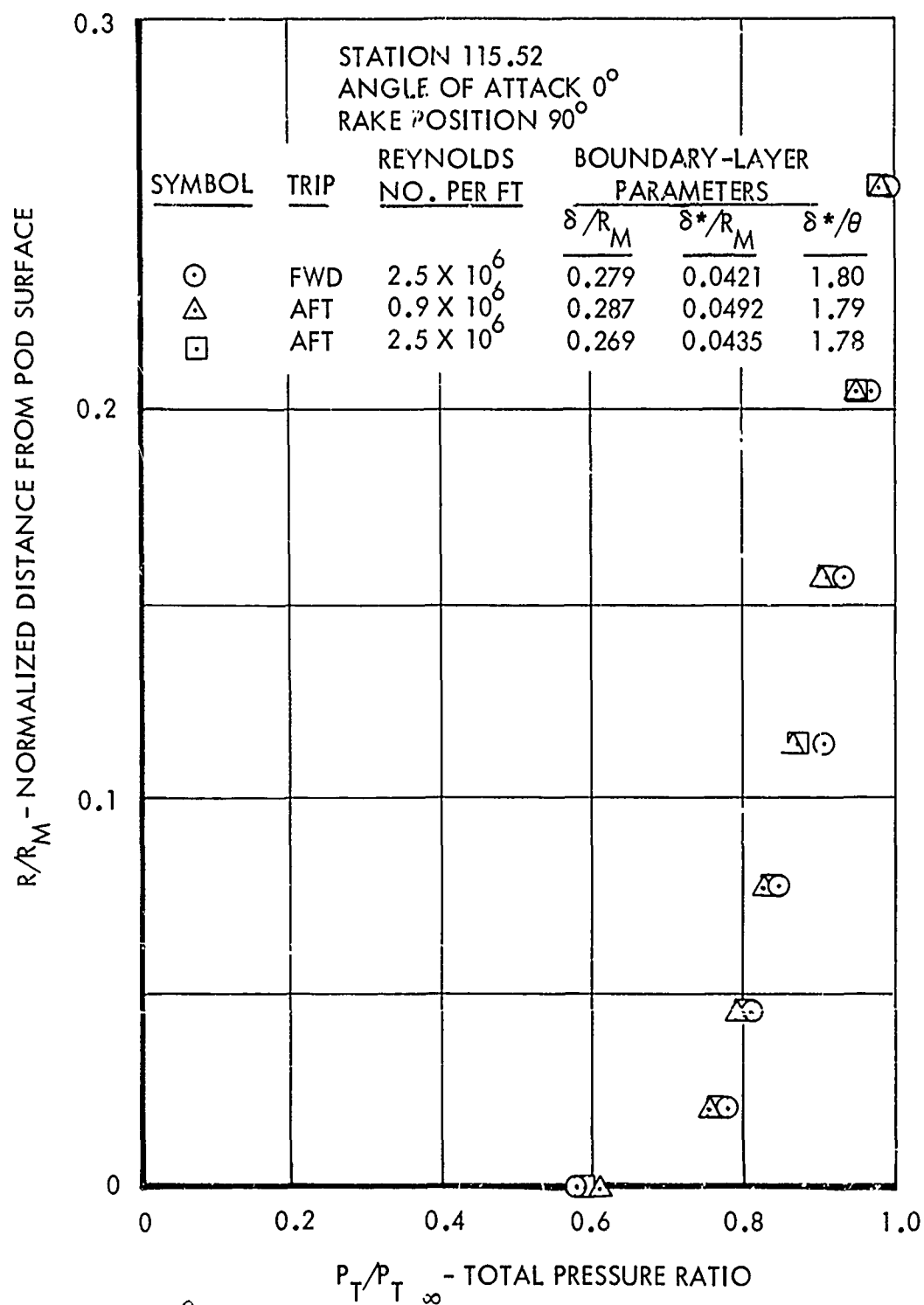


Figure 23. Effect of Boundary-Layer Trip on Total Pressure Profiles - Mach 0.9

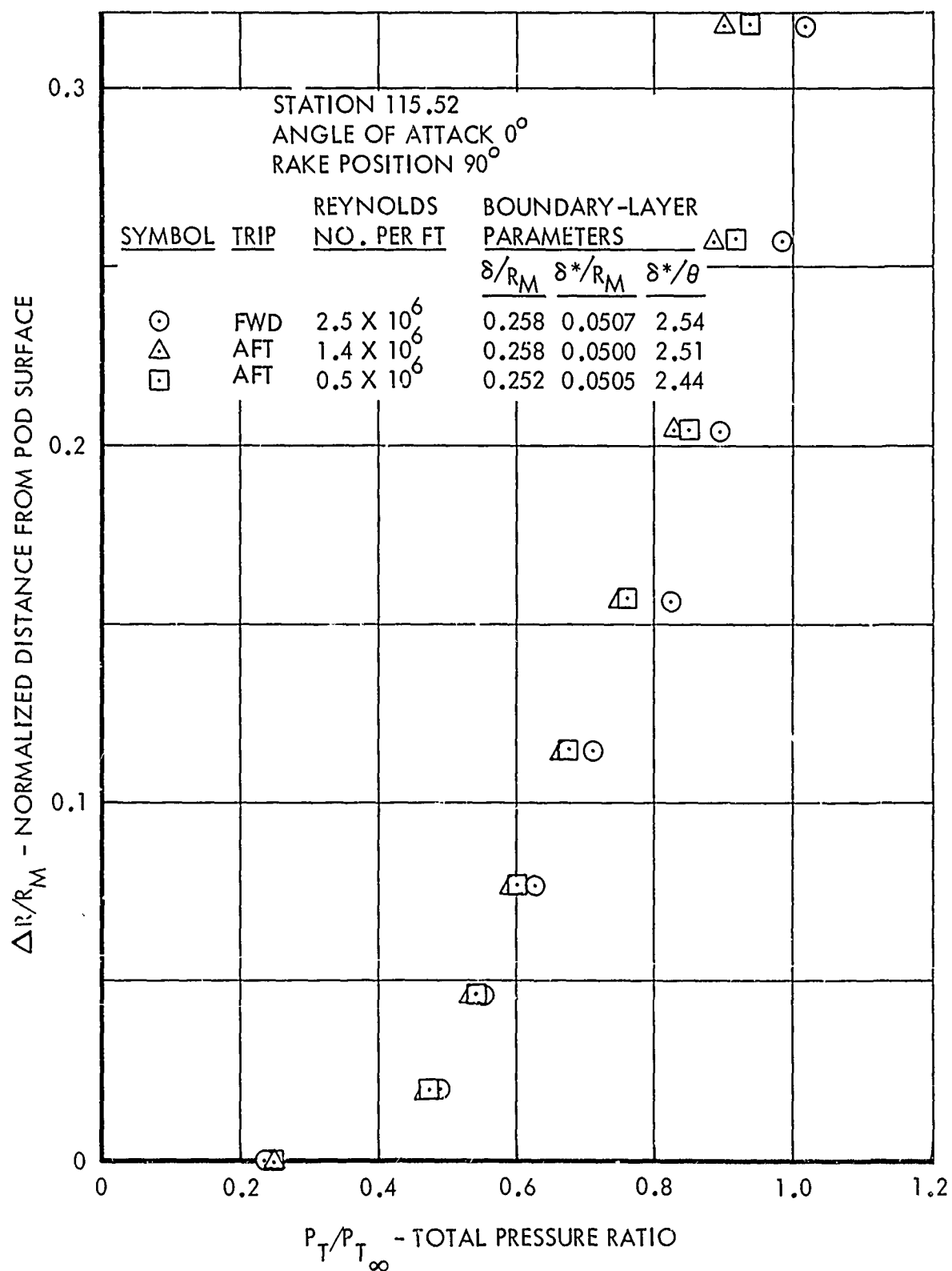


Figure 24. Effect of Boundary-Layer Trip on
Total Pressure Profiles - Mach 1.6

TABLE 5. STRUT NON-UNIFORMITY DRAG INCREMENT SUMMARY

Nozzle Configuration	Mach Number	Nozzle Pressure Ratio	Nozzle Pressure Drag Increment Coefficient	Nozzle Friction Drag Increment Coefficient	Total Pressure Plus Friction Drag Increment Coefficient
CF ₁	0.8	5	-0.0093	-0.0004	-0.0097
CF ₃	1.8	10	-0.0131	-0.0002	-0.0133
CI ₁	0.6	4	-0.0022	0.0005	-0.0017
	0.9	4	-0.0097	-0.0008	-0.0105
CI ₃	0.9	4	-0.0004	-0.0005	-0.0009
	1.2	5	-0.0014	-0.0003	-0.0017
	1.8	10	-0.0026	-0.0003	-0.0029
CD ₁	0.6	4	0.0009	0.0007	0.0016
	0.9	4	0.0013	-0.0009	0.0004
CD ₃	1.2	6	-0.0007	-0.0005	-0.0012
	1.8	10	-0.0013	-0.0005	-0.0013
CD _{1E}	0.6	4	-0.0118	0.0007	-0.0111
	0.9	4	-0.0039	-0.0010	-0.0049
CD _{3E}	1.8	10	0.0001	-0.0006	-0.0005
CDE ₁	0.6	3	0.0028	0.0005	0.0033
CDE ₃	1.8	10	0.0006	-0.0004	0.0002
UP _A C ₁	0.9	4	-0.0077	-0.0005	-0.0082
UP _A C ₃	0.6	4	0.0011	0.0004	0.0015
	0.9	4	0.0008	-0.0005	0.0003
	1.2	5	0.0036	-0.0003	0.0033
	1.8	12	-0.0009	-0.0002	-0.0011
SP _A C ₃	1.2	5	0.0010	-0.0003	0.0007
	1.8	10	-0.0002	-0.0003	-0.0005

total pressures at the 180-degree rake to be higher near the wall and lower at the edge of the boundary layer than at the 0-degree and 90-degree rakes. The boundary layer is thinner at the 180-degree rake than at the 0-degree and 90-degree rakes. Both of these effects increase with increasing free-stream Mach numbers. The higher total pressures in the near-wall part of the boundary layer on the strut side are apparently due to the additional turbulence and mixing caused by the strut, and the lower total pressures outside the boundary layer are from the wake. The total pressure profiles and above boundary-layer parameters at the 0-degree and 90-degree rakes are in good agreement with one another for the test Mach numbers.

2.3 PERFORMANCE PREDICTION METHODS

Analytical methods for predicting the thrust and drag of isolated axisymmetric nozzle installations are described and evaluated in this section. In evaluating these methods, the overall problem was divided into the following four basic categories: external flow, internal flow, exhaust plumes, and base pressures. Within each category the problem was further reduced to individual flow regimes (i.e., subsonic, transonic, and supersonic) and individual analysis methods. Methods which formed a logical assemblage were subsequently embodied in a combined method, such as a combined inviscid/boundary layer method.

In the evaluation of analytical methods, each method was considered for its capability to describe the underlying phenomena of a particular component flow for the integrated nozzle/aftbody problem. Thus, the methods evaluated for each category were examined for their capability to describe the flow accurately, in addition to giving accurate final results. This approach avoids arriving at confusing or erroneous conclusions which can occur if a single analytical method is compared to combined phenomena (i.e., experimental results which usually show the combined effects such as inviscid flow, boundary layer, and separation).

A summary list of the analytical methods investigated is shown in Table 6. Those with an asterisk (*) are the recommended methods for the particular application, based on the results of this study.

2.3.1 External Flow Methods

Analytical methods for computing external flow fields over axisymmetric aftbody/nozzle boattail surfaces are described and evaluated in this section. Included are methods for the inviscid flow, the boundary layer, interactions between the two, and separated flow. While several boundary layer methods are available and were considered early in the study, no comparison was made between methods. Instead the Calac boundary layer routine (Reference 14) was adopted because of its agreement with test data and availability in a computer program. Methods for predicting subsonic, transonic, and supersonic flow fields are described and evaluated in the following subsections.

TABLE 6. SUMMARY LIST OF PERFORMANCE PREDICTION METHODS

Application	Method
C-D Nozzles	Exact Shock MOC* Source Flow 1-D/Correlation* 1-D Start Line for MOC* Characteristic Start Line for MOC Time Depending - Throat Mass Flow* Error Minimization - Throat Flow
C-D Ejector Nozzles	MOC Primary/1-D Secondary* Bernstein Method Weber Method
Plug Nozzles	Exact Shock/MOC* Isentropic Shock/MOC* 1-D
External Subsonic Flow	Potential Flow/Boundary Layer* Crown Mesh Method/Boundary Layer
External Transonic Flow	P&WA Modified Spreiter/Alksne Method of Local Linearization* Crown Mesh Method Crown Integral Method Spreiter Integral Method IMS Correlation* CABF Correlation
External Supersonic	Exact Shock MOC/Boundary Layer* Isentropic Shock MOC Ogive and Conical Boattail Drag Curves
Supersonic Annular Base Pressure	Korst Zero Boundary Layer Theory Korst Theory/Equivalent Bleed Korst Theory/Virtual Origin Brazzel/Henderson Empirical*
Subsonic Annular Base Pressure	McDonald/Hughes Correlation Modified Brazzel/Henderson Empirical*
Boundary Layer	Calac/Cohen - Laminar* Calac - Turbulent*
External Separation	Goldschmid - Subsonic* Bonner-Karger - Supersonic*
Plumes	Exact Shock MOC (Internal and External) Isentropic Shock MOC (Internal and External) Shock Expansion/One-Dimensional* Shock Expansion/MOC Newtonian Impact/MOC

*Recommended methods

2.3.1.1 Subsonic Flow

Two axisymmetric inviscid methods for subsonic flow were evaluated: potential flow and Crown's mesh method. The potential flow analysis method is based on the Neumann incompressible solution and adjusted by Gotherts similarity rule for compressible flow (Reference 15). The Crown mesh method (Reference 18) is an inviscid compressible flow solution which involves the solution of a differential equation applied to a large number of cells or a mesh which extended in all directions from the body to freestream conditions. Both of these inviscid methods were shown in a previous study (Reference 5) to give essentially identical results for subsonic flow. The objective of the present study was, therefore, to develop combined inviscid/boundary layer solutions. Common to both the potential flow and the Crown mesh solutions is the method of combining the inviscid flow with the boundary layer and plume calculations. In solving for the external flow field, the plume is treated as a solid body attached to the end of the boattail with a slope discontinuity at the juncture. This juncture produces a very steep pressure rise when the inviscid potential flow solution is applied (See Figure 25). In order to alleviate this problem and to improve the predictions of pressure distributions over the entire body, the Calac boundary layer solution was combined with both the potential flow and Crown mesh solutions. The steep pressure gradient at the plume/body junction was eliminated by using a straight line extrapolation of the boundary layer displacement streamline into the plume just past the exit station. The development of the extrapolation technique is described in detail in the Phase I summary report (Reference 1). The improved pressure predictions which result from combining the inviscid solutions with a boundary layer solution are illustrated in Figure 25. Both the Crown mesh and potential flow results are close to the Shrewsbury test data (Reference 17).

The combined potential flow boundary layer program, which includes a routine for computing the exhaust plume boundary, is recommended for computing the subsonic pressure distributions over axisymmetric nozzle boattails. The exhaust plume boundary is computed by the shock expansion-one-dimensional plume calculation described in subsection 2.3.3. Computed results from this program are compared with Phase I isolated convergent-divergent nozzle test data in Figure 26 for a Mach number of 0.8 and a nozzle pressure ratio of 4.0. The measured boundary layer thickness and profile immediately upstream of the aftbody were used in the combined potential flow/boundary layer solution.

2.3.1.2 Transonic Flow

Transonic flow is the most difficult regime for analytical determination of the flow field since the equations for subsonic, sonic, and supersonic flow are, respectively, elliptical, parabolic, and hyperbolic in nature, and thus one solution does not suffice over the entire range. As a consequence, most transonic theories and solution methods have simplifying approximations to the exact flow equations. A list of some of the noteworthy and more promising methods drawn up early in the program are shown below.

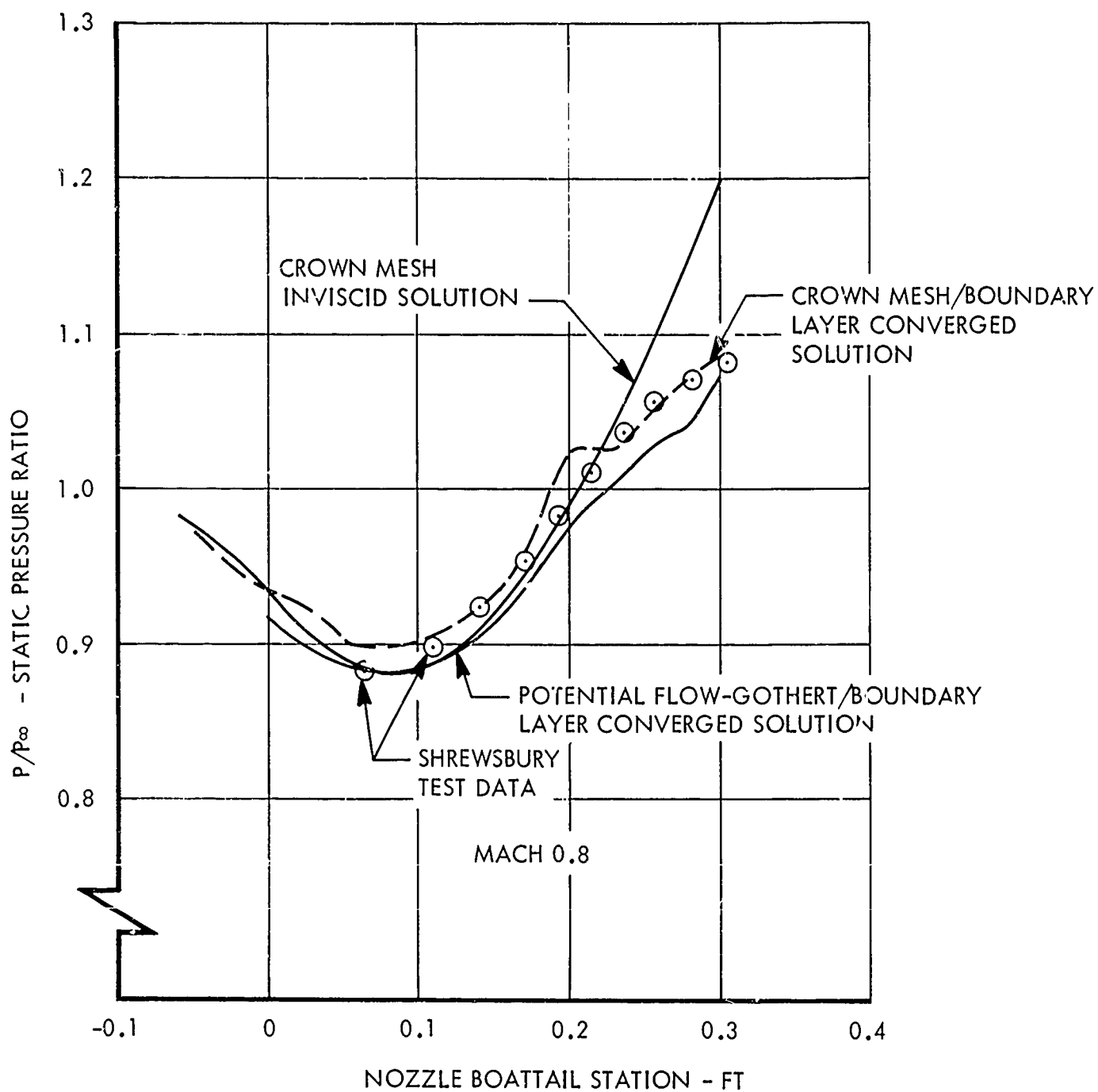


Figure 25. Comparison of Potential Flow - Gothert and Crown Mesh Method Predicted Boattail Pressures with Test Data

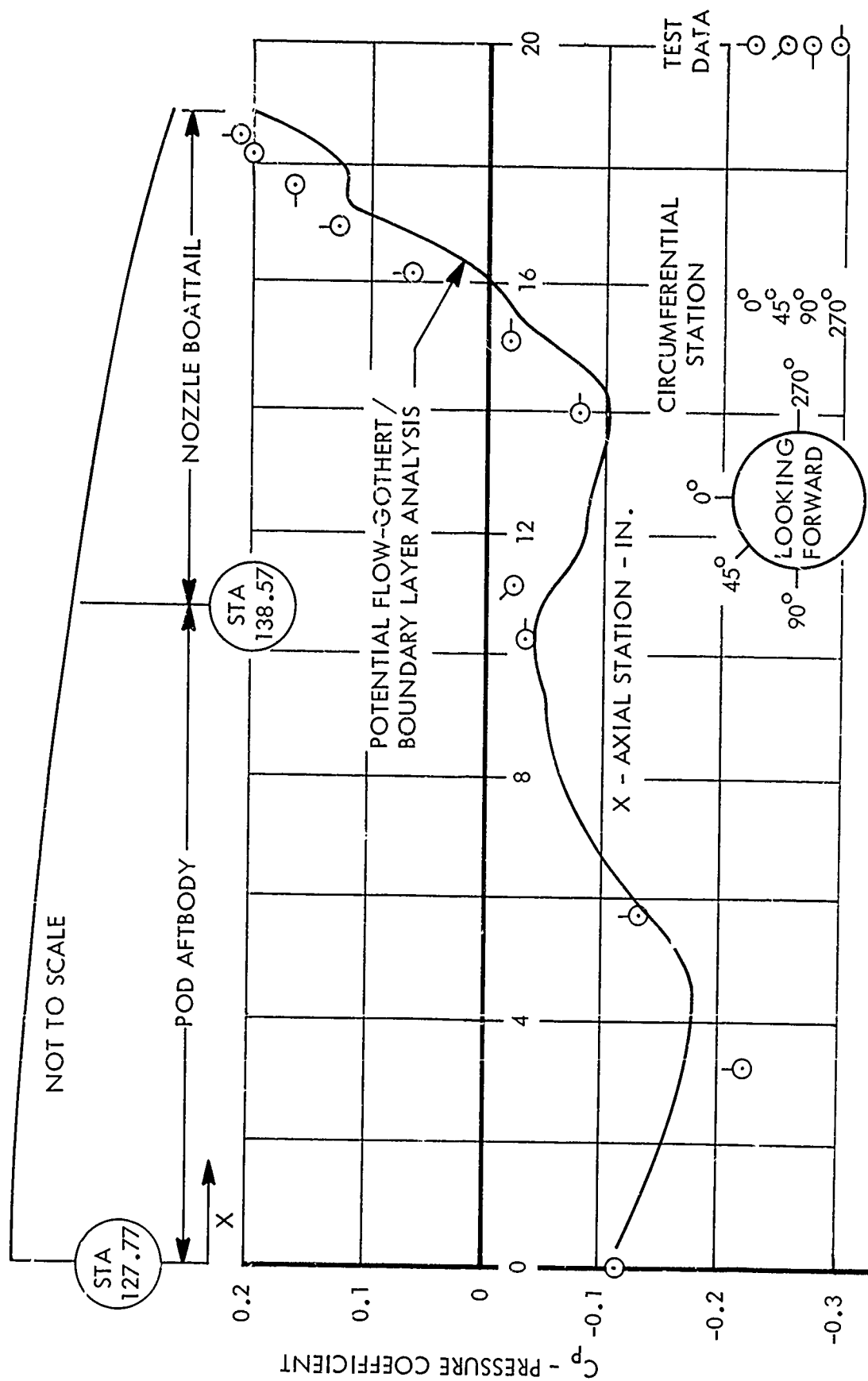


Figure 26. C_D Aftbody/Boattail Predicted and Experimental Pressure Profiles - Mach 0.8 - Nozzle Pressure Ratio 4.0

- Linearization of equations
- Small disturbance theory
- Integral method
- Method of local linearization
- Mesh method
- Relaxation
- Godunov
- Integral mean slope (IMS) correlation
- Circular arc boattail-fantail (CABF) correlation

Preliminary evaluation of the above list immediately eliminates some of the methods based on work performed by previous investigators. Linearization has been shown to fail near Mach one because some of the terms dropped from the exact equations are significant at transonic speeds. The small disturbance theory is applicable primarily for thin wings and slender bodies and, therefore, cannot be applied to the present study. The integral method consists of rewriting the basic differential equations of transonic flow theory into the form of a nonlinear integral equation. This was originally undertaken by Oswatitsch (Reference 19 and 20) and later by Spreiter and Alksne (References 21 and 22), and Crown (References 23 and 24). Regions surrounding the body, its wake, and the associated shock waves are considered. The method, therefore, was worth considering for the present study. The method of local linearization was devised by Spreiter and Alksne (see References 25, 26, and 27) and is the method presented in a previous integrated nozzle/airframe study at NAR (North American Rockwell) (Reference 28). Although attempts to analyze body shapes with simulated plumes were unsuccessful in that study, the method deserved further investigation. Crown devised the mesh method to overcome some of the problems of the integral method which he discusses in Reference 18. His approach involves solution of a differential equation rather than an integral form of the equation. It allows more versatility in body shape than the previously mentioned methods.

Relaxation (Reference 15) and the Godunov method (Reference 29) fall in the category of time-dependent finite difference solutions. These time-dependent solutions are theoretically possible for mixed flow transonic cases, but they are usually very laborious and time-consuming to apply. Application of these methods is primarily a mathematical and computer programming problem. Most time-dependent methods are in the early stages of development and are tied to advances in computers and mathematics. However, they are worthy of continued consideration as they develop into practical engineering analysis tools.

The IMS and CABF correlation methods were developed by P&WA from several series of tests of various boattail shapes and are discussed in detail in Reference 7. Of the two, P&WA recommends the IMS method because it is more accurate and applicable to a larger variety of boattail shapes.

P&WA Spreiter-Alksne Method of Local Linearization - A modified form of Spreiter and Alksne's inviscid method of local linearization (Reference 25), coupled with a modified Reshotko-Tucker treatment of the boundary layer displacement thickness, showed good agreement with test data for Mach 1 flow over a parabolic arc body of revolution and fair agreement for Mach 0.9 flow over a body with a rounded shoulder conical boattail. This method (Reference 30) was developed into computer program form by P&WA and all analytical results from this method which are included in this report were prepared by P&WA. The method starts with the Spreiter and Alksne inviscid solution and iterates the inviscid flow solution with the boundary layer calculation until a converged solution is obtained. Results for Mach 1 flow over a parabolic arc sting mounted body of revolution of thickness r to $1/6$ are compared in Figure 27 to Drougge test data from Reference 31. While both inviscid and fourth iteration viscous solutions are in good agreement with the data over most of the body, the viscous solution gives slightly better agreement in the vicinity of the sting body junction. To circumvent the computational difficulties associated with the discontinuity in surface slope at the aft body and rear sting juncture, the contour was smoothed in this region. The remaining disagreement is probably due to shock/boundary layer interaction in this region.

Crown Mesh and Integral Methods - The model for treating transonic flow by the Crown Mesh method (Reference 18) assumes flow initially subsonic accelerates over a body to supersonic speeds and returns to subsonic speeds through a normal shock discontinuity. Thus, the flow is not only mixed but contains an imbedded supersonic region. The technique for obtaining a solution is to set up a series of cells or a mesh extending in all directions from the body, assumes an initial pressure distribution over the body, solve the flow equations in differential form within the mesh, and adjust the body pressure distribution from the current cell properties. The process is continued until a converged distribution is found. Similar results are obtained using Crown's integral method; however, the mesh method is preferred.

P&WA IMS Correlation Method - The integral mean slope (IMS) correlation method was developed by P&WA from a broad range of isolated nozzle shapes and test conditions. (Reference 7). The effects of geometry are correlated in terms of the integral mean slope of the boattail. The IMS is defined as the average value of the rate of change of body area with length, i.e.

$$IMS = \frac{1}{A_F/A_M} \int_{(1 - A_F/A_M)}^1 \frac{d(A/A_M)}{d(X/D_M)} d(A/A_M) \quad (1)$$

where A is the cross-sectional area, A_F is the boattail projected frontal area, A_M is the maximum cross-sectional area, X is the distance aft of the maximum diameter station, and D_M is the maximum diameter. The correlation is based on a large body of combined pressure and friction drag coefficients

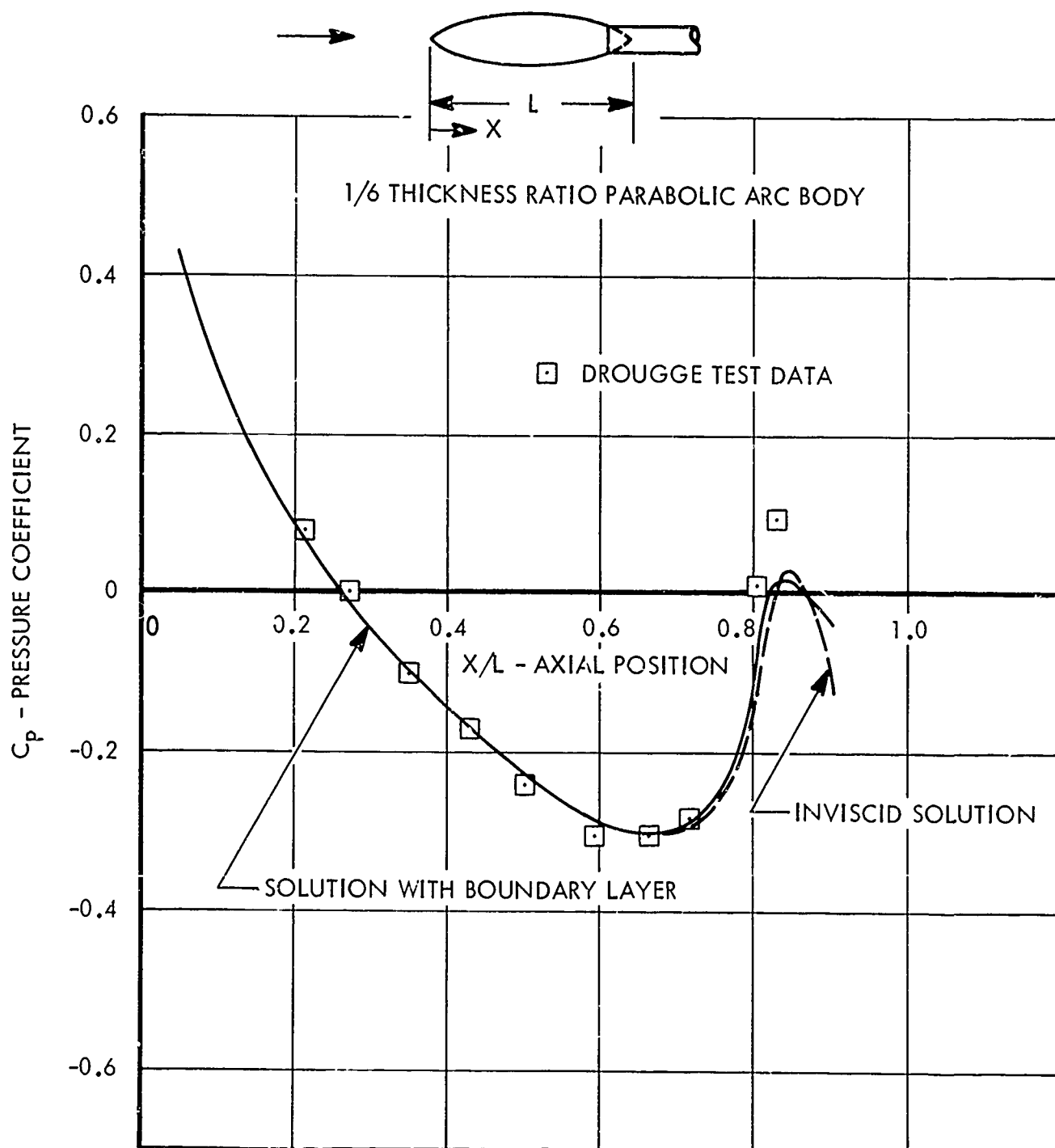


Figure 27. Comparison of P&WA Spreiter-Alksne and Measured Pressure Distributions at Mach 1.0

for a variety of nozzle/aftbody configurations. Data built into the correlation computer program is for freestream Mach numbers of 0.7, 0.9, and 1.2 and nozzle pressure ratios of 2 and 4.

Comparison of Methods - Analysis of a typical plume-body by the Crown mesh method gave a pressure distribution having a sharp pressure rise along the boattail. A P&WA Spreiter-Alksne analysis of the same body gave a steep but smooth pressure rise along the boattail and was in better agreement with test data. Integral and mesh method analyses of 6 and 8 percent circular arc airfoils gave approximately the same velocity profiles and freestream Mach numbers for selected shock locations.

A 6 percent circular arc airfoil with a shock located at the 70 percent chord point was analyzed using Crown's mesh method as programmed in Deck V of Reference 18, and the results are compared with Crown's integral method (Reference 23) and the Spreiter and Alksne integral method in Figure 28. The Crown mesh method and the Spreiter and Alksne integral method are in close agreement with each other except in the vicinity of the shock. The Crown integral method gives a distribution of critical Mach number slightly above that predicted by the other two methods.

Pressure distributions obtained from the mesh method and from the P&WA modified Spreiter and Alksne method of local linearization (Reference 25) are compared with Shrewsbury's test data (Reference 17) in Figure 29 for a conical boattail with a rounded shoulder followed by a cylindrical simulated plume. For supersonic flow, the inviscid mesh method assumes that a normal shock occurs somewhere along the boattail surface. This results in a pressure discontinuity at the assumed shock location. At the test freestream Mach number of 0.9, the mesh method indicates a shock located 0.2 feet downstream of the start of the boattail. The experimental data shows a steep but smooth pressure rise along the boattail which is qualitatively different from the mesh method results. The Spreiter and Alksne method inviscid results (prepared by P&WA) more closely follow the trend of the test data. In this method shocks are assumed to be sufficiently weak to be neglected; consequently, a smooth recompression of the flow occurs in the solution. The effect of a boundary layer displacement thickness on the pressure distribution was investigated using the Spreiter and Alksne method and found to be minor, as indicated by Figure 29.

Since agreement between the test data and the P&WA-modified Spreiter and Alksne method is moderately good and the trend appears more realistic than the mesh method, it is the recommended analytical method for external transonic flow calculations. This does not necessarily imply that the Spreiter and Alksne model is closer to simulating the actual flow conditions. Since Reference 17 had no photographic evidence to indicate the presence or absence of a single strong shock or several weaker shocks, the correctness of each model for the inviscid flow could not be evaluated. It is possible that a strong shock with a boundary layer interaction and pressure feedback could give the more gradual pressure rise indicated by the data. More likely, several weaker shocks with a boundary layer interaction and pressure feedback are occurring.

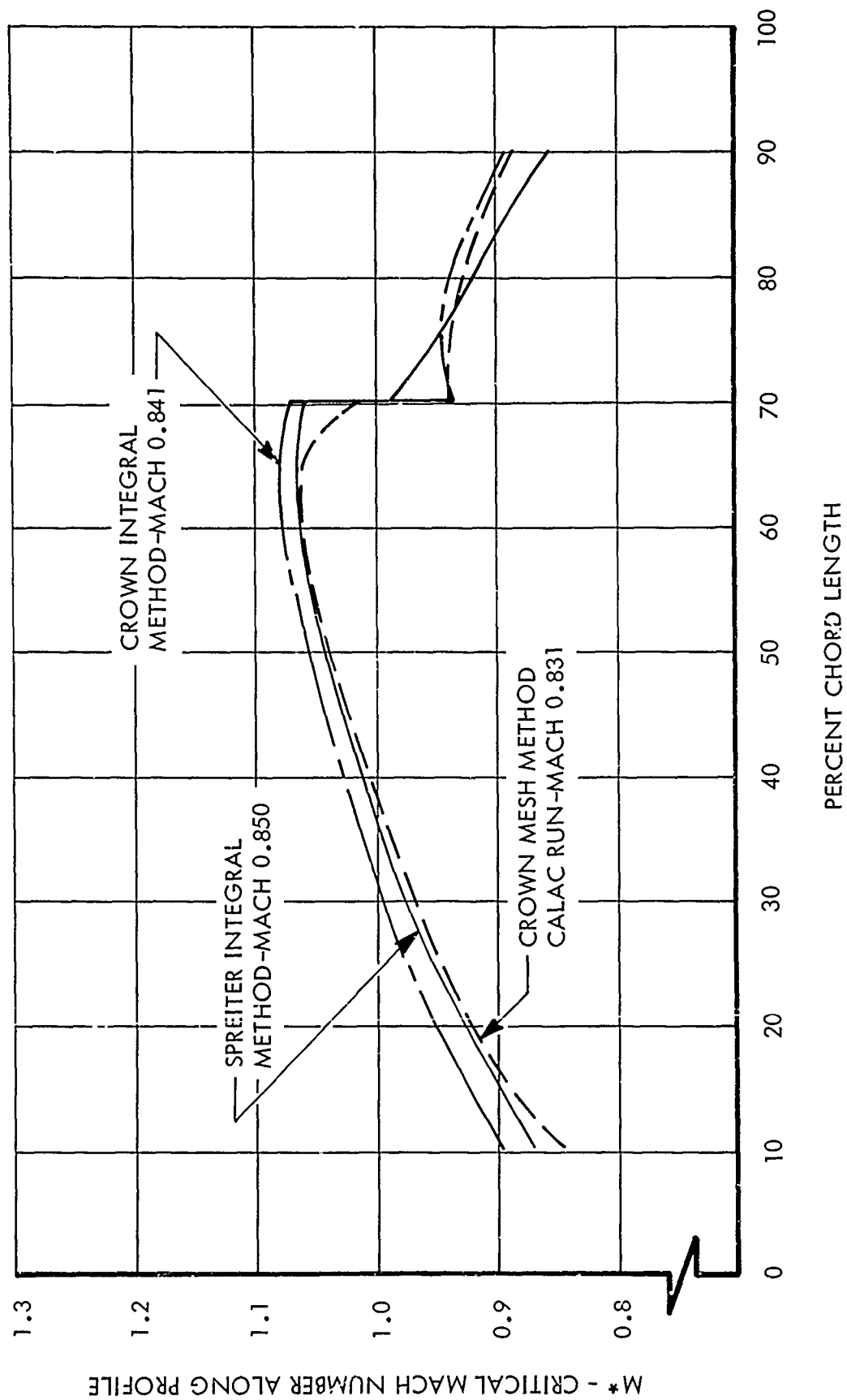


Figure 28. Comparison of Flow Computation Methods -
6% Circular Arc Airfoil

The P&WA Spreiter-Alksne modified equivalent body analysis was used by P&WA to compute pressure distributions over the pod aftbody and nozzle for various Phase I nozzle configurations tested in the transonic flow regime. Comparisons between measured and computed pressure distributions for the Phase I UP C₃ and CI₁ nozzle configurations are presented in Figures 30 and 31 for a freestream Mach number of 0.9 and a nozzle pressure ratio of 5.0. The analysis results agree with the data except near the exit of the plug nozzle. Computer results for Mach numbers of 1.1 and 1.2 were in poorer agreement with the experimental data.

Comparison of drag predictions from the P&WA Spreiter-Alksne analytical method and the P&WA IMS correlation method for Mach 0.9 flow over the pod aftbody and CI₁ and CI₃ nozzle configurations, operating at nozzle pressure ratios from 2 to 5 (Figure 32) shows the analytical method to give consistently higher drag than the correlation. When compared to test data, the correlation results are in closer agreement. Based on this limited comparison, it would be premature to recommend one of these methods over the other.

In summary, both the Spreiter-Alksne modified equivalent body analysis and the IMS correlation are limited in their usefulness for analytical predictions. The equivalent body method yields results in agreement with experimental pressure distributions only at subsonic speeds. Consequently, it yields acceptable drag predictions only at subsonic speeds. The IMS correlation provides somewhat more accurate drag predictions.

2.3.1.3 Supersonic Flow

The external supersonic flow analysis methods considered were a method-of-characteristics (MOC) analysis and a combined MOC/boundary layer analysis. Comparison of the inviscid MOC and combined MOC/boundary layer methods for Mach 1.8 flow over the CD₃ nozzle shows the pressure distributions predicted by both methods to be very close except in the vicinity of the body slope discontinuity (Figure 33). The greater deviation between the two methods in this region is due to smoothing by the boundary layer in this region. The wall pressure distributions predicted by both methods are in good agreement with the test data. The steep rise in measured pressures just upstream of the boattail slope discontinuity point occurs before the predicted rise due to pressure feedback through the boundary layer which is not accounted for in the analysis. Separation pressure predicted by the Bonner-Karger separation criterion (Reference 32) and pressures downstream of the separated flow region predicted by the unseparated combined analysis are in good agreement with the test data.

The capability for predicting jet-induced flow separation is incorporated in the combined MOC/boundary layer method. This capability is achieved thru iteratively locating the jet induced separation point by matching the separation pressure computed by the Bonner-Karger separation correlation to the base pressure computed by the Brazzel-Menderson base pressure correlation (Reference 33). As shown in Figure 33 this method over-predicts the jet induced separation pressure.

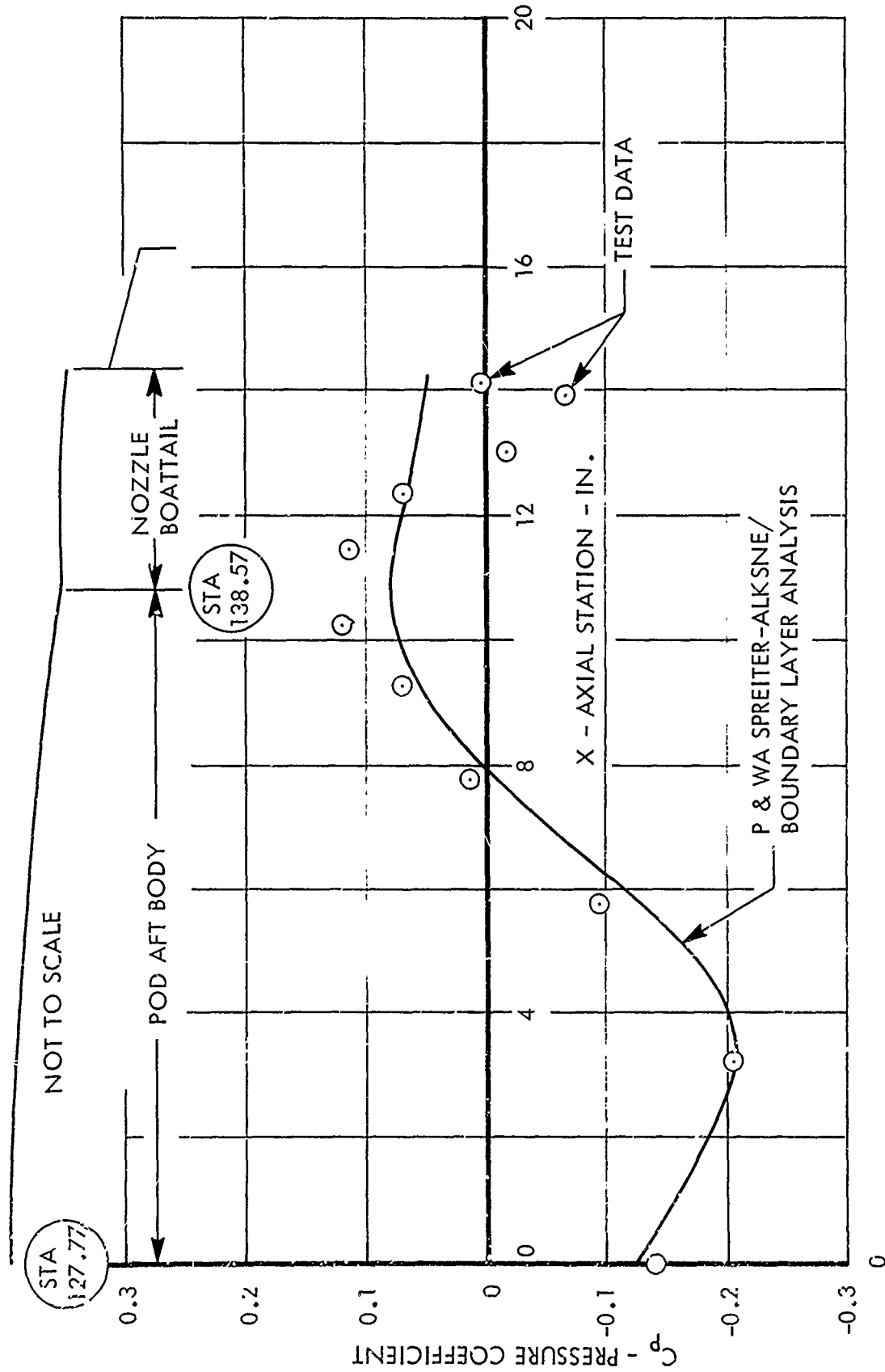


Figure 30. JP_A C₃ Aftbody/Boattail Predicted and Experimental
Transonic Pressure Distributions - Mach 0.9 -
Nozzle Pressure Ratio 5.0

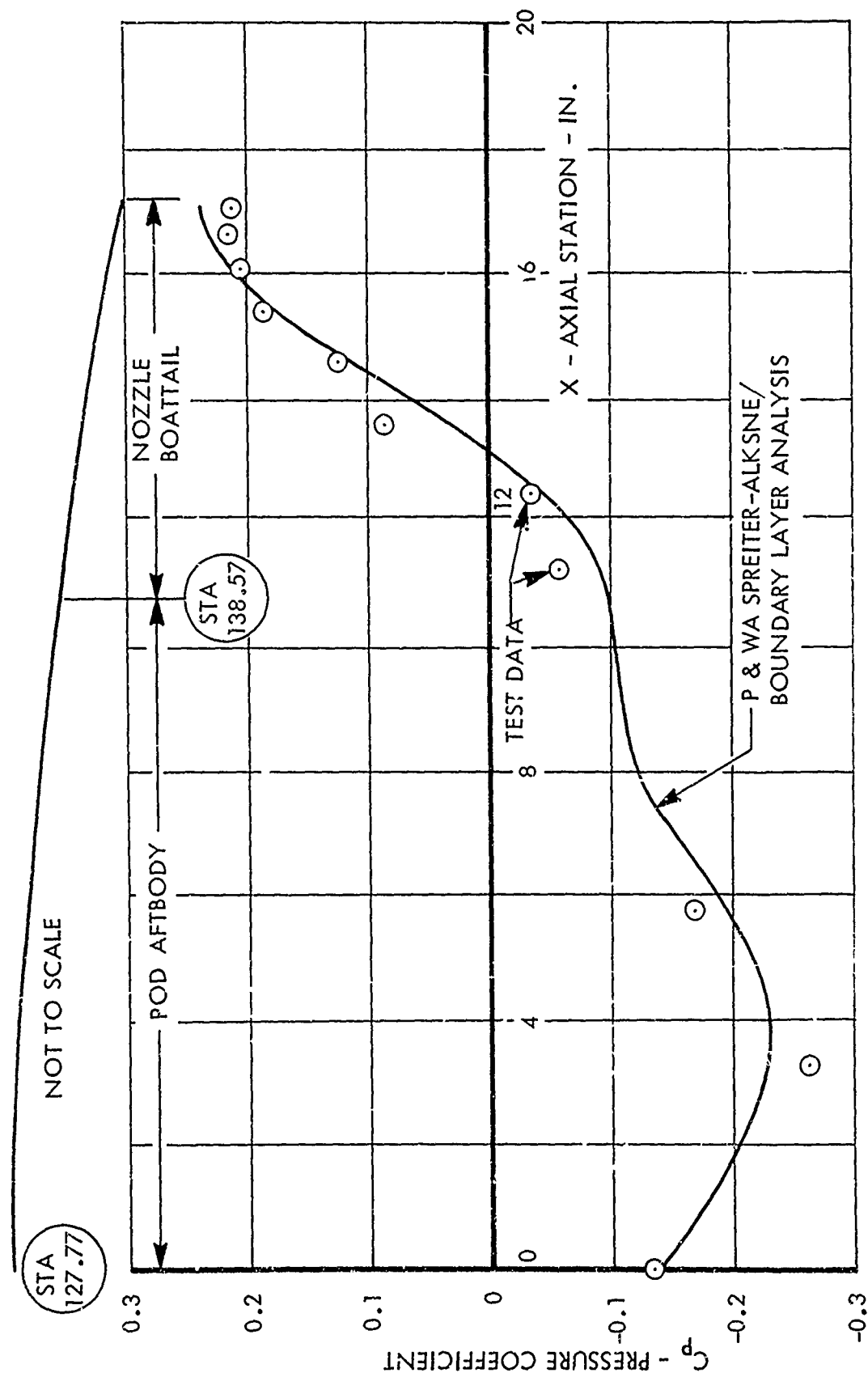


Figure 31. CI_1 Aftbody/Boattail Predicted and Experimental
Transonic Pressure Distributions - Mach 0.9 -
Nozzle Pressure Ratio 5.0

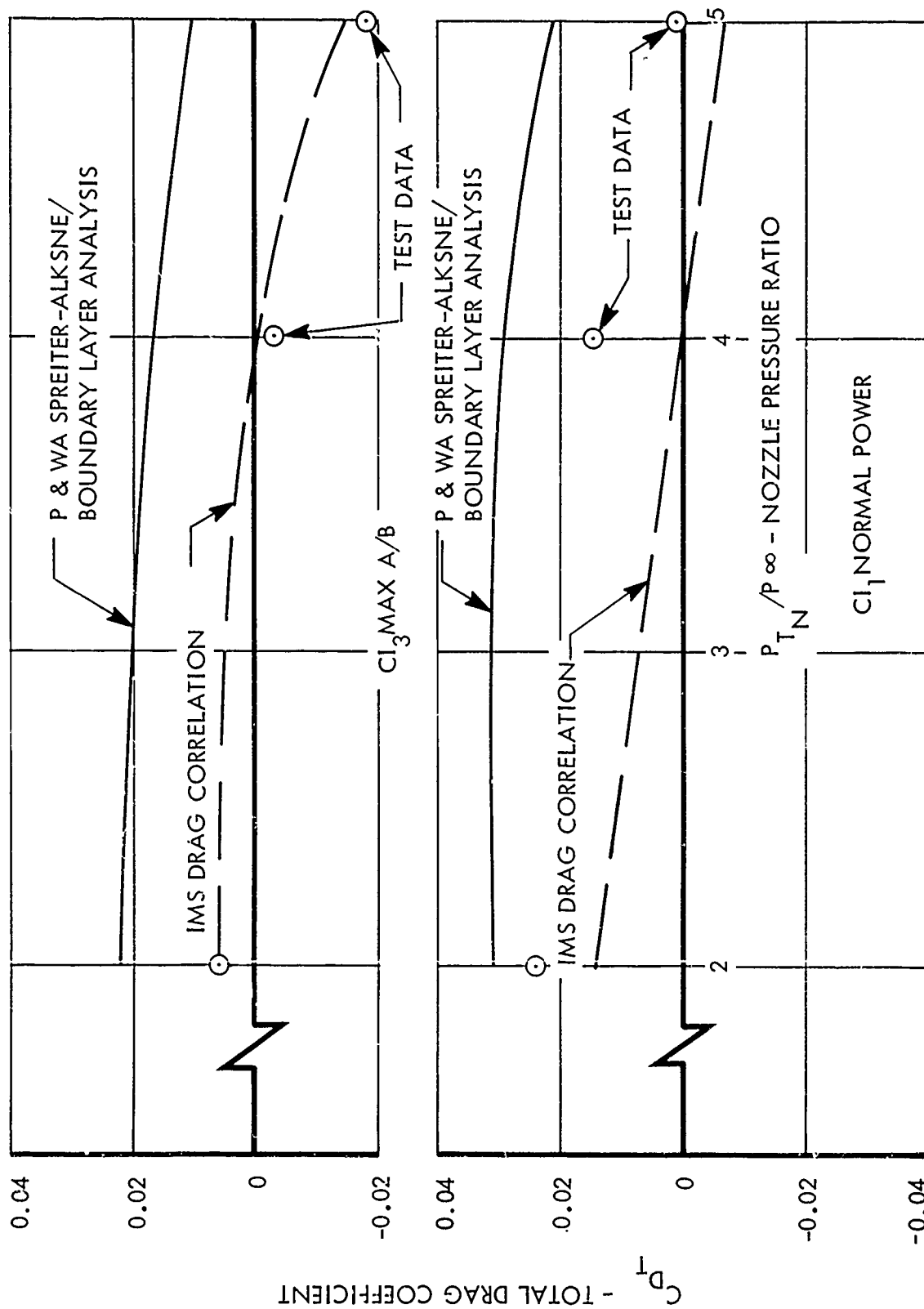


Figure 32. CI_1 and CI_3 Aftbody/Boattail Analytical and Experimental Transonic Total Drag - Mach 0.9

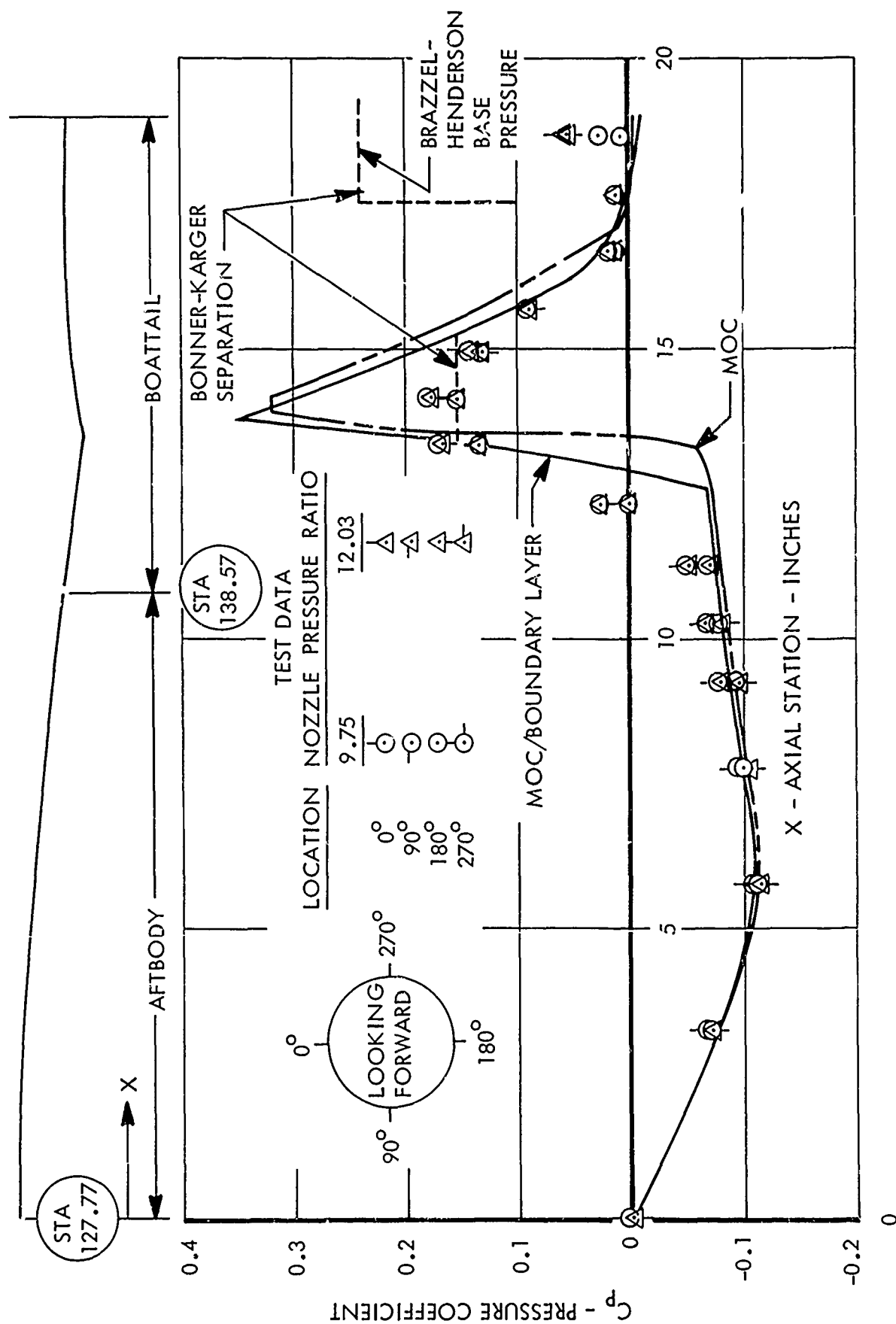


Figure 33. CD₃ Aftbody/Boattail Predicted and Experimental Pressure Profile - Mach 1.8

Aftbody and nozzle boattail drag predicted by combining the MOC/boundary layer analysis, the Bonner-Karger separation criterion, and the Brazzel-Henderson empirical base pressure correlation were in reasonably good agreement with test data for the convergent-divergent (CD), convergent flap (CF), and convergent iris (CI) nozzles. A summary of results for selected test conditions is shown in the table below. The aftbody drag coefficient, $C_{D_{BTA}}$, is the aftbody friction plus wave drag referenced to the maximum

aftbody cross-sectional area. The nozzle boattail drag coefficient, $C_{D_{BTN}}$,

includes the combined effects of pressure, friction, separation, and base pressure on the nozzle. As indicated in the table, aftbody drag can be accurately predicted, but nozzle boattail drag predictions are less accurate. However, the prediction of the combined effects may be adequate for practical applications for estimating total aftbody plus nozzle boattail drag.

Model	P_{T_N}/P_{∞}	MEASURED		PREDICTED	
		$C_{D_{BTA}}$	$C_{D_{BTN}}$	$C_{D_{BTA}}$	$C_{D_{BTN}}$
CD	12.03	0.034	0.007	0.035	0
CF	10.04	0.040	-0.006	0.038	0.007
CI	10.01	0.041	0	0.039	0.004

A correlation of inviscid MOC pressure drag was developed to provide a rapid means of estimating drags for arbitrary boattail contours. Figure 34 presents a correlation of conical boattail drag coefficients obtained by use of the MOC for exit to maximum area ratios ranging from 0.0 (limiting case of a closed axisymmetric body) to 1.0 (limiting case of a two-dimensional boattail contour). Correlation of the data for a given area ratio is achieved through use of similarity parameters which are obtained from linearized supersonic flow theory. IMS, rather than the conventional thickness ratio, is used as the geometric parameter. The MOC drag data used in generating the curves for each area ratio shown in Figure 34 included data for boattail angles ranging from 3 to 9 degrees and Mach numbers ranging from 1.2 to 2.0. Although the data shown in Figure 34 were generated from MOC solutions for conical boattails, the results are applicable for arbitrary boattail contours since, for a given area ratio, the IMS parameter accounts for the contour effect. The ability of IMS to correlate data for various contours and at a fixed area ratio is illustrated in Figure 35 and 36 for Mach numbers of 1.2 and 2.0, respectively. Drag coefficients computed by the MOC are presented in these figures for conical and circular arc boattails and for exit to maximum area ratios of 0.15, 0.5, and 0.9. Although the area ratio data are not correlated, especially at the lower supersonic Mach number of 1.2, the circular arc and conical boattail drags are correlated reasonably well for the same area ratio. This result indicates that IMS is a suitable geometric parameter for relating the drag of different contours at the same area ratio.

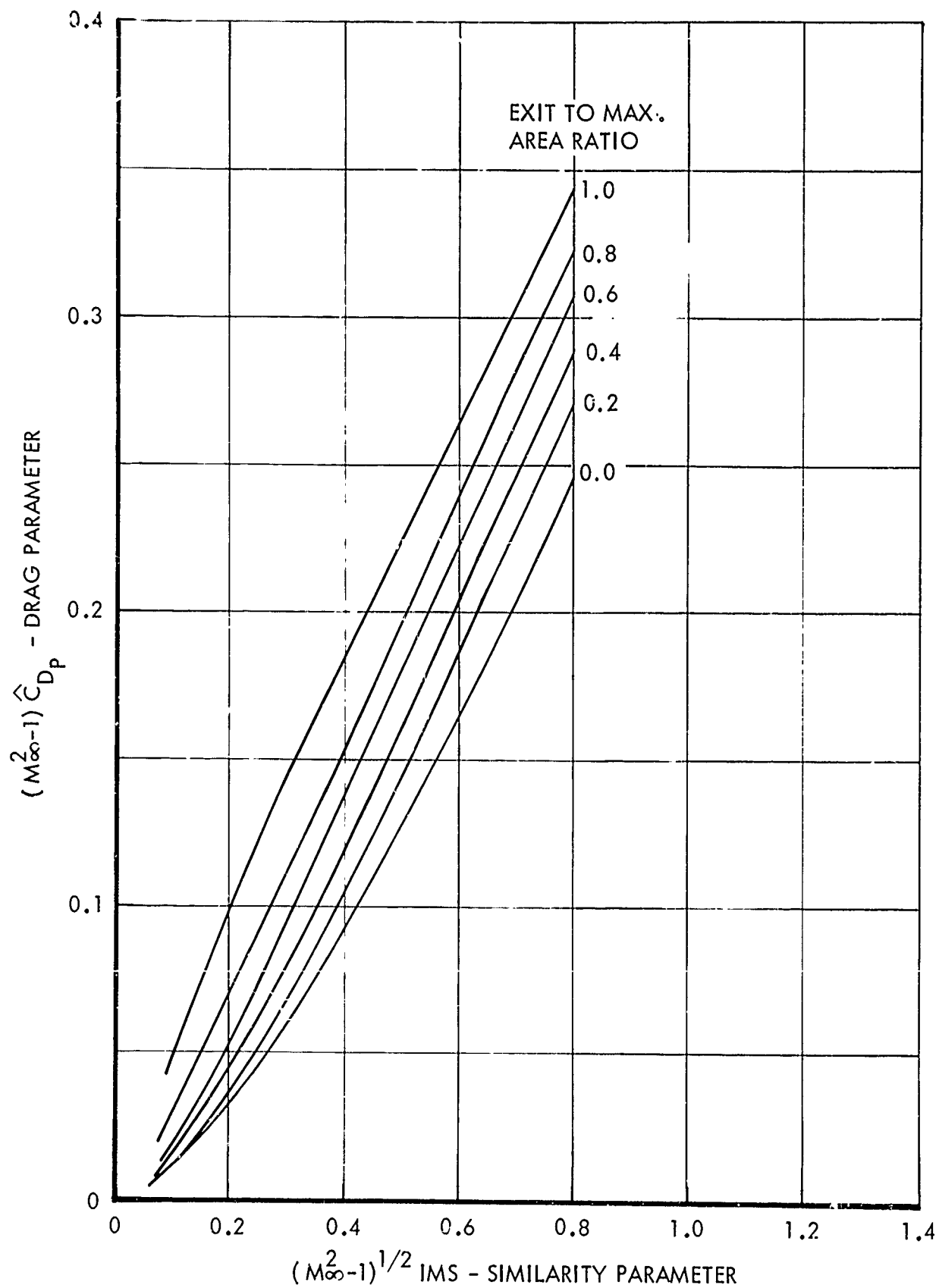


Figure 34. IMS/Supersonic Similarity Correlation of Conical Boattail MOC Pressure Drag

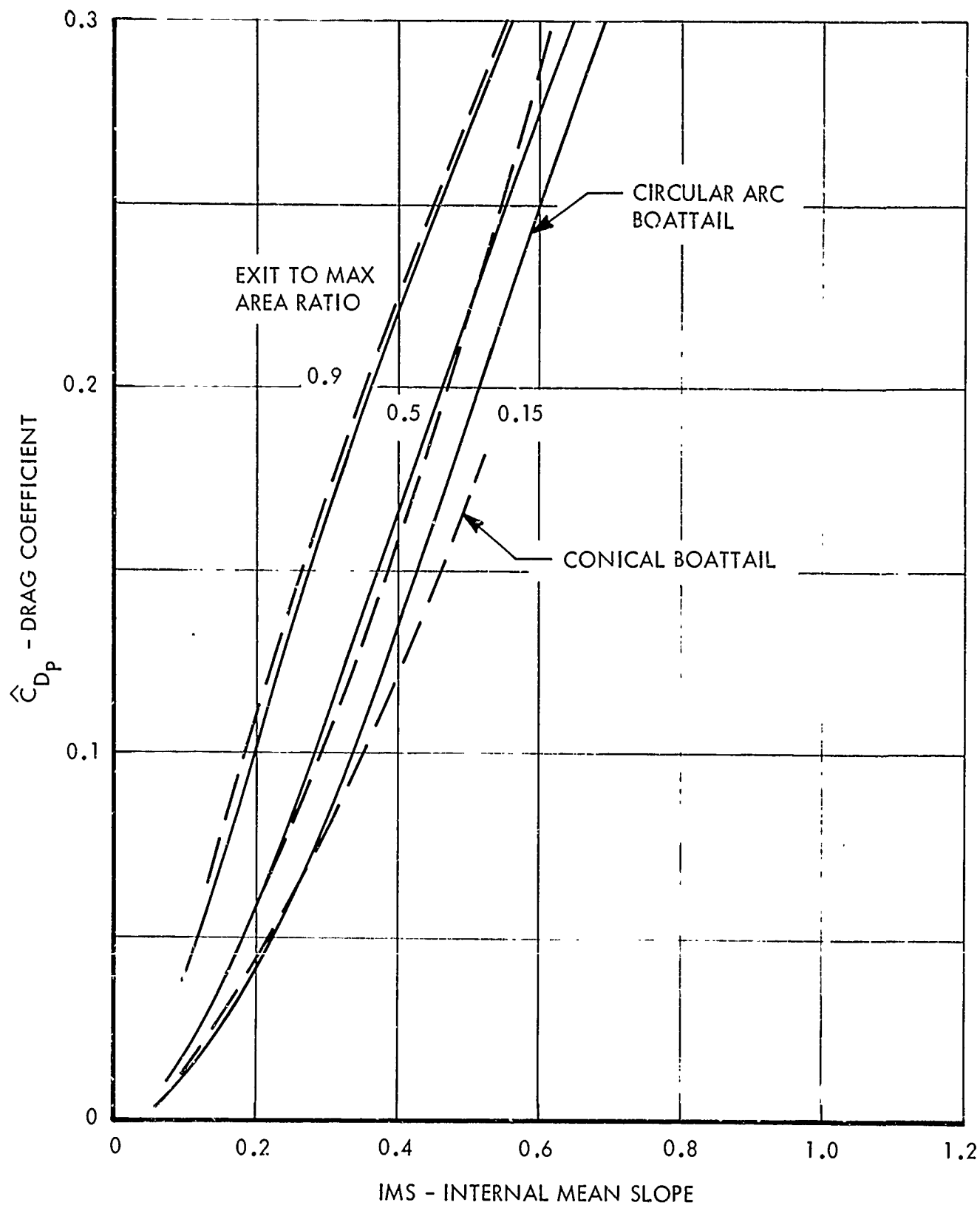


Figure 35. Correlation of Circular Arc and Conical Boattail
MOC Pressure Drag - Axisymmetric Boattails -
Mach 1.2

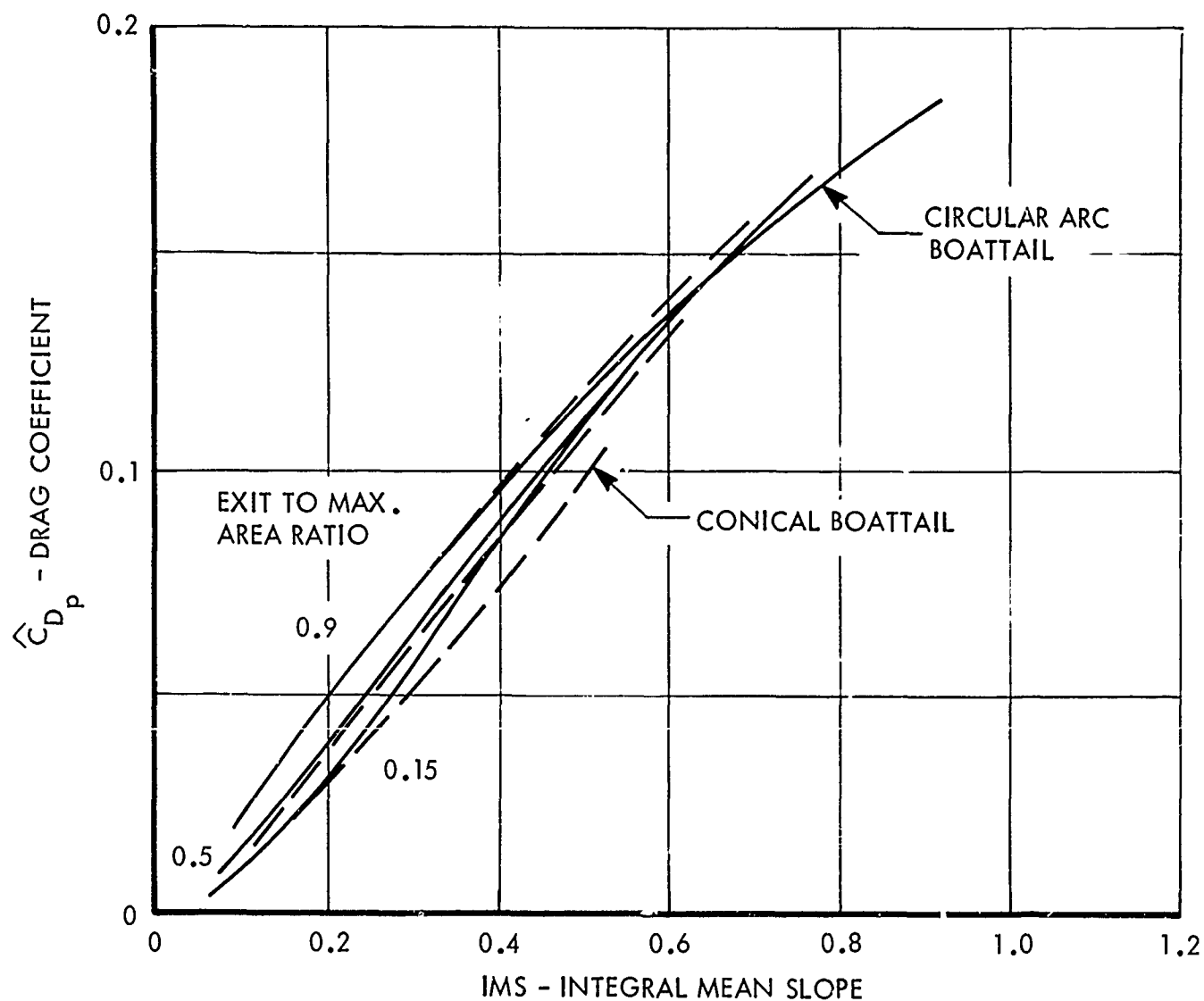


Figure 36. Correlation of Circular Arc and Conical Boattail MOC Pressure Drag - Axisymmetric Boattail - Mach 2.0

A general correlation for axisymmetric boattail drag using Spreiter's transonic similarity theory (References 25, 26, and 34) combined with IMS was evaluated using boattail drags computed by use of the MOC. This correlation approach is attractive since the theory is not limited to the transonic regime since it merges smoothly with both the linear subsonic and linear supersonic theories. The appropriate drag coefficient and similarity parameters with the conventional thickness ratio replaced with IMS are written, respectively, as

$$\tilde{C}_D = \hat{C}_{D_{2-D}} \left\{ (\gamma + 1) M^2 \right\}^{1/3} (IMS)^{-2/3} \quad (2)$$

and,

$$K = (M^2 - 1) \left\{ (\gamma + 1) M^2 \right\}^{1/3} (IMS)^{-2/3} \quad (3)$$

As shown in Reference 2, the thickness ratio can be replaced with IMS since, for affinely related bodies, IMS is proportional to thickness ratio.

Since Spreiter's similarity parameters are applicable only to two-dimensional flows, and since, as shown in Figure 34, IMS does not account for the difference in drag between two-dimensional and axisymmetric bodies, a correlation of drag data for axisymmetric bodies requires that these drag data be adjusted by the ratio of two-dimensional to axisymmetric drag. The appropriate drag coefficient parameter for correlating axisymmetric boattail drags is written as:

$$\tilde{C}_D = \hat{C}_{D_P} \left(\frac{\hat{C}_{D_{2-D}}}{\hat{C}_{D_{AXI}}} \right) \left\{ (\gamma + 1) M^2 \right\}^{1/3} (IMS)^{-2/3} \quad (4)$$

The results shown in Figure 34 can be used to obtain the two-dimensional to axisymmetric drag ratio for a given Mach number, IMS, and area ratio.

The results shown in Figure 37 indicate the accuracy of correlating axisymmetric boattail drags by application of Spreiter's similarity parameters combined with the results shown in Figure 34. The results are seen to be correlated within a narrow band for exit to maximum area ratios ranging from 0.15 to 0.8. MOC circular arc boattail drag data are presented in the figure for equivalent conical boattail angles ranging from 3 to 9 degrees and for Mach numbers ranging from 1.2 to 2.0 for each area ratio.

2.3.1.4 Boundary Layer

The boundary layer solutions in this study are used to obtain skin friction drag displacement thicknesses for the inviscid flow calculations, and momentum thicknesses used in the virtual origin base pressure correction method. Both laminar and turbulent boundary layer cases for a known transition point are treated in the external supersonic flow/boundary layer program (Reference 4). For subsonic external flow and subsonic or supersonic internal flow, only turbulent boundary layers are considered.

EQUIVALENT CONICAL
BOATTAIL ANGLE - θ

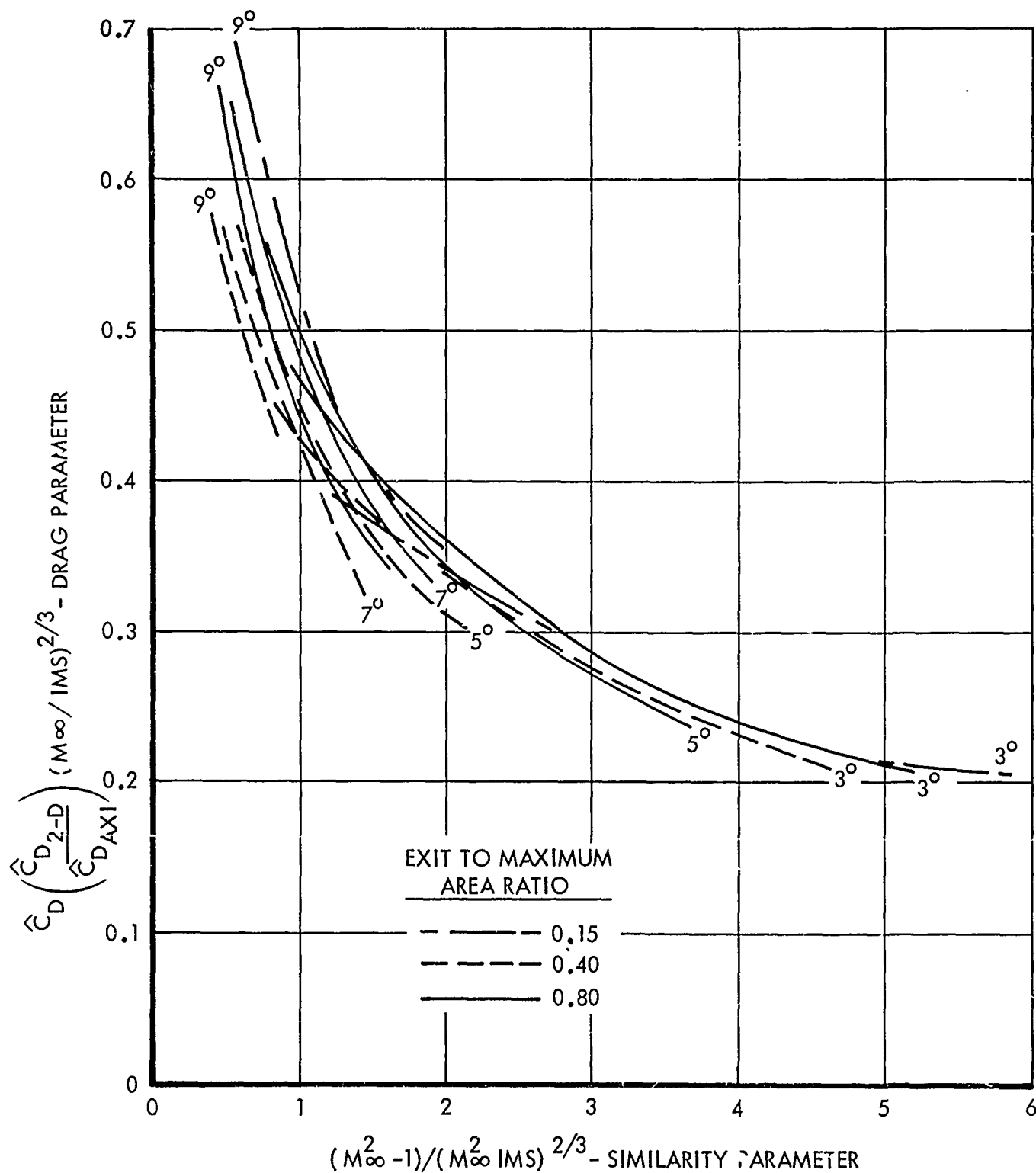


Figure 37. IMS/Transonic Similarity Correlation of
Circular Arc Boattail Scaled MOC Pressure
Drag - Axisymmetric Boattails

Early in the program four turbulent boundary layer methods (References 14, 35, 36, and 37) were considered. However, the Reference 14 Calac boundary layer method was subsequently adopted without comparison to the other methods because it was shown in Reference 14 to be in good agreement with test data and this method was already integrated with inviscid methods under investigation in this study. For laminar boundary layers, only Cohen's solution, described below, was considered.

The laminar boundary layer solution used in the Calac combined MOC/boundary layer program (Reference 4) is essentially Cohen's solution, Reference 38. Briefly, the method is described as follows. The Prandtl boundary layer equations are reduced to a set of ordinary differential equations by introducing a transformation of independent variables. The momentum and energy equations are reduced to a pair of third order ordinary differential equations by establishing conditions for which the velocity and total enthalpy profiles are functions of a single similarity parameter. A pressure gradient parameter is determined at each station and the boundary layer equations are solved using the boundary conditions at the wall and boundary layer edge in a Newton-Raphson iteration procedure. Finally, the displacement thickness, momentum thickness, boundary layer thickness, local heat transfer rate, and skin friction coefficient are determined.

The Lockheed compressible turbulent boundary layer program (Reference 14) is used to compute the boundary layer by simultaneous solution of the boundary layer momentum and energy integral equations. A velocity power law and a modified Crocco equation relating velocity to enthalpy are used. The T' skin-friction method (Reference 13) is used to correct the incompressible skin friction correlation of Sivells and Payne (Reference 12) for compressibility. A modified Reynolds analogy relating heat transfer to skin friction is applied. Given the local inviscid flow properties, the wall temperature, and the body radius, the above relations and the momentum and energy integral equations are solved numerically for the boundary layer thickness, displacement thickness, momentum thickness, and skin friction coefficient along the body.

2.3.1.5 Separation

Flow separation due to steep pressure gradients along a boattail occurs from sharp changes in boattail shape and from the spreading of under-expanded exhaust jets. Since separation causes significant changes in boattail pressures and drag, prediction of separation is important. Two methods were investigated: the Goldschmied criterion for subsonic flow and the Bonner-Karger criterion for supersonic flow. Descriptions of both methods are given below.

Goldschmied Criterion

The Goldschmied criterion states that separation pressure, P_s , is related to the shear stress, τ_m , at the minimum pressure point, P_m , as follows

$$P_s - P_m = 200 \tau_m \quad (5)$$

Restated in terms of the pressure coefficient (referred to freestream conditions)

$$C_{p_s} = 200 C_{f_m} + C_{p_m} \quad (6)$$

According to Reference 32, the above equation is applicable only to two-dimensional flow; however, Goldschmied suggests that it may be utilized for boundary layers which are thin relative to an axisymmetric body radius. Prior to this study substantiation of Goldschmied's criterion had been limited to low Mach number flows. Nevertheless, its use at high subsonic Mach numbers was tentatively recommended in Reference 32 because a review of the derivation did not indicate any obvious limitations due to compressibility.

The Bonner-Karger criterion was developed in Reference 32 by a correlation which collapses a large body of data into a single curve, as follows:

$$\frac{P_s}{P_L} = 13 \left[\frac{M_L^2}{(M_L^2 - 1)^{1/2}} \left(\frac{M_L^2}{Re_X} \right)^{1/7} \right]^{2.24} + 1 \quad (7)$$

where P_s is the separation pressure, P_L is the local external flow pressure, M_L is the local external flow Mach number, and Re_X is the turbulent boundary layer Reynolds number based on an equivalent flat plate length which yields the momentum thickness at the separation point. This expression was derived using flow similarity parameters related by experimental model data. Since the correlation was derived using model data only, its reliability for full scale aircraft is unknown. Also, the correlation does not apply at Mach numbers below 1.16 (lower bound of the data) or Reynolds numbers below about 10^5 (since naturally turbulent boundary layers do not usually appear at such low Reynolds numbers). For convenience, Equation 7 is plotted in Figure 38 using Reynolds number as a parameter.

2.3.2 Internal Flow Methods

Subsonic, transonic, and supersonic flow analysis methods were investigated for computing the internal flow fields of single flow and dual flow nozzles.

2.3.2.1 Single Flow Nozzles

The method of characteristics, an error minimization method, an AEDC-ETF (Arnold Engineering Development Center Engine Test Facility) time dependent method, and a one-dimensional method were the procedures investigated for the analysis of the internal flow of single flow convergent, convergent-divergent, and plug nozzles.

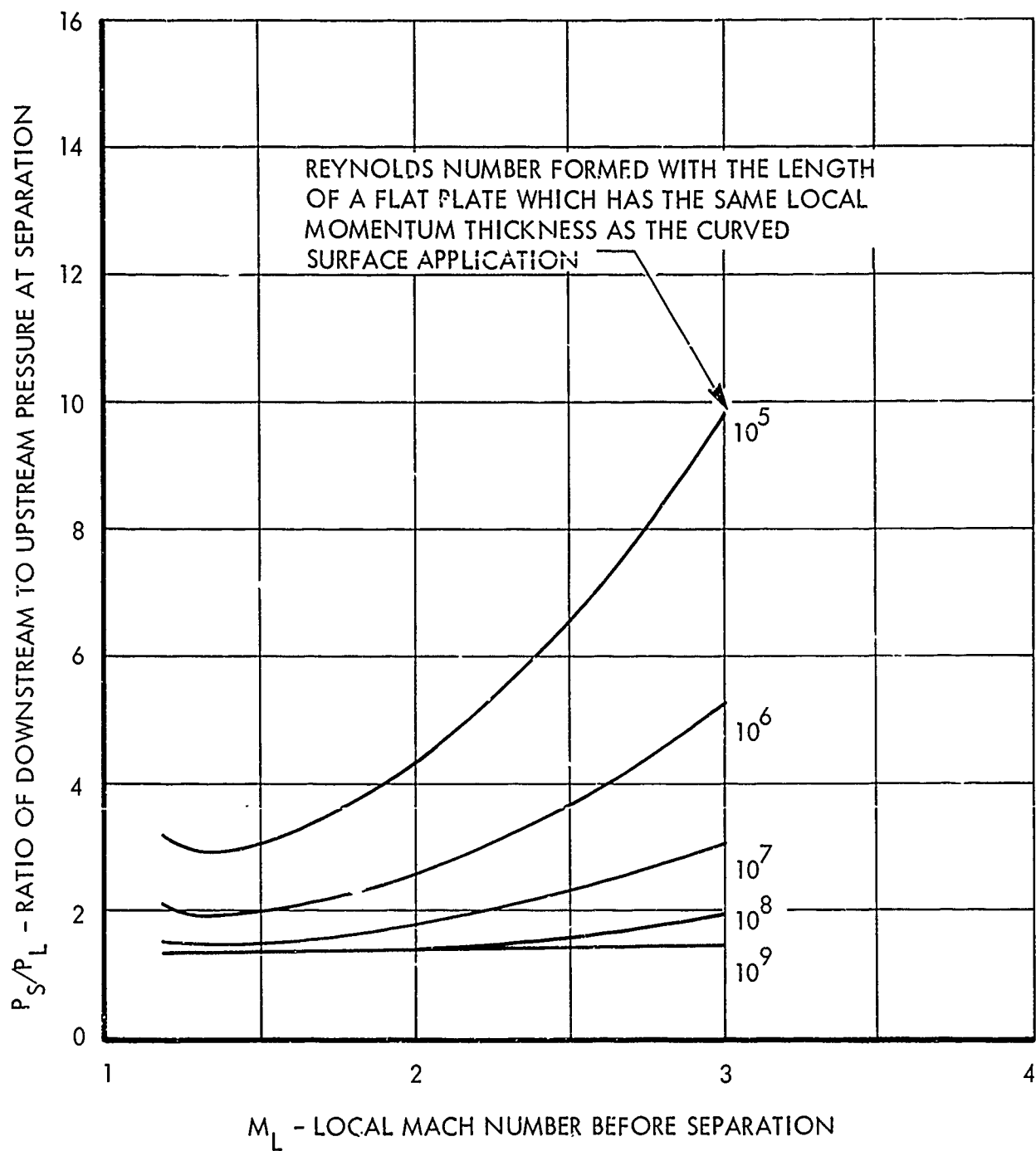


Figure 38. Bonner-Karger Separation Correlation

An internal flow MOC computer program (Reference 39) was used to analyze the supersonic flow downstream of the throat of the convergent-divergent and plug nozzles. The effect of assuming different starting lines for the MOC was investigated. A convergent-divergent nozzle was analyzed by assuming first a vertical starting line at the throat with a Mach number of 1.01, and then by assuming starting conditions of constant axial Mach number of 1.005, 1.01, 1.04, and 1.08 along lines inclined at the respective Mach angles from the axial flow direction. The latter inclined starting lines are more representative of actual transonic conditions than the vertical one. The results of the study indicated that the gross thrust coefficient and exit plane Mach number distribution of the nozzle were insensitive to the starting conditions considered. Therefore, it was concluded that an acceptable solution to the supersonic flow field in a small angle convergent-divergent nozzle can be computed using a simple starting line.

The plug nozzle analysis was conducted by assuming starting conditions for the MOC along a line normal to the plug wall which passes through the downstream end of the cowl. The jet boundary pressures were assumed to be constant for static and subsonic external flow conditions and were determined by shock-expansion theory for supersonic external flow. A linear variation of Mach number from 1.04 to 1.01 from the cowl to the plug was found to be necessary to prevent the solution from going subsonic in the vicinity of the start line. A comparison of measured and predicted plug pressures shows poor agreement slightly upstream and good agreement downstream of the cowl exit.

The error minimization transonic flow method is essentially a relaxation calculation using a mathematical technique to minimize the error (residuals) as the nonsteady state equations approach a steady state condition. The wall pressure distribution was found to be sensitive to flow field mesh sizes selected. Further, the computed results did not compare favorably with experimental pressure data downstream of the throat.

The AEDC-ETF time dependent method is an application of the mathematical technique to the solution of unsteady flow equations of motion which may be applied to subsonic, transonic, and supersonic flows (Reference 40). Typically, the flow field is subdivided into a number of cells having initially assigned flow properties (e.g., from a one-dimensional approximation). Subsequently, the unsteady differential flow equations are solved in each cell, flow adjustments are made, and a new solution obtained for the entire flow field. The process is continued until all unsteady terms are negligible and a steady state solution is thereby obtained.

Nozzle wall pressures upstream of the throat of a convergent-divergent nozzle predicted by one-dimensional analysis or the AEDC-ETF method, and downstream of the throat predicted by the AEDC-ETF or MOC methods agree well with test data, as is shown in Figure 39. The throat mass flow rate predicted by the AEDC-ETF inviscid flow analysis was within 0.6 of one percent of the measured mass flow rate. A boundary layer correction to the AEDC-ETF solution gave a calculated mass flow rate identical to measured

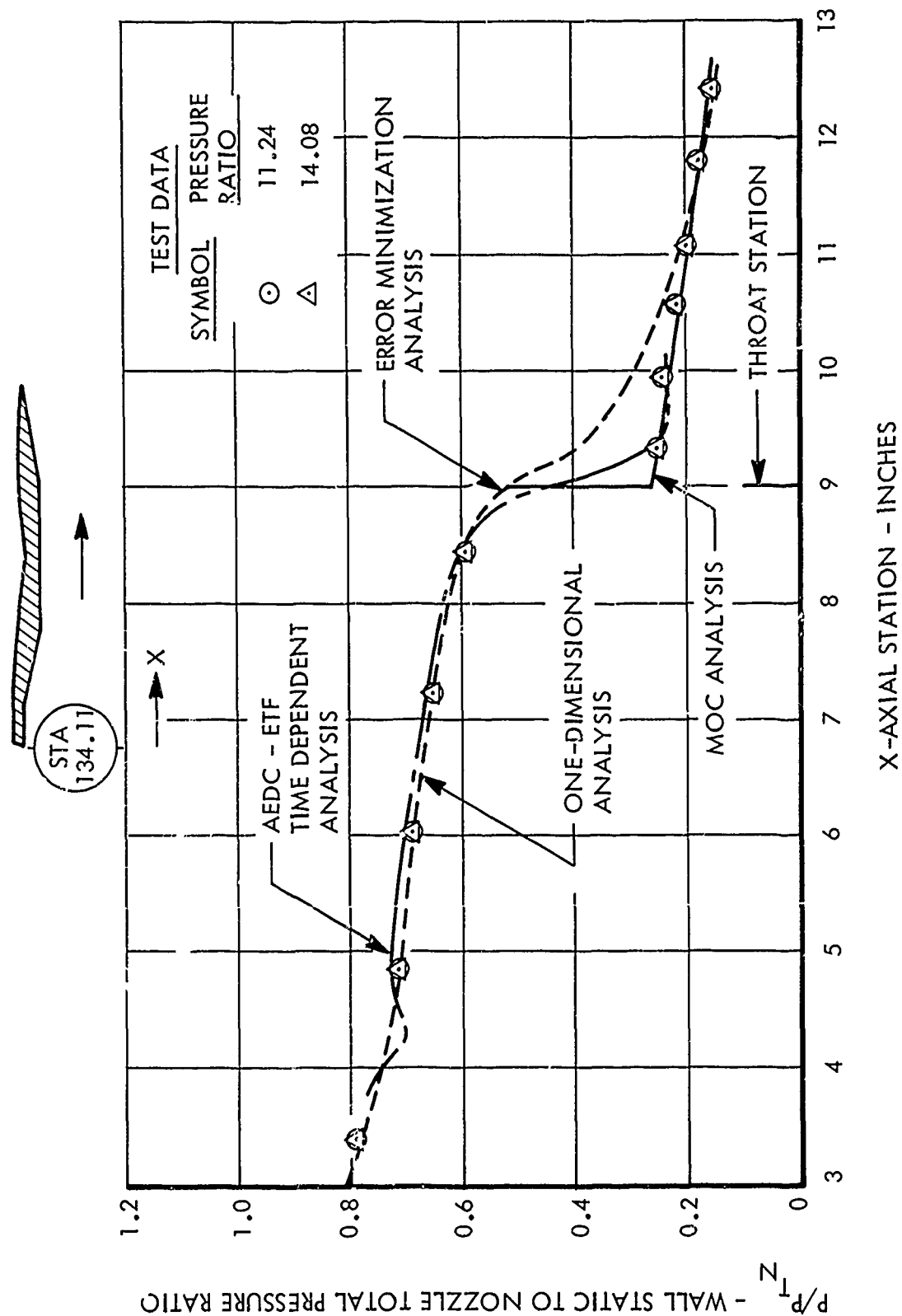


Figure 39. CD_3 Nozzle Predicted and Experimental Internal Pressure Profiles

values. The one-dimensional analysis predicted pressures which are too high over most of the region downstream of the throat, but agree well at the exit.

Since the above methods are too cumbersome to use for preliminary design studies, a combined one-dimensional/empirical method developed by P&WA and described in Reference 41 is recommended for predicting nozzle thrust and discharge coefficients. Application of the method depends on the nozzle type and internal flow regimes. For convergent nozzles, separate methods are employed when the nozzle flow is entirely subsonic, when the flow is critical (mixed subsonic/supersonic flow) but not choked, and when the flow is choked (discharge coefficient invariant with nozzle Pressure ratio). For convergent-divergent nozzles, separate methods are employed when the flow is subsonic throughout the nozzle, the flow is critical with separation occurring in the diverging section (flow overexpanded), and the flow is critical with no internal flow separation.

For all flow regimes and nozzle types, a stream thrust correction factor is employed for predicting thrust coefficients. The stream thrust correction factor, C_s , is defined as the ratio of actual total momentum to ideal total momentum (sums of momentum and pressure/area terms) at the nozzle exit (assuming for both that no internal flow separation occurs) and is written as

$$C_s = \frac{(\dot{m}V + PA)_{\text{actual}}}{(\dot{m}V + PA)_{\text{ideal}}}$$

where the ideal total momentum is obtained from one-dimensional isentropic flow relationships. For convergent nozzles, a fixed value of 0.997 for the correction factor is employed, while, for convergent-divergent nozzles, the correction factor is obtained from correlations of experimental data as a function of area ratio and internal divergence angle.

For separated internal flows, the nozzle gross thrust is computed as the sum of the total momentum at the separation point plus the pressure force acting on the nozzle inner surfaces downstream of the separation point. The flow total momentum at the separation point is obtained through application of the stream thrust correlation. Specifically, the stream thrust factor is obtained as a function of the nozzle area ratio at the separation point and the divergence angle. The location of the separation point and the pressure acting on the inner wall surface downstream of the separation point are obtained from two empirical correlations. The separation point is located through use of a correlation for prediction of the surface pressure just upstream of the separation point as a function of nozzle pressure ratio. The pressure downstream of the separation point is obtained as a function of the pressure upstream of the separation point and freestream ambient pressure.

Figure 40 shows good agreement between predicted and measured convergent and convergent-divergent nozzle thrust coefficients.

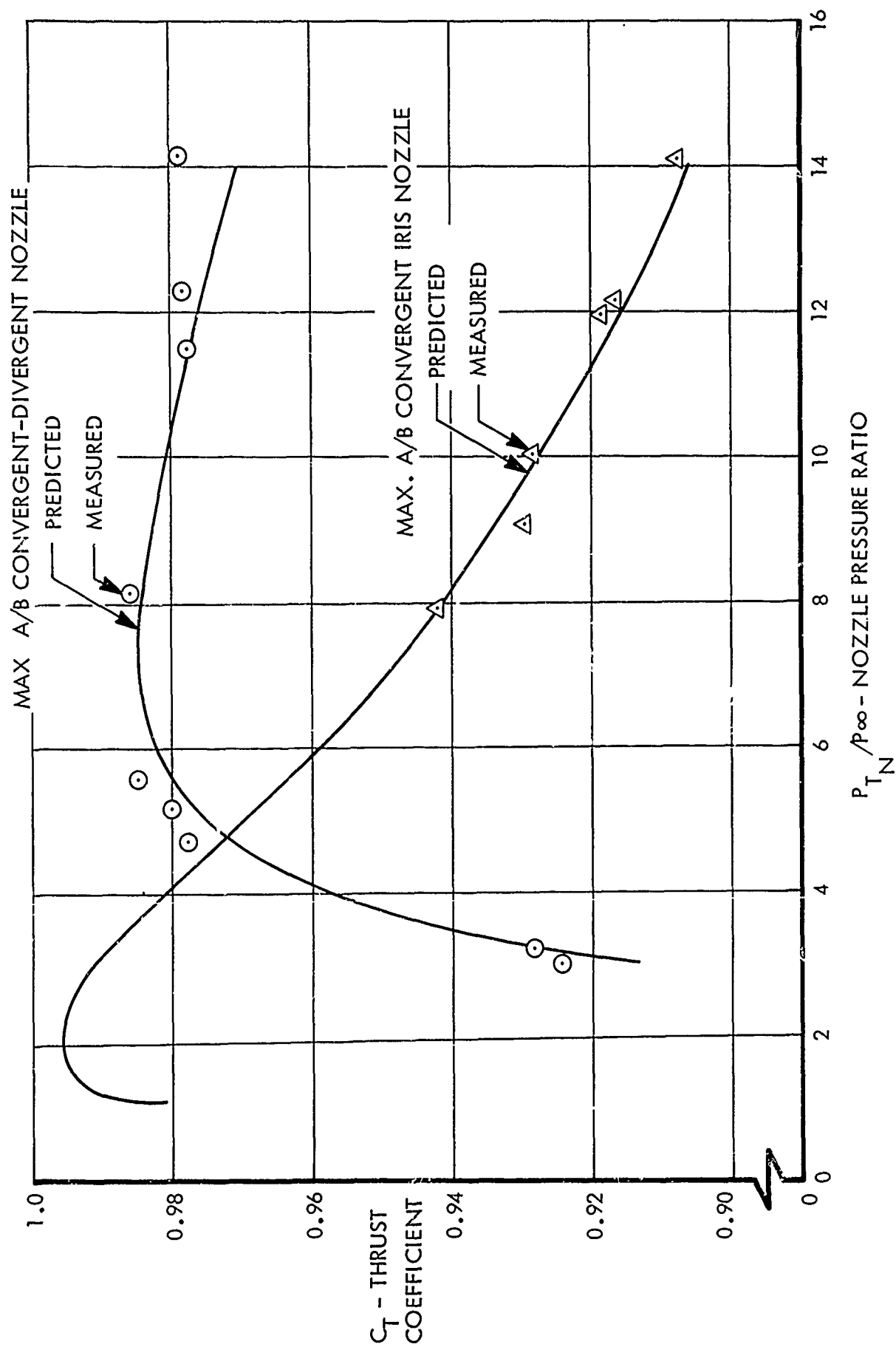


Figure 40. Comparison of Predicted and Measured Nozzle Thrust Coefficients

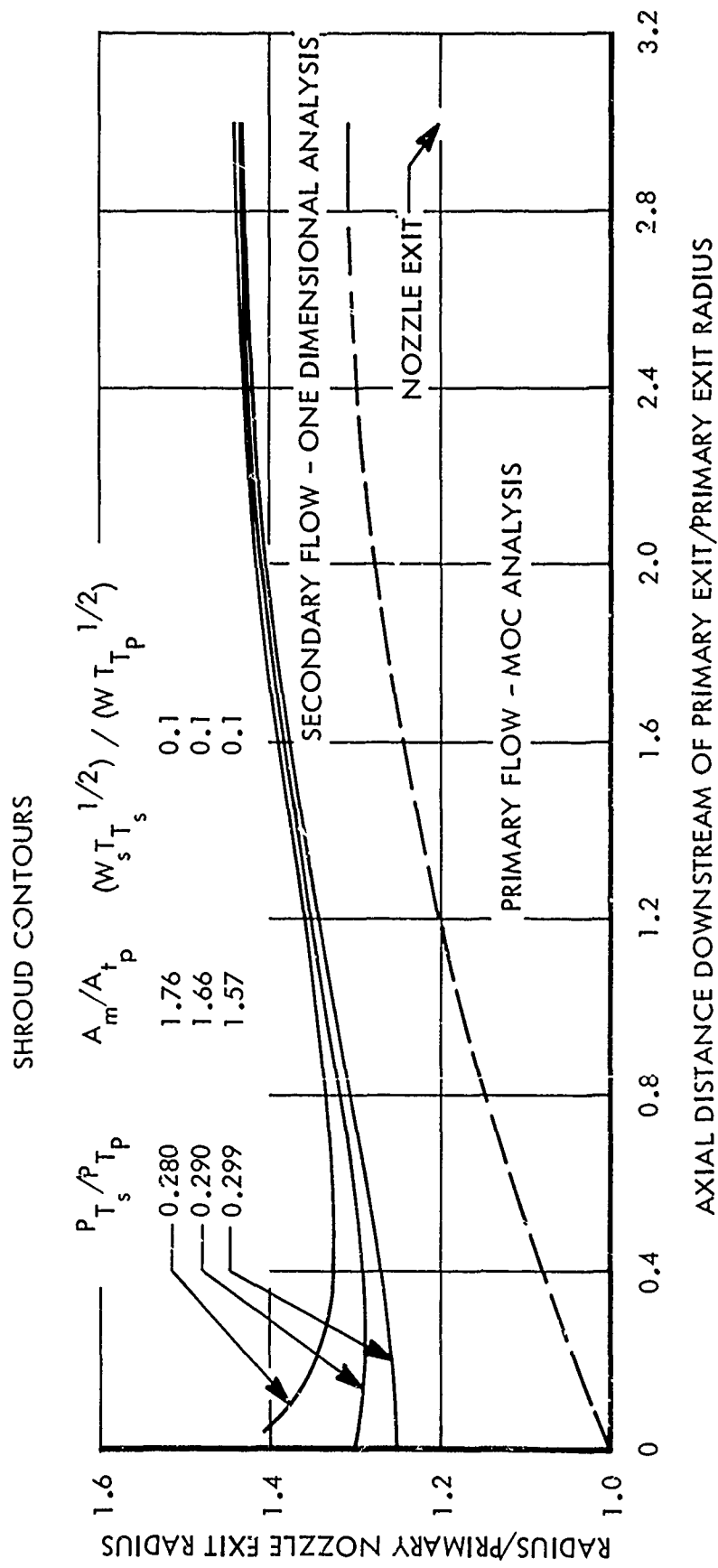


Figure 41. Convergent-Divergent Ejector Nozzle Shroud Designs

2.3.2.2 Dual Flow Nozzles

The following three ejector (dual flow) nozzle analysis methods were evaluated: MOC primary/one-dimensional secondary solution, the Bernstein one-dimensional approximation, and Weber's modified one-dimensional method. The MOC/one-dimensional method of ejector nozzle analysis was originally devised by Addy (Reference 42) to overcome some of the shortcomings of the one-dimensional and quasi-one-dimensional analysis. The method is applicable where the secondary mass flow is large compared to the entrained mass flow due to mixing. Typically, the secondary mass flow should be greater than two percent of the primary mass flow. For small secondary flows the mode of operation of the ejector can be more accurately described as a base pressure problem, and the traditional base pressure solutions are applicable. In addition to the inviscid MOC/one-dimensional solution, a mixing correction, such as the method of Addy and Chow (Reference 43), may be added to account for mixing between the two streams. The digital computer program of Reference 44 incorporates the above procedure for analysis of ejector nozzles. The Bernstein theory (Reference 45) for multistream compound-compressible nozzle flow assumes the exit of the primary nozzle to be located far enough upstream of the minimum shroud area so that two-dimensional effects can be ignored. The method of Weber (Reference 46) predicts pumping characteristics of ejectors with short axial distances between the primary exit plane and the plane of the minimum shroud area.

For purposes of comparing the three ejector methods, the shroud contours shown in Figures 41 were used. The pressure distribution along the outer boundary of the primary flow was determined by exact shock MOC. Then, using one-dimensional flow relations, the shroud contours were calculated by determining the area necessary to pass the secondary flow at the local static pressure as obtained from the primary flow MOC calculation. The resulting contours show that as the secondary to primary total pressure ratio is increased, the shroud minimum area, A_m , decreases and the location of the minimum area moves upstream.

Comparison of the Bernstein, Weber, and MOC/one-dimensional methods to the ejector nozzle configuration described above shows that the Weber method predicts substantially lower secondary to primary total pressures (higher pumping) than the other two methods (Figure 42), and that the Bernstein prediction is in close agreement with the MOC/one-dimensional for cases having the minimum shroud area downstream of the primary nozzle exit. As expected, agreement between the Bernstein and MOC/one dimensional analysis was not good for the case of the minimum shroud area in the primary nozzle exit plane.

In order to further evaluate the MOC primary/one-dimensional secondary method, two ejector nozzles were analyzed and the results compared to test data. Predicted and experimental internal shroud pressures and secondary to primary corrected mass flow ratios were in good agreement. Typical results are shown in Figure 43 for the ejector nozzle.

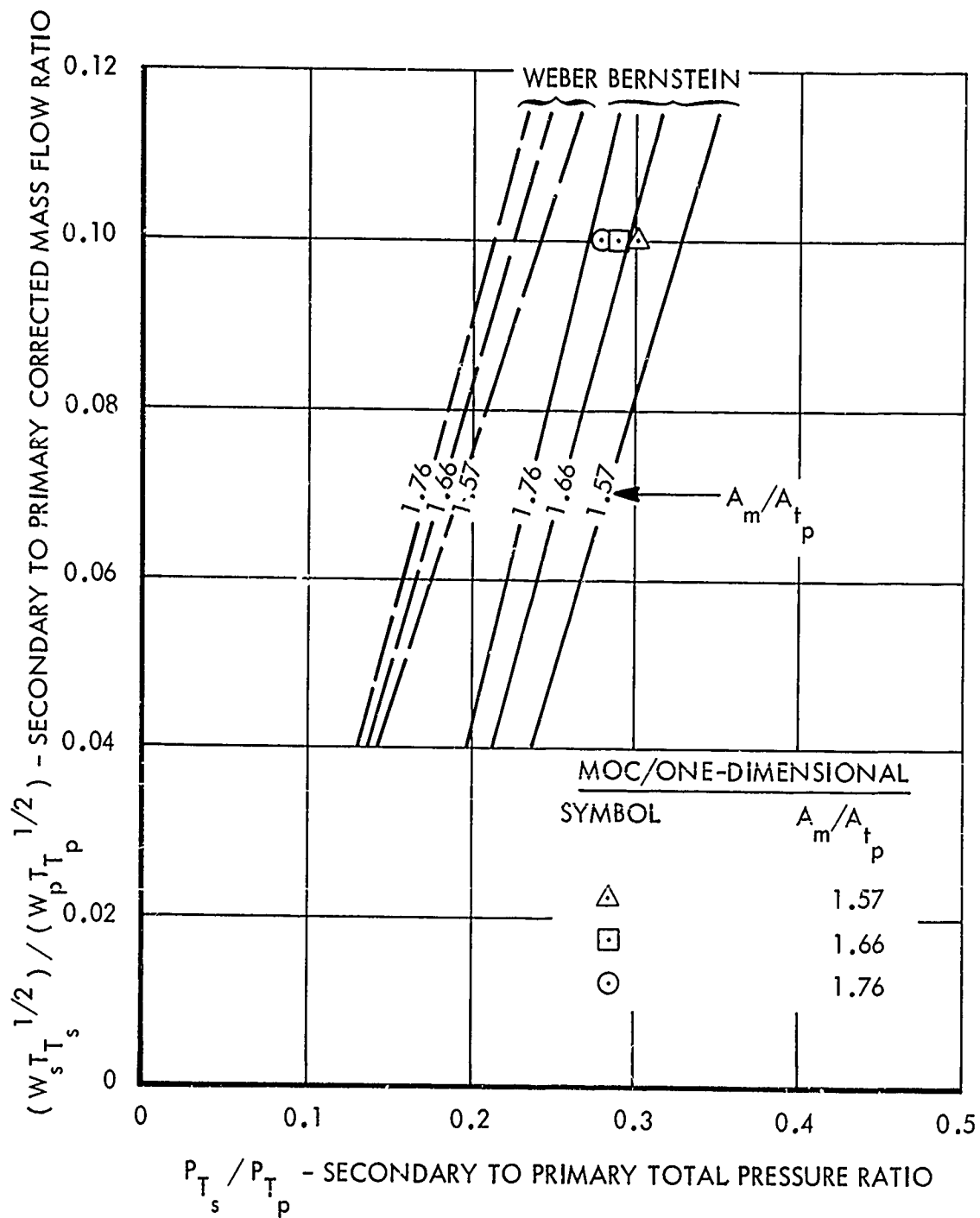


Figure 42. Comparison of Ejector Nozzle Pumping Characteristics Prediction Methods

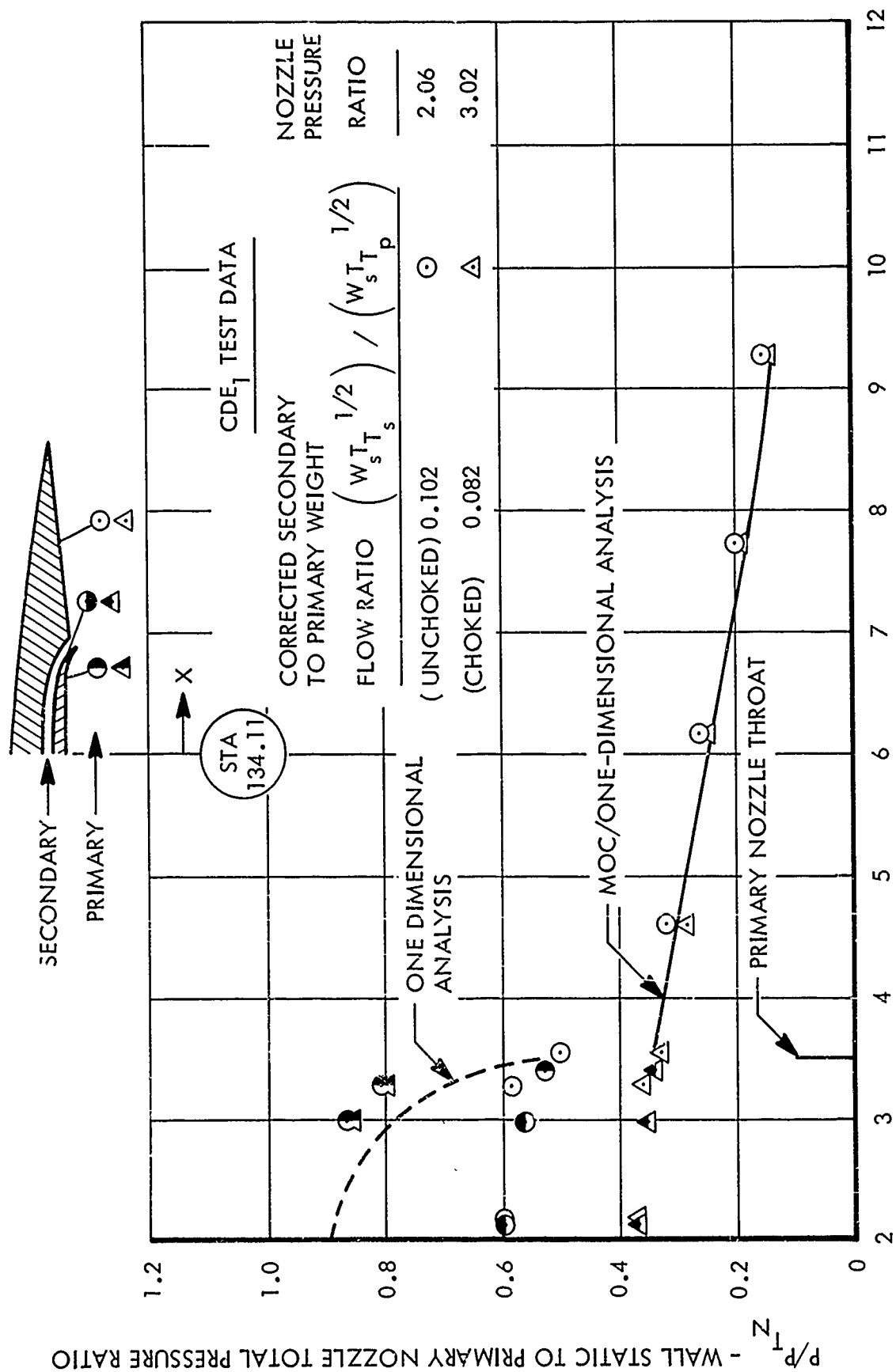


Figure 43. CDE₁ Ejector Nozzle Predicted and Experimental Internal Pressure Distributions

For preliminary design work, ejector nozzle performance can be adequately predicted using Bernstein's method combined with the one-dimensional/stream-thrust-correction. This simplified prediction method and its extension to include internal flow separation is described in the supplement to this report.

2.3.3 Exhaust Plumes

The analysis of exhaust plumes is important in the determination of nozzle thrust and drag because of their influence on boattail, plug nozzle, and base pressures. The interaction between the external flow and the exhaust plume is treated in this section as it relates to the boattail and plug effects; the effect on base pressure is treated separately in Subsection 2.3.4.

2.3.3.1 External Flow Conditions

The air surrounding a plume may be static (quiescent), subsonic, or supersonic. The quiescent air solution, which assumes a constant ambient static pressure along the entire plume boundary, is used for the first guess in a subsonic external flow analysis. Subsequent subsonic external flow plume solutions use external pressure distributions determined iteratively from potential flow solutions around the plume until a converged plume shape is determined.

Supersonic external flow can be treated by shock expansion theory, Newtonian impact theory, or the MOC. Shock expansion theory uses the oblique shock relations to calculate the initial plume pressure (at the boattail/plume junction) and Prandtl-Meyer expansion downstream of the initial shock point. The Prandtl-Meyer relation is applied by calculating a jet boundary pressure which corresponds to turning of the external flow through the change in jet boundary flow angle between adjacent calculation stations. For both oblique shock and Prandtl-Meyer calculations, the external pressure must be balanced with the internal plume pressure at each station.

Newtonian impact theory relates external pressure on the jet boundary to pressure and Mach number upstream of the plume in the following manner:

$$P = P_L \left[1 + \gamma M_L^2 \sin^2 (\theta - \theta_L) \right] \quad (9)$$

where P_L , M_L , and θ_L are pressure, Mach number, and flow angle just upstream of the plume, γ is the ratio of specific heats for the external stream, and P and θ are the local pressure and flow angle along the jet boundary. Again, internal and external pressures must be balanced at each point along the plume boundary.

Application of the MOC to external flow calculations requires a description of the flow field upstream of the plume so that a starting line can be defined. The initial portion of the flow field is determined either by

oblique shock relations or an isentropic compression-characteristic coalescing (isentropic shock) technique. The rest of the plume is calculated by applying the MOC and balancing the internal and external static pressures along the jet boundary.

2.3.3.2 Internal Flow Conditions

Three methods were investigated for computing internal plume flow: shock-expansion-1D, exact shock MOC, and isentropic shock MOC. Exhaust plumes are usually supersonic, in which case any of the methods may be applied. Plumes with subsonic internal flow would be restricted to one-dimensional analysis.

The shock-expansion-1D method utilizes a combination of shock/expansion theory and one-dimensional analysis similar to the methods of Henson and Robertson (Reference 47), Adamson and Nicholls (Reference 48), and Love (Reference 49). The method starts with a Prandtl-Meyer expansion of the internal flow at the nozzle trailing edge to determine the initial plume boundary angle which will match the plume and external static pressures. Downstream of this point, the static pressure of the internal flow at the plume boundary balances the local external static pressure by virtue of two equal opposing effects: the compression caused by the curvature of the plume boundary and the expansion produced by the arrival of the trailing edge expansions which have been reflected at the nozzle centerline. These effects are approximated as follows. Using the local jet boundary slope, the jet boundary is extrapolated a small distance downstream and the internal plume pressure is calculated for the plume flow area at the second station from one-dimensional relations. Taking this pressure as the upstream pressure and the local external pressure as the downstream pressure, oblique shock relations are used to calculate the jet boundary slope just downstream of the second station. The above process is repeated in a step-by-step process until the desired plume station is reached. Plume boundaries were generated using both plane and spherical areas to calculate one-dimensional properties but the difference was so slight that the simpler plane area method was selected. The exact shock MOC method couples the MOC with the oblique shock relations. In the computer program used for this study (Reference 39), as in most exact shock MOC programs, only one oblique shock is calculated by exact shock relations, the trailing edge external shock. All other shocks are treated by a characteristic line coalescing technique. Jet boundary points are calculated by a pressure balance between the local internal and external static pressures, which is an iteration process for the case with external flow.

Isentropic shock MOC calculations are identical to the exact shock method except that oblique shock calculations are replaced by a characteristic line coalescing technique.

2.3.3.3 Comparison and Recommendation of Methods

Five combinations of external and internal methods were used to calculate plume shapes in the presence of supersonic external flow. The results are

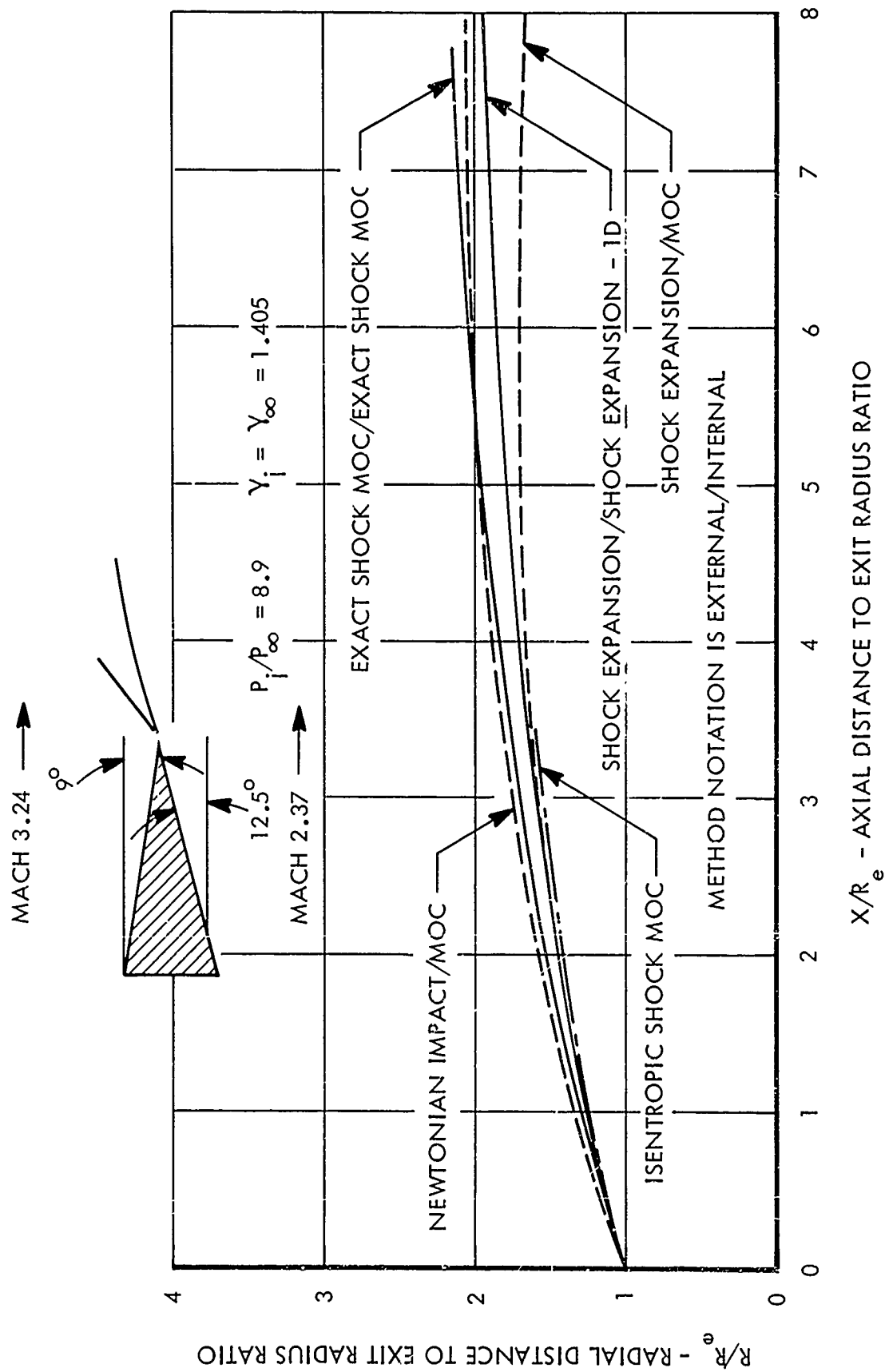


Figure 44. Comparison of Plume Shape Prediction Methods for Supersonic External Flow

shown in Figure 44. In this discussion the combined method notation will be external/internal. Taking the exact shock MOC (for both external and internal flow) from Reference 49 as the standard of accuracy, the other methods in order of increasing error in the plume shape are: (1) Newtonian impact/MOC, (2) shock-expansion/shock-expansion-1D, (3) shock-expansion/MOC, and (4) external and internal isentropic shock MOC. The isentropic shock MOC plume obtained from the NAR slipstream computer program (Reference 50), ceased at a distance of 3.5 nozzle exit radii downstream of the nozzle exit due to a program restriction. In the NAR program, left running characteristics are generated from the nozzle exit start line to the plume. No lines are generated downstream of the last characteristic which originates at the axis point on the start line. All of the methods are in reasonably close agreement up to an (X/R_e) of 1. Beyond this point the Newtonian impact/MOC and exact shock MOC methods give plume shapes which are in close agreement. The other three methods are in close agreement with each other up to an X/R_e value of 3.5, but differ considerably from the method selected as the standard of accuracy. The shock-expansion/MOC method had the greatest deviation from the "accurate" exact shock MOC method over the complete solution length.

A comparison of the initial plume conditions from each method is made in the table below. It is clear that the Newtonian theory gives inaccurate initial plume properties and all of the other methods compare favorably. The Newtonian/MOC method compares even less favorably at the lower Mach numbers. For example, for a local Mach number of 2.5 and other conditions the same as in Figure 44, the Newtonian/MOC method gives an initial plume angle of 25 degrees and a pressure ratio of 3.74, compared to the shock expansion values of 20 degrees and 5.3 pressure ratio.

Method	δ Initial Plume Angle (degrees)	P_δ/P_L Initial Plume To Local Static Pressure Ratio
Exact Shock MOC	17.6	5.85
Isentropic Shock MOC	17.7	6.16
Shock-Expansion/MOC	18.2	6.07
Shock-Expansion/Shock-Expansion-1D	17.6	5.85
Newtonian/MOC	21.5	4.81

The conclusions which can be drawn from these results are: (1) all of the methods give plume contours in reasonably good agreement for short distances downstream of the nozzle exit; (2) initial plume conditions predicted by the Newtonian theory are substantially in error; (3) Newtonian theory gives the best overall plume contour (at a local Mach number of 3.24); and (4) the shock-expansion/shock-expansion-1D method gives the best combination of initial plume conditions and plume shape. In view of the above results, the shock-expansion/shock-expansion-1D method is recommended for calculating plumes with supersonic external flow.

The shock-expansion/shock-expansion-1D method was also selected by Calac to compute the internal plume flow with subsonic external flow. Since the subsonic external flow case involves an external/internal flow field iteration beginning with a quiescent air exhaust plume, it is of interest to compare plumes obtained by the selected method with quiescent air plumes computed by another. Figure 45 provides such a comparison with the isentropic shock MOC method of Reference 49. For a jet to ambient pressure ratio of 1.17 the two methods are very close, and for a pressure ratio of 10.0 the shock-expansion-1D gives a somewhat similar diameter plume. These cases are typical for the integrated nozzle/airframe study and the comparison shows that the shock-expansion/shock-expansion-1D method should be adequate, especially since lower plume pressure ratios usually occur with subsonic external flow.

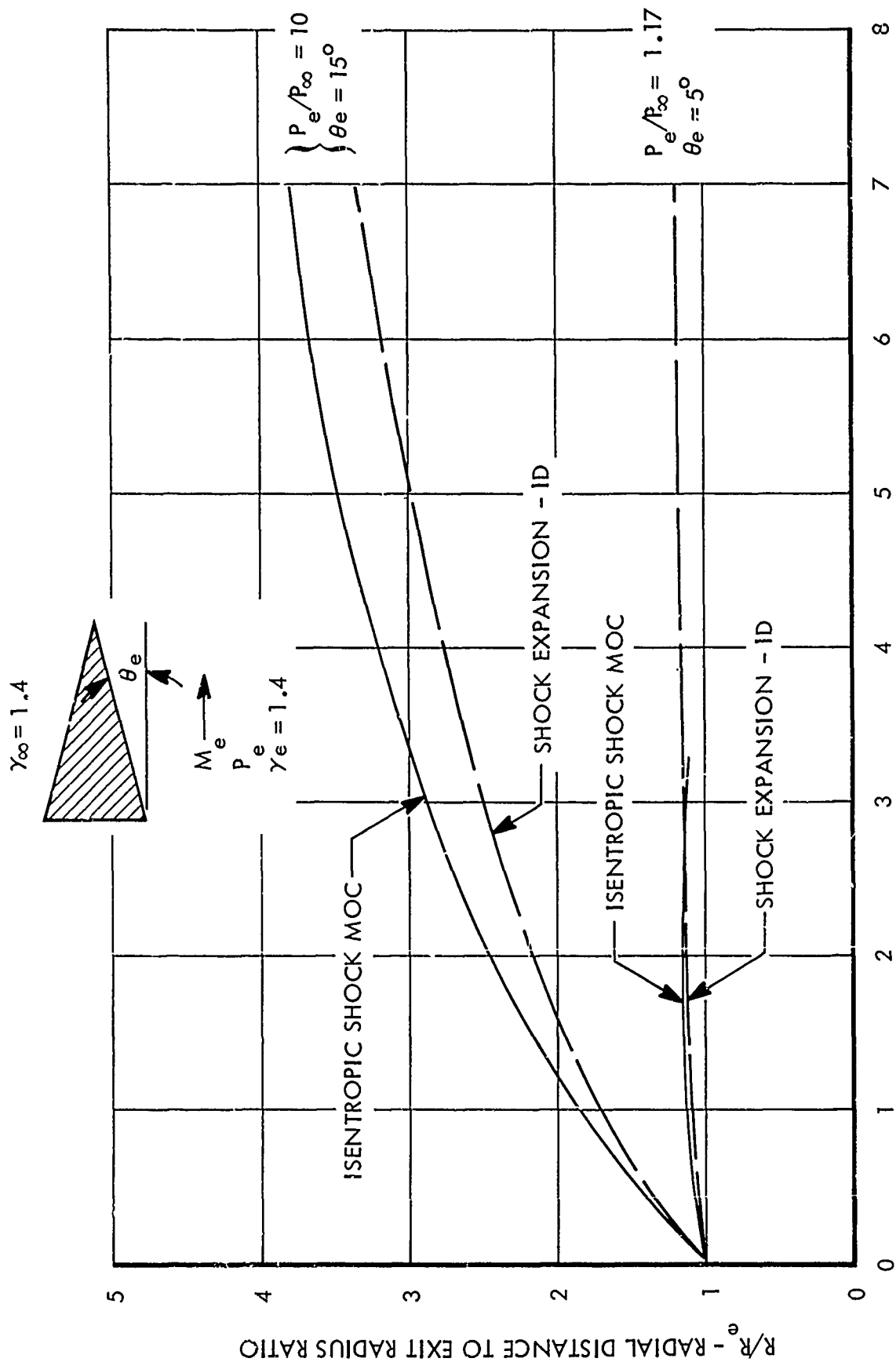
2.3.4 Base Pressure

This subsection presents an evaluation of analytical and empirical methods for predicting annular and plug base pressures.

2.3.4.1 Annular Base Pressure

As applied to this study, annular base pressures occur at the nozzle trailing edge region between the exhaust jet and the external stream. Base pressure is important because it can have a significant influence on the nozzle-boattail drag. For subsonic external flow, annular base pressure is predicted by a modified Brazzel-Henderson correlation method or the McDonald-Hughes correlation. For the supersonic external flow, it can be predicted by the Brazzel-Henderson Correlation or by the Korst theory with a virtual origin correction for boundary layer.

Subsonic External Flow - The Brazzel and Henderson empirical supersonic method (Reference 30), extended to subsonic external flow cases, indicates that base pressure is a weak function of jet to freestream momentum ratio and boattail geometry. Since practical cases for subsonic external flow have a sonic jet, this study is restricted to such cases.



X/R_e - AXIAL DISTANCE TO EXIT RADIUS RATIO

Figure 45. Comparison of Isentropic Shock MOC and Shock-Expansion-ID Plume Shapes for Still Air

Basically, the correlation is divided into two parts. The first part is a correlation of annular base pressure for cylindrical (no boattail) afterbodies as a function of the nozzle exit to freestream momentum ratio, defined as

$$R_{m_f} = \frac{(mV)_e}{(mV)_\infty} = \frac{\gamma_e P_e A_e M_e^2}{\gamma_\infty P_\infty A_M M_\infty^2} \quad (10)$$

For subsonic flow, Cubbage's data from Reference 51 and 52 for cylindrical and 3-degree conical boattail afterbodies show a slight increase in base pressure with jet to freestream momentum ratio as illustrated in Figure 46. (The 3-degree boattail data were included because they were sufficiently close to the cylindrical data for correlation). This trend can be approximated by the following relation for cylindrical afterbodies.

$$\frac{P_b}{P_{\infty \text{ cyl.}}} = 0.9 + 0.0167 (R_{m_f}) \quad (11)$$

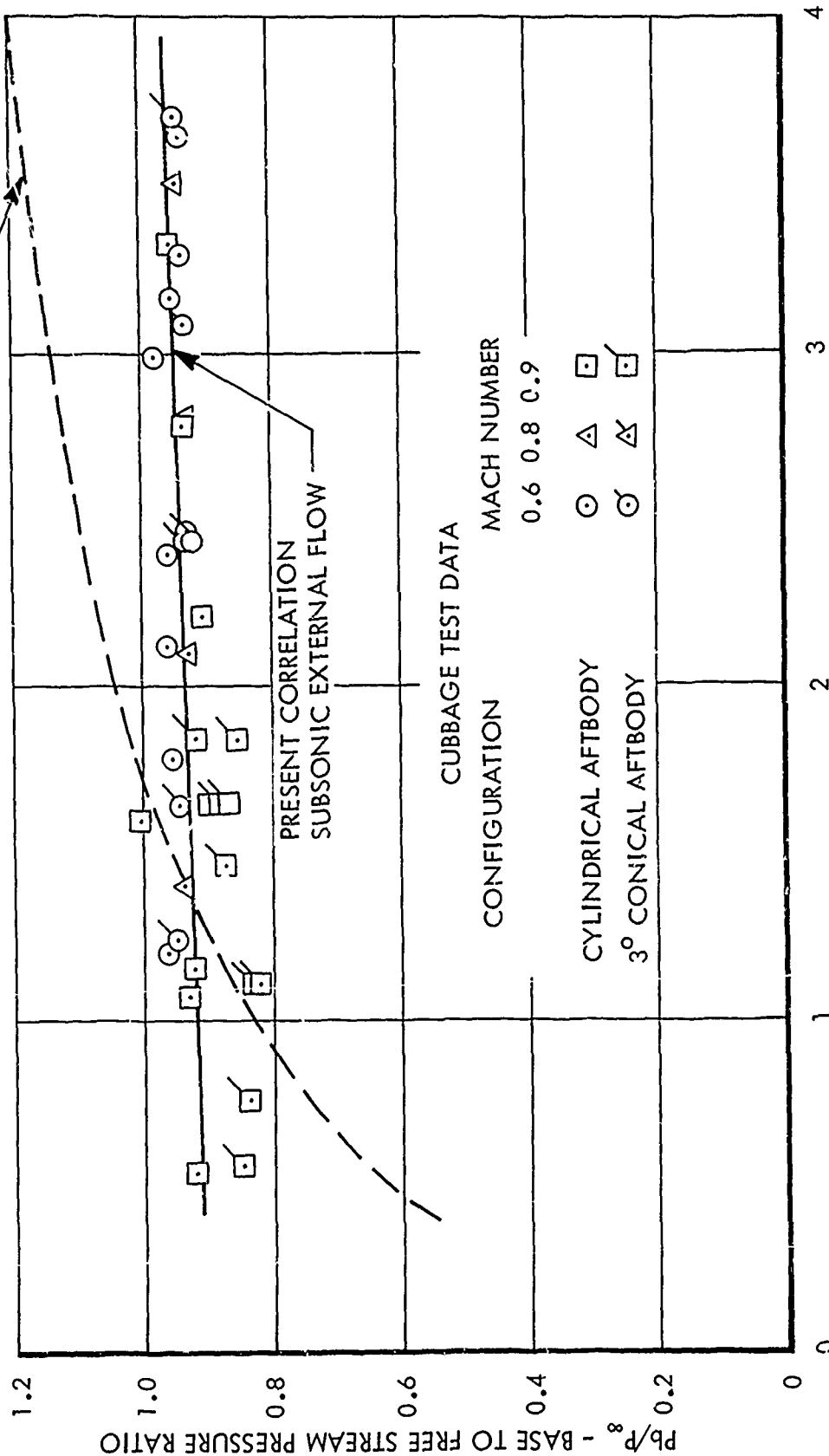
The second part of the correlation relates annular base pressures for cylindrical afterbodies to annular base pressures for non-cylindrical (boattail) afterbodies as a function of the base to maximum body area ratio, A_b/A_M . This function was determined by plotting the ratio of cylindrical to non-cylindrical base pressure versus the area ratio as shown in Figure 47. A slight decrease in base area is indicated. Cylindrical base pressures are taken from Figure 46 for momentum ratios corresponding to the non-cylindrical bodies. These values are ratioed to experimental base pressures of the corresponding non-cylindrical bodies taken from Reference 52. Unfortunately, about a twenty percent data scatter exists for the lower area ratio values. This will result in some inaccuracy in using the average line drawn through the data given by

$$\frac{P_{bcyl.}}{P_{b \text{ non-cyl.}}} = 0.94 + 0.06 (A_b/A_M) \quad (12)$$

combining equations (11) and (12) yields a modified Brazzel-Henderson subsonic base pressure correlation as follows:

$$\frac{P_b}{P_\infty} = \left[0.9 + 0.0167 (R_{m_f}) \right] / \left[0.94 + 0.06 (A_b/A_M) \right] \quad (13)$$

BRAZZEL AND HENDERSON CORRELATION
SUPERSONIC EXTERNAL FLOW



R_{m_f} - JET TO FREE STREAM MOMENTUM RATIO

Figure 46. Annular Base Correlation for Cylindrical and 3-Degree Conical Aftbodies

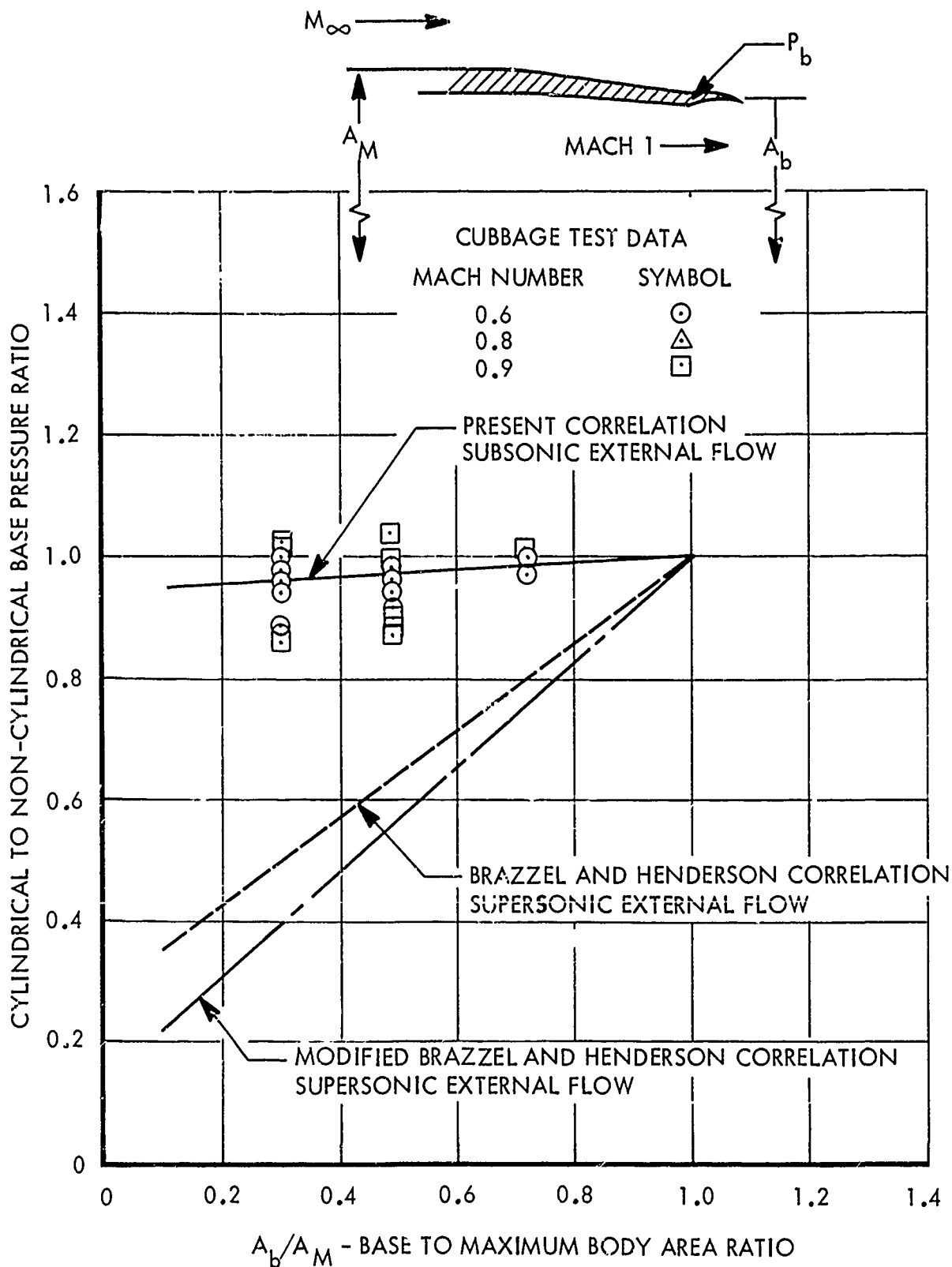


Figure 47. Annular Base Pressure Correction for Noncylindrical Afterbodies

The McDonald-Hughes correlation method (Reference 53) is based on correcting the base pressure coefficient for zero jet flow for the presence of the jet. The zero jet flow coefficient, C_{pbz} , is correlated as a function of base to maximum body diameter, D_b/D_M , and boattail angle. Two terms are added to this to account for the presence of the jet. The first, F_1 , is a function of jet pressure ratio and boattail angle. The second is the product of F_2 , a function of jet pressure ratio, and the geometric parameter $(D_e^2/D_M D_b)$ where D_e , D_M , and D_b are the jet, maximum body, and base diameters, respectively. In equation form this is stated as

$$C_p = C_{pbz} + F_1 + F_2 (D_e^2/D_M D_b) \quad (14)$$

Plots of the functions F_1 and F_2 are presented in both References 28 and 53. (The nomenclature herein has been changed to simplify the presentation of the correlation).

Subsonic external flow base pressures predicted for the CF_1 model (Figure 48) are slightly above the test data for the McDonald-Hughes method and slightly below the test data for the Brazzel-Henderson method. The trends predicted by the McDonald-Hughes method with freestream Mach number and nozzle pressure ratio agree with test data trends. The Brazzel-Henderson method shows essentially no effect of freestream Mach number. Since the test data trends with Mach number are small, this deficiency in the Brazzel-Henderson subsonic method is not considered important. Further, since the method is much simpler to apply, it is recommended.

Supersonic External Flow - Analytical and empirical methods of predicting base pressure on the annular base for the case of supersonic internal and external flows are discussed in this section. Neither the Korst zero boundary layer base pressure prediction method nor the modification of this method with the Korst equivalent bleed correction yields uniformly good results for typical nozzle installations. However, the mixing layer virtual origin correction to the Korst zero boundary layer theory improves the results. The empirical relation proposed by Brazzel and Henderson (Reference 33) successfully correlates the available experimental data.

In an NAR study (Reference 28), annular base pressures predicted with the Korst base pressure theory (Reference 54) were compared to experimental values. Good agreement between predicted values and test data was noted for cases where the boattail boundary layer was small compared to the annular

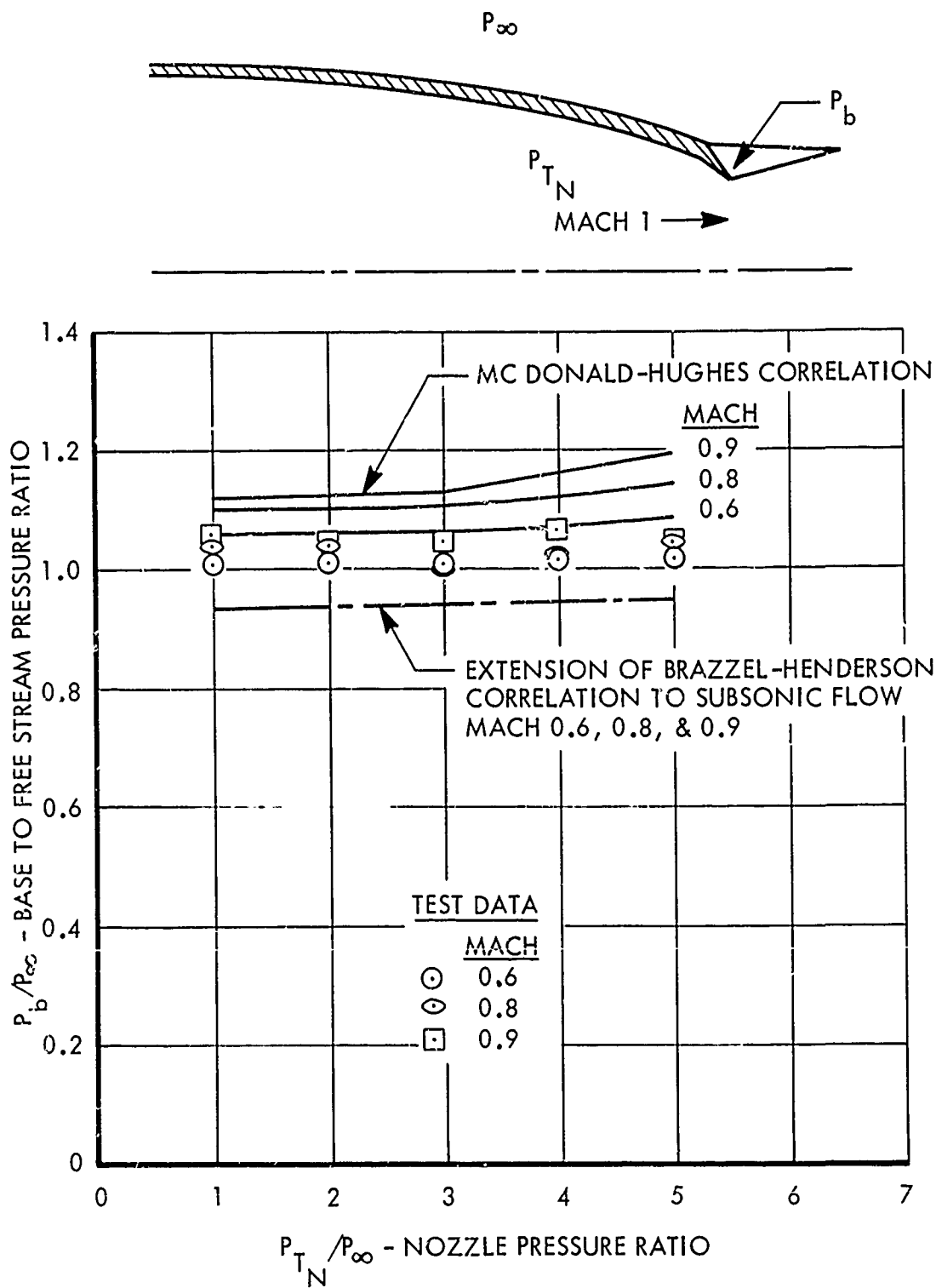


Figure 48. Comparison of Subsonic Base Pressure Prediction Methods with CF_1 Test Data

base height, and poor agreement where it was not. This is not surprising, since in the Korst theory the ratio of initial boundary layer thickness to mixing length along the free jet boundary must approach zero. This condition is violated in typical nozzle installations where the initial boundary layer thickness is not small compared to the base height (small base heights yield short mixing lengths).

Korst and Chow (Reference 55) propose accounting for the initial boundary layer with an equivalent bleed flow. This proposal is based on the fact that in the mixing integral equations of the base flow problem, the two terms expressing the effects of the boundary layer and of base bleed are additive. Consequently, either may be replaced by an equivalent change of the other. The equivalent bleed flow rates required to theoretically account for the base pressures obtained by Baughman and Kochendorfer (Reference 56) were compared with those calculated from the boundary layer momentum thickness. The comparison showed that the equivalent bleed method failed for these cases. This failure is attributed to the fact that these thick boundary layers violate the basic assumption that the shapes of the flow profiles are not strongly affected by the initial boundary layer. Since these cases are typical of conditions likely to be encountered in aircraft operation, the equivalent bleed method obviously will not yield satisfactory results for cases of interest in this study.

The virtual origin method, described in detail in Reference 19 accounts for the initial boundary layer by shifting the origin of the shear layer from the base separation point to an upstream point chosen such that the mass and momentum fluxes at the base separation point are the same as those in the actual boundary layer at the base separation point. Virtual origin calculations were performed by modifying the NAR two-stream base pressure program, as detailed in Reference 19, and were compared with Baughman and Kochendorfer experimental data (Reference 56). In all cases, the virtual origin boundary layer correction to the Korst zero boundary layer method improved the agreement with data.

An empirical technique for predicting annular base pressure for bodies-of-revolution with a single jet has been developed by Brazzel and Henderson (Reference 33). The method is based on correlation of data for cylindrical and non-cylindrical boattails with exhaust jets. The relationship is as follows:

$$\frac{P_b}{P_\infty} = \left[\frac{T_e}{T_e^*} \right] \left[\frac{3.5}{1 + 2.5 A_b/A_M} \right] \left[0.19 + 1.28 \left(\frac{R_{mf}}{1 + R_{mf}} \right) \right] + 0.047 (5 - M_\infty) \left[2 \left(\frac{\Delta X_e}{D_M} \right) + \left(\frac{\Delta X_e}{D_M} \right)^2 \right] \quad (14)$$

where A_M is the maximum body area.

The first term on the right side of equation (14) normalizes the jet temperature to the jet temperature of a sonic nozzle. The second term corrects for boattail effects, and the third term is a correlation based on the ratio of nozzle exit momentum flux to freestream momentum flux where

$$R_{m_f} = \frac{(mV)_e}{(mV)_\infty} = \frac{\gamma_e P_e A_e M_e^2}{\gamma_\infty P_\infty A_\infty M_\infty^2} \quad (15)$$

A nozzle position (relative to the end of the boattail) correction is obtained by the fourth term.

Examination of Brazzel's correlation plot for the boattail correction term shows that a better estimate of this effect is obtained by replacing the second term of Equation (14) with

$$\frac{3.5}{0.5 + 3.0 A_b/A_M} \quad (16)$$

The modified Brazzel-Henderson empirical method, Korst zero boundary layer theory, and Korst/virtual origin theory predictions are compared in Figure 49 to Baughman and Kochendorfer test data from Reference 56. Predictions from the empirical method are in very good agreement with test data. Although the empirical method makes no special correction for boundary layer effects, the effects are inherently included in the correlation since it is based on model test data. Since the boundary layer momentum thickness-to-base height ratio for full scale aircraft are different than those for models, an adjustment in the correlation may be necessary if applied to full scale aircraft. Both corrected and uncorrected Korst theory predictions give scattered results. Korst theory cases in best agreement with the test data have small momentum thickness to base height ratios (giving small momentum thickness to mixing length ratios).

For supersonic flow cases having a large annular base area (either geometric or effective) the Brazzel-Henderson supersonic correlation predicted base pressures which are in good agreement with Phase I test data, but for a small annular base area the prediction is only in fair agreement with the data. These results are shown below. In obtaining these predicted base pressures a check was made first to see if flow separation should occur before the end of the boattail. This check was done by combining the Bonner-Karger and Brazzel-Henderson correlations in a common calculation. The point along the boattail at which the separation and base pressures, P_s and P_b , matched was found. No separation was predicted for the CF_3 Mach 2.2 case, and the calculated base pressure therefore applies to the physical annular base area. Separation was predicted for the other cases and the annular base area was taken as the projected area from the separation point to the nozzle exit internal radius.

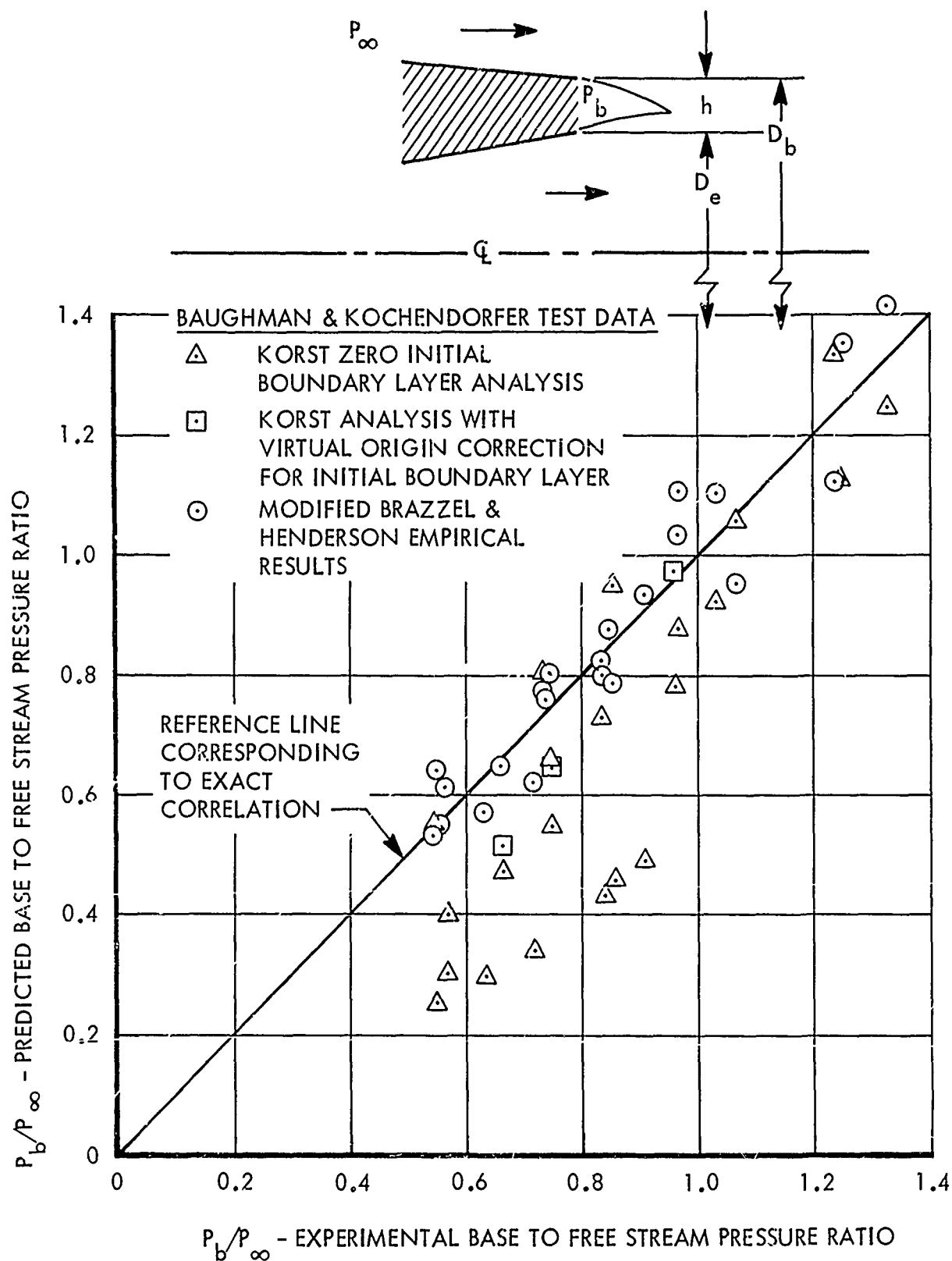


Figure 49. Comparison of Base Pressure Prediction Methods

Model	Base Area Ratio A_b/A_M	Nozzle Pressure Ratio	Mach Number	P_b/P_∞ - Base Pressure Ratio	
				Measured	Predicted
CF ₃	0.111*	10.04	1.8	1.24	1.22
CF ₃	0.071	13.12	2.2	1.18	1.20
CI ₃	0.185*	10.01	1.8	1.16	1.16
CD ₃	0.047*	12.03	1.8	1.34	1.54

*Effective base area which includes boattail separation effect.

Some general comments can be made concerning annular base drag. The drag contribution from a thin annular base is small compared to overall aircraft drag, and errors in predicting the base drag will thus not seriously affect overall aircraft performance predictions. However, for a large annular base (for example, if boattail flow separation occurs), errors in base pressure prediction may give large errors in base calculations. The Korst theory agrees better with measured base pressures as the momentum thickness to base height ratio decreases (thin boundary layer or large base height). Thus, in the overall view, the base drag prediction problem using the Korst method is somewhat compensating in that predictions become more accurate as the contribution from the base increases. On the other hand, because of the simplicity of the calculation and the good agreement with data, the Brazzel-Henderson empirical correlation is recommended as an easily applied and useful tool for predicting annular base pressures.

2.3.4.2 Plug Base Pressure

A semi-empirical plug base pressure method was developed from the Phase I test data. The base pressure method relates the base to total nozzle pressure ratio to the nozzle (total to freestream static) pressure ratio as illustrated in Figure 50 for Mach numbers of 1.1 to 2.5 and nozzle pressure ratios of 4 to 18.5. At low nozzle pressure ratios, the base pressure decreases with increasing nozzle pressure ratio; at high nozzle pressure ratios, the base pressure becomes independent of nozzle pressure ratio (horizontal lines). The latter result is due to shielding of the base region from the interaction between the internal and external flow. Base pressures for low nozzle pressures can be represented by the following equation:

$$\frac{P_b}{P_{T_N}} = \frac{4.312}{(P_{T_N}/P_\infty)^{1.975}} \quad (17)$$

Base pressures for high nozzle pressure, which are defined as locked-in base pressures since they are invariant with nozzle pressure ratio, fall along the straight line represented below when plotted as a function of plug surface static pressure at the end of the plug, P_p , as shown in Figure 51.

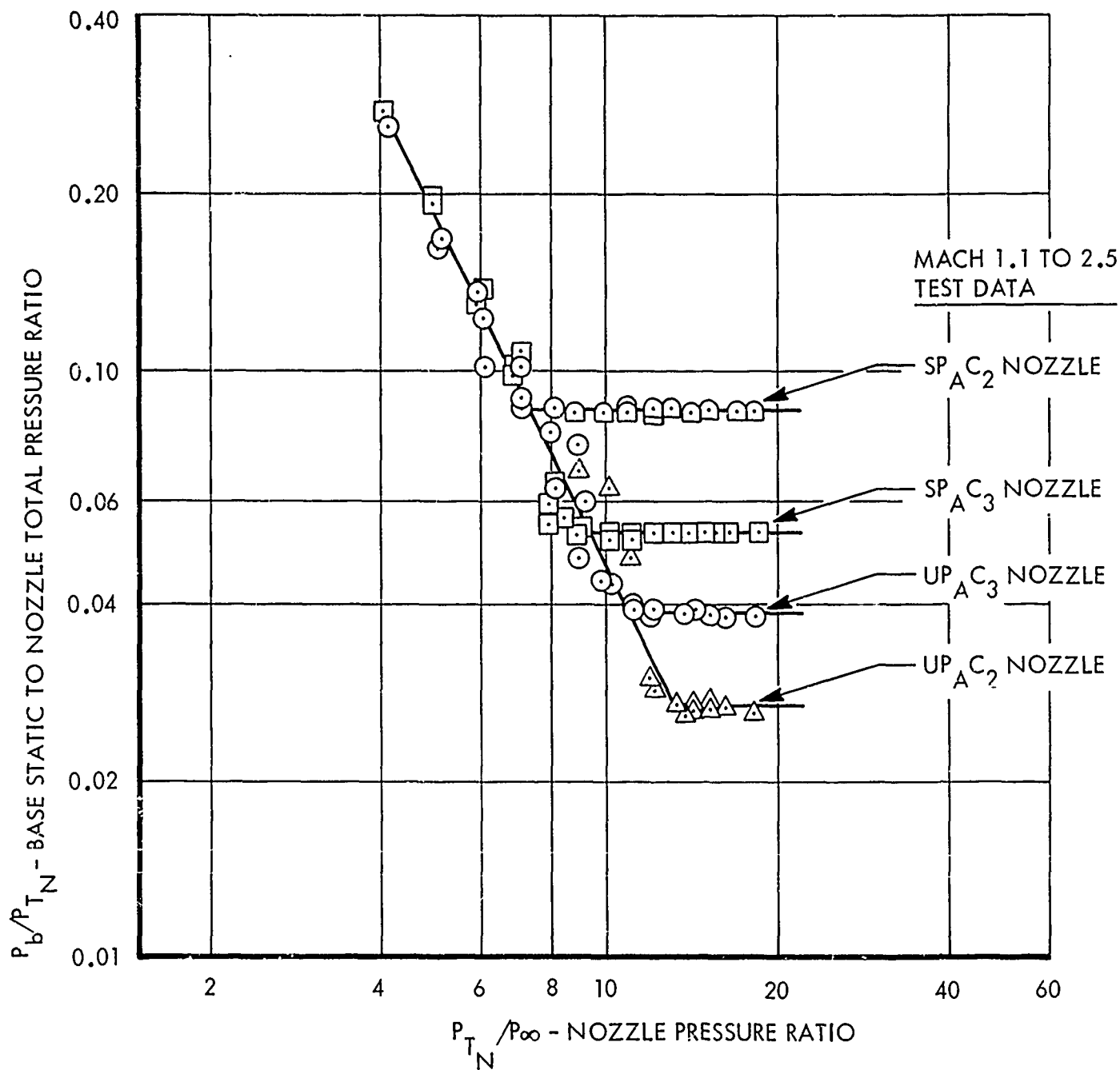


Figure 50. Isolated Plug Nozzle Base Pressure Correlations

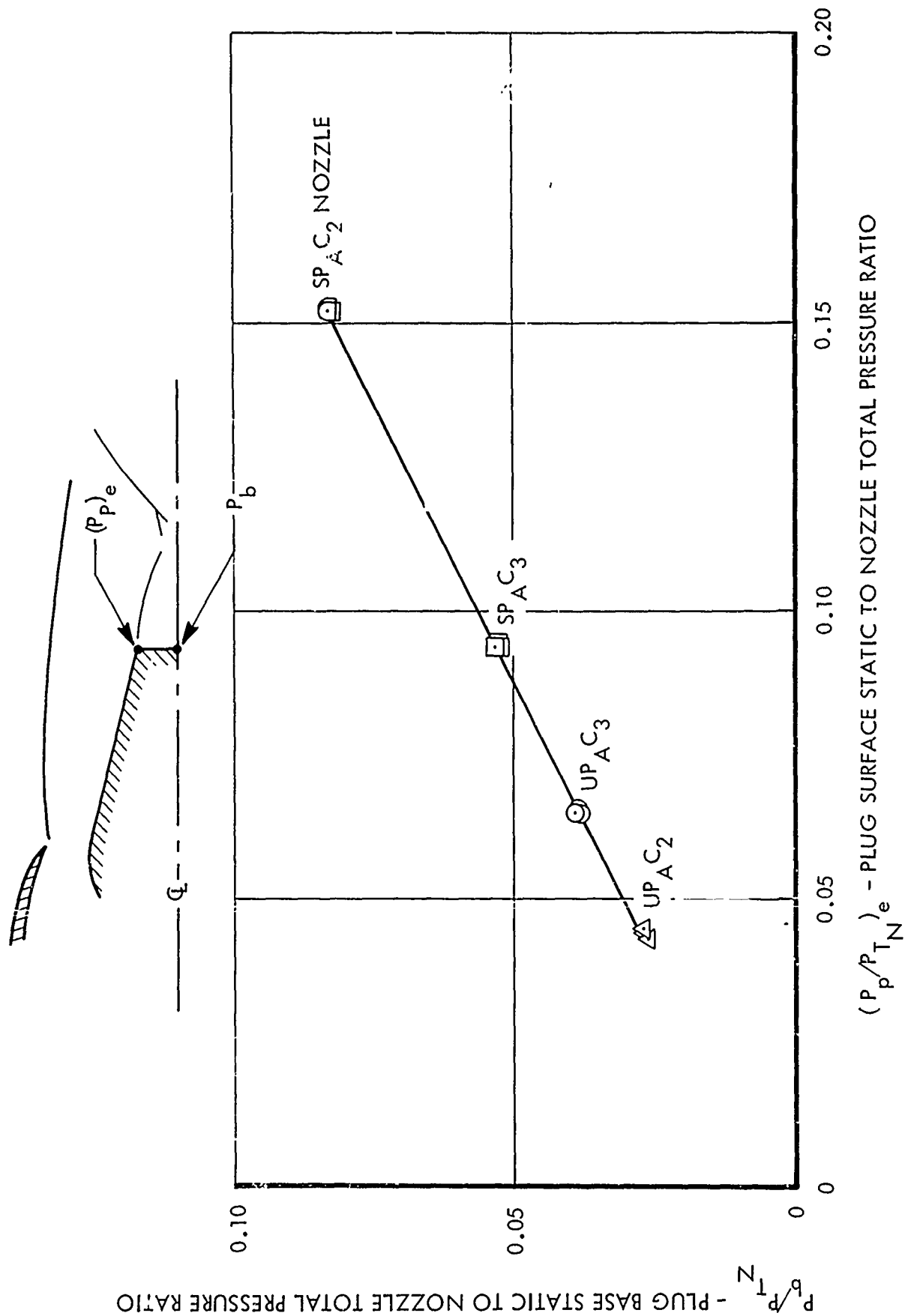


Figure 51. Plug Nozzle Locked-in Base Pressures

$$\frac{P_b}{P_{T_N}} = 0.517 \left(\frac{P_p}{P_{T_N}} \right)_e + 0.0046 \quad (18)$$

where $(P_p/P_{T_N})_e$ is the ratio of plug surface static pressure just upstream

of the plug base to nozzle total pressure. This pressure ratio is independent of nozzle pressure ratio and is a function of only nozzle geometry.

The plug surface pressure can be obtained from a fully expanded MOC plug nozzle analysis. Thus, by combining Equation (18) with a fully expanded plug nozzle analysis, the total plug thrust can be calculated.

SECTION 3

TWIN-NOZZLE/AFTBODY INVESTIGATION

A strut-supported twin-jet fighter aircraft model was developed for testing various aftbody, nozzle, and empennage configurations over a 0 to 2.5 Mach number range in the AEDC 16-foot PWT. A photograph of the model installed in the 16T is shown in Figure 52. The model is approximately 12 feet in length and has a wing span of 7.9 feet.

The configuration variables investigated in the test program include the following:

- Nozzle Type - convergent flap, convergent iris, convergent-divergent, convergent-divergent ejector, and unshrouded plug
- Nozzle Position - normal power, partial afterburning, and maximum afterburning
- Nozzle Lateral Spacing Ratio (nozzle centerline-to-centerline distance divided by the maximum nozzle diameter) - 1.25, 1.625, and 2.0
- Nozzle Axial Position - nozzle fully or partially exposed to the external flow field
- Aftbody Contour - basic or alternate side fuselage fairing
- Horizontal Stabilizer Area - full, 70 percent, stabilizer off
- Horizontal Stabilizer Deflection - -0.4, -2.0, and -5.0 degrees
- Vertical Stabilizer Type - single or twin
- Vertical Stabilizer Position - forward or aft mounted
- Vertical Stabilizer Area - full, 78 percent, stabilizer off
- Rudder Deflection - 0, 4.0, 11.0, and -11.0 degrees
- Interfairing Type - horizontal wedge and vertical wedge
- Interfairing Length - trailing edge terminating at -4.0, 0, 3.5, 8.216, and 13.0 inches aft of the customer connect station

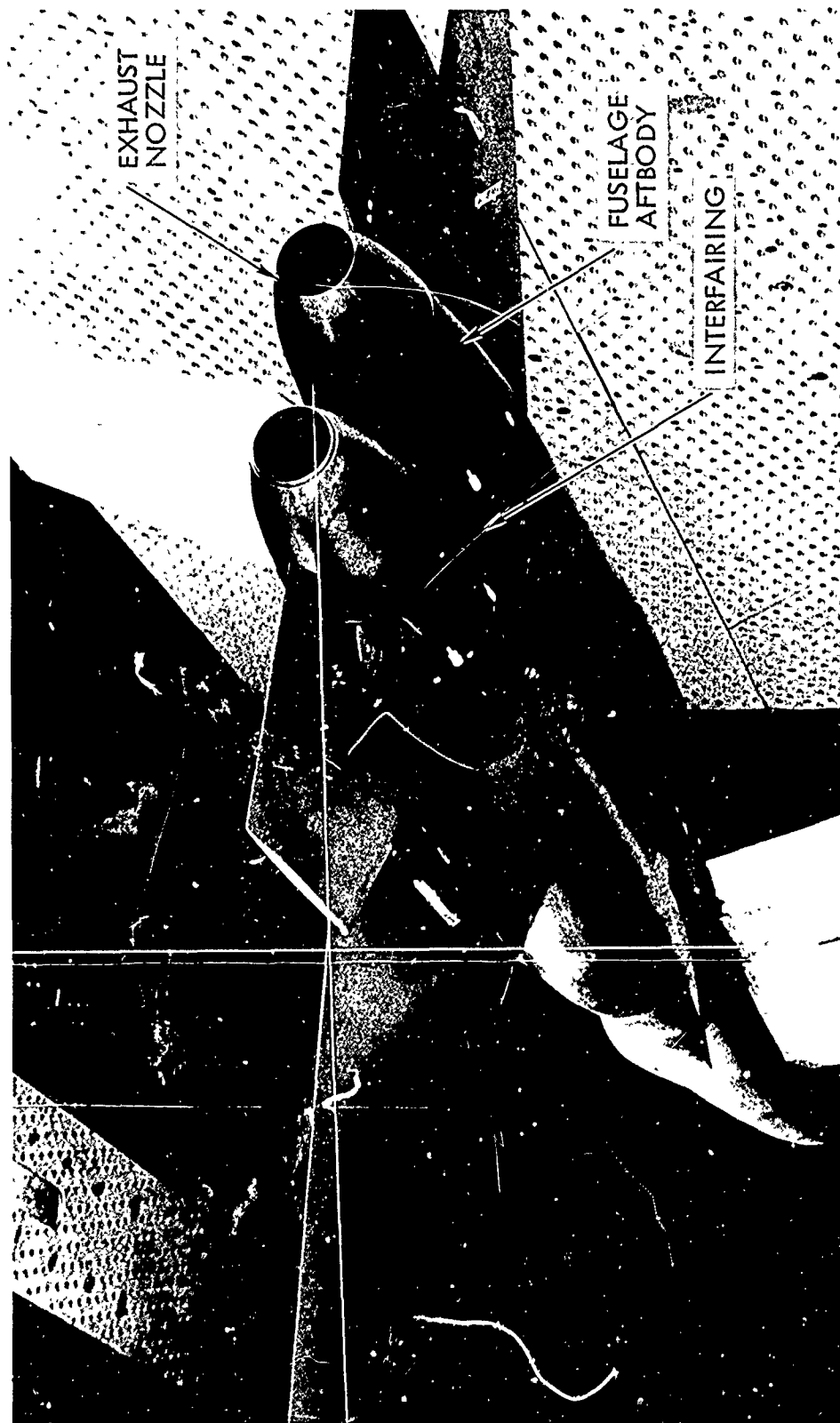


Figure 52. Photograph of Phase II Aircraft Model Installed in AEDC 16T Propulsion Wind Tunnel

- Interfairing Height - trailing edge 1.8 inches above and along the nozzle centerline
- Interfairing Base Area - three interfairings

The 8-inch maximum diameter nozzle models were selected from among those tested during the Phase I Isolated Nozzle Investigation. Six force balances were installed in the model, and a maximum of 247 model pressures were measured using the AEDC plenum-mounted P²B (precision pressure balance) system. The nozzle thrust and external nozzle and aftbody drags were both calculated in two separate ways: (1) using the indicated balance forces and cavity pressures, and (2) using only the measured model surface pressures. Boundary layer rake surveys were taken just upstream of the model aftbody for each of the three nozzle spacings investigated.

A summary of the apparatus and procedures employed in obtaining and reducing the test data and a discussion of experimental results and performance prediction methods are included in this section.

3.1 APPARATUS AND PROCEDURE

The apparatus and procedure used in conducting the test program, i.e., the test facility, twin-jet fighter aircraft model and support system, instrumentation and calibration, data reduction, and test activities, are presented below.

3.1.1 Test Facility

The test facility, its operating characteristics, test support equipment, and data acquisition systems are basically the same as summarized in Subsection 2.1.1, with the following exceptions.

- Orifice meters were not used to measure model airflows
- Scanivalves were not used to measure model pressures
- Nozzle balance data were digitized by the Beckman Model 210 data system rather than by the 20 channel readout system used for the thrust and aftbody balances.

3.1.2 Model and Support System

The strut-supported model designed for testing in the AEDC PWT 16T and 16S tunnels is representative of a twin-buried-engine fighter aircraft. In Figure 53, the major external model components are identified. The number of part replacements fabricated for each of the model components is listed below:

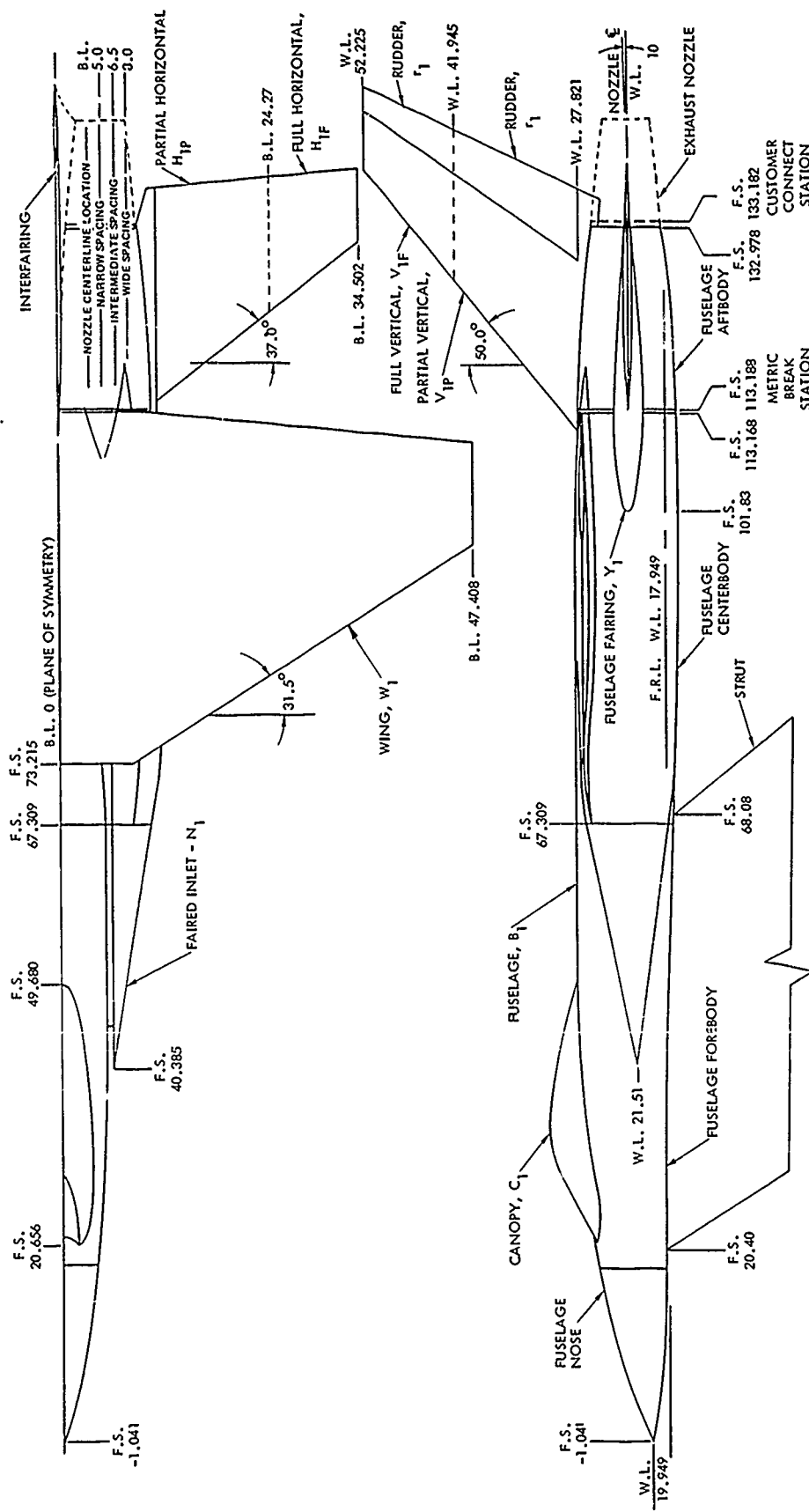


Figure 53. Diagram of Phase II Aircraft Model External Components

<u>Component</u>	<u>Number of Configurations</u>
Fuselage	
Nose	1
Forebody	1
Centerbody	3
Aftbody	1
Fairing	4
Canopy	1
Inlet Fairing	1
Wing	1
Horizontal Stabilizer	6
Vertical Stabilizer	10
Interfairing	18
Exhaust Nozzle	13

Figure 54 shows the general internal model arrangement, which includes the basic support structure, the airflow ducting, and the six force measuring balances.

Each model configuration is identified by a configuration code with a separate symbol for each of the seven major model components. The configuration variables for each of these components are itemized symbolically in Table 7. The design of the model components and the support strut are discussed in the subsections which follow.

3.1.2.1 Airframe

The basic airframe (S_1) consists of the fuselage (B_1), canopy (C_1), inlet fairing (N_1), and wing (W_1). Expressed symbolically,

$$S_1 = B_1 C_1 N_1 W_1$$

The basic test configuration was developed by Calac from the A-2 vehicle design evolved by General Dynamics under the AFFDL-sponsored Supersonic Inlet Design and Airframe-Inlet Integration Program (Reference 57). The A-2 vehicle was selected after comparing the candidate configurations on the basis of aft-end flow simulation and compatibility with test requirements and, to a lesser degree, on mission performance and ease of model fabrication.

Modifications to the A-2 vehicle design included relocating the wing from a low to high position, fairing over the half-axisymmetric inlets, and providing for three nozzle lateral spacings. The wing was relocated in

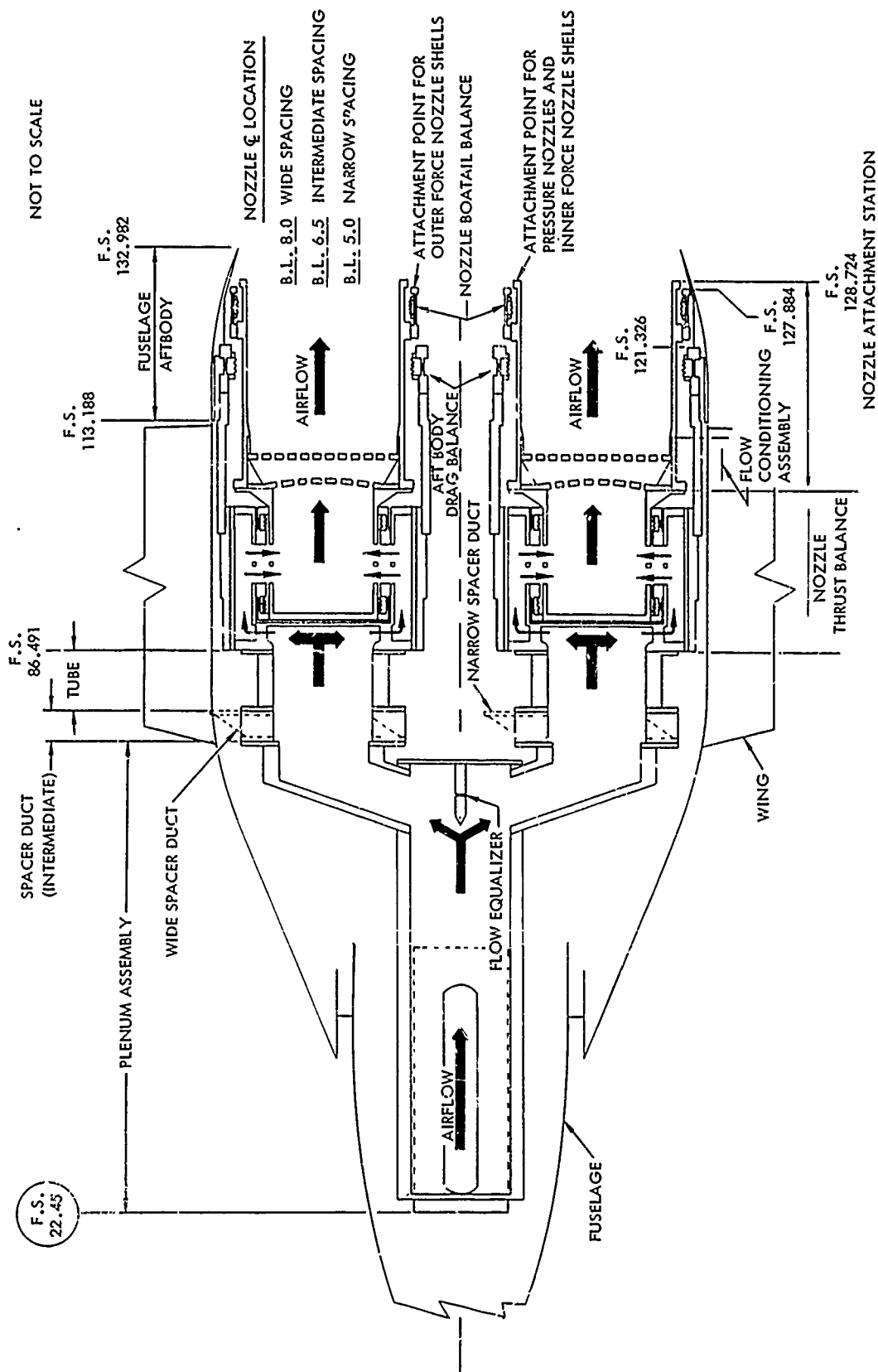


Figure 54. Diagram of Phase II Aircraft Model Internal Arrangement

TABLE 7. PHASE II MODEL CONFIGURATION SUMMARY

A-frame	Fuselage Fairing	Horizontal Stabilizer	Vertical Stabilizer	Interfairing			Exhaust Nozzles	Boundary Layer Trip
				S/D=1.25	S/D=1.625	S/D=2.0		
S ₁ =B ₁ C ₁ N ₁ W ₁ l ₁ l ₁ l ₁	Y ₁ Y ₂ Y _{2M} -	H _{1F} ^{-0.1} -2 H _{1F} ⁻⁵ H _{1F} ^{-0.4} -2 H _{1P} -	V _{1F} ^h V _{1F} ^r V _{1F} ^{ll} V _{1F} ^{r-ll} V _{1F} ^{r-ll} V _{1P} ^h V _{1P} ^r V _{2P} V _{3P} V _{3P} -	N1B	I1B	W1B	CF ₁	-
				N1C	I2B	W2A	CF ₃	T ₁
				N1D	I2D	W2F	CI ₁	T ₂
				N1D/C	I4B	W2C	CI ₃	T ₃
				N1E/D		W2D	CD ₁	T ₄
				N3D		W2E	CD ₂	
				N3E			CD ₃	
				N3E/D			CD _{1A}	
							CD _{3A}	
							CDE ₃	
1	4	6	10	8	4	6	13	5
				18				

order to make the vehicle more representative of current and advanced air superiority fighter designs. The wing geometric characteristics are listed in Table 8. Inlet fairings were required since high pressure air supplied through the strut was used to simulate the nozzle exhausts instead of air supplied through flowing inlets. Results from a study regarding testing with faired-over inlets (Reference 58) indicate that fairing over the axisymmetric inlets has only a small effect on aftbody drag and is, therefore, an acceptable modification to the aircraft design when only aftbody/nozzle performance is desired.

Nozzle spacing ratios (distance between nozzle centerlines divided by the maximum nozzle diameter) of 1.25, 1.625, and 2.0 were selected for investigation. These choices were based on full scale aircraft requirements and wind tunnel model limitations. The minimum spacing of 1.25 was selected to allow for adequate engine installation provisions. These include a firewall between the engines and space to reach engine accessories and plumbing. The minimum spacing was further dictated by the force balance arrangement and flow tube size required by the model scale. The maximum spacing ratio of 2.0 was considered a reasonable upper limit for twin engines buried in the fuselage. The maximum spacing was also limited by the need to design a single model to accommodate the selected range of nozzle spacings. The intermediate spacing of 1.625 was chosen to be mid-way between the maximum and minimum values.

The P&WA F100-PW-100 current-technology engine, used in the design of the GD A-2 configuration, was replaced by the P&WA STF371A-20 advanced-technology engine for this investigation since the selected airframe-nozzle configuration was to be typical of the next generation of turbine powered fighter aircraft. As compared to the F100-PW-100 engine, the STF371A-20 engine has the same airflow schedule, approximately the same diameters, a 14 percent greater overall pressure ratio, a 0.3 higher bypass ratio, and a 400°F higher maximum turbine inlet temperature. The STF371A-20 engine is, therefore, a feasible follow-on, minimum change, installation for this investigation.

The selection of the STF371A-20 engine cycle parameters (overall pressure ratio, bypass ratio, and maximum turbine inlet temperature) was based on the minimum mission fuel weight plus engine weight required to perform the basic air superiority mission and the point intercept mission and was influenced by consideration of the thrust available for maneuvering. The mission indicated that increases of overall pressure ratio, bypass ratio, and maximum turbine inlet temperature relative to those of the F100-PW-100 engine would provide improved mission performance for an advanced air superiority fighter aircraft.

A full scale maximum external nozzle diameter (customer connect) of 44.57 inches was selected for this investigation in order to be compatible with both the F100-PW-100 and STF371A-20 engines. This diameter is slightly larger than the value of 43 inches quoted in Reference 1 and corresponds to a scale factor of 0.1795 for the eight-inch diameter (customer connect) nozzle models fabricated for the Isolated Nozzle Investigation.

TABLE 8. WING GEOMETRIC CHARACTERISTICS

Characteristic	Symbol	Dimension
Airfoil type	-	Bi-conver
Aspect ratio	AR	3.37
Span	b	94.816 in.
Mean aerodynamic chord	\bar{c}	51.512 in.
Root chord	c_r	11.017 in.
Tip chord	c_t	11.254 in.
Incidence angle	i_w	0.0
Area	S	2667.6 in. ²
Root thickness to chord ratio	$(t/c)_r$	3.7
Tip thickness to chord ratio	$(t/c)_t$	3.26
Taper ratio	λ	0.25
Dihedral angle	γ	0.0
Leading edge sweep angle	$\Lambda_{L.E.}$	31.5 degrees
Location of 0.25 \bar{c}		
F.S.		88.411
W.L.		27.545
B.L.		18.941

3.1.2.2 Fuselage Fairing

The non-metric support beams for the horizontal stabilizers were cantilevered from the mid-fuselage section and designed as a side fuselage fairing since an internal location was precluded by volume limitations. The following four fuselage fairing arrangements were investigated:

Y_1	Basic
Y_2	Alternate (F-111 type) - non-metric
Y_{2M}	Alternate - metric
-	Fuselage fairing removed

The basic fuselage fairing, Y_1 , was designed to support the horizontal stabilizer with a minimum disturbance to the external flow. The cross-sectional area of the basic fairing is a maximum at the metric break station (F.S. 113.188) and gradually decreases in the aft direction until the fairing height becomes equal to the thickness of the horizontal stabilizer at F.S. 130.13. Beyond this station, the fairing follows the contour of the horizontal stabilizer, if the horizontal stabilizer is installed, or continues the upstream contour if the horizontal stabilizer is not installed.

The alternate fuselage fairing, Y_2 , was designed to support the horizontal stabilizer in the same manner as the basic fairing and to resemble the fuselage fairing used on the F-111. The alternate fairing is substantially larger in cross-sectional area than the basic fairing and extends beyond the nozzle exit plane. The aft portion of the fairing is contoured so the nozzle plume will not impinge on the fairing surface.

The alternate metric fuselage fairing, Y_{2M} , has the same contour as the alternate non-metric fuselage fairing, Y_2 , but is attached to the metric aftbody instead of to the non-metric centerbody. The fairing was not designed to support the horizontal stabilizer since the forces exerted on the aftbody balance would have been excessive during a tunnel unstart.

3.1.2.3 Empennage

The empennage variables investigated were horizontal stabilizer area (0, 70, and 100 percent) and deflection (-0.4, -2, and -5 degrees) and vertical stabilizer type (single and twin), position (forward and aft mounted), area (0, 78, and 100 percent), and rudder deflection (0, 4, 11, and -11 degrees). As a result of model design considerations, (1) the empennage was attached to non-metric support beams cantilevered from the fuselage centerbody rather than to the metric aftbody, (2) the full area stabilizers were excluded from supersonic testing, and (3) all deflection angles were manually set.

Horizontal Stabilizers - The area and deflection angle combinations for the horizontal stabilizers are itemized below. The indicated negative deflections correspond to trailing edge up.

$H_{1F}^{-0.4}$	Full stabilizer deflected -0.4 degrees
H_{1F}^{-2}	Full stabilizer deflected -2.0 degrees
H_{1F}^{-5}	Full stabilizer deflected -5.0 degrees
$H_{1P}^{-0.4}$	Partial stabilizer deflected -0.4 degrees
H_{1P}^{-2}	Partial stabilizer deflected -2.0 degrees
-	Horizontal stabilizer removed

The basic geometric characteristics of the exposed portion of the full and partial horizontal stabilizers, including the location of the stabilizers with respect to the aircraft when attached to the basic fuselage fairing, are listed in Table 9. The stabilizers are located 0.2 inches further outboard when attached to the alternate fuselage fairing; however, the exposed surface area of the stabilizers is the same for both installations.

The horizontal stabilizer deflections required to trim the aircraft were determined as a function of aircraft load factor (lift to weight ratio) for selected Mach number and altitude conditions. The aerodynamic data used in the analysis were obtained from References 59 through 66. The maximum stabilizer deflections for the basic air superiority and point intercept missions and for the maneuverability or specific excess power points are tabulated below for each test Mach number. The axis about which the entire stabilizer rotates is located at F.S. 125.286 and W.L. 22.25.

Since the variation in stabilizer deflection was extremely small at supersonic conditions, a single position of -0.4 degrees was selected for the supersonic portion of the tests. This basic stabilizer position was also selected for subsonic conditions, and -2.0 and -5.0 degree deflections were provided to simulate the maneuverability points. It was found during the first tunnel entry, however, that the support bracket which deflected the horizontal stabilizer -2.0 degrees was mistakenly labeled -0.4 degrees and vice versa. In order to insure that all basic data were consistent, the -2.0 degree bracket was used for all subsequent basic runs. This approach is acceptable since the effect of the horizontal stabilizer deflection angle on external drag is quite small between -0.4 degrees and -2.0 degrees.

TABLE 9. HORIZONTAL STABILIZER GEOMETRIC CHARACTERISTICS

Characteristic	Symbol	Dimension	
		Full Span - H_{LF}	Partial Span - H_{LP}
Airfoil type	-	Bi-convex	Bi-convex
Aspect ratio	AR	1.50	0.71
Span	b	24.232 in.	14.0 in.
Mean aerodynamic chord	\bar{c}	17.590 in.	20.021 in.
Root chord	c_r	24.357 in.	24.357 in.
Tip chord	c_t	8.041 in.	14.930 in.
Tail length	l_t	36.885 in.	29.716 in.
Area	S	2.726 ft ²	1.910 ft ²
Taper ratio	λ	0.330	0.613
Leading edge sweep angle	Λ_{LE}	37.0 degrees	37.0 degrees
Location of 0.25 \bar{c}			
F.S.		125.296 in.	118.127 in.
W.L.		22.250 in.	22.250 in.
Distance from nozzle	ℓ	15.375 in.	11.71 in.
Tip chord from nozzle ℓ		29.502 in.	19.270 in.
Root chord from nozzle ℓ		5.27 in.	5.27 in.

<u>Test Mach Number</u>	<u>Deflection Angles for Basic Air Superiority and Point Intercept Missions - degrees</u>	<u>Deflection Angles for Maneuverability Points - degree</u>
0.6	-1.0 to -3.3	-5.9
0.8	-0.5 to -1.6	
0.9	0.22 to -1.2	-0.3, -1.8, -3.9
1.1	-0.59	
1.2	-0.43	
1.4	-0.25	
1.6	-0.20	-1.0
1.8	-0.17	
2.0	-0.25	
2.2	-0.40	-0.4
2.5	-0.60	

Vertical Stabilizers - The combination of position, area, and rudder deflections for the vertical stabilizers are itemized below. Positive deflection corresponds to trailing edge right as viewed looking forward.

V_{1F}	Forward-mounted single full stabilizer
V_{1F}^{+4}	V_{1F} with rudder deflected +4.0 degrees
$V_{1F}^{\pm 11}$	V_{1F} with rudder deflected ± 11.0 degrees
V_{1P}	Forward-mounted single partial stabilizer
V_{1P}^{+4}	V_{1P} with rudder deflected +4.0 degrees
V_{2P}	Aft-mounted single partial stabilizer
V_{3PV}	Twin partial stabilizers aligned vertically
V_{3PR}	Twin partial stabilizers canted 15 degrees out board
-	Vertical stabilizers removed

The basic geometric characteristics of the vertical stabilizers, including the location of the stabilizers with respect to the aircraft, are listed in Table 10. The aspect ratios, taper ratios, and leading edge sweep angles were changed substantially from those proposed by GD in order to reflect current design practice. All vertical stabilizers are geometrically similar and designed to have the same effectiveness. As a result, the aft-mounted

TABLE 10. VERTICAL STABILIZER GEOMETRIC CHARACTERISTICS

Characteristic	Symbol	Units	Dimension				
			V_{1F}	V_{1F}	V_{2P}	V_{3PV}	V_{3PR*}
Airfoil Type	-	-	Bi-convex	Bi-convex	Bi-convex	Bi-convex	Bi-convex
Aspect ratio	AR	-	1.5	0.83	0.83	0.83	0.80
Span	b	in.	29.975	19.695	17.500	16.814	16.459
Mean Aerodynamic chord	\bar{c}	in.	21.906	24.368	21.702	21.163	21.163
Root chord	c_r	in.	30.730	30.730	27.372	26.690	26.690
Tip chord	c_t	in.	9.226	16.601	14.778	14.414	14.414
Tail length	l_t	in.	35.538	32.070	40.060	32.550	32.550
Area	S	ft ²	4.159	3.237	2.561	2.432	2.349
Taper ratio	λ	-	0.300	0.540	0.540	0.540	0.540
Leading edge sweep angle	$\Lambda_{L.E.}$	degrees	50.0	50.0	50.0	50.0	50.0
Location of 0.25 \bar{c}							
F.S.	-	in.	123.949	120.481	128.471	120.961	120.961
W.L.	-	in.	34.545	31.118	30.129	29.922	29.661
B.L.	-	in.	0	0	0	8.0	12.410
Tip chord W.L.	-	in.	52.225	41.945	39.750	39.290	38.709
Root chord W.L.	-	in.	22.25	22.25	22.25	22.25	22.25

*Characteristics determined from a side view

single vertical stabilizer was smaller than the forward-mounted stabilizer. Also, each twin vertical stabilizer was smaller than the aft-mounted single stabilizer however, the total surface area of the twin vertical stabilizers is greater than that of the forward-mounted single stabilizer.

The non-metric support beam to which the single vertical stabilizers are attached was placed inside the interfairing so that the interfairing contour could be preserved. The exposed surface areas of the single vertical stabilizers thus depend on the particular interfairing installation. In general, the forward mounted single vertical stabilizers were installed with the shorter interfairings (trailing edge either at or 3.5 inches downstream of the customer connect station), and the aft-mounted single vertical stabilizers were installed with the longer interfairings (trailing edge either 8.216 or 13.0 inches downstream of the customer connect station).

The non-metric support beams to which the twin vertical stabilizers were attached were cantilevered from the wing with a 0.05-inch gap provided between the beam and the metric aftbody. These beams were designed as fairings mounted external to the fuselage aftbody since an internal location was precluded by volume limitations. The maximum cross-sectional area of the fairings occurs at the metric break station (F.S. 113.188), and the thickness gradually tapers to match the root thickness of the twin vertical stabilizers at approximately 60 percent chord.

Only the forward-mounted single vertical stabilizers had provisions for rudder deflections. The rudder hinge line was located along the 70 percent chord line. Average rudder deflections of +11 degrees between Mach 0.6 and 0.9 and +4 degrees between Mach 1.1 and 2.5 were selected for the tests. Provisions were also made to investigate a -11.0 degree rudder deflection so that the windward and leeward flow field effects could be determined from the pressure instrumentation located on the right-hand side of the model.

3.1.2.4 Interfairings

Eighteen different nozzle interfairing configurations were developed for the Phase II tests. The following interfairing variables are included:

Width

- N - Narrow - 1.25 spacing ratio
- I - Intermediate - 1.625 spacing ratio
- W - Wide - 2.0 spacing ratio

Trailing Edge Orientation

- 1 - Horizontal wedge with interfairing trailing edge 1.8 inches above the nozzle centerline
- 2 - Horizontal wedge with interfairing trailing edge along nozzle centerline

3 - Vertical wedge

4 - High horizontal wedge profile along interfairing plane of symmetry and trailing edge along nozzle radial lines

Length - Specified in terms of the distance from the customer connect station to the aft end of the interfairing

A - -4.0 in.

B - 0 in.

C - 3.5 in. (exit of plug nozzles)

D - 8.216 in. (exit of C-D nozzles)

E - 13.0 in.

Base Area

D/C - D length interfairing truncated to C length

E/D - E length interfairing truncated to D length

The eighteen interfairing configurations fabricated are identified in Table 11, in terms of the above symbols. All interfairings have the same height and surface slope at the metric break station (F.S. 113.188) and are aligned with respect to the nozzle centerline. (The nozzle centerline is canted one degree nose-down with respect to the FRL (W.L. 17.949) and intercepts W. L. 22.383 at F.S. 133.182.) The contours of the high, center, and modified horizontal wedge interfairings downstream of the metric break station consist of a circular arc followed by a straight line which is tangent to the circular arc, as shown in Figures 55 through 57. The vertical interfairing designs are shown in Figure 58.

The horizontal wedge interfairings which terminate downstream of the customer connect station (F.S. 133.182) were specially contoured to each nozzle with which they were to be tested. The vertical interfairing area distribution does not depend on the nozzle configuration since a gap was provided between the interfairing and nozzle so that the flow could expand through this region.

3.1.2.5 Nozzles

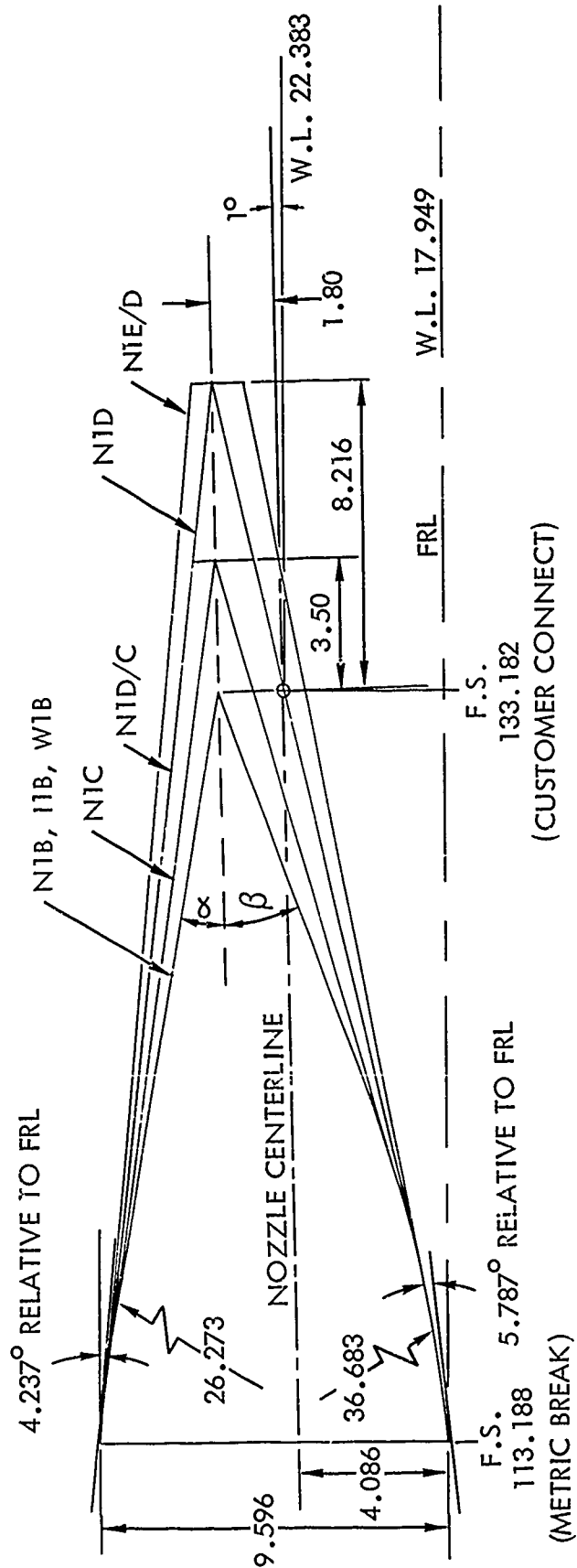
The thirteen nozzle configurations indicated below were selected for investigation from among those designed by P&WA and tested during the isolated nozzle tests. The design rationale employed by P&WA in developing the full-scale nozzle configurations and schematics of all nozzle models are presented in Subsection 2.1.2.

Each twin nozzle configuration set consists of either a pressure instrumented nozzle configuration and a force balance nozzle or a combined pressure and force balance nozzle and a dummy (non-metric and non-instrumented) nozzle. The nozzles from which force balance data were obtained have a two-piece

TABLE 11. INTERFAIRING CONFIGURATION IDENTIFICATION

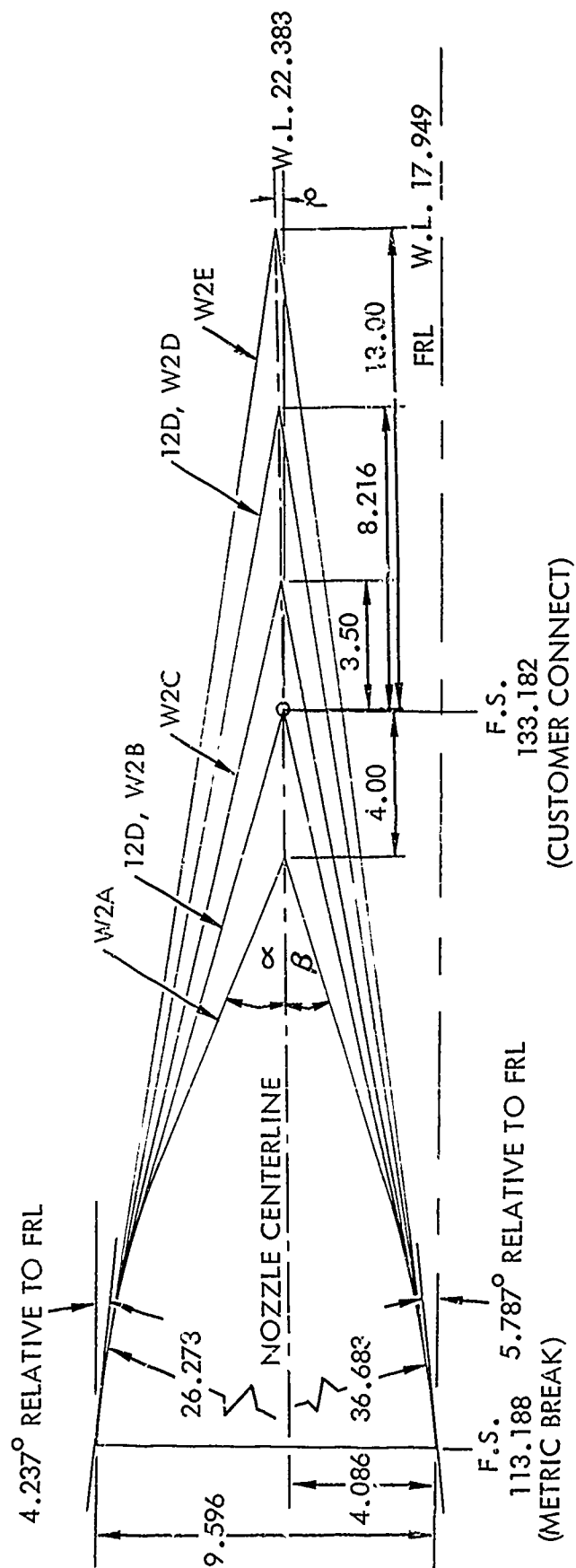
Nozzle Spacing Ratio, S/D	Interfairing Type	Length Specified in Terms of the Distance in Inches from the Customer Connect Station to the Aft End of the Interfairing				
		-4.0	0	3.5	8.216	13.0
1.25	High Horizontal Wedge		N1B	N1C N1D/C	N1D N1E/D	
	Vertical Wedge				N3D N3E/D	N3E
1.625	High Horizontal Wedge		I1B			
	Center Horizontal Wedge		I2B		I2D	
	*Modified Horizontal Wedge		I4B			
2.0	High Horizontal Wedge		W1B			
	Center Horizontal Wedge	W2A	W2B	W2C	W2D	W2E

*High horizontal wedge profile along interfairing plane of symmetry and trailing edge along nozzle radial lines.



TRAILING EDGE ANGLE-DEGREES	INTERFAIRING CONFIGURATIONS			
	N1B, I1B & W1B	N1C	N1D/C	N1D
α —UPPER SURFACE	10.792	9.091	7.519	7.519
β —LOWER SURFACE	19.683	15.508	12.339	12.339
				N1E/D
				6.45
				10.385

Figure 55. High Horizontal Wedge Interfairing



TRAILING EDGE ANGLE-DEGREES	INTERFAIRING CONFIGURATIONS				
	W2A	12B OR W2B	W2C	12D OR W2D	W2E
α - UPPER SURFACE	23.061	16.688	13.788	11.243	9.58
β - LOWER SURFACE	17.202	12.412	10.237	8.347	7.106

Figure 56. Center Horizontal Wedge Interfacing

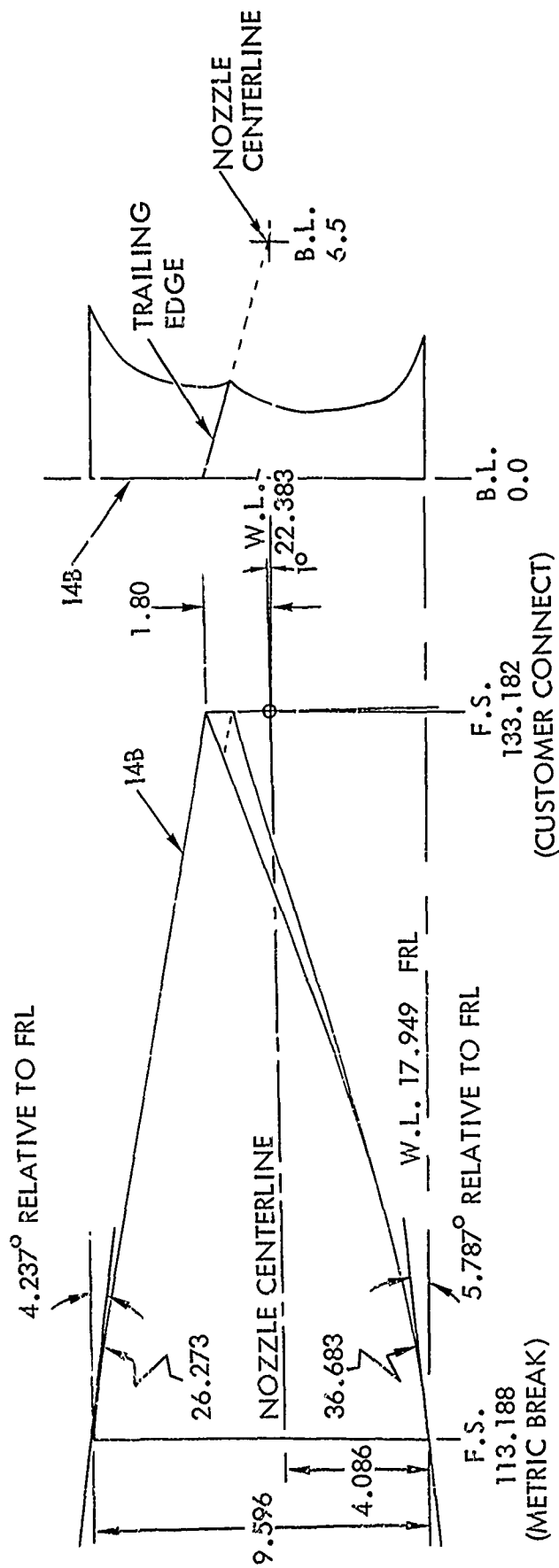


Figure 57. Modified High Horizontal Wedge Interfairing with Trailing Edge
Along Nozzle Radial Lines

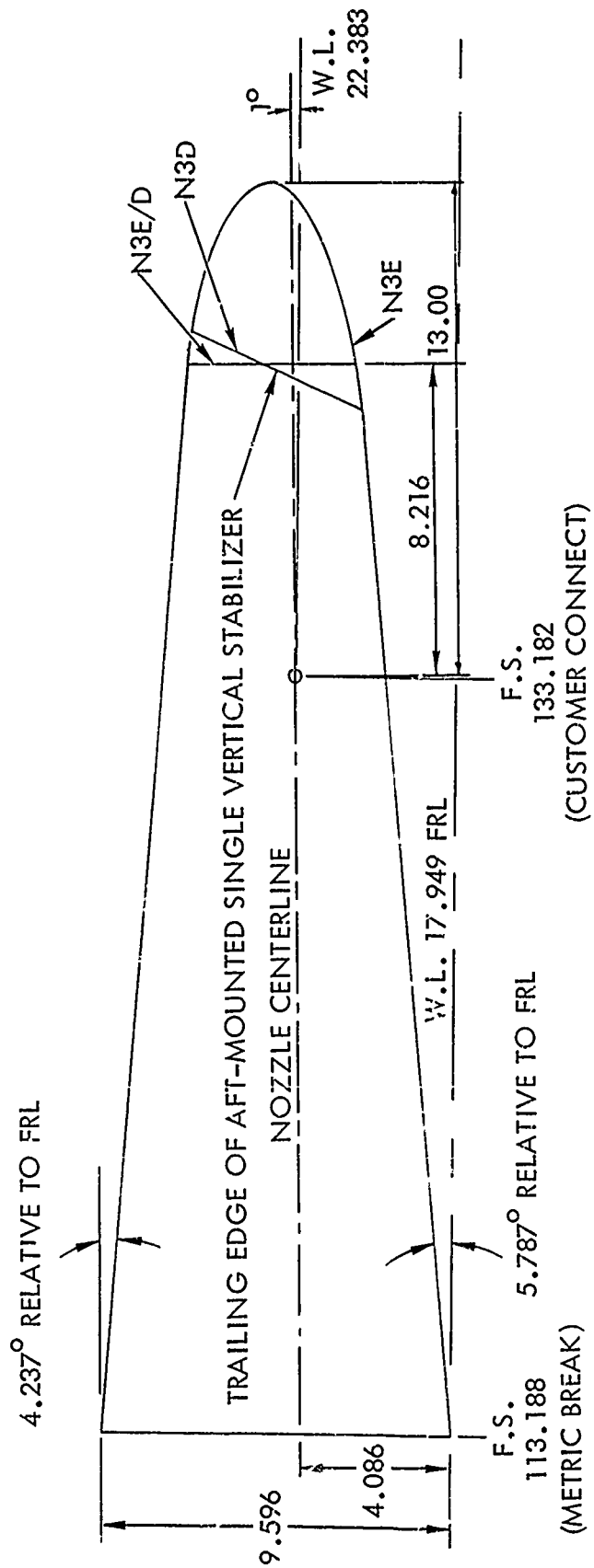


Figure 58. Vertical Wedge Interfairing

<u>Nozzle Type</u>	<u>Power Setting Position</u>		
	<u>Normal</u>	<u>Partial A/B</u>	<u>Max. A/B</u>
Convergent Flap	CF ₁		CF ₃
Convergent Iris	CI ₁		CI ₃
Convergent-Divergent	CD ₁	CD ₂	CD ₃
	CD _{1A}		CD _{3A}
Convergent-Divergent Ejector			CDE ₃
Unshrouded Plug	UP _A C ₁	UP _A C ₂	UP _A C ₃

construction - an external nozzle boattail shell, which attaches to the nozzle boattail balance at F.S. 127.884, and an internal nozzle shell, which attaches to the flow tube at F.S. 128.724. The pressure and dummy nozzles, which attach to the flow tube at F.S. 128.724, have a one-piece construction with the same inner and outer contours as the two-shell designs.

The convergent flap, convergent-divergent, and convergent-divergent ejector nozzles were arranged with a combined pressure and force balance nozzle on the right-hand side of the model and a dummy nozzle on the left-hand side. This arrangement was selected since the nozzle shell thickness was sufficient to accommodate the required pressure instrumentation and, thus, both pressure and force balance data could be obtained from only one nozzle installation during the isolated nozzle tests. The convergent iris and unshrouded plug nozzles were arranged with a pressure nozzle on the right-hand side of the model and a force nozzle on the left-hand side. All pressure-instrumented nozzles were installed on the right-hand side of the model in order to simplify the pressure hook-up requirements.

In addition to the nozzles fabricated for the isolated nozzle tests, alternate CD₁ and CD₃ (designated CD_{1A} and CD_{3A}) nozzles were fabricated for the twin-nozzle tests in order to determine the effect of nozzle axial position. The alternate nozzles had the same contours as the basic nozzles, but were moved forward 3.802 inches with respect to the model aftbody.

The convergent-divergent nozzle was selected for the axial position study because (1) the potential weight savings resulting from axial translation is greatest for this configuration, since its flap length is considerably longer than the other nozzle types investigated; (2) the aerodynamic contour of the aftbody and nozzle is significantly improved when the nozzle is in the alternate axial position for at least one power setting position (max. A/B); and (3) the nozzle is the most likely candidate for installation in an air superiority fighter aircraft. The alternate position was selected such that the nozzle exit plane location is the same as the CI₃ nozzle, which is approximately equidistant between that of the CF and UP nozzles and that of the CDE nozzle.

3.1.2.6 Boundary Layer Trips and Rakes

The boundary layer trip arrangements identified below were investigated to determine the effect of boundary layer transition location on the aftbody and nozzle external drag forces.

- No trips anywhere
- T₁ Trips installed on fuselage nose
- T₂ Trips installed on fuselage nose and inlet fairing
- T₃ Trips installed on fuselage nose, inlet fairing, and wing
- T₄ Trips installed on fuselage nose, inlet fairing, wing, and empennage (horizontal and vertical stabilizers)

The boundary layer trips installed on the forebody nose and inlet fairing are similar to the three-dimensional roughness types designed by Van Driest and Blumer (Reference 67) and consist of 0.062 inch diameter steel spheres spot welded to a trip ring at a circumferential spacing of 4 sphere diameters. The rings, which are 0.010 inches thick and sharpened at the leading edge, were located one foot aft of the vertices of the forebody nose and inlet fairings. According to Reference 67, the selected sphere diameter is sufficiently large to cause boundary layer transition for all test conditions.

The boundary layer trips installed on the wing and empennage consist of a 1/8 inch wide strip of #30 carborundum grit located one inch from the leading edge of each surface. The average grit height of 0.0232 inches, determined from NACA TN 4363 (Reference 68) is sufficiently large to cause boundary layer transition for all test conditions.

Six boundary layer total pressure rakes were located immediately upstream of the right-hand aftbody and distributed around the right-hand half of the interfairing and aftbody. All rakes have 12 probes, except for the wing wake rake which has 17 probes, and were installed on one configuration for each of the three nozzle spacings investigated.

3.1.2.7 Support Strut

The strut fabricated for the isolated nozzle tests was modified for use in the twin nozzle tests. This approach, rather than construction of a new strut, was selected based on the following considerations: (1) the Phase I strut was designed for the same 60 lb/sec maximum airflow rate selected for Phase II; (2) the Phase I strut is compatible with the selection of a common air supply for the two nozzles; (3) the Phase I strut is the correct length for mounting the Phase II model upright in the tunnel such that the reflected bow shock does not intersect the model in the supersonic tunnel; and (4) the Phase I strut could be easily strengthened to withstand the Phase II model loads by welding a 3/8-inch plate to each side of the basic strut.

A schematic of the Phase II model and support strut is shown in Figure 59. The tapered strut has a low thickness to chord ratio varying from 0.053 (2.55 inches thick) at the model to 0.088 (5.25 inches thick) at the tunnel floor and an average sweep angle of 36 degrees. The strut was tapered to keep the thickness at a minimum near the model and yet provide strength consistent with the AEDC requirements (Reference 6). The leading and trailing edge fairings have a total included angle of 20 degrees. The trailing edge of the strut at the strut-fuselage juncture is approximately eight nozzle diameters upstream of the customer connect station. The base of the strut was attached to the tunnel pitch table below the test section floor and canted six degrees so that a -4 degree to +16 degree model angle-of-attack range could be obtained within the pitch table angle-of-attack range of ± 10 degrees. The required internal flow area was provided by twelve tubes having 1.38 inch inside diameters. The maximum tunnel blockage caused by the strut is 0.67 percent.

3.1.2.8 Model Installation

A complete description of the installed model and its various configurations is given in Reference 2. Included in the description are the following items:

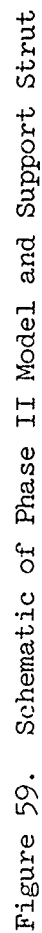
- Principal geometric parameters, area distributions, projected frontal areas, wetted surface areas, and IMS (integral mean slope) for all model components tested
- Photographs of selected configurations
- Schematic diagrams of major model components
- Tabulation of configurations tested

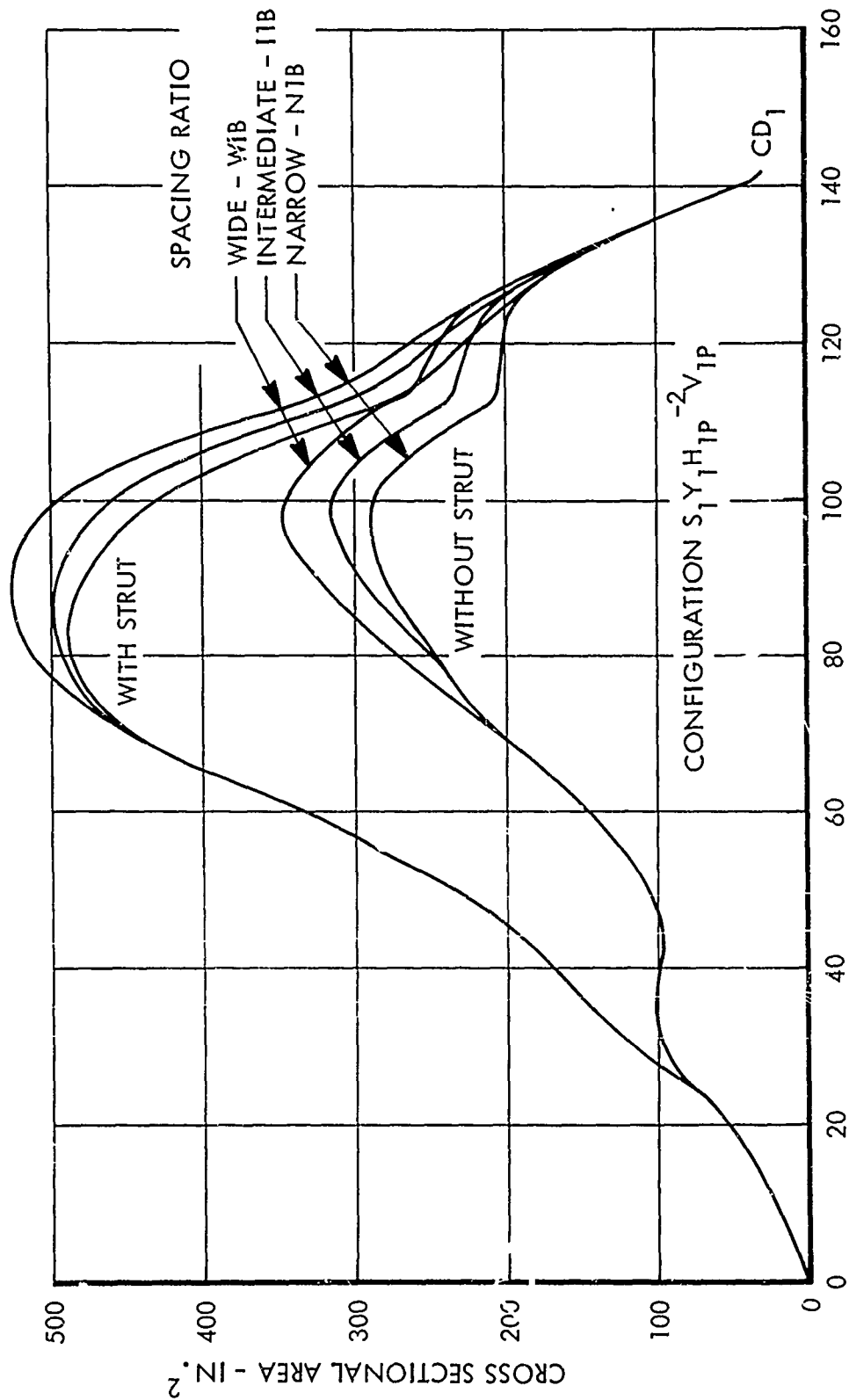
The cross-sectional area distributions for the typical model configurations are shown in Figures 60 and 61. The effects of both the support strut and nozzle spacing on the area distribution are quite significant, as illustrated in Figure 60. The maximum percent tunnel blockage for each arrangement is tabulated below.

PERCENT TUNNEL BLOCKAGE

	Nozzle Spacing		
	Narrow	Intermediate	Wide
With Strut	1.326	1.351	1.424
Without Strut	0.784	0.854	0.939

The wing, empennage, and nozzle power setting position significantly affect the slope of the area distribution, as shown in Figure 61. By contrast, the effect of interfairing type and length is relatively small.





F.S. - MODEL FUSELAGE STATION - IN.

Figure 60. Model Cross-Sectional Area Distribution -
Effect of Nozzle Spacing and Support Strut

CONFIGURATION $S_1 Y_1 H_1 P_1^{-2} V_1 NIB$

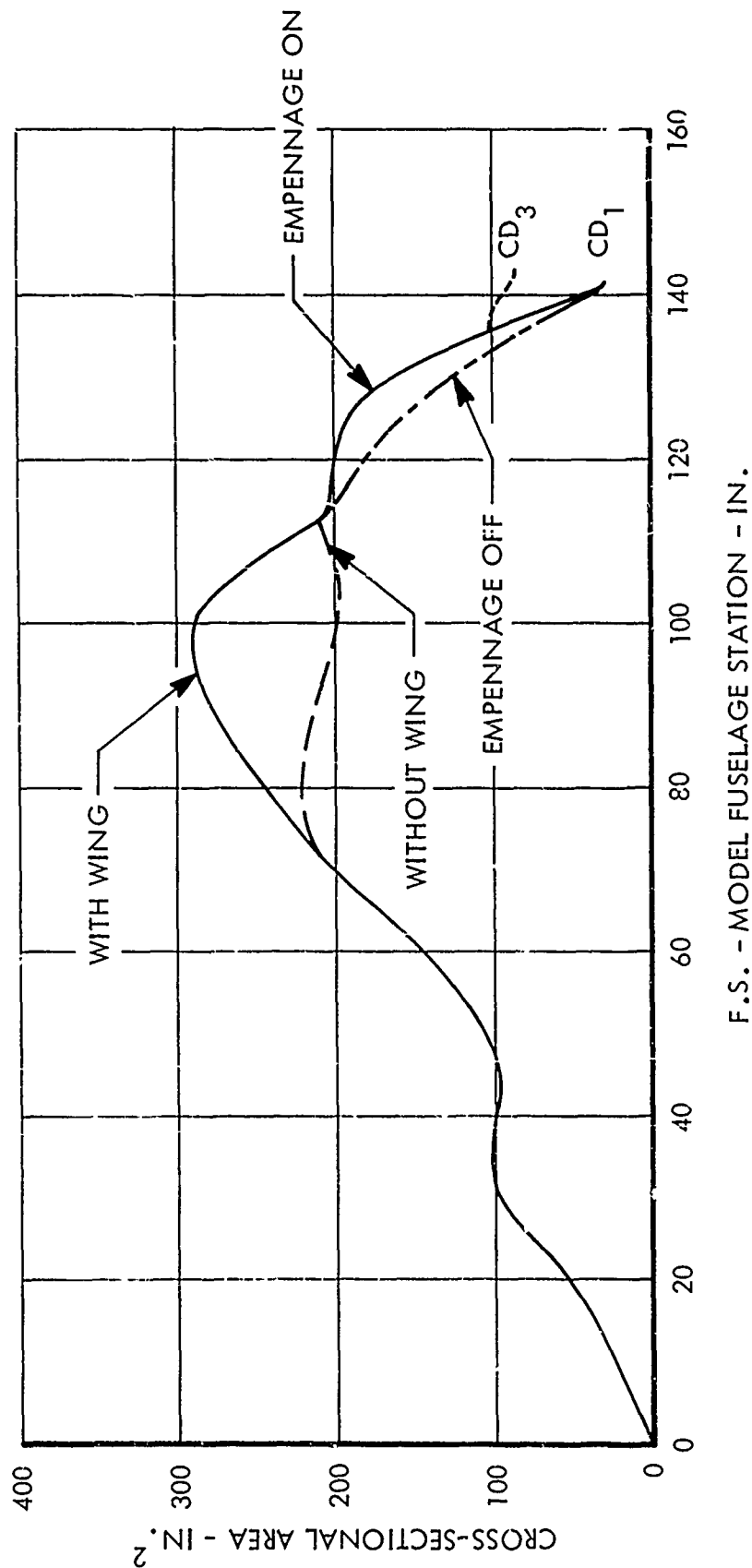


Figure 61. Model Cross-Sectional Area Distribution - Effect of Wing, Empennage, and Nozzle Power Setting Position

3.1.3 Instrumentation and Calibration

A description and an evaluation of the accuracy and repeatability of the force, pressure, and temperature instrumentation used during the tests are presented in this subsection. Also presented are the balance and flow meter calibration results.

3.1.3.1 Force Balances

Six individual force measuring balances were installed in the model: two cylindrical flow-through thrust balances, two cylindrical aftbody drag balances, and two cylindrical nozzle drag balances. Only one nozzle drag balance was active during any test run. A backup balance of each type was available in the event of a balance failure. Four of the nine force balances required for these tests (two thrust and two nozzle drag balances) were used in the isolated nozzle investigation.

Balance Description - Each thrust balance is a six-component radial inflow/axial outflow strain gage balance, through which the nozzle airflow is routed, that measures the nozzle thrust minus the nozzle external boattail and base drag. The cylindrical drag balances were instrumented to measure four components: normal, side, and axial forces and pitching moment. These balances were used to measure the external nozzle boattail and aftbody boattail (fuselage aftbody plus interfairing) drags separately. All balances incorporate metallic bellows to seal the gap between the metric and non-metric balance segments.

The axial design loads for the thrust, aftbody, and nozzle balances were 2200, 900, and 150 pounds, respectively. Although the anticipated axial running load on the aftbody balance was only 50 pounds, the 900 pound axial force design load was necessary to satisfy the safety factor requirements for a tunnel unstart condition. This condition subjects the balance to a large pitching moment which, for this type of balance, is measured by the same flexure elements used for determining the axial force.

Balance Calibration - Each balance was subjected to a dead weight calibration from which a calibration coefficient matrix was established. These matrices were used during the tests to convert the balance output to forces and moments. For this application, axial force was the component of primary interest and the other balance components were loaded chiefly to establish minor interaction corrections to the axial force. In addition, a flow-through calibration of each thrust balance and an internal pressure versus axial force calibration of all balances were performed.

The flow-through calibration of the thrust balance provided data with which to correct the balance output for the forces acting on the bellows seal and for the axial component of the momentum of the airstream entering the metric balance sleeve. Flow-through calibration tests were conducted at AEDC so that the PWT data acquisition system, air supply, control, and metering systems could be utilized with the model hardware required to perform the calibration

(strut, plenum, and thrust balances) installed in the tunnel. The flow-through calibration was accomplished at each nozzle spacing by sealing one side of the plenum with a cap and attaching a "zero thrust" nozzle/plenum assembly to the thrust balance on the other side. This zero thrust assembly consists of a plenum with two sets of diametrically opposed nozzles 90 degrees apart, which exhaust the air in a direction perpendicular to the balance centerline. Different nozzle exit areas are used to obtain balance forces at different combinations of airflow and pressure. The maximum flow-through correction was only approximately 0.7 percent of the indicated thrust minus drag.

The internal pressure calibration of the aftbody and boattail balances was required to determine the effective bellows area. This area is necessary to correct for any pressure differential across the bellows during the tunnel tests. The internal pressure calibration was accomplished by sealing the balance, applying a known axial load, and pressurizing the cavity to null the axial force output reading. The effective bellows area is then obtained by dividing the applied load by the measured internal gage pressure. The effective bellows areas are considered to be accurate within 0.1 percent of the stated areas.

Balance Accuracy and Repeatability - The accuracy of the force balances used during the test was determined from the AEDC dead weight calibration results. The error of the axial force measurements for each balance are summarized below in terms of twice the RMS (root mean square) of the difference between the indicated and applied loads expressed in pounds and as a percent of the balance design loads. If the deviations are distributed in accordance with a normal density function, then the tabulated errors fall within a 95.5 percent confidence interval.

Balance Type	Average Axial Force Errors	
	Pounds	Percent of Design Load
Thrust	12.16	0.55
Aftbody	0.44	0.05
Nozzle	0.94	0.63

The repeatability of the force balances used during the test was determined from test results obtained from configurations for which repeated runs were made. The RMS of the difference in data for repeated test conditions is presented below in terms of selected thrust and drag parameters.

The repeatability results were obtained from data where balance "zero shifts" were within a 95.5 percent confidence interval. The balance zero shifts are an indication of the electrical offset in output from beginning to end of a series of runs due to environmental effects. The following table indicates the RMS of these electrical zero shifts expressed in pounds.

Thrust and Drag Parameters		Number of Samples	Balance Repeatability
Title	Symbol		
Total nozzle drag coefficient	$C_{D_{TN_W}}$	65	0.00053
Total aftbody drag coefficient	$C_{D_{TA_W}}$	65	0.00014
Total drag coefficient	$C_{D_{T_W}}$	65	0.00048
Thrust-minus-total-drag-coefficient	$C_{(T-TD)}$	51	0.0163

AEDC Tunnel	Balance Zero Shifts - lb		
	Thrust	Aftbody	Nozzle
16T	1.66	1.97	0.41
16S	1.48	6.57	5.23

3.1.3.2 Model Pressures and Temperatures

The right-hand side of the model was instrumented to measure local static pressures on the fuselage aftbody, interfairing, centerbody, wing, empennage, flow tube, and internal and external nozzle surfaces. A maximum of 247 model pressures were measured using the AEDC plenum-mounted P²B system. A schematic of the pressure tap and rake locations is presented in Figure 62. Specific location and identification of all pressure instrumentation is provided in Reference 69.

Longitudinal rows of static pressure tubes were located on the aftbody, external nozzle, internal nozzle, and interfairing such that a representative pressure distribution could be obtained to calculate the pressure forces acting on these model components. A greater concentration of tubes was located on the inboard half of the aftbody and external nozzle surfaces which experiences large pressure variations due to the adjacent nozzle, vertical stabilizer, and interfairing.

The internal pressure instrumentation consisted of 4 static pressure taps and a 10-tube rake located in each flow tube, internal nozzle pressure taps, and balance cavity pressure taps. Balance cavity pressures were required to calculate the pressure forces acting on the bellows assemblies and base areas.

External total pressure distributions were obtained near the external model surface immediately upstream of the right-hand aftbody. Six total pressure rakes were distributed around the interfairing and aftbody as described in Reference 69.

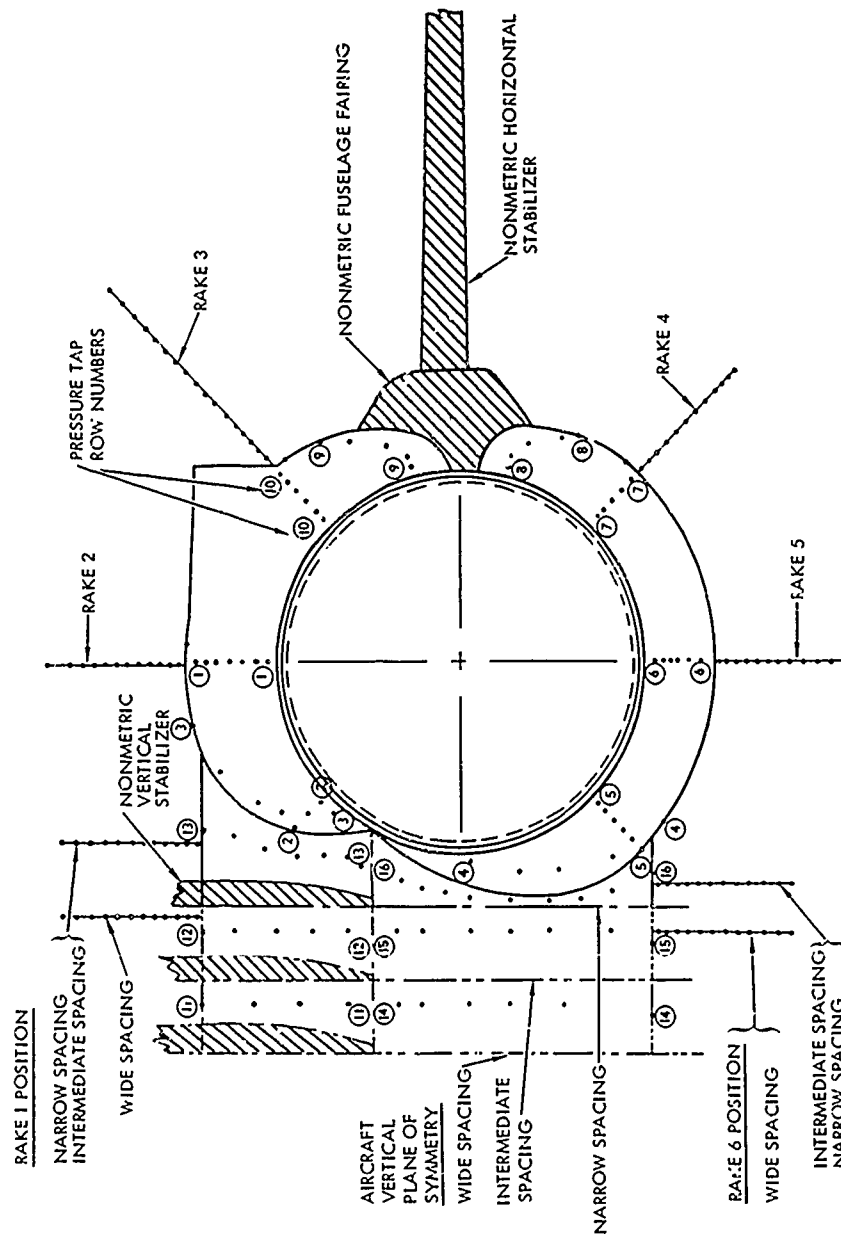


Figure 62. Pressure Tap and Rake Locations

The P²B's were calibrated prior to each running shift, and since they were contained in a controlled environment cabinet, these calibration constants were used to reduce the data to absolute pressures for all data points obtained during the shift. Since the P²B devices measure a pressure differential, a known reference pressure is required for each instrument. Based on multiple pressure measurements at the same model stations and data repeatability, the accuracy of pressures measured by the P²B's is estimated to be the larger of ± 0.02 psia or 0.15 percent of the measured differential pressure.

Total temperatures were measured in both model flow tubes and at each airflow metering station. Each flow tube temperature was determined as the average of three thermocouples at locations specified in Reference 69. The airflow metering station temperatures were also measured by thermocouples.

3.1.3.3 Flow Meters

The total nozzle airflow was metered by both a venturi meter and a swirlmeter located in series. The total nozzle airflow measured by the venturi meter was used in all data reduction programs, whereas the swirlmeter was used as only a backup metering device.

Two venturi meters were used during the tests (one in 16T and the other in 16S) in order to accommodate the required range of airflows (1.5 to 60 lb/sec in 16T and 2.6 to 18 lb/sec in 16S) for a maximum supply pressure of 700 psia and also to provide choked flow at the lower flow rates. Both venturi meters were designed in accordance with procedures outlined in Reference 11 and were fabricated by CEESI at Nunn, Colorado. The throat diameters of the venturi meters were 2.501 and 1.499 inches for the 16T and 16S tests, respectively. A swirlmeter, manufactured by Fischer and Porter Company, was used in series (upstream) with the venturi meter.

Calibration tests of the venturi meters were performed by CEESI at their primary facility to determine the throat discharge coefficient at the venturi throat Reynolds numbers anticipated during the tests. The discharge coefficients were evaluated with accuracies of 0.1 percent. Calibration of the swirlmeter was performed by the manufacturer prior to delivery of the instrument of AEDC. The stated accuracy of the average meter coefficient is within ± 1.0 percent of the coefficient throughout the entire Reynolds number range.

Venturi meter accuracies were evaluated by determining the effect of measurement and calibration inaccuracies on the total nozzle airflow. The effect of a 0.15 percent error in the measurement of the venturi pressure and temperature was to induce airflow inaccuracies of 0.15 and 0.02 percent, respectively. Including the accuracy of the discharge coefficients, the overall accuracy of the total nozzle airflow measurements is estimated to be ± 0.27 percent. Venturi meter data repeatability was evaluated by a second order least square curve fit through data points selected at random from the entire test. This evaluation yielded a 2σ value (twice the RMS of the deviations) of 0.019 lbs/sec which is indicative of the venturi measured total nozzle airflow data repeatability.

The stated accuracy of the swirlmeter is ± 0.75 percent of the indicated flow rate relative to CEESI standards. Measurement errors of 0.15 percent in the parameters utilized to calculate the swirlmeter airflow would induce airflow inaccuracies of 0.02, 0.15, and 0.15 percent for temperature, pressure, and volumetric flow rate, respectively. Therefore, system errors could result in a maximum error of ± 0.32 percent. Comparison between the indicated venturi and swirlmeter flow rates yielded an RMS difference of approximately 1.4 percent. The stated repeatability of the swirlmeter is ± 0.25 percent of the indicated flow rate. Comparison of the mass flow calculated by the swirlmeter and venturi indicated a mean deviation of approximately 0.40 percent.

3.1.3.4 Comparison of Pressure and Force Balance Data

In addition to the nozzle thrust and drag coefficients determined from direct force measurements, the model was pressure instrumented so that these same parameters could be calculated from the pressure data, as discussed in Section 3.1.4. A summary of the RMS (root mean square) deviations between pressure and force data thrust and drag coefficients is shown below.

Parameter	Symbol	RMS Deviation	
		16T	16S
Total aftbody drag coefficient based on wing area	$C_{D_{TA_W}}$	0.00039	0.00108
Total nozzle drag coefficient based on wing area	$C_{D_{TN_W}}$	0.00027	0.00063
Total (aftbody plus nozzle) drag coefficient based on wing area	$C_{D_{TW}}$	0.00051	0.00127
Thrust-minus-nozzle-drag coefficient	$C_{(T-ND)}$	0.0153	0.0136

3.1.4 Data Reduction

The test data were reduced using computer programs developed by ARO (on-site) and by Calac (off-site). The on-site program handles only those data reduction calculations which can be performed either during the tests (on-line) or immediately after the tests (off-line). An extension to the on-site program was developed at Calac which calculates the external drag coefficients based on projected areas, in addition to those calculated in the basic ARO on-site program based on the maximum cross-sectional area and on the wing reference area. The extension also provides for the calculation of those external drag coefficients dependent on the total aftbody drag balances assuming that first one and then the other of the two aftbody balances is inactive. Similarly, it calculates the thrust coefficients assuming that first one and then the other of the two thrust balances is inactive. The off-site program handles those data reduction calculations which can be

performed only after reviewing and correcting the nozzle pressure data subsequent to the tests. Specifically, the nozzle thrust, nozzle boattail drag, and aftbody drag are calculated from the integration of pressures combined with calculated skin friction drag using the off-site program; whereas these same parameters are calculated from force balance data using the on-site program.

The on-site and off-site data reduction programs are described below. All thrust and drag forces (and associated areas) were measured and are presented with respect to the direction of the engine centerline, which is canted one degree nose-down from the fuselage reference line (W.L. 17.949). That is, the forces are not resolved into components parallel to and normal to the freestream direction.

3.1.4.1 On-Site Data Reduction Program

On-site data reduction results from the Phase II tests were printed in tabular form by AEDC, both on-line and off-line. Included in the tabulated on-line data are the tunnel flow conditions; venturi meter pressures, temperatures, and flow rates; model angle of attack; model flow tube conditions; balance forces, moments, and cavity pressures; and all nozzle/aftbody performance parameters calculated from force balance data. Although all on-site data reduction calculations were performed on-line, some of the pressure data were printed off-line in order to utilize tunnel occupancy time more efficiently. All these off-line pressure data were tabulated in absolute pounds per square inch. For external pressures they are also presented as pressure coefficients and for nozzle internal pressures as pressure ratios (static to flow tube total pressure).

The more important performance parameters calculated by the on-site data reduction program are nozzle discharge coefficient, nozzle thrust-minus-drag coefficient, nozzle boattail and base drag coefficients, and aftbody boattail and base drag coefficients. The data reduction procedures used to calculate these parameters are presented in detail in Reference 69 and summarized below. Only one of the two nozzle boattail balances installed in the model was active at a time. The right-hand balance was active when the CF, CD, or CDE nozzles were installed, and the left-hand balance was active when the CI or UP nozzles were installed.

Nozzle Discharge Coefficient - The nozzle discharge coefficient is defined as the ratio of actual to ideal nozzle mass flow rate, where the ideal mass flow rate is based on one-dimensional sonic flow at the nozzle throat. The actual mass flow for each nozzle is obtained from the total mass flow measured by the venturi meter located in the tunnel plenum and the nozzle mass flow split between the two nozzles calculated from nozzle geometric and flow properties.

The total temperature for each nozzle is obtained by averaging the readings from the three thermocouples located in each flow tube duct at F.S. 126.884 and spaced 120 degrees apart, circumferentially. The flow tube static

pressure is obtained by averaging readings from the four pressure tubes located in each flow tube duct at F.S. 124.884 and spaced 90 degrees apart, circumferentially. The flow tube Mach number is calculated from the flow tube duct to nozzle throat area ratio, assuming choked flow at the nozzle throat. Although the flow tube Mach number does not take into account the effective flow area at the nozzle throat, it is still used in calculating the nozzle mass flow rate, since only the ratio of the right-hand to left-hand flow tube Mach numbers is required. The total pressure is calculated from one-dimensional relationships using the flow tube static pressure and Mach number, based on the nozzle mass flow rate and total temperature and the flow tube static pressure and area. The flow tube Mach numbers calculated in this manner varied from 0.175 for normal power nozzles to 0.42 for maximum A/B nozzles. Although an average total pressure in both flow tubes is calculated from an area-weighted rake, it is not used in the calculation of the basic nozzle performance parameters. However, the rake output is used for monitoring the nozzle total pressure during the test and indicating the flow tube total pressure profile.

Nozzle Thrust-Minus-Drag Coefficient - The nozzle thrust-minus-drag coefficient is equal to the thrust minus nozzle boattail and base drag normalized with the ideal gross thrust based on the actual mass flow rate and isentropic expansion of the flow to freestream pressure. The thrust-minus-drag force is obtained by correcting the axial force indicated by each of the thrust balances for the corresponding cavity force and for the axial force component equivalent to the pressure/area and momentum terms of the incoming flow.

Nozzle Boattail and Base Drag Coefficients - The nozzle boattail drag coefficient is the drag exerted on the nozzle boattail surface normalized with the product of freestream dynamic pressure and nozzle maximum cross-sectional area. The nozzle boattail drag is obtained by correcting the axial force indicated by the active boattail balance for the corresponding cavity forces. The left-hand nozzle boattail balance was active for the CI and UP nozzles, and the right-hand nozzle boattail balance was active for the CF, CD, and CDE nozzles. The nozzle boattail drag on the side with the inactive balance is obtained by adjusting the drag on the active side for the difference in projected boattail areas. The total nozzle boattail drag is then calculated by adding the drags for the active and inactive balance sides.

The nozzle annular base drag coefficient is calculated from the cavity pressure associated with the active boattail balance and the annular base area and normalized with the product of freestream dynamic pressure and nozzle maximum cross-sectional area.

Aftbody Boattail and Base Drag Coefficient - The aftbody drag coefficient is the drag exerted on the aftbody boattail surface, including the inter-fairing, normalized with the product of freestream dynamic pressure and aftbody maximum cross-sectional area. The aftbody boattail drag is obtained by correcting the axial force indicated by each of the aftbody balances for the corresponding cavity forces. The two aftbody balance measurements were

essentially independent since the left-hand and right-hand portions of the aftbody were separated by a soft foam rubber seal. The aftbody cavity pressures are obtained by averaging the readings from the four pressure tubes located in each cavity region.

The aftbody base drag coefficients are calculated from the thrust balance cavity pressures and aftbody base area normalized with the product of free-stream dynamic pressure and aftbody maximum cross-sectional area.

3.1.4.2 Off-Site Data Reduction Program

The off-site data reduction results were developed primarily for the purpose of validating the performance parameters calculated from force balance data in the on-site data reduction program. The off-site results are calculated from static pressure data and from measured boundary layer profiles just upstream of the aftbody. The output results from the on-site program were recorded on Calac-supplied computer tapes at AEDC and used as input data for the off-site program. Also input to the program are tables of nozzle geometric parameters (such as projected frontal areas to be associated with each pressure tube) and corrected pressure values. Using this input data, the off-site data reduction program determines the forces on the aftbody and on the nozzle boattail, base, and internal surfaces by summing pressure/area products and calculated skin friction drag.

The off-site data reduction procedures used to calculate the more important performance parameters are presented in detail in Reference 70 and are summarized below. The performance parameters are calculated for the right-hand portion of the model since complete pressure instrumentation is provided on this side only.

Aftbody Boattail Drag Coefficient - The aftbody drag coefficient includes pressure/area and skin friction forces on the aftbody boattail and interfairing surfaces. The boattail and interfairing pressure drag is calculated using data from 50 and 37 pressure measurements, respectively. The local skin friction coefficients are calculated at the same surface pressure tap locations used in determining the pressure drag. The total skin friction drag is obtained by assigning the incremental surface area between the pressure taps to the average local skin friction coefficients, and then summing the axial component of these incremental forces.

All local flow properties are calculated from the tunnel total temperature, the aftbody surface pressures, and the total pressure at the outer edge of the boundary layer, as determined from the pressures measured by the six boundary layer rakes. The local density and viscosity are evaluated at the reference temperature of the Sommer and Short method (Reference 13).

The Reynolds number at the start of the aftbody based on an equivalent flat plate length and reference temperature is obtained for each row of pressure tubes from the corresponding Reynolds number based on the boundary layer momentum thickness and static temperature using the correlation developed by Sivells and Payne (Reference 12). Since the local Reynolds number and

the flow properties at the start of the aftbody are known, the effective flat plate length can be determined. All local Reynolds numbers downstream of the initial aftbody station are calculated from the corresponding surface pressure, reference temperature, and effective flat plate length adjusted for the change in station.

The aftbody local skin friction drag coefficients are then obtained from the local Reynolds number using the static and reference temperatures in the Sivells and Payne correlation for incompressible turbulent flow over a flat plate (Reference 11).

Nozzle Boattail and Base Drag Coefficients - The nozzle boattail drag coefficient is computed as the sum of the drag coefficients for the pressure/area and skin friction forces. The nozzle boattail pressure drag coefficient is calculated with data from 46 pressure taps arranged in six longitudinal rows. These rows are aligned with the six rows selected for the basic aftbody, exclusive of the interfairing. The nozzle boattail friction drag coefficient is calculated by the same procedure employed for the aftbody. The only difference is that the upstream flow properties for the nozzle boattail are downstream values from the aftbody calculation, while the upstream values for the aftbody are obtained from the boundary layer rake data.

The nozzle base drag coefficient is calculated by summing the products of gage pressures and associated projected frontal areas. Four base pressure tubes were installed only on the UP nozzles. The base area for the CI nozzles was too small for the installation of pressure taps. The pressure-instrumented CF, CD, and CDE nozzles have a two shell arrangement which precludes base pressure taps. The base pressures for these nozzles were obtained as internal cavity pressures.

Nozzle Thrust Coefficient - The nozzle gross thrust is computed from a momentum balance on the flow tube and nozzle. The upstream boundary of the control volume for the momentum balance is in the flow tube at F.S. 124.884. Subtracting the pressure/area and skin friction internal forces from the total momentum (sum of momentum and pressure/area terms) at this station yields the nozzle gross thrust, and normalization with the ideal gross thrust yields the nozzle thrust coefficient. The ideal gross thrust and total momentum were obtained from the on-site data reduction program.

The procedure for calculating internal skin friction drag involves dividing the duct into cylindrical sections and calculating the pressure loss due to skin friction using one-dimensional, uniform area, ideal gas relationships (from for example, Reference 15, pp. 159-173). To account for changes of area, the conditions at the beginning of each cylindrical section are calculated from those at the end of the preceding cylindrical section as an isentropic change of area. The friction drag is then calculated by subtracting the exit total momentum with friction from the exit total momentum without friction. The method is applied to plug nozzles by replacing the diameter with the hydraulic diameter and extending the shroud axially to the downstream end of the plug.

3.1.5 Test Description

Four hundred and fifteen and a half hours were spent in twin-nozzle/aftbody investigation tests in the AEDC FWT 16T and 16S during the 11 May to 29 September time period. The test was divided into three tunnel entries: two in the 16T and one in the 16S. The 16T and 16S portions of the test program are identified by AEDC Project Numbers PT0175-B00 and PT0175-S00 and Test Numbers TT-267 and SF-141, respectively.

A total of 119 twin-nozzle/aftbody configurations were tested within a 0.6 to 2.5 Mach number range and a 0 to 12 angle-of-attack range for exhaust nozzle total pressure ratios corresponding to the operating range for typical advanced technology engine and to flow-through nacelle conditions. The basic tunnel Reynolds number per foot was 2.5×10^6 in the 16T (0.6 to 1.6 Mach number range) and 1.0×10^6 in the 16S (1.6 to 2.5 Mach number range), and Reynolds number excursions were made for selected configurations.

3.1.5.1 Test Procedure

For a given model configuration, the typical operational procedure is listed below.

1. Obtain static performance, if scheduled, at several nozzle total pressure ratios
2. Establish predetermined tunnel test conditions
3. Obtain jet-off data
4. Obtain data at predetermined angles of attack over the required range of nozzle total pressure ratios
5. Change tunnel test conditions
6. Repeat steps 3 through 5 for all tunnel test conditions

Several model configurations were tested each running shift. The typical model configuration change took approximately 40 minutes. During the non-running shift, an installed check calibration of the force balances was performed in addition to a thorough pressure instrumentation leak check.

3.1.5.2 Test Schedule

An overview of the test schedule is provided in Table 12 where the 119 twin-jet/aftbody configuration combinations are grouped according to tunnel installation, nozzle spacing ratio, and type of configuration category. Table 13 lists, in symbolic form, the configurations tested during this investigation. Most of the configurations were tested at zero angle of attack at the basic Reynolds numbers. The selection of test Mach numbers and associated test condition variables was based on mission analysis results for the F100-PW-100 engine installed in the General Dynamics A-1 air superiority fighter aircraft. The selection of the basic tunnel Reynolds numbers was based on utilizing the most efficient operating mode of the AEDC tunnels.

TABLE 12. OVERVIEW OF PHASE II CONFIGURATIONS TESTED

Tunnel	Nozzle Spacing Ratio, S/D	CONFIGURATION CATEGORIES				Totals
		Nozzle/Interfacing Combinations	Empennage Combinations	Boundary Layer Trip and Profile Studies	Repeat Configurations	
16T	1.25	23	14	10	2	49
	1.625	16	1	2	1	20
	2.0	15	6	3	2	26
	Subtotals	<u>54</u>	<u>21</u>	<u>15</u>	<u>5</u>	<u>95</u>
16S	1.25	10	3	1	0	14
	2.0	7	1	2	0	10
	Subtotals	<u>17</u>	<u>4</u>	<u>3</u>	<u>0</u>	<u>24</u>
16T & 16S	Totals	71	25	18	5	119

TABLE 13 PHASE II CONFIGURATIONS TESTED

Airframe	Fuselage Fairing	Horizontal Stabilizer	Vertical Stabilizer	Interfairing	Nozzle	Boundary Layer Trips	Boundary Layer Rakes	TEST MACH NUMBERS																
								16T										16S						
								0	0.6	0.7	0.8	0.9	1.1	1.2	1.4	1.5	1.6	1.6	1.8	2.0	2.2	2.5		
S ₁	Y ₁	H _{1P} ²	V _{1P}	NLB	CF ₁	T ₁	OFF	x	x		x	x												
↑	↑	↑	↑	↑	CF ₃	T ₁	↑	x	x			x		x										
					CI ₁	T ₁		x	x		x	x												
					CI ₃	T ₁		x	x			x		x										
					CD ₁	T ₁			x		x	x												
					CD ₂	T _h		x												x			x	
					CD ₃	T ₁							x	x	x		x							
					CD ₃	T _h														x	x	x	x	
					CD _{1A}	T ₁		x	x		x	x												
					CD _{3A}	T ₁		x				x		x		x								
					CD _{3A}	T _h		x												x			x	
					CD ₃	T _h		x												x			x	
					UP _A C ₁	T ₁			x		x	x												
					UP _A C ₂	T _h		x												x			x	
					UP _A C ₃	T ₁			x			x		x		x								
					UP _A C ₃	T _h														x	x	x ¹	x	
					NLC	CF ₃		x				x		x		x								
					UP _A C ₁	T ₁		x		x	x													
					UP _A C ₃	T ₁		x			x		x											
					NLD	CI ₁		x		x	x													
					CI ₃	T ₁		x			x		x											
					CD ₁	T ₁		x			x	x												
					CD ₃	T ₁						x	x	x	x		x							
					CD ₃	T _h		x												x	x	x	x	
					N3D	CD ₁			x		x	x												
					CD ₃	T ₁						x		x										
					CD ₃	T _h														x	x	x	x	

TABLE 13 PHASE II CONFIGURATIONS TESTED (CONT.)

Airframe	Fuselage Fairing	Horizontal Stabilizer	Vertical Stabilizer	Interfairing	Nozzle	Boundary Layer Trips	Boundary Layer Rakes	TEST MACH NUMBERS															
								16T									16S						
								0	0.6	0.7	0.8	0.9	1.1	1.2	1.4	1.5	1.6	1.6	1.8	2.0	2.2	2.5	
S_1	I_1	H_{1P}	V_{2P}	$N3D$	UP_{AC1}	T_1	OFF	x		x	x												
					UP_{AC3}	T_4													x				x
				$N3D$	CD_1	T_1		x		x	x												
					CD_3	T_4		x											x				x
				$N3E/D$	CD_1	T_1		x		x	x												
					CD_3	T_1					x		x										
			V_{1P}	$I1B$	CD_1	T_1		x		x	x												
					CD_3	T_1					x		x					x					
					UP_{AC1}	T_1		x		x	x												
					UP_{AC3}	T_1		x			x		x					x					
				$I2B$	CD_1	T_1		x		x	x												
					CD_3	T_1					x		x										
					UP_{AC1}	T_1		x		x	x												
					UP_{AC3}	T_1		x	x			x		x				x					
				$I2D$	CD_1	T_1		x		x	x												
					CD_3	T_1		x				x		x				x					
					UP_{AC1}	T_1		x		x	x												
					UP_{AC3}	T_1		x			x		x										
			V_{1P}	$I4B$	CD_1	T_1		x	x		x	x											
					CD_3	T_1						x		x		x							
					UP_{AC1}	T_1		x	x		x	x											
					UP_{AC3}	T_1		x				x		x									
				WLB	CI_1	T_4						x											
					CI_3	T_4		x											x				x
					CD_1	T_4		x			x	x											
					CD_3	T_4		x				x		x				x					x
					UP_{AC1}	T_4		x			x	x											

TABLE 13 PHASE II CONFIGURATIONS TESTED (CONT.)

Airframe	Fuselage Fairing	Horizontal Stabilizer	Vertical Stabilizer	Interfairing	Nozzle	Boundary Layer Trips	Boundary Layer Rakes	TEST MACH NUMBERS																
								16T								16S								
								0	0.6	0.7	0.8	0.9	1.1	1.2	1.4	1.5	1.6	1.6	1.8	2.0	2.2	2.5		
S ₁	Y ₁	H ₁ ⁻² 1P	V ₁ P	W1B	UP _A C ₃	T ₄	OFF	x	x			x		x				x			x		x	
↑	↑	↑	3PR	W2A	CD ₃	T ₄	↑														x		x	
			↑	↑	UP _A C ₃	T ₄		x			x		x					x						
			V ₁ P	W2C	CD ₁	T ₄		x				x												
			↑	↑	CD ₃	T ₄						x		x							x		x	
			↑	↑	UP _A C ₁	T ₄		x			x	x												
			↑	↑	UP _A C ₃	T ₄															x		x	
			↑	↑	W2C	UP _A C ₁	T ₄	x			x	x												
			V ₂ P	W2D	CD ₁	T ₄		x			x	x												
			↑	↑	CD ₃	T ₄						x		x							x	x	x	x
			↑	↑	UP _A C ₁	T ₄		x			x	x												
			↑	↑	UP _A C ₃	T ₄							x											
			↑	↑	W2C	CD ₁	T ₄	x			x	x												
S ₁	-	-	-	N1B	CD ₁	T ₁	OFF	x																
↑	↑	↑	↑	↑	CD ₃	T ₁	↑					x	x	x	x									
					CD ₃	T ₃															x	x	x	x
					UP _A C ₁	T ₁		x			x	x												
					UP _A C ₃	T ₁		x	x			x												
					UP _A C ₃	T ₃		x																
					N1B	CD ₃	T ₁	x				x	x	x	x	x								
					UP _A C ₃	T ₁						x												
					N1B	CD ₁	T ₁	x	x			x	x											
					N1B	CD ₁	T ₁					x	x											
					UP _A C ₁	T ₁		x	x			x	x											
					N1B	UP _A C ₃	T ₁					x	x											
					N1B	CD ₁	T ₁					x	x											
					N1B	CD ₁	T ₁					x	x											
					N1B	CD ₁	T ₁					x	x											
					N1B	UP _A C ₃	T ₁					x	x											
					N1B	CD ₁	T ₁					x	x											
					N1B	UP _A C ₃	T ₁					x	x											
					N1B	CD ₁	T ₁					x	x											
					N1B	UP _A C ₃	T ₁					x	x											

TABLE 13 PHASE II CONFIGURATIONS TESTED (CONT.)

[illegible]

3.2 EXPERIMENTAL RESULTS AND DISCUSSION

The Phase II aircraft model experimental results are presented and discussed in this section. The presentation is divided into six subsections covering the effects on the Phase II model forces and pressures of: (1) nozzle type and power setting, (2) nozzle lateral spacing, (3) interfairing type and length, (4) empennage type, position, span reduction, and deflection, (5) angle of attack, and (6) Reynolds number and boundary layer trips. Sufficient test data are presented in each subsection to illustrate the observed trends. Unless stated otherwise, the drag coefficients presented are based on wing area and include both pressure and friction drag components as measured by the force balances.

3.2.1 Nozzle Type and Power Setting Effects

In this subsection, comparisons of both internal and external performance parameters are presented to show the effects of nozzle type and power setting. The SL Y1 HIP(-2) VIP NIB model configuration was employed to evaluate these effects. The total aftbody/nozzle drag is discussed first, followed by the discharge coefficient, thrust coefficient, and thrust-minus-total-drag coefficient. All comparisons made are between model test configurations differing only in the nozzle type.

3.2.1.1 Total Drag

Total drag, which is the sum of aftbody boattail drag, aftbody base drag, nozzle boattail drag, and nozzle base drag, is presented as a function of nozzle pressure ratio in Figures 63 through 66 in the form of a drag coefficient based on wing area. Since the base drags are small compared to the boattail drags and the aftbody drags are essentially independent of nozzle type and power setting, total drag variations with nozzle type are due primarily to the variations in the nozzle boattail drag. Even the large aftbody base of the CD1A nozzle (which is 12.3 percent of the maximum cross-sectional area of the aftbody) contributes very little to the total drag, since the base pressure is very close to freestream static pressure.

The effect of nozzle type and power setting on total drag is shown for normal power nozzles at Mach 0.9 in Figure 63 and for maximum A/B nozzles at Mach numbers of 0.9, 1.2, and 1.6 in Figures 64 through 66. For a normal power nozzle setting significant differences in total drag exist at subsonic speeds. The long, smooth contours of the convergent iris and convergent divergent nozzles are pressurized by the nozzle flow, which diminishes the total drag. The sharp corner on the convergent flap nozzle, the base at the customer connect of the alternate convergent divergent nozzle, and the short turn at the end of the unshrouded plug nozzle cowl prevent the nozzle flow from pressurizing the boattail area and result in no drag reduction for any of these nozzles.

For a maximum A/B nozzle setting, only the convergent flap and convergent iris nozzles have large enough projected frontal areas to be affected significantly by the external flow. At subsonic speeds, the drag is much lower for these

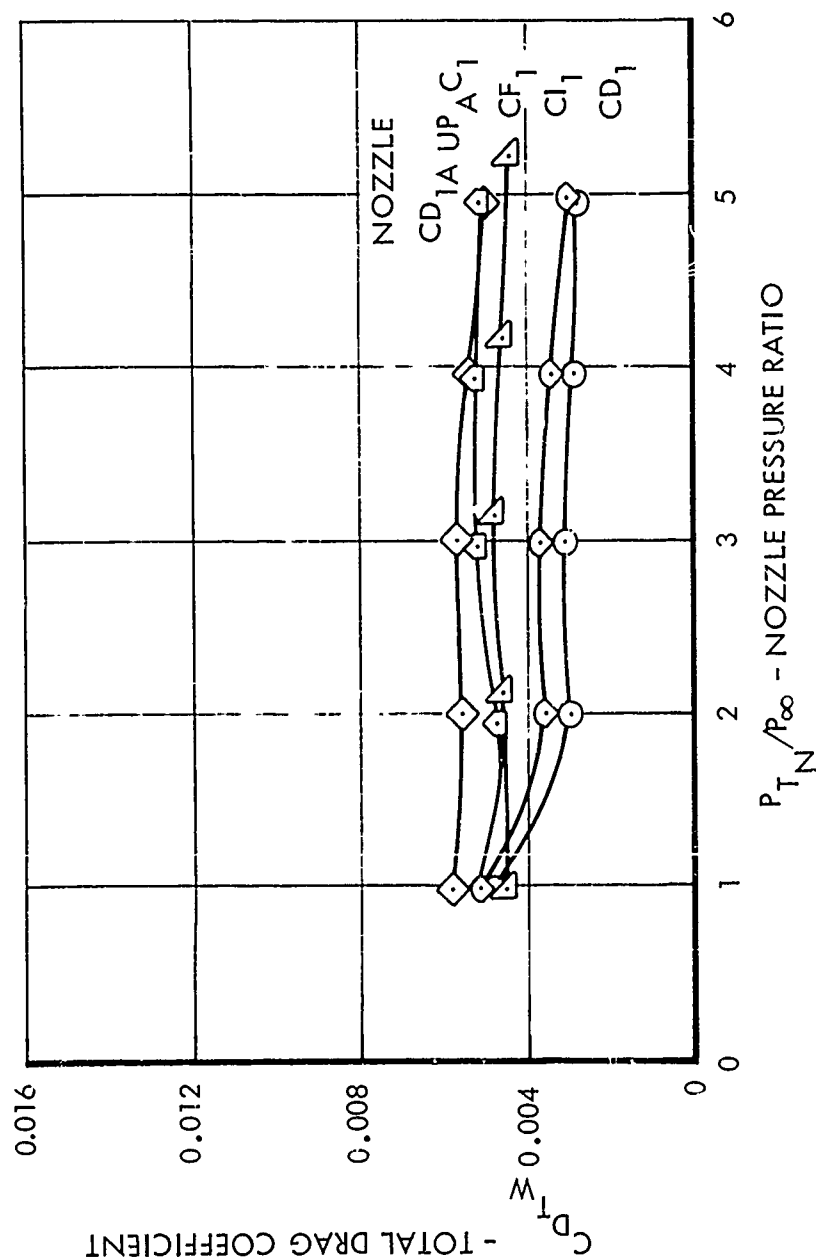


Figure 63. Effect of Nozzle Type on Total Drag - Normal Power Nozzles - Mach 0.9

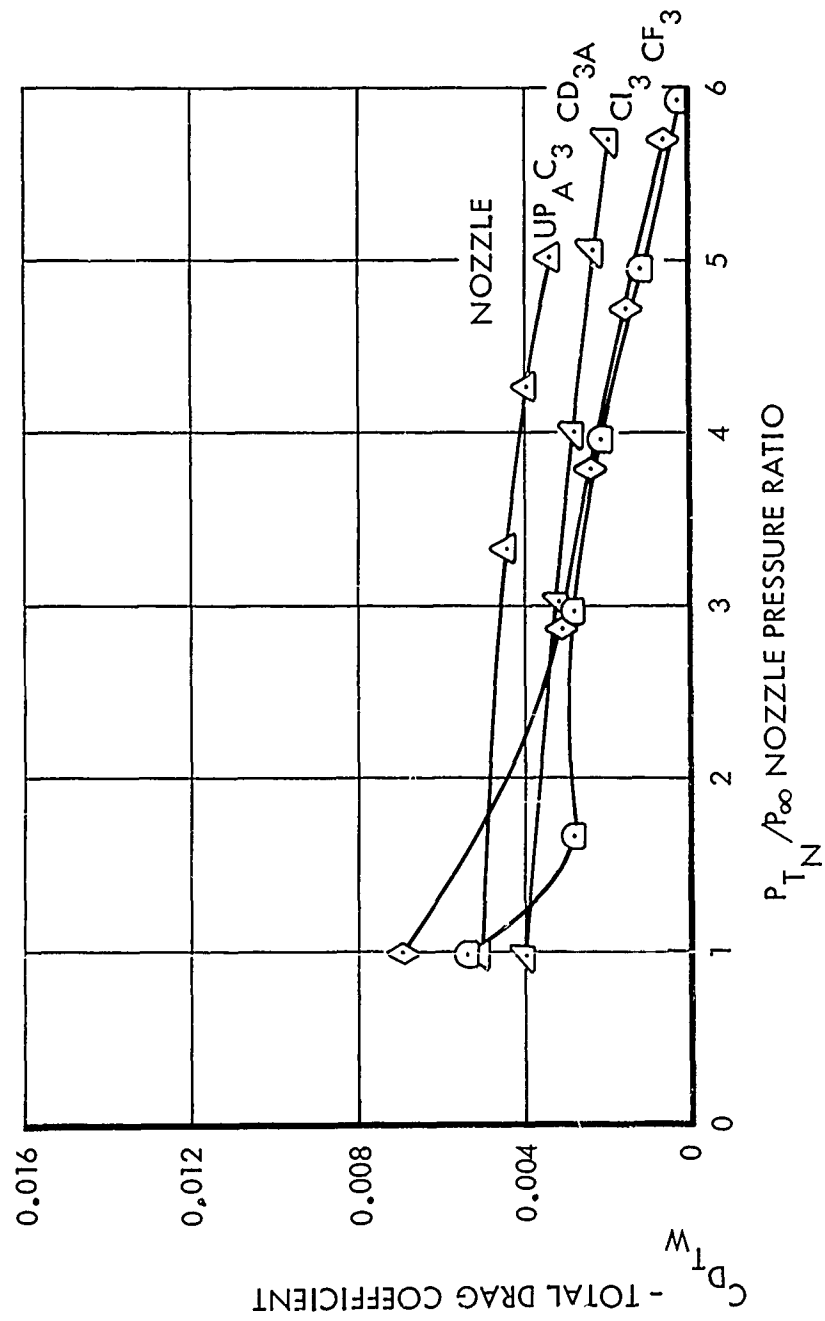


Figure 64. Effect of Nozzle Type on Total Drag - Maximum A/B Nozzles - Mach 0.9

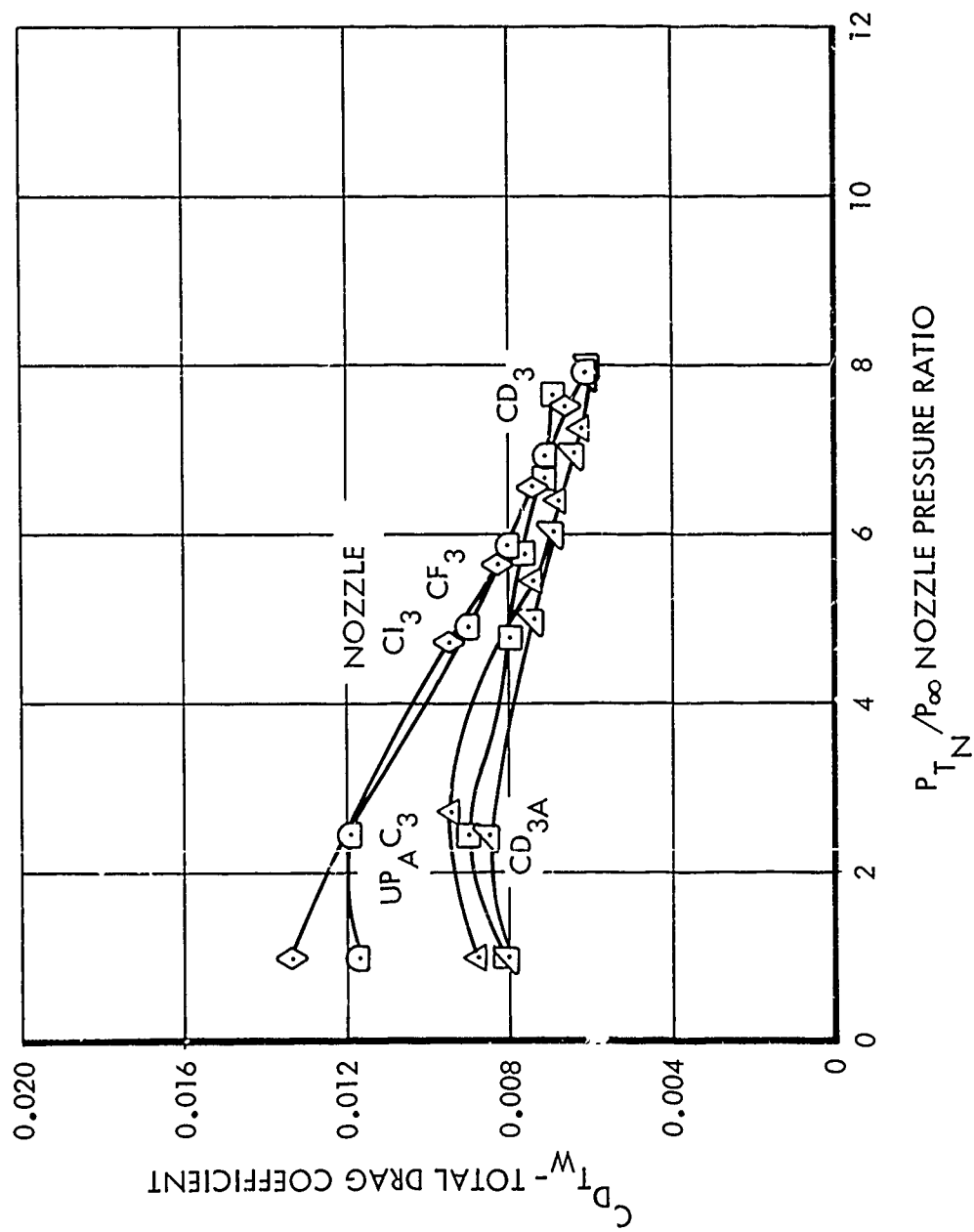


Figure 65. Effect of Nozzle Type on Total Drag - Maximum A/B Nozzles - Mach 1.2

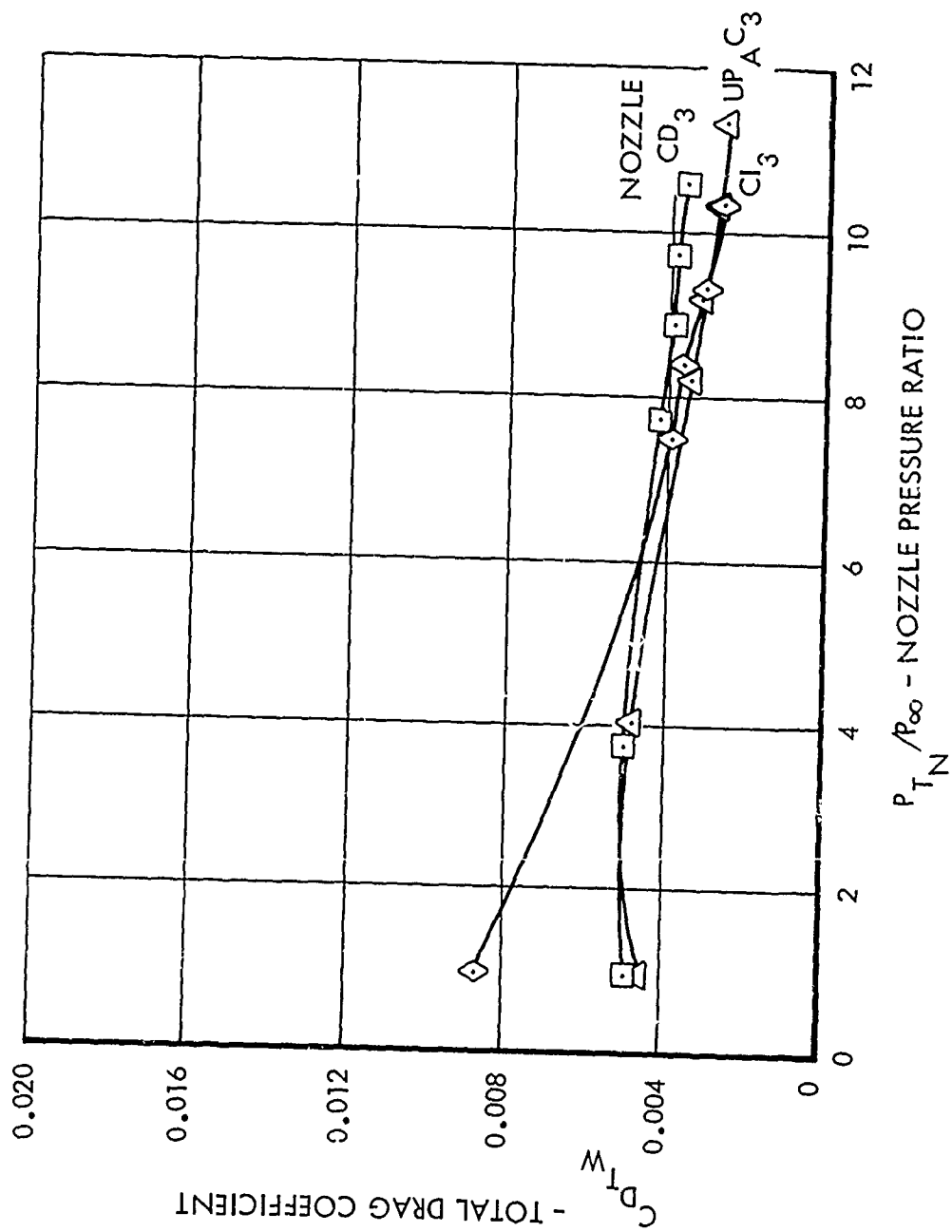


Figure 66. Effect of Nozzle Type on Total Drag - Maximum A/B Nozzles - Mach 1.6

two nozzles than for the convergent-divergent and plug nozzles because of the pressurization effect of the nozzle flow, and much higher at supersonic speeds because of the greater flow turning that occurs over the boattail surfaces.

A summary comparison of the total drag data is made in Figures 67 and 68 where drag data are presented versus Mach number for the typical schedule of nozzle pressure ratio shown in Figure 69.

3.2.1.2 Thrust and Discharge Coefficients

Thrust coefficients presented in this section are measured gross thrusts normalized by the ideal thrust based on measured nozzle mass flow. Defined in this manner, the thrust coefficients indicate the efficiency of the nozzle in developing thrust from the actual mass flow, independent of the discharge coefficient.

The thrust and discharge coefficients for the normal power nozzles operating at Mach 0.9 are presented in Figures 70 and 71, respectively. Although some of the differences between data for the different nozzles are due to measurement errors, the more significant differences are caused by two-dimensional and external flow effects. Examination of nozzle internal pressure distributions for a nozzle pressure ratio of 3 reveals that an external flow effect is present as internal lip flow separation in the CD1 nozzle and not in the CD1A nozzle. This external flow effect results in a higher thrust for the CD1 nozzle, since the CD1A nozzle is over-expanding the nozzle flow. Both nozzles have coefficients well below unity because of their sharp-edged throats. The flow is parallel to the wall as it approaches the throat but cannot generate large enough radial pressure gradients to immediately turn through the 23-degree throat angle and become parallel to the wall downstream of the throat. The result is an effective throat which is smaller than and downstream of the nozzle geometric throat.

The C11 (convergent iris) nozzle by virtue of its smooth internal contours has the highest discharge coefficients of all the nozzles. For the same reason, the thrust coefficients for the C11 nozzle are in better agreement with one-dimensional analysis results than those of the other nozzles.

The CF1 (convergent flap) nozzle has 60 percent of its internal area change on the 40-degree flap at the exit. The radial pressure gradients set up by the 40-degree turn cause the flow to converge more rapidly than the walls near the exit and result in an effective throat smaller than and upstream of the nozzle geometric throat. The flow near the nozzle wall is actually expanding just upstream of the nozzle exit. Thrust coefficients are higher for the CF1 nozzle than for the C11 nozzle because of the flow expansion near the exit of the CF1 nozzle. The CF1 nozzle has the lowest discharge coefficient of the normal power nozzles because of the pronounced two-dimensional effects in the flow around the 40-degree flap.

Thrust coefficients significantly greater than unity for the UPAC1 (unshrouded plug) nozzle at nozzle pressure ratios below 4 are the result of plug pressurization by the external flow. The external flow converging over the aftbody

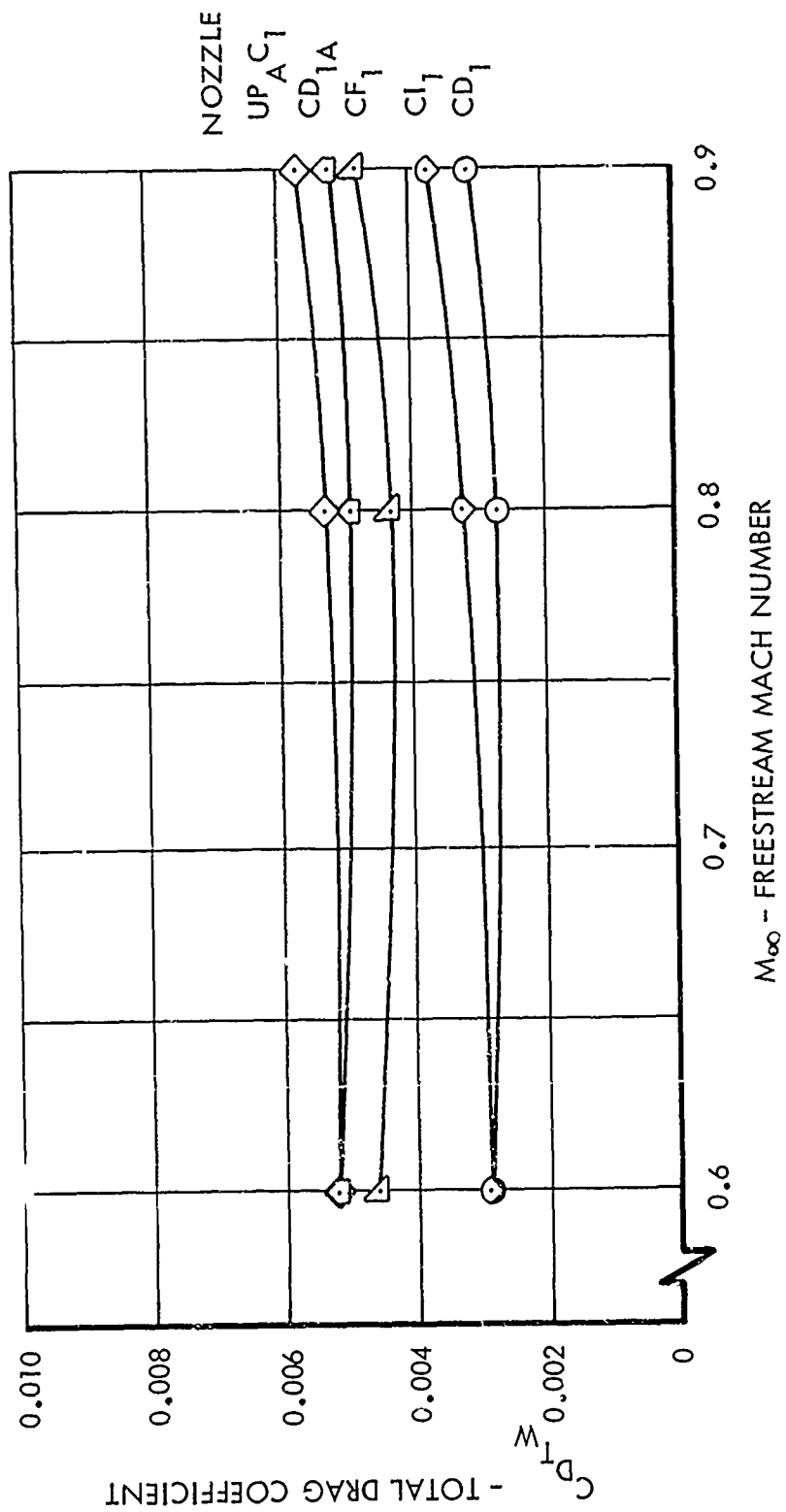


Figure 67. Total Drag - Typical Mission Applications - Normal Power Nozzles

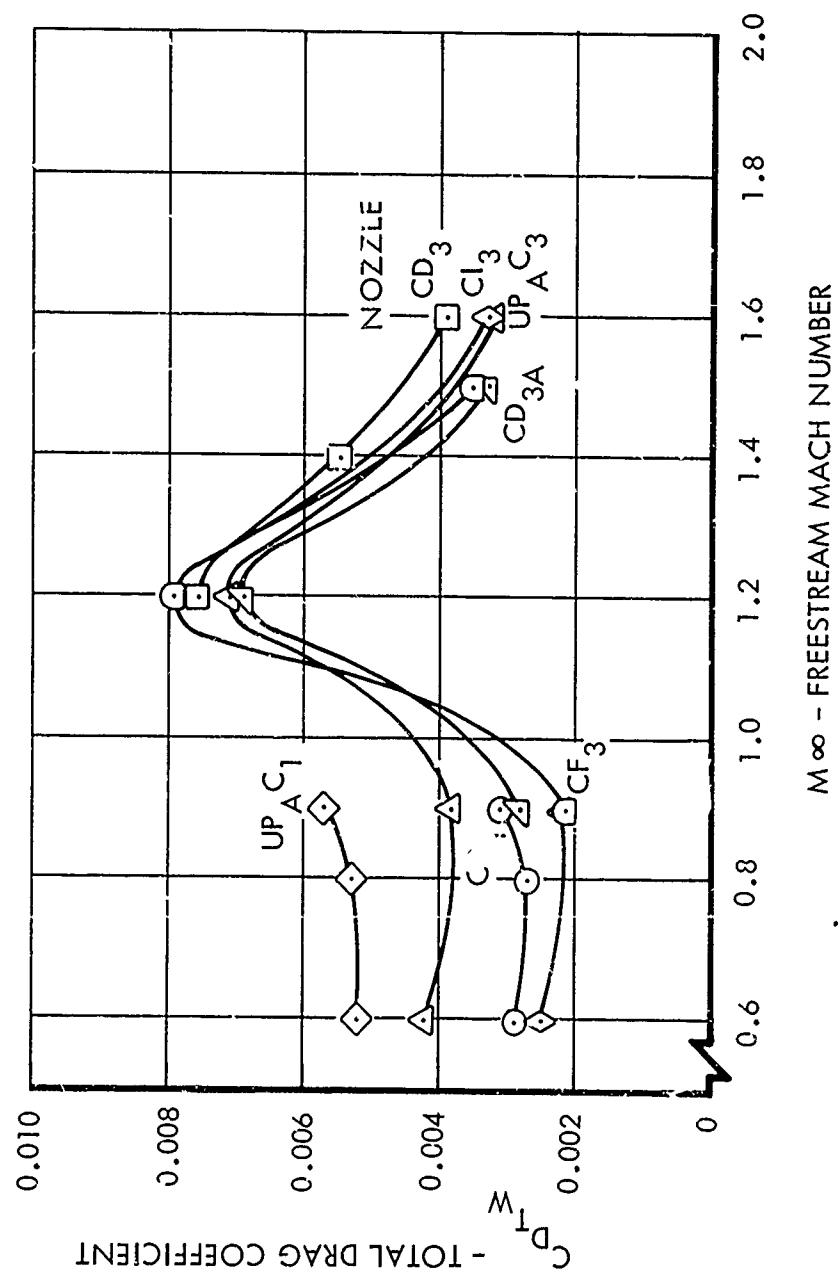


Figure 68. Total Drag - Typical Mission Applications - Normal Power and Maximum A/B Nozzles

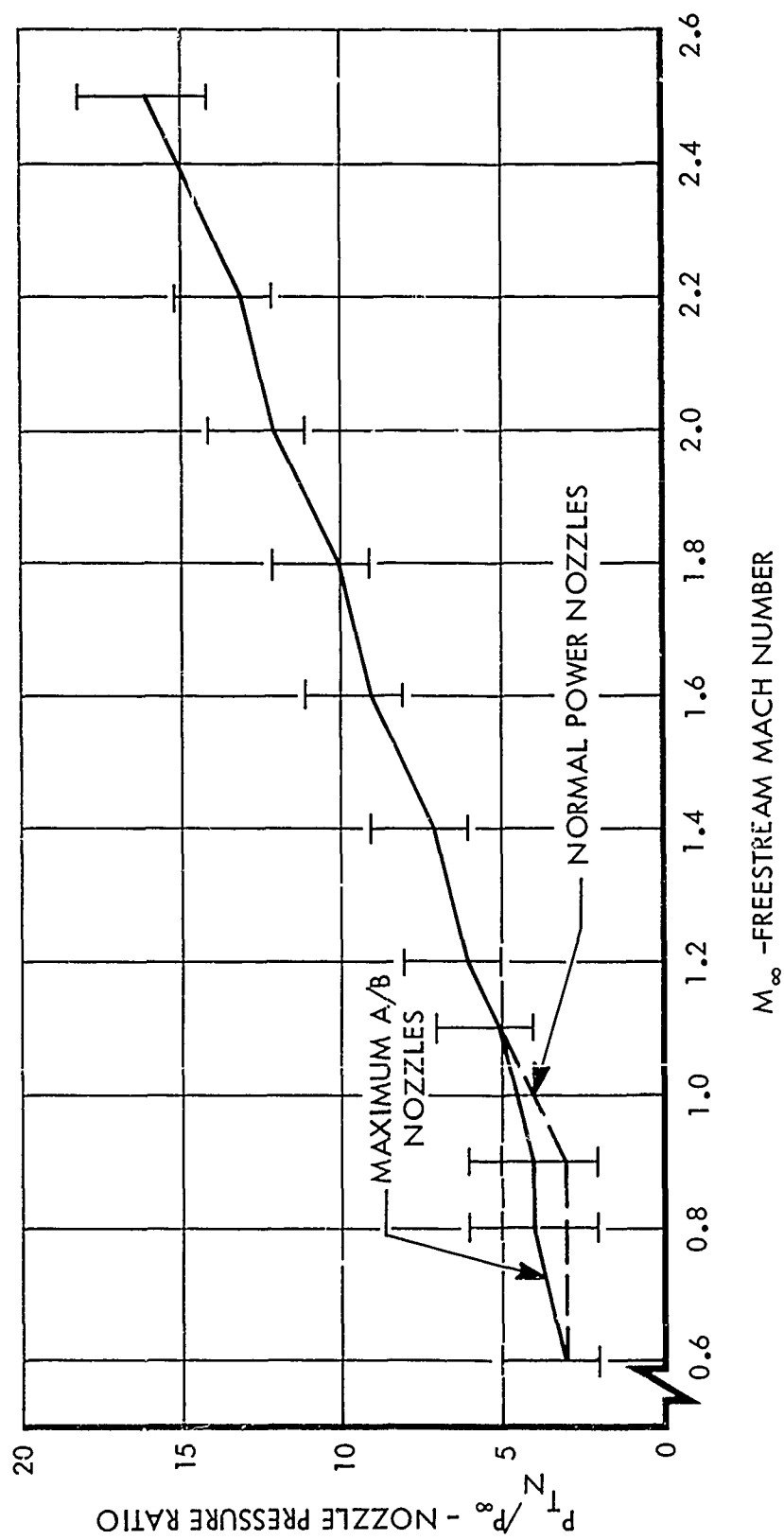


Figure 69. Nozzle Pressure Ratio Schedule for Typical Mission Applications

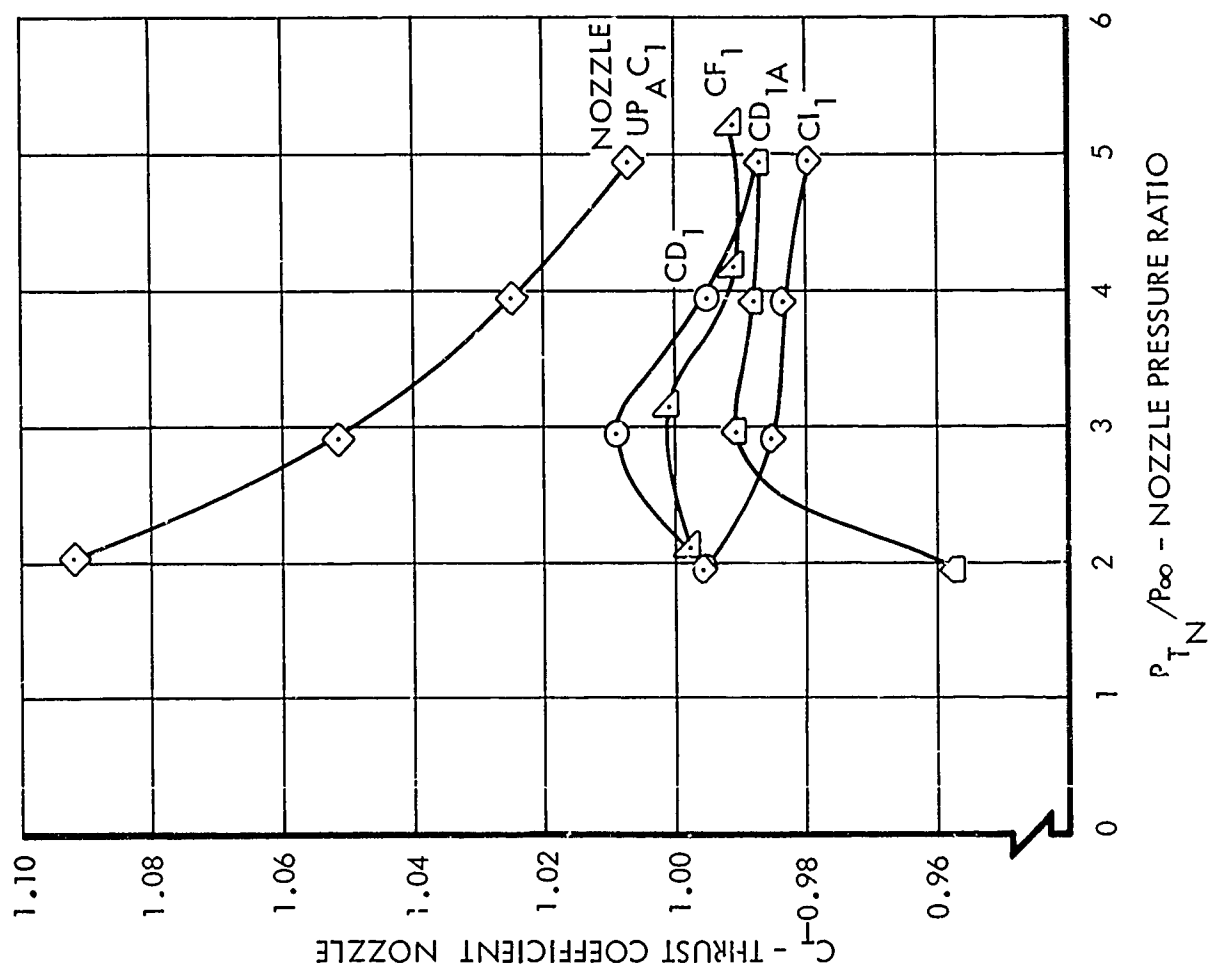


Figure 70. Effect of Nozzle Type on Thrust - Normal Power Nozzles - Mach 0.9

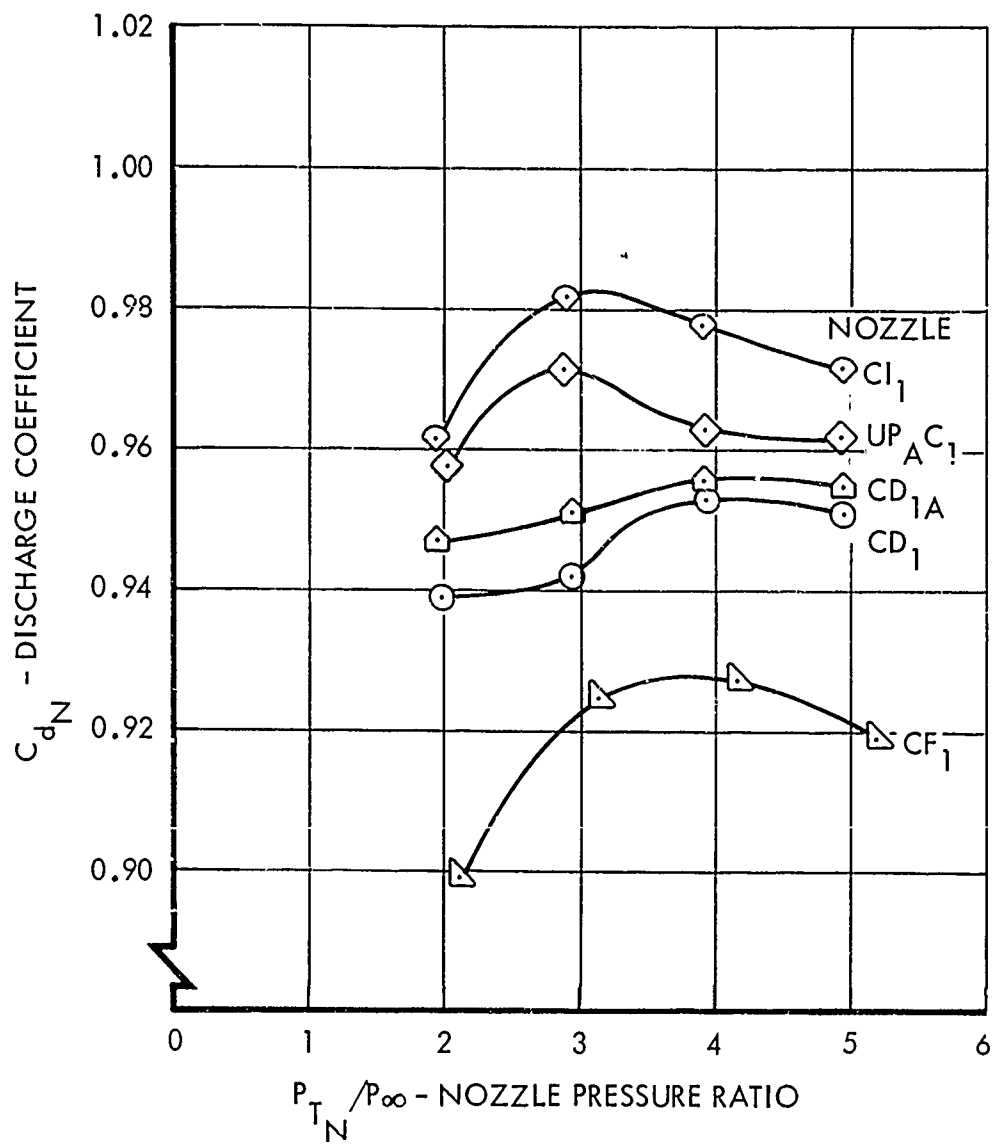


Figure 71. Effect of Nozzle Type on Discharge Coefficients - Normal Power Nozzles - Mach 0.9

and nozzle boattail is compressively turned outward by the nozzle flow, resulting in external pressures higher than freestream static pressure. The high external pressures affect the plug area downstream of the last right-running characteristic from the nozzle shroud lip and produce a nozzle thrust increment. As the nozzle pressure ratio increases, the thrust increment decreases, since the intersection of the plug and the characteristic from the shroud moves downstream and decreases the plug area affected by the external flow. The UPAC1 nozzle discharge coefficients are higher than those of all other nozzles except the C11 nozzle, since the internal geometry of the UPAC1 nozzle is free from the discontinuous slopes found in the other nozzles but has more internal flow turning than C11. Further, the boundary layer displacement effects for the UPAC1 nozzle are larger than for the C11 because of an increased internal wetted area.

Thrust and discharge coefficients for the maximum A/B nozzles are presented in Figures 72 and 73 as functions of nozzle pressure ratio. In Figure 73, data for Mach numbers of 0.9, 1.2, and 2.0 are paired with a single curve for each nozzle since the discharge coefficients should be independent of freestream Mach number. The data of Figure 72 are treated in the same manner since, except for plug nozzles at low pressure ratios, the thrust coefficients should also be independent of freestream Mach number. The CF3 (convergent flap) nozzle has its flap retracted and has no large internal flow angle changes. The CD3 (convergent-divergent) and CD3A (alternate convergent-divergent) nozzles have sharp throats but the throat angles have decreased to 14 degrees from the 23-degree normal power throat angles. Thus, the two-dimensional effects observed in the normal power nozzles are greatly diminished, and the thrust coefficients are near the one-dimensional analysis values for the CF3, C13, CD3, and CD3A nozzles. Boundary layer displacement and exit flow angularity account for most of the differences from ideal performance for these nozzles.

The UPAC3 (unshrouded plug) nozzle has its thrust increased by external flow pressurization of the plug at low nozzle pressure ratios in subsonic flow, but the effect is smaller than for UPAC1. The higher nozzle mass flow rate of UPAC3 reduces the magnitude of the plug thrust increment relative to the nozzle exit total momentum. Also, the larger shroud diameter of the UPAC3 nozzle causes the last right-running characteristic to intersect the plug farther downstream than on the UPAC1 nozzle at the same nozzle pressure ratio and, thus, decreases the plug area affected by the external flow. The UPAC3 discharge coefficient is lower than for the other maximum A/B nozzles because of the greater internal turning required of the nozzle flow and the increased boundary layer displacement effects.

Thrust and discharge coefficients for normal power, partial A/B, and maximum A/B convergent-divergent and unshrouded plug nozzles are shown in Figures 74 and 75 for freestream Mach numbers of 0.9, 1.2, 2.0, and 2.5. Thrust coefficients are highest for the normal power nozzles at Mach 0.9 and for the maximum A/B nozzles at the other Mach numbers. The maximum A/B convergent-divergent and both partial A/B nozzles have similar nearly constant discharge coefficients. The internal flow turning of the unshrouded normal power and

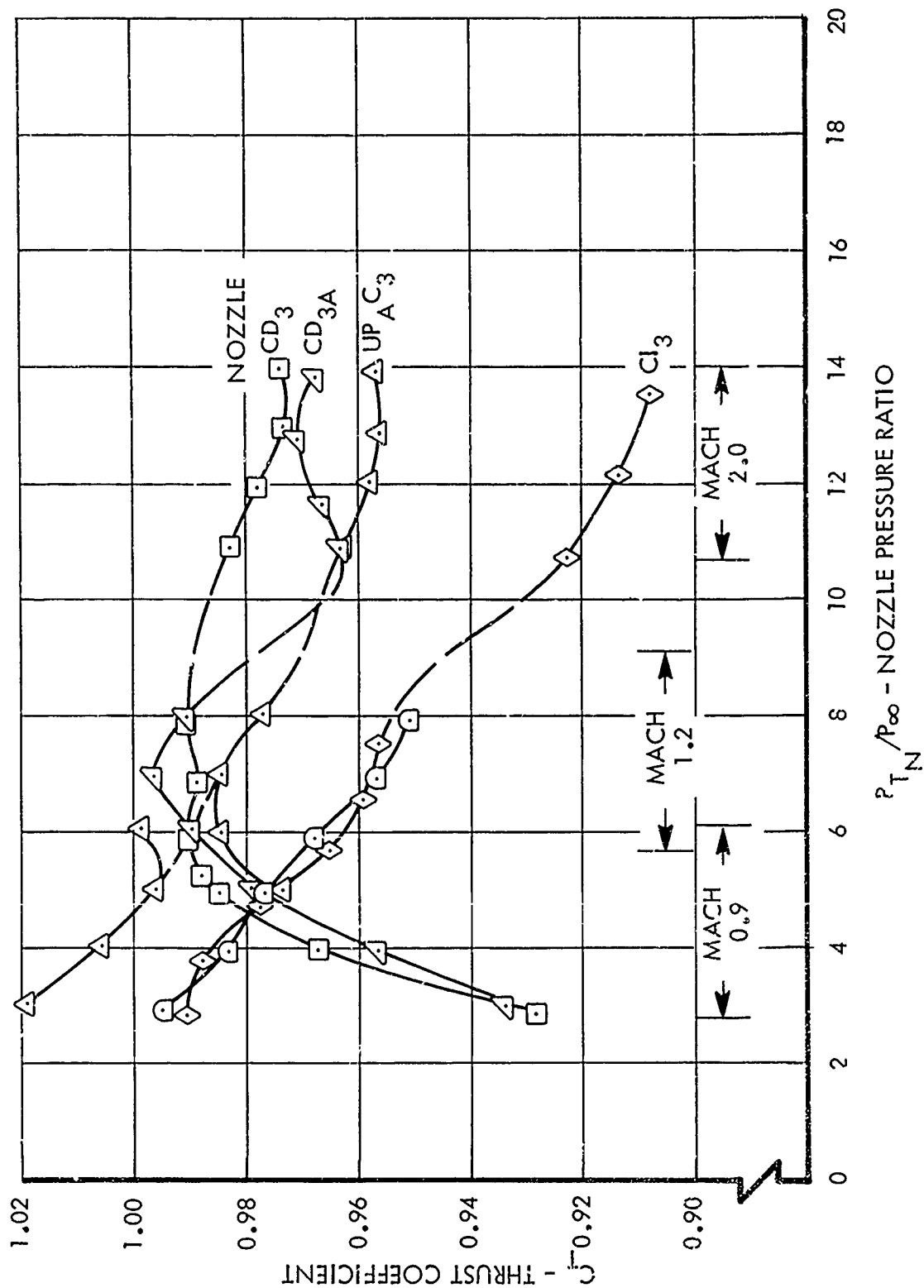


Figure 72. Effect of Nozzle Type on Thrust - Maximum A/B Nozzles - Mach 0.9, 1.2, and 2.0

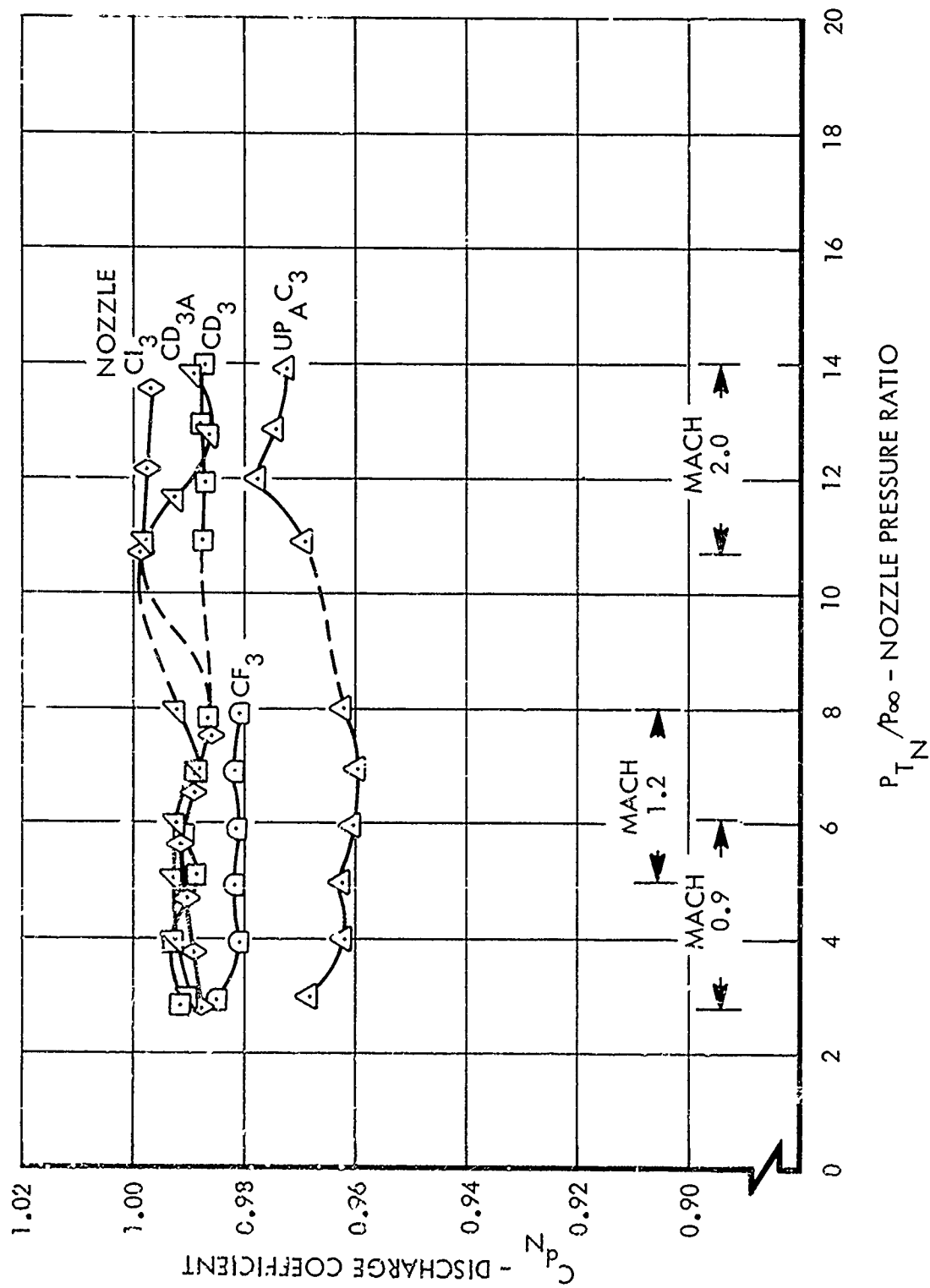
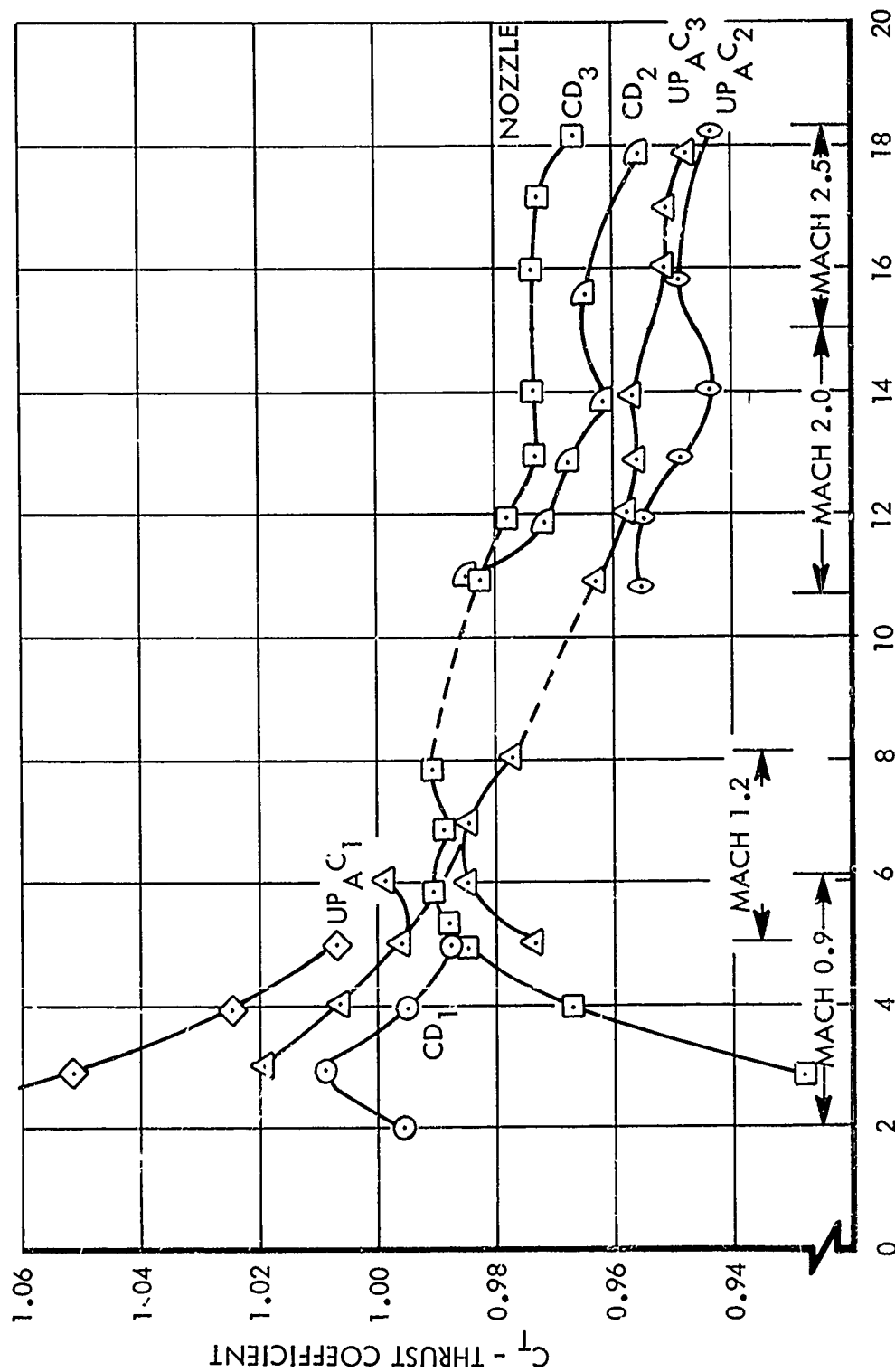


Figure 73. Effect of Nozzle Type on Discharge Coefficients - Maximum A/B Nozzles -
Mach 0.9, 1.2, and 2.0



P_T/P_∞ - NOZZLE PRESSURE RATIO

Figure 74. Effect of Nozzle Type on Thrust - CD and UP Nozzles - Mach 0.9, 1.2, 2.0, and 2.5

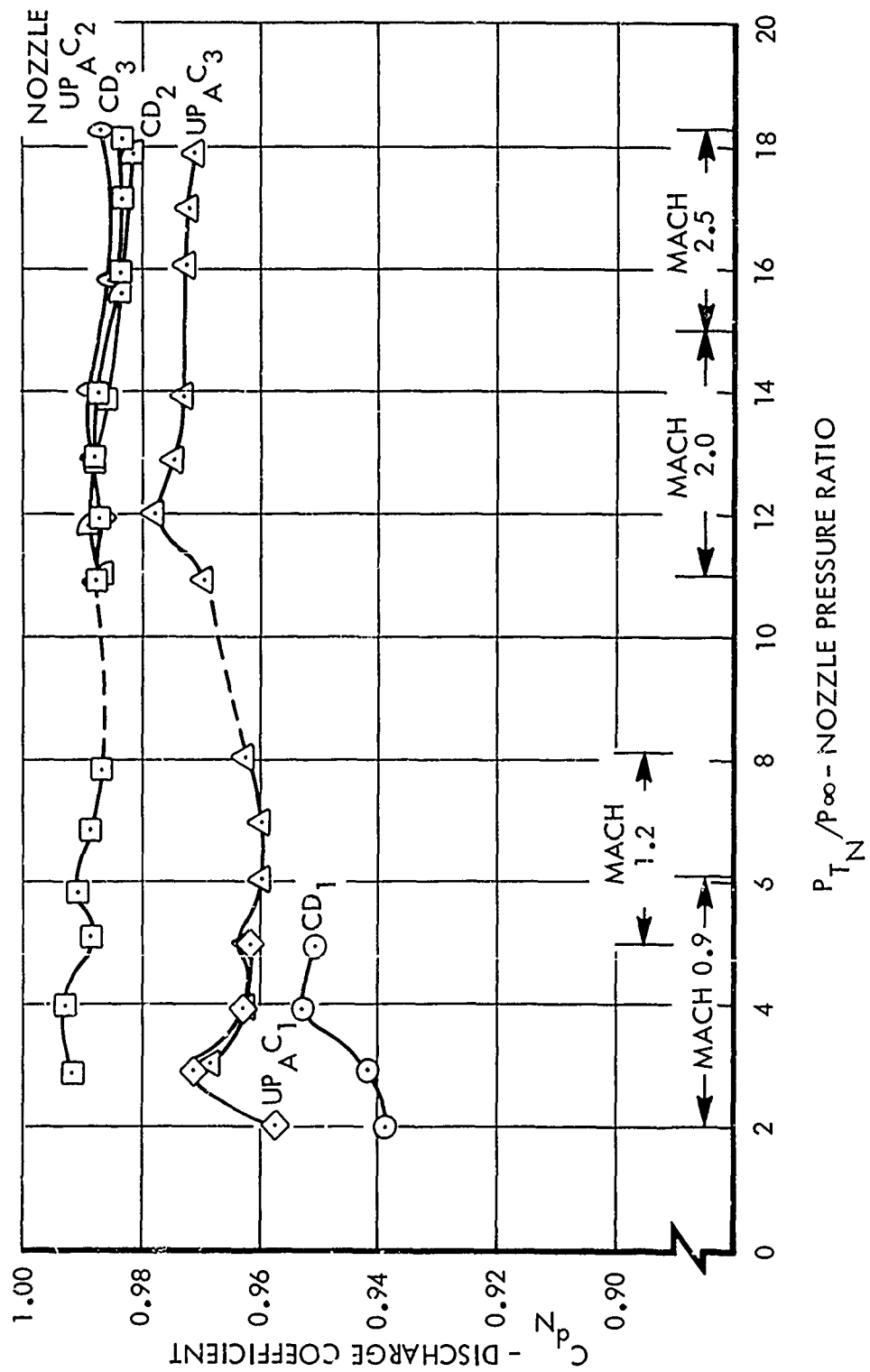


Figure 75. Effect of Nozzle Type on Discharge Coefficient - CD and UP Nozzles - Mach 0.9, 1.2, 2.0, and 2.5

maximum A/B plug nozzles results in lower but nearly constant discharge coefficients, and the CD1 nozzle, with its 23-degree angle sharp throat, has the lowest discharge coefficients.

3.2.1.3 Thrust-Minus-Drag Performance

The thrust-minus-total-drag coefficients presented in Figures 76 and 77 are formed by subtracting the aftbody boattail, aftbody base, nozzle boattail, and nozzle base drag forces from the gross thrust and normalizing the result by the ideal gross thrust based on measured mass flow. The thrust-minus-drag coefficients are indicative of the installed exhaust system performance, including the effects of the nozzle flow on the adjacent airframe surfaces.

In most cases the total drag forces are sufficiently large relative to the thrust forces at the lower nozzle pressure ratios to cause the thrust-minus-total-drag coefficient to increase with nozzle pressure ratio. This occurs even for nozzles for which thrust coefficients decrease with increasing pressure ratio. The convergent-divergent and unshrouded plug nozzles have the highest thrust-minus-total-drag coefficients except at Mach 0.9, where the maximum A/B convergent-divergent nozzle overexpands the exhaust flow.

3.2.2 Nozzle Lateral Spacing Effects

The effects of nozzle lateral spacing on the external drag, internal thrust, and thrust-minus-drag of the Phase II model are presented in this subsection. These effects are presented for the high short horizontal (NLB, ILB, and WLB), centerline short horizontal (I2B and W2B), and centerline long horizontal (I2D and W2D) wedge interfairings for each of the following nozzle configurations and operating conditions.

<u>Nozzle Configuration</u>	<u>Mach Number</u>	<u>Nozzle Pressure Ratio</u>
CD ₁ , UP _A C ₁	0.9	4
CD ₃ , UP _A C ₃	0.9	4
CD ₃ , UP _A C ₃	1.2	6
CD ₃ , UP _A C ₃	1.6	10

3.2.2.1 External Drag and Pressure Distributions

Since all external drag coefficients presented are based on wing area, (rather than the maximum aftbody or nozzle cross-sectional areas which vary with nozzle spacing) they indicate only the drag changes with nozzle spacing for the various configurations. In addition, all data were obtained using the average of the left-hand and right-hand aftbody balance results. Although the left-hand and right-hand balance results generally differed slightly from each other, the drag force trends obtained using either the average or individual balance results were found to be substantially the same.

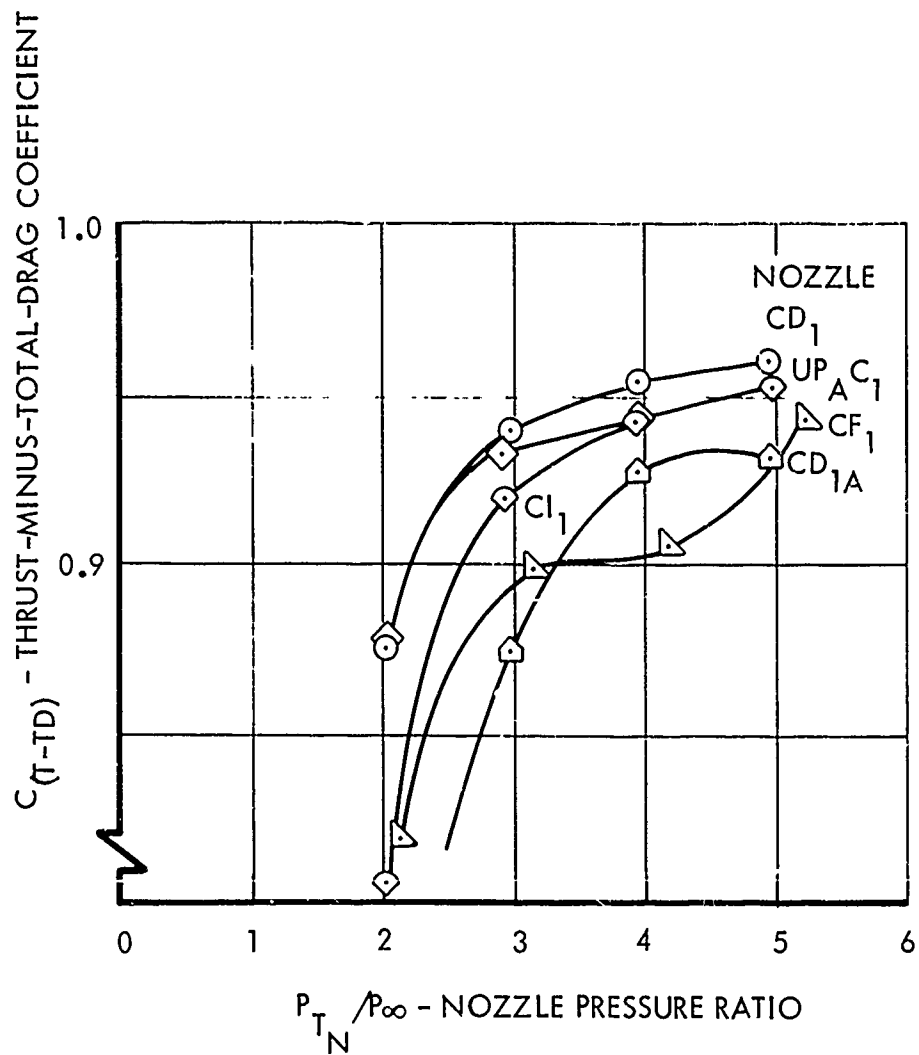


Figure 76. Effect of Nozzle Type on Thrust-Minus-Total-Drag - Normal Power Nozzles - Mach 0.9

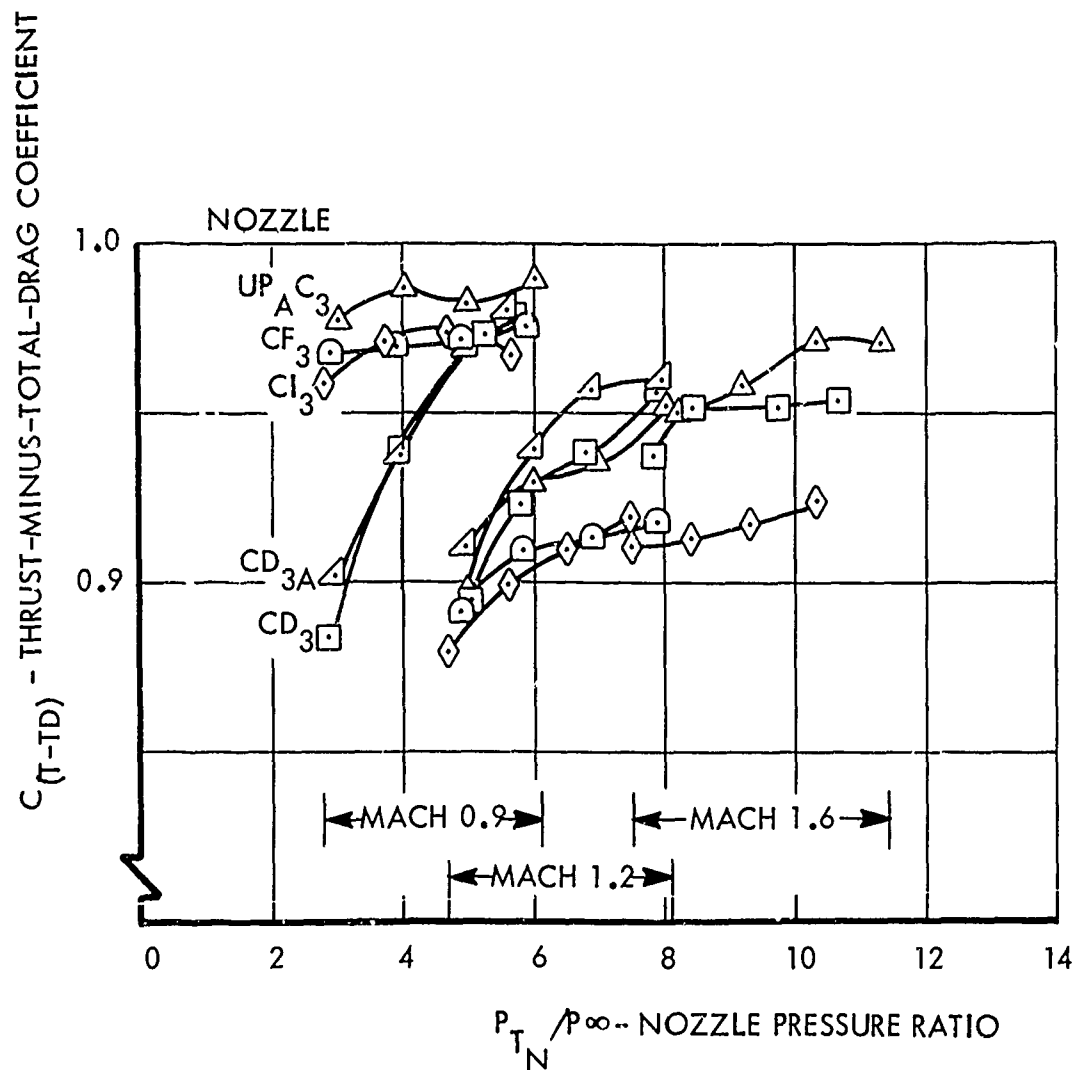


Figure 77. Effect of Nozzle Type on Thrust-Minus-Total-Drag - Maximum A/B Nozzles - Mach 0.9, 1.2, and 1.6

Subsonic External Flow - At 0.9 Mach number, the total drag is insensitive to nozzle lateral spacing, as shown in Figures 78 and 79. Little variation in total drag occurs because the total aftbody drag increase and the total nozzle drag decrease with increasing nozzle spacing cancel one another.

The observed drag trends can be explained by inviscid flow theory, as follows. In the upper portion of Figure 80, the aftbody/nozzle area distributions are illustrated for the narrow, intermediate, and wide nozzle lateral spacing. Also illustrated is the area distribution for the exhaust jet. Assuming a constant area forebody extending far upstream (equivalent to assuming that the forebody has little effect on the aftbody flow field), the axial pressure force acting on the streamline adjacent to the body and exhaust jet boundary must be zero in accordance with subsonic potential flow theory (Reference 71). The pressure force acting on the jet boundary is invariant with nozzle spacing and jet area distribution since this force is uniquely determined by the change in momentum of the exhaust jet as it expands from the same exit conditions to freestream static pressure. In order to obtain an integral pressure force value of zero for the force acting on the streamline adjacent to the aftbody/nozzle and exhaust jet boundary for each nozzle spacing, the pressure force acting on the aftbody/nozzle must be equal (but opposite in direction) to the pressure force acting on the jet boundary. The total pressure drag is, therefore, predicted to be invariant with nozzle spacing. As a result, the variation in total drag with nozzle spacing, such as that shown in Figures 78 and 79, must depend only on viscous effects. The variation in total drag for subsonic external flow will be small since the friction drag is estimated to increase only six percent on the average from a narrow-spaced to a wide-spaced configuration.

Illustrated in the lower portion of Figure 80 are pressure distributions which are representative of those that would be obtained by application of potential flow theory for axisymmetric bodies with the area distributions shown in the upper portion of the figure. As the maximum diameter increases, the pressures in the nozzle region increase due to greater flow recompression. Since the total drag must remain constant with nozzle spacing, the pressures on the forward portion of the aftbody must decrease. Thus, as the maximum diameter is increased (equivalent to increasing the nozzle spacing), the total aftbody drag is increased, but this is compensated by a reduction in the total boattail drag.

For the maximum A/B nozzle configurations, both the total aftbody and total boattail drags remain relatively constant with nozzle spacing. The variation in total boattail drag is small due to the low drag levels resulting from the small nozzle frontal areas. To be consistent with the theory discussed above, the total aftbody drag also remains constant in order to maintain an invariant total drag with nozzle spacing.

Although the total drag and pressure distribution trends for both the normal power and maximum A/B nozzle configurations are consistent with the trends predicted by inviscid potential flow theory for an equivalent axisymmetric body, the analysis method is inadequate for evaluating absolute drag levels

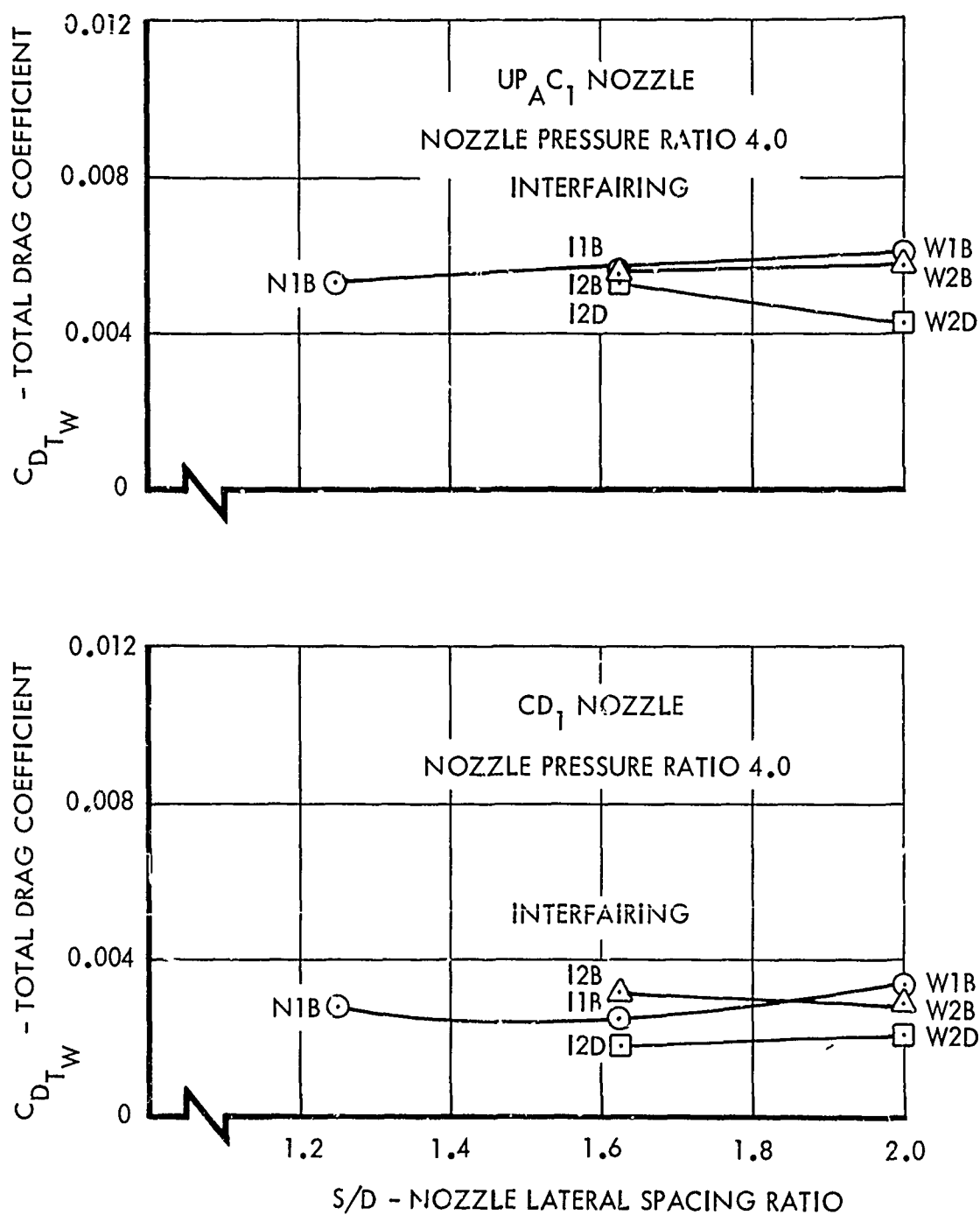


Figure 78. Effect of Nozzle Lateral Spacing on Total Drag - Normal Power Nozzles - Mach 0.9

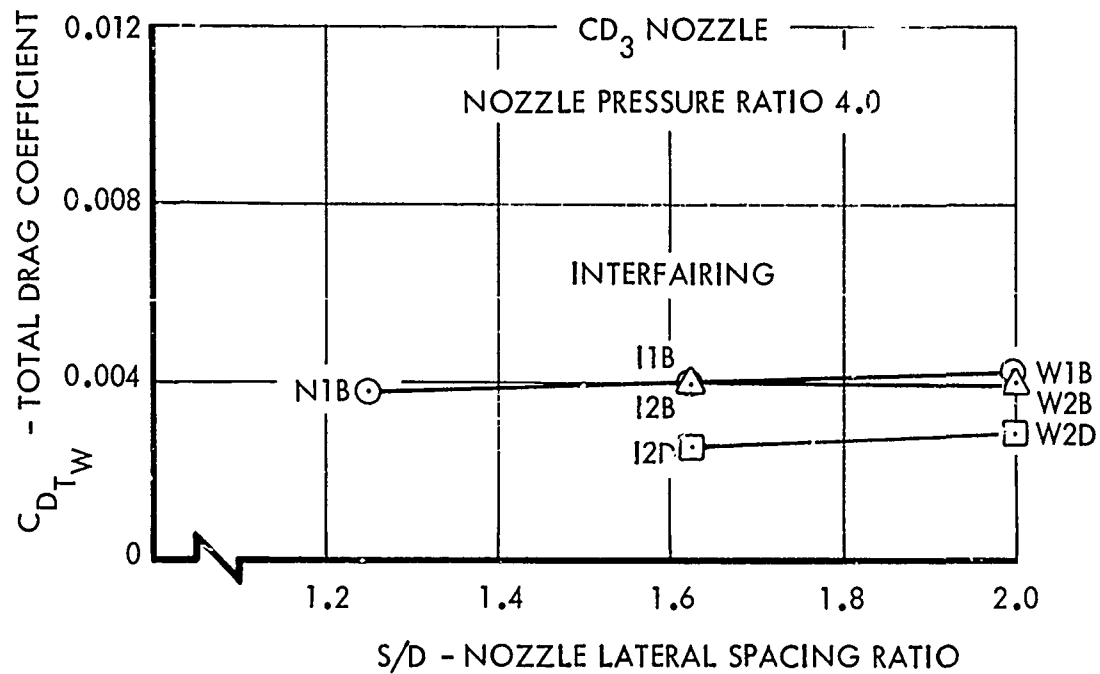
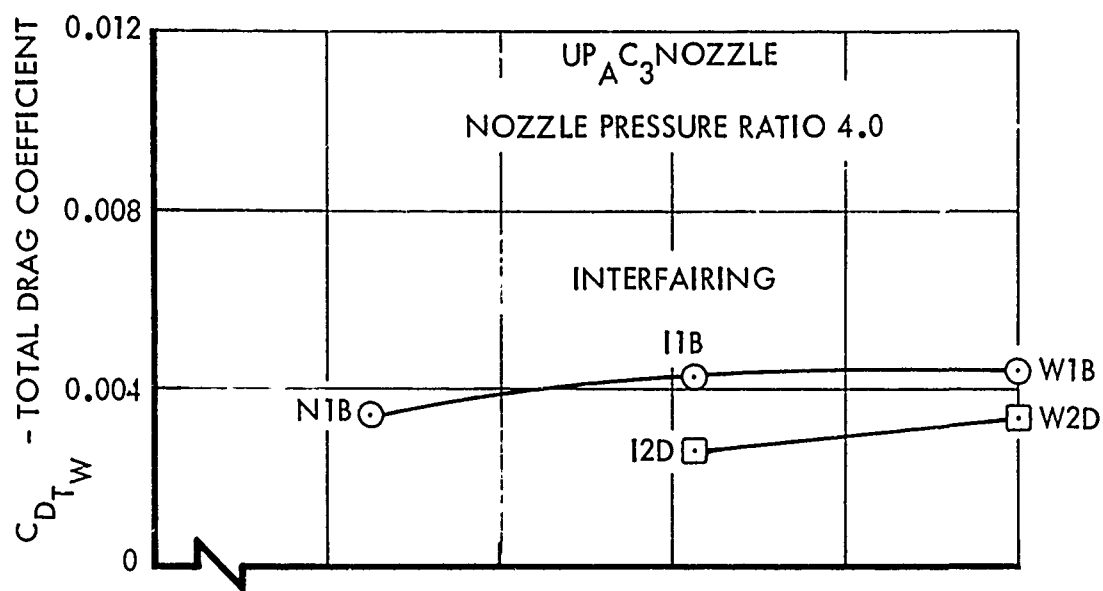


Figure 79. Effect of Nozzle Lateral Spacing on Total Drag - Maximum A/B Nozzles - Mach 0.9

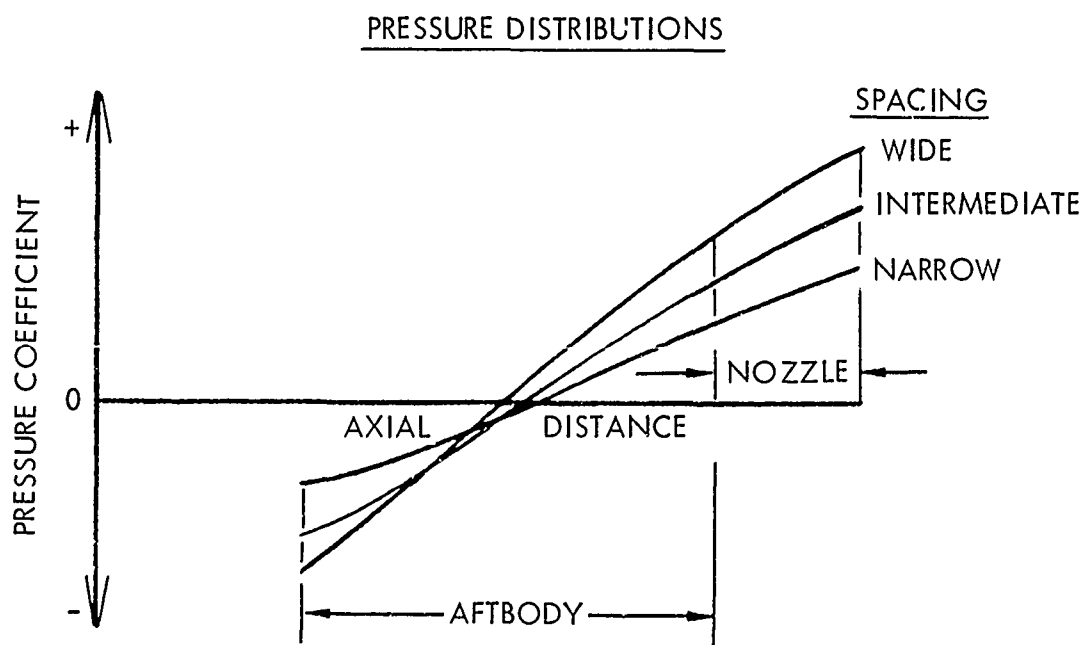
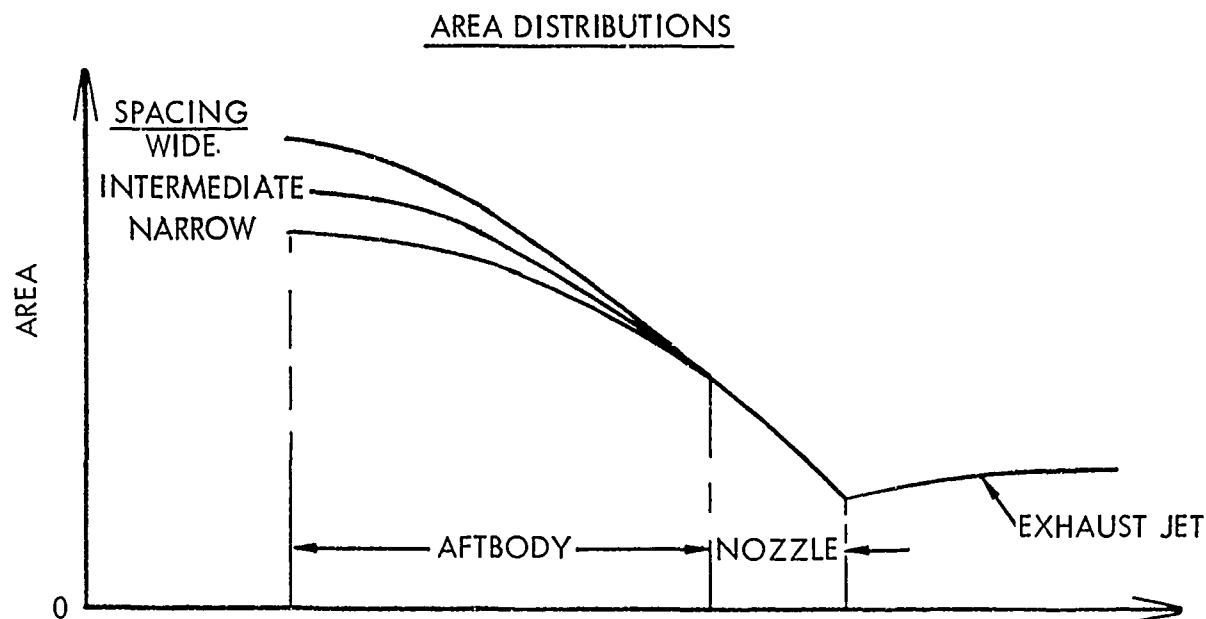


Figure 80. Illustrative Area and Pressure Distributions for Phase II Aftbody and Nozzle

of various configurations due to the simplifying assumptions employed. The method will be valid for predicting the incremental drag change with nozzle spacing if the errors associated with the assumptions employed are invariant with nozzle spacing.

Supersonic External Flow - The total drag for the maximum A/B nozzle configurations increases considerably with increasing nozzle lateral spacing for freestream Mach numbers of 1.2 and 1.6, as shown in Figures 81 and 82, respectively. An increasing total aftbody drag with nozzle spacing ratio is responsible for the total drag trend since the total nozzle drag is very small. As previously mentioned, a small boattail projected frontal area is responsible for the small nozzle drag force.

The total aftbody drag increase with increasing nozzle spacing is expected since, as the nozzle spacing increases, the maximum area is increased and the area distribution curve is steepened (as illustrated in Figure 80). According to linearized theory (e.g., Equation 17.29 of Reference 15), increasing the maximum area increases the Mach number at the start of the aftbody because of the increased effective thickness ratio of the forebody. The steepened area distribution curve effectively increases the surface slope and promotes increased flow expansion and, therefore, reduced pressures.

Since the maximum model area occurs near the fuselage centerbody (upstream of the metric break) and increases with increasing nozzle lateral spacing, and since only the aftbody/nozzle surfaces were metric, the measured aftbody/nozzle drag trends may not be representative of the aircraft drag trends. Application of equivalent body/method of characteristics analysis methods indicates, however, that the observed aftbody nozzle drag trends are representative of the aircraft drag trends. The analysis method employed consisted of computing the aftbody/nozzle and aircraft equivalent-body drags for each of axisymmetric bodies whose area distributions correspond to one-half the area distribution of the aircraft model, excluding the wing and empennage, for the NLB/CD3 and WLB/CD3 configurations. The computational method employed was the combined MOC/boundary layer program described in Reference 1. The equivalent bodies were contoured to correspond to the half-area rather than full-area distribution since computed aftbody pressure drag coefficient using a half-area distribution body were found to be in better agreement with experimental data. Computed equivalent body drags show that, as the nozzle spacing increases from the narrow to wide configuration, the increase in aftbody/nozzle pressure drag is six percent larger than the increase in aircraft drag of the equivalent bodies for a freestream Mach number of 1.6 and five percent larger for a freestream Mach number of 2.0. Application of the measured aftbody/nozzle drag trends for prediction of the aircraft drag trends with nozzle spacing can, therefore, be employed with some confidence.

3.2.2.2 Thrust and Internal Pressure Distribution

For the nozzle configurations and operating conditions selected for this study, it is concluded that nozzle spacing has little effect on the nozzle gross thrust coefficient and internal pressure distributions.

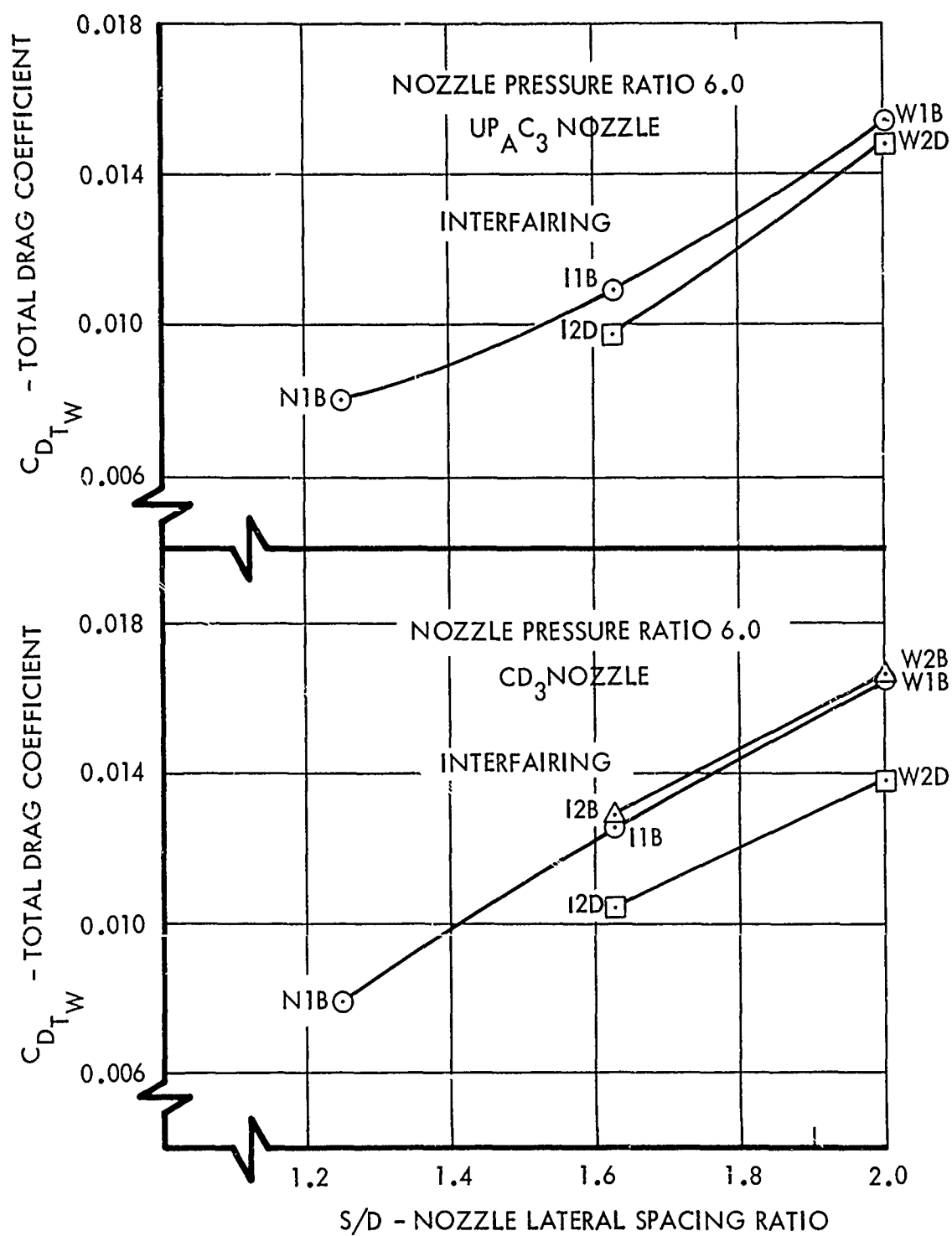


Figure 81. Effect of Nozzle Lateral Spacing on Total Drag - Maximum A/B Nozzles - Mach 1.2

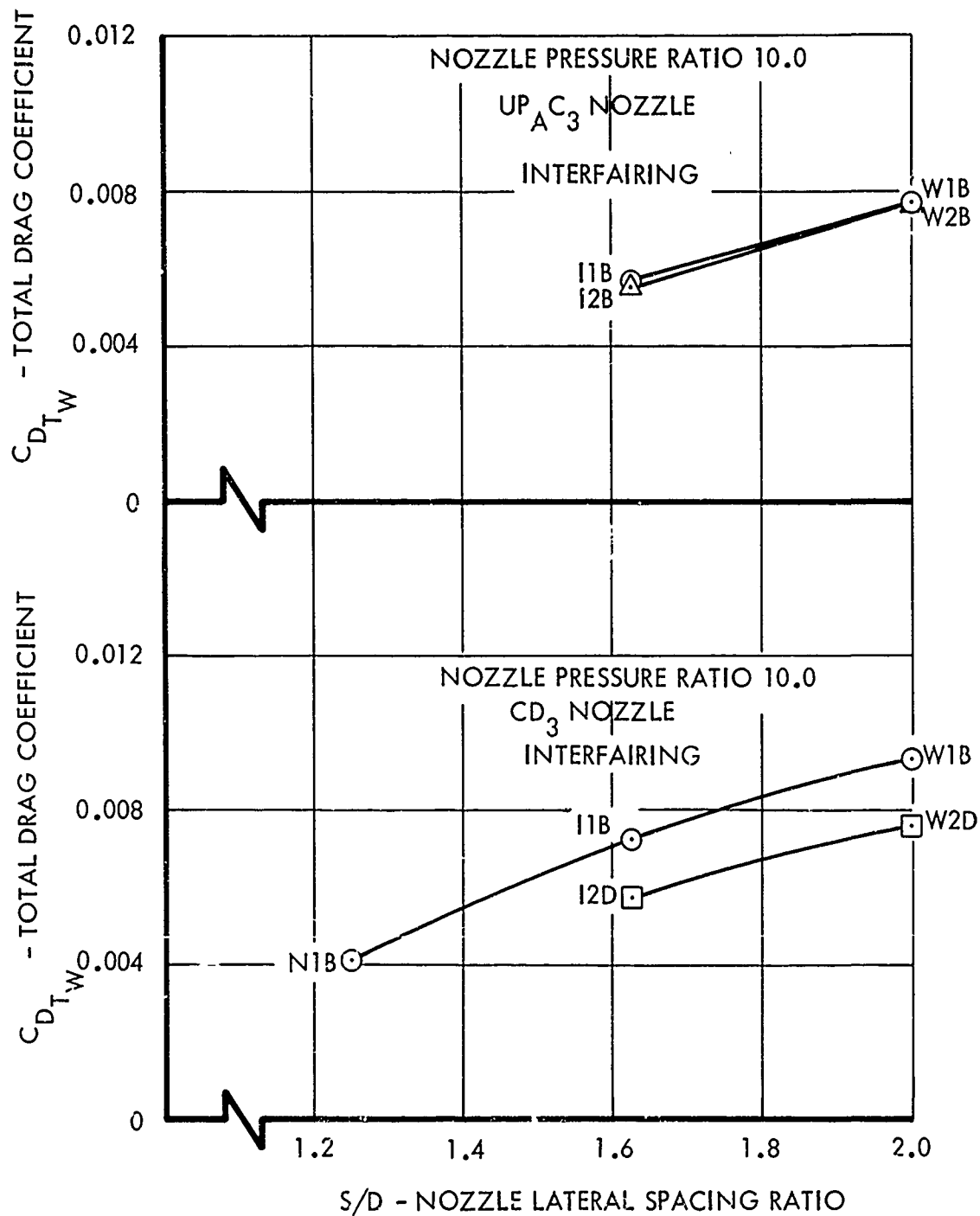


Figure 82. Effect of Nozzle Lateral Spacing on Total Drag - Maximum A/B Nozzles - Mach 1.6

The effect of nozzle spacing on the thrust coefficients of the normal power nozzles is presented in Figure 83 for a freestream Mach number of 0.9. The balance data indicate that the thrust coefficients are influenced somewhat by both nozzle spacing and interfairing type. However, the result of analysis of nozzle pressure distributions data are believed to be more accurate, and these indicate that: (1) the influence of nozzle spacing is less than that indicated by the force balance data, and (2) that the thrust coefficients are not influenced by interfairing type. Specifically, for the normal power plug nozzle, integration of the pressure forces acting on the plug surface indicates that the thrust coefficient increases 0.47 percent (metric data indicate a one percent increase) as the nozzle spacing increases from the narrow to intermediate position and remains constant as the spacing further increases.

The internal surface pressure distributions of the normal power convergent-divergent nozzle indicate that, as the nozzle spacing increases, the pressures near the exit of the nozzle are reduced. Only one row of internal pressure taps was incorporated in the CD1 nozzle. These taps are located 45 degrees from vertical in the upper quadrant nearest the aircraft centerline. The largest internal pressure variation with nozzle spacing is expected in this region since the largest pressure distribution variation on the external boat-tail surface was observed in this region. Although the observed internal pressure variation appears significant, the gross thrust variation with nozzle spacing is quite small since the frontal area of the inner nozzle wall surface is small in the region of interest. As the nozzle spacing increases from narrow to wide, the estimated decrease in thrust coefficient is 0.15 percent.

The effect of nozzle spacing on the thrust coefficients of the maximum A/B nozzles is similar to the variation obtained for the normal power nozzles. The pressure distributions for the maximum A/B nozzles indicate that, as the spacing increases from narrow to wide: (1) the plug nozzle thrust coefficient increases 0.3 percent, and (2) the convergent-divergent nozzle thrust coefficient decreases 0.5 percent. The pressure data also indicate that the thrust coefficient variation with nozzle spacing is independent of the interfairing type.

3.2.2.3 Thrust-Minus-Total Drag

Since the nozzle internal performance is relatively insensitive to nozzle spacing, the thrust-minus-total drag variations with nozzle spacing simply reflects the airbody/nozzle drag trends. Specifically, for both the normal power and maximum A/B nozzles, the thrust-minus-total drag is insensitive to nozzle spacing for subsonic external flow. For supersonic external flow and for the maximum A/B nozzles, the thrust-minus-total drag is considerably reduced as the nozzle spacing increases.

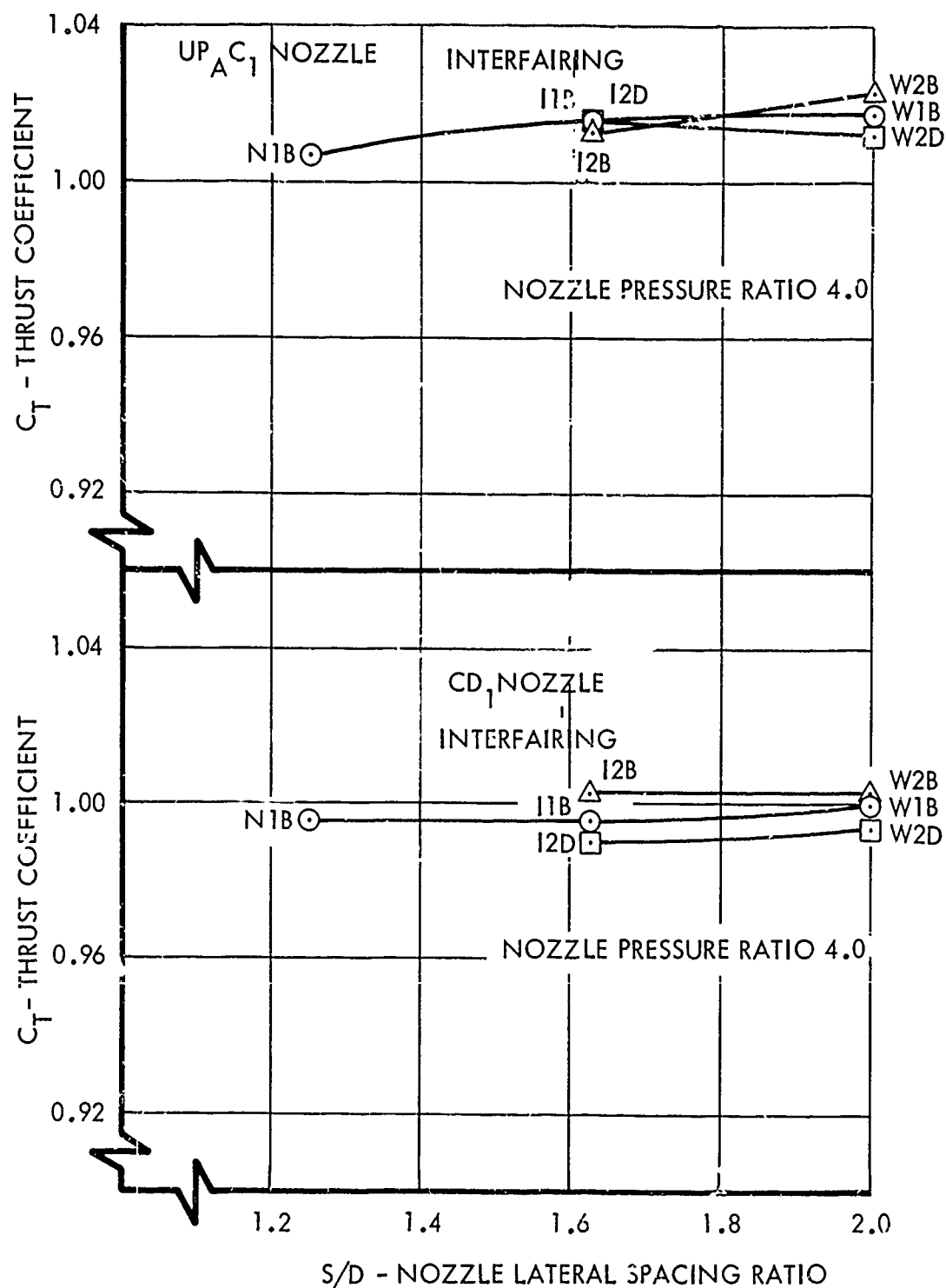


Figure 83. Effect of Nozzle Lateral Spacing on Thrust - Normal Power Nozzles - Mach 0.9

3.2.3 Interfairing Type and Length Effects

3.2.3.1 Interfairing Type Effects

The effect of interfairing type on the total drags of the Phase II model are presented for horizontal and vertical wedge-type interfairings. The horizontal wedge interfairings include three trailing edge types: horizontal trailing edge at the nozzle centerline, horizontal trailing edge above the nozzle centerline, and trailing edge along nozzle radial lines. Detailed descriptions of the interfairing configurations are presented in Section 3.1.2.4.

The most pronounced changes of total drag with interfairing type occur between the high horizontal wedge results and the vertical wedge at subsonic speeds. As shown in Figure 84, the horizontal wedge interfairing yields lower total drag than the vertical wedge interfairing for a narrow-spaced CD1 nozzle. The nozzle drag trend dominates the aftbody drag trend for this configuration since only the region between the interfairing and nozzles is affected and the nozzles have a larger projected frontal area than that associated with the side of the interfairings. For the CD3 nozzle, the drag difference shown in Figure 85, though not as great as for the CD1 nozzle, is reversed. This reversal is due to the forward facing frontal area associated with the fan-tailed nozzle surface. The drag trend for non-fan-tailed maximum A/B nozzle configurations would be similar to the trends obtained for the normal power nozzle configurations.

The total drags for the center horizontal wedge interfairing installations are, in most cases, slightly higher than the drags for high horizontal wedge installations, as shown in Figure 86. This higher drag results because the vertical tail for the center horizontal wedge installation is located in the deep channel between the nozzles. The results for the radial trailing edge interfairing are very similar to the results for the high horizontal wedge interfairing.

3.2.3.2 Interfairing Length Effects

Interfairing length effects are presented in this subsection for the high horizontal and vertical wedge interfairings at the narrow nozzle spacing, the center horizontal wedge interfairings at the intermediate nozzle spacing, and the center horizontal wedge interfairing at the wide nozzle spacing. Most of the results are presented for interfairing lengths ending at the nozzle customer connect station ("B" length) and at the exit of the CD nozzles ("D" length). A limited amount of data is presented for interfairings ending upstream of the nozzle customer connect station ("A" length), ending at the exit of the plug nozzles ("C" length), and extending downstream of the exit of the CD nozzles ("E" length).

In general, an increase in interfairing length results in a decrease in aftbody drag at all speeds, increase in nozzle drag at subsonic speeds, and little effect on nozzle drag at supersonic speeds. The overall net effect

4.0 NOZZLE PRESSURE RATIO

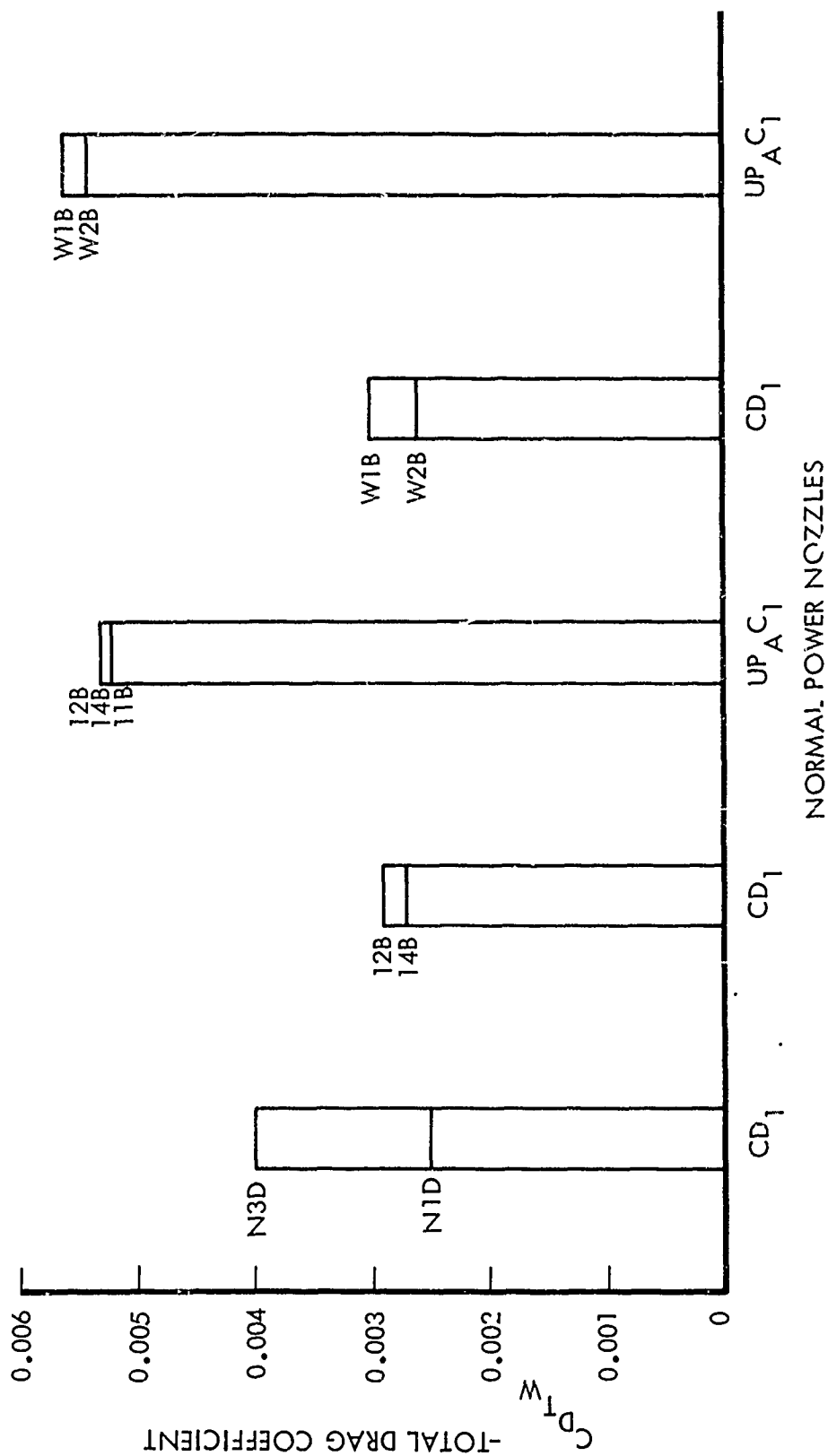


Figure 84. Effect of Interfiring Type on Total Drag - Normal Power Nozzles - Mach 0.9

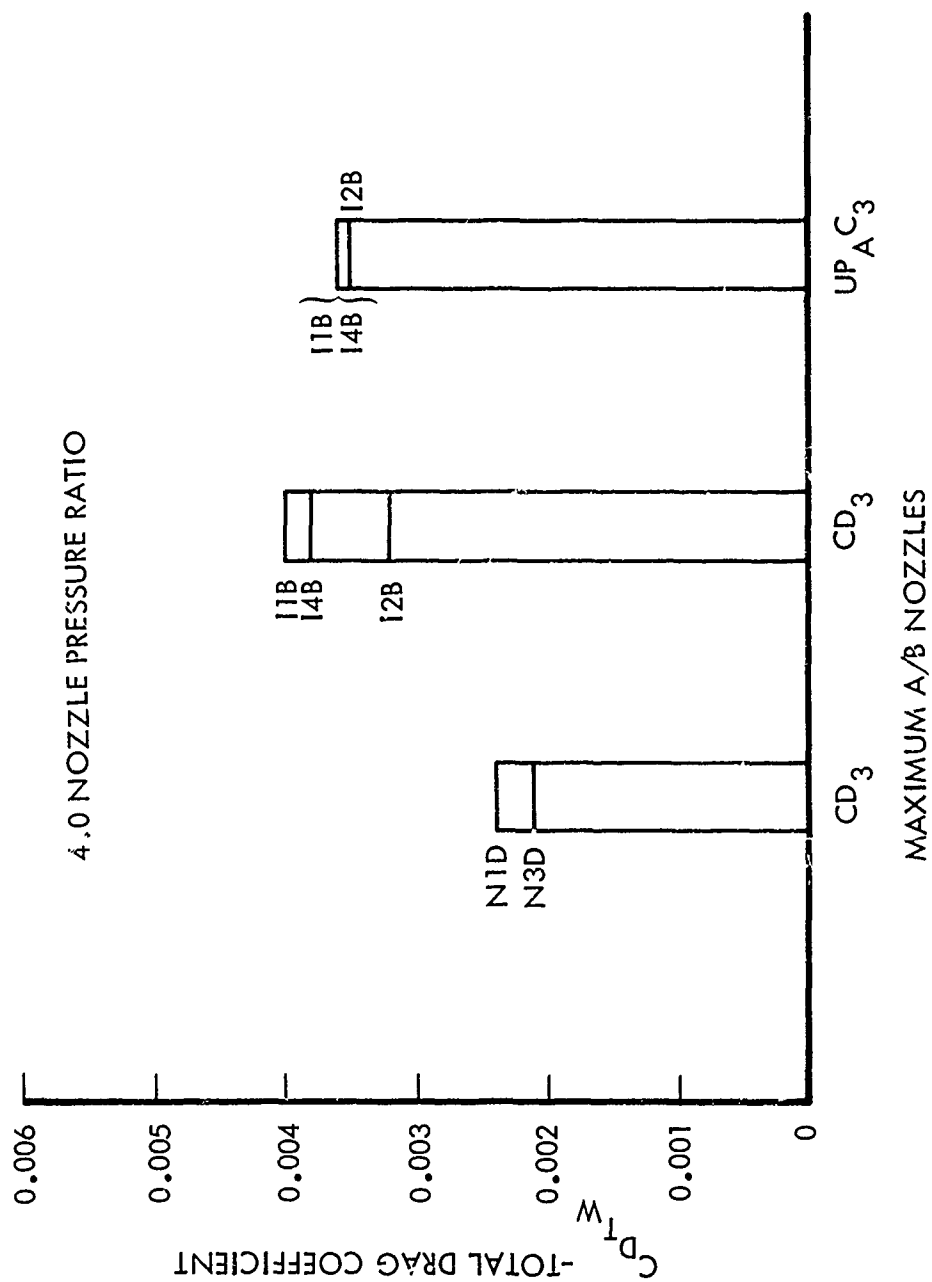


Figure 85. Effect of Interfiring Type on Total Drag - Maximum A/B Nozzles - Mach 0.9

is that the total drag decreases as the interfairing trailing edge location moves downstream from the customer connect station to the exit plane of the convergent-divergent nozzles. Longer interfairings were tested for the normal power convergent-divergent nozzle only, and minimum total drag occurred with the interfairing terminating at the nozzle exit plane.

The effect of interfairing length on total drag is shown in Figures 87 through 89 for the normal and maximum A/B nozzle configurations. Figure 37 indicates that for the normal power nozzles the total drag generally decreases as the end of the interfairing moves downstream from the nozzle customer connect station to the nozzle exit station. Further, the total drag for the CD1 nozzle installation incorporating a horizontal wedge interfairing is a minimum when the interfairing terminates at the nozzle exit. Insufficient data are available for determining if the remaining horizontal-wedge/nozzle configurations would exhibit minimum drag for an interfairing terminated at the nozzle exit. In contrast to the above horizontal interfairing results, the total drag for the CD1 nozzle installation incorporating the vertical interfairings were found to decrease as the interfairing trailing edge is extended downstream from the nozzle exit (N3D compared to N3E).

For most of the maximum A/B nozzle configurations, increasing the interfairing length resulted in reduced total drag, as shown in Figures 88 and 89. In the case of the CF3 nozzle configuration, the large base region prevents recompression along the longer interfairing resulting in an increase in drag with increasing length. Interfairing lengths sufficiently long to minimize total drag were not tested.

Interfairing length effects presented in Reference 72 for a twin-jet model at a freestream Mach number of 0.8 are consistent with the length effects observed for the Phase II model. Specifically, moving the interfairing trailing edge from the nozzle customer connect station to the nozzle exit resulted in little total drag difference. In Reference 72, a twin-jet strut supported model representing only the aft portion of an aircraft (excluding empennage) was used. The consistent results indicate that a partial model may in some cases provide useful results in evaluating interfairing length effects.

3.2.4 Empennage Type, Position, Span Reduction, and Deflection Effects

3.2.4.1 Empennage Type and Position Effects

Four partial span vertical stabilizer configurations were tested to assess their effects on the aftbody and nozzle external flow. The single vertical stabilizers, V1P and V2P, are mounted on the aftbody interfairing top centerline. V1P is the forward stabilizer (positioned between F.S. 103.820 and F.S. 134.550), and V2P is the aft vertical stabilizer (positioned between F.S. 113.655 and F.S. 141.027) and has about 20 percent less wetted area than V1P. The twin vertical stabilizers V3PV and V3PR, are nearly identical designs mounted in pairs on the aftbody pods between F.S. 106.527 and 133.217.

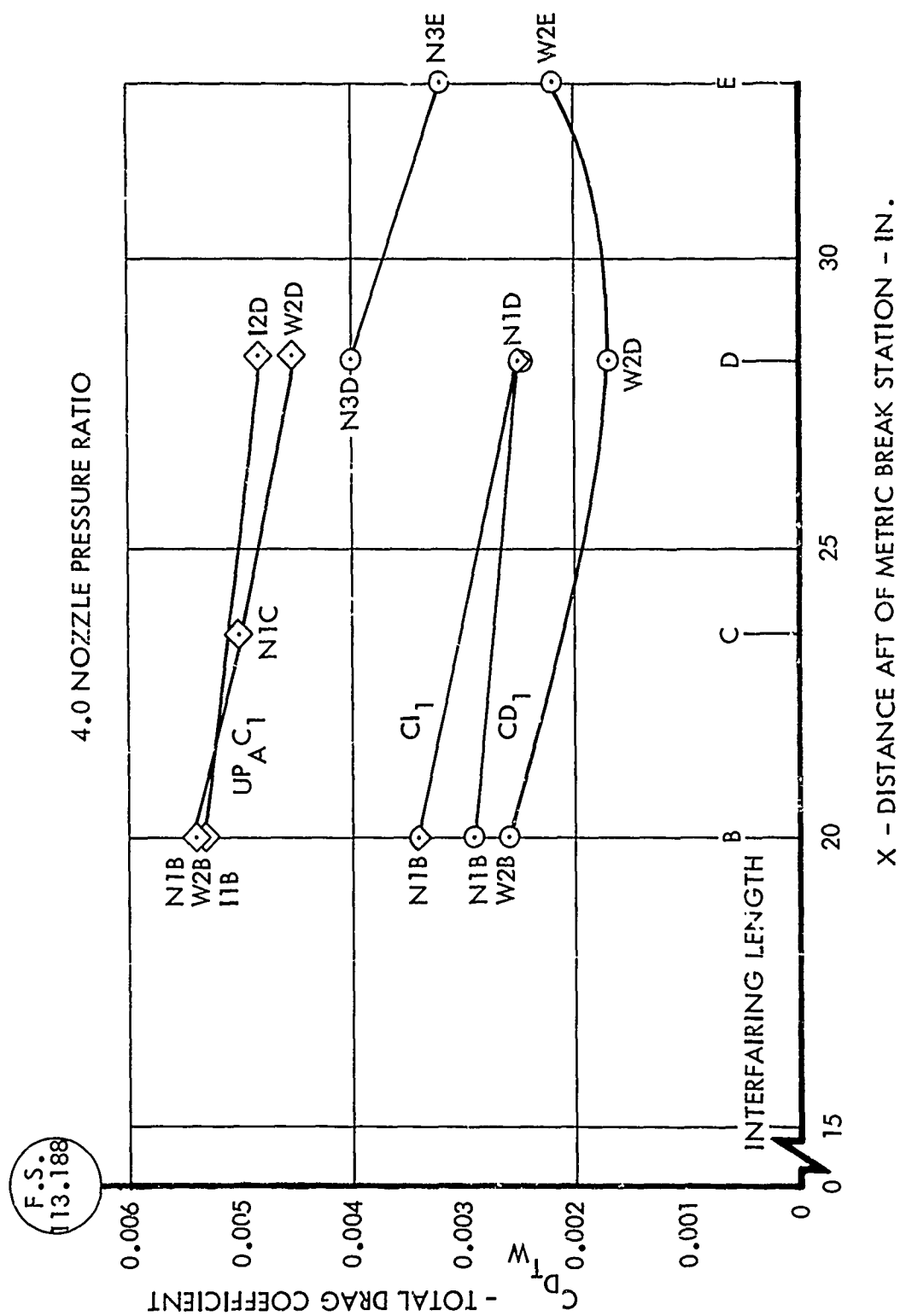
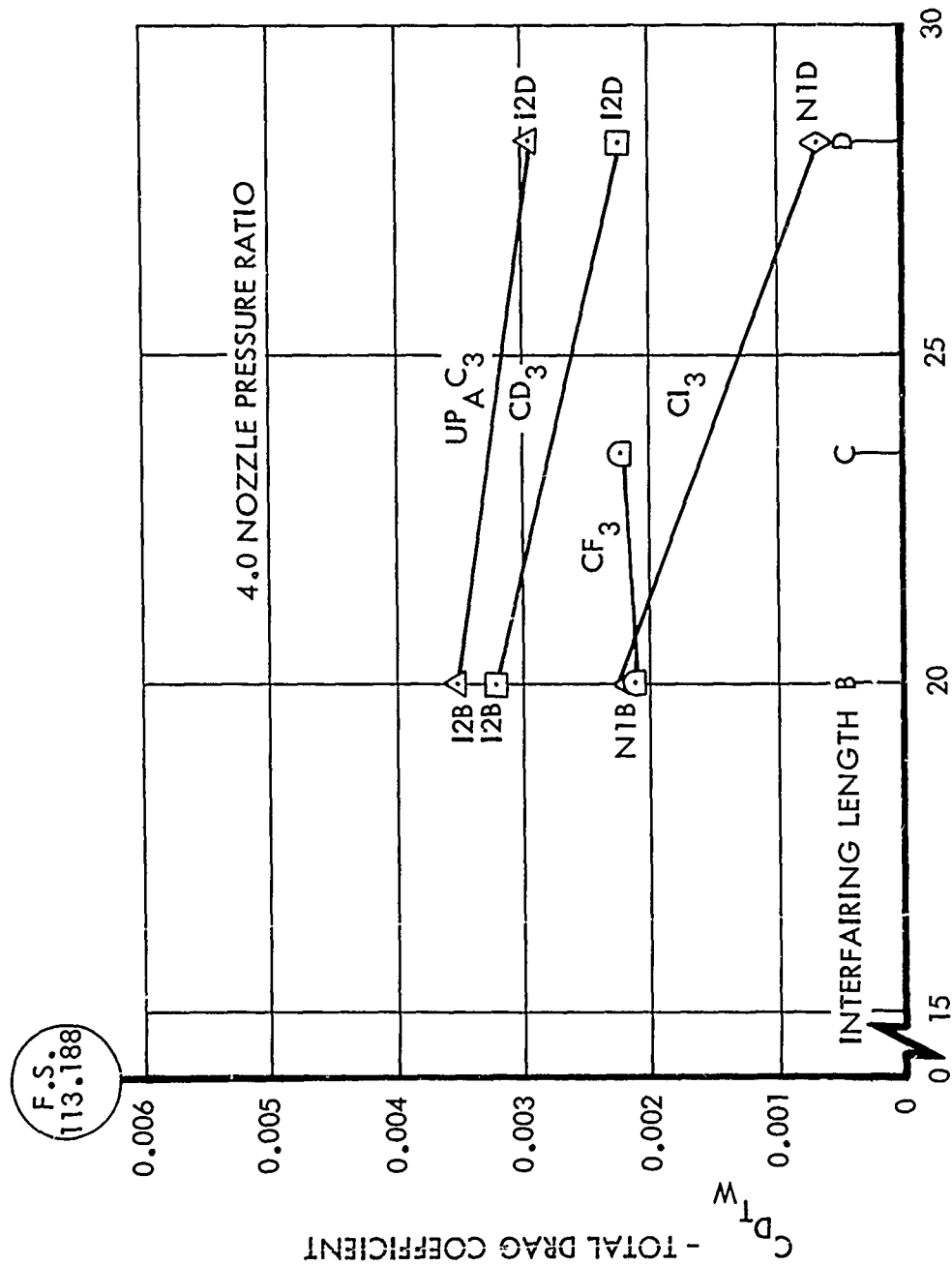
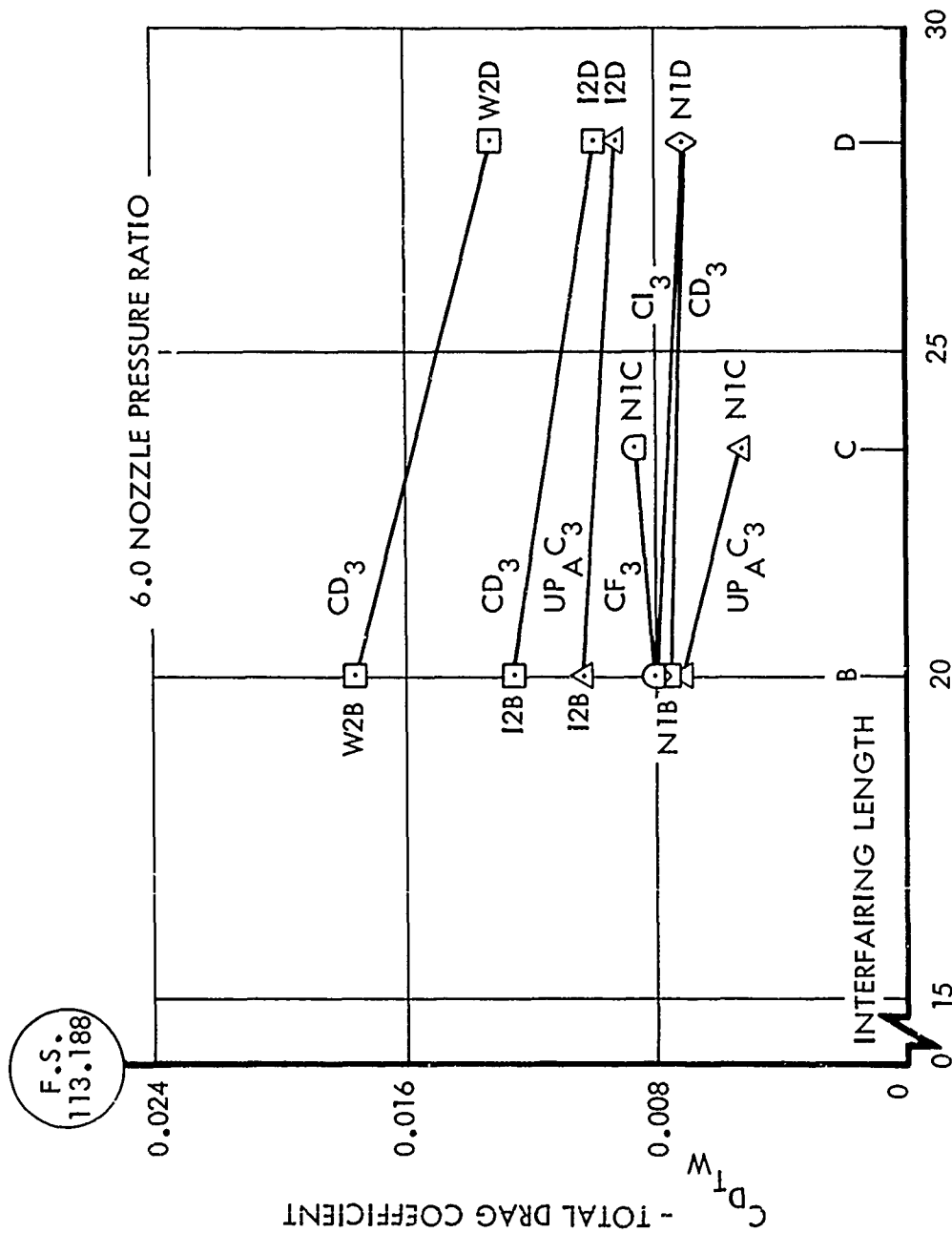


Figure 87. Effect of Interfairing Length on Total Drag - Normal Power Nozzles - Mach 0.9



X - DISTANCE AFT OF METRIC BREAK STATION - IN.

Figure 88. Effect of Interfairing Length on Total Drag - Maximum A/B Nozzles - Mach 0.9



X - DISTANCE AFT OF METRIC BREAK STATION-IN.

Figure 89. Effect of Interfairing Length on Total Drag - Maximum A/B Nozzles - Mach 1.2

The V3PV stabilizers are mounted vertically, and the V3PR stabilizers are mounted in planes passing through the engine centerlines and canted 15 degrees outboard.

Comparisons of total drag for the different vertical stabilizers are shown in Figure 90. The total drags for the twin stabilizer configurations, V3PR and V3PV, are significantly higher than those for the single vertical stabilizers, V1P and V2P, which are also nearly equal. The V3PR and V3PV twin stabilizers create greater drags than V1P and V2P because their position on the aftbody, out of the flow field plane symmetry, results in greater flow disturbances than for stabilizers mounted in the plane of symmetry.

3.2.4.2 Empennage Span Reduction Effects

The empennage span reduction study includes configurations without empennage or fuselage fairing, with the basic fuselage fairing alone, with the fairing plus partial span horizontal and partial span vertical stabilizer, and with the fairing plus full span horizontal and full span vertical stabilizers. Comparisons of total drags are presented for configurations including the partial span empennages (H1P V1P), and full (H1F V1F) span empennages with NLB/CD1 interfairing/nozzle combinations and for configurations including the Y1 fuselage fairing and partial span empennage with NLB/CD3 and NLB/UPAC3 interfairing/nozzle combinations. Drag comparisons with the empennage removed are presented for all of these interfairing/nozzle combinations.

Total drag comparisons for empennage span reductions are given in Figures 91 and 92. Little effect is evident for span reduction from full to partial or from fuselage fairing alone to no empennage or fairing. The flow blockage and turning by the horizontal and vertical stabilizers is large enough for empennage removal to significantly increase the flow expansion rate over the aftbody, which causes higher aftbody pressures and lower aftbody drag at subsonic speeds and causes lower pressures and higher drag at supersonic speeds. The changes in total drag with span reduction are essentially the same as the aftbody drag changes at subsonic speeds. At supersonic speeds, the change in nozzle and aftbody drags tend to cancel one another; consequently, total drag changes with span reduction are small.

3.2.4.3 Empennage Deflection Effects

The effects of rudder deflection and horizontal stabilizer deflection on total drag were investigated at subsonic speeds for the NLB/CD and NLB/UP configurations. Rudder deflections were tested with the horizontal stabilizer deflected -2.0 degrees, and horizontal stabilizer deflections were tested with the rudder undeflected.

The rudder deflection studies were conducted by deflecting the portion of the vertical stabilizer aft of the 70 percent chord line at angles of 0, 4, and 11 degrees (positive deflection right, looking upstream). The effect of rudder deflection was investigated for both the full (V1F) and partial (V1P) span forward single vertical stabilizers. Rudder deflections of 0 and 4

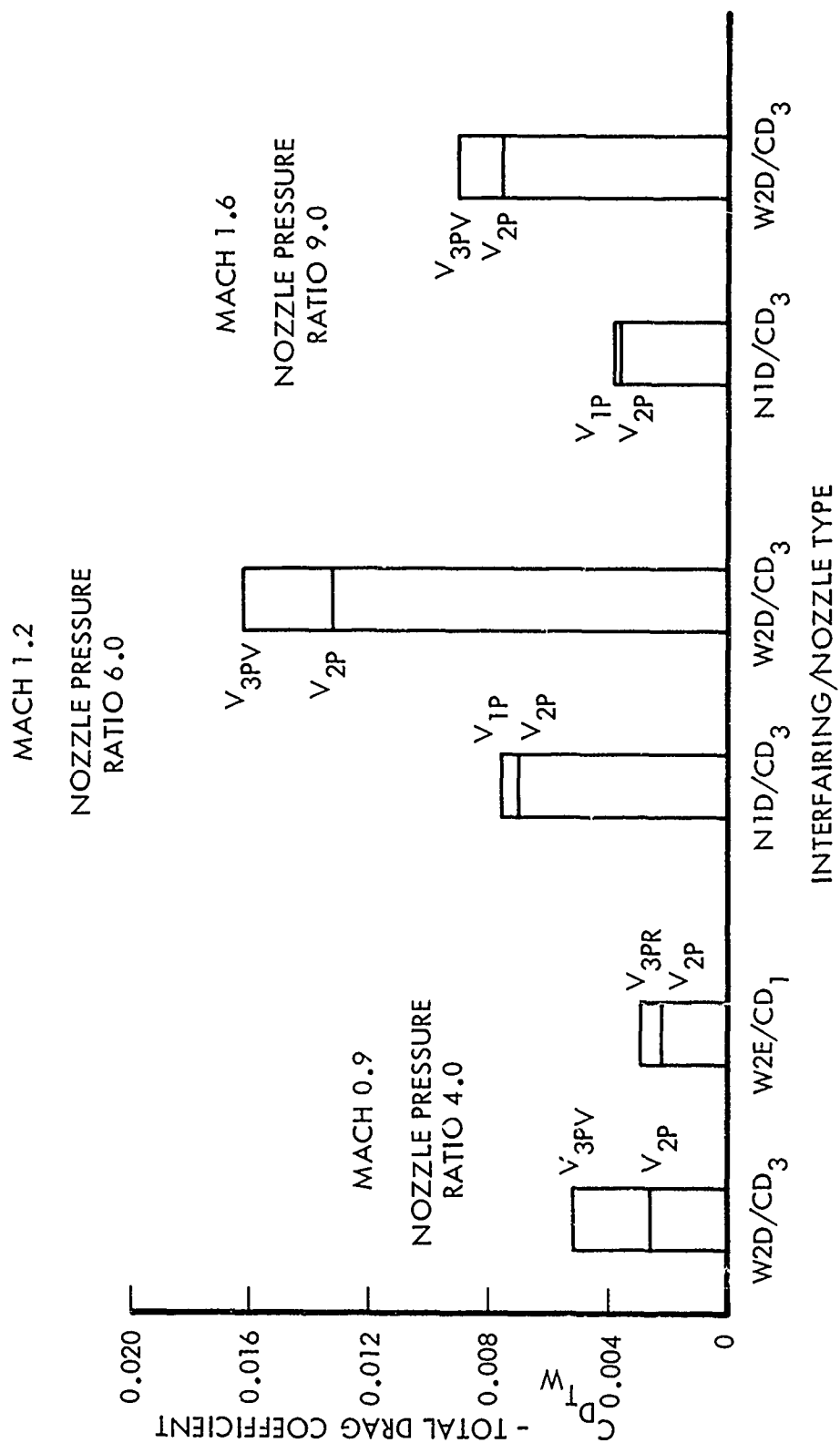


Figure 90. Effect of Vertical Stabilizer Type and Position on Total Drag

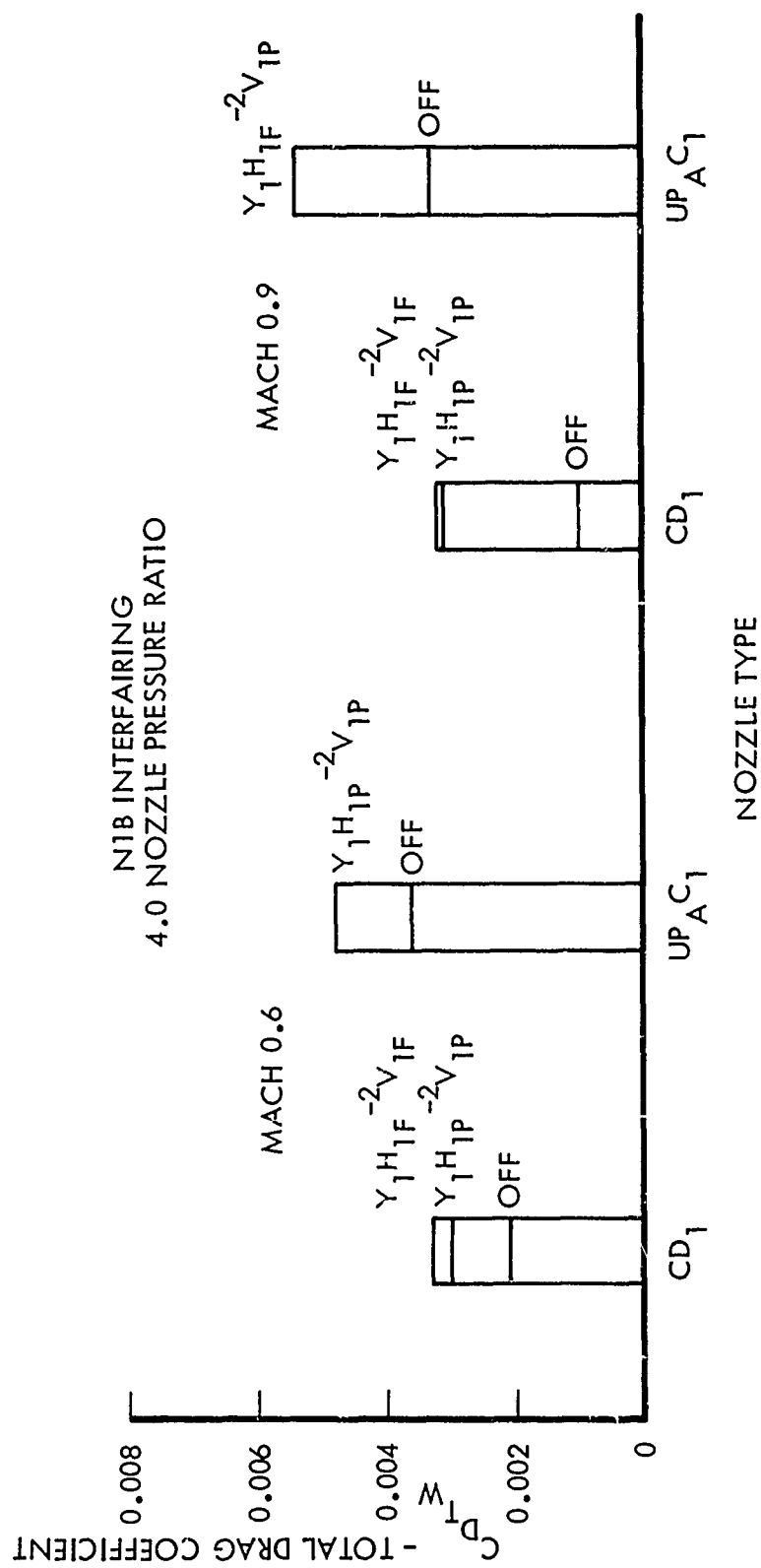


Figure 91. Effect of Empennage Span Reduction on Total Drag - Normal Power Nozzles

N1B INTERFAIRING

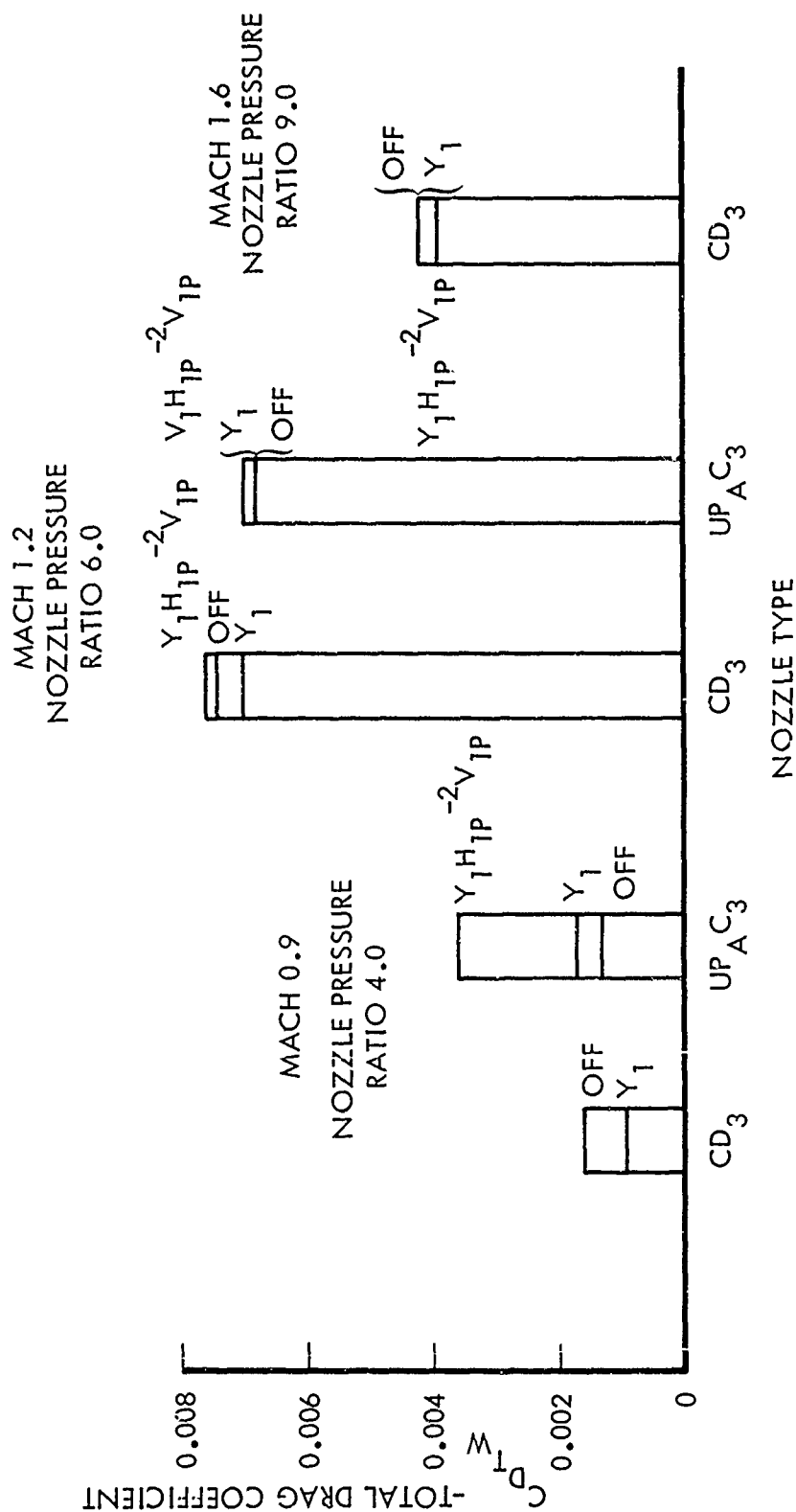


Figure 92. Effect of Empennage Span Reduction on Total Drag - Maximum A/B Nozzles

degrees were tested with the normal power unshrouded plug and convergent-divergent nozzles, and deflections of 0 and 11 degrees with the maximum A/B plug nozzle, all at Mach numbers of 0.6 and 0.9.

The total drag comparisons shown in Figure 93 are influenced primarily by the nozzle boattail drag differences with rudder deflection. The total drag decrease for rudder deflection with the CD1 nozzle installed is caused by the drag reduction on the right-hand nozzle, which contains the boattail balance. The UPAC1 has the balance in the left nozzle, and shows an increase in total drag, which is consistent with the nozzle boattail drag shift. These effects, total drag increasing on the left side and decreasing on the right side, should indicate that total drag change with rudder deflection should nearly disappear if force measurements on both aftbodies and both nozzles were added. However, this conclusion cannot be substantiated since no nozzles were tested with active force balances on both sides of the model.

The horizontal stabilizer deflection studies were conducted by testing with the entire stabilizer at angles of -0.4 and -2 degrees (negative angles are with trailing edge up) with the CD1 nozzle and at angles of -2 and -5 degrees with the UPAC3 nozzle.

The total drags, shown in Figure 94, change only slightly with horizontal stabilizer deflection. The variation in drag which does occur is confined to the portion of the nozzle aft of the horizontal stabilizer and the fuselage fairing. The change in stabilizer deflection from -0.4 to -2 degrees increases drag for the CD1 nozzle but the change from -2 to -5 degrees causes almost no drag change for the UPAC3, which terminates upstream of the fuselage fairing.

3.2.5 Angle-of-Attack Effects

The effects of angle of attack on the Phase II model total drag, thrust, thrust-minus-total-drag, and boundary layer displacement thickness are presented in this section. The drag and thrust-minus-drag results are based on the forces acting parallel to the nozzle centerline which is canted one degree nose down from the aircraft centerline. All configurations examined had a high short interfairing with either the unshrouded plug or convergent-divergent nozzles installed.

3.2.5.1 Total Drag

At Mach 0.6 the total drag decreases slightly with increasing angle of attack, and at Mach 0.9 the total drag is a minimum at the intermediate value of six degrees angle of attack. At supersonic speeds, the total drag increases with increasing angle of attack.

The slight decrease in total drag with increasing angle of attack is shown in Figure 95. The interfairing pressure distributions do not indicate a drag trend since the reduced pressures at high angle of attack on the top of the interfairing are cancelled by the increased pressures on the bottom. The same

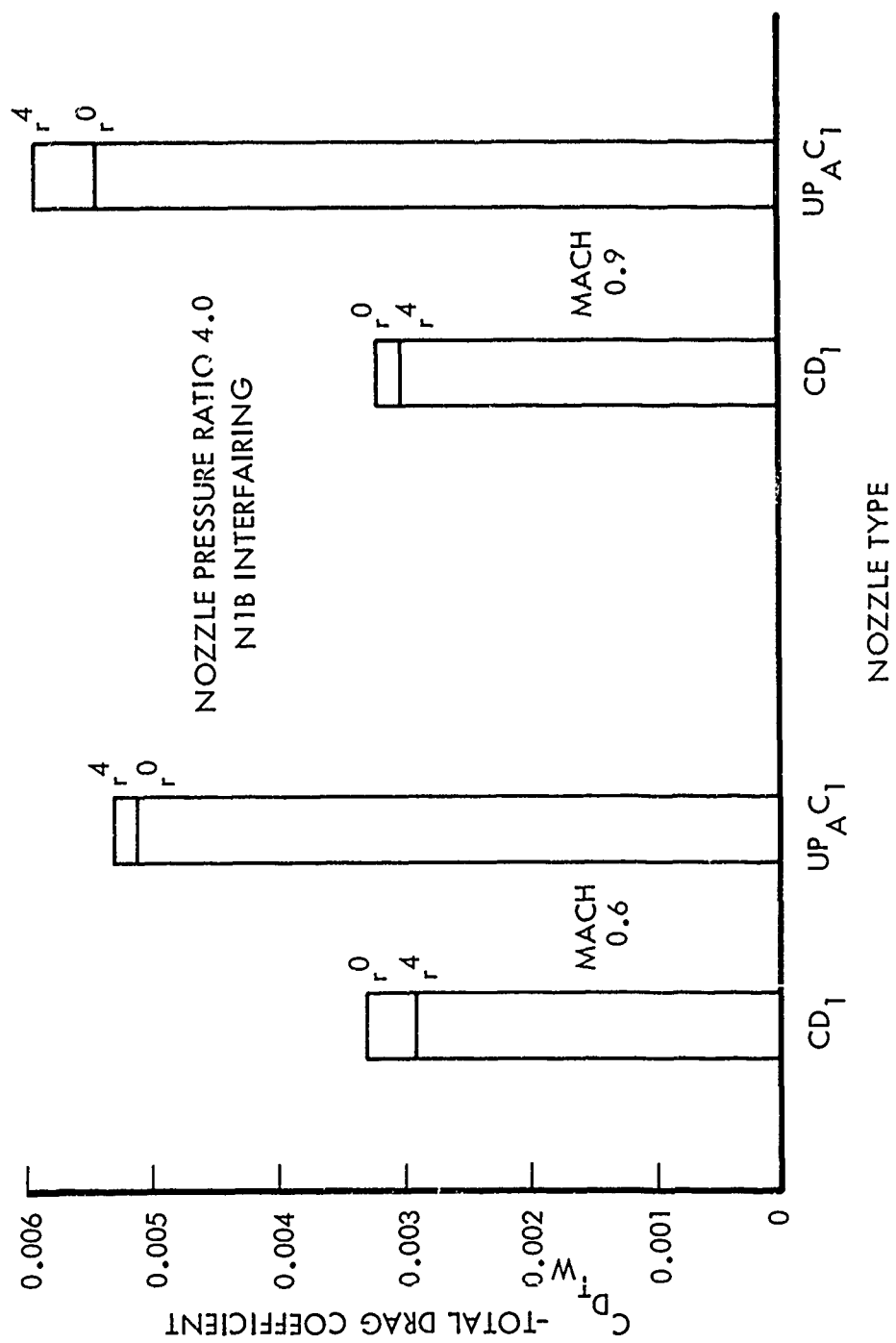


Figure 93. Effect of Rudder Deflection on Total Drag

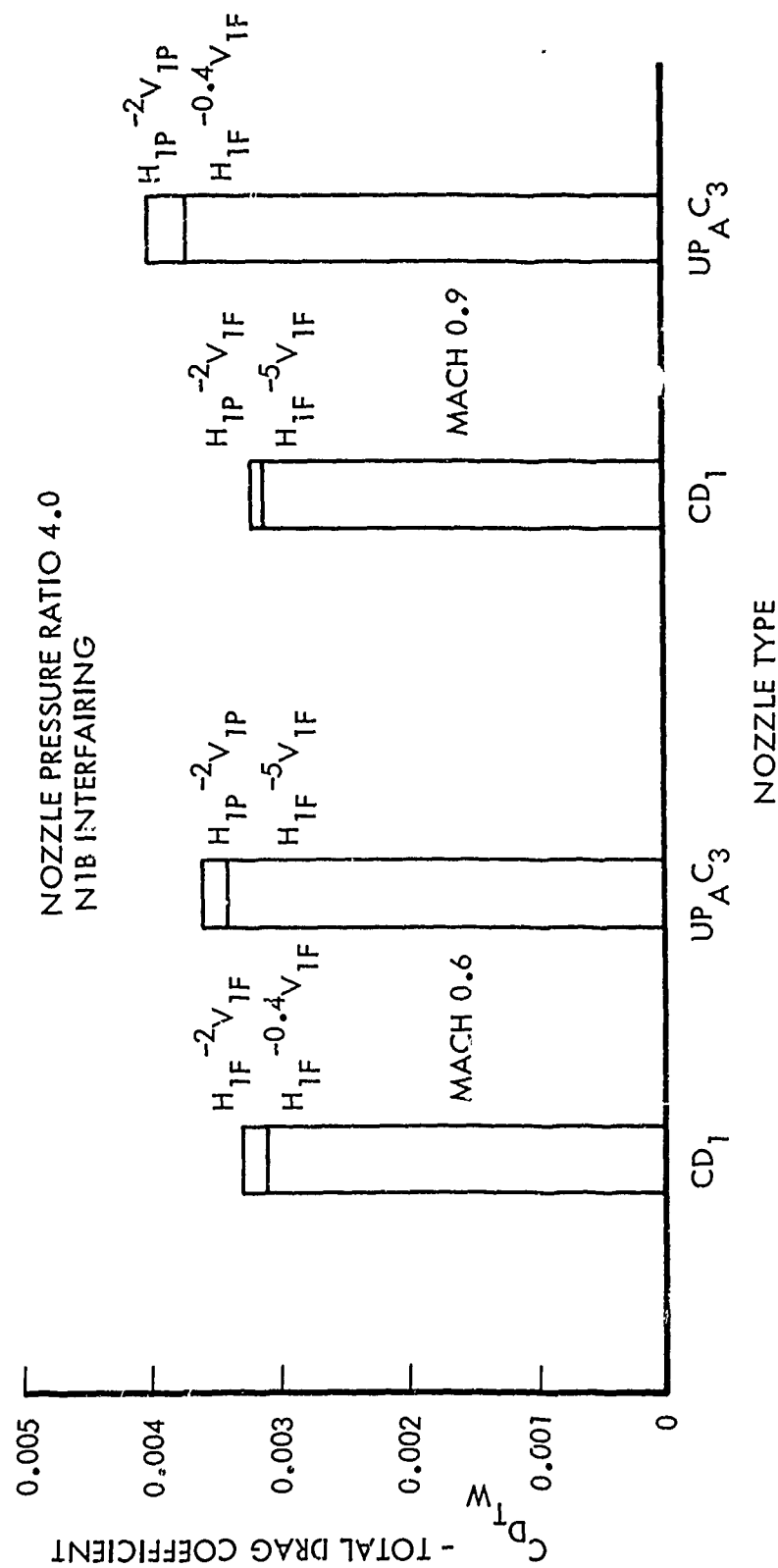


Figure 94. Effect of Horizontal Stabilizer Deflection on Total Drag

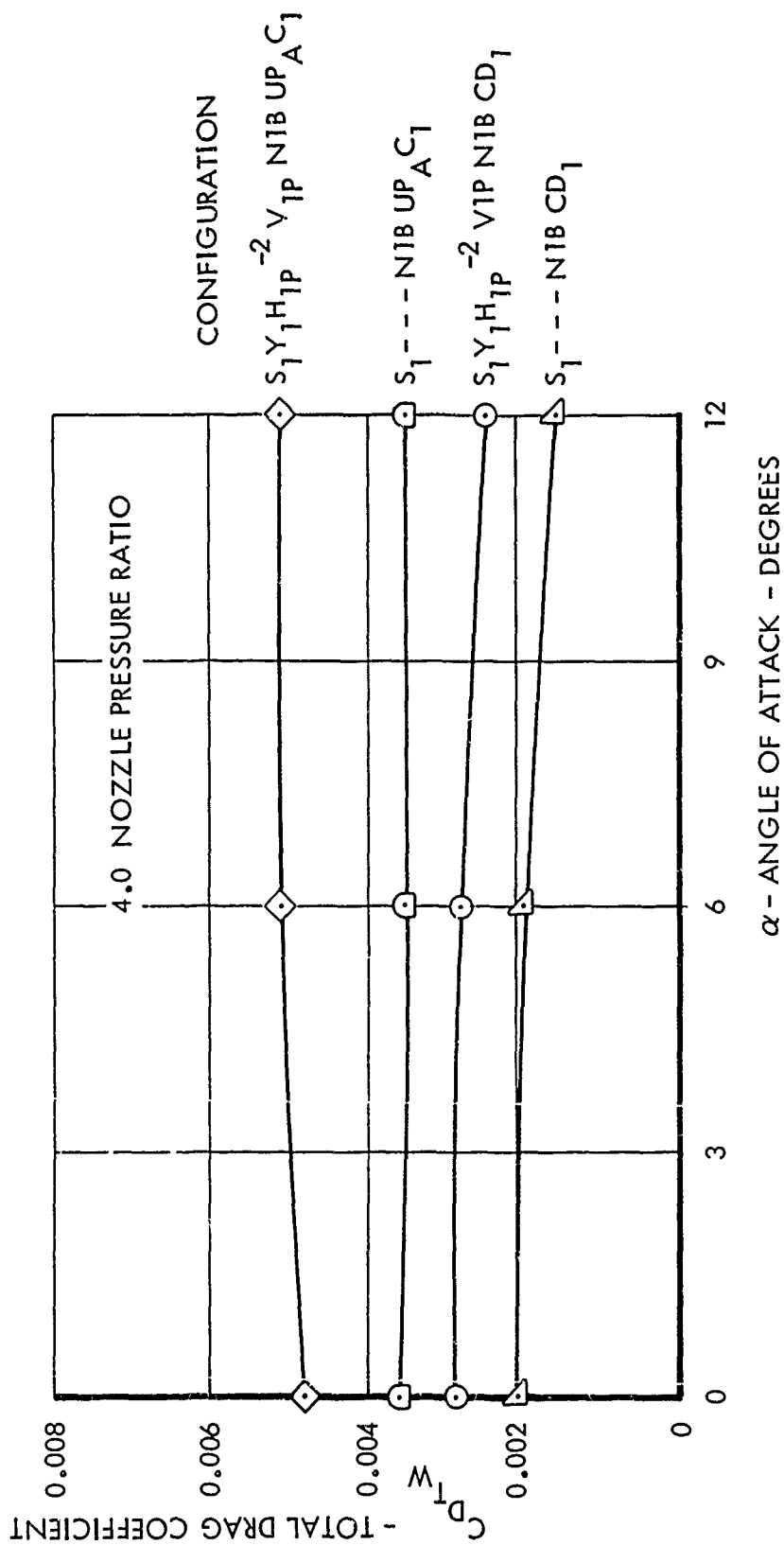


Figure 95. Effect of Angle of Attack on Total Drag - Normal Power Nozzles - Mach 0.6

pressure trends are observed along the fuselage aftbody and nozzle except near the end of the nozzle where the pressure is increased at high angle of attack on both the windward (bottom) and leeward (top) sides. Also, there is no significant difference between pressure levels on the windward and leeward sides near the end of the nozzle boattail; this indicates that the exhaust flow interaction with the external flow is a dominant factor in the pressurization of the nozzle boattail near the nozzle exit. The increased pressures in this region cause the slight drop in drag observed with increasing angle of attack.

The total drag coefficients at Mach 0.9 are shown in Figure 96 for normal power nozzles. Similar drag trends occur for the maximum A/B nozzle configurations. As the angle of attack increases from zero to 6 degrees, both the aftbody and nozzle boattail drags are reduced. As the angle of attack increases from 6 to 12 degrees, the aftbody boattail drag increases and the nozzle boattail drag decreases. The net result is an increased total drag. Pressure distributions along the NLB interfairing and aftbody and along the fuselage and nozzle for the CD1 nozzle installation indicate that the boattail drag reduction with increasing angle of attack is due to pressurization of the nozzle boattail near the nozzle exit. Increasing the angle of attack from 6 to 12 degrees considerably reduces the pressures on the upper side of the aftbody. A large supercritical flow region over the top of the wing and aftbody is responsible for the reduced pressures at 12 degrees angle of attack. These reduced pressures have a greater effect on the total drag than the slight pressure rise on the windward side of the aftbody and the pressurization of the nozzle boattail and thus cause the drag increase.

The increase in total drag with increasing angle of attack at supersonic speeds is illustrated in Figure 97 for Mach 1.2. Analysis of the aftbody and nozzle boattail drag data indicates that the total drag increase is due entirely to an increase in aftbody drag. Pressure distributions along the NLB interfairing and along the fuselage aftbody and nozzle for the CD3 nozzle installation show that as the angle of attack increases, the reduced pressures on the leeward side of the aftbody more than compensate for the increased pressures on the windward side of the aftbody and produce the drag increase.

3.2.5.2 Internal Thrust Results

Analysis of nozzle internal pressure distributions indicates that the thrust coefficients are not influenced by angle of attack. Identical internal pressure distributions were obtained at all angles of attack except for UPAC1 nozzle. For this nozzle, the plug surface pressure distributions were influenced only slightly by angle of attack. Pressure-area integrated plug forces indicate that the thrust coefficients should increase by only 0.2 percent as the angle of attack increases from zero to 6 degrees.

3.2.5.3 Thrust-Minus-Drag Results

Since angle of attack has no effect on nozzle thrust, the thrust-minus-drag changes simply reflect the total drag changes discussed in Subsection 3.2.5.1.

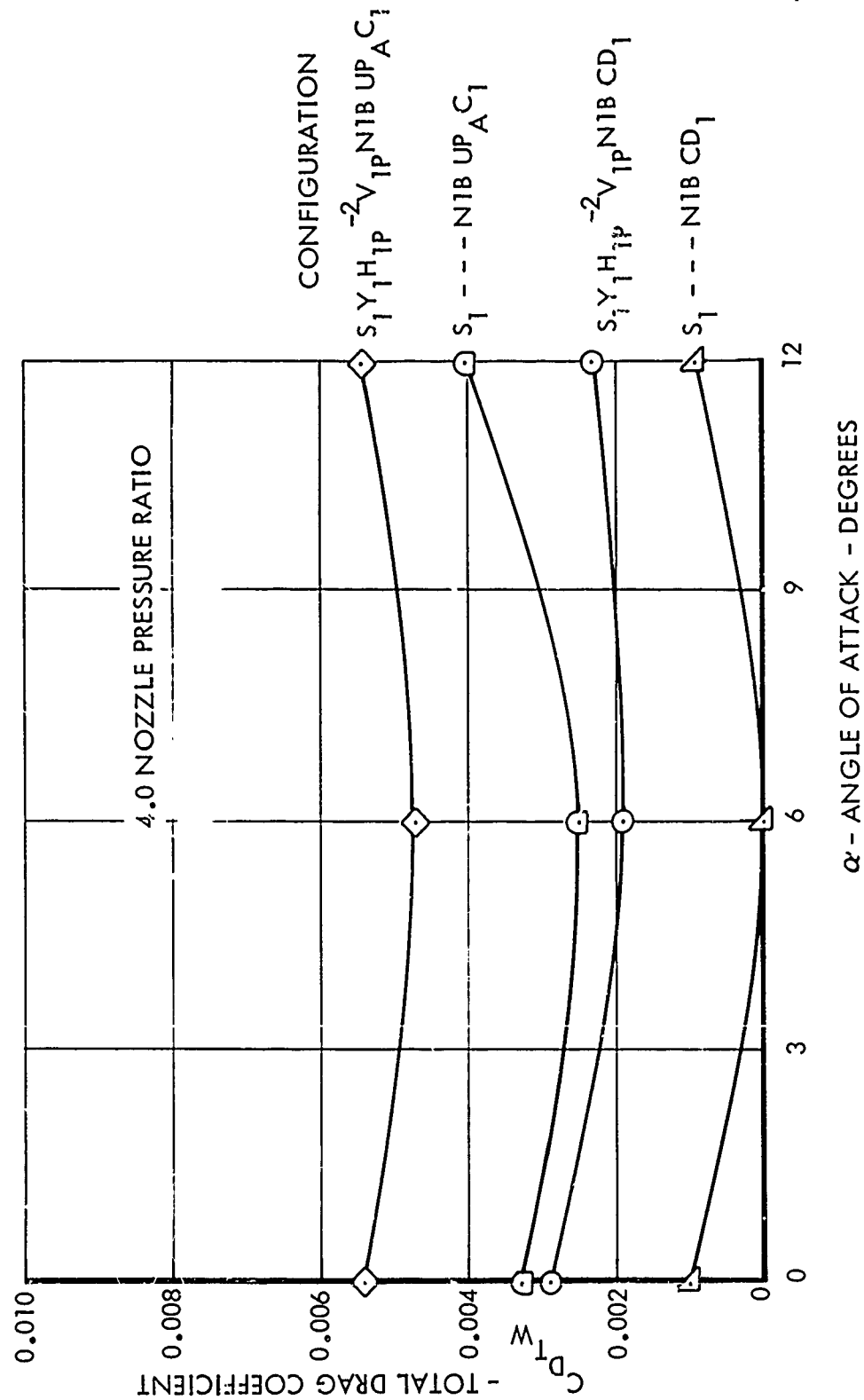


Figure 96. Effect of Angle of Attack on Total Drag - Normal Power Nozzles - Mach 0.9

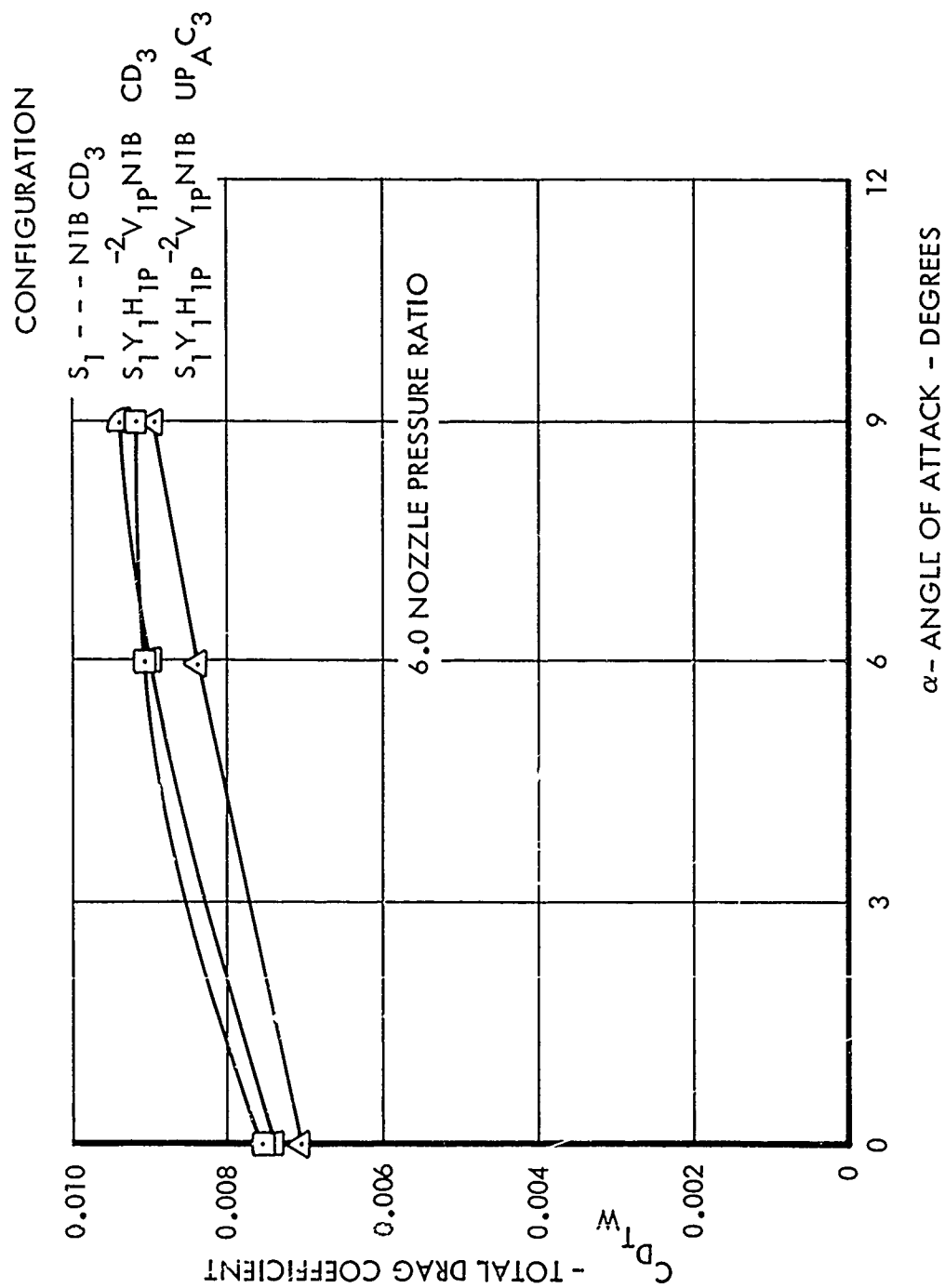


Figure 97. Effect of Angle of Attack on Total Drag - Maximum A/B Nozzles - Mach 1.2

Figures 98 and 99 show the thrust-minus-total drag results for normal power configurations at Mach 0.9 and for maximum A/B nozzles at Mach 1.2. The maximum thrust minus drag at 6 degrees angle of attack for the normal power nozzles is the result of the minimum in total drag at that condition. The maximum A/B nozzle thrust minus drag decreases with increasing angle of attack since the total drag increases and the thrust remains constant. The trends shown in Figure 99 are representative of the trends obtained for higher supersonic Mach numbers.

3.2.5.4 External Boundary Layer Properties

No consistent trend is evident for subsonic speeds in the effect of angle of attack on the boundary layer displacement thickness at the aftbody metric break station. At supersonic speeds, the boundary layer displacement thickness on the upper (rake 1.) and lower (rake 6) sides of the interfairing is reduced as the angle of attack is increased. The decrease in displacement thickness tends to reduce pressures along the interfairing at supersonic speeds since the slope of the displaced flow field streamline more nearly duplicates the surface slope and, therefore, results in greater flow turning. The momentum thickness variation with angle of attack is similar to the displacement thickness variation.

3.2.6 Reynolds Number and Boundary Layer Trip Studies

The nozzle boattail drag coefficient, in general, decreases at subsonic speeds and increases at supersonic speeds with increasing Reynolds number. The aftbody boattail and total drag coefficients increase at a decreasing rate with increasing Reynolds number for both speed regimes. The external static pressure distributions substantiate the Reynolds number effect on external drag. The effect of boundary layer trips on drag for the basic test Reynolds numbers at Mach numbers of 0.9 and 2.0 is small. Boundary layer displacement and momentum thicknesses at the metric break station decrease with increasing Reynolds number.

3.2.6.1 Reynolds Number Effects

The effects of Reynolds number on total drag coefficients at three nozzle pressure ratios are shown for subsonic speeds for selected configurations in Figures 100 through 102. For the convergent and convergent-divergent nozzles, the total drag coefficient increases with increasing Reynolds number. At supersonic speeds, the total drag coefficients also increase with increasing Reynolds number, as shown in Figure 103.

Typical external static pressure distributions at the highest Reynolds numbers are higher on the nozzle boattail and lower on the aftbody boattail than those at the lowest Reynolds number. The pressure coefficients and pressure gradients on the convergent and convergent-divergent nozzle boattail surfaces are higher than on the plug nozzle boattail surfaces, and this effect is more pronounced at the higher nozzle pressure ratios. These higher pressure gradients are a result of more interaction from the jet plume for the convergent and

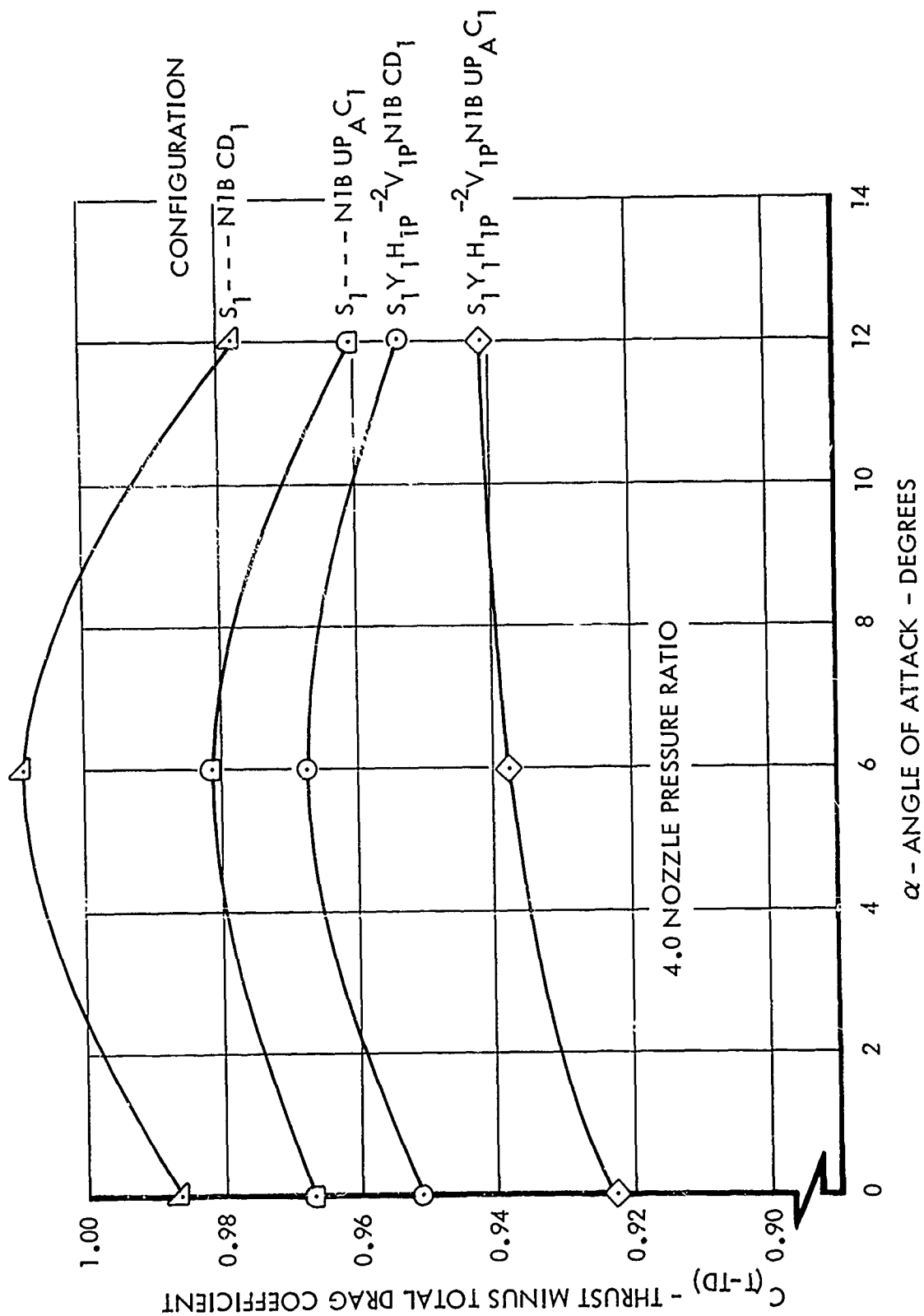


Figure 98. Effect of Angle of Attack on Thrust-Minus-Total-Drag - Normal Power Nozzles - Mach 0.9

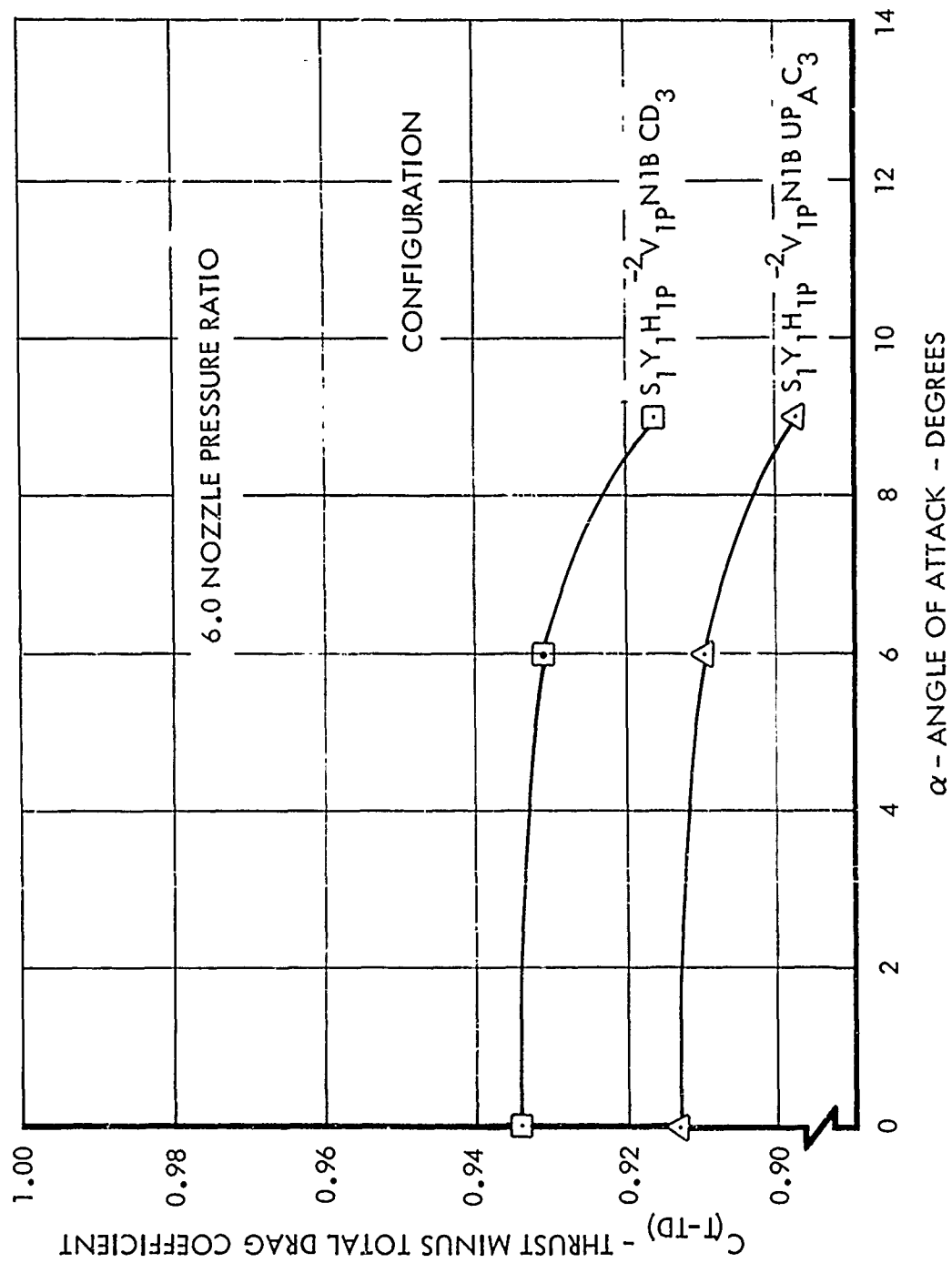


Figure 99. Effect of Angle of Attack on Thrust-Minus-Total-Drag - CDL Nozzle - Mach 0.9

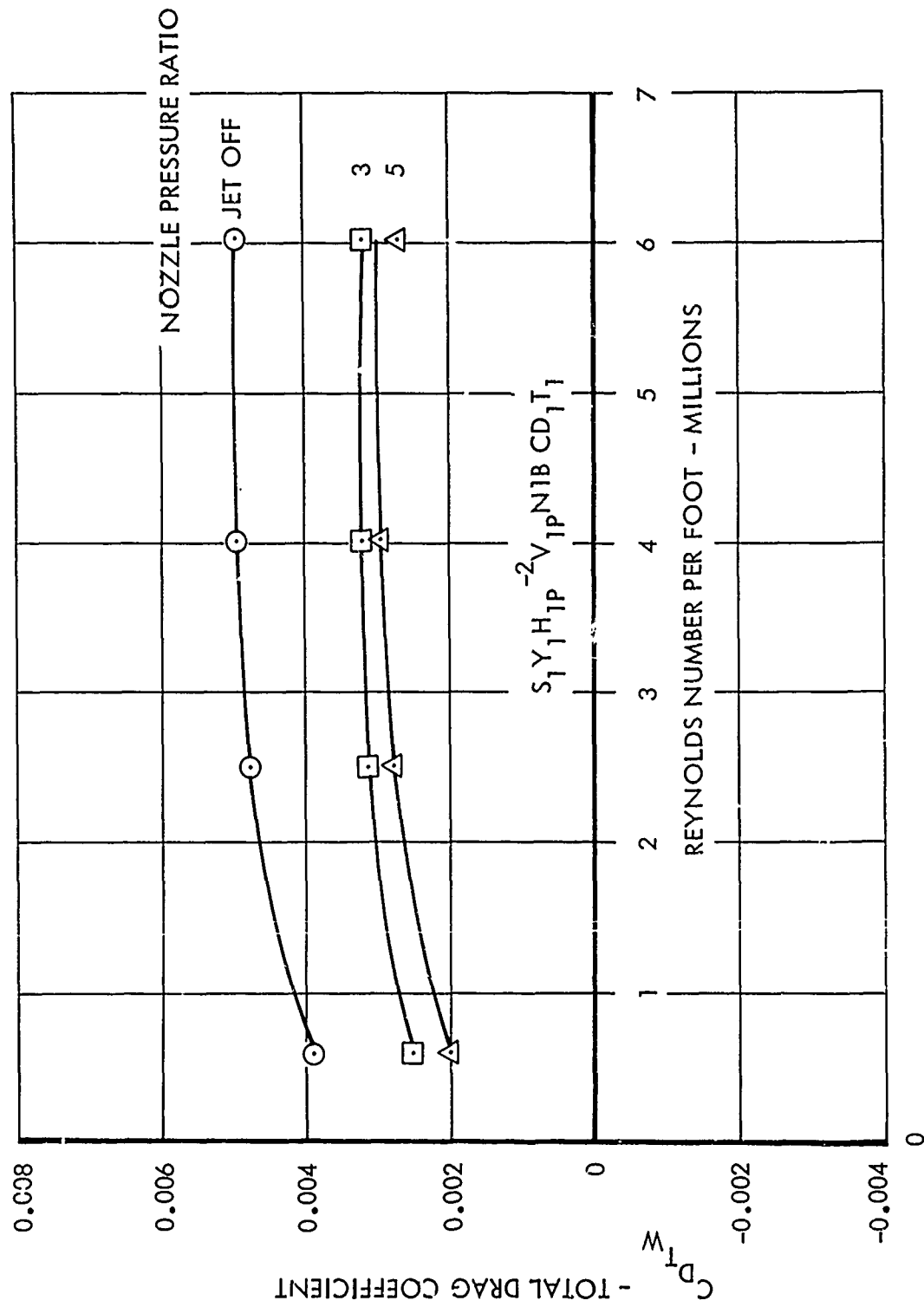


Figure 100. Effect of Reynolds Number on Total Drag - CDL Nozzles - Mach 0.9

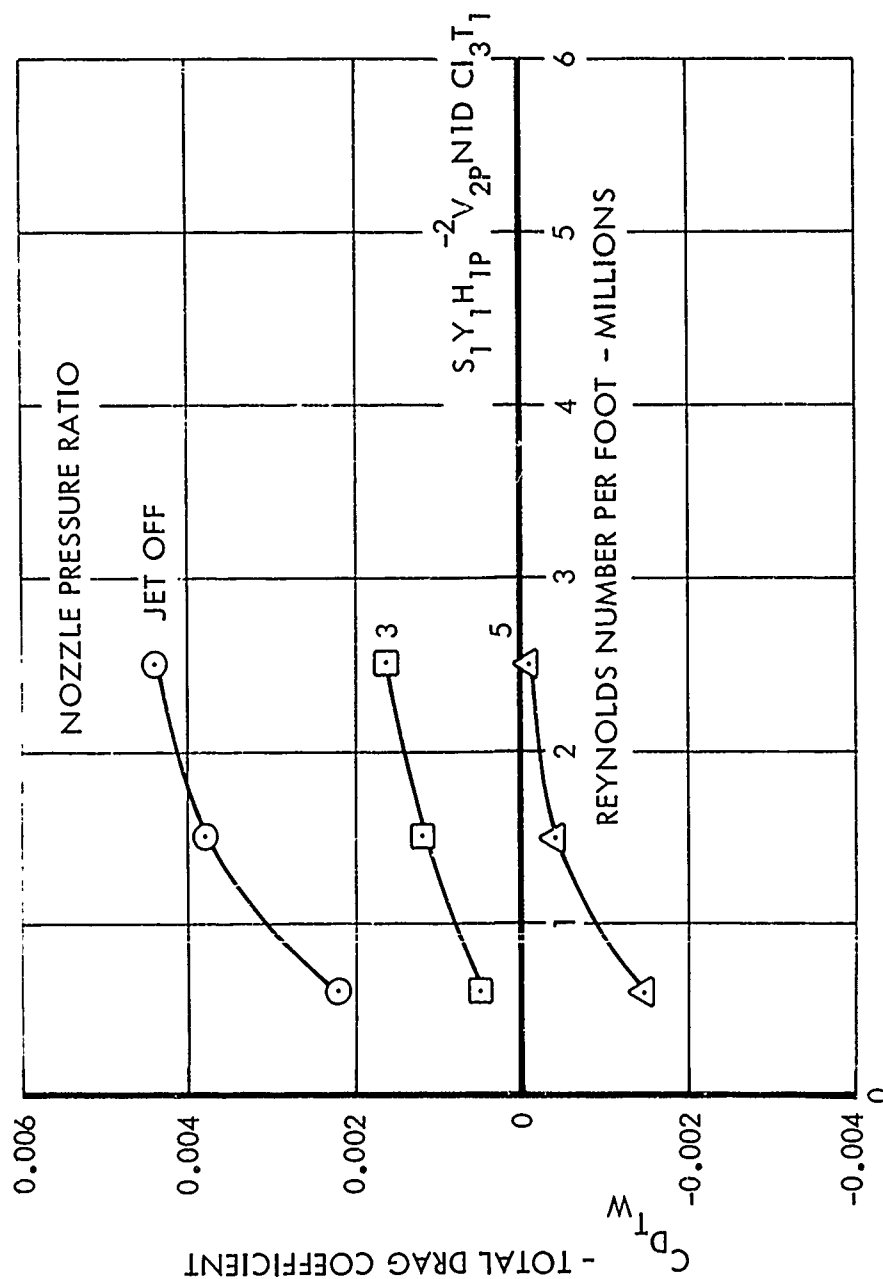


Figure 101. Effect of Reynolds Number on Total Drag - CI3 Nozzles - Mach 0.9

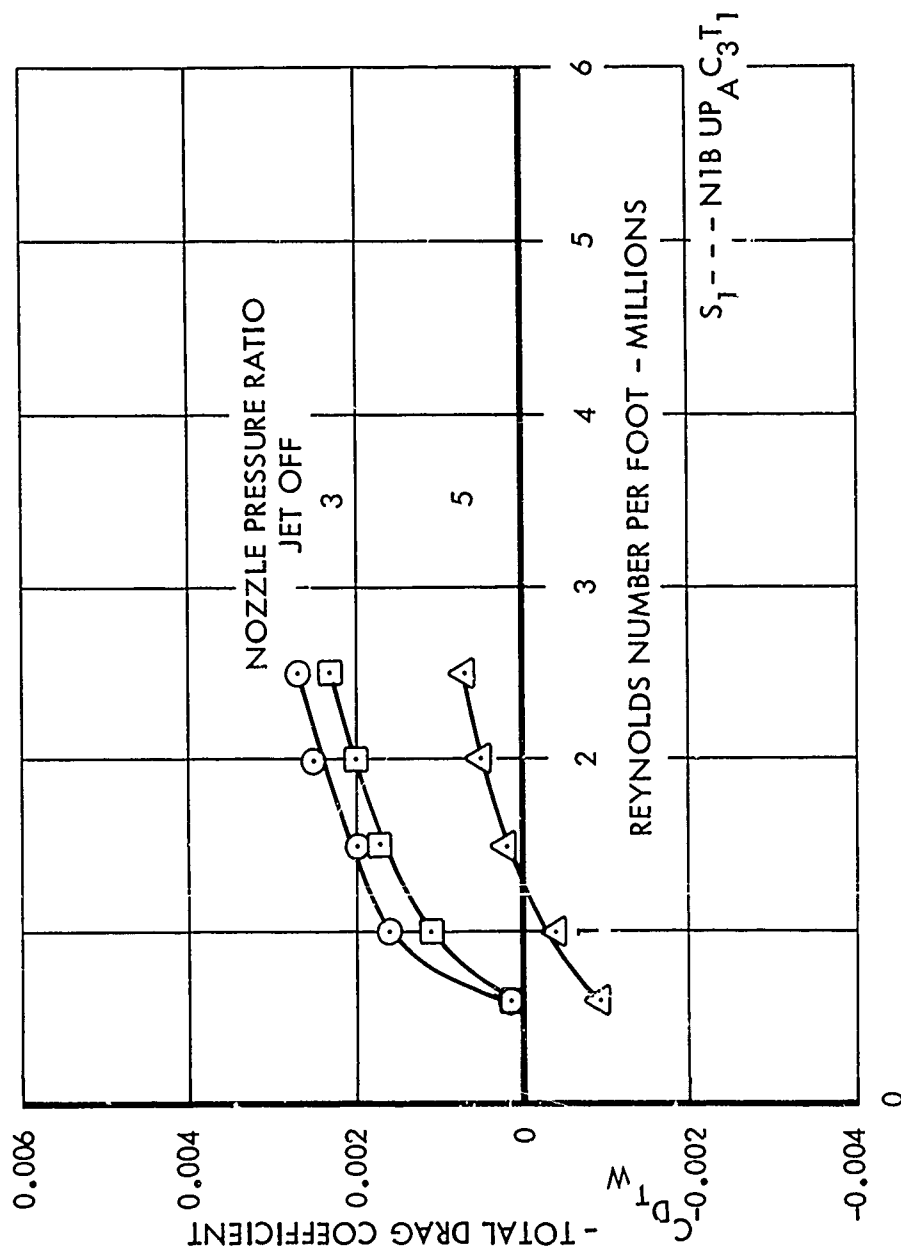


Figure 102. Effect of Reynolds Number on Total Drag - UPAC3 Nozzle - Mach 0.9

NOZZLE PRESSURE RATIO 12

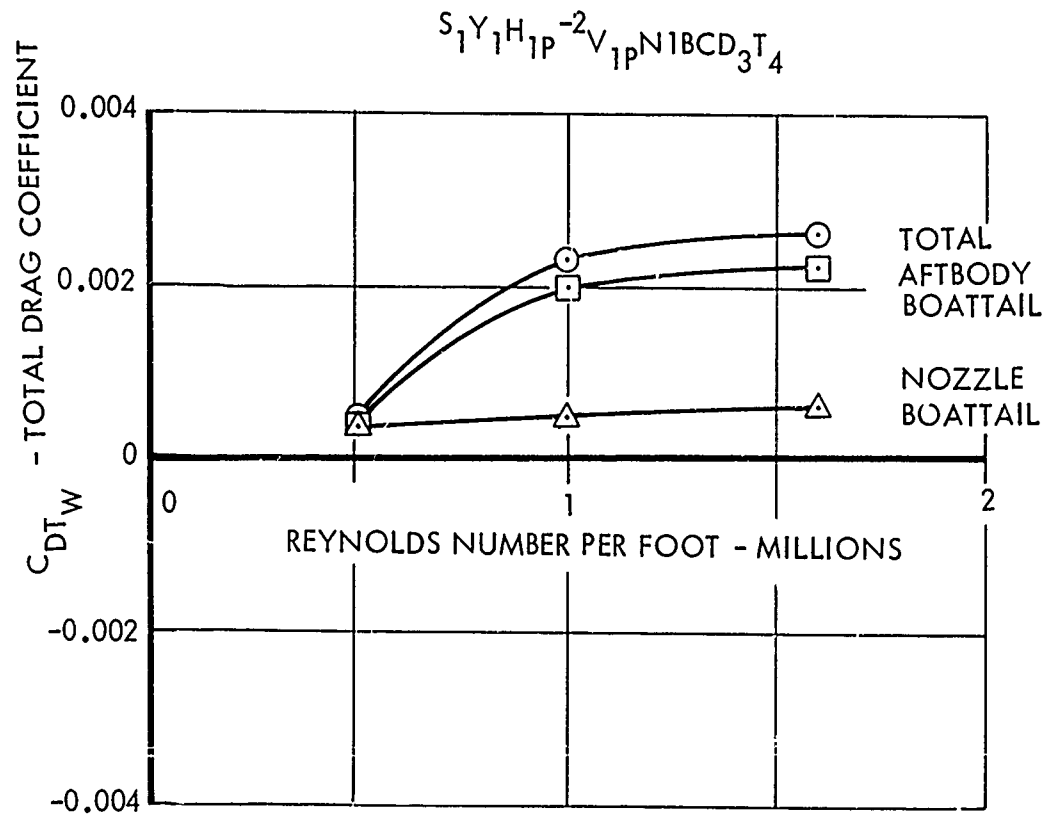


Figure 103. Effect of Reynolds Number on Integrated-Pressure Drags - CD3 Nozzle - Mach 2.0

convergent-divergent nozzles than for the plug nozzles. Larger viscous, or Reynolds number dependent, effects would, therefore, be expected for the convergent and convergent-divergent nozzles than for the plug nozzles. These static pressure trends are consistent with the drag trends obtained from the force-balance data.

The boundary layer displacement and momentum thicknesses decrease with increasing Reynolds number. The boundary layers are thinner on the outboard side of the model (rakes 3 and 4) since the boundary layers in these regions develop from the inlet fairing rather than from the fuselage nose. Also, this effect is more pronounced for the wide as compared to the narrow-spaced configurations.

3.2.6.2 Boundary Layer Trip Effects

The effects of boundary layer trips on the external drag coefficients for the basic test Reynolds numbers per foot of 2.5 million and 1.0 million at Mach 0.9 and 2.0, respectively, are small. However, there is an effect of trips on the drag coefficients at Reynolds number per foot of 0.5 million at both of these Mach numbers. The trip configurations tested are: (1) no trips; (2) fuselage nose trips; and (3) fuselage nose, inlet fairing, wing, and empennage trips. Figure 104 shows that the effects of the second and third trip configurations on the total drag coefficients at Mach 0.9 are small for all Reynolds numbers. The total drag coefficients for the no trip configuration are not shown because of excessive aftbody balance zero shifts. External static pressure distributions on the aftbody and nozzle boattails for the three different trip configurations indicate that the pressure coefficients are higher for the no trip configuration than the other trip configurations at a Reynolds number per foot of 0.5 million. The higher pressure coefficients on the nozzle boattail surface for the no trip configuration are apparently due to more recompression resulting from a thinner boundary layer. The thinner boundary layer would be expected for the no trip configuration because of delayed transition on the model.

At Mach 2.0, the effects of trips on integrated-pressure total drag are small at Reynolds numbers per foot of 1.0 million and 1.6 million, as illustrated in Figure 105. However, at Reynolds number per foot of 0.5 million, the drag coefficient for the third trip configuration is 35 drag counts lower than the drag coefficient for the second trip configuration. The lower static pressures at a Reynolds number per foot of 0.5 million are apparently due to additional supersonic expansion over the aftbody surface resulting from a thinner boundary layer on this surface. The thinner boundary layer would again be expected for the configuration with only the nose trips because of delayed transition on portions of the model. The configuration with the trips removed was not tested at Mach 2.0.

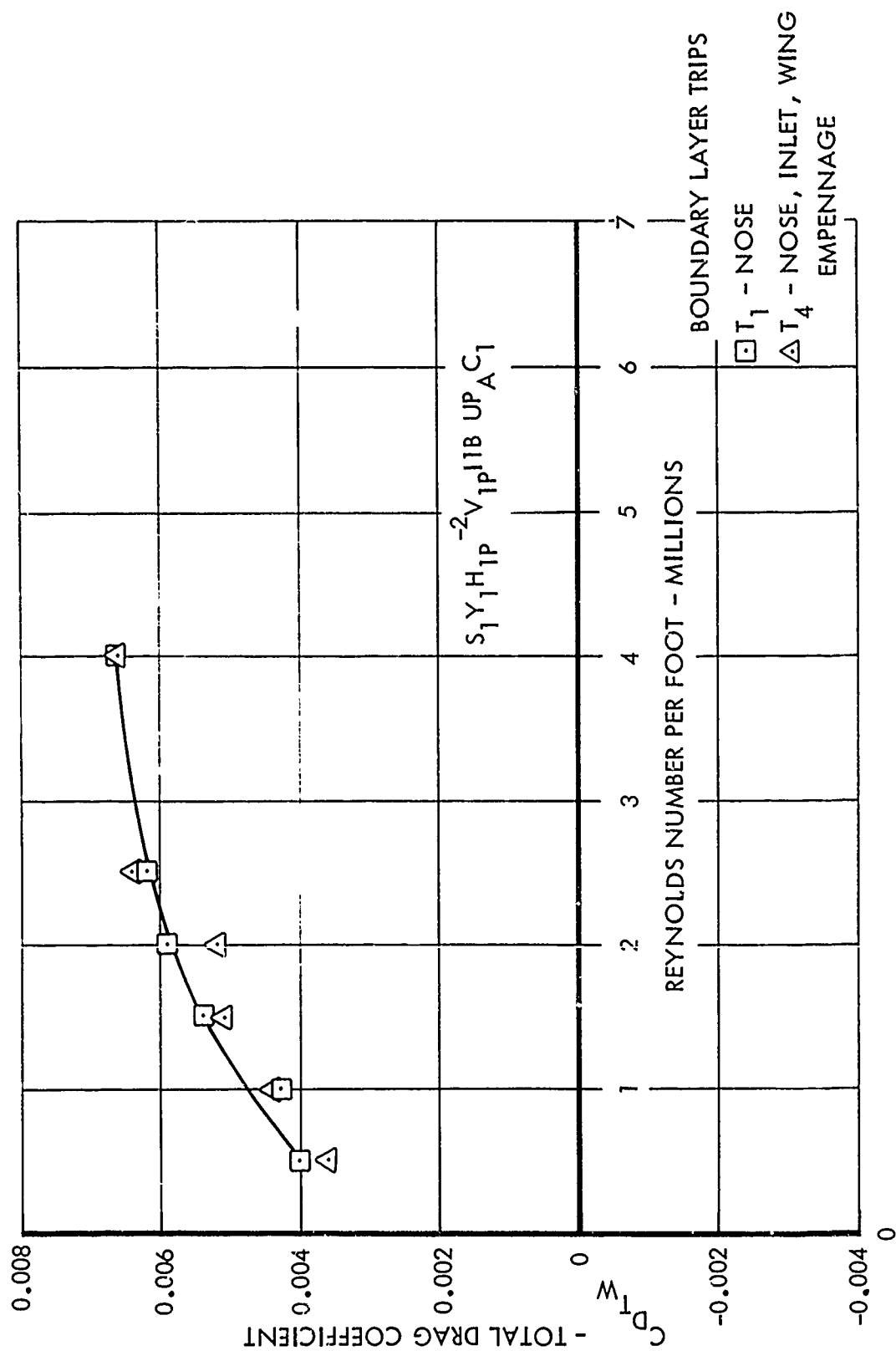


Figure 104. Effect of Boundary Layer Trips on Total Drag - UPAC1 Nozzle - Mach 0.9

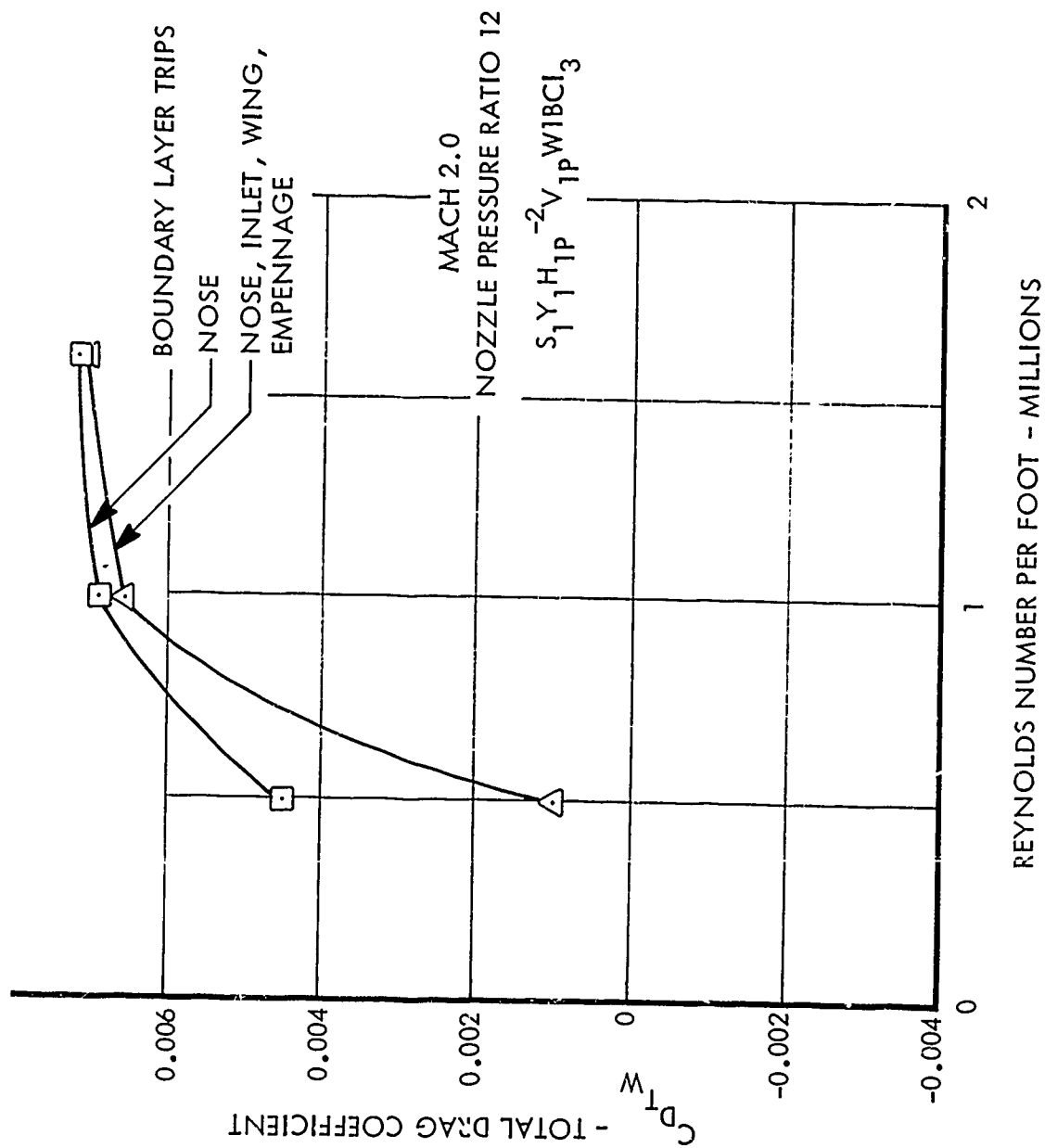


Figure 105. Effect of Boundary Layer Trips on Integrated Pressure Drags - CI3 Nozzle

3.3 PERFORMANCE PREDICTION METHODS

This subsection presents an evaluation of analytical methods for predicting the thrust and aftbody and nozzle drags for twin-nozzle aircraft configurations. Also presented are empirical correlations of the Phase II twin-nozzle test data. The analytical methods were evaluated, in general, by comparing the results directly with experimental data rather than first comparing them with the results of other more precise analytical methods, as was done in the evaluation of isolated aftbody/nozzle methods (Subsection 2.3). The latter evaluation technique is, of course, preferred since it is more effective in isolating the effects of the idealizations employed in the analyses. However, due to the paucity of accurate three-dimensional analytical results, this preferred approach is in most cases impossible. Since a direct comparison with experimental data usually involves a test of several idealizations concurrently, care must be exercised to differentiate between situations in which errors cancel one another and those in which real confirmation of the method is obtained.

A summary list of the analytical methods investigated is presented in Table 14. The recommended methods are marked with an asterisk. Of the analytical methods investigated, none are recommended for predicting aftbody drags. However, several methods for predicting aftbody pressure distribution trends are recommended. Isolated nozzle internal performance methods, in general, are applicable to twin-nozzle installations.

3.3.1 External Flow Methods

Analytical methods for computing external flow fields over twin-nozzle/aftbody surfaces are evaluated first, followed by a description of the empirical correlations of Phase II data. For subsonic external flow, three dimensional, equivalent body and sector analysis methods were investigated. For supersonic external flow, only equivalent body and sector analysis methods were investigated, since three-dimensional analysis techniques were not available.

The equivalent body analysis approach consists of representing the twin-jet model by one or more axisymmetric bodies whose total area distribution is identical to the area distribution of the twin-nozzle model. Aftbody/nozzle drag is then obtained by application of any of several axisymmetric analytical techniques. The sector analysis approach consists of first dividing the three-dimensional body into a number of sectors as shown in Figure 106. The boundaries of each sector are formed by passing cutting planes through the body parallel to the freestream direction. The orientation of the cutting planes for each sector are selected such that the surface contours bounded by the cutting planes can be approximately represented by a sector of an axisymmetric body whose center coincides with the intersection line of the cutting planes. As illustrated in the figure, the cutting plane intersection lines do not have to be coincident for each sector. The pressure distributions over the resultant axisymmetric bodies are then obtained by application of any of several axisymmetric analytical technique.

TABLE 14. SUMMARY LIST OF ANALYTICAL METHODS INVESTIGATED

APPLICATION	METHOD
Subsonic External Flow	Equivalent Body/Potential Flow Analysis * 3-D Potential Flow * P&WA 3-D Transonic Analysis Sector/Potential Flow Analysis * Correlation
Supersonic External Flow	Equivalent Body/MOC Wave Drag Analysis Sector Analysis/MOC * Correlation
Internal Flow	* AEDC-ETF Time Dependent Analysis * MOC Sector Analysis/MOC * Correlation
Annular Base	Korst Analysis * Correlation
Plug Nozzle Base	* Correlation

*Recommended methods

3.3.1.1 Subsonic External Flow

Equivalent Body Methods - For a single axisymmetric or equivalent body representation of the model, the drag force for subsonic speeds is computed by use of a combined potential flow/boundary layer computer program described in Reference 5. The potential flow analysis is based on the Neumann incompressible solution adjusted for compressibility by Gothert's similarity rule (Reference 15).

Application of the axisymmetric potential flow/boundary layer analysis to an equivalent axisymmetric body does not appear useful for predicting aft-end drag, as evidenced by the poor agreement between computed and measured results shown in Figure 107. The computed sum of pressure and friction drag is forty percent below the force balance measured total drag for the Berrier and Wood (Reference 73) A-1 twin-jet body for jet-off at Mach numbers ranging from 0.5 to 0.3. The Berrier and Wood A-1 twin-jet body is a strut supported model incorporating a horizontal wedge interfairing which terminates upstream of the nozzle exit plane. Except for area distribution, the A-1 model is similar to the CD1/I2B Phase II model configuration without the wing and empennage.

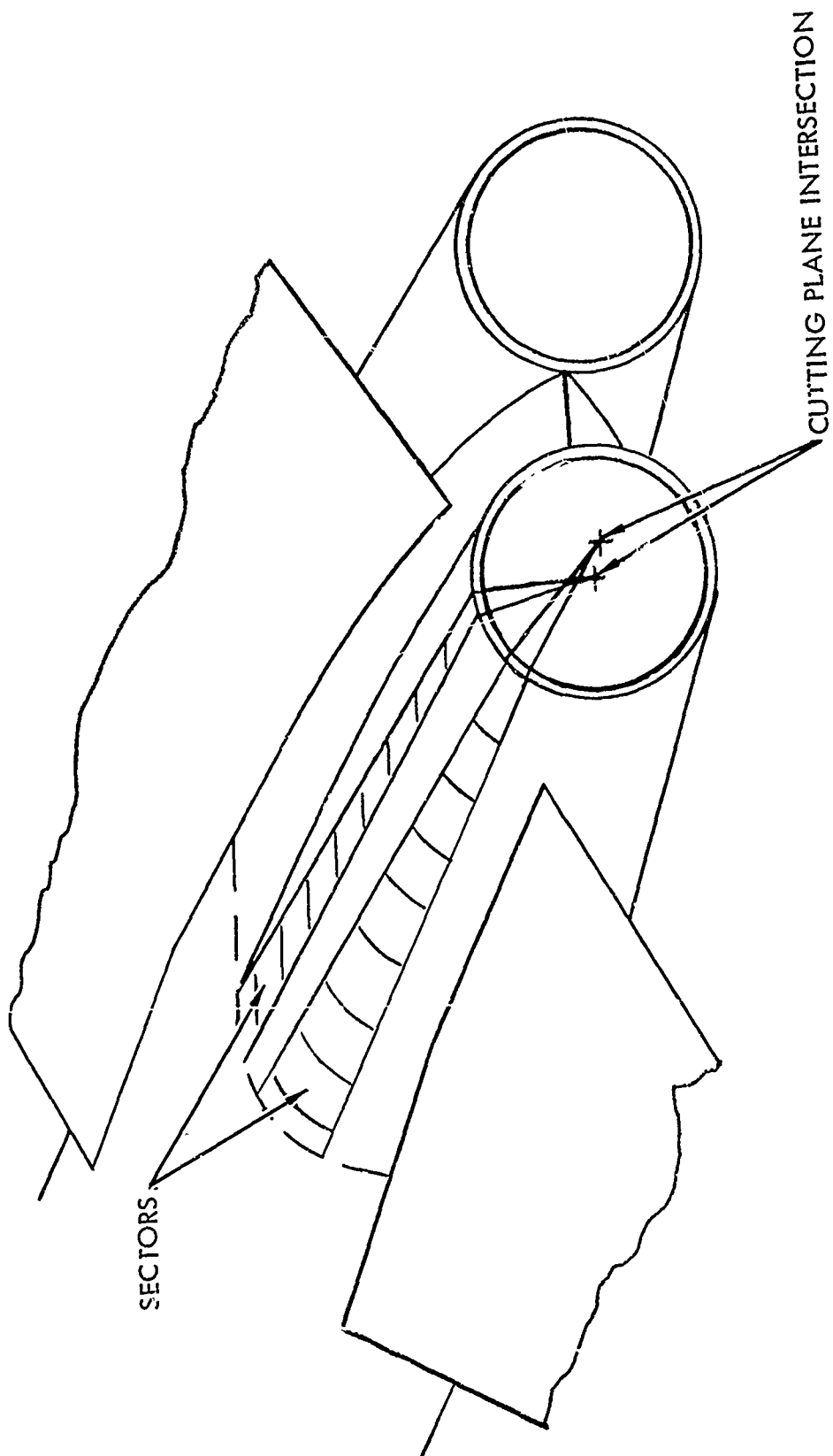


Figure 106. Sectoring Technique

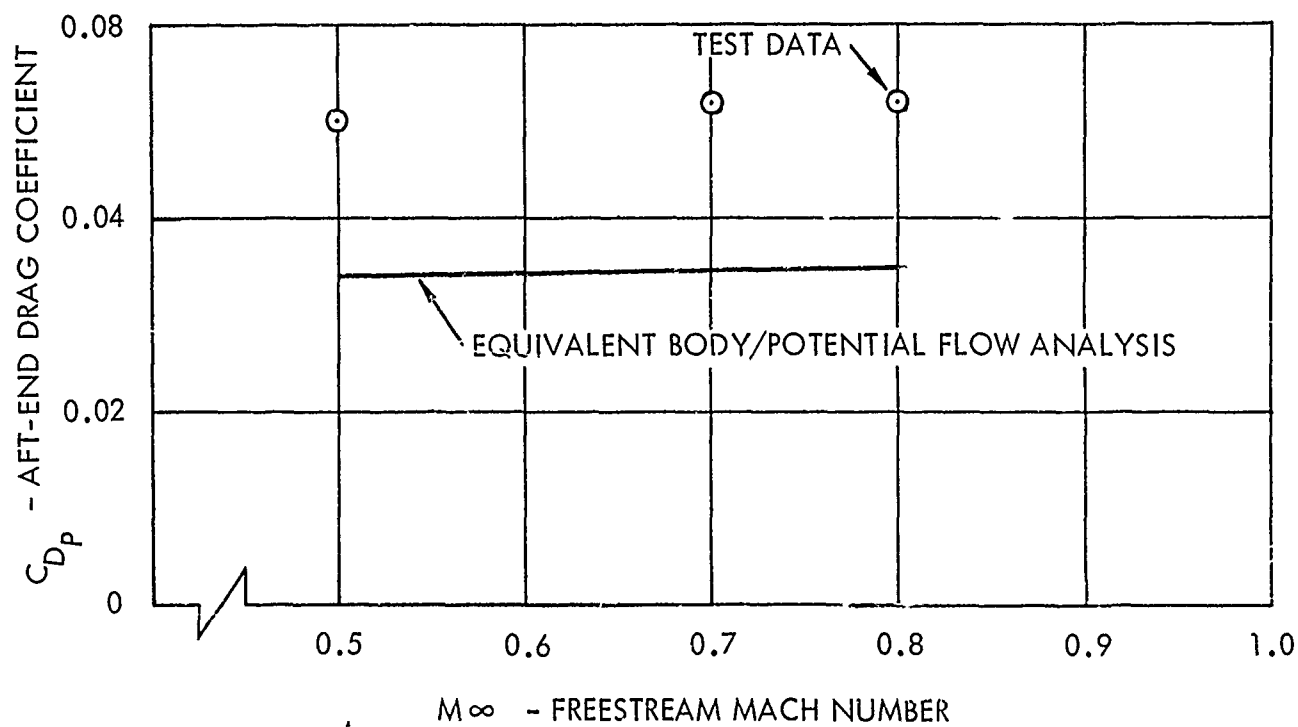


Figure 107. Comparison of Predicted and Measured Aft-End Drag - A-1 Twin-Jet Body - Subsonic External Flow

Friction drag calculated in the Reference 5 computer program for an axisymmetric body with a wetted area correction for the twin-jet body is essentially identical to the friction drag calculated in Reference 73 by the Frankl and Voishel method, and therefore should not be the source of differences between the test data and the analysis results. Strut interference effects could account for the higher drag indicated by the test data. However, poor agreement between computed and measured results were also obtained for the isolated nozzle models tested during Phase I for which strut interference effects are known to be small.

Three-Dimensional Methods - For the actual twin-jet body, a three-dimensional potential flow analysis method (Reference 74) and the P&WA transonic analysis method (Reference 75) were employed for predicting subsonic flow fields. The potential flow analysis is based on an incompressible solution which is corrected for compressibility by Gothert's similarity rule. The P&WA three-dimensional transonic analysis method consists of first computing the pressures over an axisymmetric body with the same area distribution as the original body by use of a modified form of Spreiter and Alksne's method of local linearization coupled with a Reshotko-Tucker boundary layer calculation. The pressures thus computed are then modified by a cross-flow pressure term which is the difference between the pressures on the axisymmetric and non-axisymmetric bodies. The cross-flow pressure corrections are calculated from incompressible analysis using three-dimensional and axisymmetric potential flow computer programs.

Inviscid aft-end pressure distributions, computed by use of the three-dimensional potential flow computer program and the P&WA three-dimensional transonic flow analysis method are compared in Figures 108 through 110 with Mach 0.8 experimental data obtained by Berrier and Wood (Reference 73) for the A-1 twin-jet body. Good agreement between the experimental data and results obtained with the P&WA three-dimensional transonic analysis method is evident. Computed pressures are compared with pressures measured along the instrumentation rows located on the top (row 1) and side (row 2) of the aft-end in Figures 108 and 109, respectively. In Figure 110, pressure distributions along the interfairing (row 5) and along the body (row 4) downstream of the interfairing trailing edge are presented. The P&WA three-dimensional analysis results are in better agreement with the experimental data than the three-dimensional potential flow results, and neither method is in agreement with data in the region downstream of the interfairing trailing edge. Considering the complex flow interactions which exist in this region, the disagreement is not unexpected. The computed results shown in the figures were obtained assuming a cylindrical exhaust jet.

Sector Analysis Method - The combined potential flow/boundary layer program (Reference 5) is employed in the sector analysis approach for subsonic speeds. Using this method to predict the pressure distributions on twin-jet bodies does not appear to be sufficiently accurate, as evidenced by poor agreement between computed and experimental data at Mach 0.8 for the Berrier and Wood A-1 body. In Figure 111, computed pressures are compared with

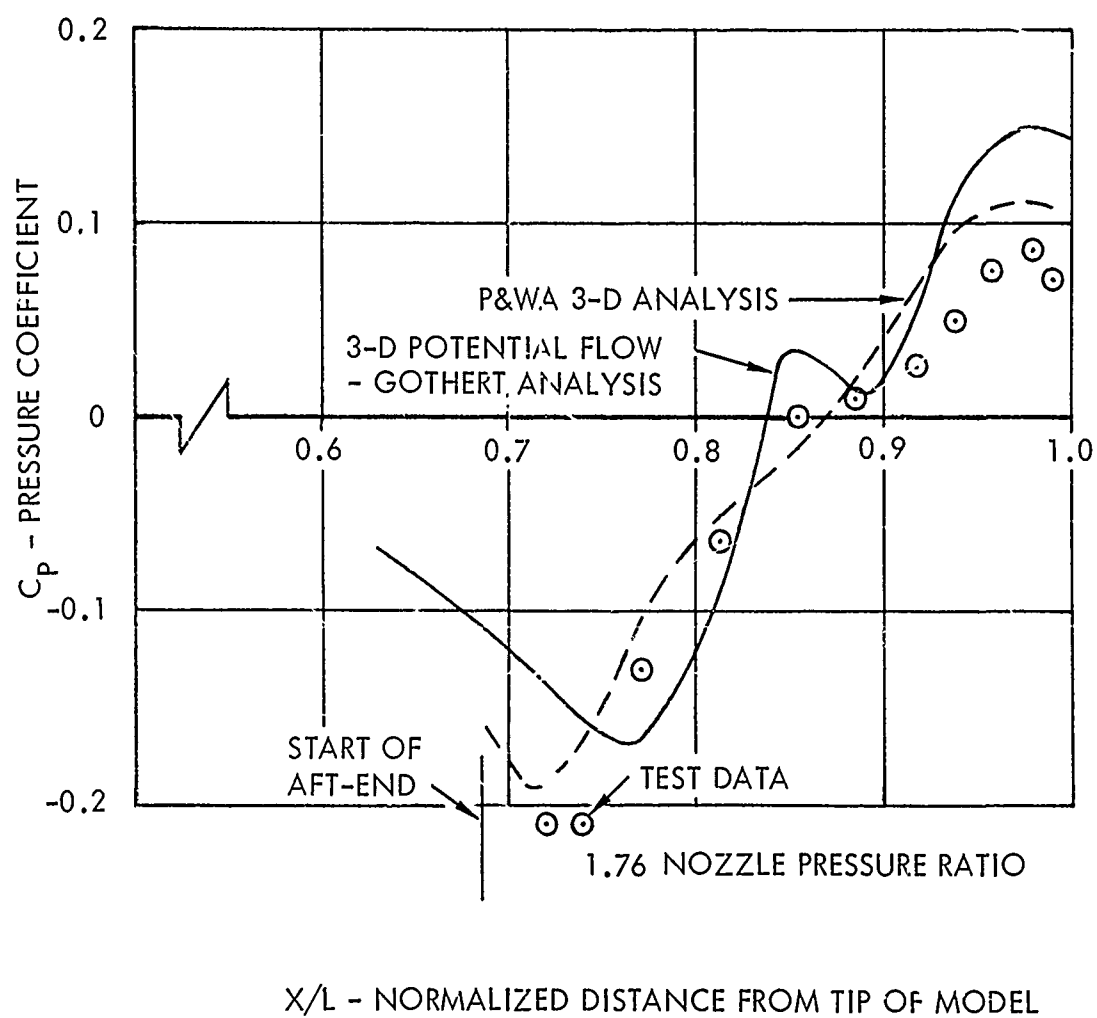


Figure 108. Comparison of Predicted and Measured Row 1 Pressure Distributions - A-1 Twin-Jet Body - Mach 0.8

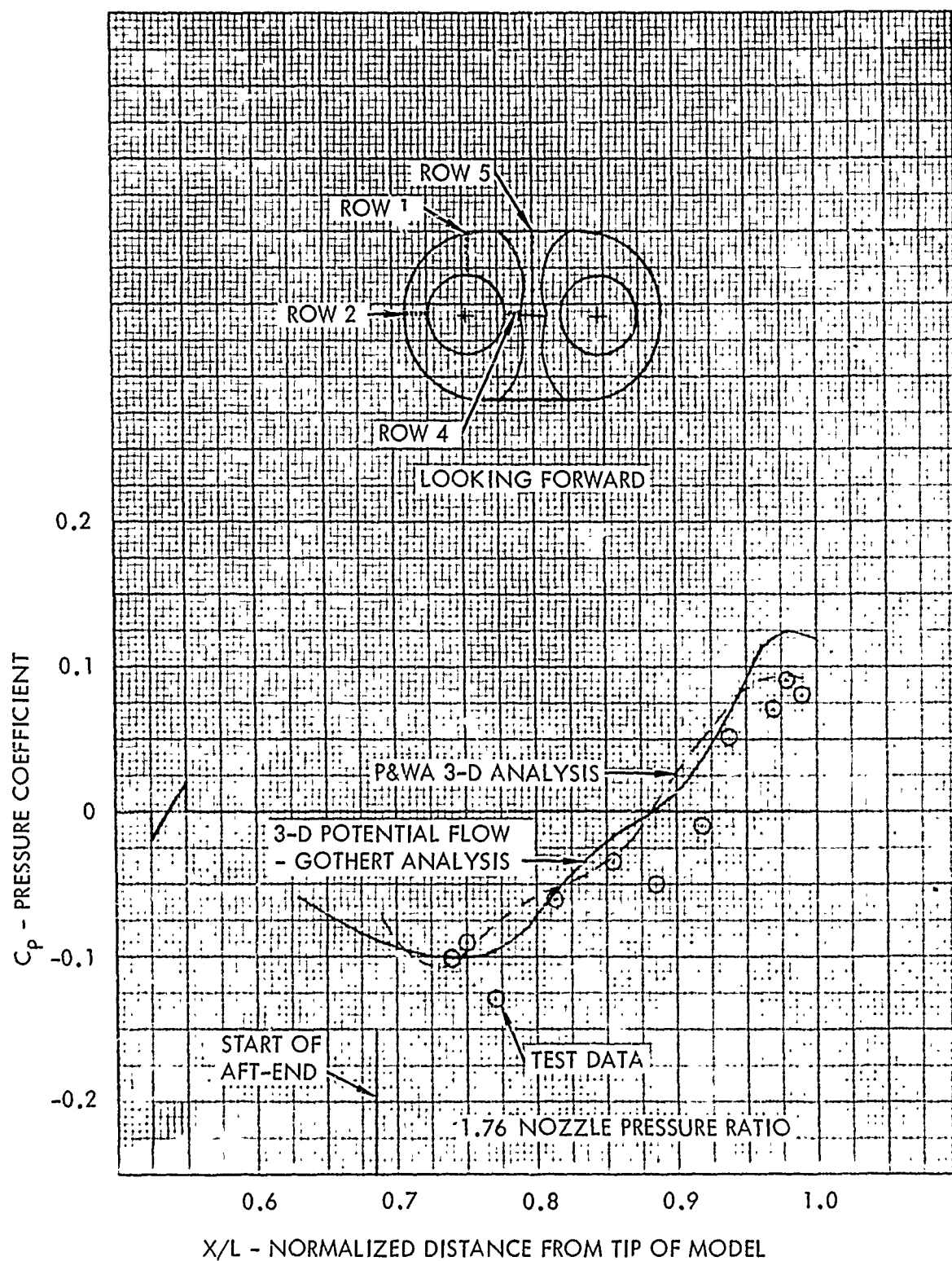


Figure 109. Comparison of Predicted and Measured Row 2 Pressure Distributions - A-1 Twin-Jet Body - Mach 0.8

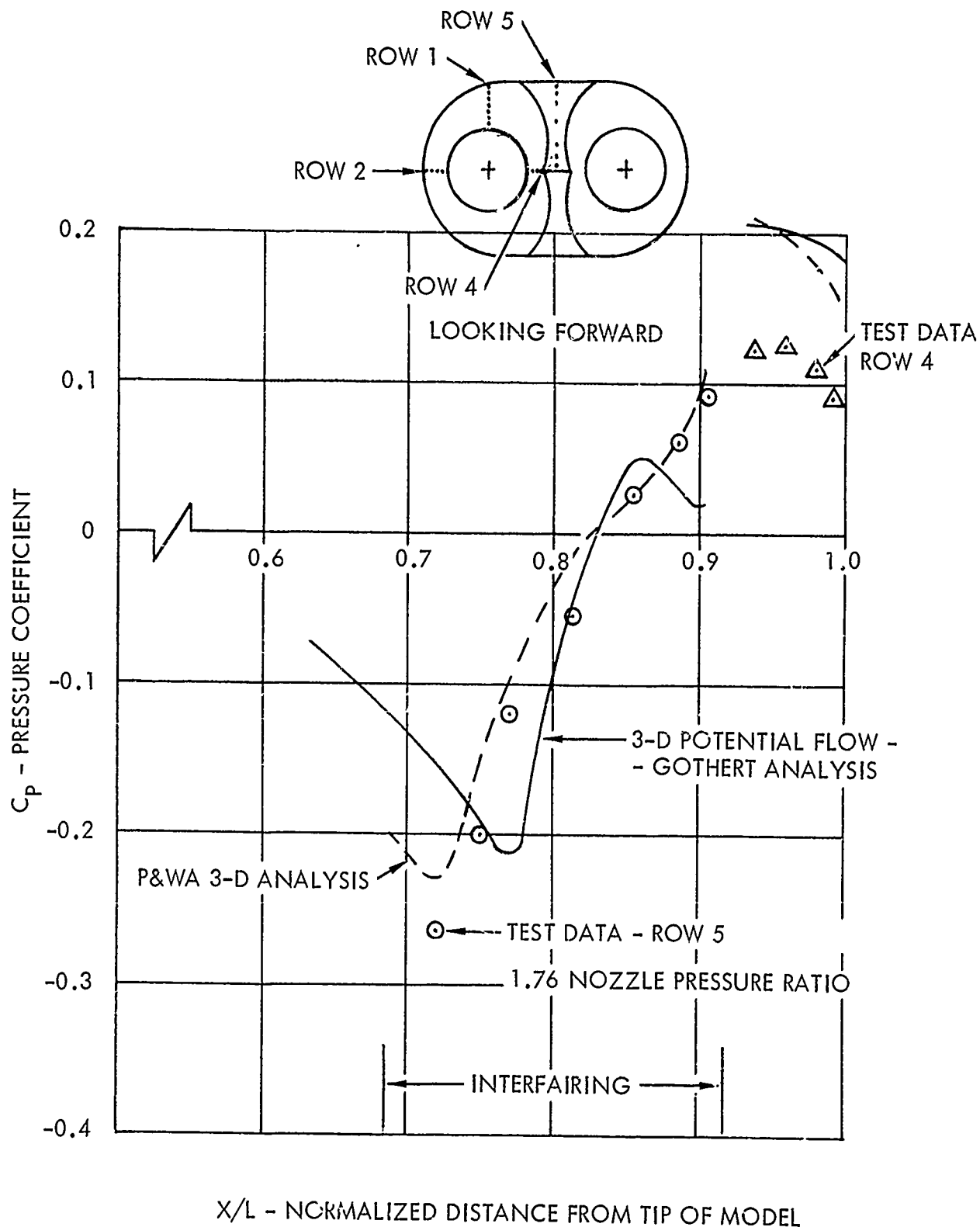


Figure 110. Comparison of Predicted and Measured Rows 4 and 5 Pressure Distributions - A-1 Twin-Jet Body - Mach 0.8

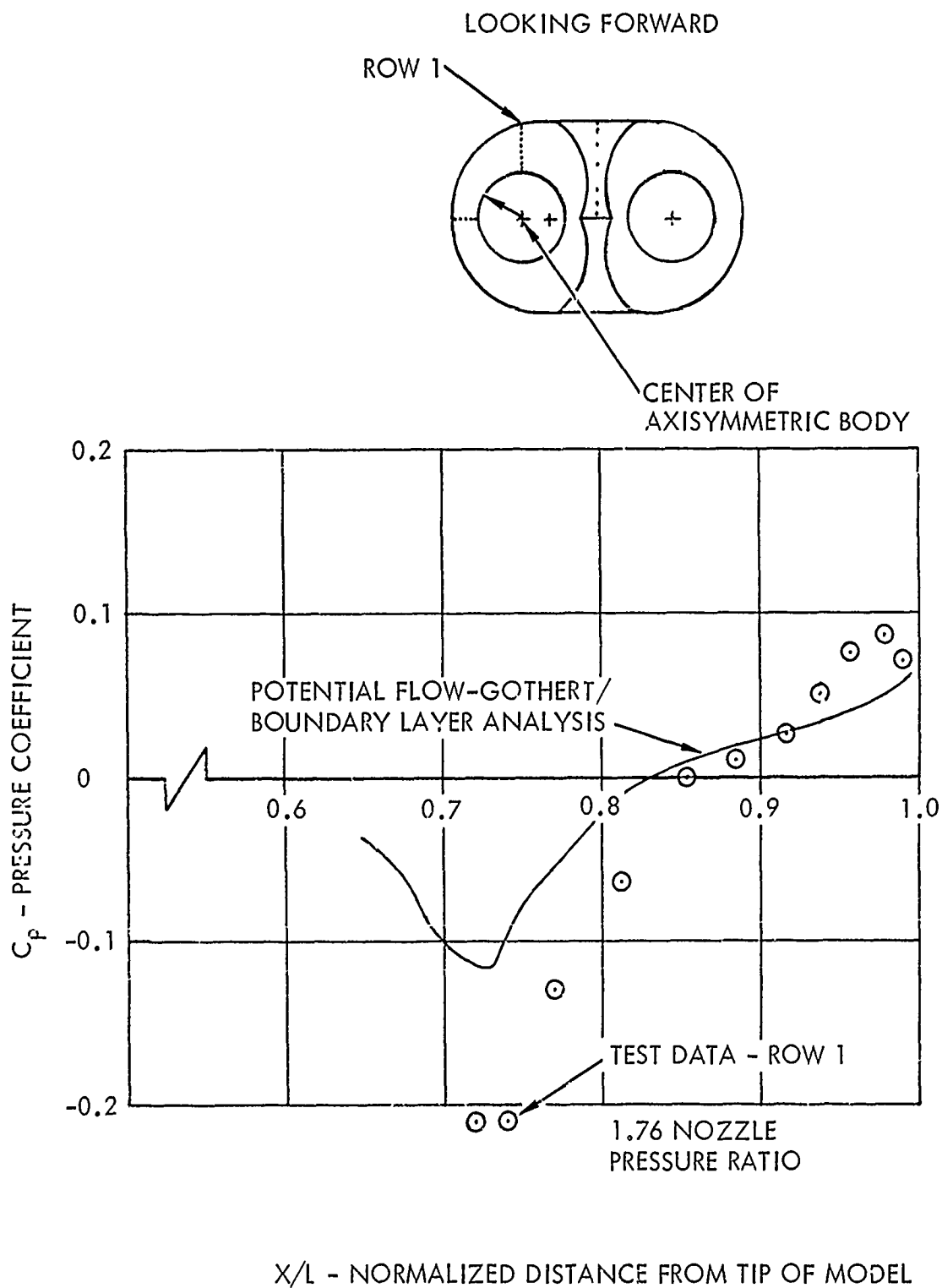


Figure 111. Comparison of Sector Analysis and Measured Row 1 Pressure Distributions - A-1 Twin-Jet Body - Mach 0.8

pressures measured along instrumentation row number 1 (located along the top of the nozzle as illustrated in the figure). The computed results shown are for an axisymmetric body whose centerline coincides with the centerline of the nozzle and whose radius distribution is identical to radius distribution along row 1 measured from the nozzle centerline. Figure 111 indicates that the sector analysis method is not sufficiently accurate for predicting aft-end pressure distributions.

Correlation Methods - A correlation of the jet-off subsonic drag data is presented in Figure 112 for several Phase II narrow spaced nozzle configurations. The drag data is presented in terms of Spreiter's transonic similarity parameters (Reference 54) combined with IMS of the equivalent body of revolution for the twin-jet models. As discussed in Subsection 2.3.1.1, application of Spreiter's similarity parameters requires that the drag parameter be referenced to a two-dimensional drag which in turn requires that the measured drag be adjusted by the ratio of two-dimensional to axisymmetric drags for the equivalent body of revolution. Since, for subsonic flow, a procedure for obtaining this ratio has not yet been determined, the measured drag coefficient was used directly in the drag parameter. Consequently, the drag data for different area ratios lie on separate curves, as illustrated in Figure 112, rather than on a single correlation curve. Jet-off data correlations for the intermediate and wide nozzle lateral spacing are presented in the computer program manual, (Reference 76) which is a supplement to this report.

If the aftbody maximum area station is used as the reference station for bookkeeping aircraft drags, then the results presented in Figure 112 must be used with caution since the metric break station of the Phase II model lies downstream of the maximum area station. Using the maximum area station as a reference station requires a procedure for obtaining the drag acting on the body between the maximum area and metric break stations. Attempts were made to obtain this increment by application of the potential flow/boundary layer program (Reference 5). The results did not, however, appear realistic. Regardless of the accounting system employed, the correlation results are adequate for predicting drag increments due to configuration changes downstream of the metric break provided that the configuration change does not influence the flow field upstream of the metric break.

The method used for correlating the jet-on aftbody/nozzle drags for convergent and convergent-divergent nozzles is based on subsonic potential flow theory. In accordance with this theory, the net axial pressure force acting on the streamline adjacent to the aircraft surface must be equal (but opposite in direction) to the pressure force acting on the jet boundary. Assuming the exhaust jet does not influence the flow field upstream of the aftbody, then a change in the force acting on the exhaust plume boundary, due to a change in the nozzle pressure ratio, must be balanced by a change in the force acting on the aftbody and nozzle. The ideal axial force acting on the jet boundary, ΔD , can be determined by a momentum balance on the jet for a control volume beginning at the nozzle exit and extending downstream to infinity where the jet momentum is equal to the ideal thrust. Expressed algebraically

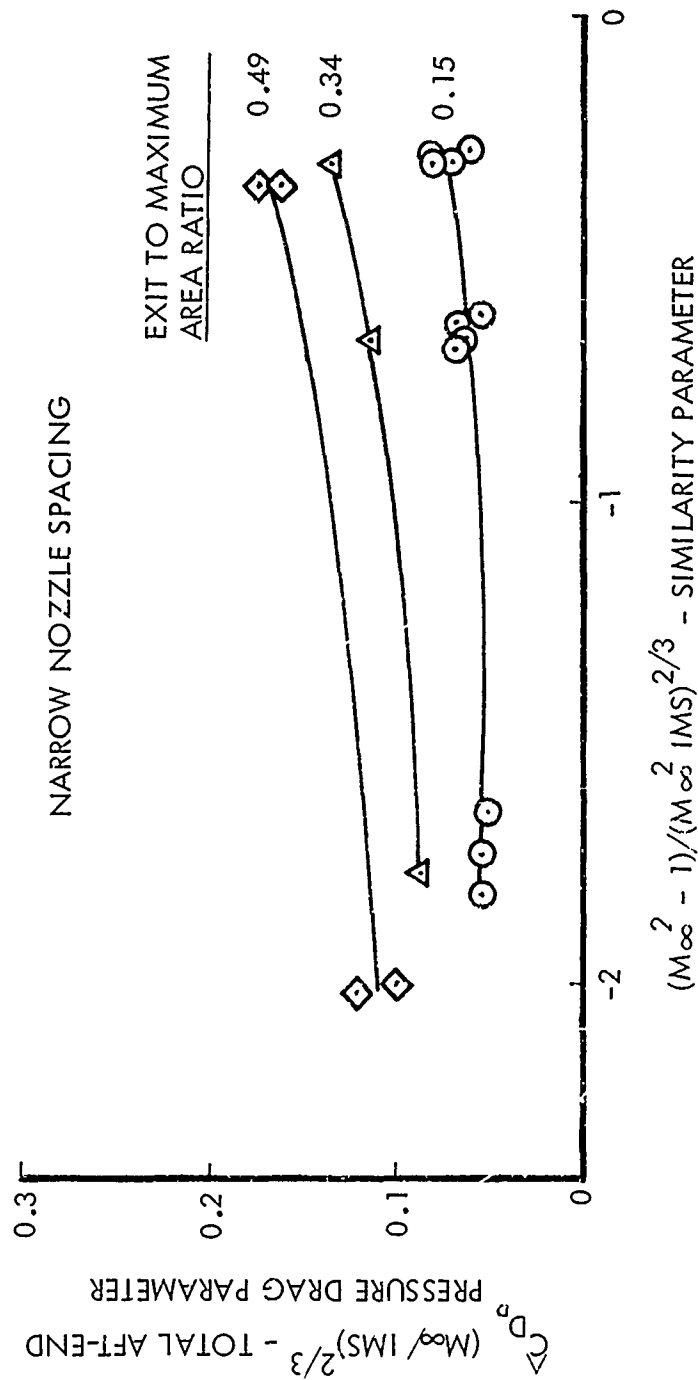


Figure 112. Transonic Similarity Correlation of Phase II Data - Subsonic Flow - Jet-Off

$$F_i - F_g + \Delta D = 0$$

where F_i is the gross thrust of the fully expanded exhaust jet, F_g is the nozzle gross thrust. In coefficient form, the above equation can be expressed as

$$(1 - C_t) + \frac{\Delta D}{F_i} = 0$$

where C_t is the thrust coefficient. While the idealizations involved render the above expression inaccurate on an absolute basis, it does strongly suggest that changes of drag, i.e., increments in drag from a reference drag, may be correlated with the nozzle underexpansion losses $(1 - C_t)$. The reference drag selected is the drag associated with the nozzle operating at its design pressure ratio (i.e., cylindrical exhaust plume). (A jet-off drag reference is not suitable since the pressure force acting on the dividing streamline between the external flow and the separated flow region is not known.) Thus, a correlation of the drag increment from jet-off to jet-on (nozzle operating at the design pressure ratio) is required. The correlation developed is shown in Figure 113 for the narrow nozzle lateral spacing. The increment in drag from jet-off to jet-on (design pressure ratio) is presented as a function of nozzle exit boattail angle and Mach number. Test data for convergent, convergent-divergent, and plug nozzles were used in developing the correlations. The drag coefficients are referenced to the shroud cross-sectional area at the nozzle exit.

Figure 114 illustrates the correlation results obtained for nozzle pressure ratios greater than the design pressure ratio. Test data are presented in the figure for the normal and maximum power convergent-iris nozzle installation and for the narrow lateral spacings. The correlation results are Mach number and power setting dependent.

For unshrouded plug nozzles, the above correlation equation is difficult to use since no adequate simplified methods are available for computing thrust coefficients. However, by rewriting the above equation as

$$(1 - C_{T_e}) + \frac{\Delta D}{F_i} - (C_T - C_{T_e}) = 0$$

where C_{T_e} is the ratio of gross thrust at the nozzle throat to ideal gross

thrust obtained by expanding the flow to freestream static pressure, the drag increment and plug surface pressure forces can be correlated in terms of a convergent nozzle underexpansion loss $(1 - C_{T_e})$.

Plug nozzle data correlations are presented in Figure 115 for narrow, intermediate, and wide spaced normal power configurations and for Mach numbers of 0.6, 0.8, and 0.9. Poor data correlations are obtained at the design pressure ratio (convergent nozzle) due to the considerable influence of the external flow on the plug surface pressure distributions.

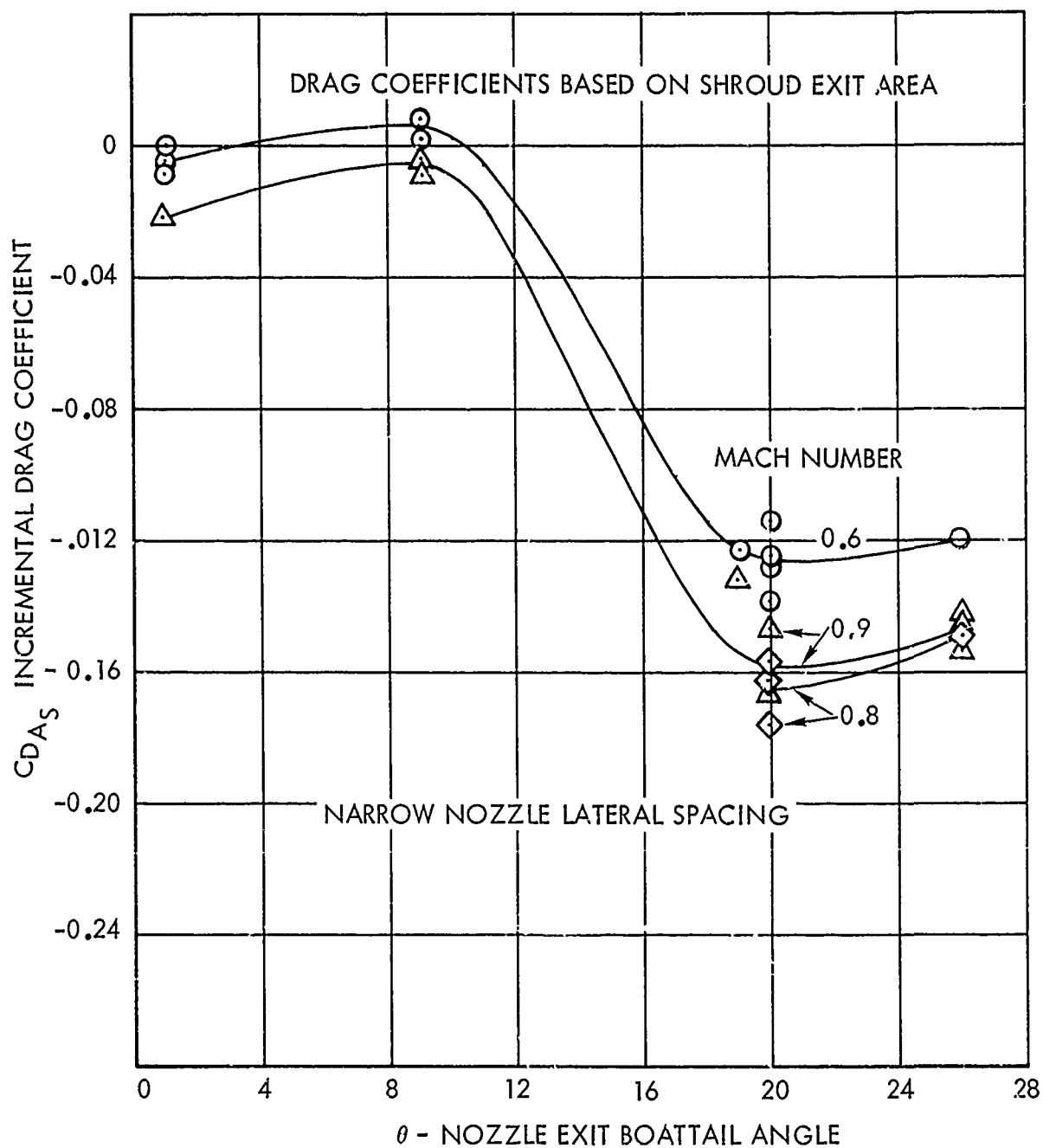


Figure 113. Correlation of Drag Increment From Jet-Off to Design Pressure Ratio Operation

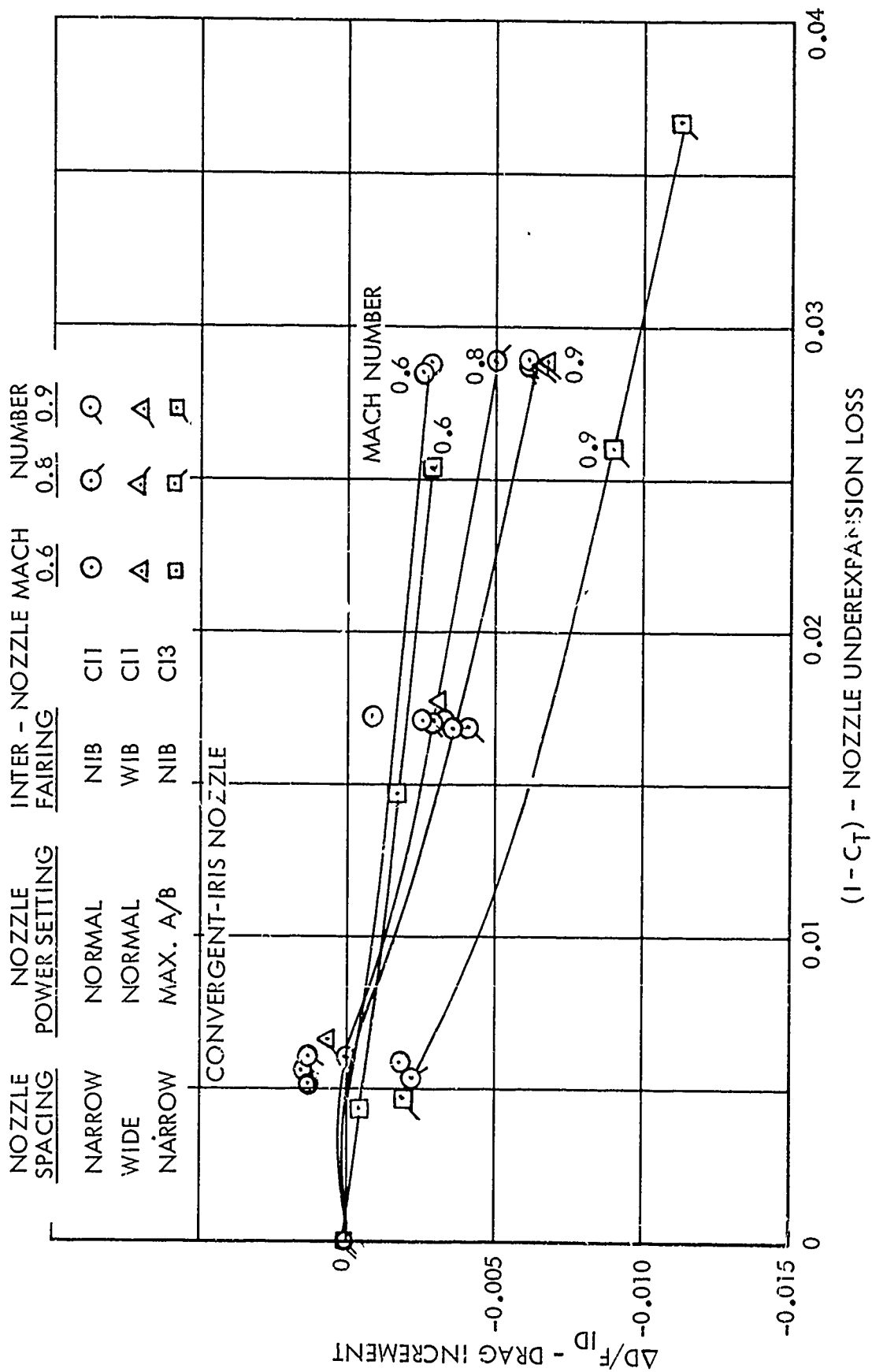


Figure 114. Correlation of Drag Increment From Design to Operating Pressure Ratio

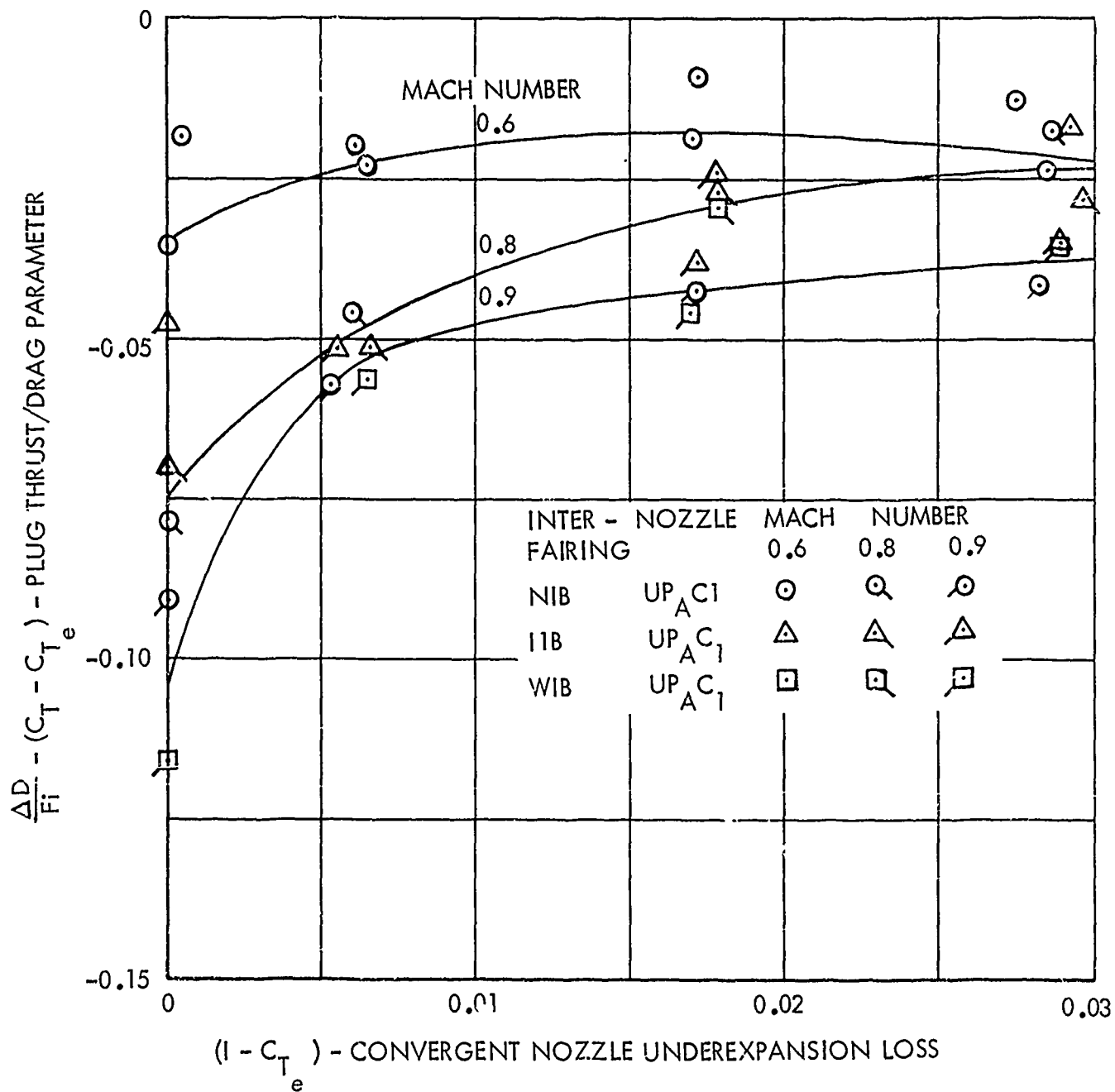


Figure 115. Correlation of Plug Thrust and Boattail Drag Increment - $UP_A C_1$ Nozzle

3.3.1.2 Supersonic External Flow

Equivalent Body Methods - For an equivalent body representation of the model, the drag force is computed using either the combined MOC/boundary layer program described in Reference 4 or the Calac Wave Drag Computer Program described in Reference 77.

In the wave drag method, an equivalent body of revolution is calculated by passing cutting planes inclined at the Mach angle through the selected representation of the twin-jet model. The total drag of the equivalent body is then calculated by application of the von Karman slender body theory (Reference 71). Since the wave drag program computes the drag of the entire body, the following procedure has been employed for separating out the aftbody/nozzle drag. First, the drag of the entire body is obtained assuming a cylindrical exhaust jet. Next, the total drag is obtained for a body which is the same except that it is cylindrical downstream of the station where the aftbody starts. The difference in drag between the two bodies is considered to be the aftbody/nozzle drag. The wing and empennage can also be included in the wave drag analysis method.

Application of the combined MOC/boundary layer program (Reference 4) in conjunction with an equivalent body (based on one-half the model area distribution) yields jet-off pressure drag coefficients which are in fair agreement with measured drag coefficients for the total boattail of the Phase II model (i.e., total aftbody plus nozzle boattail). Computed pressure drag coefficients are compared with measured drag coefficients in Table 15 below.

TABLE 15. MOC/EQUIVALENT BODY RESULTS

<u>Configuration</u>	<u>Mach Number</u>	<u>Area Distribution</u>	<u>C_{DPT} - Pressure Drag Coefficient</u>	
			<u>Computed</u>	<u>Measured</u>
CD ₃ /NLB	1.6	1/2	0.0609	0.048
CD ₃ /NLB	2.0	1/2	0.0495	0.039
CD ₃ /WLB	2.0	1/2	0.0595	0.060
CD ₃ /WLB	2.0	Full	0.087	0.060

Computed results are presented in the table for equivalent bodies with area distributions equal to the full model area distribution (excluding wing and empennage) and to half of it. The latter representation was selected since the physical arrangement of the Phase II model more nearly resembles two isolated bodies from the end view, especially at the wide nozzle lateral spacing. Further, the computed results for the half area distribution body are in better agreement with measured results than those for the full area distribution body.

Application of the combined MOC/boundary layer program in conjunction with the Bonner-Karger separation and Brazzel-Henderson base pressure correlations (described in Subsection 2.3) yields results inconsistent with the Phase II jet-on test data. The combined program iteratively locates the jet induced separation point by matching the base pressure computed assuming a base region downstream of the separation point, to the separation pressure which is computed using the Mach number and Reynolds number upstream of the separation point. Computed jet-on to jet-off drag ratios obtained by this procedure are compared with experimental results in Figure 116 for a Mach number of 1.6 and for maximum A/B convergent-iris and plug nozzle configurations. The results indicate that either the equivalent body approach or the correlations employed in the analysis method are inadequate for predicting nozzle pressure ratio effects.

Application of the Calac Wave Drag Program (Reference 77) also yields results inconsistent with experimental data for various twin-jet models. Specifically, while wave drag method results are in good agreement with measured drag forces for the Berrier and Wood A-1 twin-jet body, they are in poor agreement with measured drag forces for the Phase II model incorporating the CD₃ nozzle as discussed below.

Total aftbody drag calculated by the Calac wave drag method and the Frankl and Voishel friction drag method (Reference 72) is compared with measured drag in Figure 117 for the Berrier and Wood A-1 twin-jet body for Mach numbers ranging from 1.1 to 2.2. Computed results are presented in the figure for both single and twin equivalent body representations. The twin body representation consists of two identical axisymmetric bodies which have a combined area distribution equal to that of the A-1 twin-jet body. The lateral spacing of the twin bodies was set equal to the nozzle centerline to centerline spacing of the A-1 body. Computed results for the twin-body representation method are in better agreement with measured results. This result is not unexpected since, for a relatively wide nozzle lateral spacing, the body surface contours more nearly duplicate the surface contours of the A-1 body.

Total boattail drag coefficients computed by use of the Calac wave drag program for the Phase II model incorporating the CD₃ nozzle and narrow (NLB) and intermediate (ILB) high horizontal wedge interfairings are in poor agreement with experimental data. Computed total boattail drag coefficients, which include skin friction drag, are presented in Figure 118 for the NLB interfairing where the following methods of representing the model geometry were employed: a single axisymmetric body, twin bodies, and a fuselage and twin bodies. The twin-body representation consists of two identical axisymmetric bodies which are contoured to yield the same area distribution as the Phase II model. For the fuselage and twin-body representation, the twin bodies are contoured to yield the same area distribution as the sum of the area distributions of the nacelles (arbitrarily determined portion of the fuselage), aftbodies, and nozzles. The computed results shown in Figure 118 were obtained with the wing and empennage included in the model representation. It is seen that none of the body representations produce results which agree with the experimental data. Further, an incorrect trend of

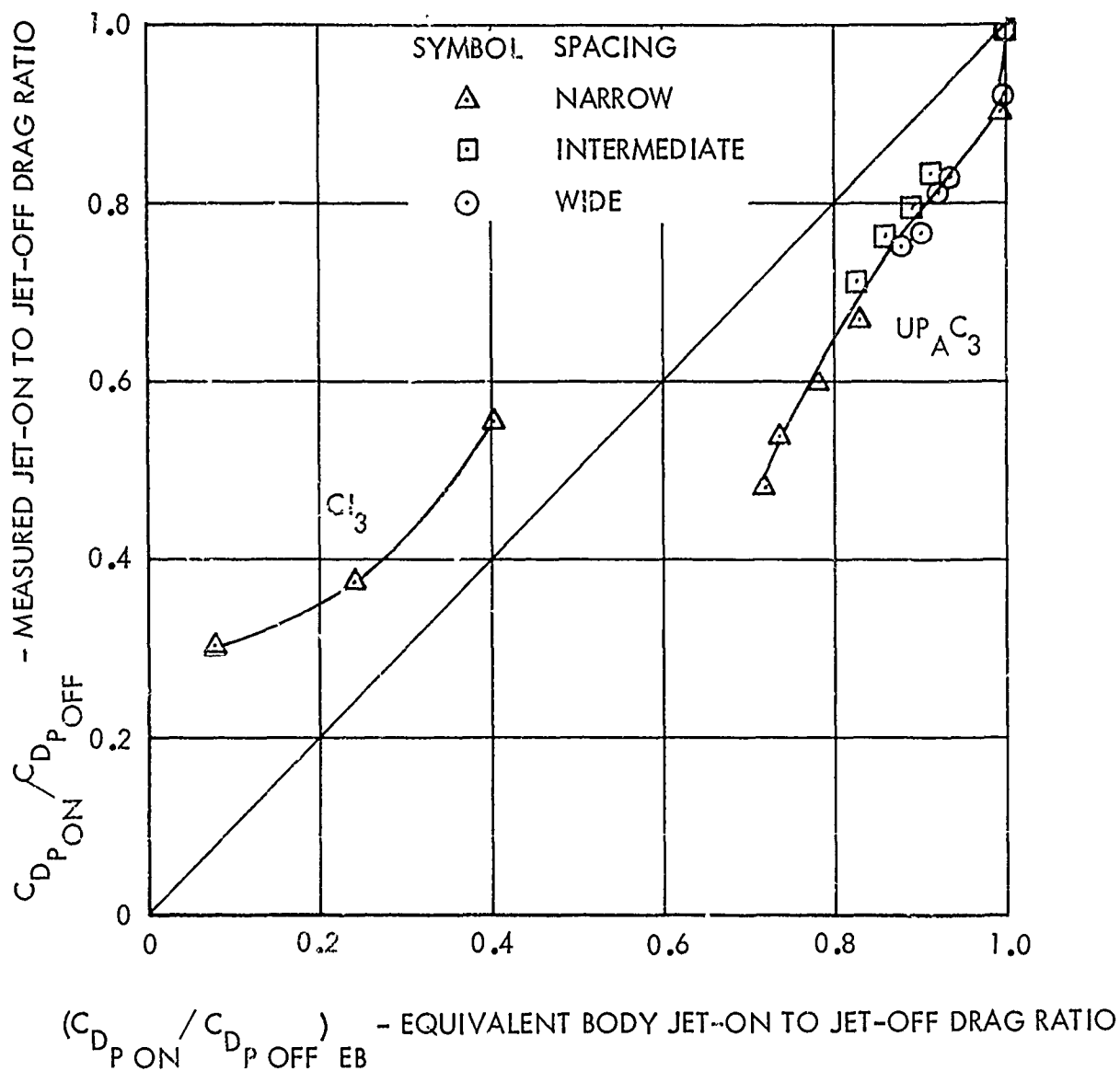


Figure 116. Equivalent Body Jet-On Drag Correlation of Phase II Data - Mach 1.6

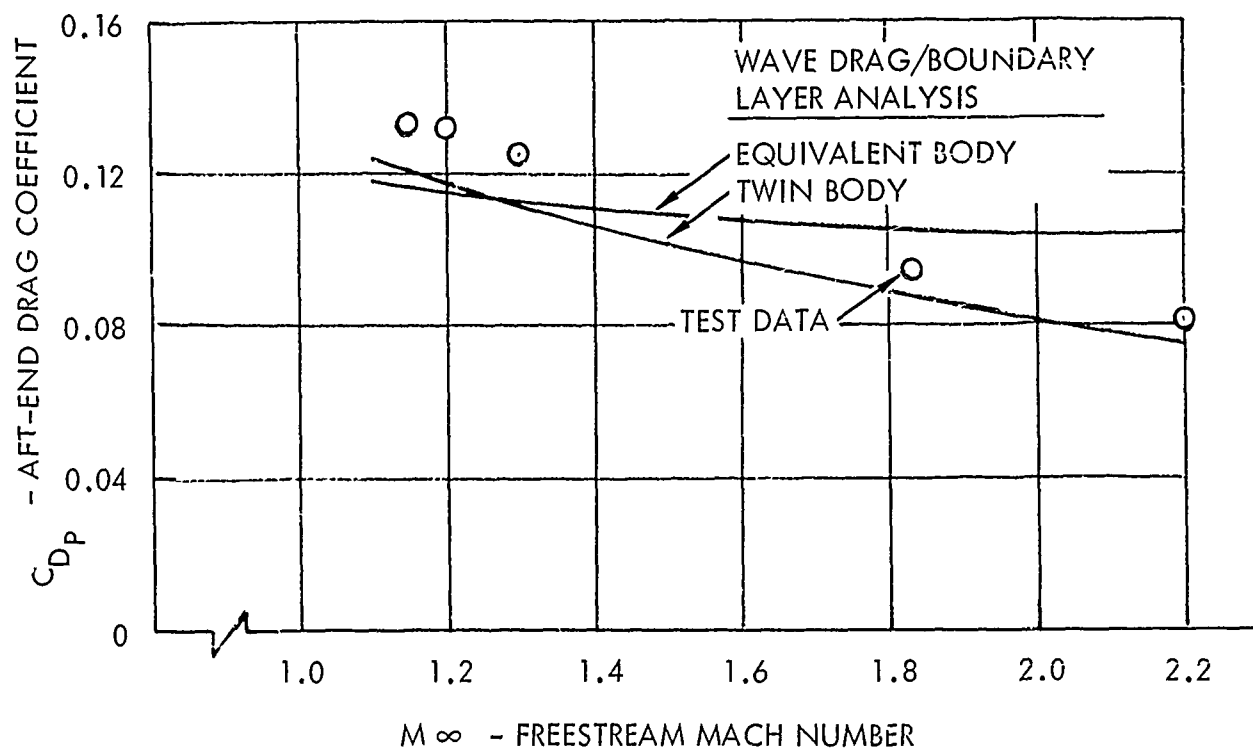
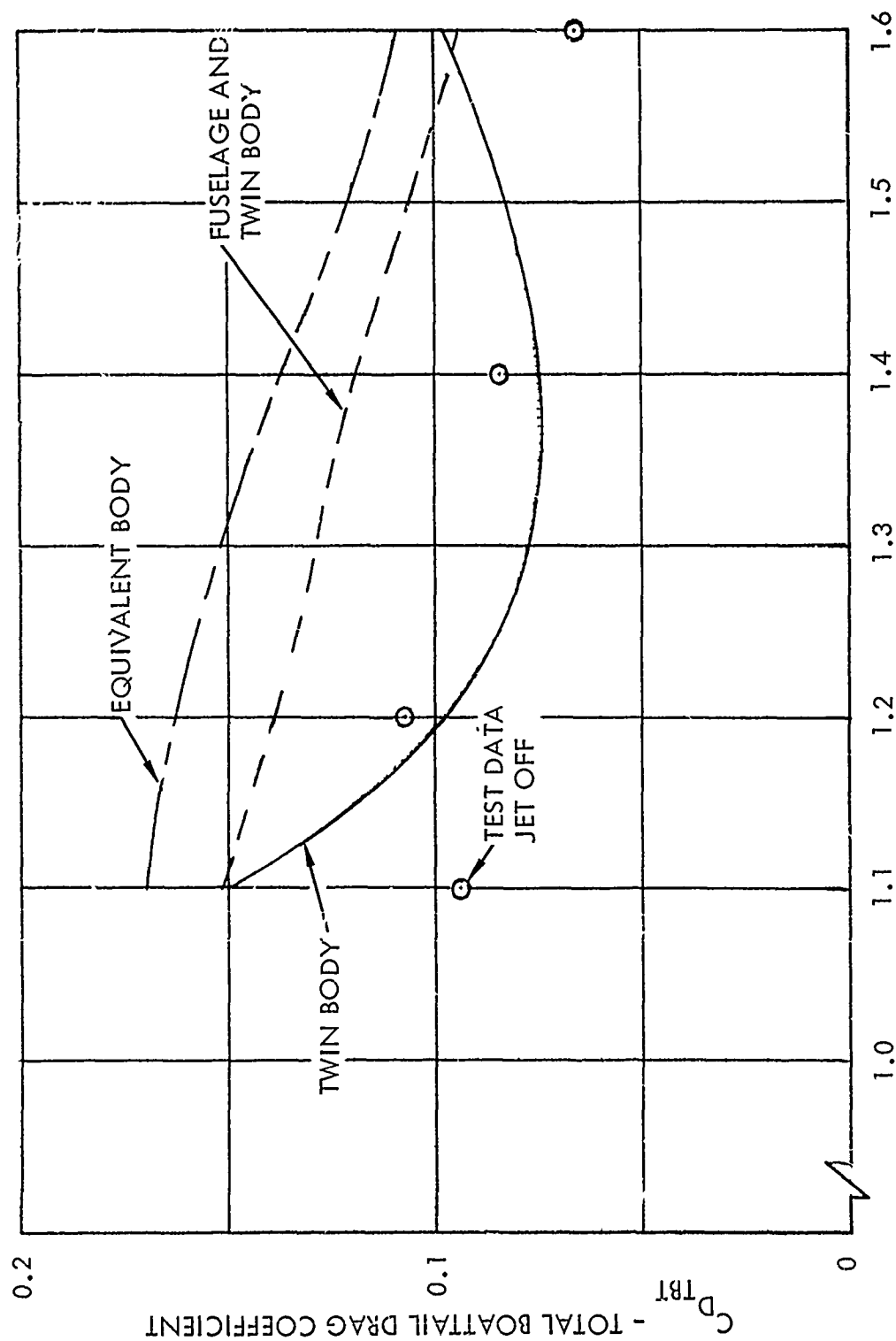


Figure 117. Comparison of Predicted and Measured Aft-End Drag
 - A-1 Twin-Jet Body - Supersonic External Flow



M_∞ - FREESTREAM MACH NUMBER

Figure 118. Comparison of Predicted and Measured Total Boattail Drag - NLB/CD₃ Configuration With Empennage

increasing drag coefficients with increasing Mach number was obtained with the twin-body representation. This result is contrary to the results obtained for a twin-body representation of the Berrier and Wood A-1 body.

The incorrect trend of increasing drag with increasing Mach number appears to be associated with including the wing and empennage in the description of the Phase II model. In particular, computed results for a twin-body description of the Phase II model incorporating the CD₃ nozzle and NLB interfairing with no wing and empennage showed the proper trend of decreasing drag coefficient with increasing Mach number. It is not yet understood why including the wing and empennage in the body description should result in an incorrect drag coefficient trend.

In order to check the validity of the wave drag computer program calculations and to obtain additional verification of the wave drag analysis method, results from the Calac wave drag program have been compared with both drag calculations and experimental data obtained by Maiden and Runckel (Reference 78) for a twin-jet body. These comparisons show that the Calac results differ from the computed results presented in Reference 78, but are in better agreement with the experimental data, as shown in Figure 119. The comparisons also show that the Calac computer results are sensitive to the number of points used to describe the body. This sensitivity arises because the program selects an area distribution between the body points which minimizes the drag. Thus, in regions of large area derivative changes, such as the juncture of the boat-tail and cylindrical exhaust jet, the body points must be closely spaced. A maximum of 30 points can be used to describe a body in the Calac program.

Sector Analysis Method - The combined MOC/boundary layer program (Reference 4) is employed in the sector analysis approach for supersonic speeds. Using this method to predict the pressure distributions on twin-jet bodies does not appear to be sufficiently accurate, as evidenced by the poor agreement between predicted and measured data at Mach 1.3 shown in Figure 120 for the Berrier and Wood A-1 body. The sector analysis method employed is identical to that described in Section 3.3.1.1 for subsonic external flow, except for substitution of the MOC boattail drag computer program for the potential flow/boundary layer program. The comparison shown in Figure 120 indicates that a problem exists in selecting a Mach number upstream of the aft-end for starting the MOC solution (freestream Mach number was assumed), as evidenced by the poor comparison at the start of the aft-end. Additional comparisons of sector analysis results with experimental data are presented in the Phase II interim report (Reference 2).

Correlation Methods - Both equivalent body and transonic similarity correlations of the Phase II jet-off data were developed. The equivalent body method provides superior correlations and is the recommended method.

The equivalent body correlation approach consists of correlating the jet-off total drag aft of the maximum area station as a function of calculated equivalent body drag. The maximum area station was chosen as a reference station since the Mach number at this station is more nearly equal to free-stream Mach number. The total drag for this procedure is the sum of the

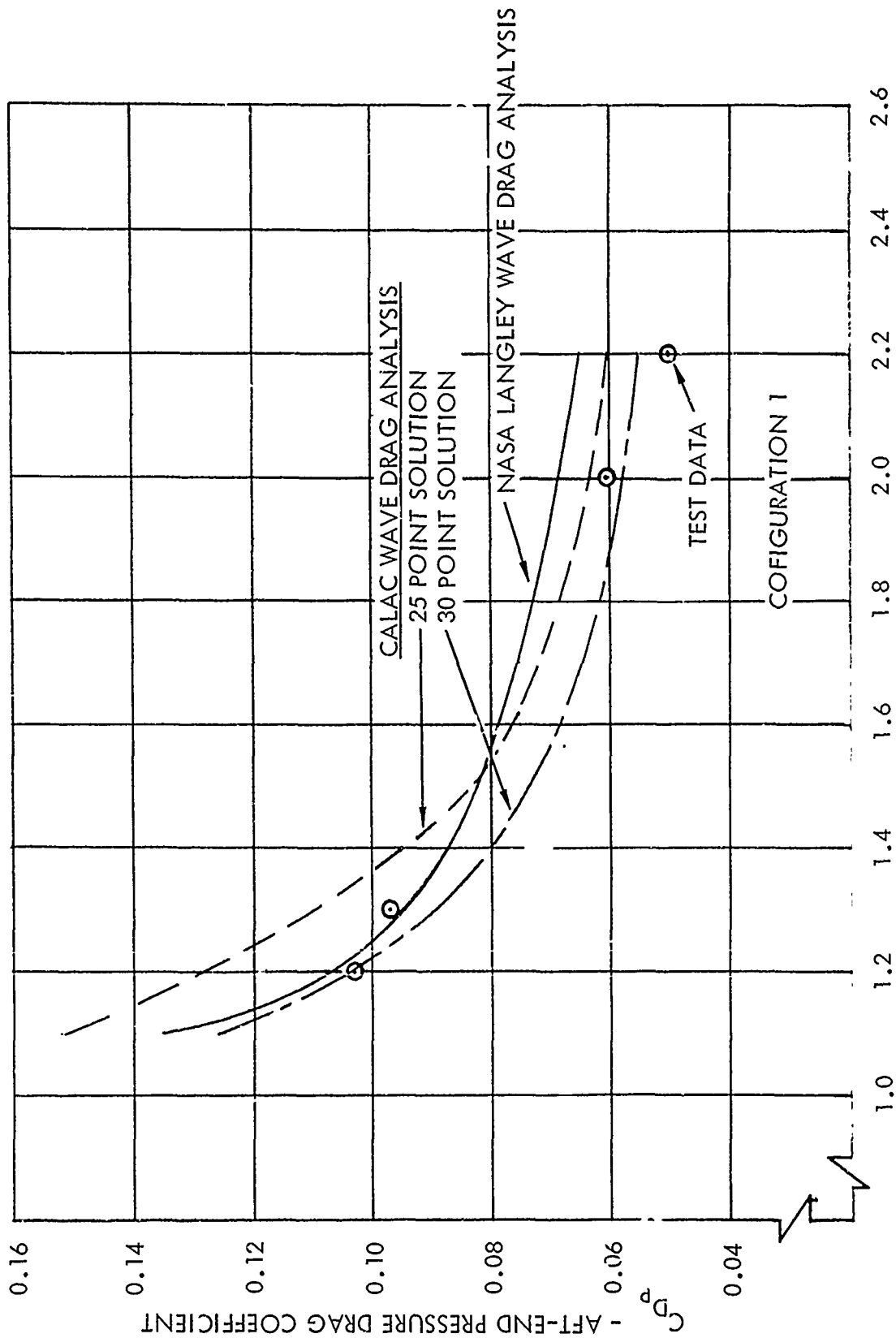


Figure 119. Comparison of Predicted and Measured Aft-End Drag - Configuration 1

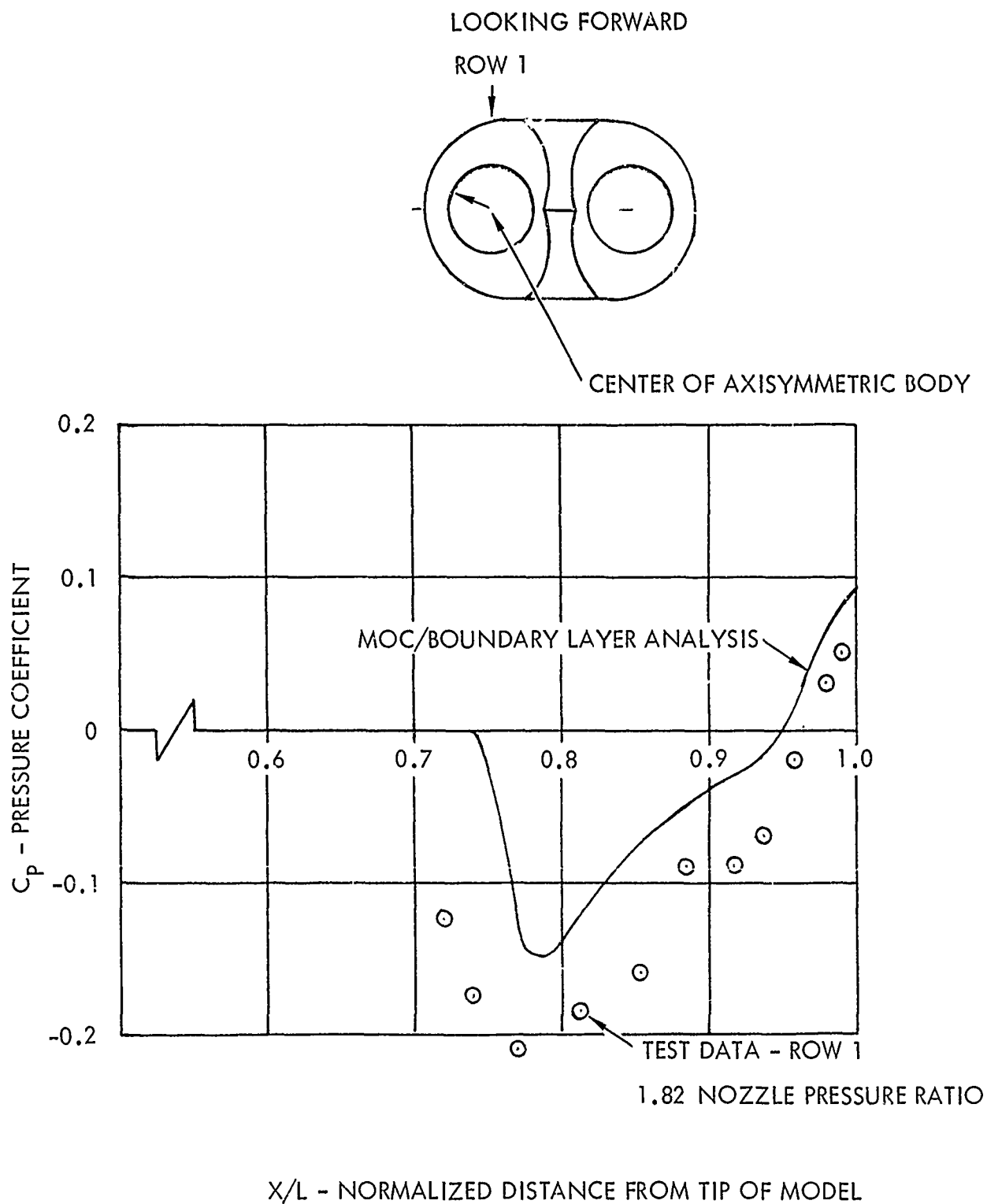


Figure 120. Comparison of Sector Analysis and Measured Row 1 Pressure Distributions - A-1 Twin-Jet Body - Mach 1.3

measured drag and the computed drag for the region between the maximum area and metric break stations. The equivalent body drag correlations presented in Subsection 2.3.1.1 are used for computing the equivalent body drag and also the drag between the maximum area and metric break stations. Correlation results obtained by application of the above procedure are presented in Figure 121 for Mach numbers of 1.2, 1.6, and 2.0, respectively. The jet-off data shown in the figure are for the maximum A/B convergent-iris, convergent-flap, plug, and convergent-divergent nozzle configurations with horizontal and vertical wedge interfairings. Except for the CF_3/NLB data points, the data for each Mach number are correlated quite well by a straight line.

Correlation of the Phase II test data using Spreiter's similarity parameters is presented in Figure 122. The measured drag data was adjusted by the ratio of two-dimensional to axisymmetric drag in order to be consistent with Spreiter's theory as discussed in Subsection 2.3.1.1. Test data presented in the figure are for the same configurations for which test data was presented in the equivalent body correlations (Figure 121). Although Mach number has been eliminated as a parameter, considerable data scatter exists. The equivalent body correlation approach is, therefore, the preferred method.

To supplement the jet-off correlations presented above, a jet-on boattail drag correlation was developed and is presented in Figure 123. The drag increments (jet-on minus jet-off) normalized by the product of the shroud exit area (jet plus base area) and the difference between the nozzle internal and external static pressures (assuming no flow separation) are correlated as a function of nozzle boattail angle at the nozzle exit. The test data presented in the figure are for freestream Mach numbers of 1.2 and 1.6 and for the maximum A/B power setting plug, convergent-flap, and convergent-iris nozzle configurations. The external nozzle boattail static pressure, P_L , used in the correlations was determined from MOC calculations. The correlation results are not valid for pressure coefficients, $(P_e - P_L)/q_L$, less than 1.4. This limit is based on the empirical observation that little or no separation occurs for values lower than this limit. The correlation results are not valid for a Mach number of 2.0 since separation was not present at this Mach number.

3.3.2 Internal Flow Methods

Examination of the Phase II model data indicates that the isolated convergent and convergent-divergent nozzle performance prediction methods described in Subsection 2.3.2 are applicable to twin nozzle installations. This conclusion is based on the observation that the external flow did not significantly influence the internal flow. Some external flow influence on the plug nozzle performance was obtained, as discussed below.

The Phase II twin-jet UPAC3 plug nozzle data indicates that, for nozzle pressure ratios greater than 4.0, isolated nozzle methods can be used for predicting plug surface pressure distributions. In Figure 124, measured plug surface pressure distributions obtained at Mach 1.6 for nozzle pressure

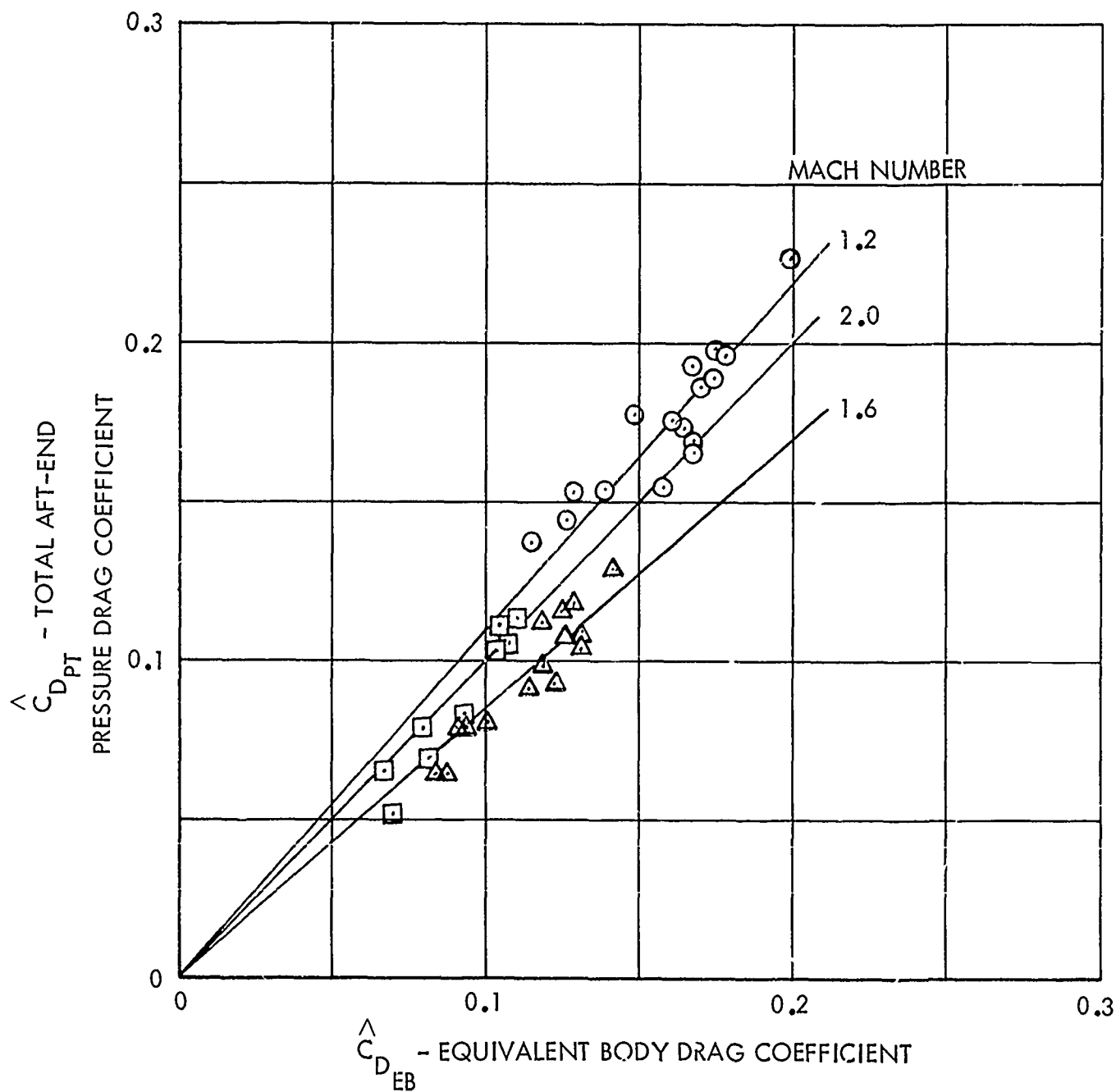


Figure 121. Equivalent Body Drag Correlation of Twin-Nozzle/Aftbody Data - Supersonic Flow - Jet-Off

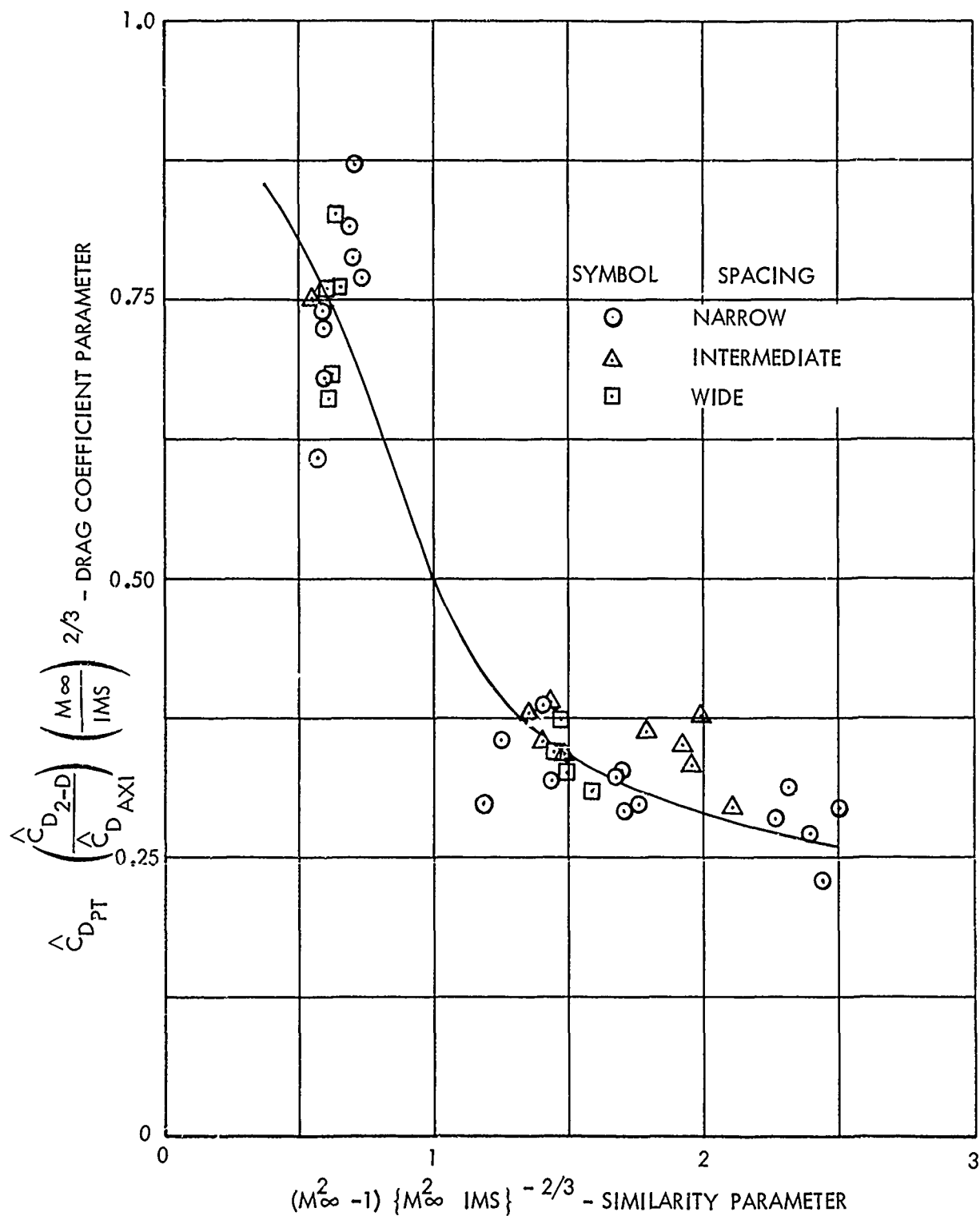


Figure 122. Transonic Similarity Correlation of Phase II Data - Supersonic Flow - Jet-Off

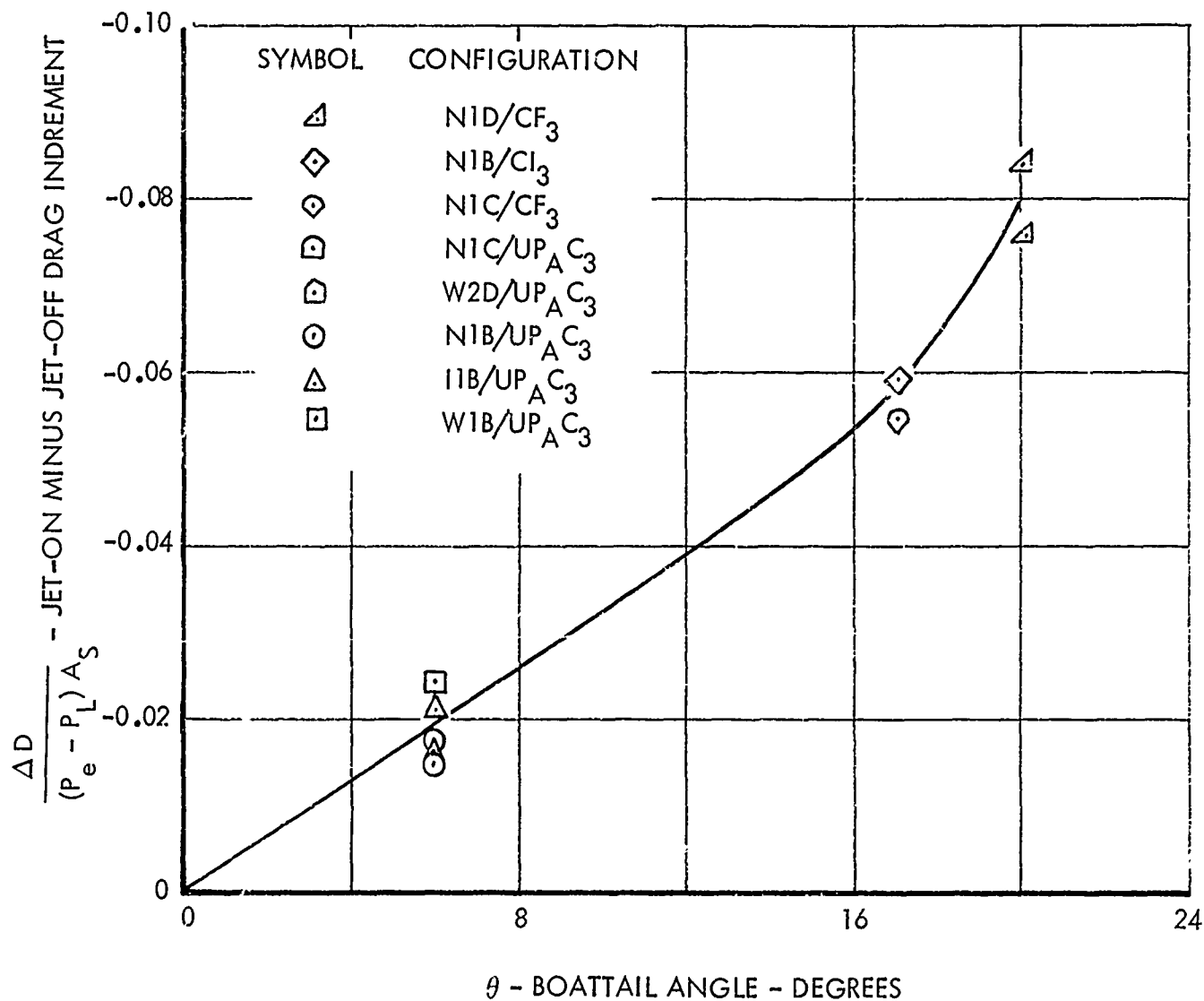


Figure 123. Correlation of Jet-On Minus Jet-Off Drag Increment - Supersonic Flow

ratios of 3.74 and 7.62 are presented for the twin-jet model which incorporates the intermediate I2B interfairing. (The pressure distributions shown in the figure are representative of those obtained for all configurations tested). Also presented in the figure is the computed pressure distribution for a nozzle pressure ratio of 7.62. The computed results were obtained by application of the MOC computer program (Reference 39) assuming freestream flow for the local external flow upstream of the nozzle exit. The good agreement between measured and experimental results is not unexpected since the monotonically decreasing pressure indicates that the plug surface is shielded from the interaction between the exhaust jet and external flow by the flow expansion around the nozzle shroud trailing edge. The plug nozzle pressure distributions were symmetrical for nozzle pressure ratios greater than 4.0 and unsymmetrical at lower values. The unsymmetrical pressure distributions shown in Figure 124 for a nozzle pressure ratio of 3.74 are representative of the distribution obtained for all configurations for pressure ratios less than 4.0. (The interaction effects influence the surface pressure distributions at pressure ratios less than about 6.0; however, this influence is symmetrical between pressure ratios of 4.0 and 6.0.) This indicates, therefore, that isolated plug nozzle analysis methods can also be applied for predicting pressure distributions and thrust coefficients for nozzle pressure ratios as low as 4.0 since the interaction effect is symmetrical. This result is significant since the nozzle pressure ratios are greater than 4.0 for most of the aircraft mission.

A sector analysis approach for prediction of the unsymmetrical plug surface pressure distributions which were obtained at nozzle pressure ratios less than 4.0 does not appear feasible. The analysis approach considered consists of application of the MOC computer program (Reference 39) assuming that each sector of the exhaust jet interacts with an external flow whose Mach number is determined using the measured boattail static pressure just upstream of the nozzle exit. The pressure data indicate, however, that the unsymmetrical plug surface pressure distributions cannot be predicted by this above method. At the angular locations between which the largest differences of plug surface pressure distributions occurred, the upstream boattail static pressures were nearly identical. For example, for the 3.74 nozzle pressure ratio data presented in the upper portion of Figure 124, the Mach numbers computed from the measured boattail static pressures on the top and bottom surfaces were 1.89 and 1.88, respectively.

3.3.3 Base Pressure Methods

Presented below is an evaluation of the applicability of isolated nozzle analytical and empirical base pressure prediction techniques for predicting twin-nozzle annular and plug base pressures.

3.3.3.1 Annular Base Pressure

Examination of Phase II model plug nozzle annular base pressure test data indicates that an isolated base pressure prediction method which assumes a

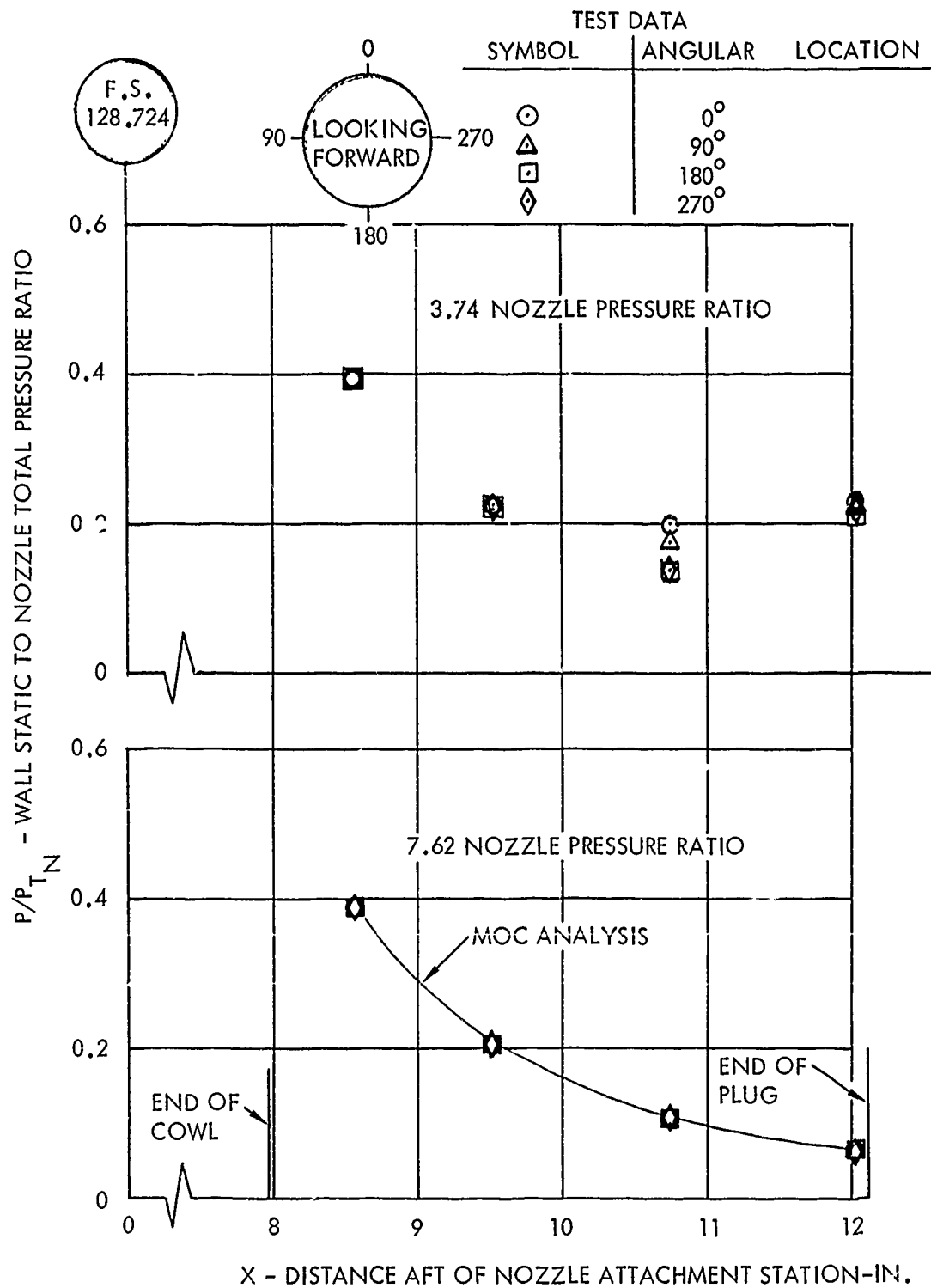


Figure 124. Comparison of Predicted and Measured Plug Surface Pressure Distributions - 12B/UP_{A3} Configuration - Mach 1.6

zero initial boundary layer thickness such as the Korst theory presented in Reference 55 and utilizes a local external flow Mach number associated with the measured static pressure upstream of the annular base, is inadequate for predicting the observed circumferential base pressure variation. This conclusion is based on the observation that large differences in base pressure were obtained at circumferential locations where the boattail static pressures upstream of the base were nearly identical. Possibly the unsymmetrical base pressures are a result of an unsymmetrical boundary layer thickness at the nozzle boattail trailing edge and a virtual origin correction to the Korst method (Reference 79) may predict the observed trends. However, since the annular base area is small, the base drag predicted by application of isolated nozzle methods should be adequate for preliminary design purposes.

3.3.3.2 Plug Base Pressure

The semi-empirical base pressure correlation equations developed for isolated plug nozzles are valid for predicting twin-jet base pressures for nozzle pressure ratios greater than 4.0 as illustrated for the Phase II twin-jet UPAC3 plug nozzle model in Figure 125. The measured results shown in the figure are for six different narrow-spaced and intermediate-spaced inter-fairings and for Mach numbers ranging from 0.6 to 1.6. The good agreement is, of course, expected since, as previously discussed, the plug surface pressure distributions were symmetrical for nozzle pressure ratios greater than 4.0.

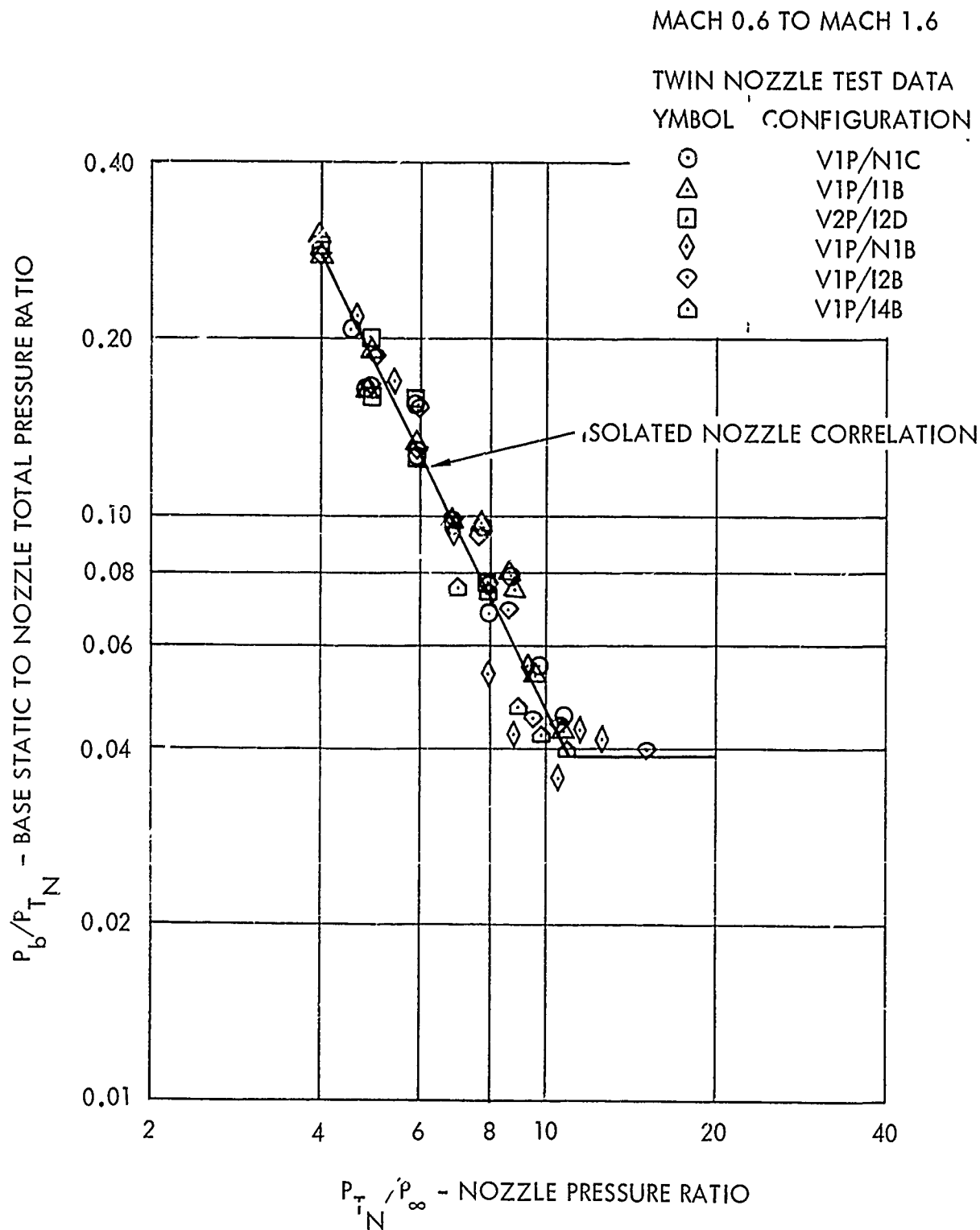


Figure 125. Twin Nozzle Base Pressure Correlation - $UP_{A_3} C_3$ Nozzle

SECTION 4

TWIN-NOZZLE/AFTBODY DESIGN TECHNIQUES

Techniques for designing the aft-end of air superiority fighters having twin buried engines and dual nozzles are presented in this section. These techniques were developed using the thrust and drag results obtained from the aircraft configuration investigated during the Phase II tests. The application of these techniques to improve the aft-end design of selected Phase II configurations is also presented along with a recommended test program for verifying the design techniques employed.

4.1 DEVELOPMENT OF DESIGN TECHNIQUES

4.1.1 Design Criteria

The development of an integrated aft-end design of an air superiority fighter must take into account such factors as weapon installation, landing gear design, internal volume requirements, structural arrangement, vulnerability, turnaround time, maintenance, performance, weight, and mission requirements.

The type of weapon installation, such as semi-submerged pylon mounted, or buried missiles, can strongly influence the nozzle lateral spacing and inter-fairing type. A wide nozzle lateral spacing was required for the F-14 aircraft, for example, in order to install the semi-submerged missiles between the engines; whereas a narrow nozzle lateral spacing was possible for the F-15 aircraft since the missiles were installed on the outboard corners of the nacelles. The location, type, and method of retracting the landing gear will effect the weapon installation which in turn may influence the nozzle lateral spacing. Installing the main landing gear between the inlets of the F-111, under the inlets of the F-15, outboard of the nacelles of the F-14, or in the wing of the F-4, for example, had a strong influence on the nozzle spacing selection for these aircraft.

The internal volume required can influence the nozzle lateral spacing. The volume may be obtained by using closely spaced engines with a long body, thus achieving a high fineness ratio, or by using widely spaced engines and a short body. The combination of length and width for the volume required may be determined by length and width restrictions, weight considerations, and area ruling the aircraft. The best fuel tank arrangement and layout for other aircraft systems or special equipment can also influence the aft-end design.

The aft-end design techniques presented herein allow the effect of performance, weight, and mission requirements to be taken into account. Predesign

guidelines and performance prediction charts were formulated for use in developing and modifying aircraft aft-end arrangements so that high thrust minus drag can be achieved. Also, post-design methods for predicting the aft-end performance of the final aircraft designs were developed (as discussed in Section 3 of Volume II) for use in conducting mission analysis studies. The mission radius for a fixed TOGW (takeoff gross weight) was selected as the criterion for evaluating the different aircraft designs. While TOGW for a fixed mission radius is a frequently applied criterion, the selected criterion yields the same relative ranking of aircraft and the associated computations are substantially simpler.

4.1.2 Design Guidelines

Considerable time and expense is involved in developing a layout of a new or modified fighter configuration and in evaluating the design using mission analysis results. In order to minimize the number of configurations subjected to the complete design process, a procedure has been formulated for screening candidate aft-end arrangements prior to developing a layout of the designs.

In this procedure, design guidelines are used initially as the rationale for developing or modifying an aft-end design. The installed thrust-minus-external drag is then estimated using drag correlation charts and nozzle thrust coefficient curves. The drag correlation charts are presented in a form such that quick tradeoffs between various nozzle types, interfairing types and lengths, and nozzle lateral spacings can be obtained. This capability is important for determining the sensitivity of drag to changes in aft-end components, especially if design requirements are such that the desired aft-end arrangement derived from the design guidelines cannot be realized. The design with the maximum installed thrust-minus-external drag at important mission conditions is then selected as the candidate configuration for the mission analysis studies.

The predesign guidelines, which were formulated from observations of the Phase II data, are listed in Table 16. The guidelines are divided into two main categories: one for aircraft missions carried out primarily at subsonic and transonic Mach numbers and the other for aircraft missions carried out primarily at supersonic Mach numbers. For missions at subsonic and transonic Mach numbers, the convergent-iris or the convergent-divergent type nozzles and the horizontal wedge interfairing with the trailing edge terminating at the exit plane of the nozzles are recommended. The cross-sectional area distribution of the aft-end should be smooth, avoiding sharp corners and steps. The nozzle lateral spacing is not critical and a single vertical stabilizer is suggested over a twin.

For missions primarily at supersonic Mach numbers, the convergent-divergent or the unshrouded plug type nozzles and either horizontal or vertical wedge interfairings with the trailing edge terminating at the exit plane of the nozzles are recommended. Again, the cross-sectional area distribution of

TABLE 16. DESIGN GUIDELINES

RECOMMENDED CONFIGURATION COMPONENTS	AIRCRAFT MISSION CATEGORIES	
	SUBSONIC-TRANSONIC	SUPERSONIC
Nozzle Type	Convergent-iris Convergent-divergent	Convergent-divergent Unshrouded plug
Interfairing Type and Length	Horizontal wedge terminating at nozzle exit plane	Horizontal or vertical wedge terminating at nozzle exit plane
Contours and Area Distribution	Smooth area distribution Avoid sharp corners and steps	Smooth area distribution Avoid sharp corners and steps Minimize boattail angle and projected frontal area
Nozzle Lateral Spacing	Not critical	Minimum
Vertical Stabilizer	Single	Single

the aft-end should be smooth, avoiding sharp corners and steps. Minimum nozzle lateral spacing and single vertical stabilizers are recommended. Unlike subsonic flow, the boattail drag increases significantly with increasing boattail angle and projected frontal area. As a result, these parameters should also be minimized.

4.1.3 Aft-End Drag Prediction Charts

The external drag for twin-nozzle/aftbody installations is provided for different nozzle lateral spacings, interfairing types, nozzle types, power settings, and nozzle pressure ratios. These twin-jet results are based on an IMS/transonic similarity correlation of the Phase II drag data and are applicable (1) over a Mach number range of 0.6 to 1.6, (2) a nozzle pressure ratio range from jet-off to typical operating nozzle pressure ratios, and (3) to fighter type aircraft having similar geometry as the Phase II model.

Empirical correlation charts have been formulated for first estimating the jet-off boattail pressure drag aft of the wing trailing edge (metric break station) and then correcting the aft-end pressure drag for jet effects. The drag correlation charts are presented in Figures 126 through 130 and are applicable to convergent, convergent-divergent, and plug type nozzles at various power settings for each of the following five aft-end arrangements. To keep the procedure simple, the skin friction and nozzle base drags were neglected.

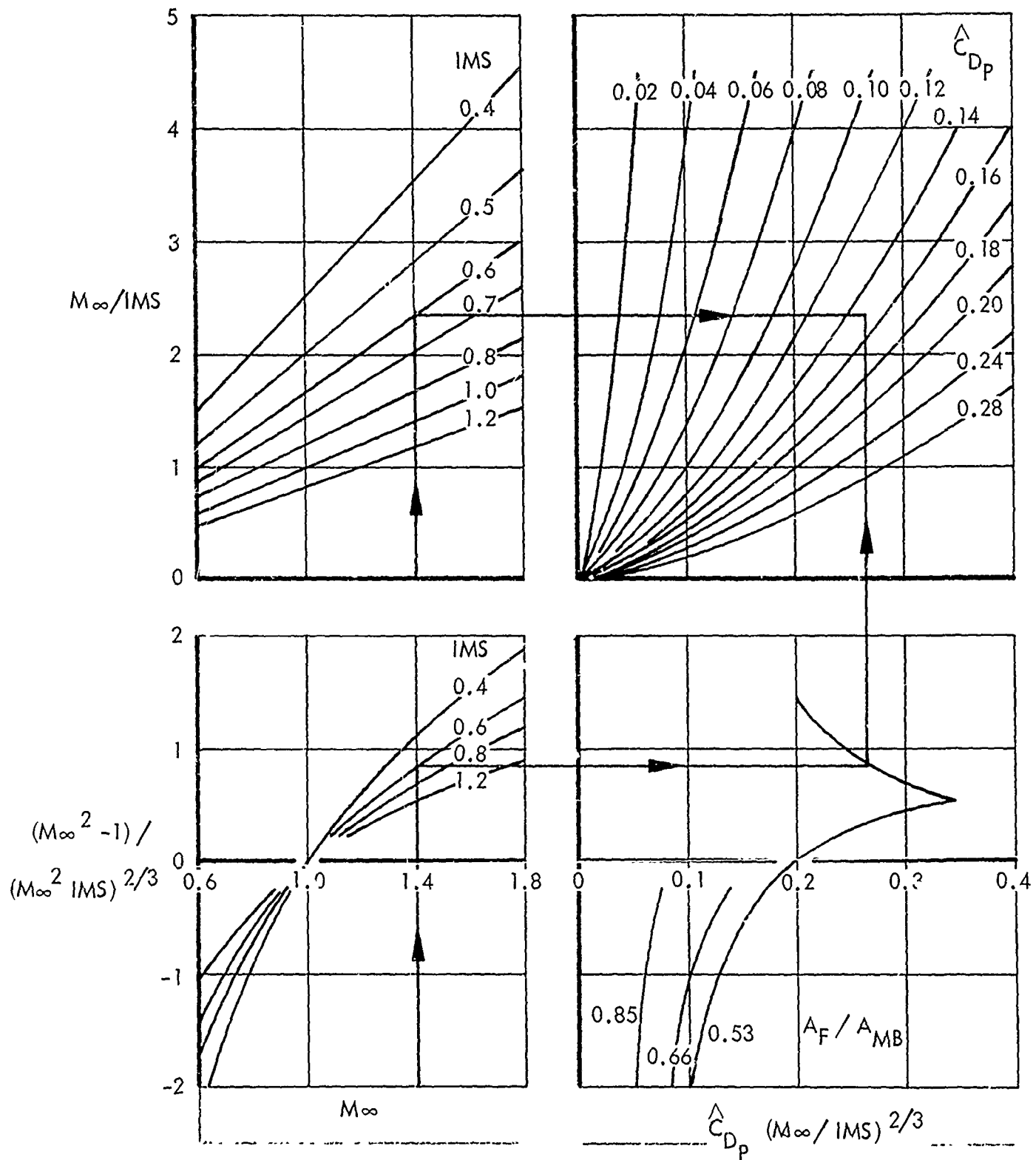


Figure 126. Chart for Estimating Twin-Jet Aft-End Drag - Narrow Spacing Ratio, Horizontal Interfiring, and Single Vertical Stabilizer

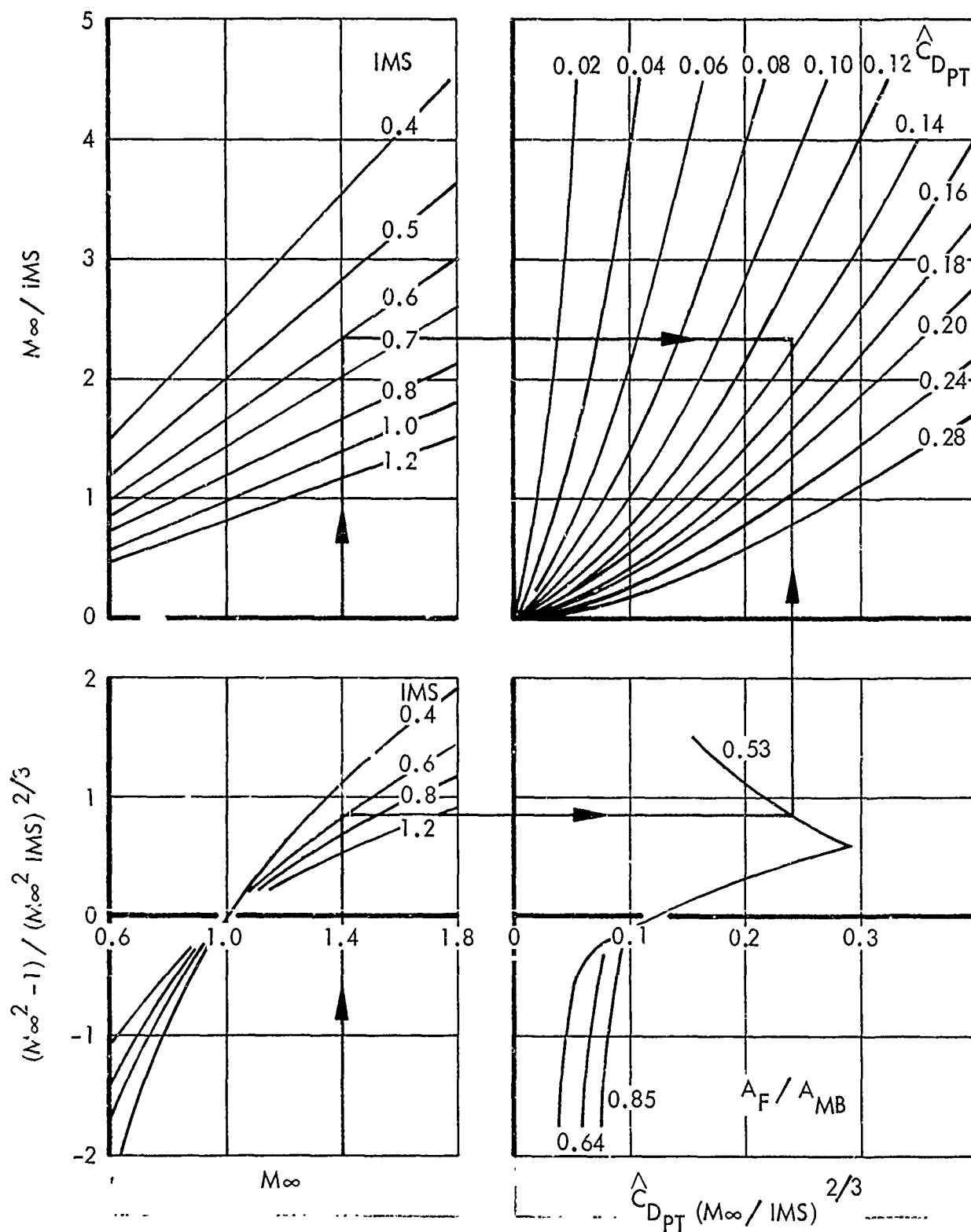


Figure 127. Chart for Estimating Twin-Jet Aft-End Drag - Narrow Spacing Ratio, Vertical Interfairing, and Single Vertical Stabilizer

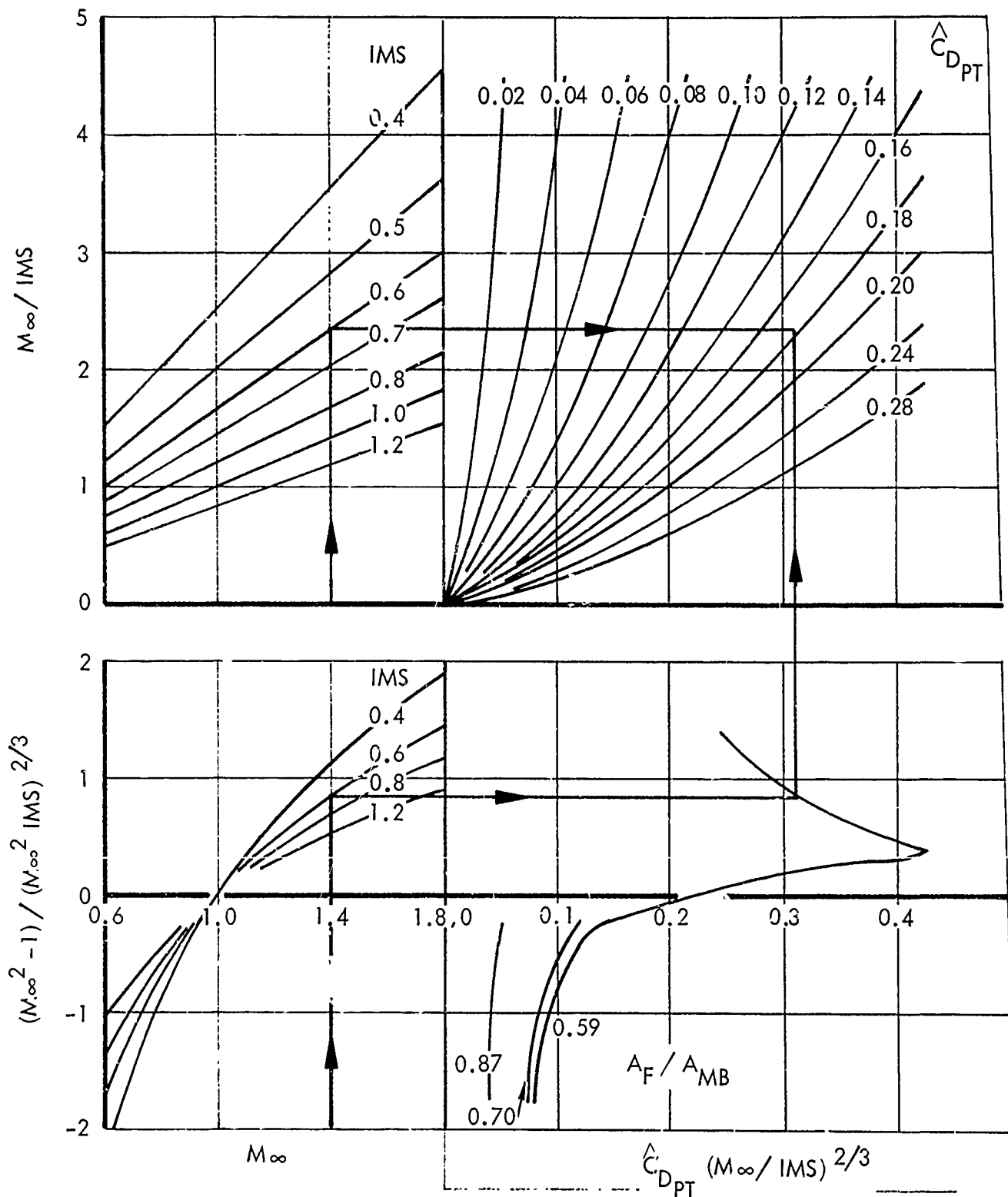


Figure 128. Chart for Estimating Twin-Jet Aft-End Drag - Intermediate Spacing, Horizontal Interfiring, and Single Vertical Stabilizer

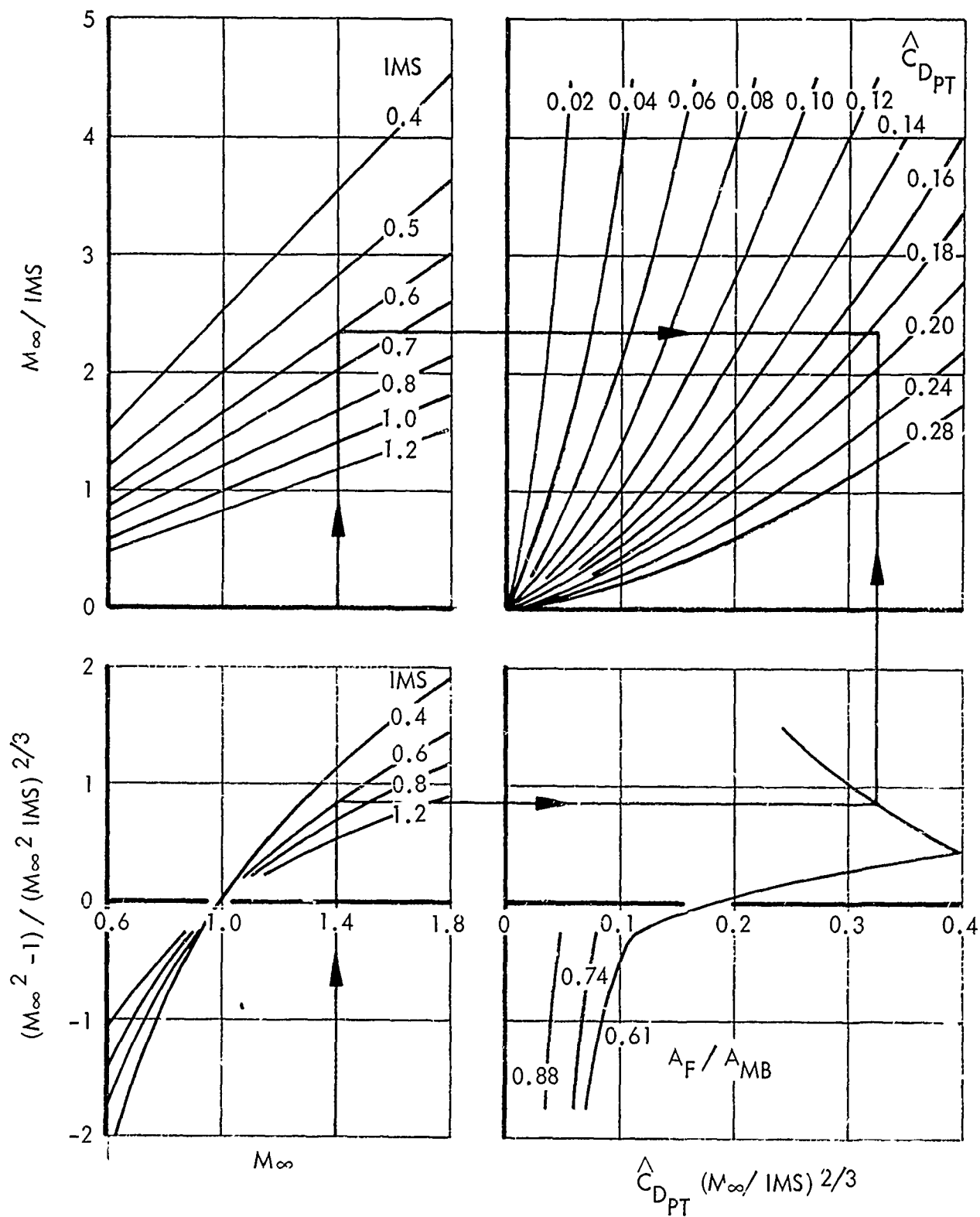


Figure 129. Chart for Estimating Twin-Jet Aft-End Drag - Wide Spacing Ratio, Horizontal Interfairing, and Single Vertical Stabilizer

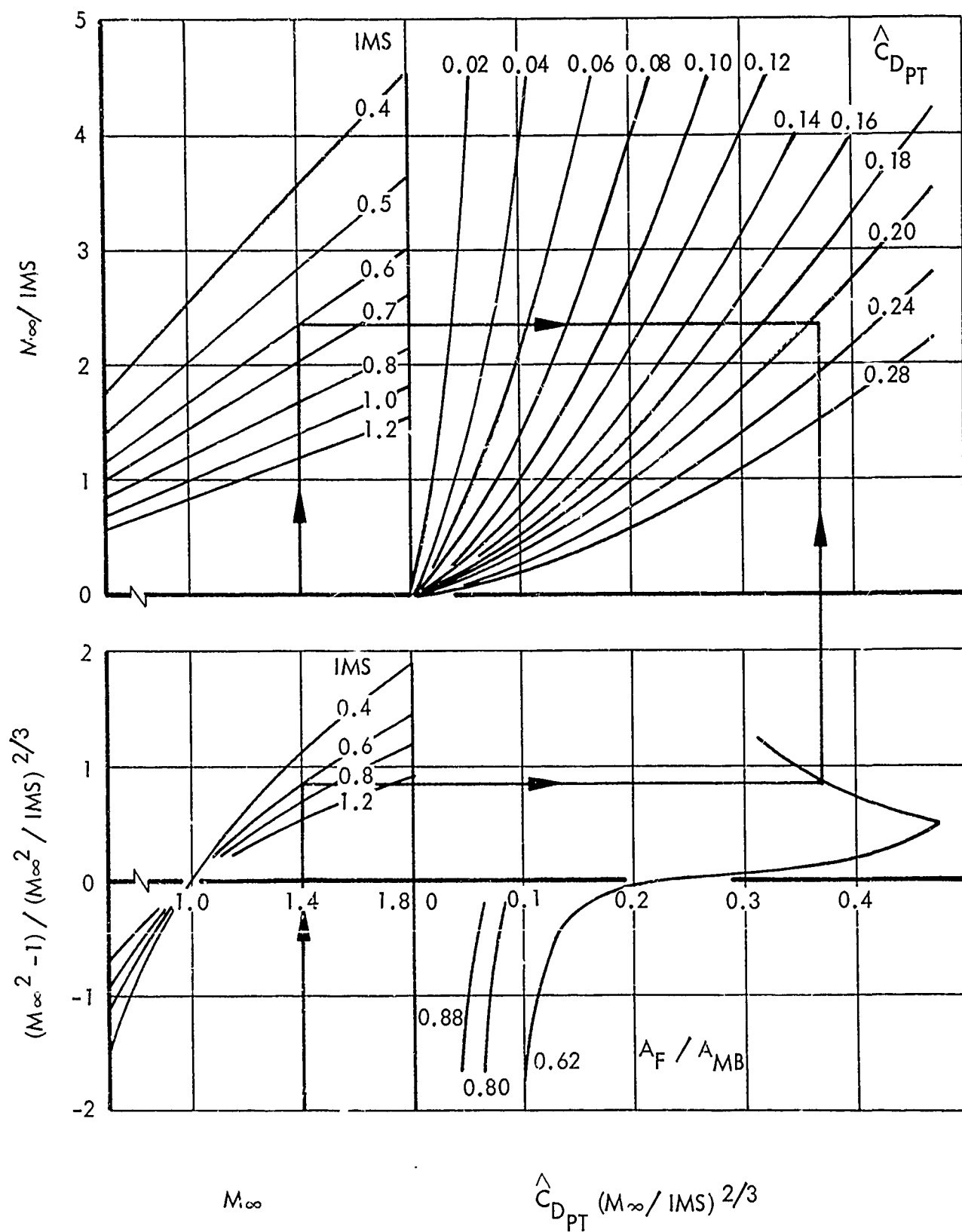


Figure 130. Chart for Estimating Twin-Jet Aft-End Drag - Wide Spacing, Horizontal Interfairing, and Twin Vertical Stabilizers

<u>Nozzle Spacing</u>	<u>Interfairing</u>	<u>Vertical Stabilizer</u>
Narrow	Horizontal Wedge	Single
Narrow	Vertical Wedge	Single
Intermediate	Horizontal Wedge	Single
Wide	Horizontal Wedge	Single
Wide	Horizontal Wedge	Twin

Only three inputs are required to obtain the jet-off aft-end pressure drag coefficient based on projected frontal area, \hat{C}_{DP} , from the charts, viz, free-stream Mach number, M_∞ , projected frontal to metric break area ratio, A_F/A_{MB} , and integral mean slope, IMS. Since the cross-sectional area distribution is not known during the predesign stage, an estimate of IMS must be employed. The IMS for typical twin-nozzle/aftbody designs is generally within the 0.4 to 0.7 range, as shown in Table 17 for selected Phase II model configurations.

In order to correct the aft-end pressure drag coefficient for jet effects, jet-on to jet-off aft-end drag ratios are presented in Figure 131 as a function of adjusted nozzle pressure ratio, $(P_{T_N}/P_\infty)_a$, internal shroud exit angle, and freestream Mach number. These drag ratios were found essentially to be independent of nozzle lateral spacing, interfairing type, and vertical stabilizer type. The adjusted nozzle pressure ratio is related to the nozzle exit to freestream static pressure ratio, P_E/P_∞ , and nozzle pressure ratio,

P_{T_N}/P_∞ , as indicated below,

$$(P_{T_N}/P_\infty)_a = (P_{T_N}/P_{TH}) (P_E/P_{TH}) (P_{T_N}/P_\infty) \quad (2)$$

where P_{T_N}/P_{TH} is nozzle throat total to static pressure ratio, which is a constant for choked flow, and P_E/P_{TH} is the nozzle exit to throat static pressure ratio. For convergent and unshrouded plug nozzles the adjusted nozzle pressure ratio is equal to the nozzle pressure ratio. For convergent-divergent nozzles, the adjusted nozzle pressure ratio is generally less than the nozzle pressure ratio due to supersonic flow expansion within the nozzle.

To demonstrate the above method, some numerical examples are given in Table 18 for the narrow spacing ratio configuration with vertical interfairing, single vertical stabilizer, and convergent-divergent nozzle. Predicted and measured twin-jet aft-end drags for these examples are compared in Figure 132 and show good agreement. The step-by-step procedure for obtaining the numerical results is outlined below.

TABLE 17. GEOMETRIC PARAMETERS FOR PHASE II AFT-END CONFIGURATION

CONFIGURATION	PROJECTED FRONTAL TO METRIC BREAK AREA RATIO	NOZZLE INTERNAL EXIT ANGLE	INTEGRAL MEAN SLOPE - IMS
N1B CI ₁	0.86	- 9.0°	0.677
N1B CI ₃	0.72	- 2.0°	0.636
N1B CD ₁	0.85	2.5°	0.583
N1B CD ₂	0.73	4.0°	0.499
N1B CD ₃	0.53	11.5°	0.465
N3D CD ₁	0.85	2.5°	0.623
N3D CD ₂	0.73	4.0°	0.514
N3D CD ₃	0.53	11.5°	0.445
N1B UPAC ₁	0.66	-24.0°	0.605
N1B UPAC ₂	0.59	-19.0°	0.501
N1B UPAC ₃	0.51	-15.0°	0.503
I1B CD ₁	0.87	2.5°	0.593
I1B CD ₃	0.59	11.5°	0.519
W1B CD ₁	0.88	2.5°	0.621
W1B CD ₂	0.64	11.5°	0.577
N5D CD ₁	0.85	2.5°	0.550
N5D CD ₂	0.74	4.0°	0.423
N5D CD ₃	0.53	11.5°	0.334
W4D CD ₁	0.87	2.5°	0.627
W4D CD ₂	0.77	4.0°	0.532
W4D CD ₃	0.59	11.5°	0.446
N6D CD ₁	0.85	2.5°	0.646
N6D CD ₂	0.74	4.0°	0.528
N6D CD ₃	0.53	11.5°	0.435

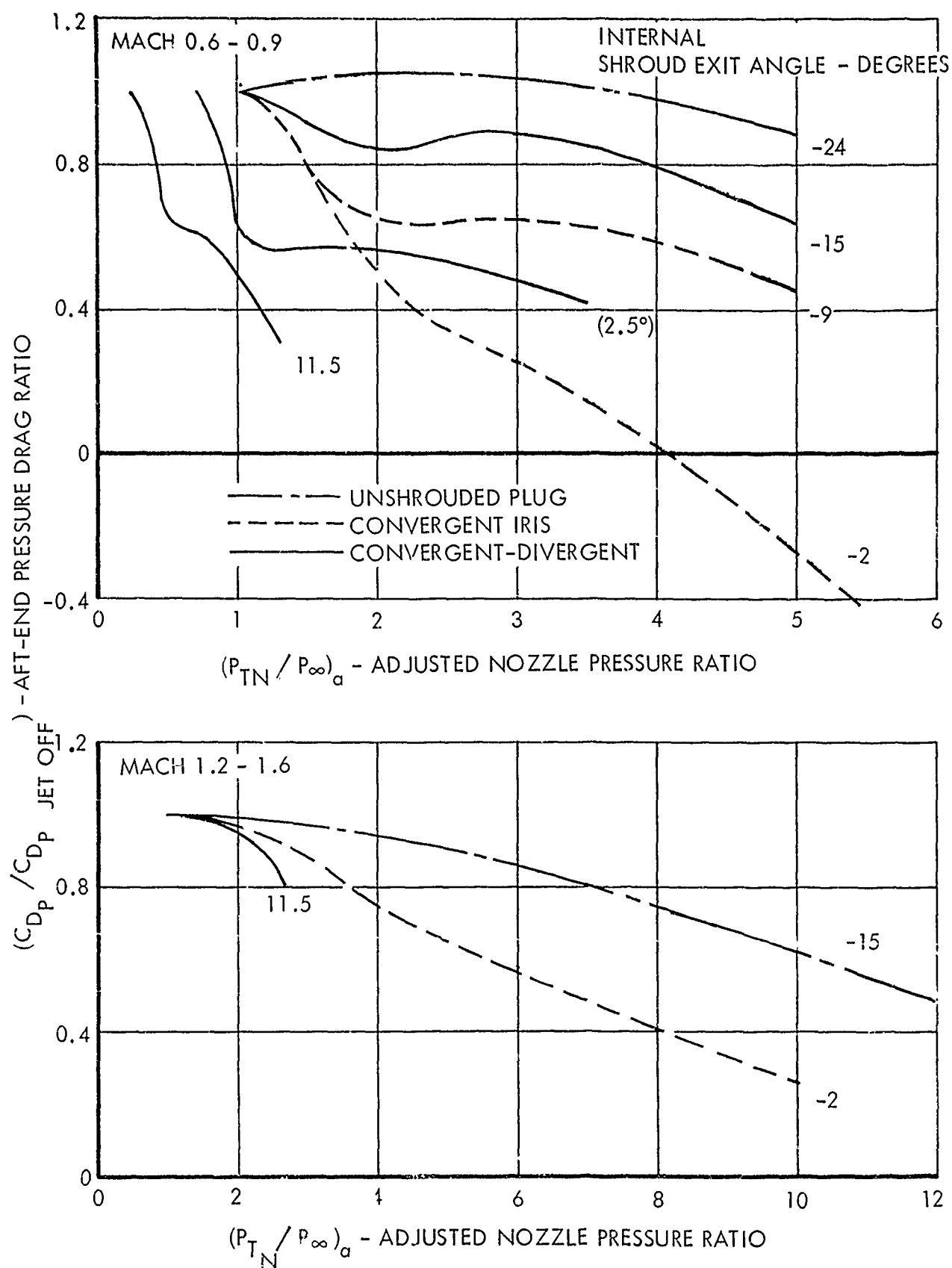


Figure 131. Effect of Adjusted Nozzle Pressure Ratio on Total Boattail Pressure Drag

TABLE 18. APPLICATION OF DESIGN CHARTS

Configuration: $S_L Y_L H_{lp}^{-2} V_{N3DCD}, \gamma_j = 1.4$

NOZZLE POWER SETTING	M_∞	P_T/P_∞	A_F/A_{MB}	θ_{INT}	IMS	$\hat{C}_{D_{PT}}$ (JET OFF)	P_E/P_{TH}	$(P_T/P_\infty)_a$	$\frac{\hat{C}_{D_{PT}}}{\hat{C}_{D_{PT}}}$ (JET OFF)	$\hat{C}_{D_{PT}}$ (JET ON)
Normal	0.6	3	0.85	2.5°	0.623	0.077	0.62	1.86	0.565	0.0435
Normal	0.8	3	0.85	2.5°	0.623	0.072	0.62	1.86	0.565	0.0406
Normal	0.9	3	0.85	2.5°	0.623	0.059	0.62	1.86	0.565	0.0335
Max A/B	0.9	3	0.53	11.5°	0.445	0.037	0.266	0.80	0.590	0.0218
Max A/B	1.2	6	0.53	11.5°	0.445	0.149	0.266	1.60	0.981	0.1468
Max A/B	1.6	8	0.53	11.5°	0.445	0.069	0.266	2.12	0.940	0.0649

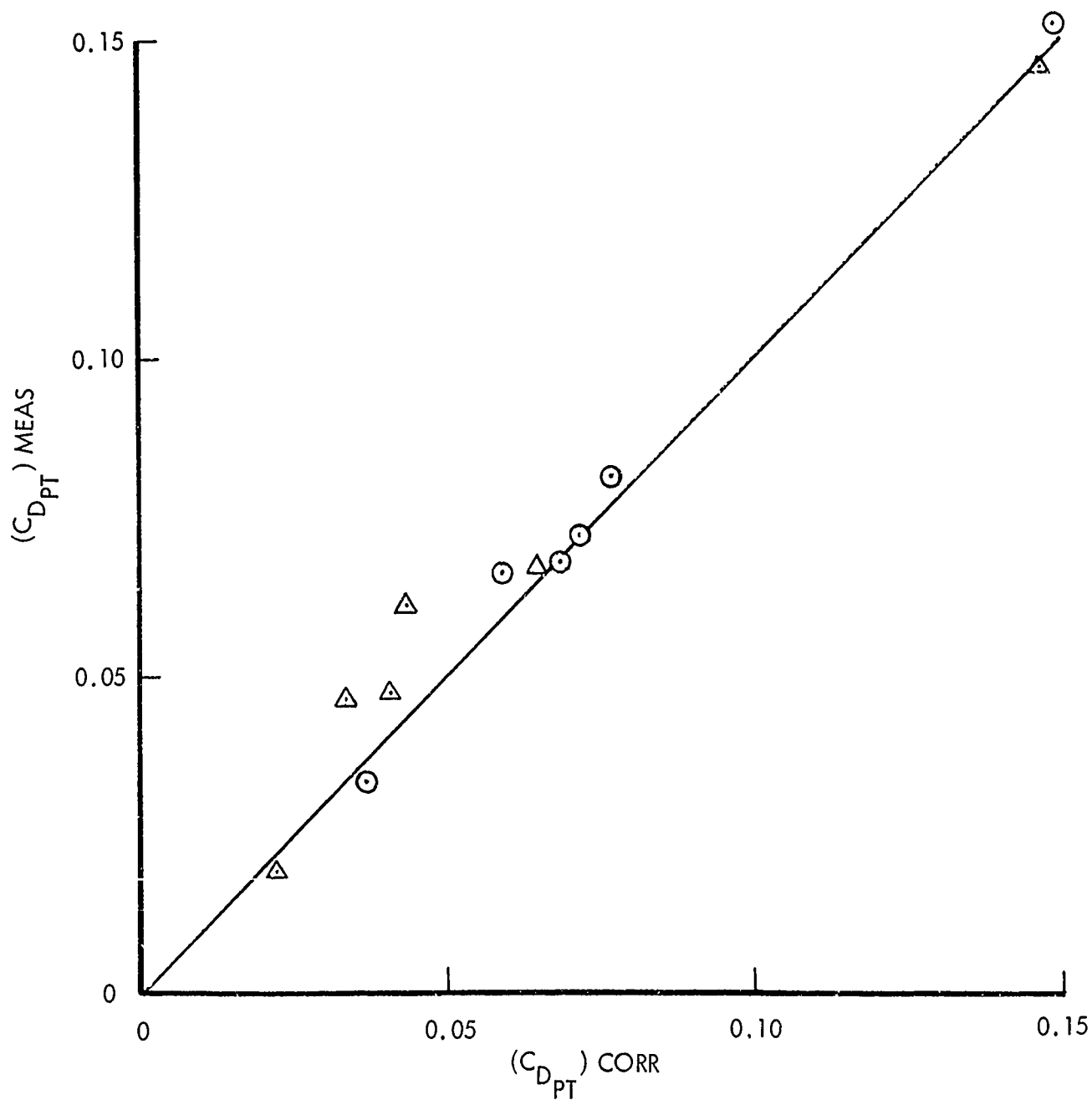


Figure 132. Comparison Between Predicted and Measured Twin-Jet Aft-End Drags — Narrow Spacing Ratio, Vertical Interfiring, and Single Vertical Stabilizer

The projected frontal to metric break area ratio, nozzle internal exit angle, and integral mean slope are found from Table 17. The jet-off aft-end drag coefficient based on projected frontal area is read from Figure 127. Knowing the exit to throat area ratio for the particular nozzle power setting, the nozzle exit to throat static pressure ratio is computed from compressible flow tables. Then, the adjusted nozzle pressure ratio, which is equal to the product of nozzle exit to throat static pressure ratio and nozzle pressure ratio, is used along with the nozzle type and internal exit angle to determine the jet-on and jet-off aft-end drag ratio from Figure 131. The jet-on drag coefficient is equal to the product of jet-off drag coefficient and jet-on to jet-off drag ratio.

4.1.4 Nozzle Thrust Coefficient Curves

Computed nozzle thrust coefficients, including under expansion and overexpansion losses, are presented in Figures 133 through 136 as functions of nozzle pressure ratio, nozzle exit to throat area ratio, A_E/A_T , and specific heat ratio, γ_j . These results enable thrust coefficients for convergent, convergent-divergent, and plug type nozzles to be estimated for quick trade-off studies. The exit to throat area ratio is unity for convergent nozzles and equal to the corresponding physical areas for convergent-divergent nozzles. For the plug nozzle, the exit to throat area ratio of unity is used at low nozzle pressure ratios and the exit to throat area ratio equal to the plug shroud to plug throat area ratio is used at high nozzle pressure ratios. The low and high nozzle pressure ratio regions are separated by the pressure ratio where the thrust coefficients for the two regions are equal.

The nozzle thrust is computed from the thrust coefficient in the following manner.

$$\text{Thrust} = \left(\frac{F_{ip}}{P_{T_N} A_T} \right) \left(\frac{P_{T_N}}{P_\infty} \right) (P_\infty A_T) C_T$$

where

$$\left(\frac{F_{ip}}{P_{T_N} A_T} \right)$$

Ideal thrust (complete expansion to freestream ambient pressure) ratio,

$$f(\gamma_j) \left[1 - \left(\frac{P_{T_N}}{P_\infty} \right)^{\frac{1 - \gamma_j}{\gamma_j}} \right]^{1/2}$$

$$f(\gamma_j)$$

Specific heat ratio function,

$$\left[\frac{2 \gamma_j^2}{\gamma_j - 1} \left(\frac{2}{\gamma_j + 1} \right)^{\frac{\gamma_j + 1}{\gamma_j - 1}} \right]^{1/2}$$

γ_j	Jet specific heat ratio
$\left(\frac{P_{T_N}}{P_\infty}\right)$	Nozzle pressure ratio
P_∞	Ambient pressure
A_T	Nozzle throat area
C_T	Thrust coefficient

For convenience the ideal thrust ratio ($F_{ip}/P_{T_N} A_T$) is given in Figure 137 as a function of nozzle pressure ratio for jet specific heat ratios of 1.25 and 1.4.

4.2 APPLICATION OF DESIGN TECHNIQUES

4.2.1 Procedure

Mission analysis studies have been used in developing and selecting twin-nozzle/aftbody installations, by means of the procedure illustrated in Figure 138.

This procedure permits the evaluation of the trade-offs between engine thrust, aircraft weight, and external drag. The sensitivity of the results to changes in mission requirements can also be evaluated. A further benefit of the adopted procedure is that it provides a framework for utilizing the performance prediction methods developed during the program (Reference 76).

In the first step of the procedure a baseline configuration is selected from among those tested during Phase II, with prime consideration being given to potential performance improvement and relevancy to current design trends. The engine thrust, aircraft weight, and external drag for each selected design is then predicted and used in conducting mission analysis studies. The mission radius for a fixed TOGW (takeoff gross weight) of 45,000 pounds was selected as the criterion for evaluating the different aircraft designs. The mission radius for each baseline configuration is determined for each of the following three representative fighter missions: escort (subsonic), point intercept (primarily supersonic), and mixed (transonic).

The next step of the procedure requires that the aft-end lines of the baseline configuration be modified so that an improved candidate installation results. The rationale for these modifications is derived from an analysis of the baseline mission results, design criteria and guidelines developed for the candidate configuration is then calculated using predicted values for the engine thrust, aircraft weight, and external drag, as was done for the baseline configuration. If the mission radius for the candidate configuration is greater than that for the baseline configuration, then the new design will be considered an improved installation.

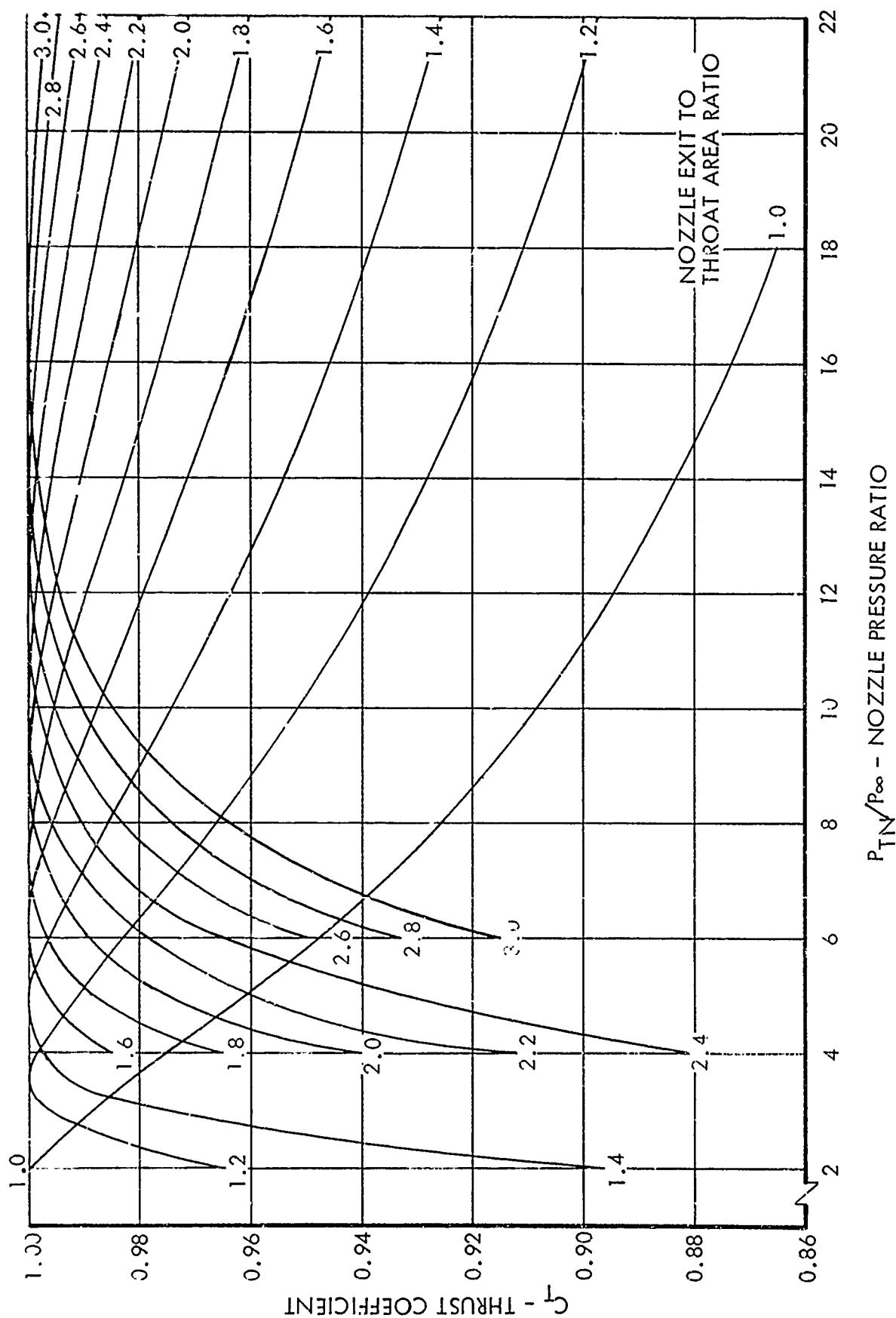


Figure 133. Nozzle Thrust Coefficients - Jet Specific Heat Ratio 1.25

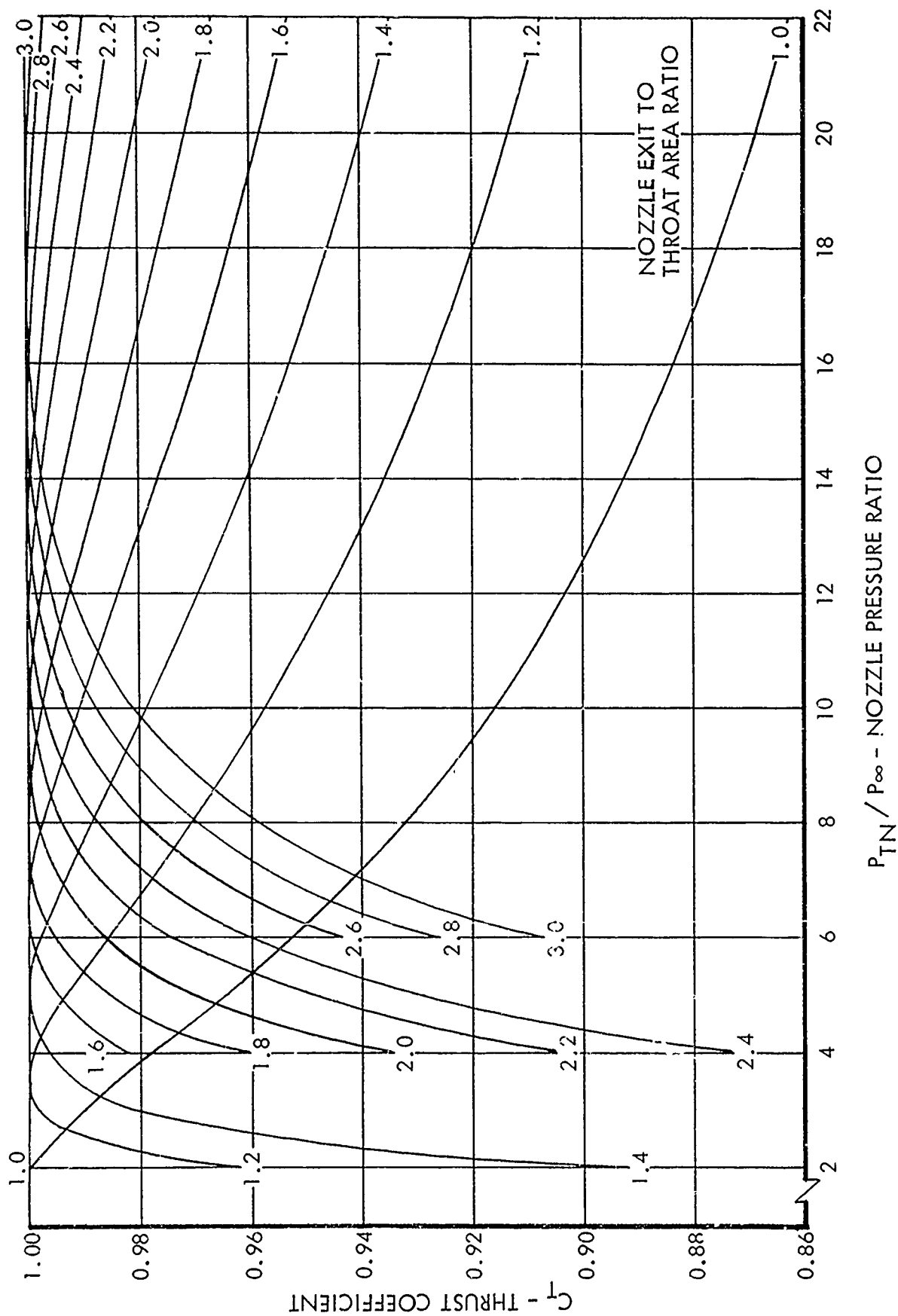


Figure 134. Nozzle Thrust Coefficients - Jet Specific Heat Ratio 1.30

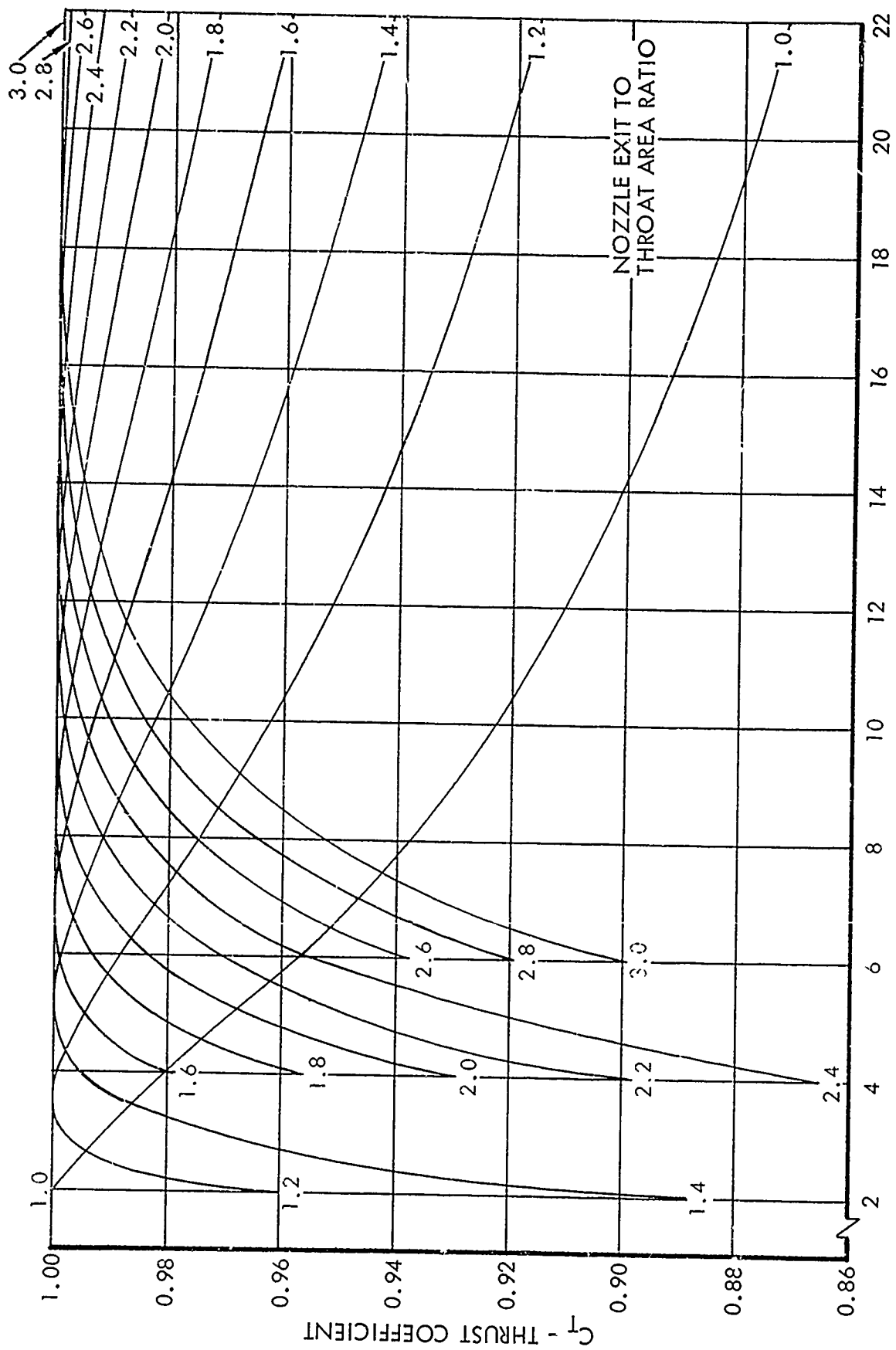


Figure 135. Nozzle Thrust Coefficients - Jet Specific Heat Ratio 1.35

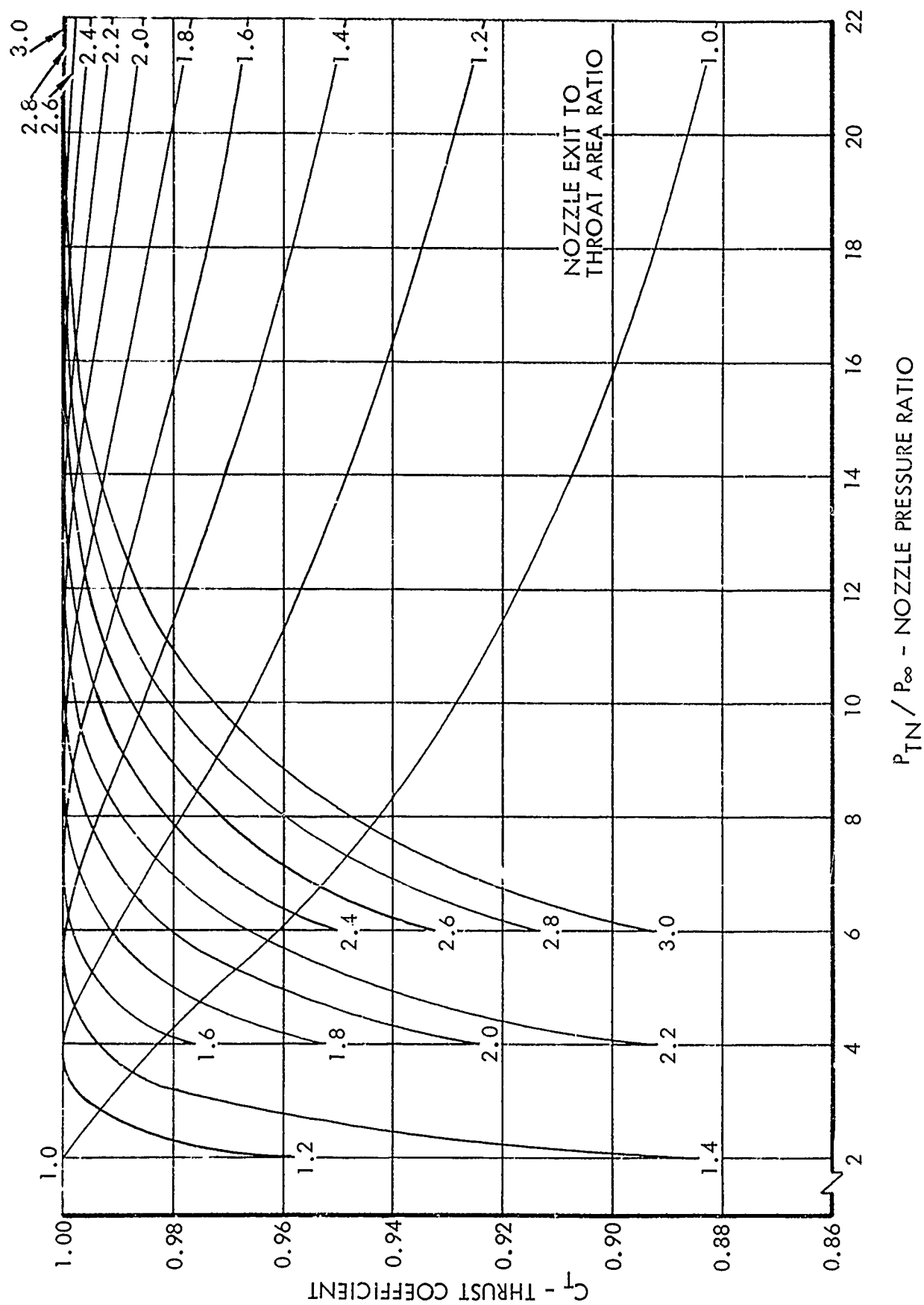


Figure 136. Nozzle Thrust Coefficients - Jet Specific Heat Ratio 1.40

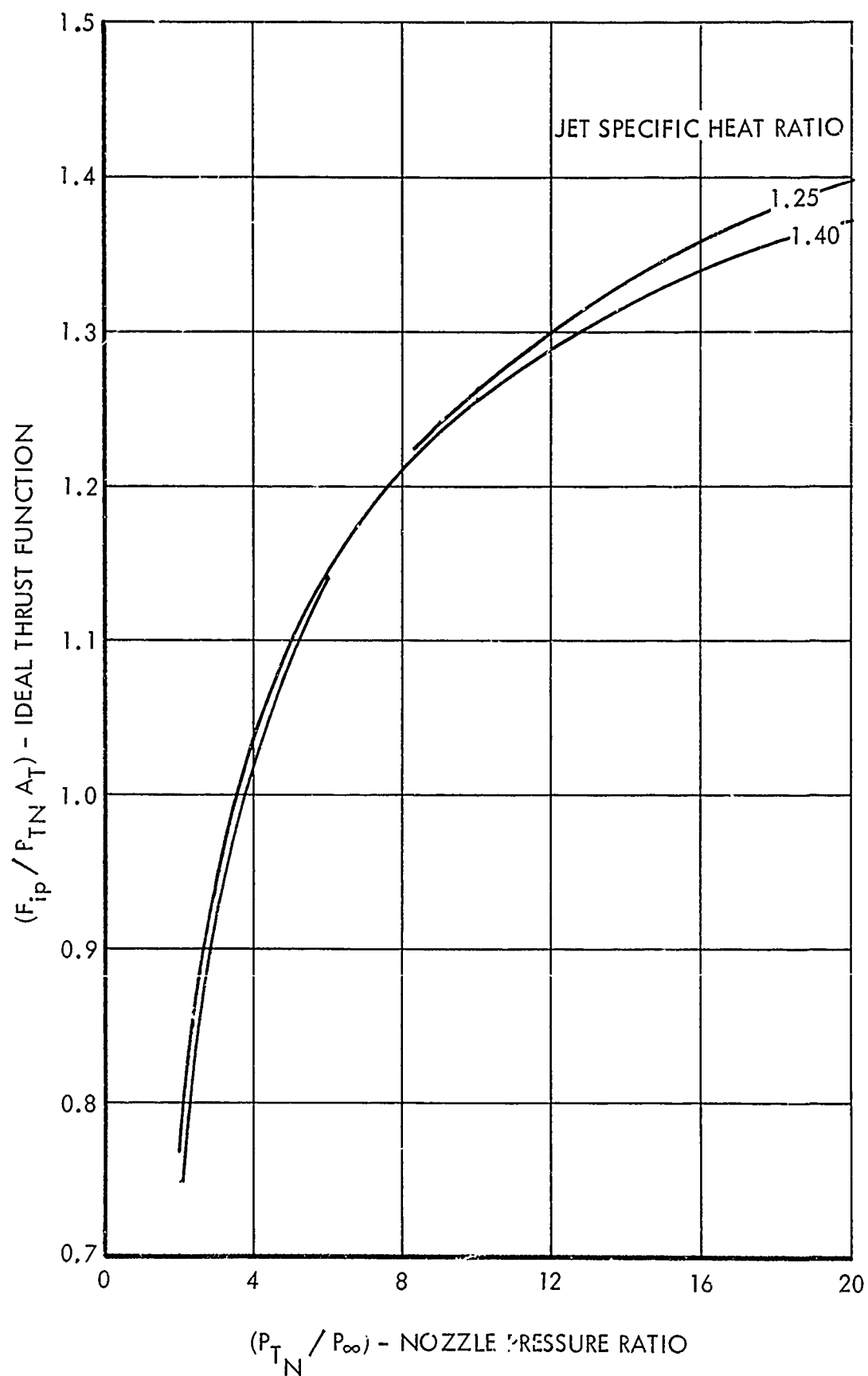


Figure 137. Thrust Function

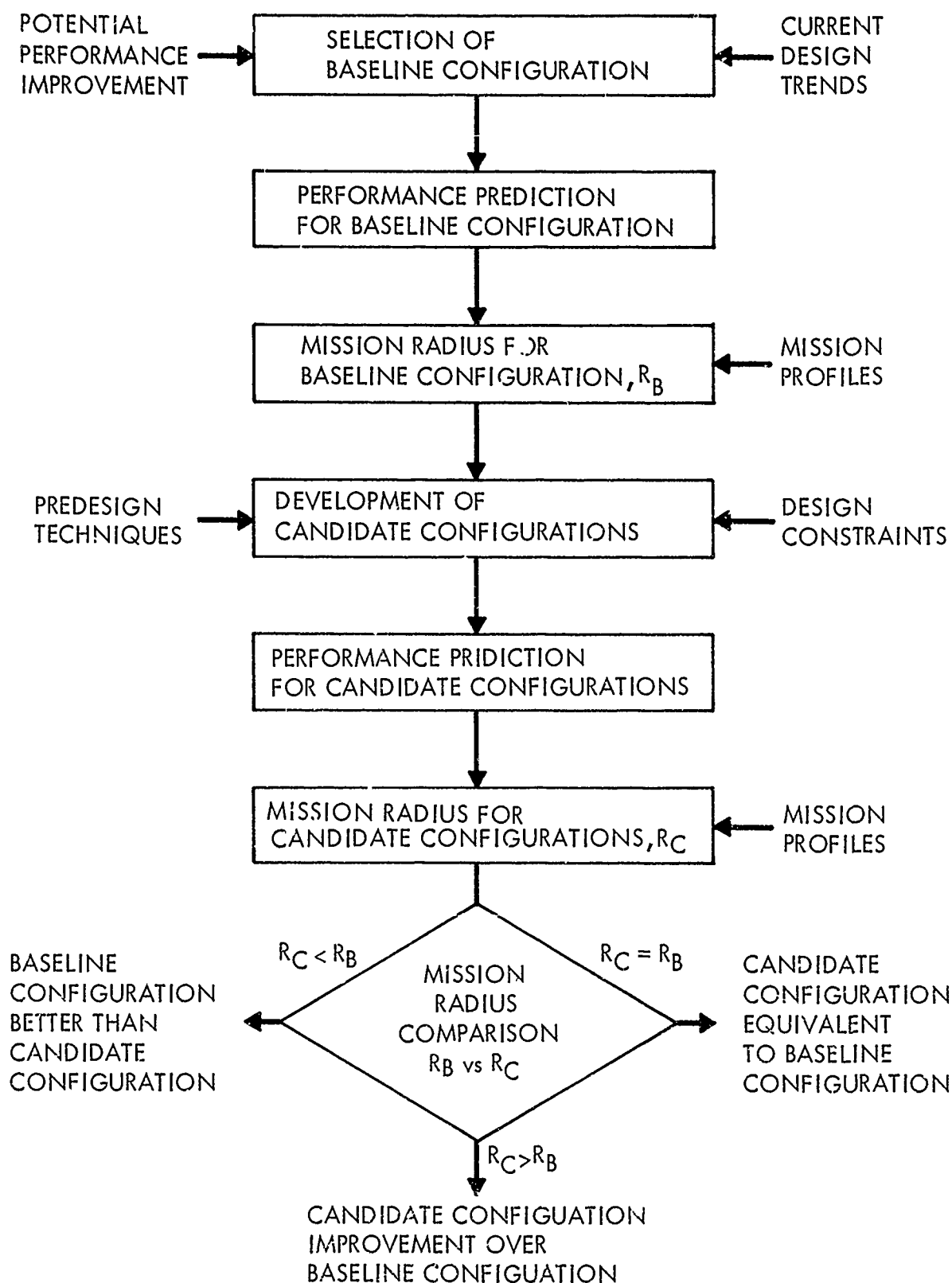


Figure 138. Procedure for Developing Improved Twin-Nozzle/Aftbody Installations

The procedure for developing improved twin-nozzle aftbody installations is applied below to five baseline configurations. The selection of the baseline configurations is presented first followed by a discussion of the development of the candidate configurations. Finally, the selection of the improved designs based on a comparison of mission analysis results is presented.

4.2.2 Baseline Configuration Selection

A total of five baseline configurations were selected from among those tested during Phase II. As discussed in Subsection 2.1.2, the basic test configuration is a modified version of the A-2 twin-jet air superiority fighter design evolved by GD under the AFFDL-sponsored Supersonic Inlet Design and Airframe-Inlet Integration Program (Reference 57). This design, designated as the Calac CL-1250, has a high wing, half-axisymmetric inlets mounted on the sides of the fuselage forward of the wing leading edge, and close coupled stabilizers, as illustrated in Figure 139.

Twin P&WA STF-371 turbofan engines are located in the fuselage of the CL-1250. The forebody is contoured to accommodate the high wing and to avoid conditions which could promote the separation of a viscous shear layer forward and low enough to be ingested by the inlet. The wing has an area of 575 square feet, aspect ratio of 3.37, leading edge sweep angle of 31.5 degrees, and leading and trailing edge flaps. The canopy is designed to give unimpaired visibility in the upper hemisphere and reasonable down vision. The nose drop angle is set by a requirement for 15 degrees down vision over the nose for landing and for air-to-air combat. The nose and main landing gear retract forward, and the main landing gear wheel rotates 90 degrees to lie flat under the inlet duct.

The five selected baseline configurations are identified in Table 19. The selection of these configurations was based primarily on potential performance improvement and relevancy to current design trends. The baseline configurations provide an interesting matrix in that the primary configuration variables investigated during Phase II, viz., nozzle type and spacing, inter-fairing type and length, and vertical stabilizer type, are all represented. The baseline configurations are listed in three forms in Table 19: (1) an abbreviated form used in the subsequent discussions; (2) the standard Calac vehicle identification form, and (3) in terms of the Phase II model component designations.

An isometric drawing of the X-1 configuration is shown in Figure 140. This configuration closely resembles the initial F-111 design and for this reason was chosen as a baseline configuration. A simulation of the F-111 aft-end was considered important since the F-111 was the most advanced fighter in production at the beginning of the contract. Also, the airframe-nozzle integration problems encountered with the F-111 provided the primary impetus for initiating this and other propulsion research programs. The narrow spaced X-1 configuration can be easily modified to reduce the aft-end drag, especially at subsonic speeds, by replacing the vertical interfairing with a horizontal wedge interfairing.

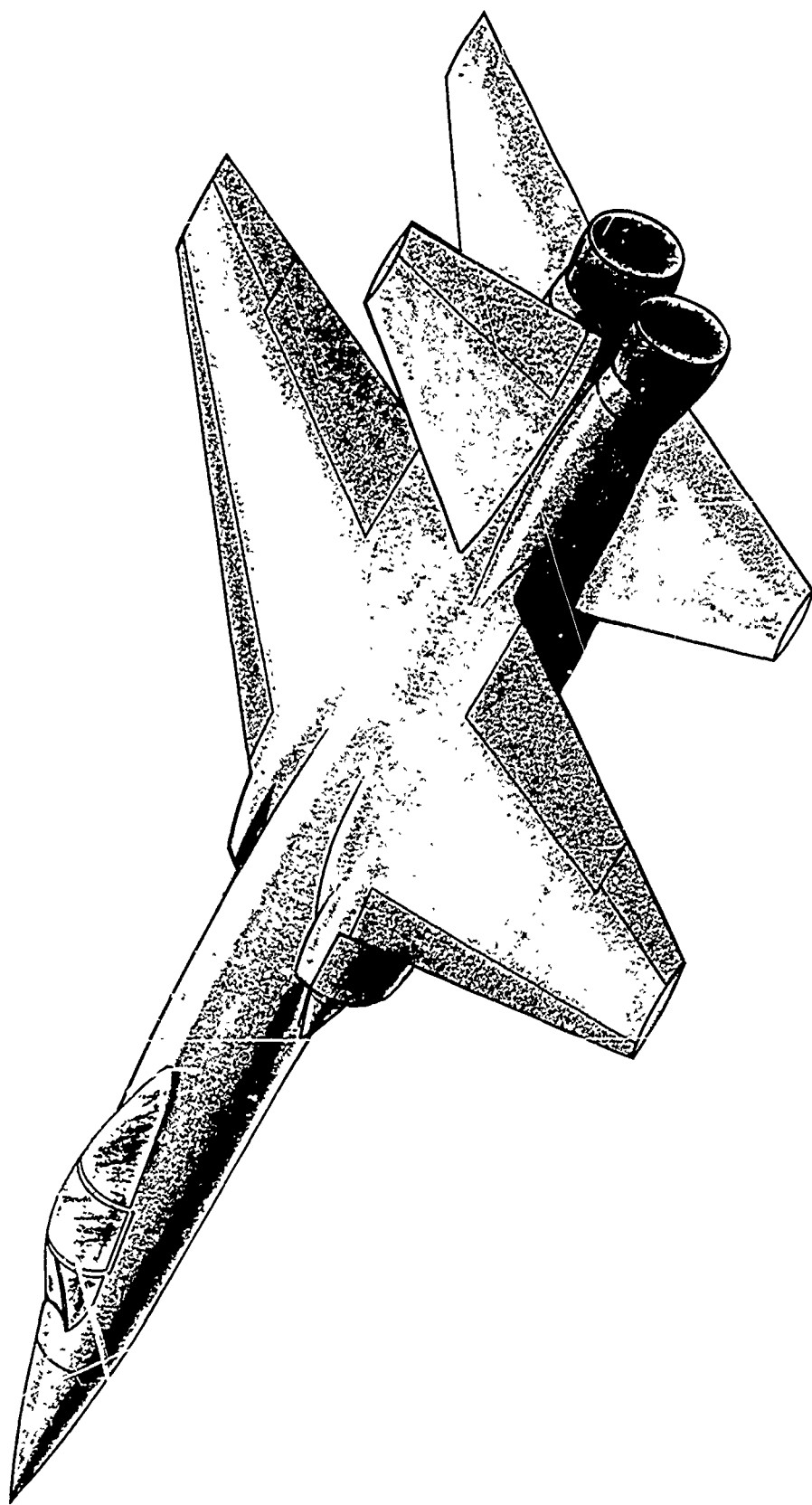


Figure 139. Calac CL-1250 Air Superiority Fighter

TABLE 19. IDENTIFICATION OF BASELINE CONFIGURATIONS

REPORT DESIGNATION	CALAC VEHICLE DESIGNATION	PHASE II MODEL COMPONENT DESIGNATIONS
X-1	CL 1250-3	$S_1 Y_1 H_{1P}^{-2} V_{2P} N3D CD$
X-2	CL 1250-4	$S_1 Y_1 H_{1P}^{-2} V_{2P} I2D CD$
X-3	CL 1250-7	$S_1 Y_1 H_{1P}^{-2} V_{3PR} W2D CD$
X-4	CL 1250-6	$S_1 Y_1 H_{1P}^{-2} V_{1P} N1B CDE$
X-5	CL 1250-6A	$S_1 Y_1 H_{1P}^{-2} V_{1P} N1B CF$

An isometric drawing of the X-2 configuration is shown in Figure 141. This design, which has an intermediate nozzle spacing and a horizontal wedge interfairing with the trailing edge terminating at the exit plane of the convergent-divergent nozzles, was selected since it represents a design intermediate between the X-1 and X-3 configurations. The X-3 configuration, which is shown in Figure 142, is somewhat similar to the F-14 in that it has a wide nozzle spacing, horizontal interfairing, and twin vertical stabilizers. The aft-end drag of the X-3 configuration can be improved by replacing the twin vertical stabilizers with a single vertical stabilizer and by reducing the fuselage area between the engine nacelles.

The X-4 and X-5 configurations are identical except for the choice of nozzles. They both are narrow spaced configurations and have horizontal wedge interfairings with the trailing edge terminating at the nozzle customer connect station, as shown in Figure 143. The lower performance of the convergent flap nozzles installed in the X-4 configuration has been compromised in order to reduce nozzle weight. A higher weight of the convergent-divergent ejector nozzle installed in the X-5 configuration has been accepted in order to obtain maximum performance. An improved design can be obtained by compromising both performance and weight.

Each baseline aircraft used in the mission analysis studies has contours identical to those corresponding wind tunnel models, with the following two exceptions. First, the aircraft design did not include the side fuselage fairing, which was cantilevered from the model centerbody and used to support the horizontal stabilizers. Secondly, the aircraft design included provision for armament, whereas such provisions were excluded from the Phase II model design so that the wind tunnel results would not be dependent on a single specific missile installation. Provisions were made in the aircraft design for a 25 mm gun to be located under the fuselage aft of the nose gear and for four Sparrow missiles to be installed semi-submerged — two along the fuselage centerline

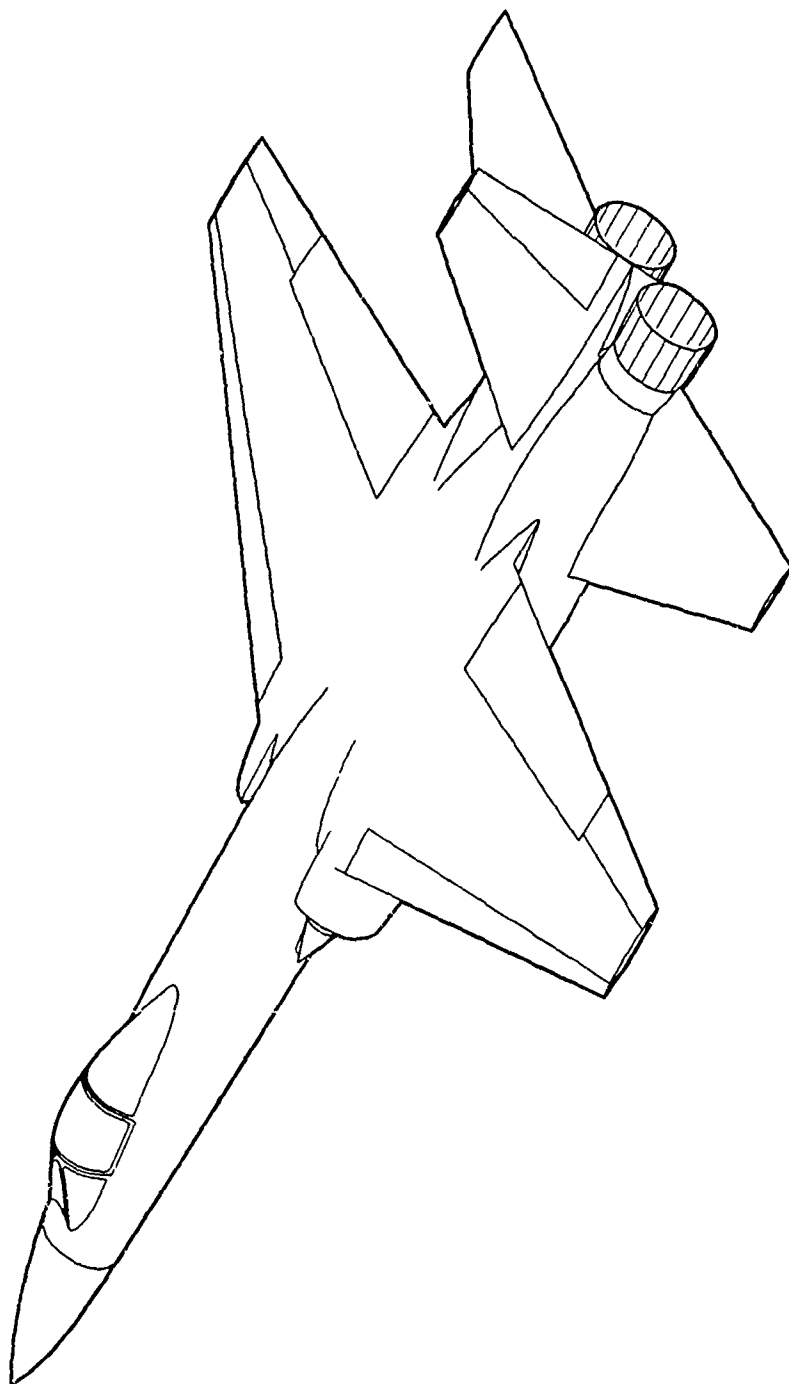


Figure 140. X-1 Baseline Turbofan Configuration

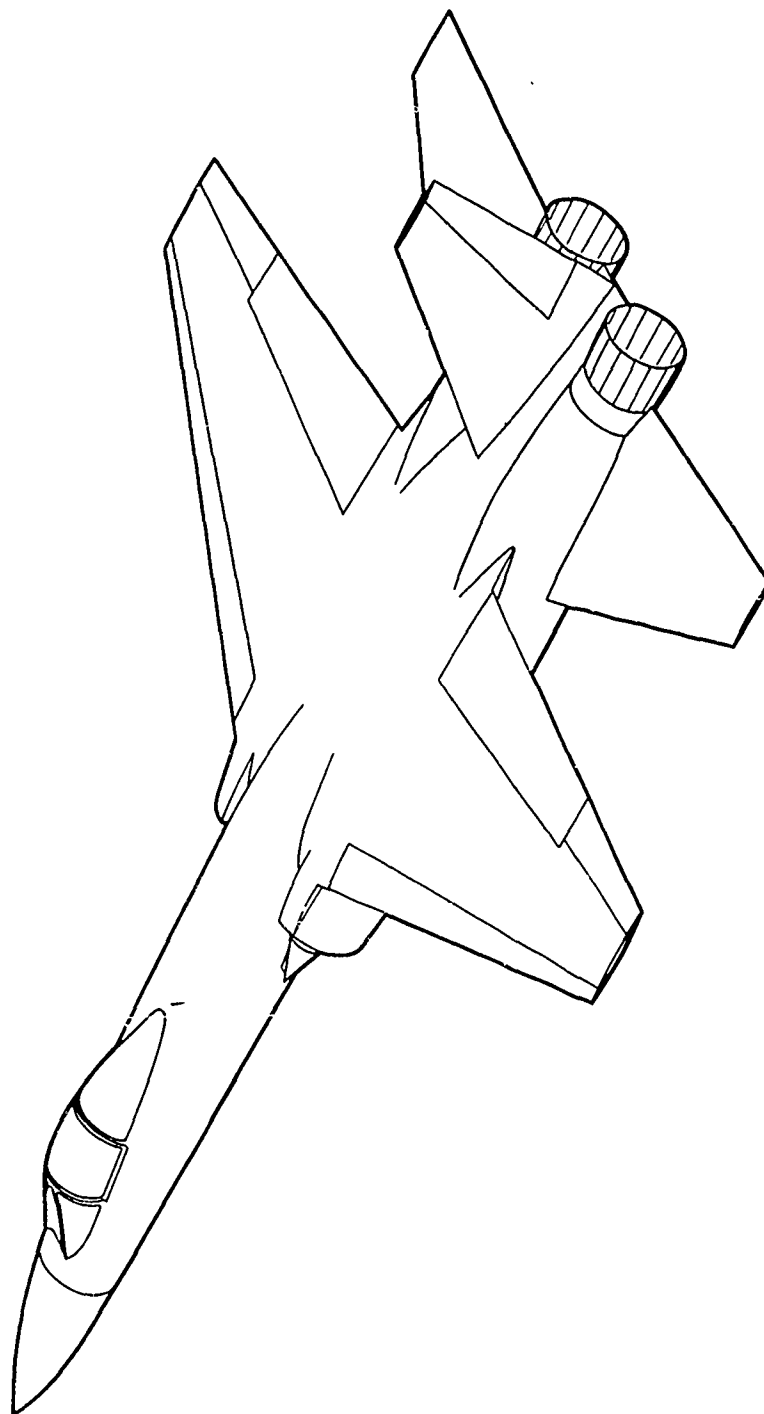


Figure 141. X-2 Baseline Turbofan Configuration

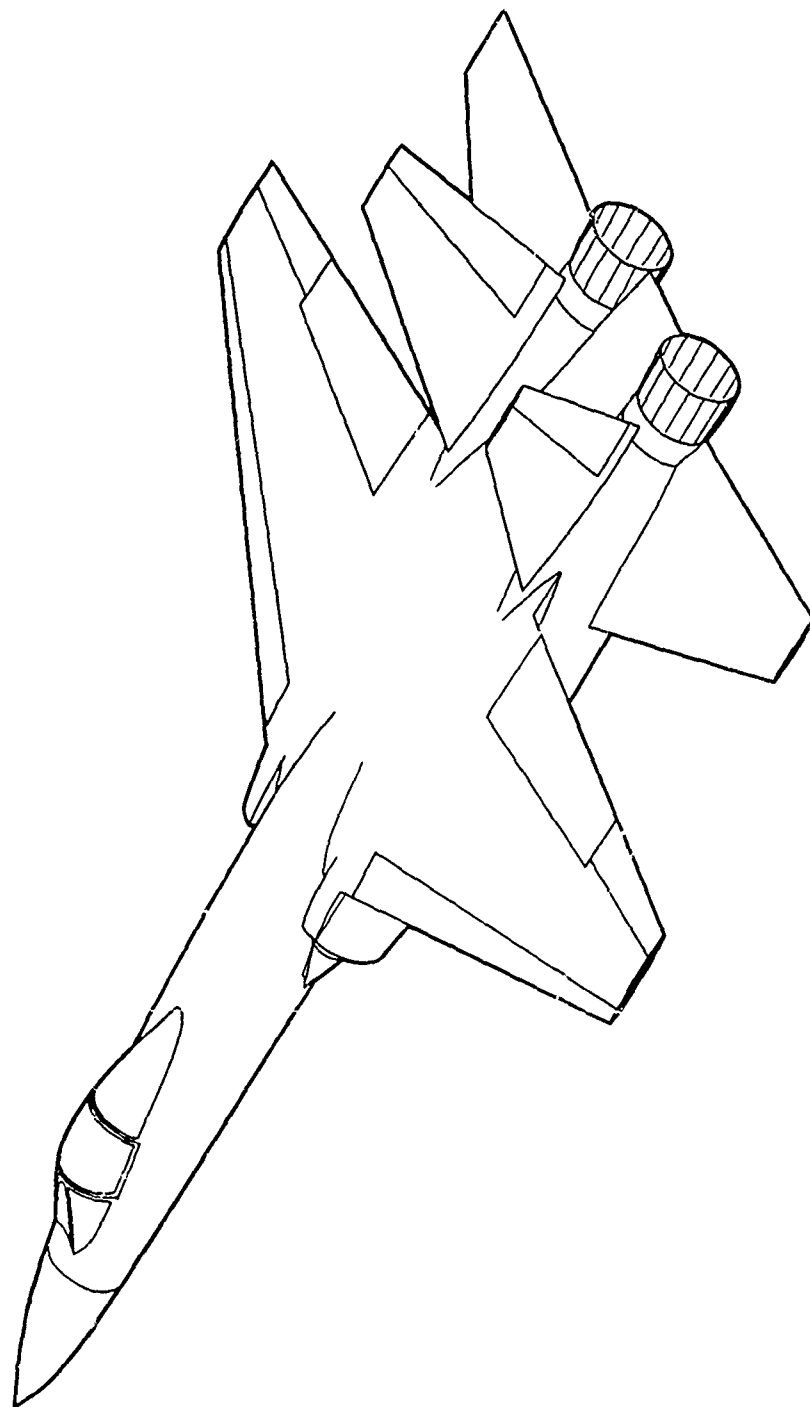


Figure 142. X-3 Baseline Turbofan Configuration

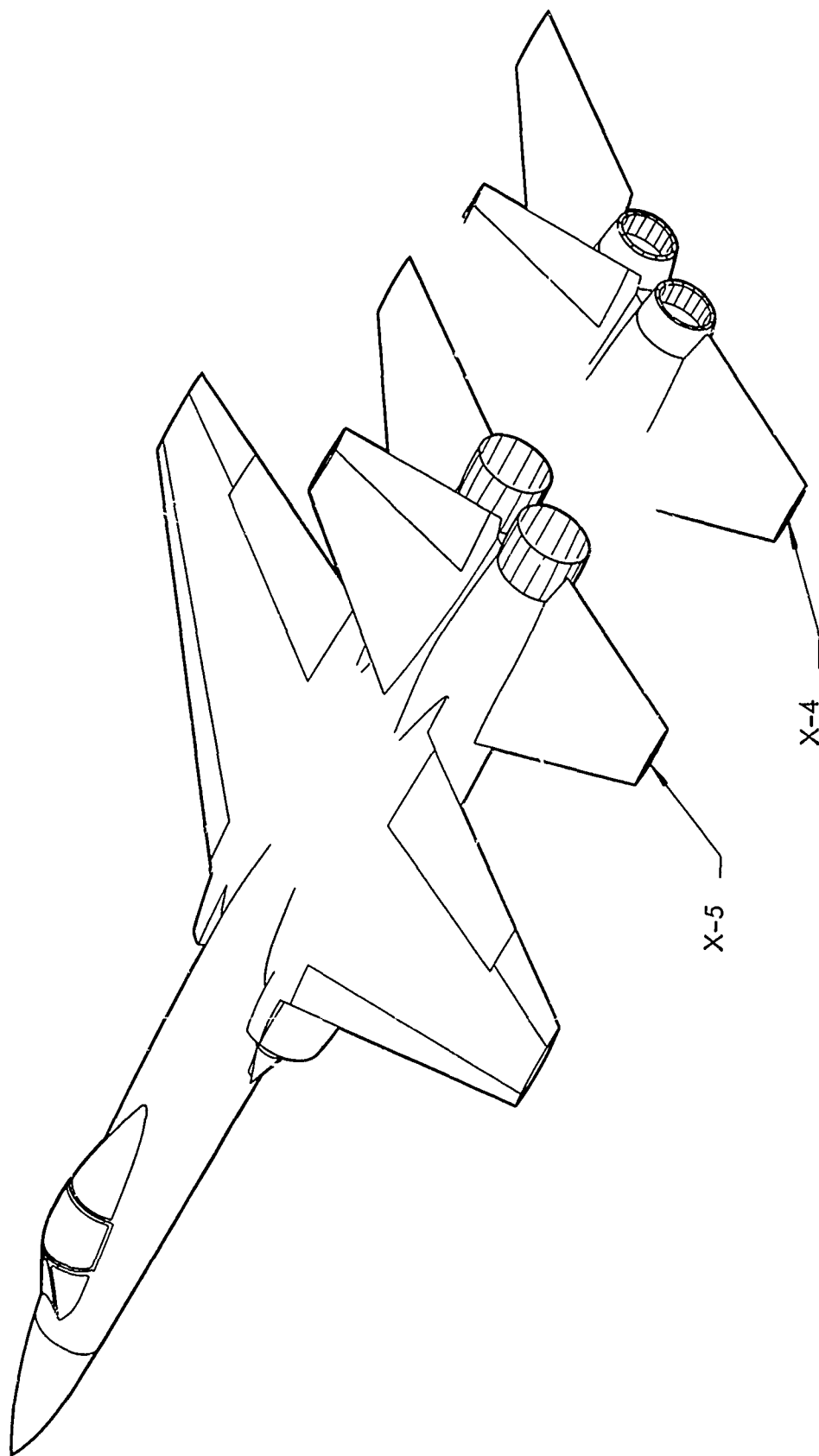


Figure 143. X-4 and X-5 Baseline Turbofan Configuration

and two in the lower corners of the nacelles. In order to house the model flow tubes and force balances, it was necessary for portions of the aircraft to be larger than that required solely from vehicle design considerations. However, no modifications were made to the contours of the baseline configurations so that the Phase II wind tunnel data could be used in evaluating the performance estimates developed for the mission analysis studies.

4.2.3 Candidate Configurations Development

The baseline configurations were modified to improve their thrust and aft-end drag characteristics. The new designs were considered only potential improvements since the rationale for the modifications is based primarily on performance consideration and whether or not they are indeed improvements is dependent on the trade-off between performance and weight, as subsequently determined from the mission analysis studies.

Four candidate configurations were developed: three STF 371 turbofan installations and one STJ 353 turbojet installation. The designations used to identify the candidate configurations in this report and on the vehicle design drawings are provided in Table 20 in addition to a summary of the modifications required to the baseline configuration.

A three-view drawing of the Y-1 configuration is shown in Figure 144. This configuration very closely resembles the Phase II S1 Y1 H1P(-2) V2P N1D CD model design and is the candidate developed for improving the performance of the X-1, X-4, and X-5 baseline configurations. Replacing the vertical interfairing of the X-1 configuration with a horizontal wedge interfairing reduces the aft-end drag, especially at subsonic speeds, with only an eight pound increase in weight. The aft-end drag of the X-4 and X-5 configurations is reduced in the Y-1 configuration by increasing the interfairing length such that the interfairing trailing edge terminates at the exit plane of the convergent-divergent nozzles instead of at the nozzle customer connect station. This increase in length results in a 20 pound weight penalty, but allows the vertical stabilizer to be located further aft on the aircraft. This results in a 144 pound weight reduction since a smaller vertical stabilizer having the same effectiveness can be utilized. The convergent-divergent nozzle installed in the Y-1 configuration, which is 300 pounds heavier than the convergent flap nozzle installed in the X-4 configuration and 360 pounds lighter than the convergent-divergent ejector nozzle installed in the X-5 configuration, is considered a potential overall improvement since it represents a compromise in both weight and performance. Further improvements were obtained by area ruling the portion of the fuselage aft of the maximum cross-sectional area station and by adjusting the nozzle expansion to obtain maximum thrust minus aft-end drag.

The Y-2 configuration shown in Figure 145 was developed to illustrate that the aft-end drag can be reduced by decreasing the nozzle spacing and increasing the aft-end length of the X-2 configuration, while keeping the volume of the two aircraft the same. This results in a higher fineness ratio and

TABLE 20. IDENTIFICATION OF CANDIDATE CONFIGURATIONS

BASELINE CONFIGURATION DESIGNATION	CANDIDATE CONFIGURATION DESIGNATIONS					
	TURBOFAN			TURBOJET		
	REPORT	VEHICLE	REQUIRED MODIFICATIONS	REPORT	VEHICLE	REQUIRED MODIFICATIONS
X-1	Y-1	CL 1250-9	Interfairing Type Area Rule Nozzle Expansion	1	CL 1250-11	Engine Installation Capture Area
X-2	Y-2	CL 1250-8	Nozzle Spacing Aft-End Length Nozzle Expansion			
X-3	Y-3	CL 1250-10	Vertical Stabilizer Type Area Distribution Nozzle Expansion			
X-4	Y-1	CL 1250-10	Interfairing Length Area Rule Nozzle Type and Expansion			
X-5	Y-1	CL 1250-10	Interfairing Length Area Rule Nozzle Type and Expansion			

therefore lower drag with a 551 pound increase in fuselage weight. The area of the horizontal and vertical stabilizers was reduced to maintain the same stabilizer effectiveness utilized for all previous configurations, which results in a 439 pound weight reduction. The nozzle expansion was again adjusted to maximize thrust minus aft-end drag.

The X-3 configuration was modified by removing area between the nozzles, substantially reducing the height of the horizontal wedge interfairing, and replacing the twin vertical stabilizers with a single vertical stabilizer. The resulting Y-3 configuration is shown in Figure 146. A 147 pound weight penalty is associated with reducing the fuselage area because of the added structure required to support the single vertical stabilizer, which is 333 pounds lighter than the twin vertical stabilizer. The cross-sectional area distribution for the Y-3 configuration is equivalent to that of the intermediate-spaced X-2 configuration. Further improvements were obtained by adjusting the nozzle expansion to obtain maximum thrust minus aft-end drag.

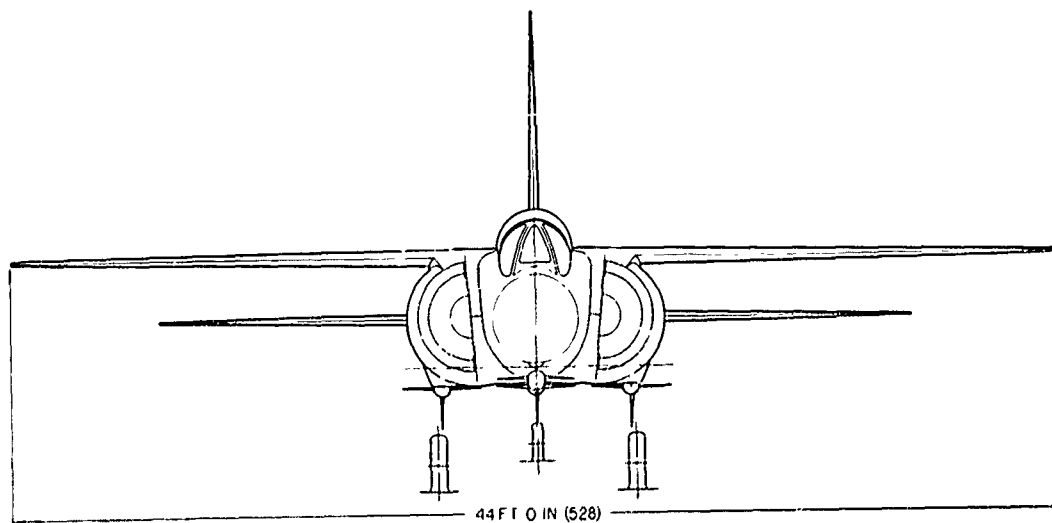
The Z-1 turbojet powered configuration shown in Figure 147 was developed by modifying the Y-1 turbofan design. The two STF 371 turbofan engines installed in Y-1 were replaced with twin STJ353 turbojet engines, which resulted in a 574 pound increase in engine weight, and the cross-section area from the inlet face to the convergent-divergent nozzle exit station was significantly reduced (16 percent reduction in maximum cross-sectional area), which resulted in a 293 pound decrease in fuselage weight. The stabilizer surfaces remained the same as those on the baseline configurations, and the same general clearances were used in installing the turbojet engine. Since the engine airflow requirements for the turbojet were markedly different than that for the turbofan engine, it was necessary to reduce the inlet capture area and also change the inlet ramp schedules, as discussed in Subsection 4.2.4.3.

CHARACTERISTICS	WING	HORIZ TAIL EXPOSED	VERT TAIL EXPOSED
AREA (SQ FT)	575	169.2	102
ASPECT RATIO	3.37	3.0	15
SPAN (FT)	44.0	22.5	23.7
ROOT CHORD (IN)	250.8	135.7	152.5
TIP CHORD (IN)	62.7	44.8	45.7
TAPER RATIO	0.25	0.33	0.30
MAC (IN)	175.56	98.0	108.7
SWEEP-LE (DEG)	31.5	37	50
T/C ROOT (°)	37	41	40
T/C TIP (°)	32.6	25	25

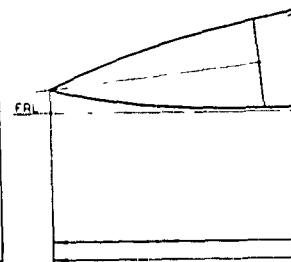


TAKEOFF GROSS WEIGHT 45,000 LB

POWER PLANT (2) PRATT & WHITNEY STF 371A 20 TURBOFAN



44 FT 0 IN (528)



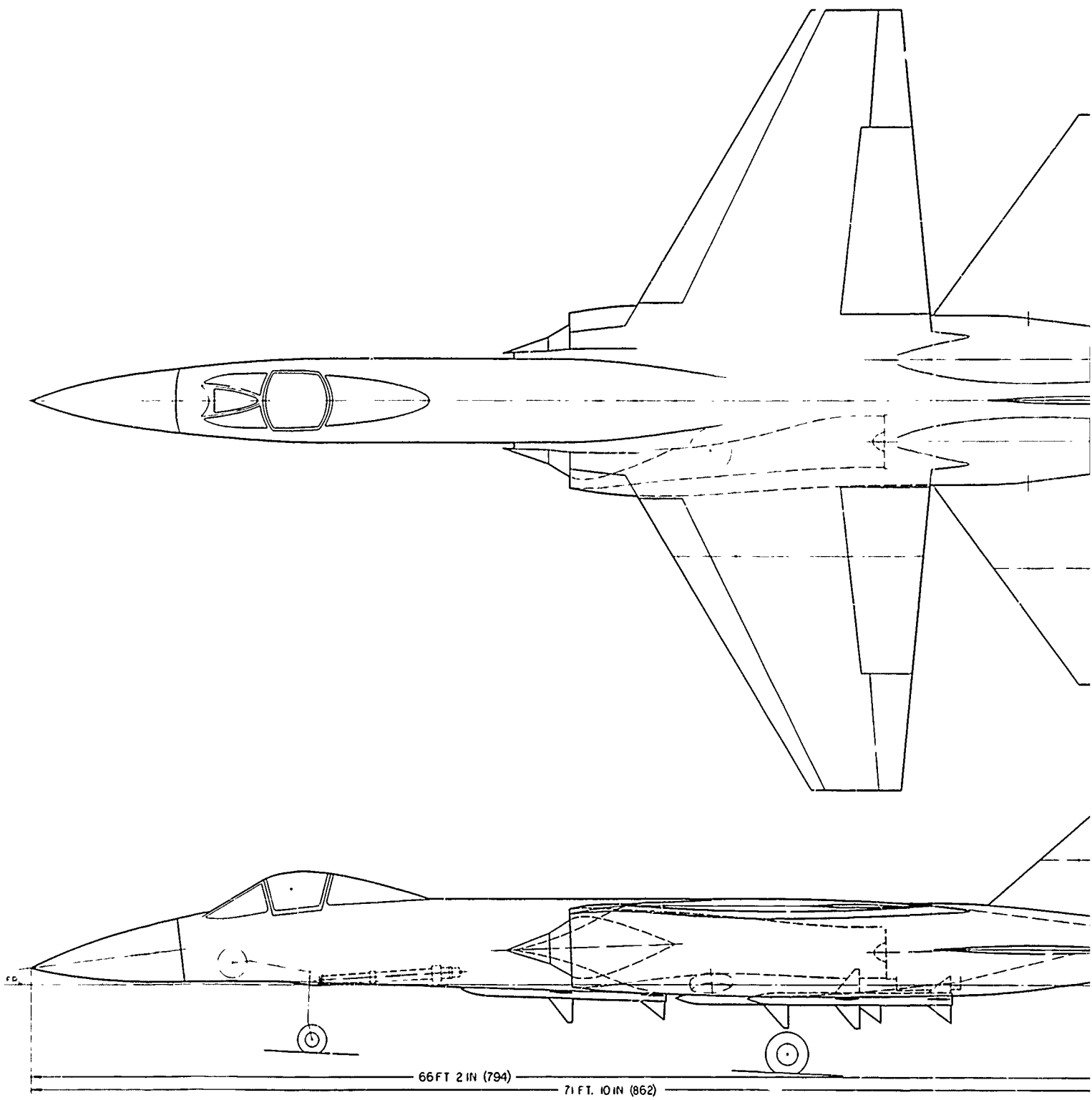


Figure 1

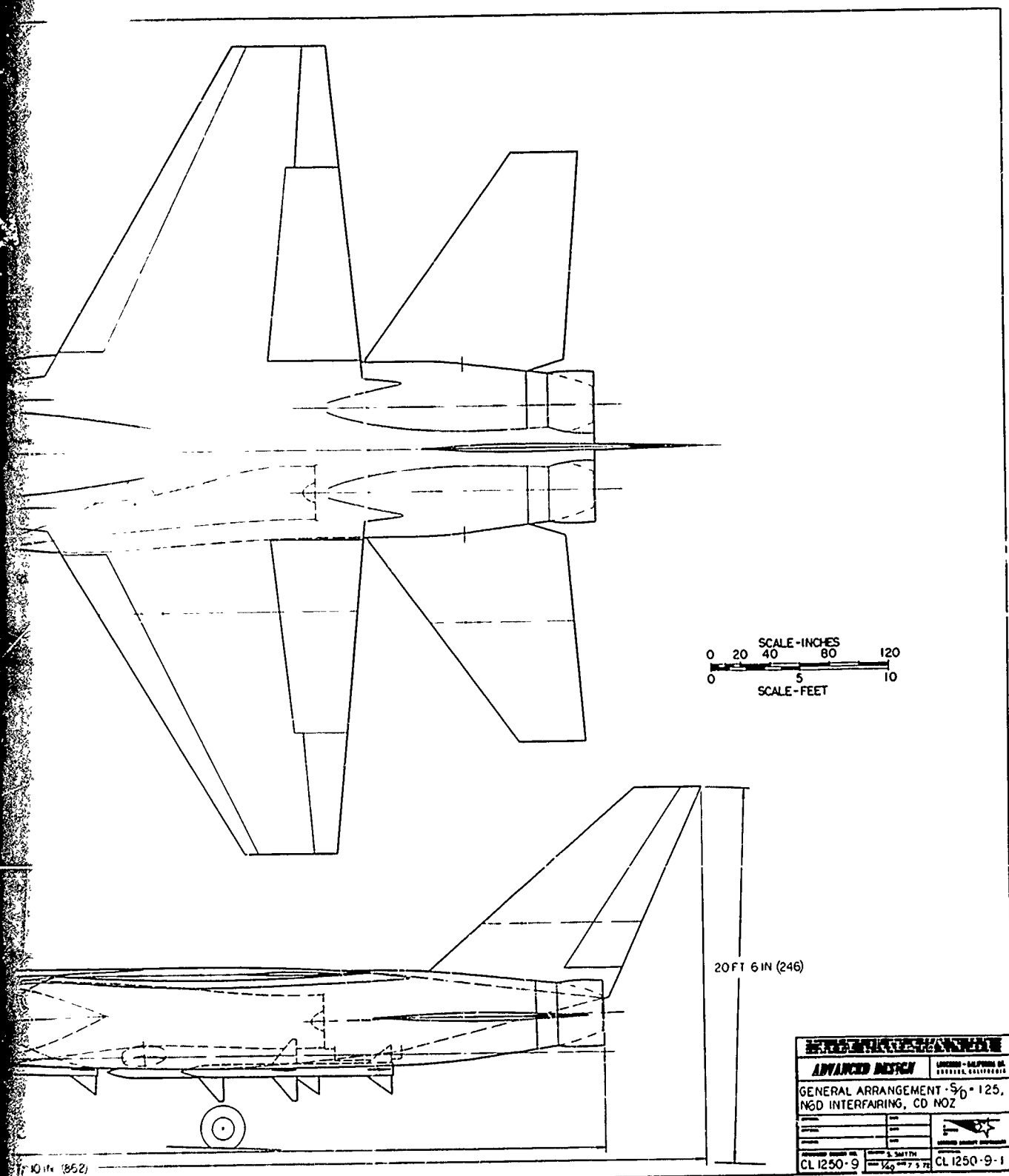
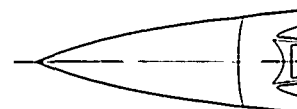


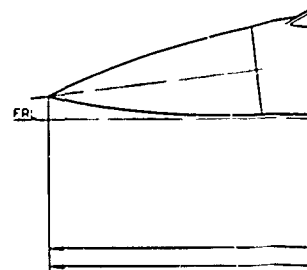
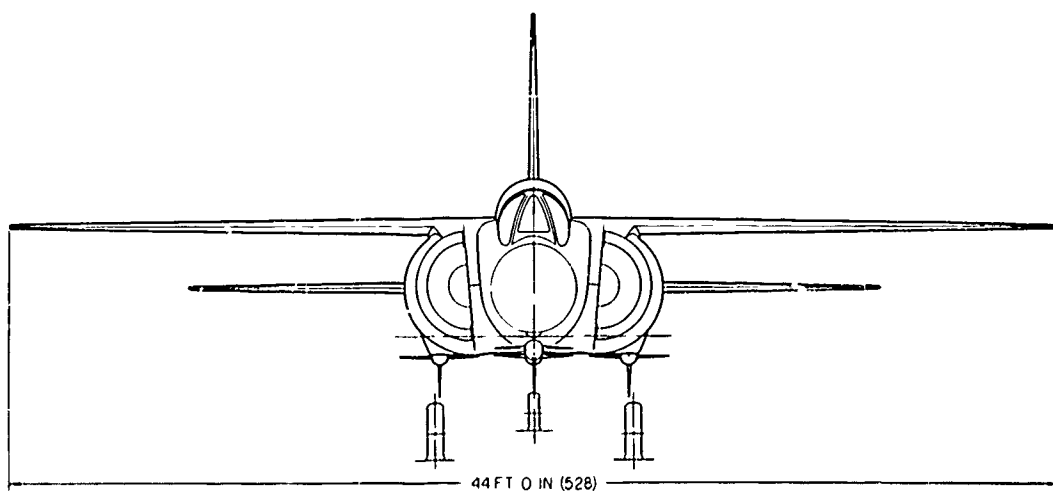
Figure 144. Y-1 Candidate Turbofan Configuration

CHARACTERISTICS	WING	HORIZ TAIL SLOPE (DEG)	VERT TAIL SLOPE (DEG)
AREA (SQ FT)	575	13.1	82.1
ASPECT RATIO	3.37	3.0	1.5
SPAN (FT)	44.0	19.8	11.1
ROOT CHORD (IN)	250.8	119.2	136.6
TIP CHORD (IN)	62.7	39.4	41.0
TAPER RATIO	0.25	0.33	0.30
MAC (IN)	175.56	86.2	97.3
SWEEP L E (DEG)	31.5	3.7	5.0
T/C ROOT (X)	3.7	4.0	4.0
T/C TIP (X)	3.26	2.5	2.5



TAKEOFF GROSS WEIGHT 45,000 LB

POWER PLANT (2) PRATT & WHITNEY STF 371A-20 TURBOFAN



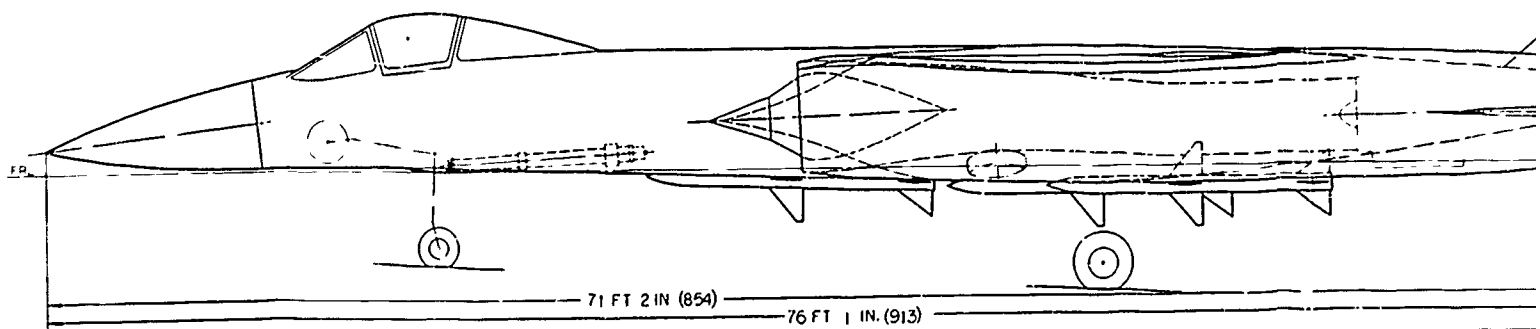
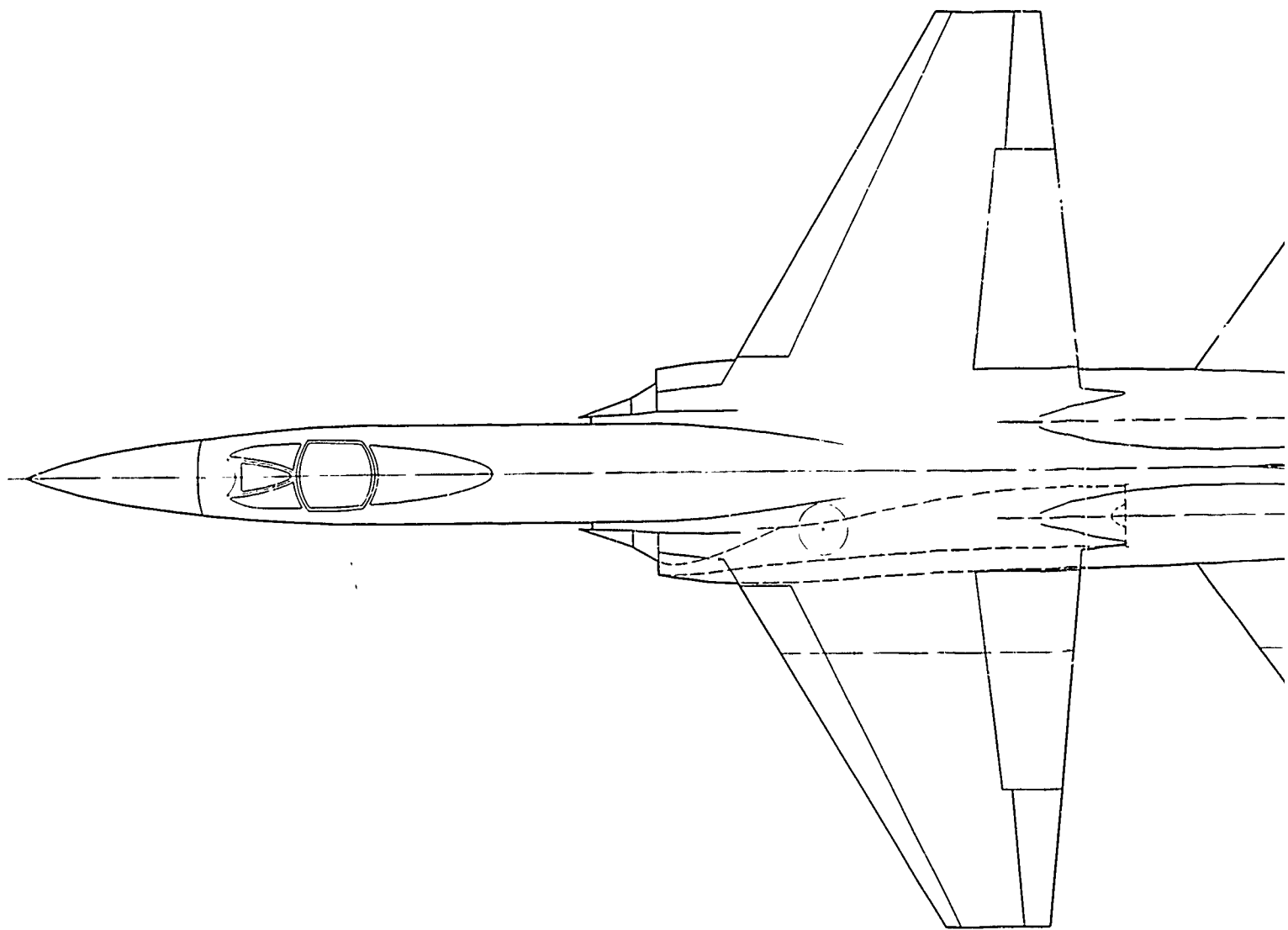


Figure 14

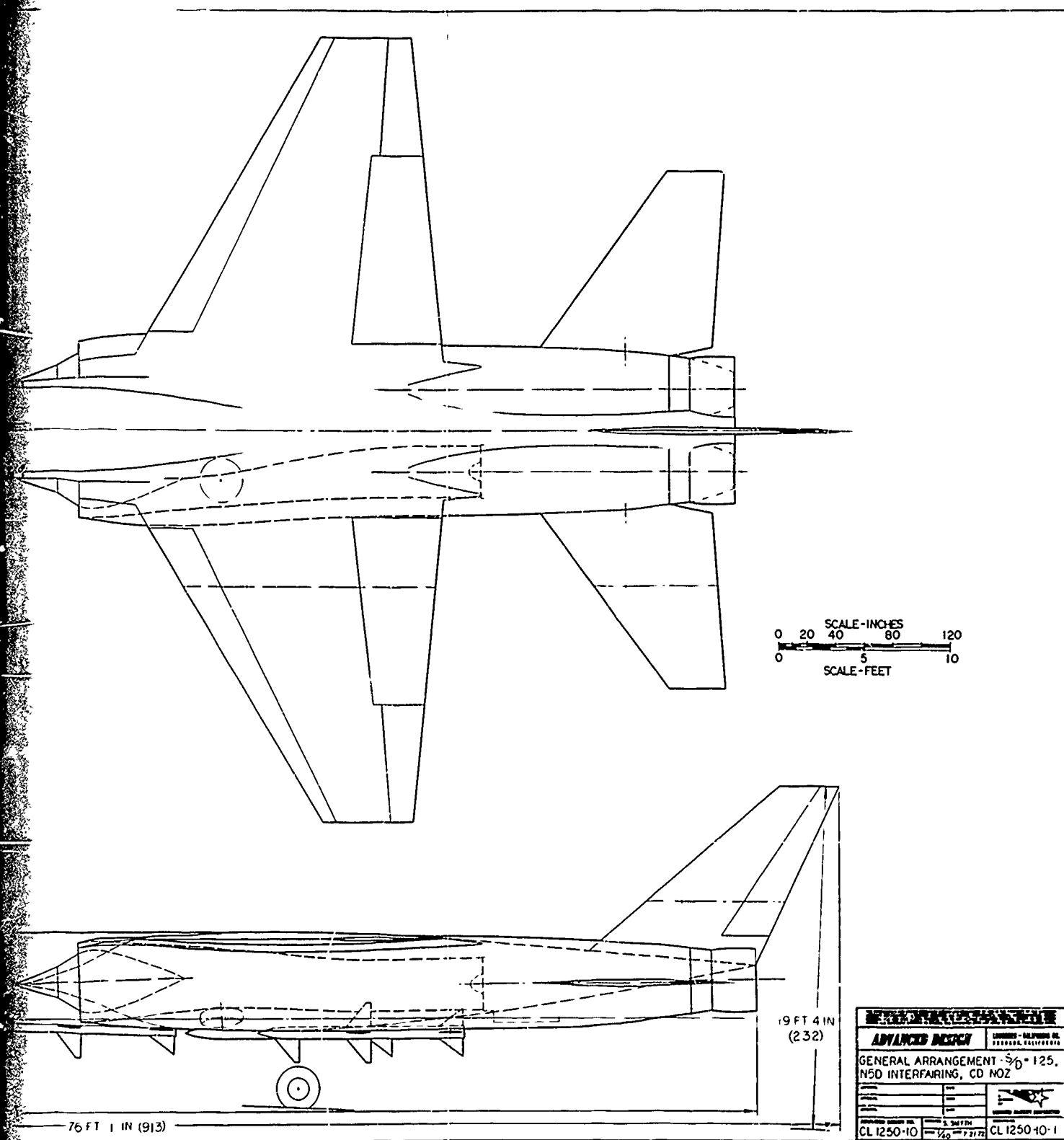
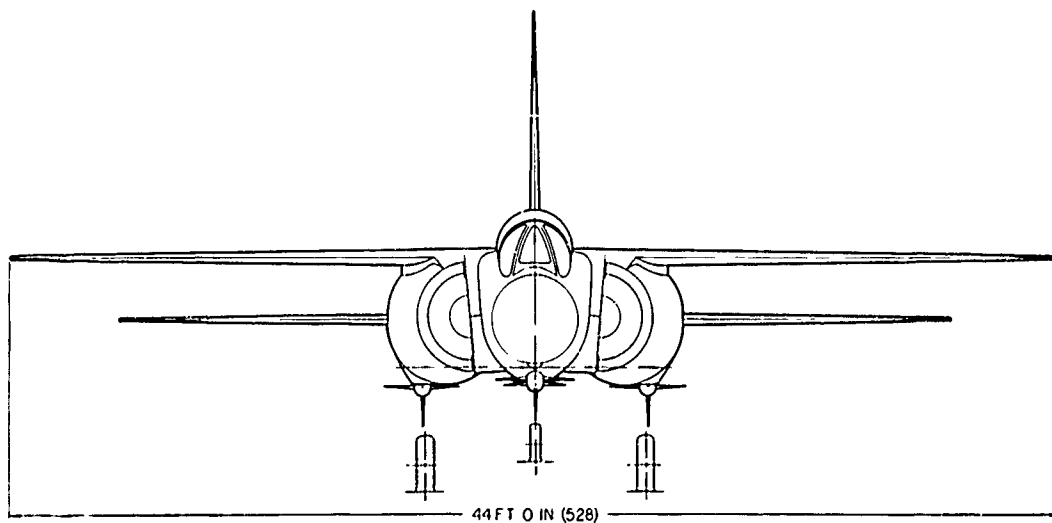
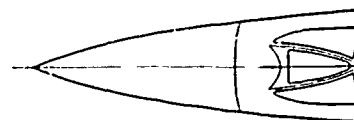


Figure 145. Y-2 Candidate Turbofan Configuration

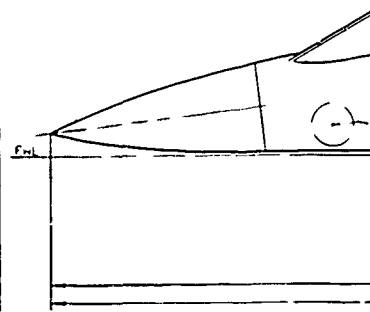
CHARACTERISTICS	WING	HORIZ TAIL DISPOSED	VERT TAIL DISPOSED
AREA (SQ FT)	575	169.2	102
ASPECT RATIO	3.37	3.0	1.5
SPAN (FT)	44.0	22.5	12.37
ROOT CHORD (IN)	2508	135.7	152.5
TIP CHORD (IN)	62.7	44.8	45.7
TAPER RATIO	0.25	0.33	0.30
MAC (IN)	175.56	98.0	108.7
SWEEP-LE (DEG)	31.5	37	50
T/C ROOT (°)	37	40	40
T/C TIP (°)	32.6	25	25

TAKEOFF GROSS WEIGHT 45,000 LB

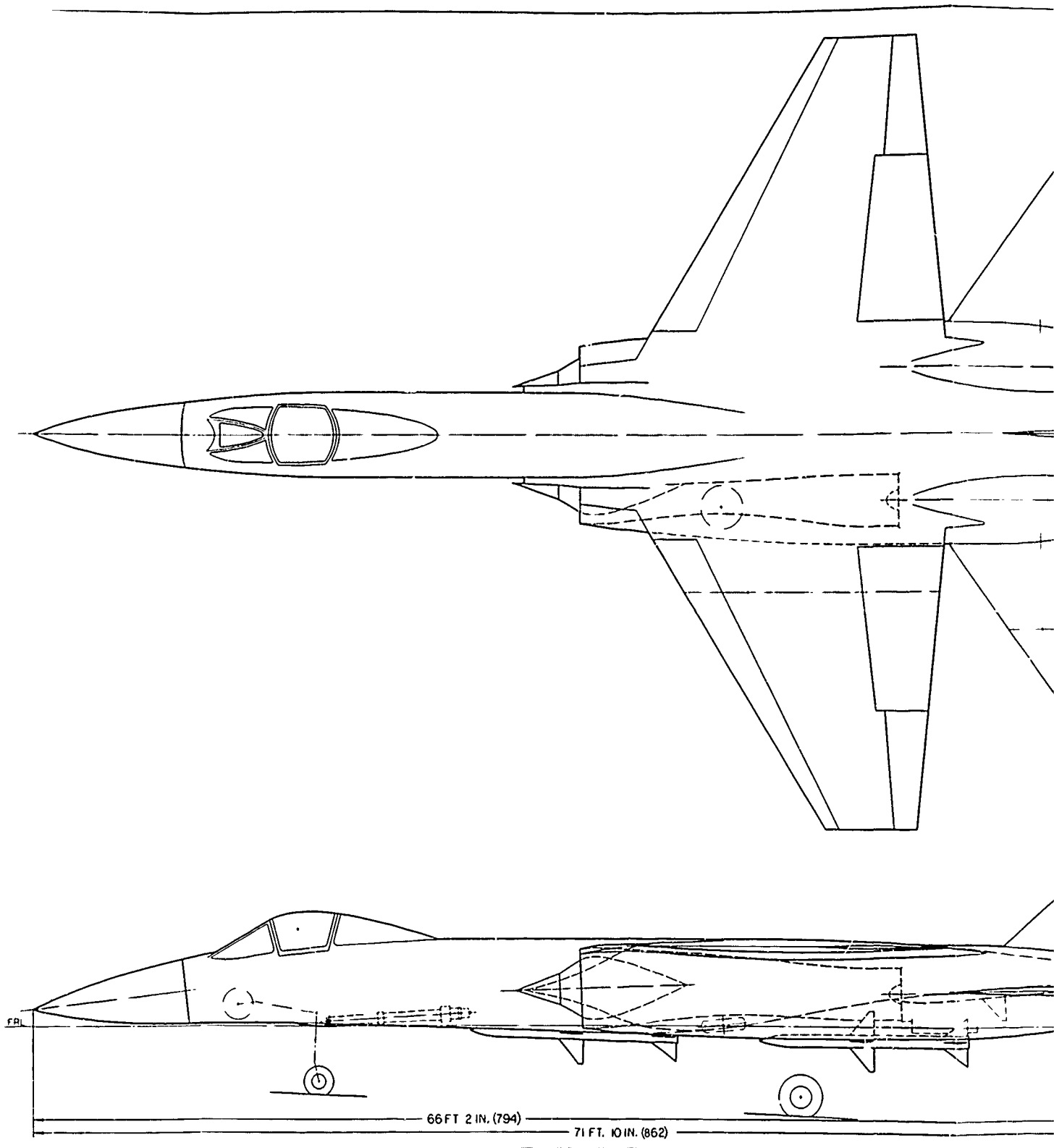
POWER PLANT (2) PRATT & WHITNEY STF 371A-20 TURBOFAN



44 FT 0 IN (528)



"PRECEDING PAGE BLANK-NOT FILMED."



Figur

8

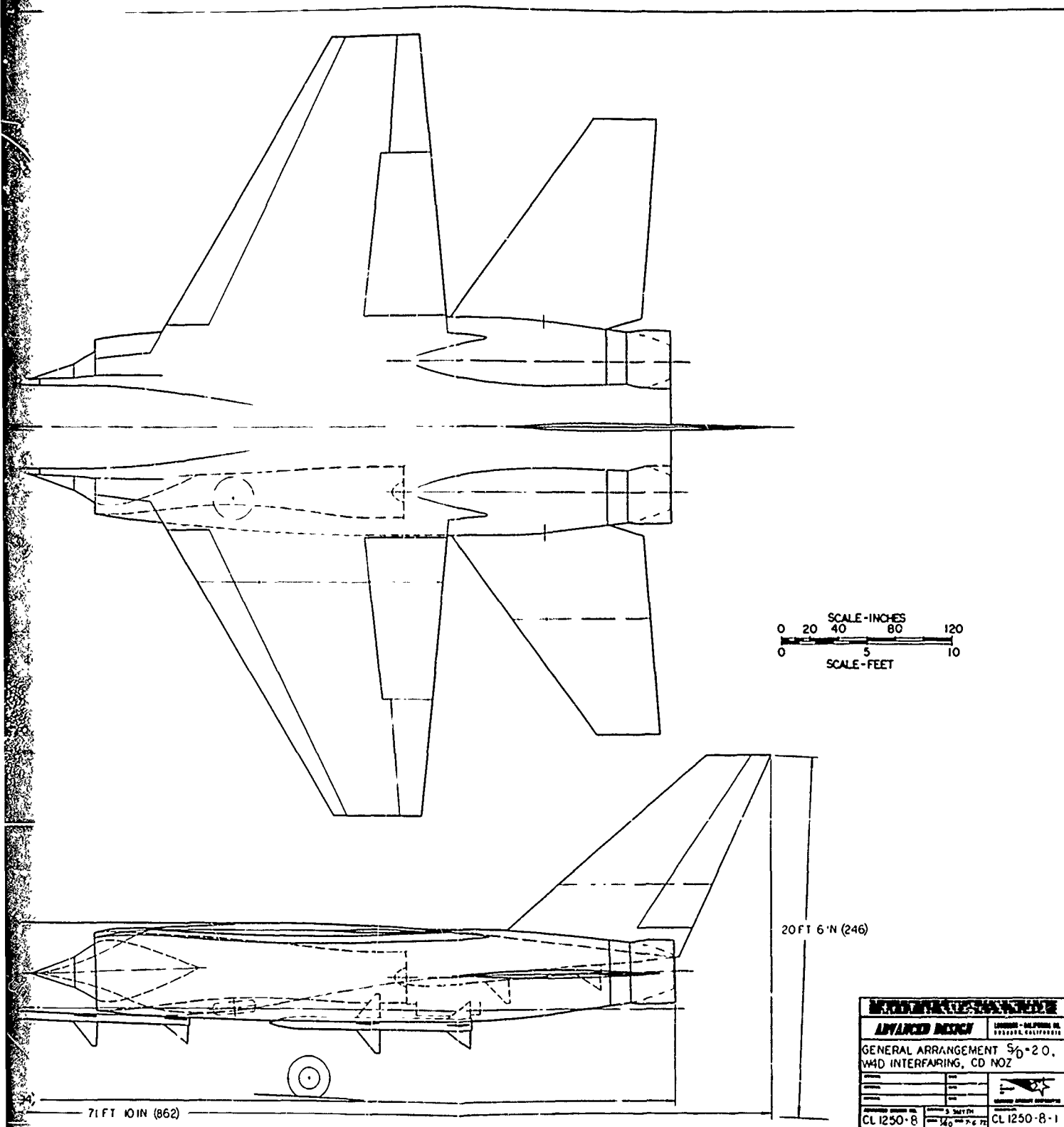
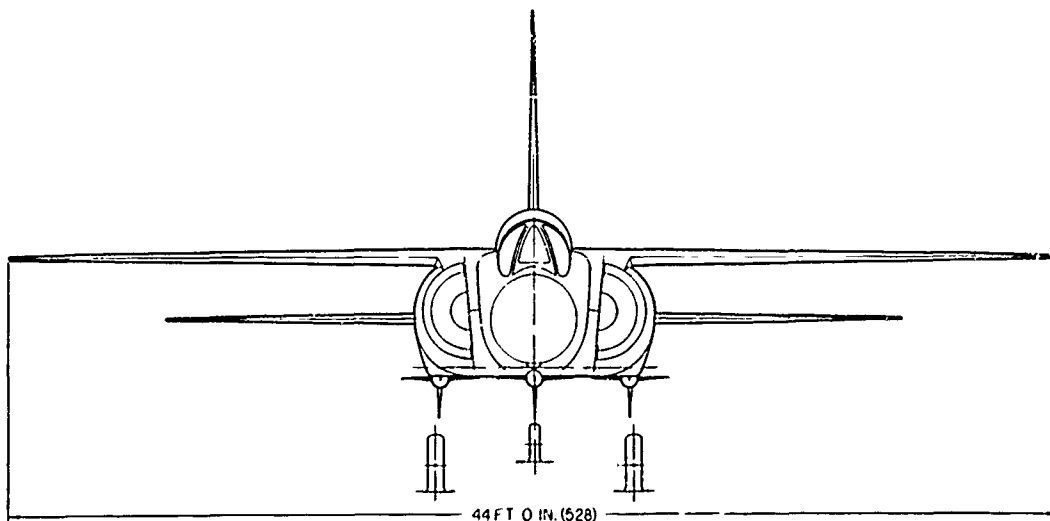
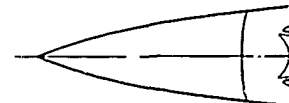


Figure 146. Y-3 Candidate Turbofan Configuration

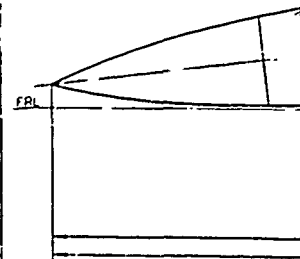
CHARACTERISTICS	WING	HORIZ. TAIL (ft/pos)	VERT. TAIL (ft/pos)
AREA (SQ FT)	575	169.2	102
ASPECT RATIO	3.37	3.0	1.5
SPAN (FT)	44.0	22.5	12.37
ROOT CHORD (IN)	250.8	135.7	152.5
TIP CHORD (IN)	62.7	44.8	45.7
TAPER RATIO	0.25	0.33	0.30
MAC (IN)	175.56	98.0	108.7
SWEEP-LE (DEG)	31.5	37	50
T/C ROOT (°)	37	40	40
T/C TIP (°)	32.6	2.5	2.5

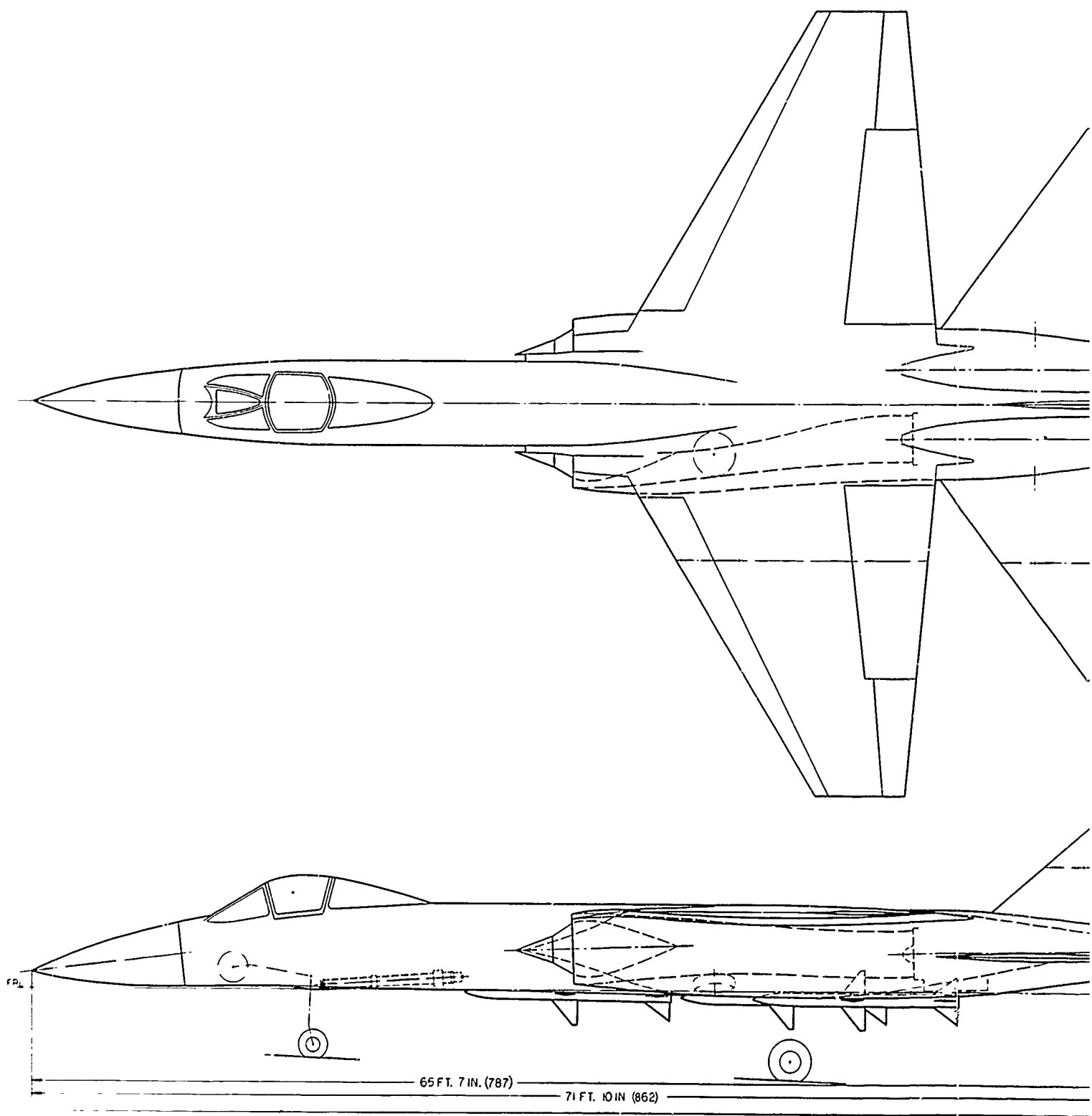
TAKEOFF GROSS WEIGHT 45,000 LB

POWER PLANT (2) PRATT & WHITNEY STJ 353 TURBOJET



44 FT 0 IN. (528)





Figure

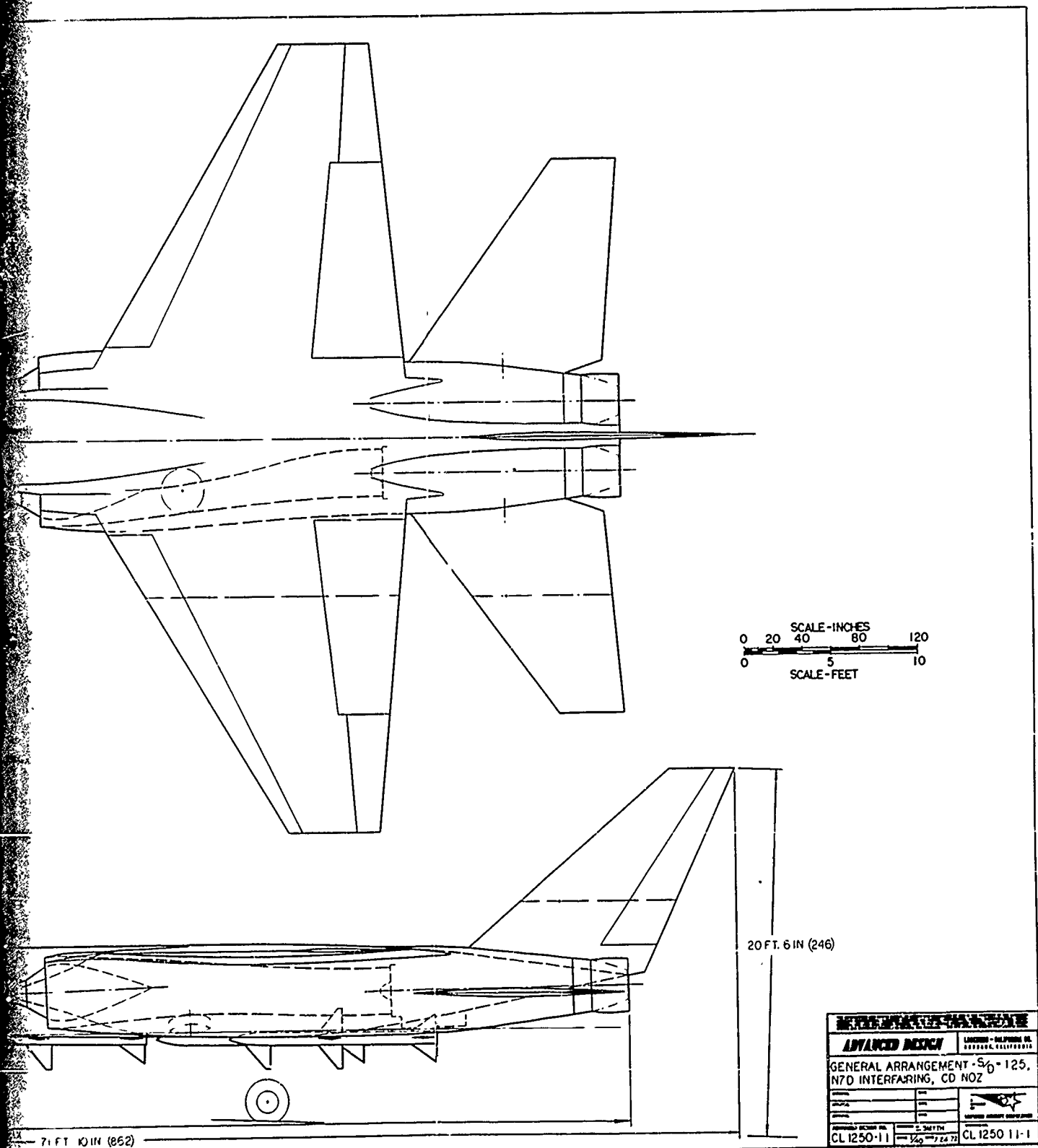


Figure 147. Z-1 Candidate Turbojet Configuration

The Phase II model contours were retained in the development of both the baseline and the candidate configurations so that the improvements obtained are representative only of the associated general configuration changes and not of specialized configuration details. However, as a consequence of this, some additional improvements are believed possible through detailed treatment of the individual improved designs, for example, through area ruling specific to each individual configuration.

4.2.4 Performance Prediction

This section presents the thrust, drag, and weight of five Phase II baseline aircraft configurations and the four candidate aircraft configurations. The force accounting procedure is described first followed by aero-model, inlet, and aft-end drag data presentations.

4.2.4.1 Force Accounting Procedure

The accounting system employed in this program separates the components into those that are independent of power setting and those that vary with power setting. Normally, the total aircraft drag is computed using equivalent body techniques which include the wing/fuselage and empennage/aftbody interaction effects. Corrections are then required to account for nozzle/aftbody interaction effects and inlet/forebody interaction effects. The interference drag due to twin nozzle/aftbody/empennage interference effects can be determined by subtracting an axisymmetric equivalent body aft-end drag from that predicted using empirical correlations of the Phase II data. In order to use this aft-end interference drag in building up the total aircraft drag, the empennage/aftbody interaction effects, which are included in the Phase II data, must be excluded from the total drag computed using equivalent body techniques. The accounting procedure described can be expressed algebraically as

$$D_T = D_{AERO} + D_{INLET} + \Delta D_{BT}$$

The first term in the above equation represents the aircraft pressure plus friction drag, including wing/fuselage interference effects but excluding empennage/aftbody interference effects and base drags. Drag due to lift, trim drag, and external stores drag are also included. The aircraft drag is computed assuming the inlet is operating at unity mass flow ratio. The inlet/forebody interference drag was assumed negligible. This assumption is valid since the inlet forebodies are similar and the vehicles are compared in terms of an incremental drag. The second term in the above equation includes the inlet spillage drag and the inlet bleed and ECS (environmental control system) drags. The last term in the above equation represents the difference in boattail drag between that obtained from correlations of the Phase II data and that obtained from an axisymmetric equivalent body analysis.

4.2.4.2 Aero-Model Drag

Drag estimates for all nine configurations are presented in Figures 148 through 156 in terms of zero lift drag as a function of Mach number for sea level operation and in terms of an increment in zero lift drag as a function of Mach number and altitude. Figure 157 presents the drag due to lift factor, K , as a function of Mach number and lift coefficient. The following equation is employed for computing the aero-model drag coefficient.

$$C_{D_{AERO}} = C_{D_W} + K C_L^2$$

where C_{D_W} is the zero lift drag coefficient. Drag increments due to external stores are presented in Figure 158. The data presented in the figures do not include the propulsion system drag increments. These drags are accounted for in the installed propulsion data.

Aero-model drag values were obtained using the general methods outlined in Reference 80. The drag values shown include both pressure and friction drag components but do not include the empennage/aftbody interference drag. The Calac wave drag program (Reference 77) was employed for computation of the wave drag. Transonic drag values were estimated using the Mach Divergence method described in Reference 81 for computing the drag rise of planar surfaces and empirical data from Reference 82 for body drag rise characteristics. Subsonic drag-due-to-lift values were calculated using the procedures in Reference 83. These procedures are compilation of data obtained from numerous military aircraft and include trim drag allowances. Supersonic drag due to lift was set at 1.10 times the theoretical value of $\sqrt{M_\infty^2 - 1}/4$. Data compiled in Reference 84 indicates this to be a reasonable assumption.

4.2.4.3 Propulsion System Performance

The inlet performance, aft-end drag, and internal nozzle performance, which are used in determining the installed thrust-minus-aft-end drag for the baseline and candidate configurations, are discussed in this subsection.

Inlet Total Pressure Recovery and Spillage Drag

The total pressure recovery and spillage drag have been estimated for the inlet design on the General Dynamics A-2 aircraft configurations. The total pressure recovery was estimated for subsonic Mach numbers from the theoretical analysis of Fradenburgh and Wyatt, Reference 85, and for supersonic Mach numbers from MOC solutions. The additive drag was obtained for subsonic and transonic Mach numbers from the drag correlations of Muller and Gasko, Reference 86, and for supersonic Mach numbers from the method of Sibulkin, Reference 87. The additive drag was corrected for cowl lip suction effects from correlations in Reference 88. The inlet bleed and ECS (Environmental Control System) bleed drags were estimated and incorporated in the inlet drag.

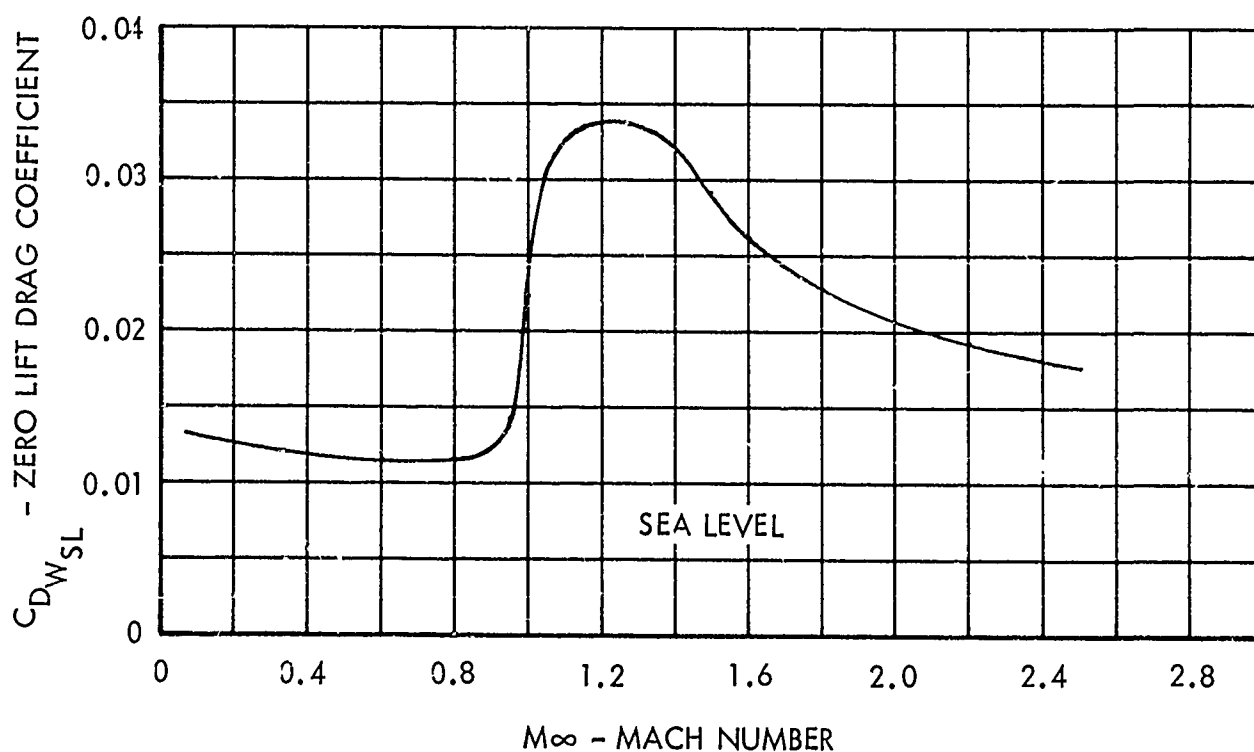
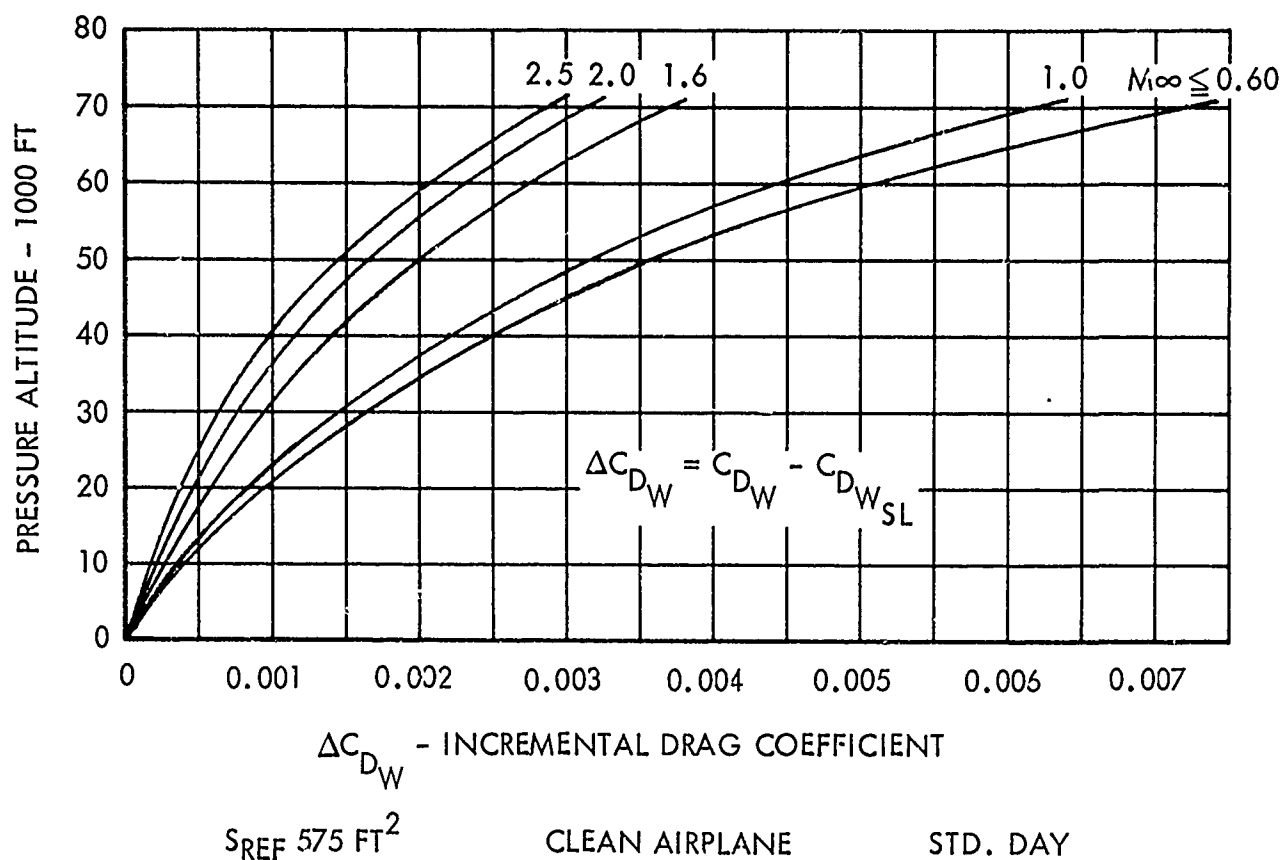


Figure 148. Configuration X-1 Aero-Model Zero Lift Drag Variation

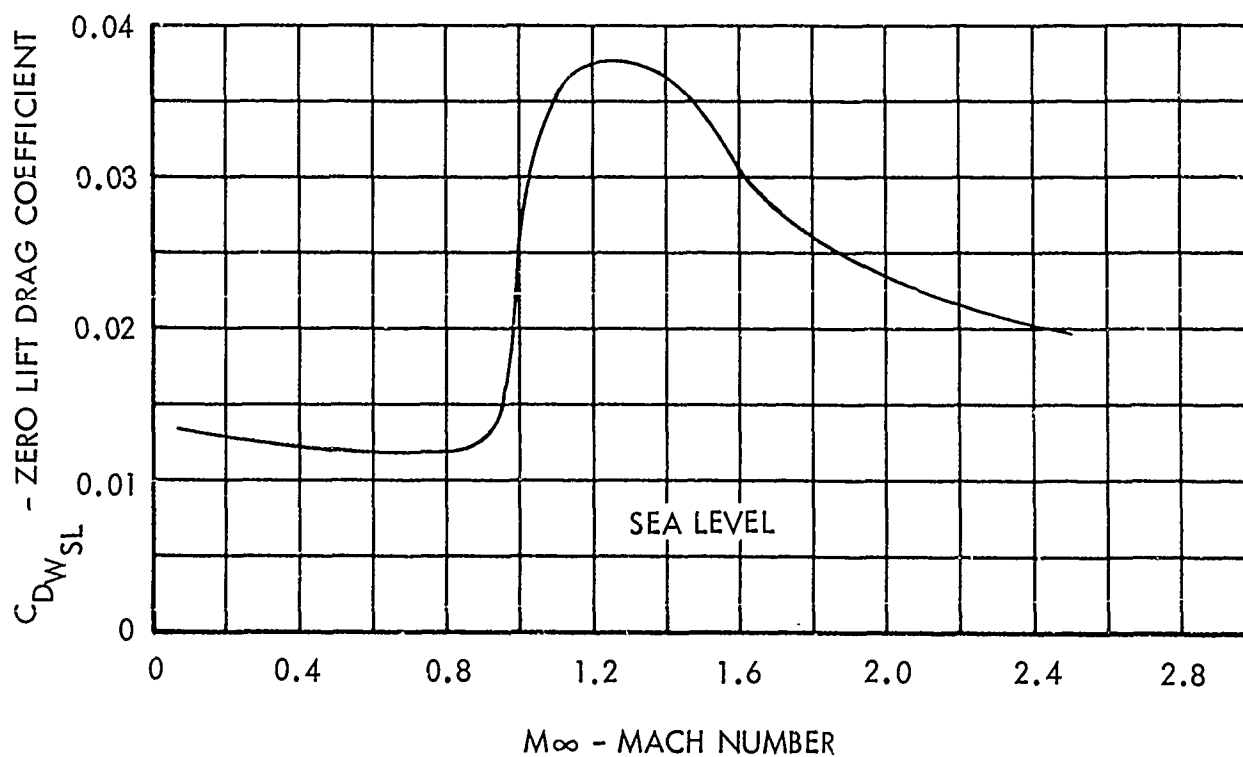
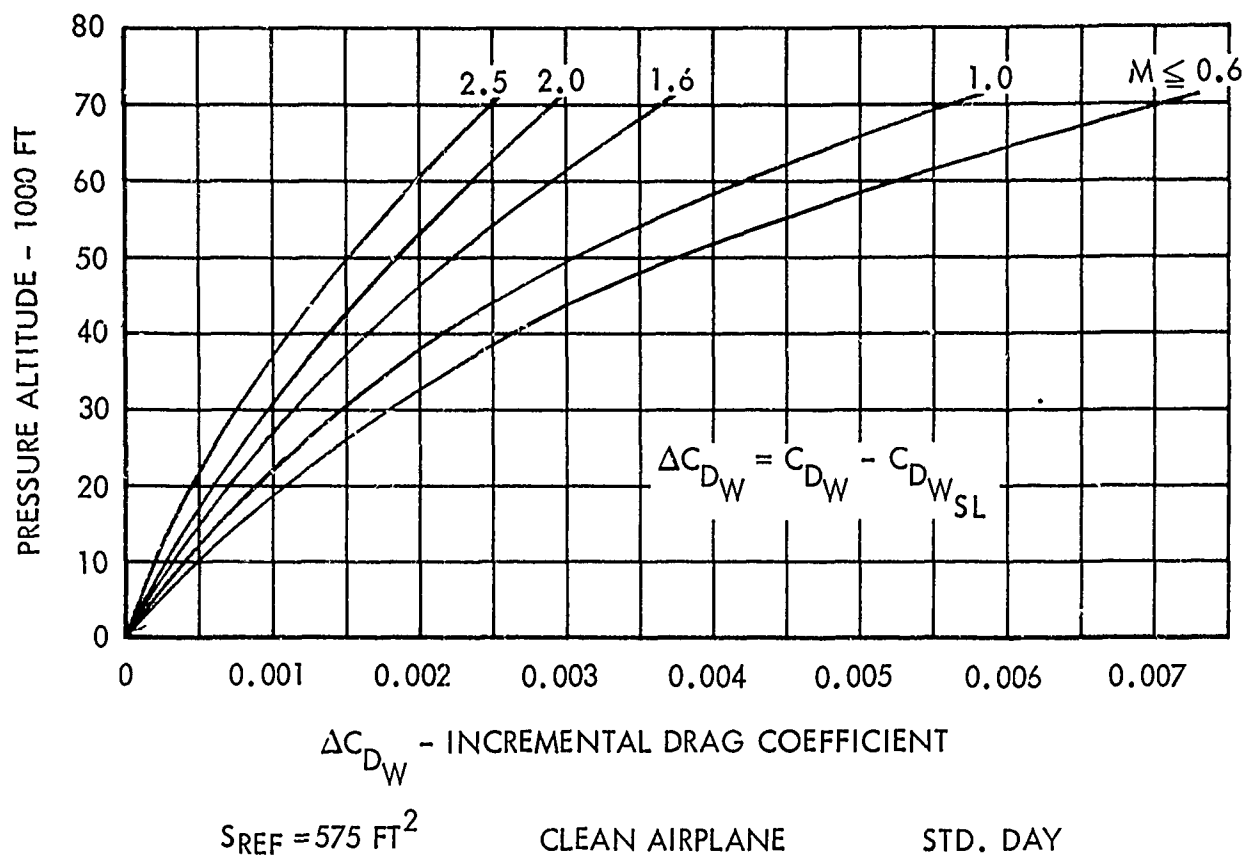


Figure 149. Configuration X-2 Aero-Model Zero Lift Drag Variation

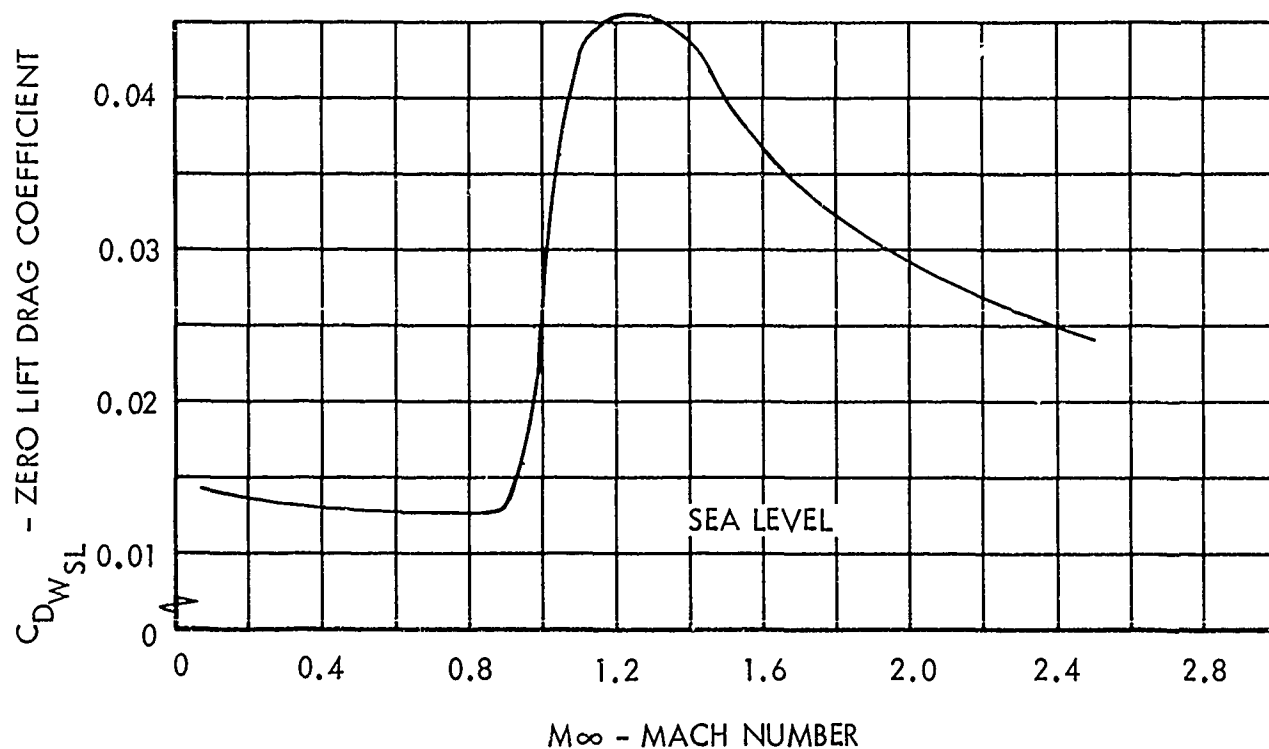
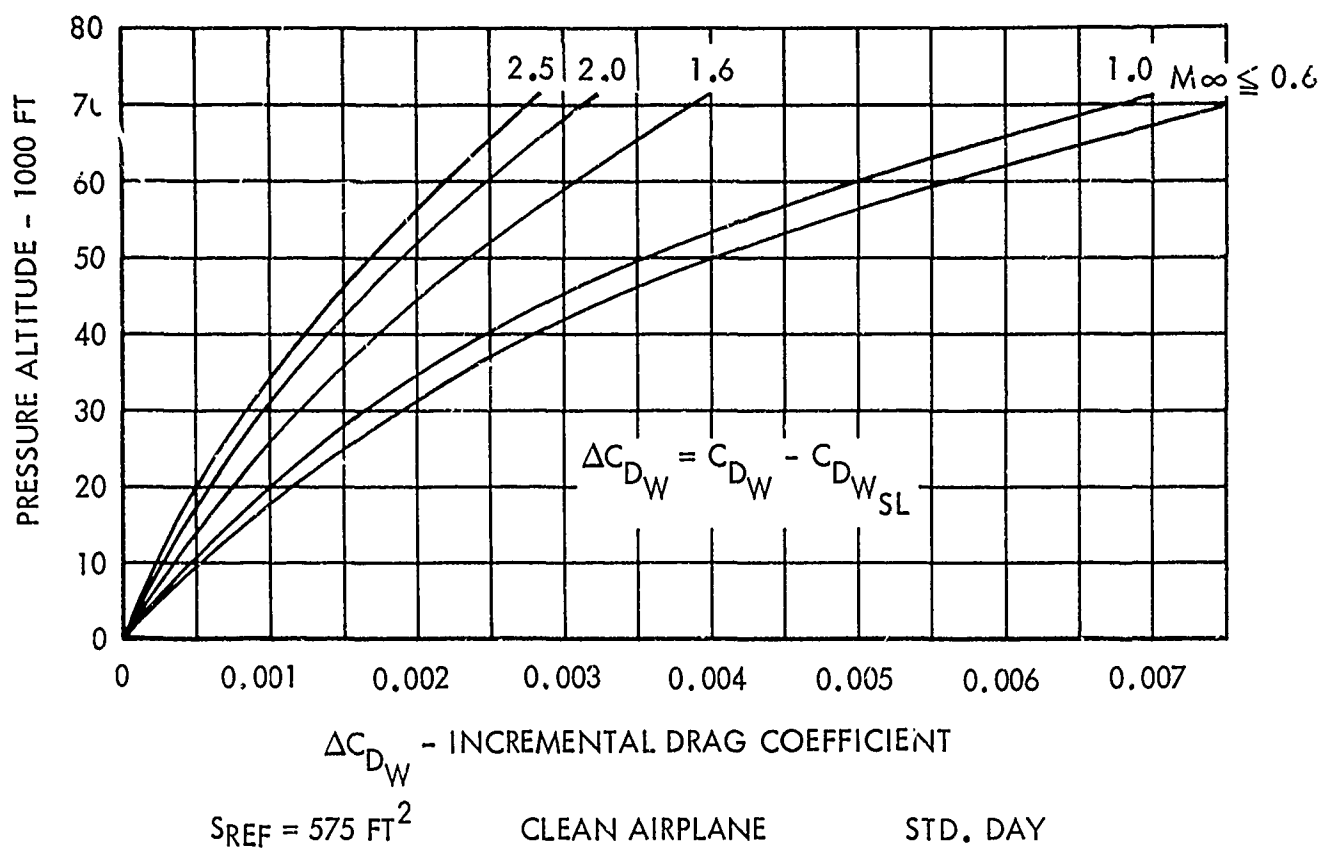
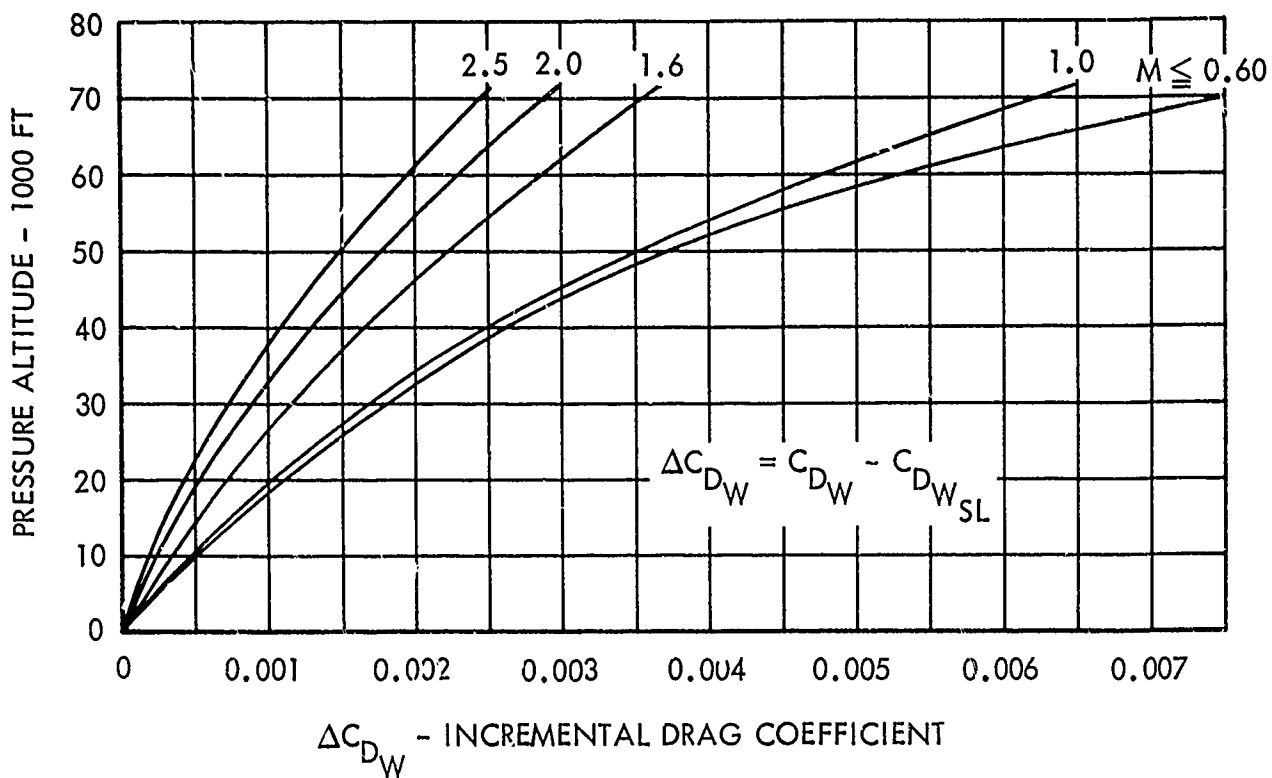


Figure 150. Configuration X-3 Aero-Model
Zero Lift Drag Variation



$S_{REF} = 575 \text{ FT}^2$

CLEAN AIRPLANE

STD. DAY

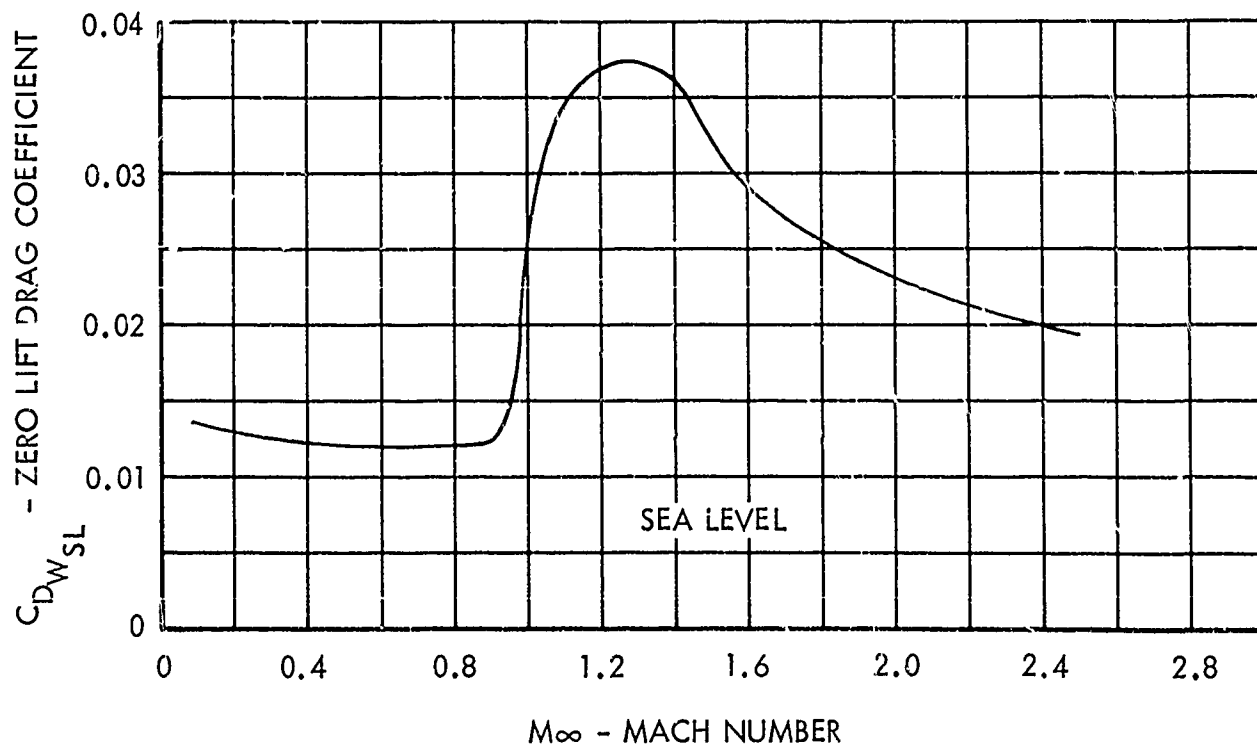
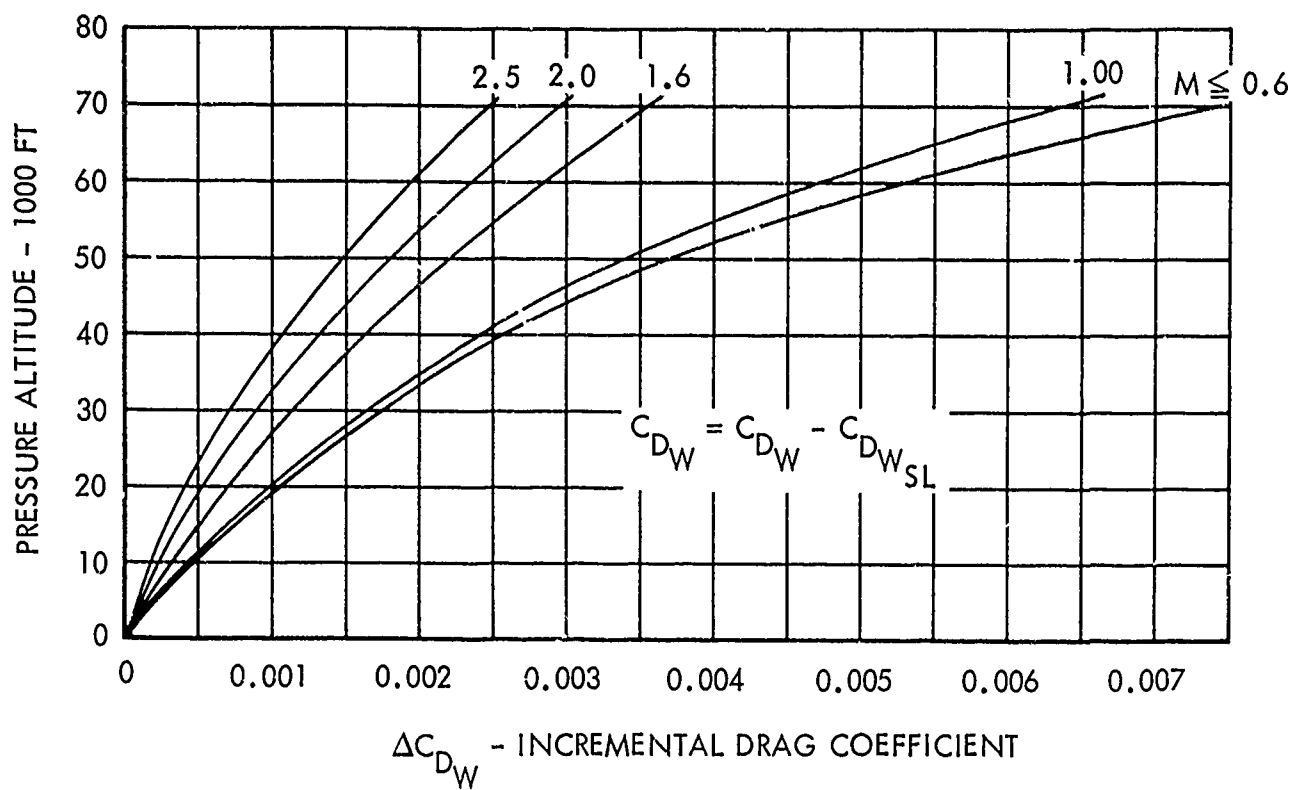


Figure 151. Configuration X-4 Aero-Model
Zero Lift Drag Variation



$S_{REF} = 575 \text{ FT}^2$

CLEAN AIRCRAFT

STD. DAY

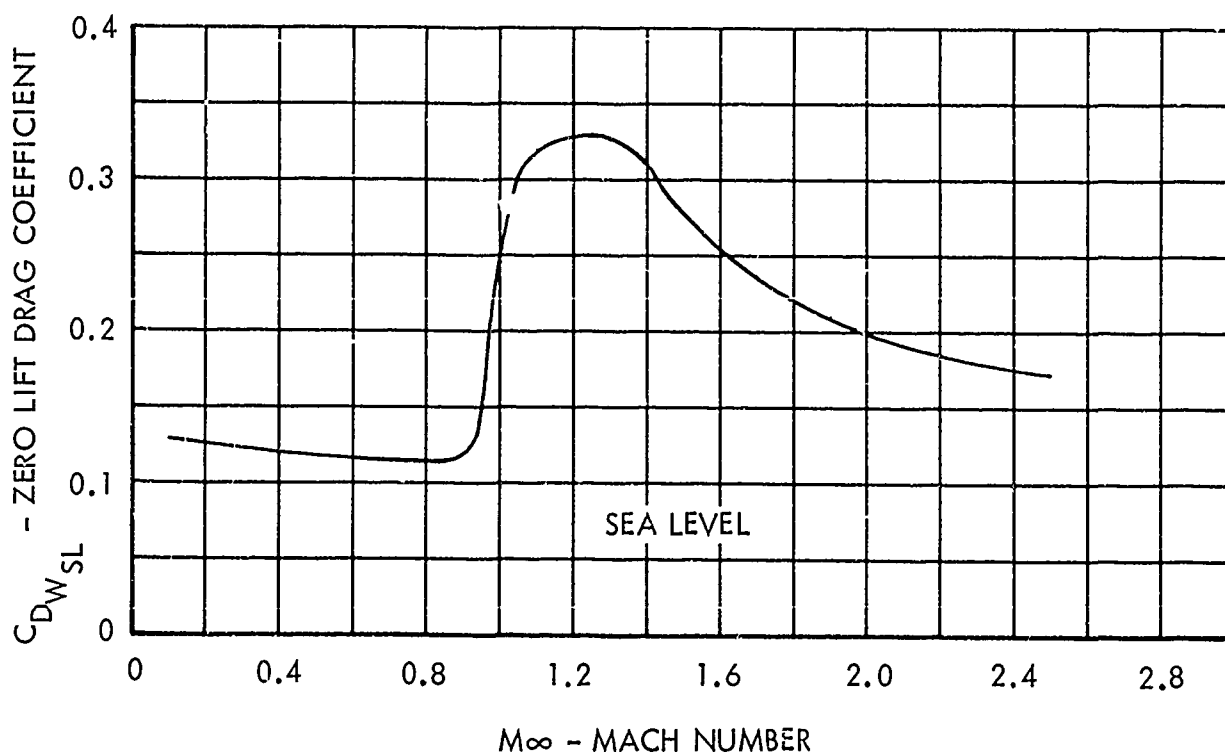
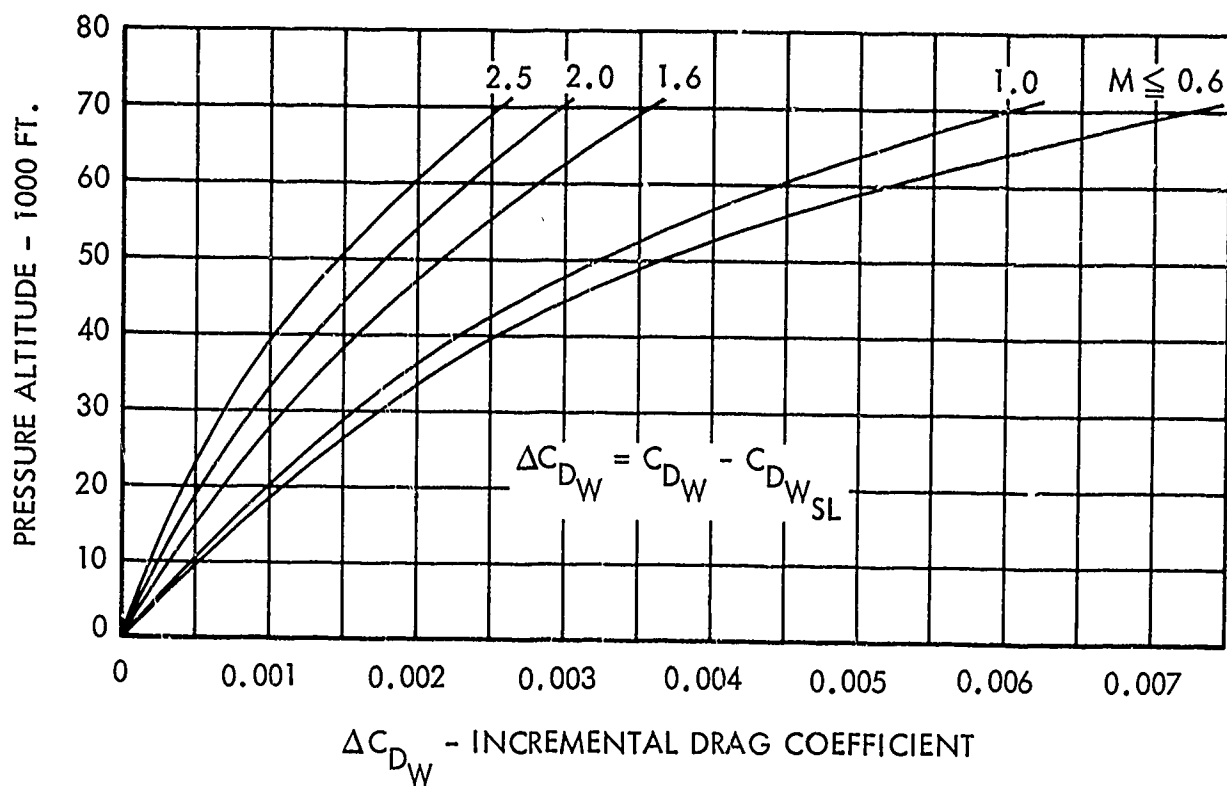


Figure 152. Configuration X-5 Aero-Model
Zero Lift Drag Variation



$S_{REF} = 575 \text{ FT}^2$

CLEAN AIRPLANE

STD. DAY

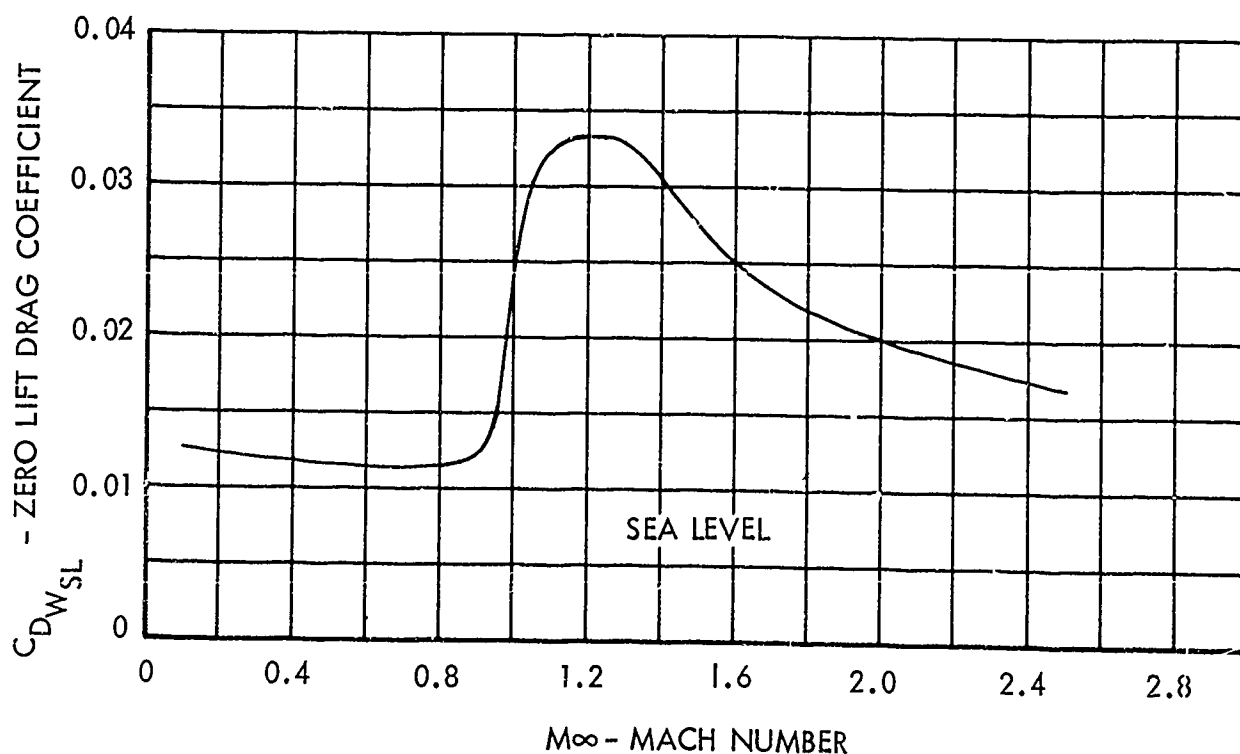
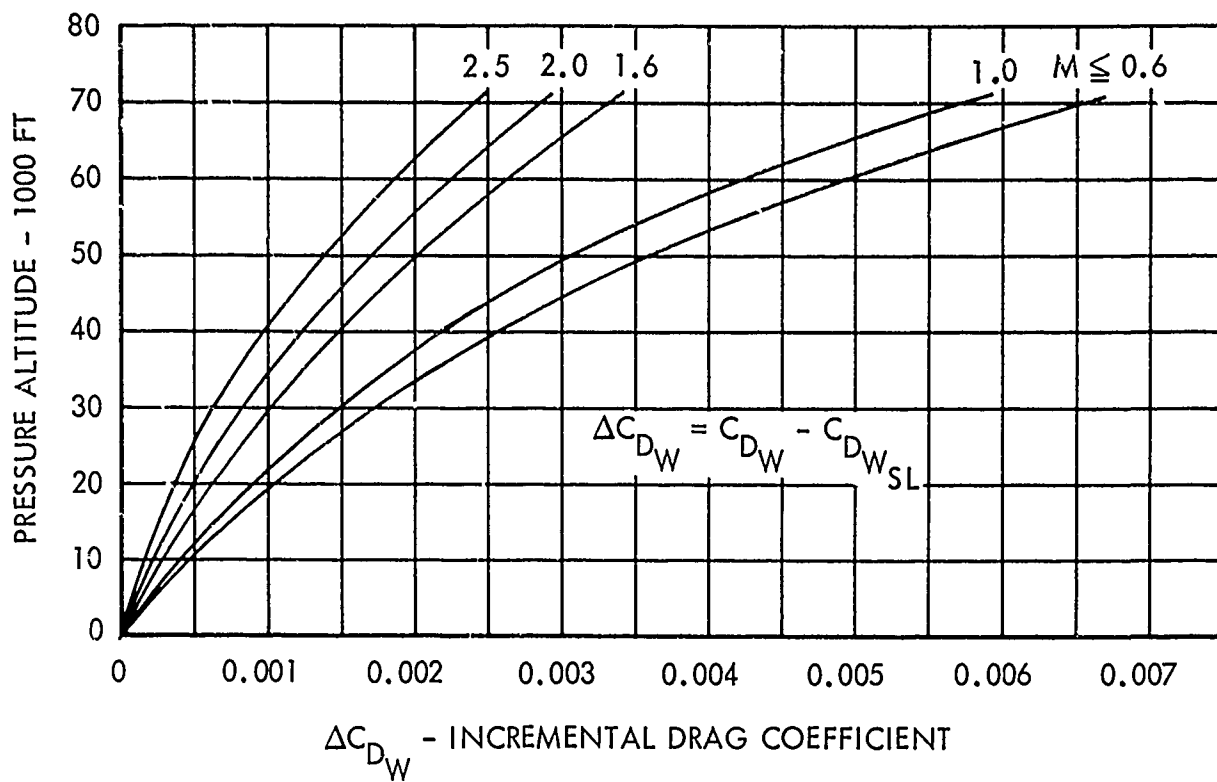


Figure 153. Configuration Y-1 Aero-Model
Zero Lift Drag Variation



$S_{REF} = 575 \text{ FT}^2$

CLEAN AIRPLANE

STD. DAY

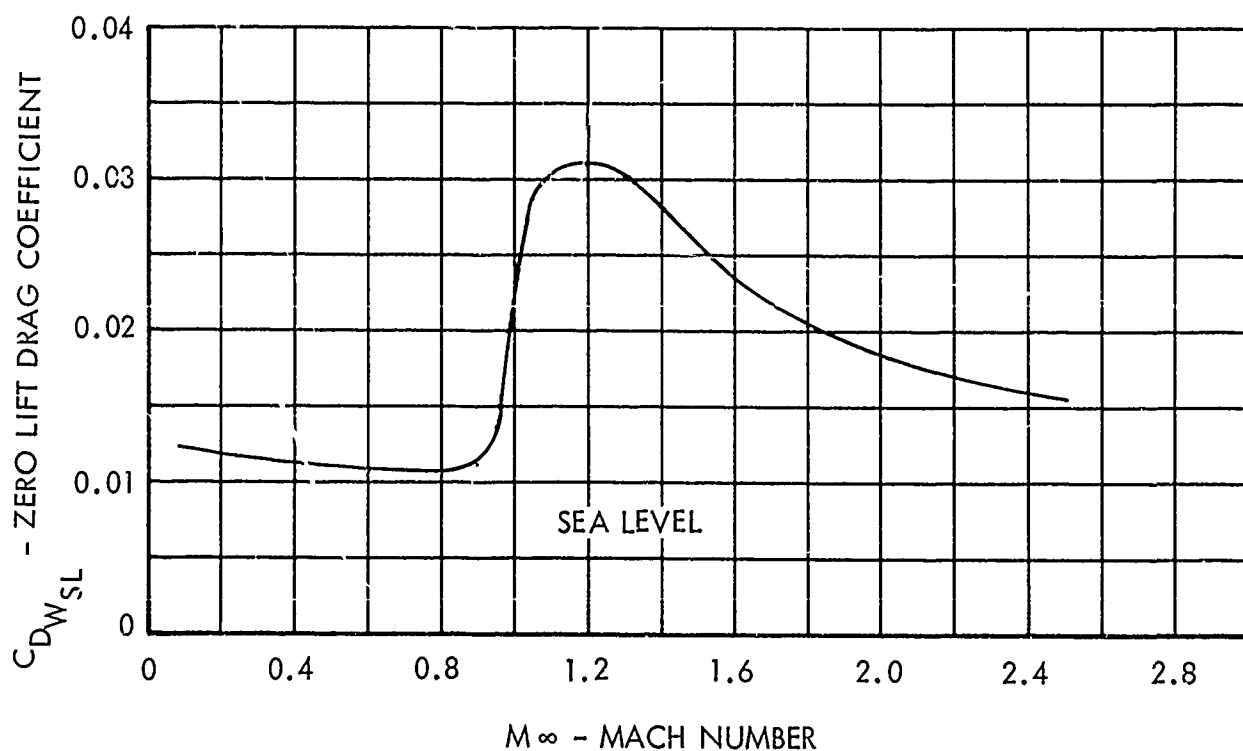
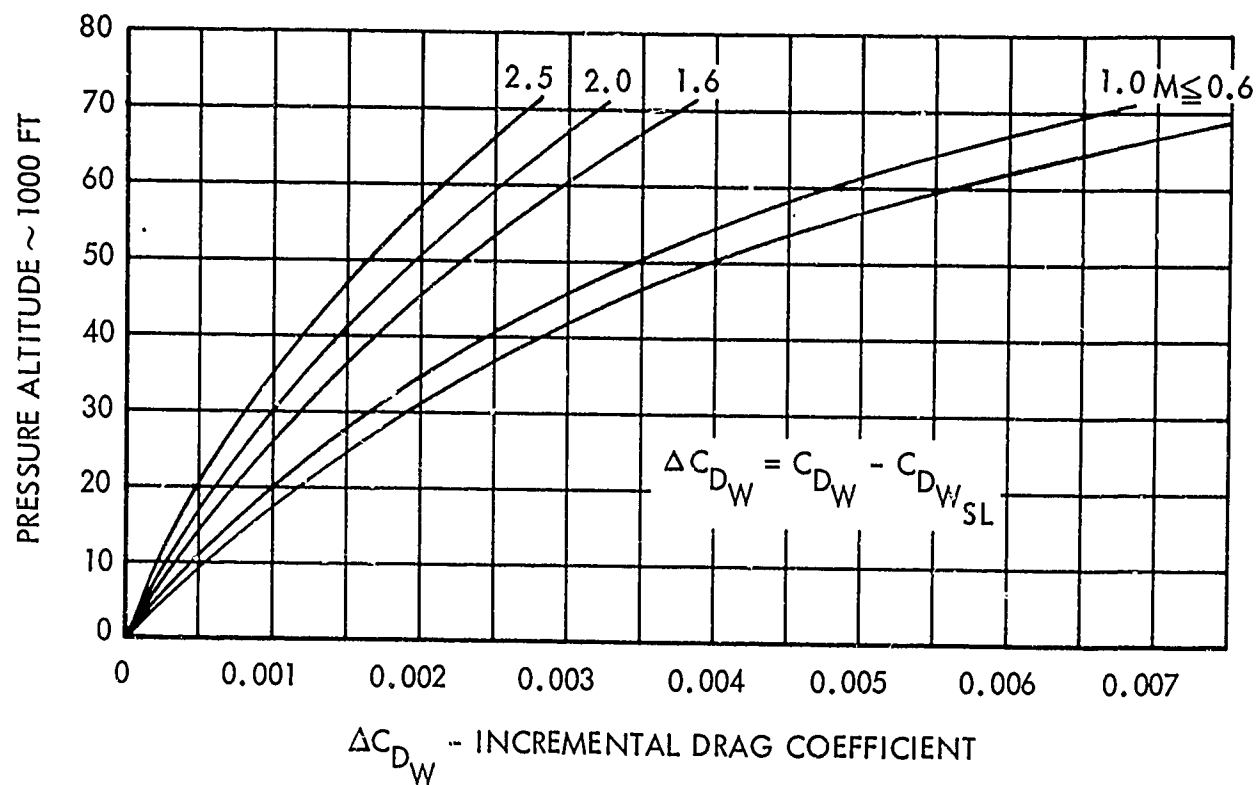


Figure 154. Configuration Y-2 Aero-Model
Zero Lift Drag Variation



$S_{REF} = 575 \text{ FT}^2$

CLEAN AIRPLANE

STD. DAY

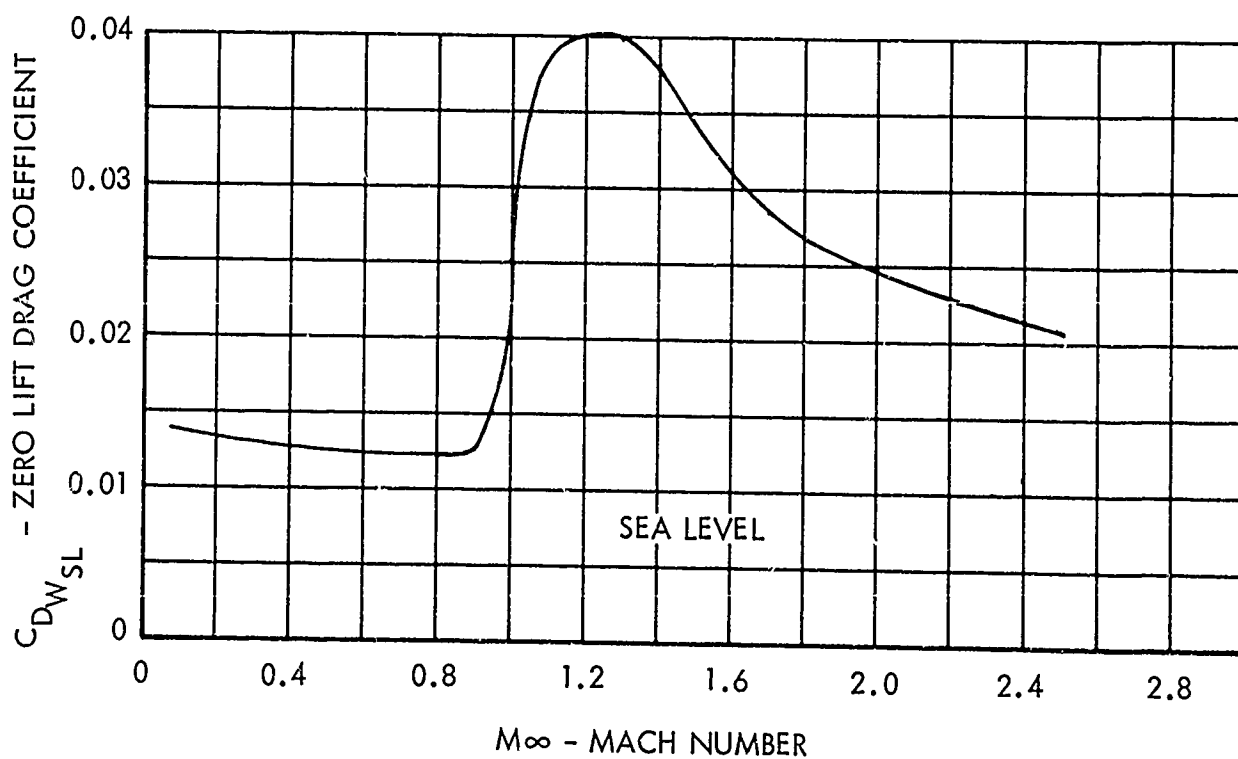
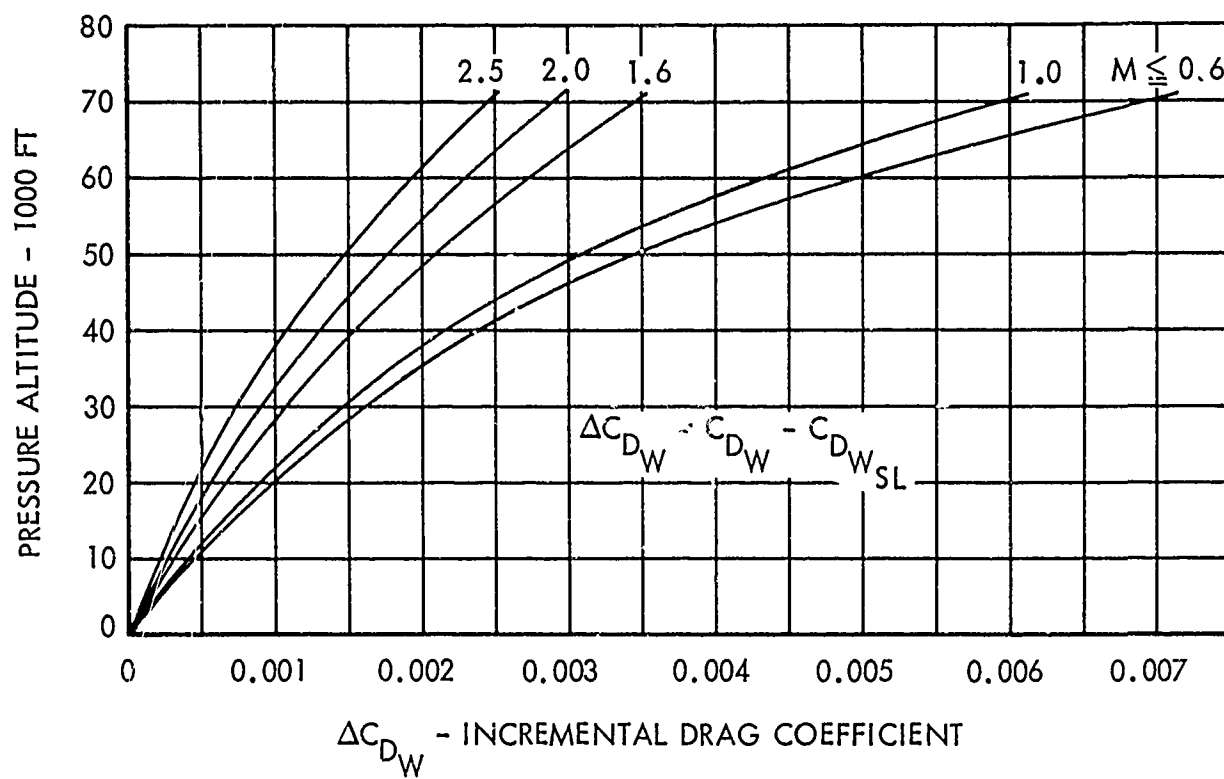


Figure 155 . Configuration Y-3 Aero-Model
Zero Lift Drag Variation



$S_{REF} = 575 \text{ FT}^2$

CLEAN AIRPLANE

STD DAY

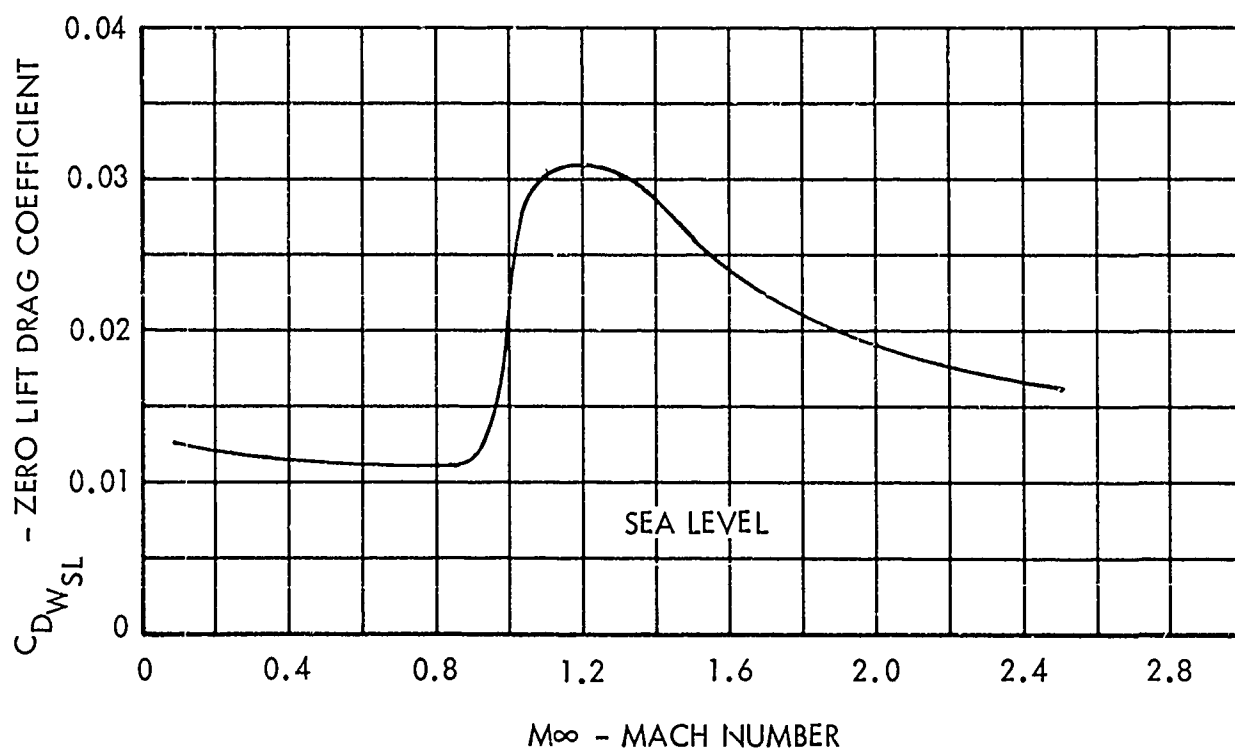


Figure 156 . Configuration Z-1 Aero-Model
Zero Lift Drag Variation

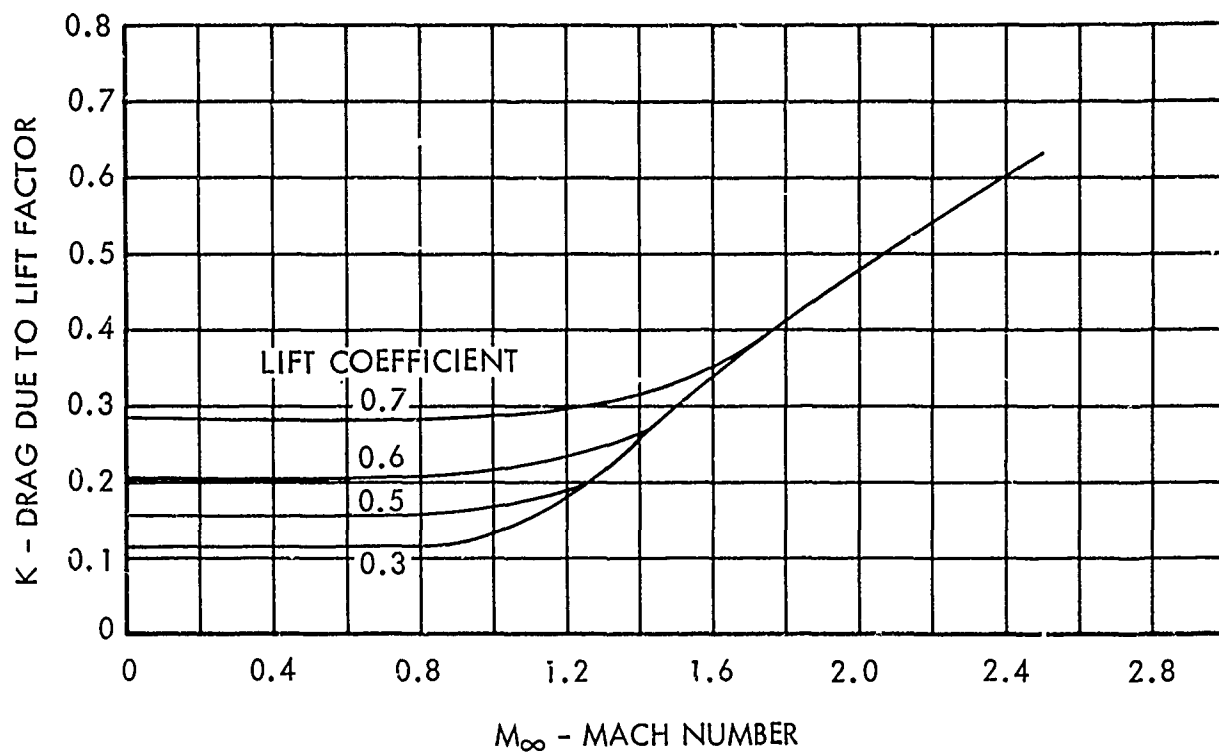


Figure 157. Drag Due to Lift Factor

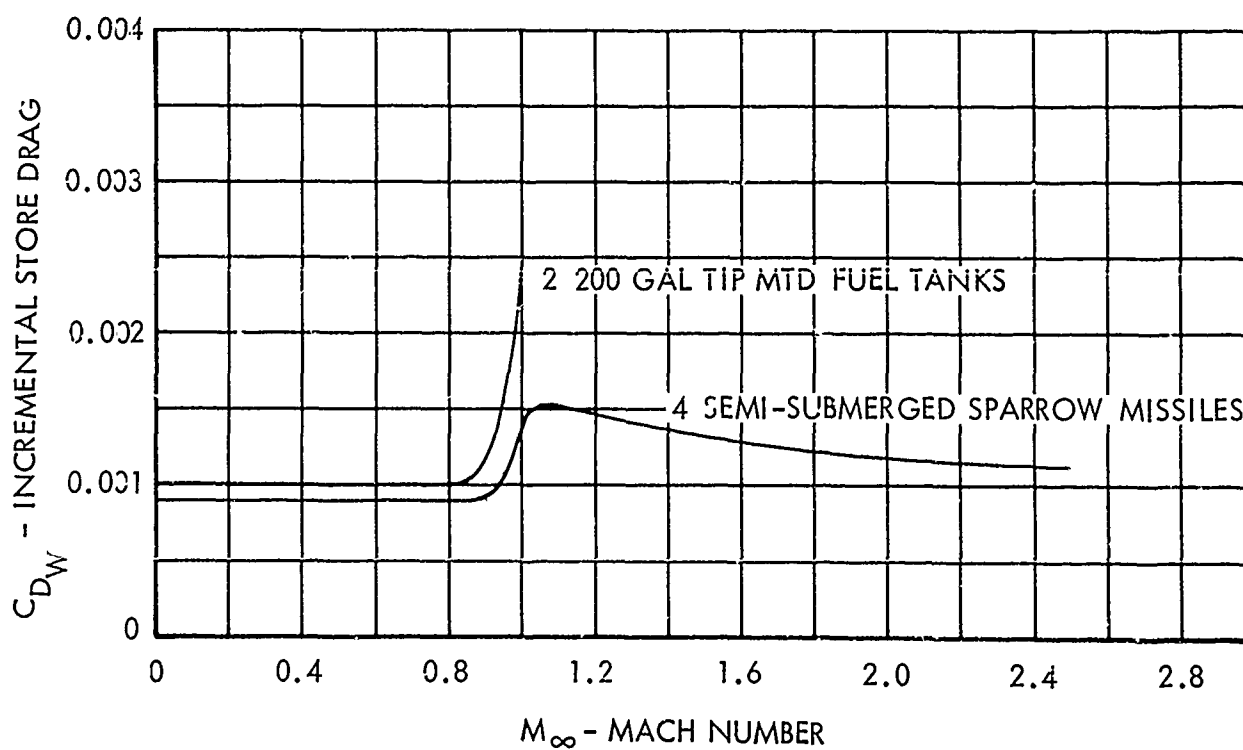


Figure 158. Increment External Stores Drag

The inlet, mounted on the sides of the fuselage upstream of the wing leading edge, is semi-circular with a double-cone centerbody, as shown in the top of Figure 159. The inlets for both the STF 371 Engine and the STJ 353 Engine are geometrically similar and were sized for 0.9 flight Mach number. The first cone is fixed at an angle of 18 degrees and the second cone angle follows the schedule with local Mach number shown in the top of Figure 159. The relationship between freestream Mach number and the inlet local Mach number is plotted in Figure 160. The cone angle schedules for both the STF 371 engine and the STJ 353 engine inlets are shown, and the corresponding throat to capture area ratios are given on the bottom of Figure 159. The cone angle schedule for the STJ 353 engine is slightly different than that for the STF 371 engine in order to provide the required throat area at subsonic speeds and to avoid excessive subcritical spillage drag at supersonic speed. For the ejector nozzle with the STF engine, however, the cone angle schedule for the STJ 353 engine was used to provide the additional air flow required by the ejector at subsonic speeds.

The total pressure recovery and inlet mass flow ratio for subsonic speeds was estimated from the theoretical analysis of Fradenburgh and Wyatt, Reference 85. The subsonic diffuser total pressure loss was assumed to equal 12.2 percent of the throat dynamic pressure. The total pressure recovery for supersonic speeds, shown in Figure 161, was estimated from MOC solutions and was assumed independent of inlet mass flow ratio for subcritical mass flow ratios. A 3 percent subsonic diffuser loss was assumed. The inlet mass flow ratio is known from the relation

$$\frac{m}{m_{O_L}} = \frac{\left(\frac{W\sqrt{\theta}}{\delta}\right)_{ENG} \left(1 + \frac{m_{BLD}}{m_{ENG}}\right)}{\left(\frac{W\sqrt{\theta}}{\delta A}\right)_L A_c} P_{t_2}/P_{t_\infty}$$

where

$$\left(\frac{W\sqrt{\theta}}{\delta A}\right)_L = 85.4145 M_L (1 + M_L^2/5)^{-3}$$

and for M_∞ equal or less than 0.8

$$\frac{m_{BLD}}{m_{ENG}} = 0$$

and for M_∞ greater than 0.8

$$\frac{m_{BLD}}{m_{ENG}} = -0.0235 + 0.0294 M_\infty$$

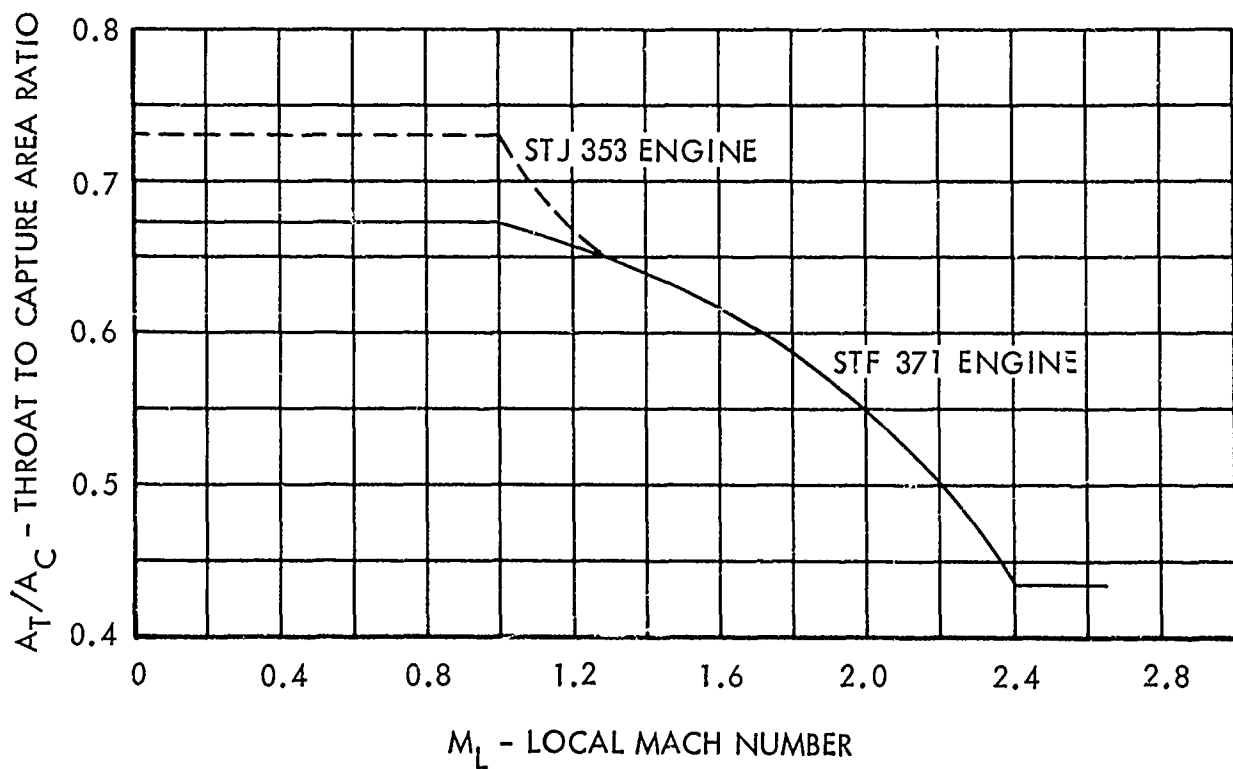
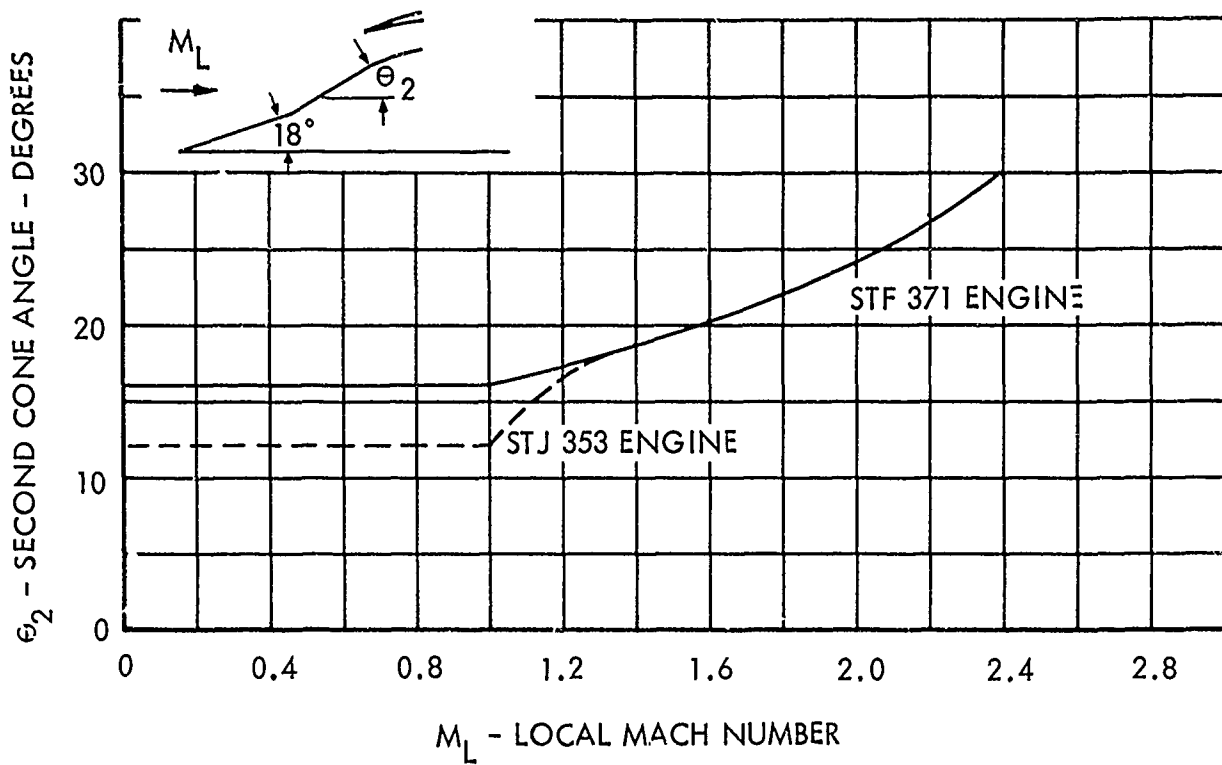


Figure 159. Second Cone Angle and Throat To Capture Area Ratio Schedules

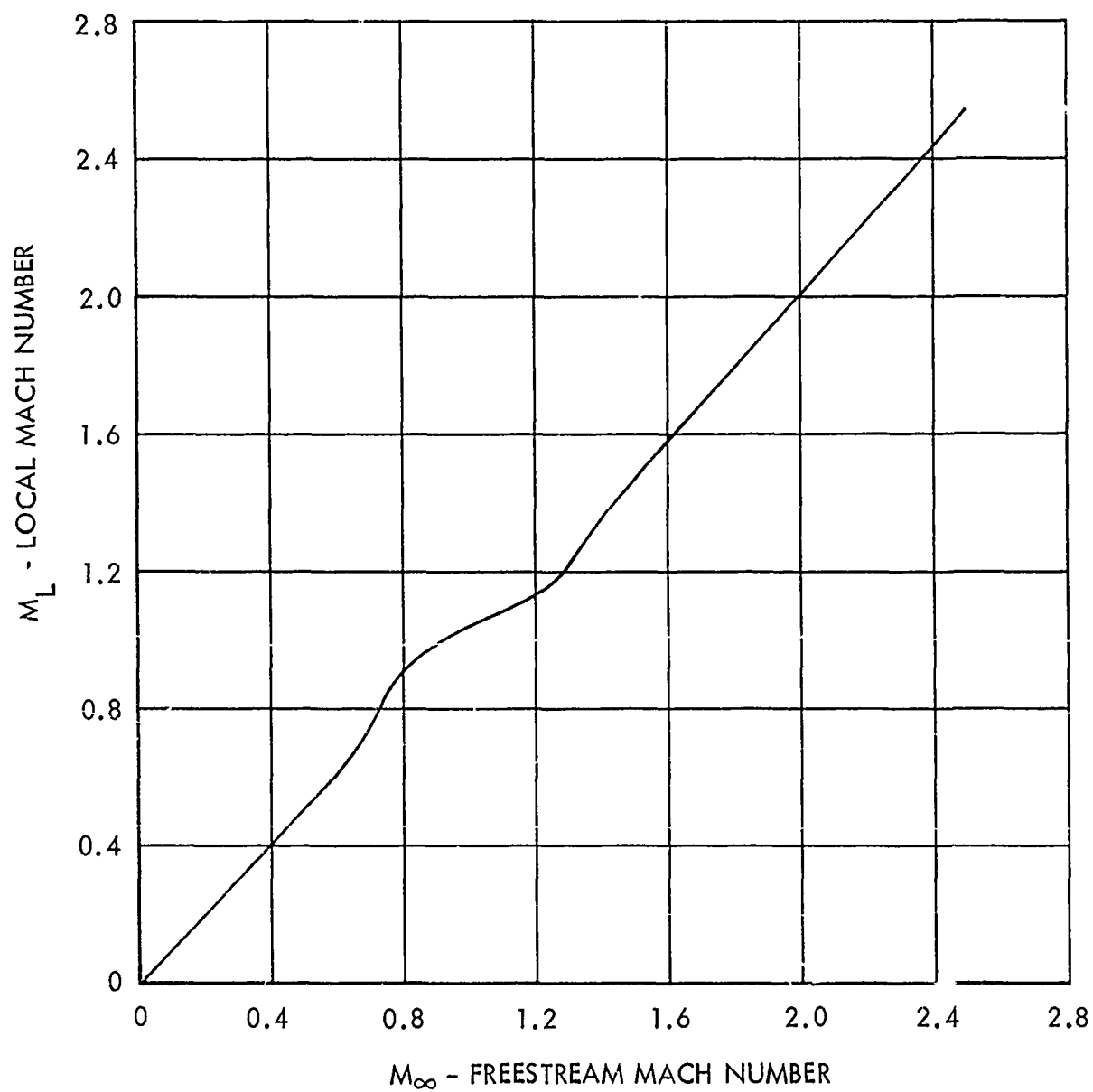


Figure 160. Inlet Local Mach Number

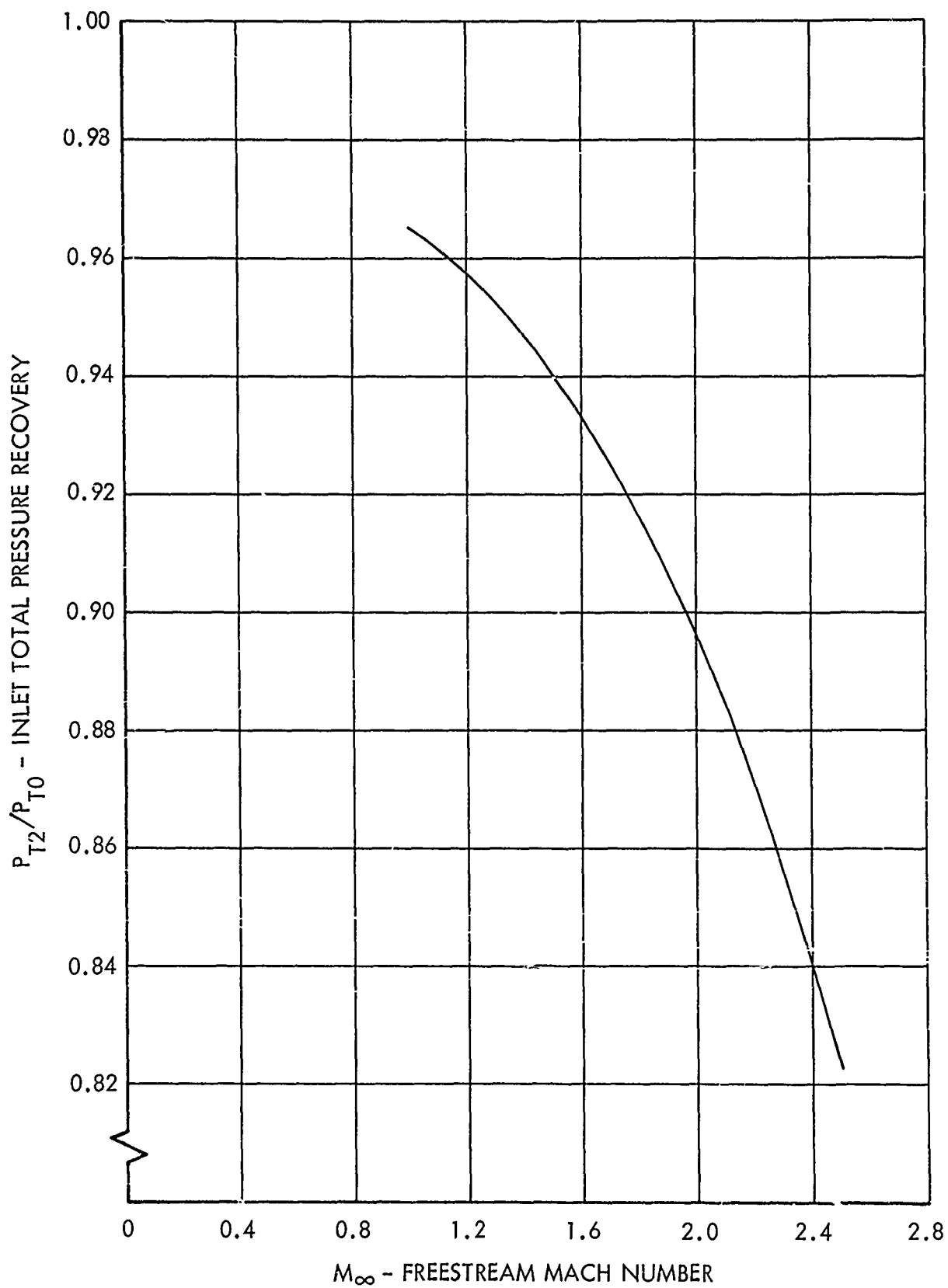


Figure 161. Inlet Total Pressure Recovery

The additive drag coefficient, shown in Figure 162 as a function of inlet mass flow ratio for various freestream Mach numbers, was obtained for Mach numbers 0.5 to 1.3 from drag correlations of Reference 86, and for Mach numbers from 1.4 to 2.5 from the method of Sibulkin, Reference 87.

The cowl lip suction to additive drag ratio, $C_{LS}/C_{D_{A_L}}$, was taken from

Reference 88. The spillage drag, which is defined as the additive drag minus the cowl lip suction, is computed from the relation

$$C_{D_{S_L}} = C_{D_{A_L}} (1 - C_{LS}/C_{D_{A_L}})$$

Finally, the drag coefficient based on freestream conditions is computed from the value based on local conditions as follows (See for example Reference 88).

$$C_{D_{S_\infty}} = C_{D_{S_L}} \frac{q_L}{q_\infty} + \frac{A_L}{A_C} \left\{ \left(\frac{P}{q} \right)_\infty \left[\frac{P_L}{P_\infty} (1 + \gamma M_L^2) - 1 \right] - 2 \frac{A_O}{A_L} \right\} + \left(\frac{P}{q} \right)_\infty \left(1 - \frac{A_L}{A_C} \right) \left(\frac{P_L}{P_\infty} - 1 \right)$$

where

$$\frac{A_L}{A_C} = \frac{m}{m_{O_L}}$$

$$\frac{A_O}{A_L} = \frac{M_L}{M_\infty} \left[\frac{1 + \frac{\gamma - 1}{2} M_\infty^2}{1 + \frac{\gamma - 1}{2} M_L^2} \right]^3$$

M_L Local Mach number

$\frac{P_L}{P_\infty}$ Local to freestream static pressure ratio

$\left(\frac{P}{q} \right)_\infty$ Freestream static to dynamic pressure ratio

$\frac{q_L}{q_\infty}$ Local to freestream dynamic pressure ratio

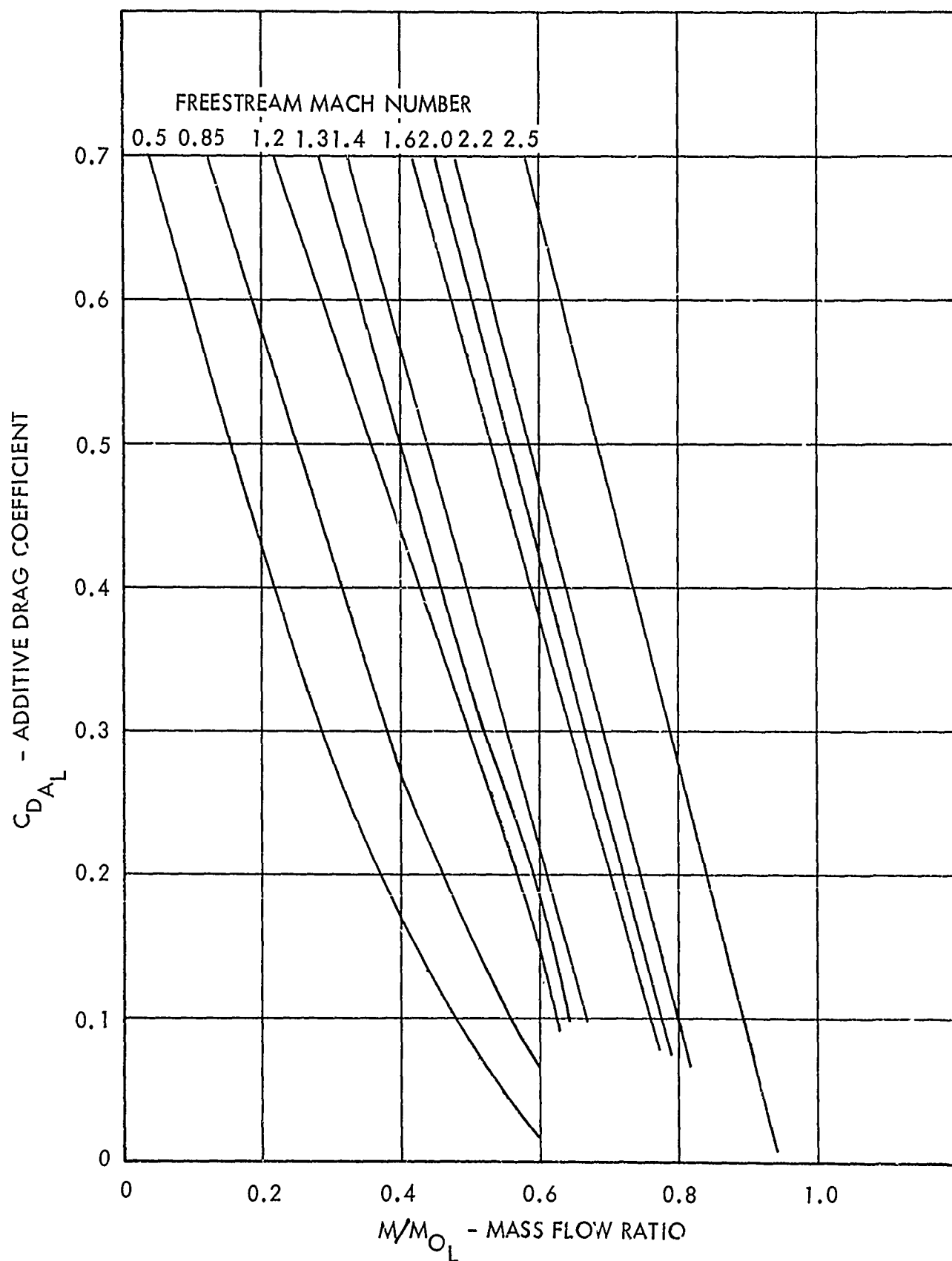


Figure 162. Additive Drag Coefficient

Aft-End Drag

The aft-end drag adjustment to the aero-model drag for different configurations was obtained using the methods described in Subsection 3.3.1. The procedure is as follows: (1) compute the installed aft-end drag for the twin-jet body for the nozzle operating at the given power setting and nozzle pressure; (2) compute the aft-end drag for an equivalent body with the same cross-section area distribution as the twin-jet body but with the nozzle in the maximum A/B power setting; and (3) determine the difference between the drags from steps (1) and (2). The installed aft-end drag, including base drag, for the twin-jet body for both subsonic and supersonic Mach numbers was found from the methods presented in Subsections 3.3.1 and 2.3.4. The aft-end drag includes the drag downstream of the metric break station for subsonic Mach numbers and includes the drag downstream of the maximum area station for supersonic Mach numbers. The aft-end drag for the equivalent body for supersonic Mach numbers was found from the equivalent body drag correlation given in Subsection 3.3.1. Because the aero-model drag for the subsonic Mach numbers is essentially independent of configuration for the configurations investigated in the present study, the aft-end drag for the equivalent body for subsonic Mach numbers was set equal to zero. This is justifiable since only drag differences are required and this drag is very small. Also, because of the similarity between the twin-jet body and the equivalent body, the drag adjustment for skin friction was assumed negligible for all Mach numbers. Since no base region was included in the aero-model drag, no base drag was computed for the equivalent body drag.

Aft-end drag coefficients (boattail plus base drag), given in the top of Figure 162, for the selected Phase II baseline configurations, and given in the bottom of Figure 163, for the four candidate configurations, show that the candidate aft-end configurations have, in general, lower drag than the Phase II configurations. The convergent-divergent nozzles are in the normal power position for subsonic Mach numbers and are in the maximum A/B power position for the supersonic Mach numbers. For the candidate configurations, however, the convergent-divergent nozzle position was selected such that the installed thrust-minus-external drag was maximized. As a result the nozzle exit to throat area ratio for the convergent-divergent nozzle at Mach 1.2 (maximum A/B power position) is higher than the corresponding area ratio for the Phase II configurations. The area ratios for the other Mach numbers were comparable. The Phase II intermediate spaced configuration number X-2 has the lowest drag at subsonic Mach numbers, and the wide spaced configuration number X-3, with twin vertical stabilizers has the highest drag at supersonic Mach numbers. The narrow spaced candidate configuration number Y-2, which has a long aft-end design, is among the lowest drag configurations at subsonic Mach numbers and is the lowest drag configuration at supersonic Mach numbers.

The aft-end drag adjustments to be added to the aero-model drag are presented in Figure 164. The largest positive drag adjustments occur for the Phase II baseline configurations, particularly for configuration numbers X-1 and X-3 at subsonic Mach numbers and configuration number X-3 at low supersonic Mach numbers. The drag adjustments for both baseline and candidate configurations at high supersonic Mach numbers are, in general, small.

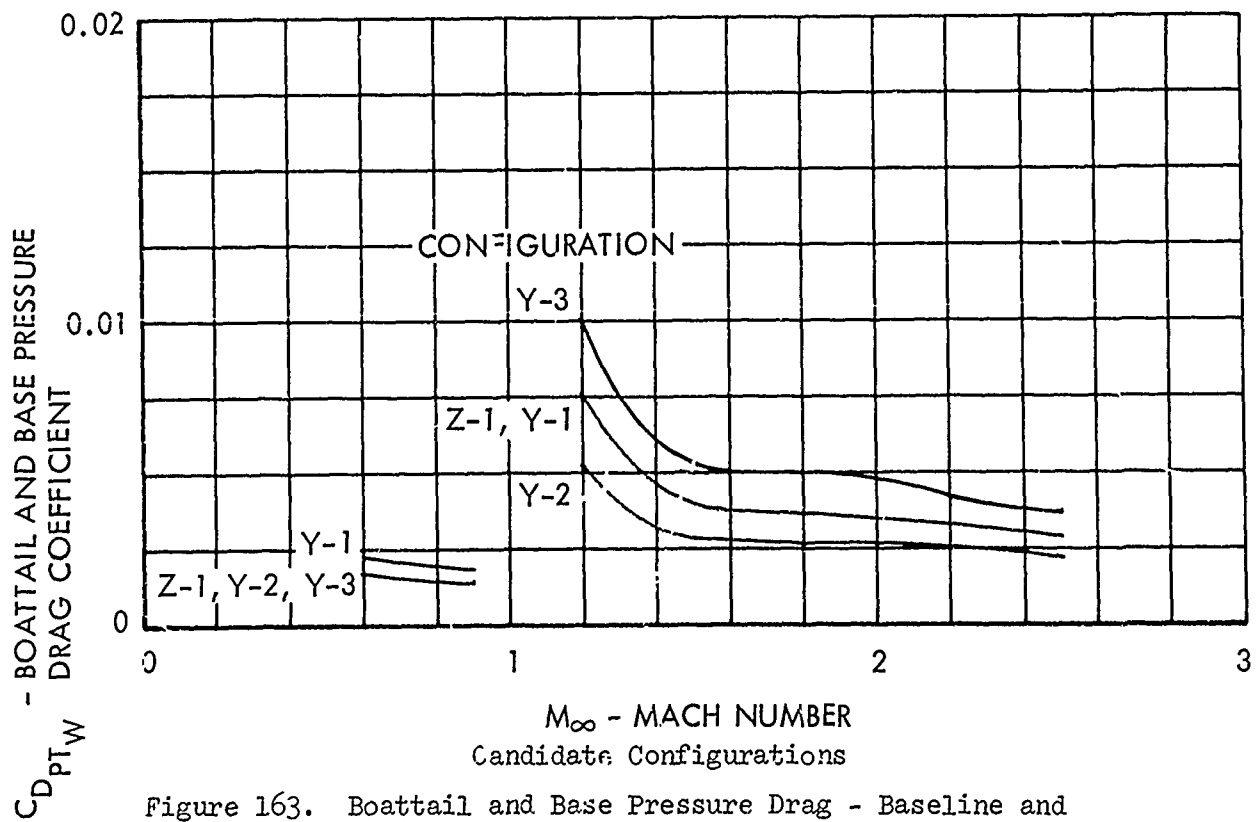
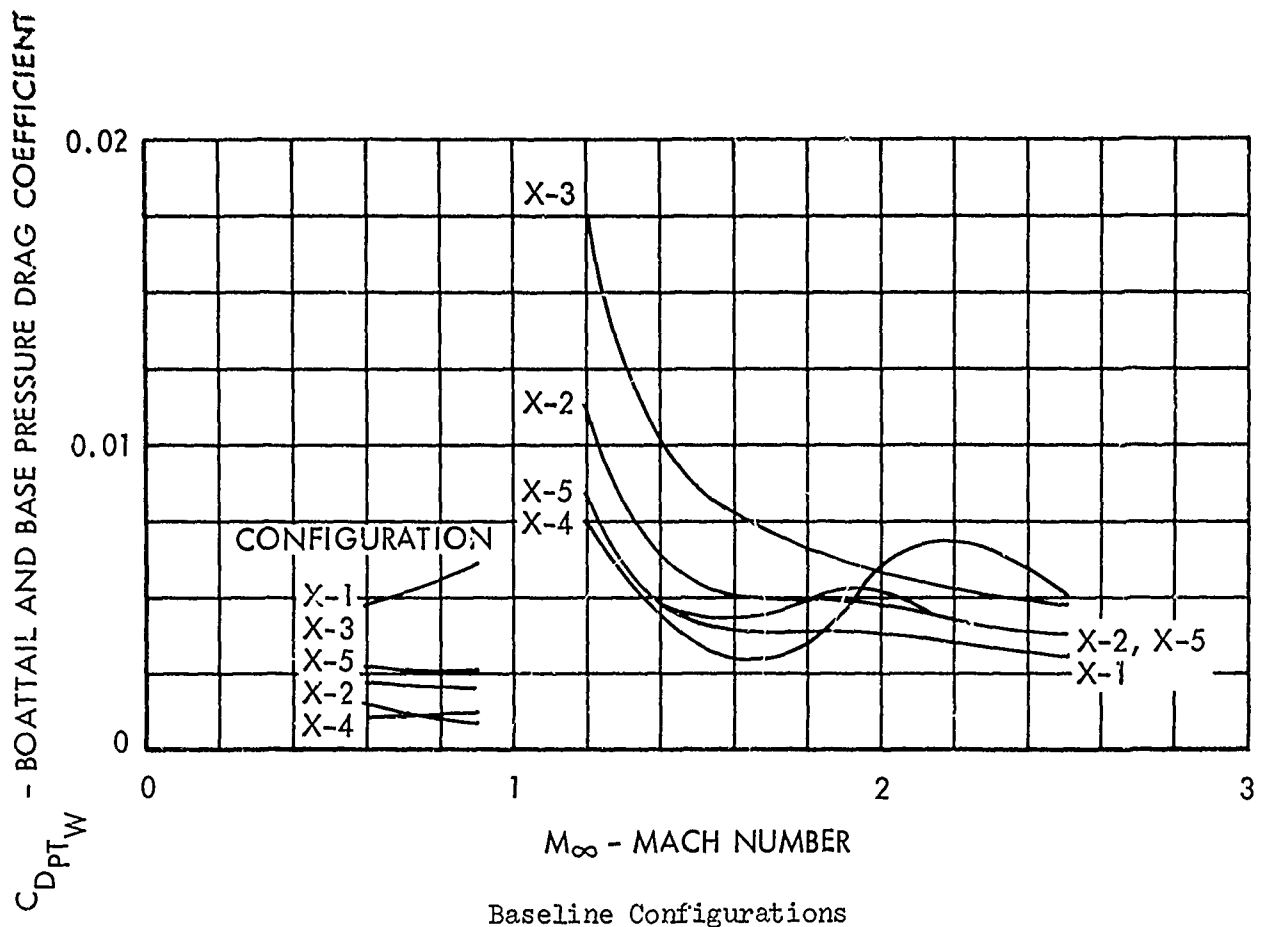


Figure 163. Boattail and Base Pressure Drag - Baseline and Candidate Configurations

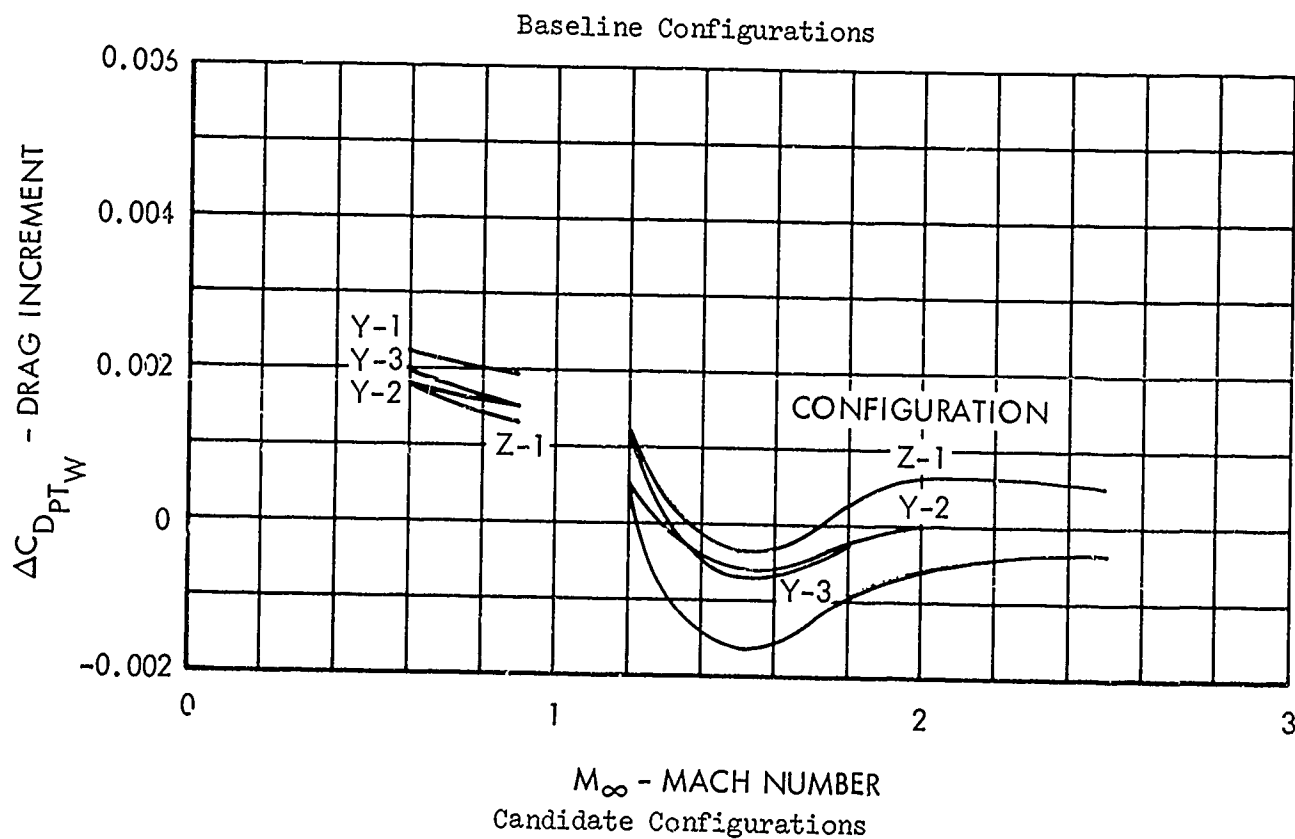
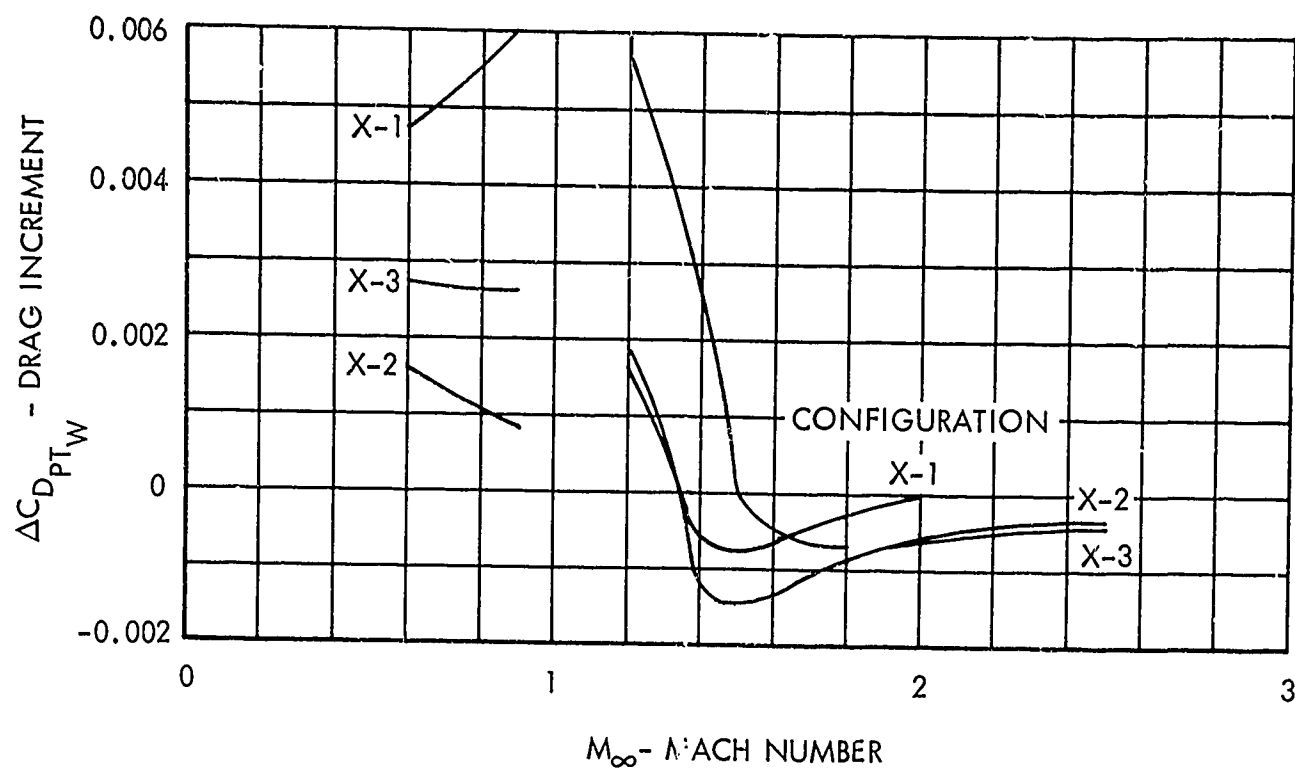


Figure 164. Drag Increment Between Propulsion and Aero Models - Baseline and Candidate Configurations

Internal Nozzle Performance

The thrust and nozzle discharge coefficients for the baseline and candidate configurations given in Figures 165 and 166 were computed using the methods described in Subsection 3.3.2. The nozzles are in the normal power position for subsonic Mach numbers and are in the maximum A/B power position for the supersonic Mach numbers. Both thrust and nozzle discharge coefficients are in general, comparable, among the configurations with the convergent-divergent nozzle, except for configuration number Z-1. The coefficients for configuration number Z-1 are generally lower because of the smaller throat area associated with the turbojet engine. The low thrust coefficients for configuration number X-4 at the supersonic Mach numbers were expected because of the underexpansion of the convergent-flap nozzle.

Weight Increments

Component weight increments for the selected configurations are presented in Table 21. The component weight increments are referenced to the X-1 configuration. Weights for the remaining components such as armament, auxiliary systems, etc., are assumed identical for all configurations.

4.2.5 Improved Design Selection

This subsection includes the comparative mission performance of the five baseline turbofan configurations (X-1 through X-5), the three candidate turbofan configurations (Y-1 through Y-3), and the one candidate turbojet configuration (Z-1). Mission performance, including SEP (specific excess power) comparisons, for all nine designs are presented relative to that of configuration X-1. Since the engine data used in the mission analysis studies was classified confidential, this method of comparison was employed so that the report could remain unclassified.

TABLE 21. AIRCRAFT WEIGHT COMPARISON

Incremental Weight from That of Baseline Configuration X-1 - Pounds

Component	Configuration								
	X-1 ⁽¹⁾	X-2	X-3	X-4	X-5	Y-1	Y-2	Y-3	Z-1
Tail	0	0	333	144	144	0	-439	0	0
Body	0	246	515	- 12	- 12	8	636	662	-285
Propulsion	0	0	0	-300	360	0	161	0	574
Total	0	+246	+848	-163	+492	+8	+358	+662	+289

(1) Baseline configuration

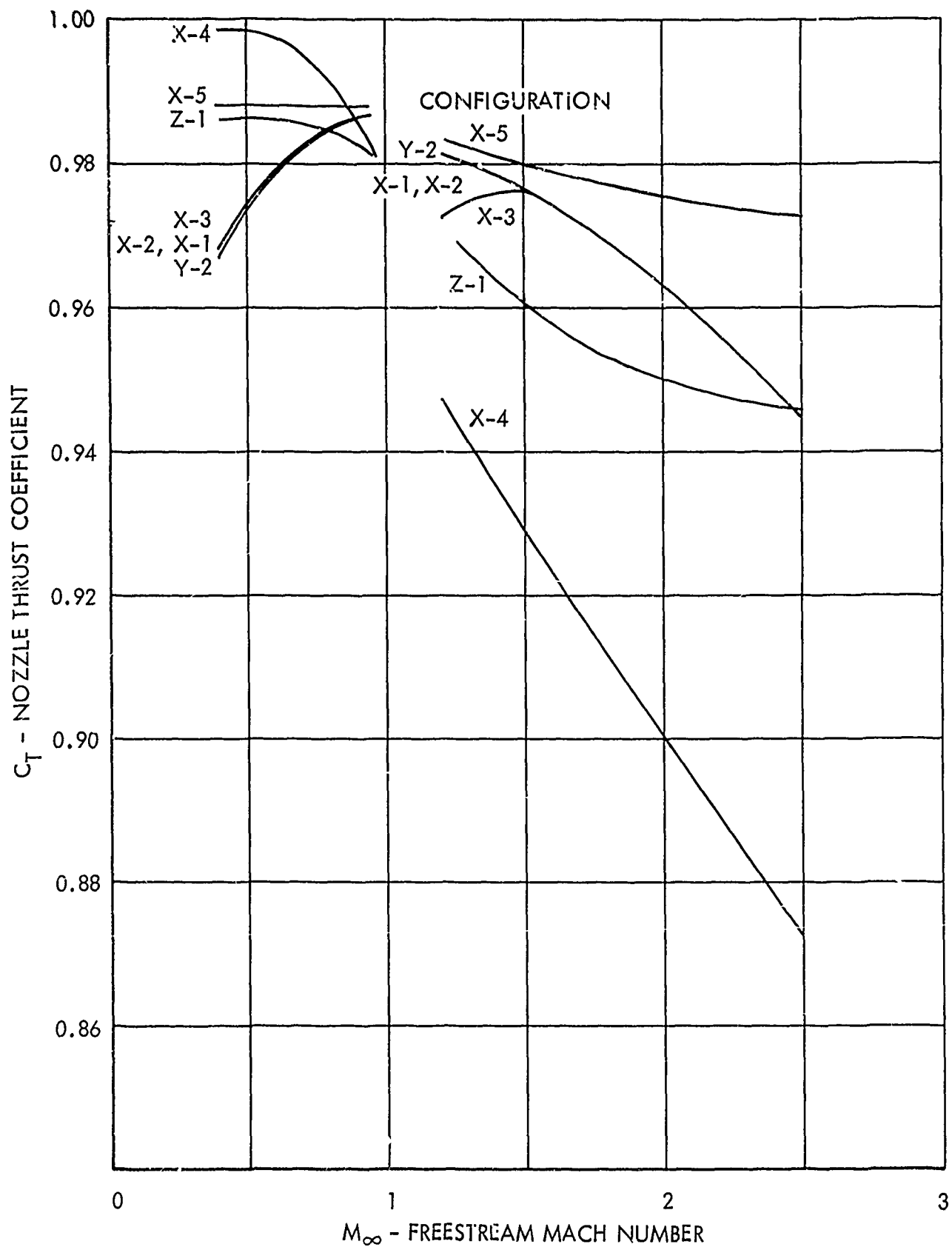


Figure 165. Nozzle Thrust Coefficients For Baseline and Candidate Configurations

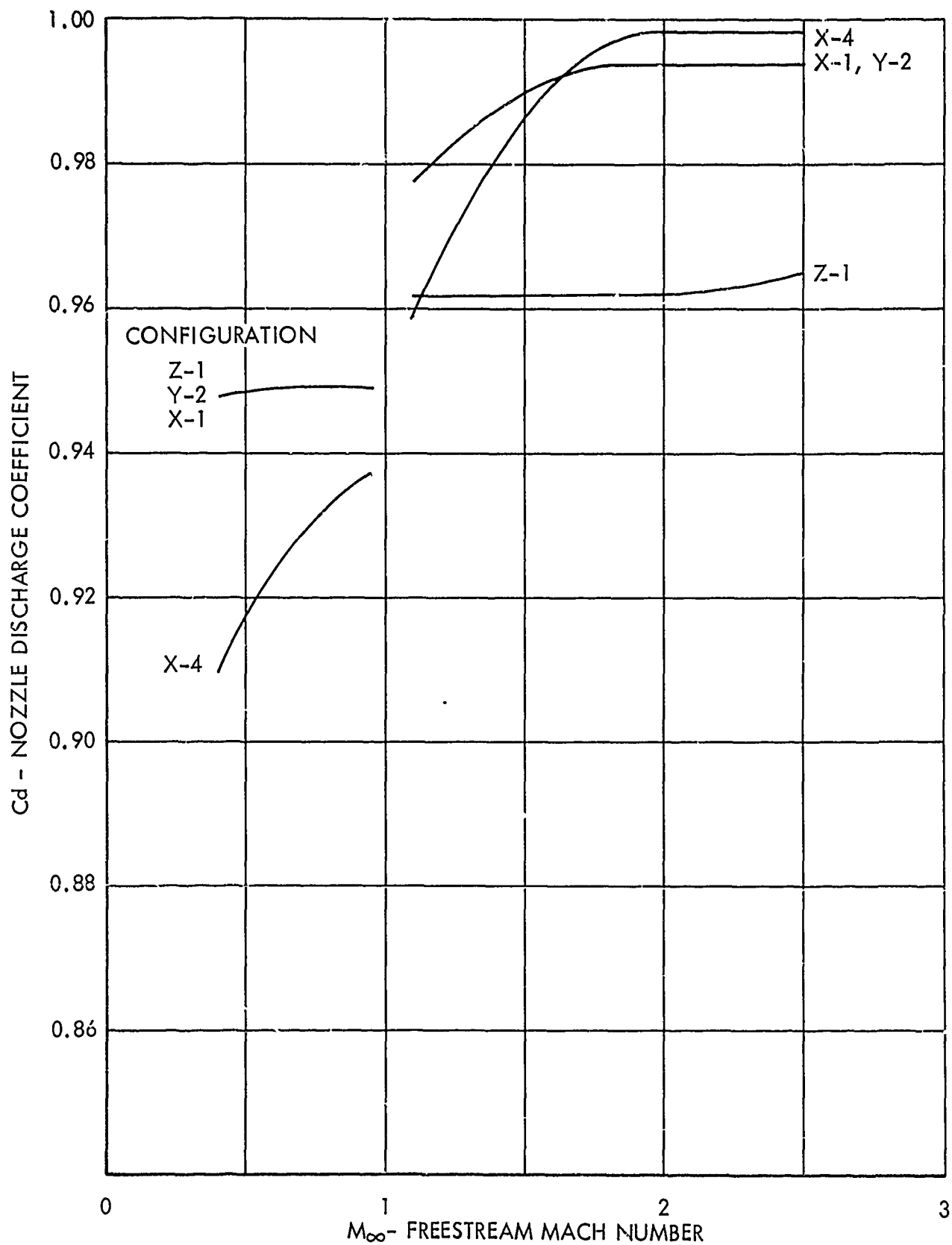


Figure 166. Nozzle Discharge Coefficients For Baseline and Candidate Configurations

4.2.5.1 Mission Description and Results

Each candidate vehicle has been analyzed in three different missions. These include: (1) Basic Air Superiority Mission; (2) Tactical Air-Air Mission; and (3) Supersonic Point Intercept Mission. Figures 167, 168, and 169 describe these missions by individual segment. Takeoff gross weight was held constant for all designs at 45,000 lbs. As can be noted in the Tactical Air-Air Mission, external fuel was allowed. Two 200-gallon, tip-mounted fuel tanks were used which increased the takeoff gross weight in this mission to 47,900 lb. Weapon armament consisted of 4 semi-submerged Sparrow missiles, an internal gun, and ammunition. Combat fuel allowance for all missions is that fuel necessary to gain 144,000 feet of maneuver energy utilizing maximum power.

$$\text{Combat fuel} = \frac{E_M W_f}{\text{SEP}}$$

where E_M = 144,000 feet of maneuver energy

W_f = fuel flow at 10,000 foot altitude, Mach 0.9, maximum A/B

SEP = specific excess power (ft/sec) at half fuel weight, at 10,000 foot altitude Mach 0.90, 1g wing loading clean airplane

Takeoff fuel was constant for all vehicles.

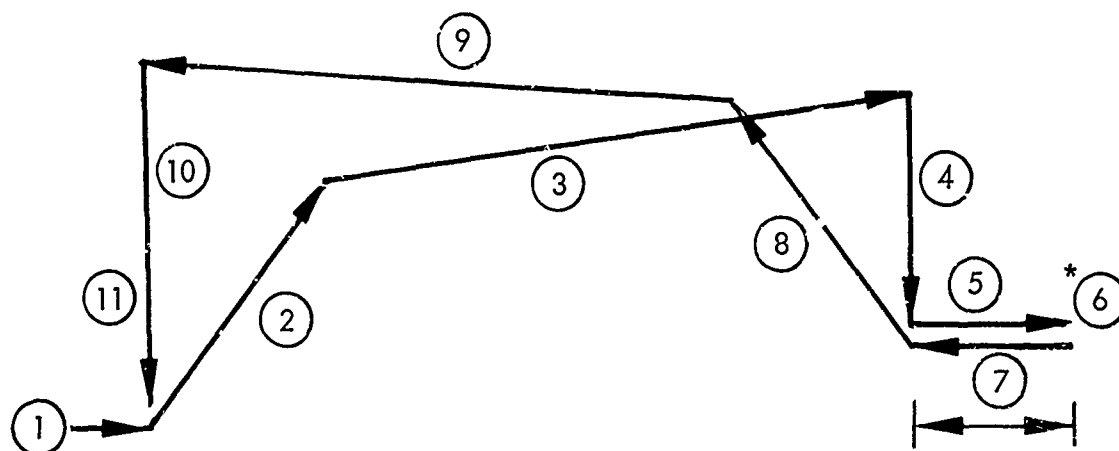
Calculations were made using the Calac Aircraft Mission Analysis Computer Program. This digital program is designed to work from basic data such as drag polars, thrust, and fuel flow tables. Mission segments consisting of various flight modes such as climb, accelerate, cruise, are connected in logical sequence to simulate the complete mission. Calculations are made in chronological order. For missions with a range optimization, iterations are made until the zero fuel weight falls within a preselected tolerance range.

The mission radius for each of the nine configurations are compared in Table 22 for each of the three selected missions. For the basic air superiority and tactical air-air missions, the narrow-spaced X-4 configuration with the convergent flap nozzle installed had the largest radius. This vehicle not only had the highest thrust but also the lowest zero fuel weight and external drag of all nine configurations. Although the thrust and zero fuel weight of the Z-1 turbojet installation were competitive, the mission radius for this configuration was extremely low due to the inefficiency of the engine cycle at part dry power settings. For the supersonic point intercept mission, the narrow-spaced Y-1 and Y-2 configurations had the largest mission radius, and the wide-spaced X-3 configuration, which had both the highest drag and highest zero fuel weight, had the lowest mission radius.

The mission radii of the Y-1, Y-2, and Y-3 candidate configurations are greater than those of the X-1, X-2, and X-3 baseline configurations, respectively, for all three missions investigated. The lower drag and higher thrust of the Y-1

Takeoff of gross weight = 45,000 lb

Payload: 4 Sparrow missiles + gun
+ ammunition



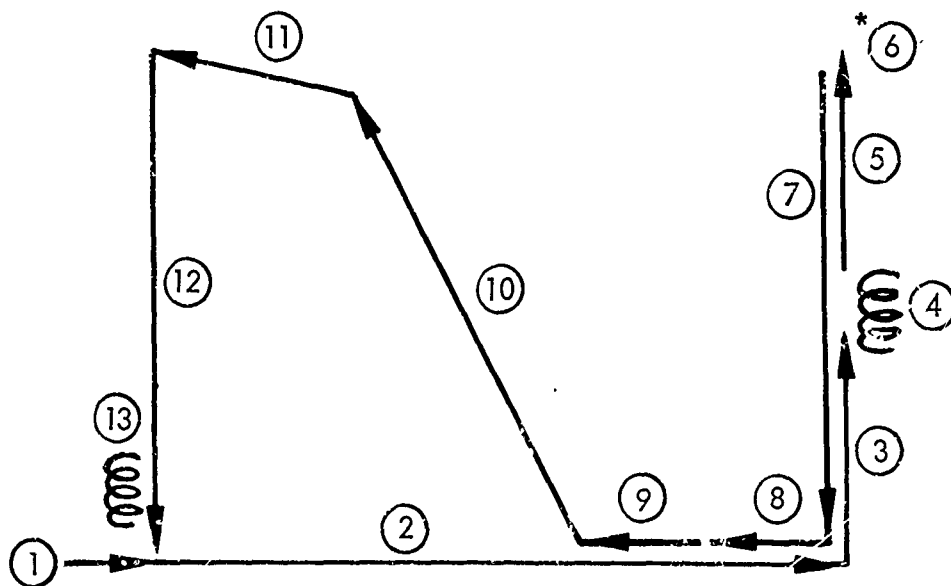
INTERNAL FUEL ONLY

1. Warmup and Takeoff: 2 minutes at normal rated power: 1 minute at maximum A/B (sea level static)
2. Climb to optimum cruise altitude: Mach 0.80 at normal power
3. Cruise at optimum Mach and altitude: partial power
4. Descent to 10,000-foot altitude (no time, distance, or fuel allowance)
5. Cruise at 10,000-foot altitude, Mach 0.95, for 60 nautical miles at partial power
6. Combat
7. Return Cruise at 10,000-foot altitude, Mach 0.85, for 60 nautical miles at partial power
8. Climb to optimum cruise altitude: Mach 0.80 at normal power
9. Return cruise at optimum Mach and altitude: partial power
10. Descent to sea level (no time, distance, or fuel allowance)
11. Reserve fuel: 20 minutes maximum endurance sea level: partial power

Figure 167. Breakdown of Basic Air Superiority Mission Profile

Takeoff of gross weight = 47,900 lb

Payload: 4 Sparrow missiles + gun
+ ammunition



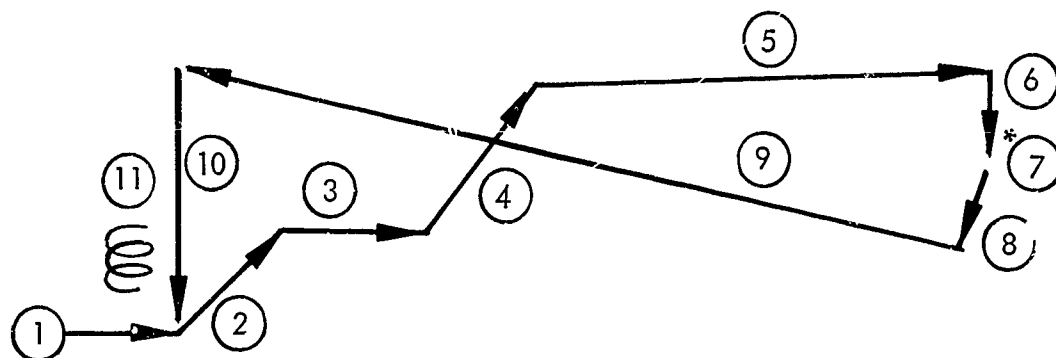
INTERNAL FUEL PLUS 2 - 200 GALLON EXTERNAL TANKS

1. Warmup and Takeoff: 2 minutes at normal rated power, 1 minute at maximum A/B (sea level static)
2. Cruise at Mach 0.70 and 500-foot altitude: partial power
3. Climb at Mach 0.90 to 10,000-foot altitude at normal power (no distance credit)
4. Cruise on station, Mach 0.90, 10,000-foot altitude, for 15 minutes (no distance credit): partial power
5. Climb at maximum A/B , Mach 1.10, to 20,000-foot altitude (no distance credit)
6. Combat
7. Descent to 500-foot altitude (no time, distance, or fuel allowance)
8. Return cruise for 50 nautical miles at 500-foot altitude at normal rated power
9. Return cruise for 50 nautical miles at 500-foot altitude at optimum cruise Mach number and partial power
10. Climb at Mach 0.80 to optimum cruise altitude: normal power
11. Return cruise at optimum Mach and altitude: partial power
12. Descent to sea level (no time, distance, or fuel allowance)
13. Reserve Fuel: 20 minutes maximum endurance at sea level: partial power

Figure 168 . Breakdown of Tactical Air-Air Mission Profile

Takeoff gross weight = 45,000 lb

Payload: 4 Sparrow missiles + gun
+ ammunition



INTERNAL FUEL ONLY

1. Warmup & Takeoff: 2 minutes at normal rated power, 1 minute at maximum A/B (sea level static)
2. Climb to 35,000-foot altitude at maximum A/B, Mach 0.925
3. Accelerate to Mach 2.50, altitude 35,000 ft at maximum A/B
4. Climb at maximum A/B, Mach 2.30, to combat ceiling altitude (rate of climb of 500 ft/min)
5. Cruise at combat ceiling, Mach 2.30, partial A/B
6. Descent to 50,000-foot altitude (no time, distance, fuel allowance)
7. Combat & store drop
8. Descent to optimum cruise altitude (rate of climb of 2000 ft/min @ partial power, Mach = 0.80)
9. Return cruise at optimum Mach and altitude: partial power
10. Descent to sea level (no time, distance, or fuel allowance)
11. Reserve fuel: 20 minute maximum endurance at sea level partial power

Figure 169 . Breakdown of Supersonic Point Intercept Mission Profile

TABLE 22. MISSION RADIUS COMPARISON

Configuration Incremental Radius From That of Baseline Configuration - X-1 - Percent

Configuration	X-1 ⁽¹⁾	X-2	X-3	X-4	X-5	Y-1	Y-2	Y-3	Z-1
Basic Air Superiority Mission	0.00	+4.62	-14.41	+11.80	-10.90	+6.30	+ 5.55	- 5.36	-24.60
Tactical Air-Air Mission	0.00	+8.44	-18.57	+18.05	- 8.02	+9.70	+10.54	- 5.49	-47.20
Supersonic Point Intercept Mission	0.00	-8.19	-35.78	-14.70	- 5.60	+2.59	+ 2.15	-19.83	- 2.15

(1) Baseline Configuration

and Y-2 configurations over that of the X-1 and X-2 configurations, respectively, more than compensated for the associated weight penalty. Although the subsonic aft end drag for the narrow-spaced Y-2 configuration is greater than that for the intermediate-spaced X-2 configuration, the total aircraft drag of the Y-2 configuration is less due to nozzle lateral spacing effects. The thrust, drag, and weight of the Y-3 configuration were all better than that of the X-3 configuration. Based on the mission analysis results, configurations Y-1, Y-2, and Y-3 are considered improvements over configurations X-1, X-2, and X-3, respectively.

The thrust and drag of the Y-1 configuration are better than those for the X-4 configuration for transonic and supersonic conditions only. As a result of these performance trends and the zero fuel weight penalty, the mission radius for the Y-1 configuration is greater than that for the X-4 configuration only for the supersonic point intercept mission. Therefore, the determination of whether the Y-1 design is an improvement over the X-4 design depends on the mission profile being considered.

The lower drag and lower zero-fuel weight of the Y-1 configuration over that of the X-5 configuration more than compensated for the lower nozzle thrust. Consequently, the mission radius for the Y-1 configuration is greater for all three missions investigated. Configuration Y-1 is therefore considered an improvement over configuration X-5.

The larger but lighter STF371 turbofan engine installed in the Y-1 configuration was replaced by the smaller but heavier STJ353 turbojet engine. The resultant Z-1 configuration was heavier due to the difference in engine weight but had improved performance since the body was more slender. Also, since the nozzle throat area excursion for the turbojet was considerably smaller than that for the turbofan, the maximum nozzle expansion was increased so that the same nozzle external contours could be utilized. The improved performance of the Z-1 configuration over that of the Y-1 configuration was not sufficient to overcome the associated weight penalty for all three missions investigated. For the subsonic missions, the turbojet installation was clearly inferior due to the inefficiency of the turbojet cycle at part dry power settings.

4.2.5.2 Maneuverability Requirements and Results

Table 23 shows the incremental values of SEP for the nine vehicles relative to configuration X-1. The drag was based on a clean aircraft with one half fuel load. Thrust was based on maximum available installed power at the flight condition. The comparisons and rationale made regarding the mission radius apply also to the SEP comparisons. Configuration X-3, having the highest drag and zero fuel weight, showed the poorest results of all the turbofan configurations. The Y-2 configuration showed the best SEP values for the supersonic flight conditions. SEP values are shown in Table 23 for several SEP points which utilize maneuver flaps. The drag due to lift penalty associated with the maneuver flaps combined with a high zero fuel weight results in lower SEP values for the Y-3 compared to the X-2 configuration. The significant increases in the supersonic regime however, can be considered an improvement

TABLE 23. SPECIFIC EXCESS POWER COMPARISON

Differential SEP from That of Baseline Configuration X-1 - ft/sec

Flight Condition			Configuration								
Mach	Altitude	Load Factor	X-1 ⁽¹⁾	X-2	X-3	X-4	X-5	Y-1	Y-2	Y-3	Z-1
(2)0.6	10,000 ft	5 g's	0.0	- 8.1	- 19.4	+ 11.5	- 55.5	- 4.5	-17.1	- 15.2	-25.5
0.9	10,000 ft	1 g	0.0	- 30.0	- 46.0	+ 1.0	- 89.0	-20.0	-12.0	- 38.0	-19.0
0.9	10,000 ft	5 g's	0.0	- 36.0	- 55.0	- 1.0	-100.0	-20.0	-20.0	- 41.0	-25.0
(2)0.9	30,000 ft	5 g's	0.0	- 10.0	- 53.0	+ 1.0	- 30.0	-11.0	-24.0	- 50.5	-67.0
1.6	35,000 ft	5 g's	0.0	- 73.2	-273.0	- 72.7	+ 96.4	+33.9	+60.1	-105.1	- 4.3
2.2	40,000 ft	1 g	0.0	-100.0	-351.0	-423.0	+103.0	+26.0	+85.0	-169.0	-432.0

All calculations based on Max A/B power, clean aircraft and half fuel weight, standard day

(1) Baseline configuration

(2) Maneuver flaps utilized for all configurations

over the X-2 configuration. Configuration Y-3 shows improved SEP values at each flight condition tested compared to configuration X-3.

The Y-1 configuration showed improvements over configuration X-1 at supersonic speeds. The subsonic conditions were all lower than the X-1 but were quite competitive. The convergent flap nozzle in the X-4 configuration clearly outperformed the heavier convergent-divergent nozzle in configuration Y-1 at subsonic speeds. However, the supersonic capabilities of the X-4 were much poorer than those of the Y-1 configuration.

4.3 EXPERIMENTAL PROGRAM FOR VERIFICATION OF DESIGN TECHNIQUES

A program has been developed for testing the four candidate configurations shown in Figures 144 through 147. The results from this program will be used to verify and/or improve performance prediction methods and design guidelines and criteria developed during the current program. The proposed recommendations, which are discussed below, are based in part on the knowledge gained from analysis of the Phase I and Phase II test results.

4.3.1 Background and Objectives

The design guidelines and criteria presented in Subsection 4.1 were applied to the selected baseline configurations shown in Figures 140 through 143 to determine the detailed modifications required for improved performance. Four candidate configurations evolved: three with the STF371 turbofan engine installed and one with the STJ353 turbojet engine installed. The installed thrust minus drag was then estimated for these new designs using the performance prediction methods discussed in Subsection 3.3. In order to evaluate these design and performance prediction techniques, a test program with the following objectives is recommended.

- Experimentally determine the effect of Mach number, nozzle pressure ratio, and nozzle power setting on the aft-end drag of the candidate configurations and use the results to improve the empirical drag correlations developed during the current program, if necessary.
- Experimentally determine the influence of the forward fuselage, wing, and empennage on the aft end drags, and conversely, the influence of these variables (including the aft end variations) on the total vehicle drag so that the design and performance prediction techniques developed during the current program can be generalized and applied to other aircraft configurations of the same basic type.
- Experimentally determine the effect of the support strut, inlet spillage, and Reynolds number on the total vehicle drag and use the results in building up the total aircraft drag.

4.3.2 Experimental Approach

The overall approach for meeting the above objectives is to test the candidate configurations in the AEDC 16T PWT using the existing Phase II model modified to measure (with force balances) the total aircraft drag in addition to the aft-end drag.

Analysis of results from the current program indicate areas where additional data would allow the performance prediction methods to be improved. Specifically, to obtain a complete matrix of test data, each candidate configuration should be tested, using the normal, partial A/B, and maximum A/B convergent-divergent nozzles, at Mach numbers from 0.6 to 1.5 at a nominal Reynolds number of 2.5 million per foot. The nozzle pressure ratio should be varied from jet-off to above the normal operating pressure ratio. All data should be recorded at a model angle of attack of zero degrees. This set of data would make it possible to verify and improve, if necessary, the empirical drag correlations for aft-end drag developed during the current program.

To generalize the design and performance prediction techniques developed during the current program for application to other aircraft configurations of the same basic type, it is recommended that the influence of the forward fuselage, wing, and empennage on aft-end drag be determined. Also, the influence of these variables (including the aft-end variations) on total aircraft should be determined. To do this, it will be necessary to have the total model mounted on force measuring balances. This can be done by mounting the Phase II non-metric model components on a single balance, by using the existing aft end balance arrangement, and utilizing the capability of testing with wing and/or empennage removed.

During the Phase II test program, the model was strut-mounted and had faired-over inlets. Pressurized, non-heated air provided the nozzle air flow. With this general arrangement, the effect of strut interference and inlet spillage on aft-end drag could not be determined. In order to provide data to evaluate these effects and ultimately obtain a total build-up of the aircraft drag, the recommended program includes the following-model configurations: (1) a strut-mounted model with flow-through inlets with the capability to vary the amount of inlet spillage; (2) a strut-mounted model with faired-over inlets and twin dummy stings extended aft from the nozzles; and (3) a sting mounted model with faired-over inlets. With the results from tests of these configurations, the strut interference, inlet spillage, and sting effects on aft-end drag and total drag can be determined. Also, the sting mounted model can be used to obtain basic aerodynamic data for an aircraft of this type.

Although full-scale Reynolds numbers can not normally be obtained in the wind tunnel, drag tends with Reynolds numbers variations should be included in this program. As an aid to analyzing the Reynolds number effects, flow visualization should also be utilized.

4.3.3 Model Description

The basic model installation, S_1 , will be strut supported with faired-over inlets. The internal airflow system will be non-metric. Five active force balances will be installed to measure nozzle, aftbody, and airframe (forward fuselage, wing, and empennage) aerodynamic loads separately. The aft-end pressure instrumentation arrangement will be similar to the Phase II model, and venturi meters will measure the nozzle air flow. The four candidate configurations for this program are listed symbolically below:

<u>Report Designation</u>	<u>Wing Tunnel Model Designation</u>	<u>Description</u>
Y-1	$S_{I4N}B_{I1}W_{I1}Y_{I1}H_{I1}^{-2}V_{2P}N6DCD$	Narrow nozzle spacing with area-ruled aft end
Y-2	$S_{I3N}B_{I1}W_{I1}Y_{I1}H_{I1}^{-2}V_{2P}N5DCD$	Narrow nozzle spacing with increased length but same volume as existing $S_{I1N}B_{I1}W_{I1}Y_{I1}H_{I1}^{-2}V_{2P}N3DCD$
Y-3	$S_{I2W}B_{I1}W_{I1}Y_{I1}H_{I1}^{-2}V_{2P}W4DCD$	Wide nozzle spacing with cross-sectional area distribution equal to existing intermediate spaced nozzle configuration $S_{I1N}B_{I1}W_{I1}Y_{I1}H_{I1}^{-2}V_{2P}I2DCD$
Z-1	$S_{I5N}B_{I1}W_{I1}Y_{I1}H_{I1}^{-2}V_{2P}N7DCD$	Narrow nozzle spacing with reduced cross-sectional area

The first three configurations accommodate turbofan engines and the fourth configuration accommodates a turbojet engine.

In addition to the basic data obtained from testing the above configurations, the inlet spillage effects and sting interference effects can be determined using this model installation. To obtain inlet spillage effects, flow-through inlets would be installed. By using cylindrical nozzle extensions, $S2B$, to reduce the effects of nozzle exhaust flow on aft end drag, and varying the internal flow area, the spillage effects can be determined. The flow-through inlets with no internal flow restrictions are designated by the symbol N . An additional subscript is used to indicate the amount or internal flow restriction.

In preparation for the strut interference investigation, the effect of the twin stings will first be determined using the strut mounted model. Dummy stings, identical to the actual stings, will extend aft from the nozzles to simulate the sting mount installation. The strut mounted model with dummy stings will be designated S_2 .

The sting supported model, S_3 , with faired-over inlets will provide basic aerodynamic data in addition to results that will be used to determine the strut interference effects. Although flow-through inlet and simulated nozzle exhaust data can not be obtained with this sting mount arrangement, a realistic aft end shape will exist.

4.3.4 Test Procedure and Schedule

The test procedure for the S_1 installation will be the same as the Phase II test procedure. For the S_2 and S_3 installations, the only variables will be the tunnel test conditions and model attitude. The recommended test program involves only the 16T tunnel for the following reasons: (1) obtaining data at the transonic speeds has been the primary objective of the current program; (2) data can be obtained more efficiently in 16T; and (3) the more severe environmental conditions in 16S tend to reduce the reliability of the data obtained at supersonic speeds.

To obtain the data discussed above, a wind tunnel test of approximately 100 hours will be required to test the 39 configurations listed in Table 24.

TABLE 24. RECOMMENDED RUN SCHEDULE

Model Support	Fuselage	Inlet	Wing	Empennage	Interfacing	Nozzle			(1) Mach Number Schedule	(2) Reynolds Number Schedule	Nozzle Pressure Ratio	Angle of Attack	Angle of Yaw	Number of Configurations
						CD ₁	CD ₂	CD ₃						
S ₁	E _{4N}	N ₁	On	On	N6D	X	X	X	A	B	Variable	Variable	0	3
S ₂			Off	Off		X	X	X	B	A				3
S ₁			On	On		X	X	X	A			0		3
S _{2B}		N ₂				X		X						2
S ₃		N _{2X}				X		X						1
S ₁		N ₁				X		X		B				4
S ₃						X		X						2
S ₁	F _{1N}	N ₁			N1D	X	X	X	B	A	Variable			3
S ₁	B _{3N}	N ₁	On	On	N5D	X	X	X	B	A	Variable	0	0	3
S ₃						X		X	A	A		Variable	Variable	2
S ₁	F _{5N}	N ₁	On	On	N7D	X	X	X	B	A	Variable	0	0	3
S ₃						X		X	A	A		Variable	Variable	2
S ₁	B _{2W}	N ₁	On	On	W4D	X	X	X	B	B	Variable	0	0	3
S ₃						X		X	A	B		Variable	Variable	2
S ₁	B _{1W}				W2D	X	X	X	B	A	Variable	0	0	3

(1) Mach Number Schedules: A - 0.6, 0.8, 0.9, 0.95, 1.1, 1.2, 1.4, 1.6
B - 0.6, 0.9, 1.2, 0.6

(2) Reynolds Number Schedules: A - 2.5, Million Per Foot
B - 0.5, Million Per Foot To Tunnel Maximum

SECTION 5

CONCLUSIONS AND RECOMMENDATIONS

This experimental and analytical investigation of the installed thrust and drag of various isolated nozzle and twin-nozzle/airbody configurations has been completed under Air Force Contract F33657-70-C-0511. An assembly of performance prediction techniques and design criteria and guidelines for the integrated design of airframe-nozzle combinations were developed during the program and applied to selected air superiority fighters having twin buried engines and dual nozzles. The major conclusions and recommendations derived from the program are presented below.

5.1 TEST FACILITY AND APPARATUS

- Venturi meters provided more accurate and reliable nozzle mass flow measurements than sharp-edge orifice meters, and the mass flow measurements from an AEDC-supplied Swirlermeter were in close agreement with those from the venturi meters.
- The AEDC precision pressure balance system provided more accurate and reliable pressure measurements than scanivalves.
- Good agreement was obtained between the thrust and drag coefficients determined from direct force measurements and those obtained from pressure integrated forces and calculated skin friction drag. Results were especially good for the Phase II AEDC 16T FWT entries where the RMS (root-mean-square) of the deviations between the pressure and force balance results was 2.7 counts of nozzle drag, 3.9 counts of airbody drag, and 5.0 counts of total drag. The RMS of the deviations for the thrust-minus-nozzle-drag coefficient was 0.0059 (equivalent to about 0.6 percent).
- In order to obtain accurate force balance measurements, it is recommended that separate force balance designs be developed for 16T and 16S installations. The model forces measured in 16S are generally small due to the low tunnel operating pressures and yet the balances must be designed to withstand the potentially large tunnel unstart loads. The development of such a balance is extremely difficult, especially since the 16S operating total temperatures generally exceed 130 degrees Fahrenheit. A balance designed for this application most likely would be inferior to one designed specifically for 16T, where tunnel unstarts are not encountered and the balance design loads are more nearly equal to the anticipated running loads.

- Greater emphasis should be placed on obtaining flow visualization recordings so that separated flow regimes, which have a significant effect on aft-end drag, can be more easily identified.

5.2 EXPERIMENTAL RESULTS

- The strut wake had a negligible effect upon the external static pressure distributions on the isolated pod aftbody and nozzle boattail.
- Differences in total aftbody plus nozzle drag for different nozzle types and power setting positions were due primarily to differences in nozzle boattail drag. As would be expected, external flow had little effect on nozzles with small projected frontal areas. At subsonic speeds, only those nozzles with long, smooth contours were pressurized by the nozzle flow, which diminished the nozzle drag. At supersonic speeds, the drag difference between nozzles was small due to the compensating effect of flow expansion and jet induced separation.
- Thrust coefficients were highest at low nozzle pressure ratios for the plug nozzle at all power settings because of plug pressurization by the external flow. Convergent-divergent nozzles had the highest thrust coefficients at pressure ratios higher than those required for full expansion. The convergent nozzle thrust coefficients decreased monotonically with increasing nozzle pressure ratio and were lower than those of the other nozzle types at all pressure ratios, except for overexpanded convergent-divergent nozzles.
- Dishcharge coefficients for all nozzles and power settings were significantly lower for nozzles with internal contours having sharp corners or turns.
- Nozzle lateral spacing had little influence on the total drag of the Phase II aircraft model at subsonic speeds; this is consistent with potential flow theory. At supersonic speeds, the total drag increased significantly with increasing nozzle spacing due to the larger flow expansion (reduced pressures) caused by the increased frontal area, increased frontal area, increased local Mach number at the start of the aft-end, and the steepened area distribution curve.
- The total drag for the vertical wedge interfairing configurations was significantly greater than that for the horizontal wedge interfairing configurations due to the low pressure in the base region between the vertical wedge interfairing and the nozzle boattail. The total drag was essentially the same for all horizontal wedge type interfairings.

- The total drag decreased as the interfairing trailing edge moved downstream from the customer connect station to the exit plane of the convergent-divergent nozzles. Longer interfairings were tested for the normal power convergent-divergent nozzle only, and a minimum total drag existed for the interfairing terminating at the nozzle exit plane.
- The total drag for the canted and vertically-mounted twin stabilizer configurations was nearly equal and significantly higher than the total drag for the forward and aft-mounted single vertical stabilizer configurations, which were nearly equal.
- Little effect was observed for empennage span reduction from full to partial span or from fuselage fairing alone to no empennage and no fairing. Empennage removal resulted in a significant reduction in total drag at subsonic speeds and little change in drag at supersonic speeds.
- Little change in total drag with horizontal stabilizer deflections was observed. Little change is also expected due to rudder deflection; however, this result cannot be substantiated since no nozzles were tested with active force balances on both sides of the model.
- The effect of angle of attack on total drag depended on the Mach number range considered. At Mach 0.6, the drag decreased slightly with increasing angle of attack, and at Mach 0.9 a minimum drag occurred at the intermediate value of six degrees angle of attack. At supersonic speeds, the drag increased with increasing angle of attack. Angle of attack had no effect on nozzle thrust.
- The nozzle drag coefficient, in general, decreased at subsonic speeds and increased at supersonic speeds with increasing Reynolds number. The aftbody and total drag coefficients increased at a decreasing rate with increasing Reynolds number, even though the friction component of the drag coefficients decreased. At Reynolds numbers equal to or greater than the basic test Reynolds numbers (2.5 million to 6.0 million per foot in the AEDC 16T PWT and 1.0 million to 1.6 million per foot in the AEDC 16S PWT), the change in nozzle and aftbody drag coefficients was small and within accuracy of the data.
- The effects of boundary layer trips on external drag were small at the basic test Reynolds numbers and large at the reduced Reynolds number per foot of 0.5 million, where the distance between natural and forced transition becomes significant. At this reduced Reynolds number, the configurations with boundary layer trip arrangements which allow transition to be delayed on portions of the model had thinner boundary layers, which resulted in lower drags at subsonic speeds and higher drags at supersonic speeds.

5.3 PERFORMANCE PREDICTION METHODS

- None of the analytical methods evaluated is recommended for predicting boattail drag over axisymmetric bodies for subsonic external flow. However, potential flow theory, corrected for compressibility and for displacement effects of the surface boundary layer and external plume, provided reasonably good estimates of external pressures for unseparated flows at freestream Mach numbers below about 0.8. Pressures predicted by the Pratt & Whitney inviscid transonic analysis with the Reshotko-Tucker boundary layer method agreed well with test data below Mach 1.0 but not so well just above Mach 1.0. For supersonic flow, the MOC (method of characteristics) with a boundary layer displacement correction accurately predicted both pressure distributions and drag in unseparated flow. Use of the Bonner-Karger method adequately predicted the separation point location. The solution can then be corrected for flow separation effects by means of the Brazzel-Henderson base pressure correlation.
- The Pratt and Whitney IMS (integral mean slope) correlation was in good agreement with both subsonic and transonic Phase I isolated nozzle drag data. A correlation of inviscid MOC pressure drag, achieved through use of IMS combined with similarity parameters obtained from linearized supersonic flow theory, provided an accurate and rapid means of estimating drags for arbitrary axisymmetric boattail contours at supersonic speeds.
- The equivalent body (single and multiple axisymmetric body representations) and three-dimensional analysis methods evaluated are not recommended for predicting twin-nozzle/aftbody drag for either subsonic or supersonic external flow. However, for a subsonic external flow, both the P&WA three-dimensional transonic flow method and the Caldec three-dimensional potential flow method provide reasonably good estimates of the pressure distribution over twin-nozzle bodies. A sector analysis approach employing axisymmetric potential theory for subsonic flow and method of characteristics for supersonic flow was inadequate for predicting pressure distributions.
- The Phase II twin-nozzle/aftbody drag data was correlated for jet-off conditions at both subsonic and supersonic speeds. The subsonic correlation was developed by combining Spreiter's transonic similarity parameters with the IMS of the equivalent body of revolution. The supersonic data was correlated with the equivalent drag obtained from the axisymmetric MOC correlation. Additional correlations of the Phase II data were developed to account for nozzle pressure ratio effects.
- The AEDC-ETF (Engine Test Facility) transonic nozzle flow analysis technique combined with boundary layer and method of characteristics analyses accurately predicted the thrust and discharge coefficients of convergent-divergent and plug nozzles provided there was no flow separation and the influence of the external flow was axially

symmetric. A sector analysis technique employing a method of characteristics method was not adequate for predicting plug surface pressure distributions when the influence of the external flow was unsymmetrical. For ejector nozzles with choked secondary flow, good agreement in pressure distribution and pumping characteristics was obtained with a method using one-dimensional analysis for the secondary flow and the method of characteristics for the primary flow.

- The use of shock-expansion theory for external flow and a combination of shock-expansion theory and one-dimensional theory for internal flow yielded isolated nozzle exhaust plume contours in good agreement method of characteristics solutions.
- The Brazzel-Henderson subsonic and supersonic base pressure correlations provided accurate predictions of annular base pressure for axisymmetric models with small base areas. No adequate techniques are available for predicting the unsymmetrical annular base pressures observed for the Phase II model. Twin-nozzle plug base pressures can be predicted by application of isolated plug nozzle empirical correlations over most of the nozzle operating range.

5.4 IMPROVED AIRCRAFT DESIGNS

- The narrow-spaced X-1 configuration was improved by replacing the vertical wedge interfairing with a horizontal wedge interfairing of equal length and by optimizing the nozzle internal flow expansion. The resultant Y-1 configuration had a lower aft-end drag, especially at subsonic speeds, slightly better thrust, and required 8 pounds less fuel than the X-1 configuration.
- The intermediate-spaced X-2 configuration was improved by increasing the aft-end length, and reducing the maximum cross-sectional area and nozzle spacing, so that the aircraft volume would remain unchanged. The resultant Y-2 configuration had lower aft-end drag, especially at supersonic speeds, approximately the same thrust, and required 112 pounds less fuel than the X-2 configuration.
- The wide-spaced X-3 configuration was improved by replacing the twin vertical stabilizers with a single vertical stabilizer, reducing the fuselage area between the nozzles, and optimizing the nozzle internal flow expansion. The resultant Y-3 configuration had significantly lower drag, slightly better thrust, and required 186 pounds more fuel than the X-3 configuration.
- The X-4 configuration with the convergent flap nozzle installed performed well only for the subsonic missions, and the X-5 configuration with the convergent-divergent ejector nozzle installed performed well only for the supersonic mission. The Y-1 configuration with the convergent-divergent nozzle installed was not superior to either the X-4 or X-5 configurations. For mixed mission operation, however,

the Y-1 configuration would be an improvement over either the X-4 or the X-5 configuration.

- The mission radii for the Z-1 turbojet installation and Y-1 turbofan installation were nearly the same for the supersonic mission. For the subsonic missions, the Z-1 configuration was clearly inferior to the Y-1 configuration due to the inefficiency of the turbojet cycle at part dry power settings.

REFERENCE LIST

1. Lockheed-California Company, "Program for Experimental and Analytical Determination of Integrated Airframe-Nozzle Performance, Phase I Interim Report, Volume I," 18 December 1970.
2. Lockheed-California Company, "Program for Experimental and Analytical Determination of Integrated Airframe-Nozzle Performance," Phase II Interim Report, February 1972.
3. Arnold Engineering Development Center, "Test Facilities Handbook, Eighth Edition," December 1969.
4. Maslowe, S. A. and Benson, J. L., "Computer Program for the Design and Analysis of Hypersonic Inlets," Lockheed Report LR 18079, 1964.
5. Glasgow, E. R. and Fox, R. A. "Development of a Computer Program for Subsonic and Transonic Boattail Drag of Isolated Nozzle Aftbodies," Lockheed Report 23361, 1970.
6. "Design and Strength Requirements for Wind Tunnel Models," ARO, Inc. Propulsion Wind Tunnel Facility, November 1969.
7. Pratt & Whitney Aircraft, "Experimental and Analytical Determination of Integrated Airframe-Nozzle Performance, Phase I Summary Report," Pratt & Whitney Aircraft Support Program, PWA-4065, 15 November 1970.
8. Herbert, M. V., Goleworth, G. T., and Herd, R. J., "The Performance of a Center Body Propelling Nozzle with a Parallel Shroud in External Flow, Part II," Rep. N.G.T.E., M.384 Minister of Aviation, Great Britain, 1964.
9. Brenahan, D. L. and Jones, A. L., "Cold Flow Investigation of a Low Angle Turbojet Plug Nozzle with Fixed Throat and Translating Shroud at Mach Numbers from 0 to 2.0," NASA TM X-1619.
10. Lockheed-California Company, "Phase I Test Plan of Program for Experimental and Analytical Determination of Integrated Airframe-Nozzle Performance," LR 23564, Revision No. 1, 24 April 1970.
11. Smith, R. E. Jr., and Matz, R. J., "Verification of a Theoretical Method of Determining Discharge Coefficients for Venturis Operating at Critical Flow Conditions," AEDC-TR-61-8, September 1961.
12. Sivells, J. C. and Payne, R. G., "A Method of Calculating Turbulent Boundary-Layer Growth at Hypersonic Mach Numbers," AEDC TR-59-3, 1959.
13. Sommer, S. C. and Short, B. J., "Free-Flight Measurements of Turbulent-Boundary-Layer Skin Friction in the Presence of Severe Aerodynamic Heating at Mach Numbers from 2.8 to 7.0," NACA TN 3391, 1955.

14. Miller, L. D., "Predicting Compressible Turbulent Boundary Layers with Strong Pressure Gradient," Lockheed Report 20701, 1967.
15. Shapiro, A. H., "The Dynamics and Thermodynamics of Compressible Fluid Flow," Volumes I and II, Ronald Press Co., New York, 1954.
16. Schlichting, H., "Boundary Layer Theory," McGraw-Hill, 1960.
17. Shrewsbury, G. D., "Effect of Boattail Juncture Shape on Pressure Drag Coefficients of Isolated Afterbodies," NASA TM X-1517, September 1967.
18. "Users Manual for the External Drag and Internal Nozzle Performance Deck-Transonic/External Flow Analysis," (Deck XI) (applicable to Deck V), Pratt & Whitney Aircraft Report FWA-3465, Supplement F, Part II, 1968.
19. Oswatitsch, K., "Die Geschwindigkeitsverteilung an symmetrischen Prifilen beim Auftreten lokaler Uverschallgebiete, Acta Physica Austriaca, Bd. 4, Nr. 2/3, pp. 228-271, December 1950.
20. Oswatitsch, K., "Die Geschwindigkeitsverteilung an symmetrischen Prifilen beim Auftreten lokaler Uverschallgebiete, Acta Physica Austriaca, Bd. 4, Nr. 2/3, pp. 228-271, December 1950.
21. Spreiter, J. R. and Alksne, Alberta, "Theoretical Prediction of Pressure Distributions on Nonlifting Airfoils at High Subsonic Speeds," NACA Rep. 1217, 1955 (supersedes NACA TM 3096).
22. Spreiter, J. R., Alksne, Alberta Y., and Myett, V. Jeanne, "Theoretical Pressure Distributions for Several Related Nonlifting Airfoils at High Subsonic Speeds," NACA TN 4148, 1958.
23. Crown, J. C., "Calculation of Transonic Flow Over Thick Airfoils by Integral Methods," AIAA Journal, Volume 6, pp. 413-423, March 1968.
24. Crown, J. C., "Calculation of Transonic Flow over Bodies of Revolution by an Integral Method," Pratt & Whitney Aircraft Report, August 1967.
25. Spreiter, J. R., and Alksne, Alberta Y., "Slender Body Theory Based on Approximate Solution of the Transonic Flow Equation," NASA Report 2, 1959.
26. Spreiter, J. R. and Alksne, Alberta Y., "Thin Airfoil Theory Based on Approximate Solution of the Transonic Flow Equation," NACA Rep. 1359, 1958 (supersedes NACA TN 3970)
27. Spreiter, J. R. and Alksne, Alberta Y., "Aerodynamics of Wings and Bodies at Mach Number One," Proceedings of the ASME Third U. S. National Congress of Applied Mechanics, 1958.

28. Goebel, T. P. and Divita, J. S. "Analytical Investigation of Aircraft Exhaust Nozzle Performance," NA 69-140-11, North American Rockwell, Los Angeles Division, January 1970 (Rought Draft for Air Force Contract F33615-69-C-1376).
29. Godunov, S. K., Zabrodyn, A. W., and Prokopov, G. P., "A Difference Scheme for Two-Dimensional Unsteady Problems of Gas Dynamics and Computation of Flow with a Detached Shock Wave," Zhurnal Vychyslitelnois Matematiki i Matematicheskoi Fiziki, Vol. I, No. 6, p. 1020 (Nov., - Dec. 1961) (also available as a Cornell Aeronautical Lab. Translation).
30. Presz, W. Jr., Konarski, M., and Grund, E., "Prediction of Installed Nozzle Flow Field," Paper 70-700 presented at the AIAA 6th Propulsion Joint Specialist Conference, June 18, 1970, San Diego, Calif.
31. Drougge, G., "Some Measurements on Bodies of Revolution at Transonic Speeds," Ninth International Congress of Applied Mechanics, University of Brussels, 1957, pp. 70-77.
32. Bonner, E. and Nixon, J. A., "Wind Tunnel Testing Techniques for Integrated Airframe-Exhaust Nozzle Systems," AFFDL-TR-68-94, July 1968.
33. Brazzel, C. E. and Henderson, J. H., "An Empirical Technique for Estimating Power-on Base Drag of Bodies of Revolution with a Single Jet Exhaust," AGARD Conference Proceedings, No. 10, Sept. 1966.
34. Spreiter, J. R., "On the Application of Transonic Similarity Rules to Wings of Finite Span," NACA Report 1153, 1953
35. "Users Manual for the External Drag and Internal Nozzle Performance Deck-Supersonic Flow Analysis," (Deck XI), Pratt & Whitney Aircraft Report PWA-3465, Supplement F, Part I, 1968.
36. Weingold, H. D. and Zupnik, T. F. "The ICRPG Turbulent Boundary Layer Reference Program, prepared by Pratt & Whitney and available from Dynamic Science, Monrovia, Calif., July 1968.
37. Wazzan, A. R. and Ball, W. H., "Body Shape Effects on Skin Friction in Supersonic Flows," AIAA Journal, pp. 1770-1772, Sept. 1965.
38. Cohen, N. B., "Boundary-Layer Similar Solutions and Correlation Equations for Laminar Heat Transfer Distribution in Equilibrium Air at Velocities up to 41,000 Feet Per Second," NASA TR R-118, 1961.
39. Prozan, R. J., "Development of a Method of Characteristics Solution for Supersonic Flow of an Ideal, Frozen, or Equilibrium Reacting Gas Mixture," IMSC/HREC A782535, 1966.

40. Wehofer, S. and Moger, W. C., "Transonic Flow in Conical Convergent and Convergent-Divergent Nozzles with Nonuniform Inlet Conditions," AIAA Paper No. 70-635, June 1970.
41. Pratt & Whitney Aircraft, "Experimental and Analytical Determination of Integrated Airframe-Nozzle Performance, Phase III Summary Report," Pratt & Whitney Aircraft Support Program, PWA-4503, July 1972.
42. Addy, A. L., "On the Steady State and Transient Operating Characteristics of Long Cylindrical Shroud Supersonic Ejectors," Ph.D Thesis, University of Illinois, 1963.
43. Chow, W. L. and Addy, A. L., "Interaction Between Primary and Secondary Streams of Supersonic Ejector Systems and Their Performance Characteristics," AIAA Jour., Vol. 2, No. 4.
44. "Overall Ejector Performance Calculation Deck," Pratt & Whitney Aircraft Report PWA-2888, Supplement A.
45. Bernstein, A., Heiser, W. H., and Hevenor, C., "Compound-Compressible Nozzle Flow," Jour. of Applied Mech., Paper No. 67-APM-L.
46. Weber, H. E. "Ejector-Nozzle Flow and Thrust," Trans. of the ASME, March 1960, p. 120.
47. Henson, J. R. and Robertson, J. E., "Methods of Approximating Inviscid Jet Boundaries for Highly Underexpanded Supersonic Nozzles," AEDC TDR-62-7, 1962.
48. Adamson, T. C., Jr. and Nicholls, J. A., "On the Structure of Jets from Highly Underexpanded Nozzles into Still Air," J. Aero. Sci., Vol. 26, No. 1, pp. 16-24, January 1959.
49. Love, E. S., Grigsby, C. E., Lee, L. P., and Woodling, M. J., "Experimental and Theoretical Studies of Axisymmetric Free Jets," NASA TR R-6, 1959.
50. Butler, H. W., "Users Manual, Description of a Digital Computer Program for Nozzle and Plume Analysis by the Method of Characteristics," TM 54/20-108, IMSC/HREC A783573, IMSC, Huntsville Research Park, Alabama, 11 Dec. 1966.
51. Cubbage, J. M. Jr., "Jet Effects on Base and Afterbody Pressures of a Cylindrical Afterbody at Transonic Speeds," NACA RM L56C21, May, 1956.
52. Cubbage, J. M., Jr., "Jet Effects on the Drag of Conical Afterbodies for Mach Numbers of 0.6 to 1.28," NACA RM L57B21, April 1957,

53. McDonald, H. and Hughes, P. F., "A Correlation of High Subsonic Afterbody Drag in the Presence of a Propulsive Jet or Support Sting," Journal of Aircraft, Vol. 2, No. 3, pp. 202-207, May-June, 1965.
54. Korst, H. H., Chow, W. L. and Zumwalt, G. W., "Research on Transonic and Supersonic Flow of a Real Fluid at Abrupt Increases in Cross-Section," University of Illinois ME Tech. Report 392-5, Dec. 1959.
55. Korst, H. H. and W. L. Chow, "Nonisoenergetic Turbulent ($P_r = 1$) Jet Mixing Between Two Compressible Streams at Constant Pressure," NASA CR-419, April 1966.
56. Baughman, L. E. and Kochendorfer, F. D., "Jet Effects on Base Pressures of Conical Afterbodies at Mach 1.91 and 3.12," NACA RME 57E06, August 1957.
57.

77A-587 002
58. Glasgow, E. R., "Program for Experimental and Analytical Determination of Integrated Airframe-Nozzle Performance," R&D Contract Status Report No. 5, LR 23150-5, April 1970.
59. "USAF Stability and Control DATCOM," prepared by McDonnell Douglas Corporation under contract to the U. S. Air Force, Project No. 8219, Task No. 821902, Section 4.1.5.1, Revised Edition, Aug., 1968
60. De Young, J., Theoretical Symmetric Span Loading due to Flap Deflection for Wings of Arbitrary Plan Form at Subsonic Speeds, NACA TR 1071, 1952.
61. De Young, J., and Harper, C. W., Theoretical Symmetric Span Loading at Subsonic Speeds for Wings Having Arbitrary Plan Form, NACA TR 921, 1948.
62. Silverstein, A., and Katzoff, S., Design Charts for Predicting Downwash Angles and Wake Characteristics Behind Plain and Flapped Wings, NACA TR 648, 1940.
63. Fischel, J., and Ivey, Margaret F., Collection of Test Data for Lateral Control with Full-Span Flaps, NACA TN 1404, April, 1948.
64. Dods, J. B. Jr., and Tinling, B. E., Summary of Results of a Wind-Tunnel Investigation of Nine Related Horizontal Tails, NACA TN 3497, July, 1955.
65. Conference on Aircraft Aerodynamics, NASA SP-124, May, 1966.
66. Weil, J., Campbell, G. S., and Diederich, M. S., An Analysis of Estimated and Experimental Transonic Downwash Characteristics as Affected by Plan Form and Thickness for Wing and Wing-Fuselage Configurations, NACA TN 3628, April, 1956.

67. Van Driest, E. R. and Blumer, C. B., "Boundary-Layer Transition at Supersonic Speeds - Three-Dimensional Roughness Effects (SPHERES)," J. Aero. Sci., Volume 29, No. 8, Aug. 1962, p. 909
68. Braslow, A. L. and Knox, E. C., "Simplified Method for Determination of Critical Height of Distributed Roughness Particles for Boundary Layer Transition at Mach Numbers from 0 to 5," NACA TN 4363, 1958.
69. Glasgow, E. R., "Phase II Test Plan of Program for Experimental and Analytical Determination of Integrated Airframe-Nozzle Performance, LR 24427, March 1971.
70. Hill, D. K., Phase II Off-Site Data Reduction Program of Program for Experimental and Analytical Determination of Integrated Airframe-Nozzle Performance, LR 25182, February 1972.
71. H. Ashley and M. T. Landahl, Aerodynamics of Wings and Bodies, Addison-Wesley Publishing Company, Inc. 1965.
72. D. Migdal, E. H. Miller, and W. C. Schnell, "An Experimental Evaluation of Exhaust Nozzle/Airframe Interference," AIAA Paper No. 69-430
73. Berrier, B. L. and Wood, F. H. Jr., "Effect of Jet Velocity and Axial Location of Nozzle Exit on the Performance of a Twin-Jet Afterbody Model at Mach Numbers up to 2.2," NASA TN D-5393, Sept. 1969.
74. Hess, J. L. and Smith, A.M.O., Calculation of Non-Lifting Potential Flow About Arbitrary Three-Dimensional Bodies. Douglas Report E.S. 40622, 15 March 1962.
75. W. Presz, M. Konarski, and E. Grund, "Prediction of Installed Nozzle Flow Fields, AIAA 70-7000," AIAA Sixth Propulsion Joint Specialist Conference, June 15, 1970.
76. Lockheed-California Company, "Program for Experimental and Analytical Determination of Integrated Airframe-Nozzle Performance," Volume II of LR 25370, 31 July 1972.
77. Baxendale, M. L., Bruckman, F. A., and Shaar, R. H., Wave Drag Computer Program, Lockheed Report 20553, March 1967.
78. Maiden, D. L. and Runckel, J. F., "Effect of Nozzle Lateral Spacing on Afterbody Drag and Performance of Twin-Jet Afterbody Models with Convergent Nozzles at Mach Numbers up to 2.2," NASA TM-X 2099, 1970.
79. Korst, H. H., Page, R. H., and Childs, M. E., "A Theory for Base Pressures in Transonic and Supersonic Flow," University of Illinois, M. E. Tech. Note 392-2, March 1955.

80. Anon, "USAF Stability and Control Datcom," Air Force Flight Dynamics Lab, Wright-Patterson Air Force Base, Oct. 1960 (rev. Aug. 1968)
81. Lockheed Aircraft Corp. Report LR 9000A, Lockheed Aerodynamics Handbook-Performance.
82. Stoney, William E., Jr., "Collection of Zero-Lift Drag Data on Bodies of Revolution from Free-Flight Investigations," NASA TR-R-100, 1961
83. Linden, J. E. and O'Brimski, F. J., "Some Procedures for Use in Performance Prediction of Proposed Aircraft Designs," The Society of Automotive Engineers Paper 650800, 1965.
84. Hoerner, Sighard F., "Fluid-Dynamic Drag," Pub. by the author, 1965.
85. Fradenburgh, E., and Wyatt, D., "Theoretical Performance Characteristics of Sharp-Lip Inlets at Subsonic Speeds," NACA Report 1193, 1954.
86. Muller, G. and Gasko, W., "Subsonic-Transonic Drag of Supersonic Inlets," Pratt & Whitney Aircraft TDM-1973, 1966.
87. Sibulkin, J., "Theoretical and Experimental Investigation of Additive Drag," NACA Report 1187
88.

8C

... ..red
89. Lockheed-California Company, "Program for Experimental and Analytical Determination of Integrated Airframe - Nozzle Performance", Volume I of LR 25370, 31 July 1972.

Unclassified

Security Classification

DOCUMENT CONTROL DATA - R & D

Security classification of title body of abstract and indexing annotation must be entered when the overall report is classified

1. ORIGINATING ACTIVITY (Corporate author) Lockheed-California Company P. O. Box 551 Burbank, California 91503		2a. REPORT SECURITY CLASSIFICATION Unclassified	
		2b. GROUP	
3. REPORT TITLE Experimental and Analytical Determination of Integrated Airframe Nozzle Performance			
4. DESCRIPTIVE NOTES (Type of report and inclusive dates) Final Report 1 November 1969 to 31 July 1972			
5. AUTHOR(S) (First name, middle initial, last name) Edsel R. Glasgow, Don M. Santman, Leonard D. Miller, et.al.			
6. REPORT DATE October 1972		7a. TOTAL NO OF PAGES 325	7b. NO OF REFS 89
8a. CONTRACT OR GRANT NO F33657-70-C-0511		9a. ORIGINATOR'S REPORT NUMBER(S) LR 25370	
b. PROJECT NO			
c.		9b. OTHER REPORT NO(S) (Any other numbers that may be assigned this report)	
d.			
10. DISTRIBUTION STATEMENT Distribution limited to U.S. Government agencies only; test and evaluation; statement applied October 1972. Other requests for this document must be referred to AF Flight Dynamics Laboratory, (FXM), Wright-Patterson AFB, Ohio 45433.			
11. SUPPLEMENTARY NOTES		12. SPONSORING MILITARY ACTIVITY Flight Dynamics Laboratory Air Force Systems Command Wright-Patterson Air Force Base, Ohio	
13. ABSTRACT An experimental and analytical investigation of the installed thrust and drag of various isolated nozzle and twin-nozzle/aftbody configurations indicated that empirical correlations provide the best means of predicting aft-end performance, especially for the early stages of the aircraft design. Both subsonic and transonic isolated nozzle drag data were correlated using IMS (integral mean slope) as the geometric parameter. A correlation of twin-nozzle/aftbody drag data at subsonic and transonic speeds was developed by combining Spreiter's transonic similarity parameters with the IMS of the equivalent body of revolution. A correlation of inviscid MOC pressure drag, achieved through use of IMS combined with similarity parameters obtained from linearized supersonic flow theory, provided an accurate and rapid means of estimating drag for arbitrary axisymmetric boattail contours at supersonic speeds. Twin-nozzle/aftbody drag data at supersonic speeds was correlated with the equivalent body drag obtained from the axisymmetric MOC correlation. Improved thrust and drag performance was obtained by modifying the aft-end design of five selected aircraft configurations. The rationale for these modifications was derived from design guidelines and criteria developed during the program. Improvements in mission radius for a fixed takeoff gross weight aircraft were obtained, in general, by utilizing convergent-divergent nozzles, a horizontal wedge interfairing with the trailing edge terminating at the exit plane of the nozzles, a single vertical stabilizer, and a narrow lateral nozzle spacing.			

KEY WORDS	LINK A		LINK B		LINK C	
	ROLE	WT	ROLE	WT	ROLE	WT
Airframe-Nozzle Integration						
Air Superiority Fighter Having Twin Buried Engines and Dual Nozzles.						
Installed Nozzle Performance						
Nozzle Thrust Coefficient						
Nozzle Discharge Coefficient						
Aft-End Boattail Drag						
Twin-Nozzle/Aftbody Drag						
Design Criteria and Guidelines						
Turbojet/Turbofan						